

# 3D Ultrasound Guidance System for Pedicle Screw Insertion in Scoliosis Surgery

by

Andrew Yuen-Hong Chan

A thesis submitted in partial fulfillment of the requirements for the degree of

Doctor of Philosophy

Department of Biomedical Engineering  
University of Alberta

© Andrew Yuen-Hong Chan, 2020

## Abstract

This thesis describes the research and development process in creating a 3D ultrasound-based navigation system to assist screw insertion for scoliosis surgery, with a focus on children who have adolescent idiopathic scoliosis (AIS). Screw placement accuracy is critical to prevent spinal cord or other neurologic injury in spine surgery. Traditional image guidance can reduce pedicle breach rates in posterior fusion surgery for AIS, but at the expense of added ionizing radiation to patients and staff, prolonged surgeries and hindrances to surgical workflow.

A new image guidance system was developed by combining motion capture cameras, conventional medical ultrasound, and image registration to display navigation information in a three-dimensional virtual environment. In this system, motion capture markers are mounted onto the medical ultrasound transducer to pair 2D images with motion capture information, allowing for a 3D reconstruction of the vertebral surface. A pre-operative 3D model of the vertebra is then image registered to the 3D ultrasound vertebral surface to localize the vertebra in the operating room. The vertebra is then display on a screen, alongside motion captured surgical tools to allow surgeons to have visual feedback on the entry-point and trajectory of their screw placements.

The system was evaluated for accuracy and speed in four stages: motion capture was evaluated first, followed by 3D ultrasound localization accuracy. The image registration speed and accuracy were then evaluated, and lastly the screw placement accuracy was evaluated. This research focused on using 3D-printed ultrasound phantoms to evaluate accuracies, alongside a pilot study on porcine spines.

The accuracy of the motion capture cameras was evaluated, with translational accuracies of 0.25mm for translations within 15mm and rotational accuracies within  $3.7^\circ$  for rotations within  $60^\circ$ . The accuracy of 3D ultrasound in localizing landmarks was found to be  $0.8\pm 0.6$ mm, while using a motion capture probe to

localize landmarks on the phantom found a positional error of  $1.1\pm 1.1\text{mm}$  and rotational error of  $0.0\pm 1.7^\circ$ . The accuracy of the image registration algorithm was  $0.3\pm 0.2\text{mm}$  and  $0.9\pm 0.8^\circ$ , while the surgical localization accuracy was  $1.2\pm 0.5\text{mm}$  and  $2.2\pm 2.0^\circ$ . A qualitative study on a porcine spine showed that image registration was successful for 91% of the porcine registrations.

Lastly, the navigation accuracy of the system was tested using a live motion capture probe, which found a final entry-point and trajectory errors of  $0.5\pm 0.3\text{mm}$  and  $2.0\pm 0.8^\circ$ , with 95.6% of screw placements meeting an entry-point target accuracy of 1mm, and all screw placements meeting a trajectory target of  $5^\circ$ . The average processing time was  $8.9\pm 1.4\text{s}$ .

This system has the speed and accuracy for usage in spine surgery. However, further evaluation needs to be completed before clinical evaluation. First, improvements to the user interface and integration into surgical workflow needs to be tested. Second, the most appropriate pre-operative imaging for the system needs to be selected, whether it is X-rays, computed tomography or magnetic resonance imaging. Lastly, quantitative evaluation of the ultrasound system on soft tissues including porcine spines or cadaver spines, needs to be completed.

## Preface

This thesis is an original work by Andrew Yuen-Hong Chan. The porcine spine study received research ethics approval from the Research Ethics Office under the “Exceptions to ACUC Review” as it was considered as a Category “A” study (little to no animal manipulation) and thus no formal Animal Care and Use Committee approval was necessary for this project. (REO Reference Number: 2019.006 Chan).

Some of the research in this thesis is formed from collaborative work with various co-authors.

Chapter 3 is a modified version of two published papers:

- Chan A, Parent E, Narvacan K, San C, Lou E (2017) Intraoperative Image Guidance and Navigation in Adolescent Idiopathic Scoliosis Posterior Surgery: A Systematic Review on Screw-Related Complications and Breach Rates. *Spine J* 17(9): 1215-1229
- Chan A, Parent E, Wong J, Narvacan K, San C, Lou E (2019) Does Intraoperative Imaging Decrease Pedicle Screw-related Complications in Surgical Treatment of Adolescent Idiopathic Scoliosis: A Systematic Review Update and Meta-Analysis. *Eur Spine J* – E-published Nov 28, 2019

I conceived of the direction, performed screenings, extractions, quality appraisals, and compiled the data into the journal article. I collaborated with many reviewers to perform these tasks. Screening co-reviewers included Huda Mohamed, Michael Ryu, Arjan Ahluwalia, Muhammad Moolla and Suzana Trac. Jason Wong, Cindy San and Karl Narvacan were co-reviewers for extraction and quality appraisal for both reviews. There was also consultation with the scoliosis research group team for clinical advice and guidance: Dr. Marc Moreau, Dr. Jim Mahood, Sarah Southon and Kathleen Shearer. I consulted Liz Dennett, a medical librarian for constructing the search, and Ben Vandermeer for help with meta-analysis. Direction and guidance were provided by Dr. Parent, and Dr. Lou reviewed this article.

Chapter 4 is a modified version of a published paper:

- Chan A, Aguillon J, Hill D, Lou E (2017) Precision and Accuracy of Motion Tracking System for Pedicle Screw Placement in Adolescent Idiopathic Scoliosis. *Med Eng Phys* 46:33-43

I conceived of the experiments, collected data for auxiliary and dynamic testing, and compiled the journal article. Janelle Aguillon conducted some of the initial motion capture setup and data collection for static testing and auxiliary testing. Advice and guidance were provided by Doug Hill and Dr. Lou.

Chapter 5 is a modified version of two published papers:

- Chan A, Parent E, Lou E (2018) Reconstruction and positional accuracy of 3D ultrasound on vertebral phantoms for adolescent idiopathic scoliosis spinal surgery. *Int J Comput Assist Radiol Surg.* 14(3): 427-439
- Ottacher D, Chan A, Parent E, Lou E (2020) Positional and Orientational Accuracy of 3D Ultrasound Navigation System on Spinal Phantoms for Scoliosis Surgery. *IEEE: Trans Instr. and Meas.* doi:10.1109/TIM.2020.2973839, [Epub ahead of print], 2020.

For the first article, I conceived of the experiments, designed the phantoms and setup, collected the data, and compiled it into a journal article. For the second, I conceived of the experiments, designed the phantoms and setup, and provided guidance on the journal article writeup. Drake Ottacher collected and analyzed the data and compiled draft for the publication. Advice and guidance were provided by Dr. Parent and Dr. Lou.

The material in Chapter 6 has been submitted for publication and requested revision at this time.

- Chan A, Parent E, Lou E: Image Registration of CT Images of Phantom Vertebrae on 3D Ultrasound Images of the Vertebral Surfaces for Posterior Spine Surgery. Accepted in the ***Annals of Biomedical Engineering***, 2020.

I conceived of the experiments, developed the registration algorithms and analyzed the data in this experiment. Brendan Coutts helped with researching surface-based registration methods, implementing the method on a pilot set of data, and providing registration evaluations. Advice and guidance were provided by Dr. Parent and Dr. Lou.

## Dedication

*We conclude that God is known first through Nature, and then again, more particularly, by doctrine; by nature in His works, and by doctrine in His revealed word.* – Galileo Galilei, 1615 - quoting Tertullian

## Acknowledgements

First of all, thank you to my funders including the Natural Sciences and Engineering Research Council, the Faculty of Medicine and Dentistry, the Faculty of Graduate Studies and Research Alberta Innovates, TD, and the Women and Children's Health Research Institute. I could not conduct this research without their generous support, including for conference travel.

To all the other students of the Lou lab, thank you for all your help and for bringing much vibrancy and life to our lab. To Nitya, Tehzeeb, Amber, Sophia, Reegan, Payal, Liam, Mitchell, Ayushi, Andrew, Ugo, Carmen, Solvin, Brett and Kieran, it was a pleasure working with you all. To my colleagues Vivian, Henry, Johnny and Kai-Ernn, thank you for all the good memories.

Special thanks to the students who worked under me, who put up with my dry humor, my weekly literature review sessions and my constant requests for more: Janelle Aguillon for being the first to start up the motion capture cameras and conduct the days-long static recording experiments; Drake Ottacher for your dedication in working after hours to put together the 3D ultrasound paper; and Brendan Coutts for being an excellent 'electrical engineer', finding new algorithms and coding new approaches.

Thank you, to the staff at the Glenrose Rehabilitation Hospital Research Center at the "old red brick building". To Doug, Jim, Gary, Darryl and Justin, thank you all for your wisdom and support for the past 15 years. Thank you Raylene and Mike for all the interesting conversations and encouragements.

My fellow graduate students. Thank you Rachel Zheng, Quang Vo, Ahmed Badr and Steffen Adria, my predecessors and inspirations to bring this PhD to completion. Mahdiah Khodaei, my fellow systematic reviewer and ultrasound student, for all the bubble tea and empathy in finishing this thesis. Jason Wong, my foosball rival, my Splatoon and desk buddy and fellow tsundere, thank you for making it so that I can look forward to every workday. Lastly, Kenwick Ng, my brother-in-Christ, my fellow Europe traveler and sojourner, 3D printing maintenance man and friend. We made it! I finish this thesis with satisfaction at the completion of this endeavor, but also sadness that we will now be parting ways.

Thank you Dr. Le, who got me started in biomedical engineering in high school. I would not be here without your enthusiasm and support. Thank you, Dr. Parent, for believing in me from the start of the systematic review, always being available for a meeting, providing laser-fast turnarounds on my abstracts and articles, and for spending the time to mentor me.

Thank you, Dr. Lou, for giving me the chance to learn, to mentor, to travel and to grow in my research ability. Thank you for your constant encouragement, for putting your trust in me, and for your countless hours of work in pushing my career forward. It has been an honour and a blessing to work at the Edmonton Scoliosis Lab.

I would like to thank my family. All the meals and hours of childcare from mom and the Wai family that kept our family running. For my wife, Cindy for bringing home the bread and being a constant encouragement through all the conferences, papers, and deadlines; and for Tobias for always reminding me of the awe and joy of being alive; to know and to be known.

Finally, and most importantly, I give thanks to God to whom belongs all praise. To the Creator God, sovereign over all things, to Christ my Savior and Lord, and to the Holy Spirit my guide and Helper be all power, authority and glory.



## Table of Contents

Abstract.....	ii
Preface .....	iv
Dedication.....	vi
Acknowledgements.....	vii
Table of Contents.....	ix
List of Tables .....	xvii
List of Figures .....	xix
List of Equations.....	xxvii
List of Abbreviations and Nomenclature .....	xxviii
Chapter 1: Introduction .....	1
1.1. Motivation.....	1
1.2. Problem Statement.....	1
1.2.1. System Requirements .....	2
1.2.2. Scope of Work.....	2
1.3. Thesis Organization.....	3
1.3.1. Thesis Outline.....	3
Chapter 2: Background Information .....	4
2.1. Overview .....	4
2.2. Clinical Background.....	4
2.2.1. Spinal Anatomy .....	4
2.2.2. Types of Scoliosis .....	7
2.2.3. Adolescent Idiopathic Scoliosis.....	7
2.2.4. Surgical Treatment.....	10
2.2.5. Free-Hand Pedicle Screw Insertion Methods .....	14
2.2.6. Image Guidance Methods.....	16
2.2.7. Breach Rates and Complications.....	17
2.2.8. Free-hand vs Image Guidance Comparison .....	18
2.2.9. Non-Ionizing Technologies to Improve Pedicle Screw Insertion Safety.....	19

2.3.	Technical Background for Image Guidance for Scoliosis Surgery .....	20
2.3.1.	Motion Capture Hardware .....	21
2.3.2.	3D Position and Orientation Mathematics .....	22
2.3.3.	Motion Capture Accuracy .....	25
2.3.4.	Ultrasound Physics .....	25
2.3.5.	3D Ultrasound .....	27
2.3.6.	3D Ultrasound Imaging Accuracy .....	29
2.3.7.	CT and MRI Tomographic Imaging .....	29
2.3.8.	Image Processing .....	30
2.3.9.	Volumetric Image Registration .....	32
2.3.10.	Surface Image Registration .....	35
2.3.11.	Image Registration Speed and Accuracy .....	35
2.3.12.	3D Environment Display .....	36
2.4.	Section 2.4: Conclusion .....	37
Chapter 3: Systematic Review and Meta-Analysis of Image Guidance in Pedicle Screw Insertion' .....		38
3.1.	Overview .....	38
3.2.	Objectives.....	39
3.3.	Methods.....	39
3.3.1.	Search Strategy .....	39
3.3.2.	Study Screening.....	40
3.3.3.	Study Extraction and Quality Appraisal .....	42
3.3.4.	Inter-Rater Reliability Assessment.....	43
3.3.5.	Summary Tables.....	43
3.3.6.	Meta-Analysis.....	43
3.3.7.	Summary Statements.....	44
3.4.	Results.....	44
3.4.1.	Article Screening and Extraction .....	44

3.4.2.	Study Characteristics.....	47
3.4.3.	Quality Assessments .....	54
3.4.4.	Breaches and Complications .....	55
3.4.5.	Meta-Analysis.....	63
3.4.6.	Summary Statements.....	68
3.5.	Discussion.....	70
3.5.1.	Review Update Improvements .....	70
3.5.2.	Population Applicability .....	72
3.5.3.	Key Findings .....	72
3.5.4.	Study Quality Assessment.....	74
3.5.5.	Limitations on Findings .....	74
3.5.6.	Recommendations on Future Study Reporting .....	75
3.6.	Conclusion.....	75
Chapter 4: Evaluation of Accuracy and Precision of Motion Capture Cameras .....		77
4.1.	Summary .....	77
4.2.	System Setup.....	77
4.2.1.	Motion Capture Camera Setup .....	77
4.2.2.	Motion Capture Camera Calibration.....	78
4.2.3.	Operating Room Compatibility .....	79
4.3.	Static Testing.....	82
4.3.1.	Static Testing Methodology .....	82
4.3.2.	Static Testing Findings.....	83
4.4.	Auxiliary Testing.....	84
4.4.1.	Statistical Methodology for Motion Capture Evaluation .....	84
4.4.2.	Markers, Rigid Body and Calibration Wand Evaluation .....	85
4.4.3.	Camera Configuration Evaluation .....	87
4.4.4.	Auxiliary Evaluation Summary .....	90

4.4.5.	Navigation Camera Frame Setup .....	90
4.5.	Displacement Testing.....	91
4.5.1.	Displacement Testing Methodology .....	91
4.5.2.	Dynamic Testing Results .....	93
4.5.3.	Pegboard Pilot Test .....	95
4.6.	Clinical Relevance.....	95
4.6.1.	Phantom Studies on Motion Capture Accuracy.....	95
4.6.2.	In-Vivo Navigation Accuracy .....	96
4.7.	Conclusion.....	97
Chapter 5: Development of 3D Ultrasound for Surface Reconstruction and Positioning of Vertebrae <sup>5</sup> ...		98
5.1.	Summary .....	98
5.2.	System Setup.....	99
5.2.1.	Motion Capture Setup .....	99
5.2.2.	Ultrasound Settings.....	99
5.2.3.	Preliminary Streaming Testing .....	102
5.3.	Software Development for 3D Ultrasound Reconstruction.....	102
5.3.1.	3D Ultrasound Reconstruction Schematic .....	102
5.3.2.	Data Acquisition Graphical User Interface.....	103
5.3.3.	Image Filtering Evaluation .....	104
5.3.4.	Ultrasound Volume Reconstruction.....	107
5.4.	Calibration of 3D Ultrasound .....	108
5.4.1.	Temporal Calibration .....	108
5.4.2.	Spatial Calibration .....	111
5.4.3.	Filter Calibration.....	114
5.5.	Reconstruction of Vertebral Phantoms .....	116
5.5.1.	Phantom Modeling and Experimental Design .....	116
5.5.2.	Linear and Angular Reconstruction Results .....	118

5.5.3.	Vertebrae-Like Reconstruction Results.....	119
5.5.4.	Reconstruction Accuracy Experiment Discussion .....	119
5.6.	Localization of Phantom Position and Orientation.....	121
5.6.1.	Localization Accuracy Experimental Design.....	121
5.6.2.	Localization Positional Accuracy Result .....	122
5.6.3.	Localization Orientation Accuracy Result .....	124
5.6.4.	Localization Sources of Error.....	125
5.7.	Vertebral Position and Orientation Experiments .....	126
5.7.1.	Capture Volume, Phantom Vertebra and Probe Design.....	126
5.7.2.	Experimental Design .....	129
5.7.3.	Individual Experiment Results.....	130
5.7.4.	Full Experiment Results.....	133
5.8.	Discussion on 3D Ultrasound Results.....	134
5.8.1.	Technical Comments.....	134
5.8.2.	Clinical Relevance.....	135
5.9.	Conclusion.....	136
Chapter 6: Image Registration of Intraoperative Ultrasound to Pre-operative 3D Imaging .....		137
6.1.	Summary .....	137
6.2.	Initial Registration Testing .....	137
6.2.1.	Phantom Volume Generation .....	137
6.2.2.	Pre-built Software Algorithms .....	138
6.2.3.	Registration Process.....	139
6.2.4.	Registration Evaluation Metrics.....	140
6.3.	Pre-Registration Development .....	141
6.3.1.	Pre-Registration Concepts .....	141
6.3.2.	Pre-Registration Robustness Testing .....	143
6.3.3.	CT Symmetry Pre-Registration .....	144

6.3.4.	3DUS Symmetry Pre-Registration .....	147
6.3.5.	Slope Pre-registration .....	148
6.3.6.	Centroid Pre-registration .....	149
6.3.7.	Ultrasound Scanning Variability.....	149
6.4.	Registration Development .....	150
6.4.1.	Conventional Registration Process .....	150
6.4.2.	Single Vertebra Registration Evaluation .....	151
6.4.3.	Multi-Vertebra Phantom Registration Evaluation .....	154
6.4.4.	Surgical Registration Evaluation.....	158
6.4.5.	Iterative Closest Point Evaluation .....	162
6.5.	Phantom Registration Discussion .....	166
6.5.1.	Technical Evaluation of Registration Experiments.....	166
6.5.2.	Clinical Comparison of Registration Experiments.....	167
6.6.	Porcine Spine Pilot Feasibility Study .....	168
6.6.1.	Experimental Setup.....	168
6.6.2.	Image Intensity Evaluation.....	169
6.6.3.	Pig Spine Registration Feasibility .....	173
6.6.4.	Pig Spine Registration Discussion.....	180
6.7.	Conclusion.....	182
Chapter 7:	Navigation .....	183
7.1.	Summary .....	183
7.2.	Navigation User-Interface Development .....	183
7.2.1.	Environment Selection.....	183
7.2.2.	Navigation Setup.....	184
7.2.3.	Vertebral Placement .....	186
7.2.4.	User Interface.....	187
7.3.	Navigation Calibration .....	188

7.3.1.	Motion Capture Probe Calibration.....	188
7.3.2.	Grid Accuracy Testing.....	189
7.3.3.	Motion Capture Live Accuracy Testing .....	191
7.3.4.	Repeatability of 3D Ultrasound.....	193
7.4.	Image Segmentation and Modeling.....	194
7.4.1.	Patient Screening .....	194
7.4.2.	MRI Segmentation .....	195
7.4.3.	CT Segmentation.....	196
7.5.	Navigation Pilot Study.....	198
7.5.1.	Navigation Pilot Study on Original Phantom .....	198
7.5.2.	Navigation Pilot Study on Large CT Spine Phantom.....	202
7.6.	Navigation Study.....	207
7.6.1.	Experimental Design .....	207
7.6.2.	Origin Experiment Results.....	210
7.6.3.	Corner Experiment Overall Errors.....	215
7.6.4.	Corner Experiment: Left vs Right Holes .....	215
7.6.5.	Corner Experiment: Errors vs Position (Cardinal Directions).....	216
7.6.6.	Corner Experiment: Errors vs Height .....	218
7.6.7.	Corner Experiment: Errors vs Orientation .....	219
7.6.8.	Corner Experiment: Errors vs Vertebral Level .....	221
7.6.9.	Discussion.....	224
7.7.	Surgeon Demonstration.....	226
7.7.1.	Demonstration Setup.....	226
7.7.2.	Surgeon Feedback.....	227
7.8.	Conclusion.....	228
Chapter 8 Conclusion.....		229
8.1.	Summary .....	229

8.2.	Summary of Thesis Work .....	229
8.2.1.	Current Status of the Navigation System.....	229
8.2.2.	Original Contributions.....	230
8.3.	Challenges and Future Works .....	231
8.3.1.	Hardware Improvements .....	231
8.3.2.	Software Improvements .....	232
8.3.3.	Clinical Considerations.....	233
8.3.4.	Technological Advancement.....	234
8.4.	Final Remarks.....	234
	References .....	235
	Figure References .....	249
	Appendix 1: Search Strategy .....	251
	Appendix 2: Quality Appraisals .....	255
	Appendix 3: Systematic Review List of Extracted Articles .....	261
	Appendix 4: Ultrasound Reconstruction Code.....	268
	Appendix 5: Image Pre-Registration Code .....	277
	Appendix 6: Image Registration Code.....	289
	Appendix 7: Navigation Code.....	307



## List of Tables

Table 2-1: Odds ratio of curve progression from common risk factors [49] .....	10
Table 2-2: Lenke classification of surgical curves .....	11
Table 2-3: Comparison of benefits and drawbacks of screw insertion techniques .....	17
Table 3-1: Study inclusion and exclusion criteria.....	41
Table 3-2: Extraction categories .....	42
Table 3-3: Levels of evidence .....	44
Table 3-4: Patient characteristics for head-to-head studies and image guidance studies .....	48
Table 3-5: Patient characteristics for all types of free-hand studies .....	49
Table 3-6: Surgical and imaging characteristics for head-to-head studies and image guidance studies ...	50
Table 3-7: Surgical and imaging characteristics for all types of free-hand studies .....	51
Table 3-8: Breach definitions from head-to-head and image guidance studies.....	53
Table 3-9: Breach definitions from all types of free-hand studies .....	54
Table 3-10: Breaches in head-to-head comparison studies .....	56
Table 3-11: Breaches in image guidance studies (CT-navigation and fluoroscopy) .....	57
Table 3-12: Breaches in free-hand methods for articles with unreported imaging and no imaging in surgery .....	58
Table 3-13: Breaches in free-hand methods for articles reporting screw placement with fluoroscopic confirmation or using 3D printed templates .....	59
Table 3-14: Complications in head-to-head studies .....	60
Table 3-15: Complications in image guidance (CT-navigation and fluoroscopy) and free-hand methods (unreported imaging).....	61
Table 3-16: Complications in free-hand methods (no imaging, fluoroscopic confirmation, 3D printed templates).....	62
Table 3-17: Summary statements .....	69
Table 4-1: Rotational variables tested in the motion capture system.....	92
Table 4-2: Displacement accuracy and standard deviation for pegboard .....	95
Table 5-1: Transformation matrix mean and standard deviation and ultrasound transducer surface position standard deviation .....	112
Table 5-2: Positional RMS accuracy and repeatability in X, Y and Z directions .....	122
Table 5-3: Orientation RMS accuracy and repeatability in X, Y and Z directions .....	124
Table 5-4: Full experiment positional and rotational accuracy .....	133

Table 6-1: List of orientations in degrees (pitch, yaw, roll) .....	145
Table 6-2: Success rate at different scaling values .....	146
Table 6-3: Pre-registration algorithm summary .....	148
Table 6-4: List of transformation sequences .....	150
Table 6-5: Processing time (s) for completing registration when varying inlier ratio and down-sampling grid size on T6 vertebra.....	163
Table 6-6: Mean-squared error for varying inlier ratio and down-sampling grid size on T6 vertebra (lowest five errors in bold).....	163
Table 6-7: Pig spine registration success rate and sample images .....	174
Table 7-1: Original phantom pedicle hole trajectories .....	198
Table 7-2: Pedicle hole trajectories for pilot study.....	202
Table 7-3: Pedicle hole trajectories for navigation study .....	208
Table 7-4: Vertebra, position, height and orientation combinations .....	210
Table 7-5: Probe insertion errors comparing left and right holes in origin test .....	211
Table 7-6: Probe insertion errors comparing left and right holes in corner test.....	216
Table 7-7: Mean, standard deviation, range of means of entrypoint and trajectory errors in each category and ANOVA results from origin and corner tests .....	223

## List of Figures

Figure 2-1: Sagittal view of the human spine (Wikimedia Commons, 2017).....	5
Figure 2-2: Superior view (A), Posterior view (B) and Sagittal view (C) of a T5 vertebra (Wikimedia Commons, 2012).....	6
Figure 2-3: Oblique view of vertebral neural anatomy and intervertebral discs (Dailly Anthony, 2011).....	7
Figure 2-4: Cobb angle measurement example: A – main thoracic Cobb angle, B – upper thoracic Cobb angle (Skoliose-Info-Forum.de, 2005).....	9
Figure 2-5: X-ray of instrumented spine with pedicle screws.....	12
Figure 2-6: Image of pedicle screw, hook and sublaminar wire (Chan, 2019).....	15
Figure 2-7: Entry point landmarks for pedicle screw insertion (shaded region) on a 3D printed vertebra, SA: superior articular process; TP: transverse process; PA: pars interarticularis .....	16
Figure 2-8: Euler angle representation of orientation with $\alpha$ as the angle between X and N (reference) axis, $\beta$ as the angle between z and Z axis, and $\gamma$ between the N and X axes.....	23
Figure 2-9: Sample B-mode 2-dimensional image of a vertebral phantom and corresponding landmarks on plastic phantom .....	26
Figure 2-10: Morphological processing (a) erosion, (b) dilation, (c) opening, and (d) closing using a circular structural element. Dark blue represents original shape while light blue represents the borders of the new shape. Closing shows union of two squares. (Renatokeshet, 2008) .....	31
Figure 2-11: Top-hat filter removing background artifact on ultrasound image, (a) shows the original while (b) is the filtered image.....	31
Figure 2-12: Image Registration of CT and PET Scan (Myohan, 2009).....	33
Figure 2-13: Translation, scaling, rotation, shear and reflection transformations for 2D images (Cmglee, 2016) .....	34
Figure 3-1: Preferred Reporting Items for Systematic Reviews and Meta-Analyses flow diagram for (a) 1st systematic review (2017) and (b) 2nd systematic review and meta-analysis (2019).....	46
Figure 3-2: Quality assessments for head-to-head, image guidance and free-hand studies. ....	55
Figure 3-3: Overall breach rates for moderate quality or better head-to-head studies .....	63
Figure 3-4: Breach rates for moderate quality single-arm groups comparing image guidance vs free-hand methods .....	64
Figure 3-5: Breach rates for moderate quality or better single-arm groups comparing high risk breaches from image guidance vs free-hand methods.....	65

Figure 3-6: Breaches for moderate quality or better studies reporting both thoracic and lumbar breaches for free-hand and image guidance studies .....	66
Figure 3-7: Thoracic breaches for moderate quality or better single-arm groups .....	66
Figure 3-8: Lumbar breaches for moderate quality or better single-arm groups .....	67
Figure 3-9: Surgical time for any quality head-to-head studies.....	67
Figure 3-10: Surgical time for moderate quality or better single arm groups comparing image guidance vs free-hand .....	68
Figure 4-1: Software view of motion capture cameras tracking objects. The yellow box outlines camera settings. The orange box shows the 3D view including cameras (labeled 1, 2 and 3 in the upper left corner) and motion tracked objects (teal and purple). The green box displays reflective markers as they appear in the view of each camera.....	78
Figure 4-2: Optitrack calibration equipment and reflective markers .....	79
Figure 4-3: Surgical suite showing setup of cameras with surgical lights turned on (left), surgical tools, dish of water and markers mounted on periosteal elevator (right) .....	80
Figure 4-4: Lab-based initial motion capture setup.....	81
Figure 4-5: 3D printed right triangle used for holding markers in place for static testing. ....	82
Figure 4-6: Rotational and translational deviation over 95% confidence interval for cold-start over 10 minutes, cold-start over 6 hours, pre-heat over 10 minutes, and omitting the first hour of the cold-start 6-hour trial as pre-heat over five hours. ....	83
Figure 4-7: Positional and rotational value deviation from initial value over six hours, sampled every five minutes from cold start. ....	84
Figure 4-8: Motion capture accessories: (a), linear rigid body and triangular rigid body; (b), 7.9mm vs 6.4mm markers; (c), Standard calibration wand vs custom small calibration wand.....	86
Figure 4-9: Positional RMS accuracy (bar chart) and 95% standard error (diamond with error bars) from different rigid bodies and wands. The 7.9mm marker rigid body compared with 6.4mm markers, linear rigid body (standard markers and wand) and custom 9.6cm wand for calibration (standard triangular rigid body and marker size).....	87
Figure 4-10: Schematic of camera position relative to capture volume. Blue (translucent) region shows capture volume. ....	88
Figure 4-11: Positional RMS accuracy (bar chart) and 95% standard error (diamond with error bars) comparing eight camera configurations: three to four cameras, aligned or staggered heights, aligned or staggered depths, in X, Z and Y directions. ....	89

Figure 4-12: 3D rendering of motion capture frame .....	91
Figure 4-13: Motion capture measurements a) Rigid body mounted on a digital caliper for translational testing, (b) Mounting of rigid body on a three-directional protractor for rotational testing.....	92
Figure 4-14: Positional RMS accuracy (bar chart) and 95% confidence interval of standard error from the actual mean (diamond with error bars) at 10mm, 20mm, 40mm, 80mm and 150mm in X, Z and Y directions. ....	93
Figure 4-15: Rotational RMS accuracy (bar chart) and 95% confidence interval of standard error from the actual mean (diamond with error bars) comparing rotation in only X, Y and Z directions, two angle combinations at <math><10^\circ</math> degrees, three angle combinations at 30°, 45° and 60°,two angles combinations at >math>>60^\circ</math> degrees and two angle combinations at >math>>70^\circ</math>.....	94
Figure 5-1: User interface display for Ultrasonix SonixTablet System.....	100
Figure 5-2: Ultrasound marker holder mounted onto linear transducer .....	101
Figure 5-3: Schema of the 3D ultrasound reconstruction process. PNG: Portable Network Graphics, CSV: Comma-Separated File.....	103
Figure 5-4: Screenshot of ultrasound and motion capture streaming user interface: Screenshot of ultrasound and motion capture streaming user interface .....	104
Figure 5-5: Screenshot of image processing graphical user interface showing the original image (top) and filtered image (bottom) .....	105
Figure 5-6: Sample of the phantoms used for filter evaluation. Each square has 1-inch dimensions, with dots denoting quarter inches.....	107
Figure 5-7: Ultrasound transducer mounted to OpenBeam translating frame.....	109
Figure 5-8: Temporal calibration shifting ultrasound frames.....	110
Figure 5-9: Temporal calibration shifting motion capture frames .....	110
Figure 5-10: Calibration Setup: (a) Mounting bracket to set ultrasound orientation. (b) Crosshairs phantom for calibration.....	112
Figure 5-11: Spatial calibration, RMS errors of X (width), Y(depth) and Z (length) position of origin (bar graph), and precision of measurements (diamond with standard error bars).....	113
Figure 5-12: Spatial calibration, RMS rotation errors about each axis of rotation at the origin (bar graph), and precision of measurements (diamond with standard error bars) .....	113
Figure 5-13: Sample of averaging, contrast and surface filter applied to a scan of a phantom vertebra along the X-Y (transverse) plane. From (a) original image to (b) filtered image. ....	115

Figure 5-14: Sample of averaging and quantization filter applied to a US scan of a phantom vertebra along the Y-Z (sagittal) plane. From (a) original image to (b) filtered image. .... 116

Figure 5-15: Ultrasound scan setup, (A) Motion capture cameras with capture space, (B) a 3D printed vertebra (top) and 3D printed phantoms for ultrasound imaging (I) calibration phantom, (II) linear dimension phantom, (III) angular dimension phantom, (IV) vertebrae mimicking phantom, (C) LEGO pegboard in ultrasound water bath..... 117

Figure 5-16: Linear reconstruction RMS error (bar graph) and precision (diamond with standard error bars) on flat square and flat circle phantoms ..... 118

Figure 5-17: Angular reconstruction RMS error (bar graph) and precision (diamond with standard error bars) on angled phantoms ..... 118

Figure 5-18: Sample 3D ultrasound reconstructions of linear (a) and angular (b) phantoms..... 119

Figure 5-19: Reconstruction accuracies on concave and convex vertebrae-mimicking phantoms along width, length and depth directions and angles on concave and convex surfaces. .... 119

Figure 5-20: Positional pegboard setup including the 28 placement locations. Dots denote where the phantom was placed directly on the pegboard..... 122

Figure 5-21: Histogram of the frequency distribution of positional RMS error values in each dimension throughout the volume..... 123

Figure 5-22: Positional error values at the 28 positions in mm..... 123

Figure 5-23: Histogram of the frequency distribution of orientation RMS error values in each dimension throughout the volume..... 125

Figure 5-24: Orientation error values at the 28 positions, in degrees..... 125

Figure 5-25: Test area on LEGO pegboard. Black rectangle includes full test region while purple region is the critical region. Yellow bricks indicate raised heights..... 127

Figure 5-26: Phantoms and tilters, (a) 3D-printed phantom vertebrae used in experimentation, i) Neutral, ii) Pitch, iii) Roll, and iv) Divots. (b) Custom printed tilters for pitch or roll (i), yaw (ii) and calibration square (iii). .... 128

Figure 5-27: Motion capture devices used, i) 3D-printed pointer device with threaded tip and ii) Micron Series Digitizing Probe. .... 129

Figure 5-28: A 3D rendering using ImageJ of a sample reconstruction of a phantom vertebra that was analyzed in ImageJ. .... 131

Figure 5-29: 3D Ultrasound individual experiments results. Full and critical indicate the full range and the critical region respectively. .... 131

Figure 5-30: 3D-printed device individual experiments results. Full and critical indicate the full range and the critical region respectively.....	132
Figure 5-31: Probe position test results.....	132
Figure 5-32: Full experiment test results for all three devices. Full and critical indicate the full range and the critical region respectively.....	133
Figure 6-1: Sample manual landmark registration showing grayscale model (thin outline) registered to grayscale ultrasound surface (thick line) on transverse, sagittal and coronal views respectively. Red dots denote transverse process landmark locations (spinous process landmark is out of frame). .....	138
Figure 6-2: Conventions relative to vertebrae showing X (lateral or transverse), Y (postero-anterior) and Z (cranio-caudal or axial) directions .....	140
Figure 6-3: Flowchart of required rotations to pre-orient CT with 3DUS scan in three steps.....	142
Figure 6-4: Sample of CT and 3DUS centroid translational alignment (CT in green and 3DUS in pink) ...	143
Figure 6-5: Phantom spinal model (a), Segmented T6 vertebra in different views (b) including transverse view (top), sagittal view (middle) and coronal view (bottom) shown as a sample. ....	144
Figure 6-6: Scan direction and quality, (a) Vertebrae scanning direction moving cephalad then caudal; (b-c) sample raw ultrasound images, with transducer at the top of the image: (I) laminae, (II) spinous processes, (III) left transverse process and (IV) superior articular processes .....	150
Figure 6-7: 3D-printed T6 phantom for ultrasound scans .....	152
Figure 6-8: Histogram of single-vertebrae registration translational accuracy.....	152
Figure 6-9: Histogram of single-vertebrae registration rotational accuracy. ....	153
Figure 6-10: Average positional and rotational error in each direction from successful registrations including 95% confidence interval.....	153
Figure 6-11: Multi-vertebra phantom with LEGO mount. ....	154
Figure 6-12: Tilting mounts. Four yaw mounts were included (15° and 30° yaw to the left and right), and two roll and pitch mounts (15° and 30° which could be rotated 90° to allow for roll in either direction and pitch in either direction) .....	155
Figure 6-13: Histogram of the translational registration accuracy from the multi -vertebrae model. ...	156
Figure 6-14: Histogram of the rotational registration accuracy from the multi -vertebrae model.....	156
Figure 6-15: Average positional and rotational error in each direction from multi-vertebrae registrations including 95% confidence interval.....	157
Figure 6-16: Image and surgical registrations, (a) Sample image registration, CT in green and 3DUS in pink with overlapped regions in light pink (b) Sample surgical registration with registered phantom (green)	

overlaid on theoretical position of spinal segment (pink). Registered region is where green and pink overlap (light pink) .....	158
Figure 6-17: Histogram of image registration translation accuracy from multi-vertebrae model in surgical simulation experiment.....	159
Figure 6-18: Histogram of image registration rotational accuracy from multi-vertebrae model in surgical simulation experiment.....	159
Figure 6-19: Average positional and rotational error in each direction from image registrations including 95% confidence interval.....	160
Figure 6-20: Example of image registration (a) successful registration and (b) lone failure showing misalignment between ultrasound and CT image at the spinous process .....	160
Figure 6-21: Histogram of surgical registration translational accuracy from multi-vertebrae model.....	161
Figure 6-22: Histogram of surgical registration rotational accuracy from multi-vertebrae model.....	161
Figure 6-23: Average positional and rotational error in each direction from surgical registrations including 95% confidence interval.....	162
Figure 6-24: Histogram of the difference in MSE of pixel intensities between full-range and reduced-range ICP registrations. ....	164
Figure 6-25: Histogram of image registration translational and rotational accuracy from multi-vertebrae model in surgical simulation experiment using iterative closest point registration. ....	165
Figure 6-26: Exposed pig spine with T10 on the left and L2 on the right (five thoracic levels and two lumbar levels were exposed).....	169
Figure 6-27: Raw ultrasound image from a pig spine scan showing spinous process on the left (I), lamina in the middle (II), and soft tissue on the right (III). ....	170
Figure 6-28: Raw ultrasound image from a pig spine scan showing the inferior articular processes (region I), with the soft tissue region inferior to the spinous process (II).....	171
Figure 6-29: Raw ultrasound image from a pig spine scan showing the spinous process (I), lamina (II), and soft tissue (III).....	172
Figure 6-30: Failed porcine registration, (a) Uncropped image resulting in failed registration due to ultrasound symmetry misalignment and (b) cropped image resulting in successful registration .....	181
Figure 7-1: Screenshot of (a) Unity object panel and scene view and (b) game view including the motion capture probe (orange/yellow cylinder), vertebra (white bony object) and capture volume floor and walls (blue background). Center image is the screw-camera while the bottom displays the coronal, sagittal and transverse views of the vertebra .....	185



Figure 7-2: Drawing of calibration square(a) All dimensions in mm. Picture of calibration square (b) including the three reflective markers at each corner, triangular-pillar ultrasound stand (top left), water dish with calibration crosshairs (bottom left), and 3D probe calibration stand (center right) ..... 188

Figure 7-3: Histogram of difference between actual and theoretical width of LEGO bricks..... 190

Figure 7-4: Histogram of difference between actual and theoretical height of LEGO bricks..... 191

Figure 7-5: Probe views, (a) 3D view of the yellow and red probe on the pegboard and (b) top-down view of the probe on the pegboard. .... 191

Figure 7-6: Probe with motion capture markers (a) and pegboard grid (b) ..... 192

Figure 7-7: Histogram of motion capture positional error throughout all positions (square brackets denote that value is inclusive)..... 193

Figure 7-8: Sample of MRI segmentation of the T9 vertebra showing (a) 3D view and (b) and cross sections of vertebra with sagittal, transverse and coronal views..... 195

Figure 7-9: Sample of segmentation of the CT scan including coronal view (a) and sagittal view (b) with rightmost vertebra as T1 and leftmost vertebra as T12 ..... 197

Figure 7-10: Navigation setup: (a) Phantom vertebra with pedicle holes, (b) Capture volume including the origin (blue), the four cardinal directions (yellow) and the three tilting stands (clear) with yaw-left at the top, pitch and roll in the middle and yaw-right at the bottom..... 199

Figure 7-11: Virtual display of translucent vertebra including the probe (red and yellow concentric circles) placed into pedicle hole (a), and the Euler angles of the probe displayed (b) ..... 200

Figure 7-12: Entry-point (a) and trajectory error (b) from repeatability test: three measurements in each hole for each vertebra at the capture volume origin ..... 200

Figure 7-13: Histograms of (a) entry-point and (b) trajectory errors from pilot test ..... 201

Figure 7-14: Oversized phantoms in (a) coronal view and (b) sagittal view. In each figure, the surface finish of the left spine is matte and glossy on the right. Lego blocks for scale are 32x16mm..... 203

Figure 7-15: Histograms of (a) entry-point and (b) trajectory error from repeatability test: three measurements in each hole for each vertebra at the capture volume origin..... 204

Figure 7-16: Histograms of (a) entry-point and (b) trajectory error of the probe placement from the orientation test (phantom rotated in roll, pitch and yaw varied in both directions)..... 204

Figure 7-17: Histograms of (a) entry-point and (b) trajectory error of the probe placement from the position test (phantom placed at each cardinal direction)..... 205

Figure 7-18: Histograms of (a) entry-point and (b) trajectory accuracy from mixed orientation and position test ..... 206

Figure 7-19: Sample ultrasound images from (a) matte spine, (b) glossy spine and (c) pig spine at the spinous process.....	207
Figure 7-20: Coronal and sagittal views of the two 3D printed phantoms.....	208
Figure 7-21: Top-down view of pegboard, showing the scale of the calibration square (left) and the T7-T12 vertebra mounted in yaw-negative (left) at center, and T2-T8 vertebra mounted in pitch-negative (up) on the north-east corner.....	209
Figure 7-22: Histograms of (a) entry-point and (b) trajectory accuracy from origin experiment. ....	211
Figure 7-23: Mean error and standard deviation of entry-point (a,b) and trajectory (c,d) errors from probing the left hole (a,c) and the right hole (b,d), analyzed according to orientation.....	212
Figure 7-24: Mean error and standard deviation of entry-point (a,b) and trajectory (c,d) errors from probing the left hole (a,c) and the right hole (b,d), analyzed according to vertebra. ....	214
Figure 7-25: Histograms of (a) entry-point and (b) trajectory accuracy from corner experiment .....	215
Figure 7-26: Mean error and standard deviation of entry-point (a,b) and trajectory (c,d) errors from probing the left hole (a,c) and the right hole (b,d), analyzed according to position on pegboard .....	216
Figure 7-27: Mean error and standard deviation of entry-point (a,b) and trajectory (c,d) errors from probing the left hole (a,c) and the right hole (b,d), analyzed according to height on pegboard (0mm and 19.2mm heights) .....	218
Figure 7-28: Mean error and standard deviation of entry-point (a,b) and trajectory (c,d) errors from probing the left hole (a,c) and the right hole (b,d), analyzed according to six vertebral orientation .....	219
Figure 7-29: Mean error and standard deviation of entry-point (a,b) and trajectory (c,d) errors from probing the left hole (a,c) and the right hole (b,d), analyzed according to vertebral level.....	221
Figure 7-30: Surgeon performing 3D ultrasound scan on a phantom spine. ....	226
Figure 7-31: Navigation display showing pedicle probe (yellow/red cylinders) placed into pedicle holes .....	228

## List of Equations

Equation 2-1: Motion Capture Camera Transforms .....	22
Equation 2-2: Transformation Matrix Multiplication.....	24
Equation 2-3: Quaternion Rotation Notation .....	24
Equation 2-4: Reflectivity from Acoustic Impedance .....	26
Equation 4-1: RMS Accuracy Equation.....	85
Equation 4-2: Confidence Interval of Mean:.....	85
Equation 6-1: Mean-squared Error for Image Registration: .....	139
Equation 6-2: Centroid of CT or 3DUS Bodies.....	142
Equation 6-3: RMS Error for Position and Orientation .....	151

## List of Abbreviations and Nomenclature

<b>2D</b>	<b>Two-dimensional</b>	<b>NE</b>	<b>North-east</b>
<b>3D</b>	Three-dimensional	<b>NW</b>	North-west
<b>3DOF</b>	Three degrees-of-freedom	<b>O-Arm</b>	Intraoperative CT Scanner
<b>3DUS</b>	Three-dimensional Ultrasound	<b>OBJ</b>	Wavefront Object File
<b>6DOF</b>	Six degrees-of-freedom	<b>OR</b>	Odds Ratio
<b>AIS</b>	Adolescent Idiopathic Scoliosis	<b>PA</b>	Pars Interarticularis
<b>A-mode</b>	Amplitude Mode Ultrasound Display	<b>PET</b>	Positron Emission Tomography
<b>ANOVA</b>	Analysis of Variance	<b>Post-op</b>	Post-operative
<b>ARPF</b>	Anterior-release, Posterior Fusion	<b>Pre-op</b>	Pre-operative
<b>B-mode</b>	Brightness Mode Ultrasound Display	<b>PRISMA</b>	Preferred Reporting Items for Systematic Review and Meta-Analysis Protocols
<b>C-arm</b>	Intraoperative Fluoroscopy	<b>QUIPS</b>	Quality in Prognostic Studies
<b>CSVL</b>	Center Sacral Vertical Line	<b>RMS</b>	Root-mean Squared
<b>CT</b>	Computed Tomography	<b>ROB</b>	Risk of Bias
<b>CT-Navi</b>	CT Navigation	<b>SA</b>	Superior Articular Process
<b>Fluoro</b>	Fluoroscopy	<b>SE</b>	South-east
<b>GRADE</b>	Grading of Recommendations, Assessment, Development and Evaluations	<b>SPECT</b>	Single-Photon Emission Computed Tomography
<b>ICC</b>	Intraclass Correlation Coefficient	<b>SRS</b>	Scoliosis Research Society
<b>ICP</b>	Iterative Closest Point	<b>STL</b>	Stereolithography File
<b>L#</b>	Lumbar Vertebra Number	<b>SW</b>	South-west
<b>M&amp;M</b>	Morbidity and Mortality	<b>T#</b>	Thoracic Vertebra Number
<b>MIS</b>	Minimally-invasive Surgery	<b>TP</b>	Transverse Process
<b>Mocap</b>	Motion Capture	<b>X-axis</b>	Transverse direction (left-to-right)
<b>MRI</b>	Magnetic Resonance Imaging	<b>Y-axis</b>	Vertical direction (up-down against gravity)
<b>MSE</b>	Mean-squared Error	<b>Z-axis</b>	Axial direction (cranial-caudal or head-legs)

## Chapter 1: Introduction

Adolescent idiopathic scoliosis (AIS) is a three-dimensional spinal deformity that affects 2-3% of adolescents [1]. Because no etiology has been identified for AIS, treatment is aimed at managing the severity of the deformity to reduce the cosmetic defect and minimize limitations to exercise tolerance, either with bracing for moderate curves, or surgery in severe cases [2–4].

### 1.1. Motivation

The current standard of surgical treatment involves inserting screws posteriorly into the vertebrae to attach instrumentation to the spine and hold it in its corrected position [5,6]. While screws are the most secure method of attaching instrumentation to the spine, the screws must be placed carefully to prevent spinal cord injury, nerve root damage and even vascular injury [7–9].

Fluoroscopy and intra-operative CT-navigation systems are currently considered the cutting edge in image guidance technology for pedicle screw placement [10–12]. However, these imaging techniques are often precluded due to their bulk, expense and exposure of pediatric patients to ionizing radiation [13–16]. Alternative non-ionizing imaging methods, particularly ultrasound imaging, have been sought to provide image guidance to ensure surgical safety[17,18]. While ultrasound is traditionally used in soft tissue imaging, the potential for ultrasound to provide anatomic information for image guidance is only beginning to be explored.

### 1.2. Problem Statement

To develop and validate an intraoperative image guidance system using motion capture and 3D ultrasound. The sequence of the research and development process is as follows:

1. Determine the accuracy and precision of conventional motion capture for navigation surgery
2. Develop a bone-surface 3D ultrasound imaging system and determine its positional accuracy in localizing phantoms in the capture volume and accuracy in reconstructing dimensions on the phantoms themselves
3. Develop an image registration program for registering 3D ultrasound surface volumes to pre-operative CT vertebral image volumes
4. Validate the image guidance system for actual screw insertion in a CT-based vertebral phantom, ensuring screw entry-point accuracy of 1mm and trajectory within 5°.

### 1.2.1. System Requirements

The goal of this research is to develop and validate an image guidance method that avoids intraoperative ionizing radiation to guide pedicle screw insertion. For image guidance to be effective and useable in the operating room, the system must:

- Provide real-time feedback intraoperatively on surgical tools relative to stationary anatomy,
- Visualize internal anatomy at accuracy and precision of <1mm, equivalent to CT-navigation systems
- Use handheld guidance tools in the operating room without CT or fluoroscopy equipment
- Include a graphical user-interface that is intuitive for surgeons to use, and
- Reduce ionizing radiation exposure intraoperatively.

### 1.2.2. Scope of Work

First, an assessment of the highest quality and current clinical evidence will be undertaken to determine the surgical relevance of developing a new navigation tool. The assessment will include a systematic review and meta-analysis of original clinical studies on breach rates and complication rates due to screw placement in AIS surgery.

The accuracy of technical equipment including the motion capture system and the ultrasound machine will be evaluated, with a focus on determining localization and orientation errors. Next, research into methodologies used to create and calibrate a 3D ultrasound imaging system will be undertaken. Once the optimal 3D reconstruction methodology is selected, a custom implementation for 3D ultrasound reconstruction of the posterior surface of the vertebra including spinous process, laminae and transverse processes will be developed and its accuracy assessed.

Following development of the 3D ultrasound imager, research into applying image registration algorithms to match the 3D ultrasound vertebra surface to its corresponding 3D CT vertebral model will be undertaken. Different registration techniques will be evaluated for speed and accuracy and a novel algorithm will be developed for this navigation system. Lastly, a custom program with graphical user interface will be developed to display the registered 3D vertebral model, as well as display the tracked position and orientation of surgical tools in the surgical space. The accuracy of a probe placed through pedicle screw holes will be tested, including both entry-point positional accuracy and trajectory accuracy.

The two primary considerations throughout this study are to ensure adequate technical accuracy, providing within 1mm and 5° accuracy for guidance, and to integrate seamlessly into the surgical workflow with low profile tools, requiring less than 1 minute from imaging to display.

## 1.3. Thesis Organization

### 1.3.1. Thesis Outline

This thesis is organized in eight chapters.

Chapter 2 provides background information on both the clinical context and technical knowledge required for development of the image guidance system including motion capture, 3D ultrasound and image registration.

Chapter 3 presents the results from a systematic review and a meta-analysis on complication rates and pedicle breach rates due to screw misplacement in adolescent idiopathic scoliosis surgery.

Chapter 4 details the process used to ensure adequate accuracy of conventional motion capture in the operating room.

Chapter 5 describes the process of reconstructing 3D ultrasound images by combining conventional 2D medical ultrasound images with motion capture data, followed by evaluating the dimensional accuracy of reconstructions, and the placement accuracy of the reconstructions within the surgical space

Chapter 6 outlines the methods used for pre-processing and registering ultrasound surface images to a segmented pre-operative vertebral volume from a CT scan

Chapter 7 involves the validation of the ultrasound navigation system on a 3D-printed plastic phantom vertebra, comparing the actual entry-point and trajectory of a probe placed in the phantom vertebral pedicle, with the entry-point and trajectory shown on the display.

Lastly, Chapter 8 involves a discussion of the overall development process, current limitations and potential improvements to the technology.

## Chapter 2: Background Information

### 2.1. Overview

This chapter is an overview of the clinical background including spinal anatomy, scoliosis and surgical treatment. Detail is given to pedicle screw insertion techniques and complications for scoliosis surgery. Secondly, the technical background on motion capture technology, 3D ultrasound imaging and image registration for image guidance technologies are presented.

### 2.2. Clinical Background

#### 2.2.1. Spinal Anatomy

The human vertebral column has 24 individual vertebrae, split amongst 5 sections from superior to inferior: cervical (7), thoracic (12), lumbar (5), and fused sacral (5) and coccyx (4) regions [19] (Figure 2-1: Sagittal view of the human spine (Wikimedia Commons, 2017)). The cervical vertebrae take a lordotic curvature and comprise the neck region which allows for most the head's range of motion. The thoracic vertebrae form a kyphotic curvature with additional facets that articulate with the rib cage. The lumbar vertebrae form a largely lordotic region at the abdominal level of the torso while the sacral vertebrae and coccyx are at the level of the hip bones. The vertebrae generally increase in size when descending the spinal column.

Each vertebra includes a vertebral body anteriorly, spinous process protruding posteriorly and transverse processes protruding laterally on either side of the vertebra (Figure 2-2: Superior view (A), Posterior view (B) and Sagittal view (C) of a T5 vertebra (Wikimedia Commons, 2012)). The vertebral canal in the center of the vertebra is surrounded by the vertebral body anteriorly, laminae posteriorly, and pedicles laterally. The spinal cord lies within the vertebral canal with spinal nerves exiting the spine under each pedicle throughout the spine (Figure 2-3: Oblique view of vertebral neural anatomy and intervertebral discs (Dailly Anthony, 2011)) [19]. The superior articular process forms the facet joint with the vertebra above, while the inferior articular process connects with the vertebra below. Thoracic vertebrae have costal facets which articulate with the ribs.

Pedicle linear dimensions progress from small to large when moving inferiorly. Pedicle angles have a decreased medial angle on the transverse plane when moving inferiorly, with angles typically less than  $10^\circ$  from the sagittal plane [19]. Pedicles in the thoracic spine may be 4-8mm in diameter while lumbar



are typically 6-13mm in diameter [20]. The pedicle itself has variable density, with a thicker cortical shell medially protecting the spinal cord in the vertebral canal.

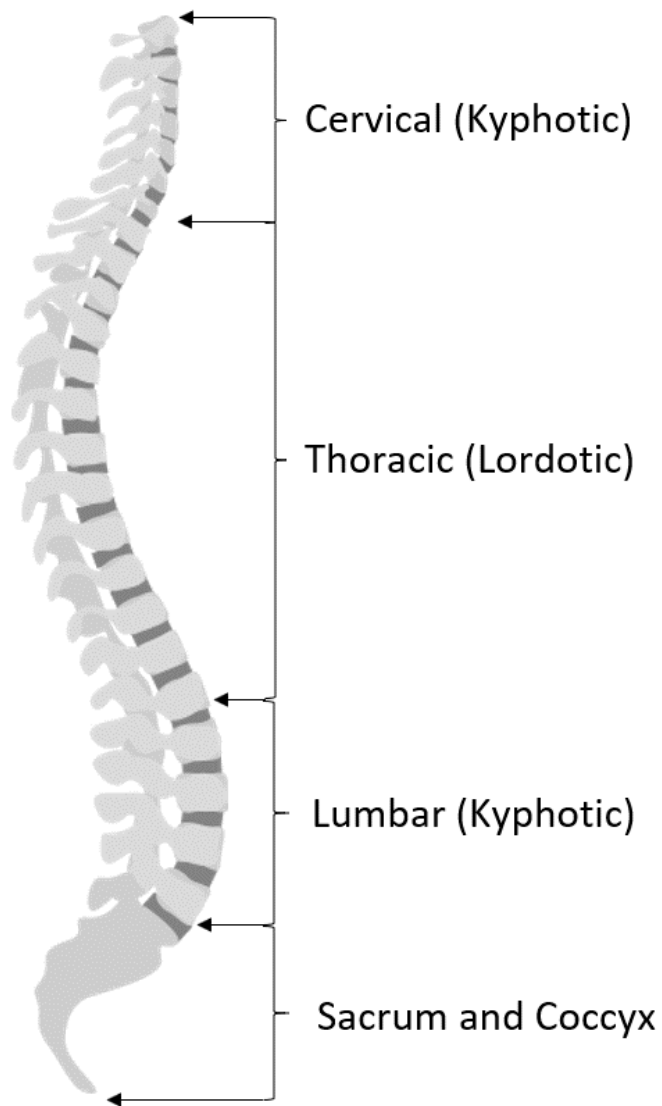


*Figure 2-1: Sagittal view of the human spine (Wikimedia Commons, 2017)*

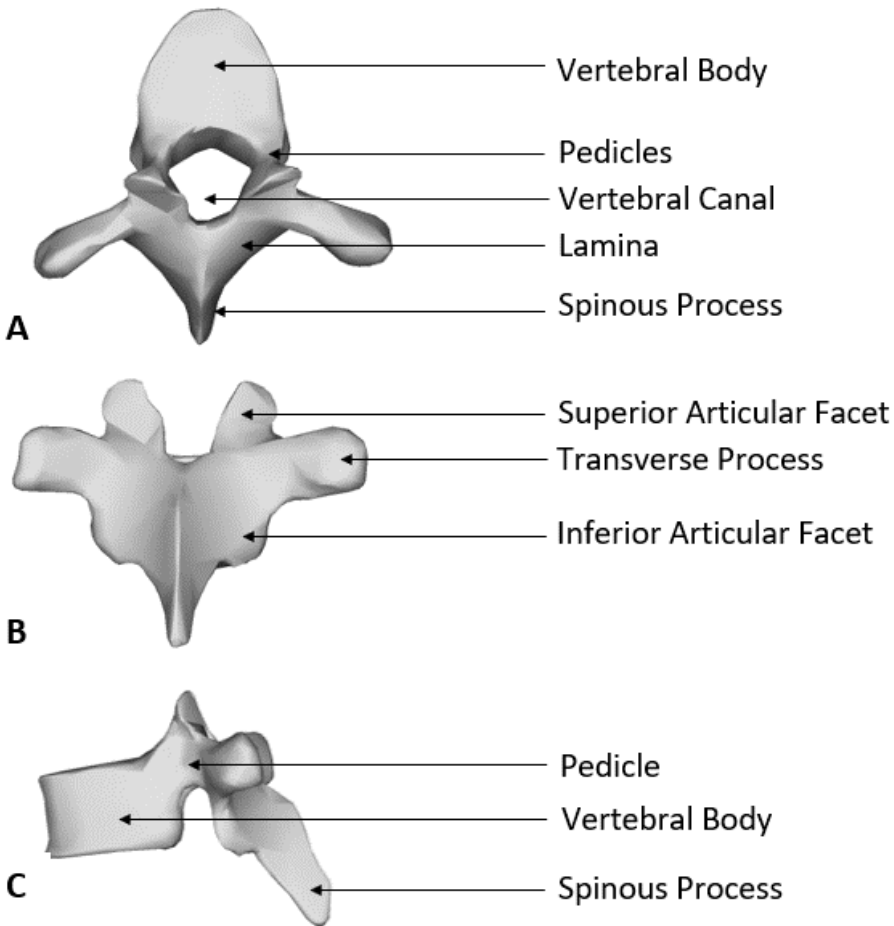


**Figure 2-2: Superior view (A), Posterior view (B) and Sagittal view (C) of a T5 vertebra (Wikimedia Commons, 2012)**

The arterial supply of the spinal cord comes primarily through two dorsal and one anterior longitudinal blood vessel [21]. The blood supply is highly redundant, with anastomoses between each level and reversible flow depending on the metabolic demands of the spinal cord [19]. At each level, segmental arteries surround the vertebral body with branch to the posterior areas of the vertebra. The poorest blood supply lies between T4-T9. Both the aorta and inferior vena cava are anterior to the vertebral body, with the aorta typically on the left side and the vena cava on the right side from T4 to L4.

Intervertebral discs lie between each vertebral body as part of the spine's load bearing and shock absorbing system (Figure 2-3: Oblique view of vertebral neural anatomy and intervertebral discs (Dailly Anthony, 2011)). Each disc is composed of an annulus fibrosus around the outside and nucleus pulposus within. The anterior and posterior longitudinal ligaments lie anterior and posterior to the vertebral body and disc respectively, running the length of the spine. The interspinous and supraspinous ligaments connect the spinous processes while the ligamentum flavum connects each lamina [21].

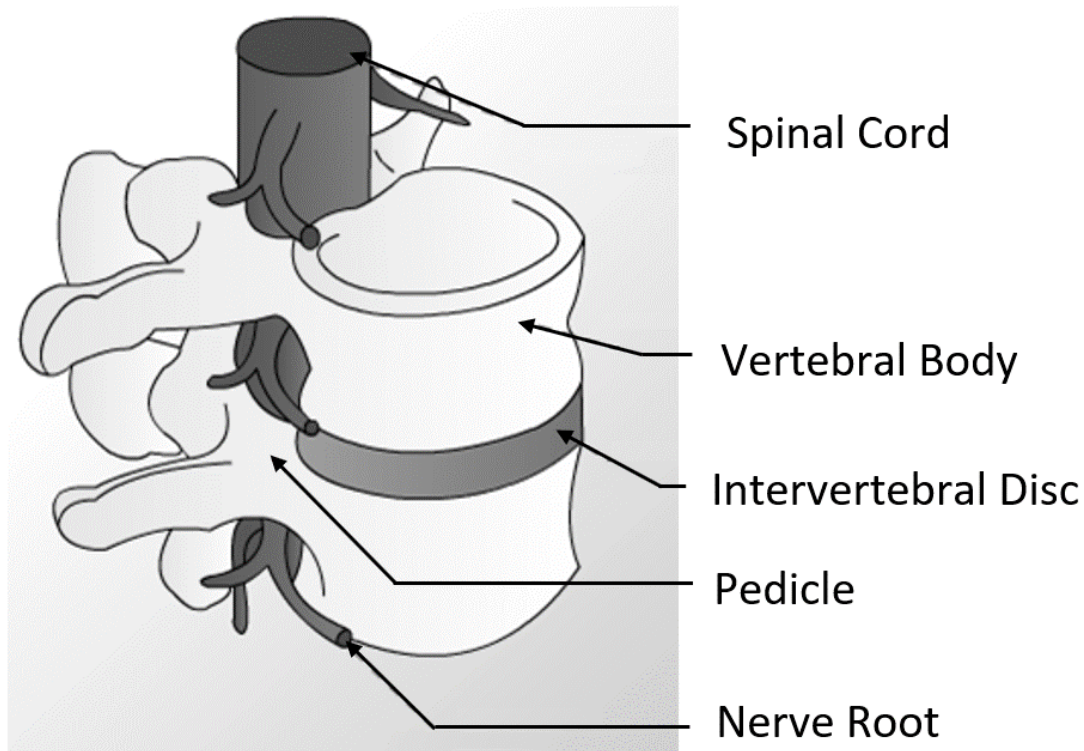


**Figure 2-3: Oblique view of vertebral neural anatomy and intervertebral discs (Dailly Anthony, 2011)**

### 2.2.2. Types of Scoliosis

Scoliosis is defined as a sideways curvature of the spine, though it is increasingly acknowledged as a three-dimensional deformity [22,23]. Scoliosis is classified into multiple types including congenital, neuromuscular and idiopathic. Congenital scoliosis involves skeletal abnormalities that are present at birth including formation of wedged hemivertebrae, partial fusion of vertebrae, or a combination of these abnormalities [24]. Neuromuscular scoliosis can be caused by genetic or syndromic diseases including cerebral palsy or Duchenne muscular dystrophy, but can also be secondary to Polio infections, central nervous system lesions or traumatic injury [25]. Connective tissue diseases including syndromic (Marfan syndrome) or secondary to low Vitamin D or Calcium (rickets) can lead to scoliosis. Congenital and neuromuscular scoliosis are often treated with surgical intervention due to the permanence of bony deformity in congenital scoliosis [26], or the severity and progression in the case of neuromuscular [27]. However, the most common form of scoliosis is adolescent idiopathic scoliosis.

### 2.2.3. Adolescent Idiopathic Scoliosis

The prevalence of idiopathic scoliosis in adolescents is reported as 2-3%, with most of these patients not needing treatment. Bracing or surgery is indicated for curves severe enough to require treatment, with a

prevalence of 0.2-0.5% [28,29]. Idiopathic scoliosis is a diagnosis of exclusion, given that no identifiable cause has been found. Empirically, concordance of idiopathic scoliosis is 73% in monozygous twins and 36% in dizygous twins, indicating that genetics is likely involved in idiopathic scoliosis pathogenesis [30]. However, no single gene or set of genes have been identified to cause idiopathic scoliosis. Studies in predicting curve progression using genetic testing have not been definitive [31]. Similarly, biochemical correlations between scoliosis and melatonin, calmodulin levels in platelets and collagen in intervertebral discs have been studied in detail [32–36]. Scoliosis has been associated with decreased melatonin, abnormalities in spinal ligaments and increased calmodulin in platelets, none of which were shown to be causative. More recently, epigenetics has been studied to determine if nutrition, physical activity, geographic latitude and maternal age may be related to idiopathic scoliosis [37]. Because the field of epigenetics is still in its infancy, the potential for discovering causation and generating therapeutics remains unknown.

Treatment of idiopathic scoliosis is aimed at halting progression after detection. Severity of scoliosis is assessed using the Cobb angle, determined by measuring the angle between the most tilted upper vertebrae and most tilted lower vertebrae in a scoliotic curve as captured on a frontal plane X-ray (Figure 2-4: Cobb angle measurement example: A – main thoracic Cobb angle, B – upper thoracic Cobb angle (Skoliose-Info-Forum.de, 2005)) [38,39]. Measuring procedures including manual ‘pencil-and-protractor’ methods, computer-assisted landmark-based software and automated systems have been used with reproducibility within 5° [40]. The presence of a scoliotic curve is defined as a Cobb angle of greater than 10° while severity is classified as mild (<20°) moderate (20-45°) or severe (>45°)[41].

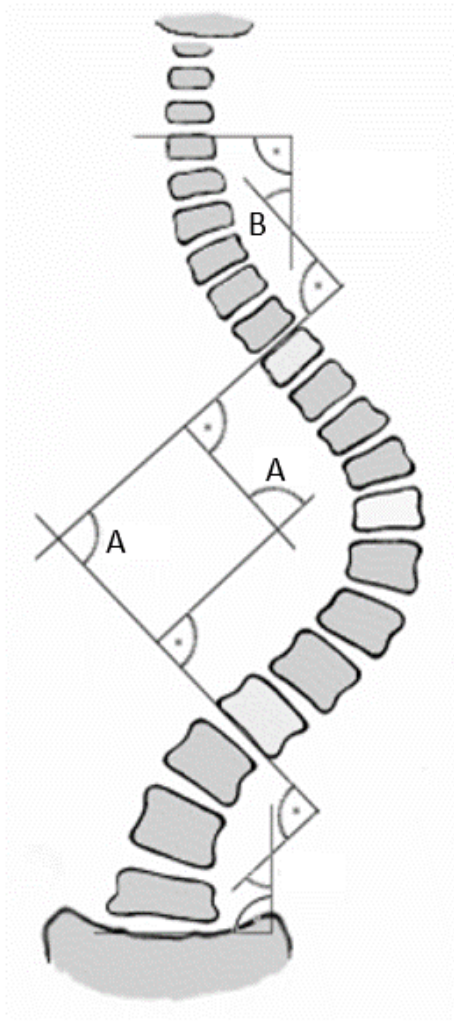


**Figure 2-4: Cobb angle measurement example: A – main thoracic Cobb angle, B – upper thoracic Cobb angle (Skoliose-Info-Forum.de, 2005)**

While the etiology of idiopathic scoliosis remains elusive, the natural history has been well delineated. Mild idiopathic scoliosis may remain stable over time, but moderate or severe curves typically worsen or progress over time. Certain risk factors including greater severity of scoliosis, gender, age at menarche, and skeletal immaturity can alter the degree of progression [1,32,42,43]. Patients with larger curves are more likely to progress (7-17% when less than 20° vs 34-40% when larger than 20°)[44]. Females are more likely to have progressive curves at a 8:1 ratio for curves greater than 30° [29] when compared to males. Being pre-menarchal also increases risk of progression [45]. Skeletal maturity is assessed using the Risser scale [46], triradiate cartilage [47] or Sanders Digital Scale, [48] with lower maturity correlated with greater progression [44]. Curve severity and the risk of progression are the primary drivers of determining

what treatment is appropriate for scoliosis [1]. Table 2-1 shows the odds ratio of curve progression from the most important risk factors for scoliosis progression [49].

**Table 2-1: Odds ratio of curve progression from common risk factors [49]**

<b>Risk Factor</b>	<b>Odds Ratio</b>	<b>Level of Evidence</b>
Age (<13)	2.7 [1.8-4.6] $p<0.01$ , 3 studies	Low
Osteopenia	2.8 [1.4-5.6] $p<0.01$ , 3 studies	Low
Initial Cobb Angle	7.6 [4.2-13.6] $p<0.01$ , 8 studies	Low
Premenarche	4.0 [2.0-7.9] $p<0.01$ , 6 studies	Low
Skeletal Immaturity	2.8 [1.6-4.8] $p<0.01$ , 4 studies	Low

Without treatment, severe curves can impair patients’ ability to perform physical activity due to decreased pulmonary function, and lead to non-disabling but increased chronic back pain [4,50,51]. Furthermore, as the incidence of idiopathic scoliosis is highest in the adolescent years, low self-esteem and poor self-image due to the deformity are important issues for these patients[52,53].

Curves that are greater than 25° are usually considered for treatment using bracing with exercise therapy as an additional option for smaller curves[1,54,55]. In a randomized controlled trial comparing brace treatment with no brace treatment, bracing was found to significantly decrease progression in skeletally immature patients with idiopathic scoliosis [2]. However, 25% of patients still had treatment failure which would require surgery to correct the deformity and prevent progression [1]. Surgery may be indicated in curves greater than 45° with the goal of correcting the deformity, preserve sagittal balance and maximize patient quality of life [3,56].

#### 2.2.4. Surgical Treatment

Scoliotic curvatures are classified typically according to the Lenke classification system [57]. The system divides the spine into three sections: proximal thoracic, main thoracic and thoracolumbar. The largest curve is considered the major structural curve, while minor curves are considered structural if the Cobb angle from a side-bending X-ray is greater than 25°. Table 2-2 shows a summary of the Lenke classification of curves including main thoracic, double thoracic, double major (major thoracic and structural thoracolumbar curve), triple major (major or structural curves in all three regions), thoracolumbar/lumbar, and thoracolumbar/lumbar-main thoracic (structural main thoracic, major thoracolumbar/lumbar) types.

In addition to curve type, the Lenke classification system includes a lumbar spine modifier with lumbar pedicle position being compared to the center sacral vertical line (CSVL): CSVL between pedicles (Type A),

CSVL touching the apical bodies (Type B) and the CSVL completely medial to the vertebral bodies (Type C). Lastly, the classification notes if the sagittal T5-T12 profile has a normal kyphotic curve (Type N) or if it is hypokyphotic (Type -) or hyperkyphotic (Type +). From the Lenke classification and its two modifiers, the levels of fusion and surgical approach are selected, with all Lenke structural curves being included in the fusion.

**Table 2-2: Lenke classification of surgical curves**

Type	Proximal Thoracic	Main Thoracic	Thoracolumbar/Lumbar	Description
1	Non-Structural	Major Curve	Non-Structural	Main Thoracic
2	Structural	Major Curve	Non-Structural	Double Thoracic
3	Non-Structural	Major Curve	Structural	Double Major
4	Structural	Major Curve	Major Curve	Triple Major
5	Non-Structural	Non-Structural	Major Curve	Thoracolumbar/Lumbar
6	Non-Structural	Structural	Major Curve	Thoracolumbar/Lumbar-Main Thoracic

The two main surgical approaches to scoliosis are classified as posterior or anterior. In the posterior approach, patients lay prone on a Jackson table, padding the arms and releasing intraabdominal pressure, allowing the lumbar lordosis to be maintained for proper sagittal alignment and giving surgeons access to the posterior surface of the spine to attach instrumentation [5,58]. Subperiosteal dissection is continued until all the fused levels are exposed. Fusion is performed by decorticating facet joints and may be facilitated using bone grafting, with autogenous iliac crest bone graft as the gold standard though a recent meta-analysis found no post-operative benefits in achieving fusion when using bone graft compared to allograft or other bone substitutes [59].

The method of correction then needs to be assessed, whether performing a derotation maneuver, distraction or translation of the curve, or in situ contouring. Regardless of the method, the corrected spinal curve needs to be held to contoured rods that run longitudinally along the spine using hooks or pedicle screws. Figure 2-5: X-ray of instrumented spine with pedicle screws shows an X-ray of an instrumented spine with longitudinal rods and pedicle screws and cross-links between rods.

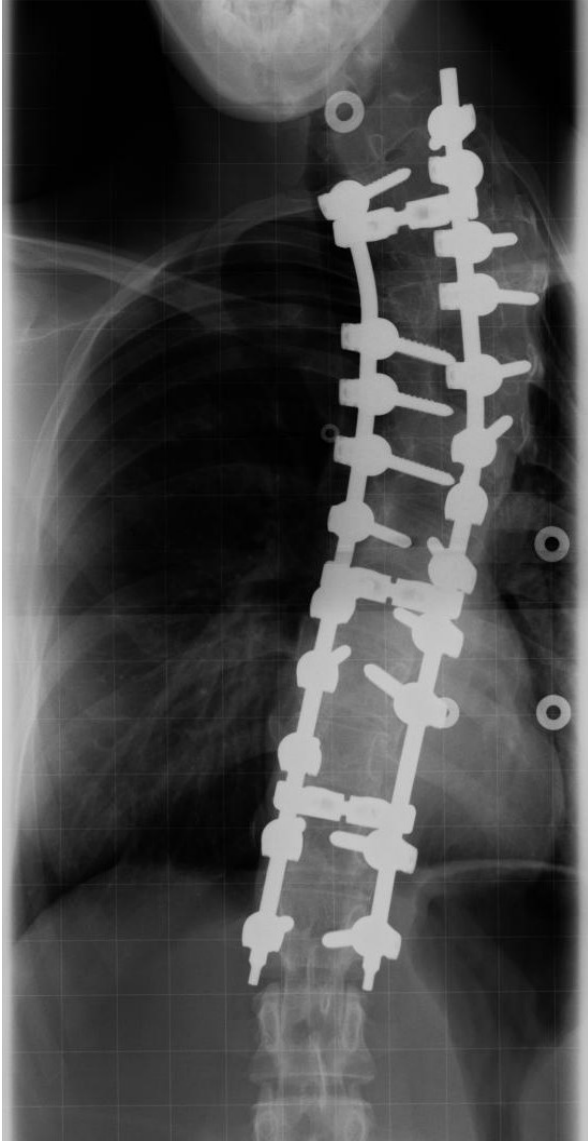


***Figure 2-5: X-ray of instrumented spine with pedicle screws***

The anterior approach is usually reserved for thoracolumbar or lumbar curves [58]. The patient lays in the lateral decubitus position and an incision is performed through the abdominal flank or along the rib that is one level higher than the most proximal instrumented rib. With the vertebral body exposed the intervertebral discs are removed and screws are placed laterally to vertebral bodies allowing instrumentation to be directly attached to the site of deforming force ,the vertebral body [5,56,60,61]. Video-assisted and endoscopic procedures have also been developed alongside the anterior approach.

While the anterior approach can reduce the amount of instrumentation inserted into the spine, surgeries tend to be prolonged with poorer post-operative pulmonary function and greater risk to retroperitoneal organs and the great vessels [56,58]. Thoracoscopic anterior approaches have a reduced incision and led



to better pulmonary outcomes, but this approach has a steep learning curve and increased risk of damaging the thoracic aorta [5,60,62].

Combined approaches involving an anterior release and posterior fusion have also been used in the past, particularly for large scoliotic curves ( $>100^\circ$ ) that may be stiffer ( $70\text{-}80^\circ$  residual side-bending curve). The combined approach may be completed in the same day, or as a two-step staged surgery. However, similar to the anterior approach, poorer pulmonary function and prolonged surgeries remain drawbacks to this method, with thoracic pedicle screw usage offering similar levels of spinal correction without the need for anterior release [63–65].

Posterior instrumentation and fusion is the preferred method of surgical treatment for AIS, comprising 13.8% of all pediatric orthopedic surgeries according to the American College of Surgeons National Surgical Quality Improvement Program. Comparatively, supracondylar humerus fracture was the only surgical indication with a higher prevalence (25.6%) and all-cause posterior spinal fusions (combining AIS, non-idiopathic scoliosis and revision surgeries) at 27.4% [66]. Anterior spinal fusions only comprised 0.28% of all procedures, with an overall adverse event rate at 8% compared to 5.97% for AIS posterior spinal fusion. Anterior fusions or anterior releases with posterior fusions comprised 31% of surgeries from the Scoliosis Research Society Morbidity and Mortality database, compared with 69% for posterior-only surgeries in 2006. Posterior fusion and instrumentation have become the prevailing method for surgical treatment of AIS.

Posterior spinal instrumentation and fusion requires longitudinal rods of the spine to be attached to the vertebrae. In the past, hooks and sublaminar wires were more commonly used than pedicle screws. Laminar hooks are placed supra-laminarly for compressive forces, and infra-laminarly when distraction is required, while pedicle hooks may be used in the thoracic spine [67]. However, hook dislodgment, poor vertebral derotation and correction loss due to diminishing hook purchase in the lumbar spine as well as intrusion into the spinal canal remain as drawbacks for usage of hooks [68]. Sublaminar wires involve passing titanium or stainless-steel cables sub-laminarly carefully to prevent travel into the spinal canal, and tying them around the rods [67]. However, the higher neurologic complication rates from wires and the difficulty in revision surgeries involving sublaminar wires due to scarring behind the lamina make their usage less popular today [56,68].

### 2.2.5. Free-Hand Pedicle Screw Insertion Methods

Pedicle screws are the most common method of attaching instrumentation to the spine in posterior spinal instrumentation and fusion surgery [6]. Although hooks were previously more common, the improved biomechanics of screw fixation and low neurological complication rate has made usage of pedicle screws the primary method of attaching the spine to instrumentation [58,69,70]. While previously reserved for lumbar levels, pedicle screws have gained favor in the thoracic spine with adequate safety and secure attachment to the spine shown in multiple studies [68,71,72].

The process of pedicle screw insertion is one of the more technically challenging portions of the surgery due to the small size of the pedicles. The transverse pedicle width may be as small as 4-6mm and sagittal width at 7-11mm in the mid-thoracic spine, with smaller pedicles in younger patients[20]. Screws are typically 4.5-5.5mm in diameter. Lumbar pedicles have transverse widths of 6-16mm and sagittal widths of 9-14mm, allowing for larger screws to be inserted. The trajectory is usually estimated using pre-operative radiographs or CT scans, though the trend is for a medial transverse angle of 0-15° and a sagittal pedicle angle at thoracic levels of 10-20° with an inferior-to-superior trajectory from the lamina [20,67]. In one study which modeled the pedicle as a cylinder based on anthropomorphic measurements, The required accuracy of screw insertion may be as low as 0.6 mm (0.05-1.50 mm) and 2.6° (0.2-7.7°) in the thoracic spine when assuming a 5.0mm screw [73]. Patients with AIS also have more dysplastic pedicles, with narrower pedicles at 22% vs 13% in control groups, with the apical vertebrae having the highest prevalence of dysplastic pedicles [74].

While screws are typically inserted at every level of fusion, the density of pedicle screws ranges quite significantly [75]. High density constructs are costly and may be overly constrained, while low density may have greater curve instability resulting in more revision surgeries. Nevertheless, recent studies have found minimal difference in curve correction between high and low density implant constructs [75-77]. A comparison of screws, hooks and wires can be seen in Figure 2-6: Image of pedicle screw, hook and sublaminar wire (Chan, 2019).

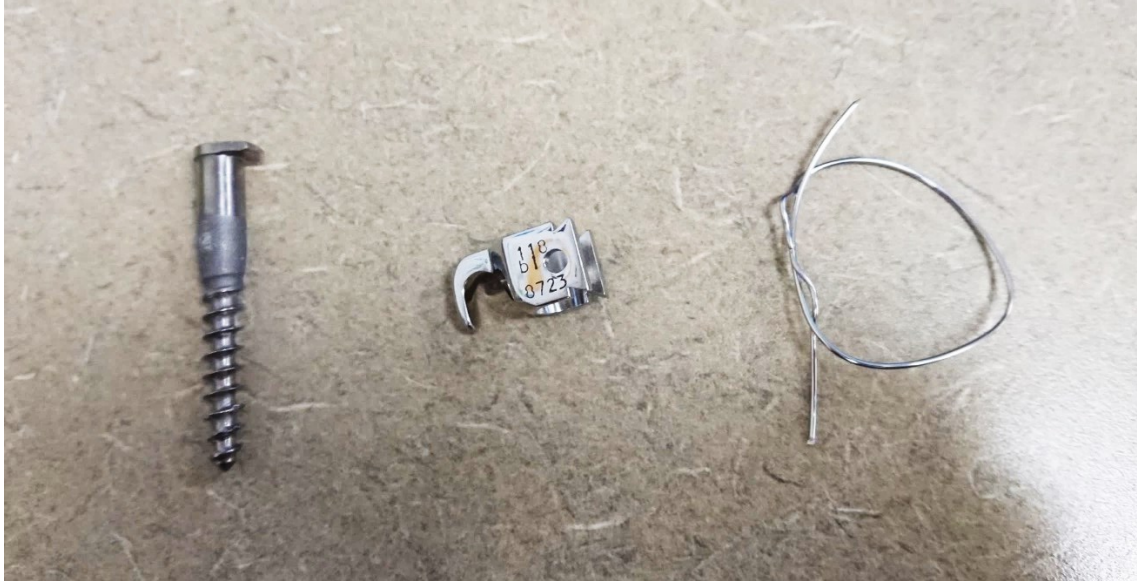


**Figure 2-6: Image of pedicle screw, hook and sublaminar wire (Chan, 2019)**

To improve accuracy, free-hand methods have been standardized for consistent screw insertion. Image guidance methods have also been developed as visual aids to guide screw insertion.

The free-hand method involves selection of the pedicle screw entry point using bony landmarks as shown in Figure 2-7: Entry point landmarks for pedicle screw insertion (shaded region) on a 3D printed vertebra, SA: superior articular process; TP: transverse process; PA: pars interarticularis. The actual entry-point is dependent on the level of screw insertion. The landmarks for entry-point include the transverse process, the inferior border of the superior articular facet, and the pars interarticularis. For the upper thoracic regions, the entry point is more lateral, while in the lower thoracic regions, the entry point is more medial. The screw trajectory can then either be straight-forward, parallel to the vertebral body endplates, or follow the anatomical axis of the pedicle, though this has less resistance to pullout [78].

An awl is used to decorticate the bone. A ball-tipped probe or pedicle finder is then inserted into the hole, palpating through the softer trabecular bone in the pedicle into the vertebral body while ensuring that there is no breach in the cortical bone [67,78]. A drill can also be used to find the smoothest way through the pedicle, resulting in a smaller hole and the potential for multiple attempts for pedicle searches without damaging the pedicles. Lastly, the threads for the screw are tapped into the hole and a pedicle screw is inserted, followed by post-insertional confirmation of the screw trajectory using fluoroscopy [71].

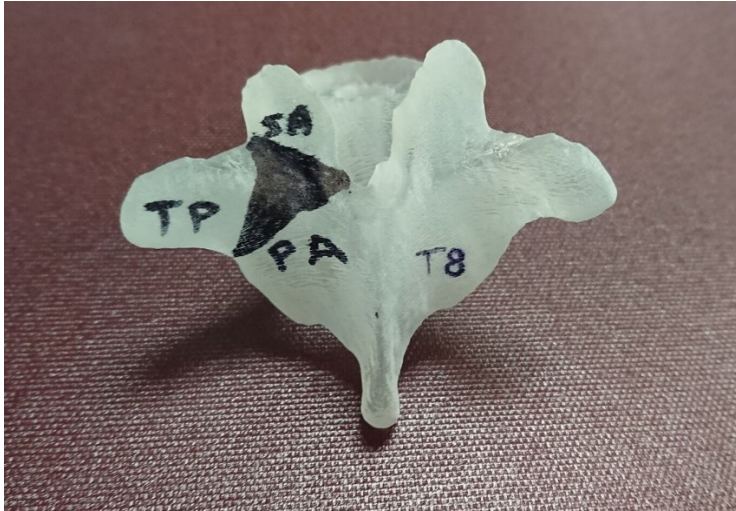


**Figure 2-7: Entry point landmarks for pedicle screw insertion (shaded region) on a 3D printed vertebra, SA: superior articular process; TP: transverse process; PA: pars interarticularis**

#### 2.2.6. Image Guidance Methods

Image guidance involves using intraoperative fluoroscopy during screw insertion or CT-navigation systems to determine screw position and trajectory during insertion. Both systems provide real-time feedback on screw trajectories and positions.

C-arm fluoroscopy allows for radiographs to be obtained in real-time, not requiring any image registration to localize anatomy. A bi-planar fluoroscopy can allow for two views to be seen at once. However, using a fluoroscopy machine continuously during screw placement results in a high amount of radiation exposure for both the patient and the surgical staff [79].

Fluoroscopy can also be combined with navigation systems intraoperatively. Any navigation system requires stereoscopic cameras, three or more reflective marker spheres attached to objects to be tracked by the cameras, and a computer platform to display motion captured objects [10]. In the case of fluoroscopy, the size and location of the fluoroscopic space is known and so the acquired images can be automatically registered and localized for the navigation system. Surgical tools are then tracked and displayed within the same virtual space, and the internal anatomy of the patient and the live position of surgical tools are displayed on a monitor [78,80–82]. Major benefits include improved anatomic accuracy due to the intra-operative nature of the images and tracking of surgical tools without the need for continuous ionizing radiation [79].

For CT-navigation, pre-operative or intra-operative CT scan is taken of the patient's spine, which uses manual landmarking of anatomy (paired-point registration or surface matching) in the pre-operative case

or using fiducial markers in the case of intra-operative systems [83]. For greater accuracy and because of the limited scan volume of intra-operative CT machines, only a few vertebral levels are registered at a time [79]. The on-screen anatomy is used to select the entry-point and the trajectory of the pedicle screw. Like fluoroscopic navigation methods, surgical tools are then tracked in 3D space to provide visual feedback of screw placement on the virtual model. Navigation does not provide actual real-time feedback of the anatomy and may be affected by breathing or slight shifts in the bony positioning [78]. A comparison of the various pedicle screw insertion techniques is shown in Table 2-3.

**Table 2-3: Comparison of benefits and drawbacks of screw insertion techniques**

	<b>Free-hand Methods</b>	<b>Fluoroscopy</b>	<b>Fluoroscopic Navigation</b>	<b>CT-Navigation</b>
<b>Benefits</b>	Fast, no special equipment required	Real-time guidance	Fast, automated registration	High quality tomographic images
<b>Drawbacks</b>	No visual feedback on pedicle trajectory	Ionizing Radiation	Ionizing Radiation Only 2D navigation Requires registration	Ionizing Radiation Most expensive equipment Requires registration

After screws are inserted, spinal segments are physically manipulated to correct their position and fixed to contoured metal rods. The sagittal and coronal balance of the spine as well as pedicle screw trajectories are then assessed based on intra-operative X-rays or visual inspection of the patient’s spinal curvature [3,84]. The position of screws post-operatively may also be assessed using CT scans [85–88].

### 2.2.7. Breach Rates and Complications

Screw insertion remains a major concern in causing potentially catastrophic neurologic complications in posterior fusion surgery. The accuracy of pedicle screw placement is most commonly assessed using a 2mm incremental method, with <2mm breaches considered acceptable [89]. The second most common classification is the ‘in’ or ‘out’ classification, where screws are allowed up to 25% screw diameter to be outside the pedicle to be considered still within the pedicle.

A systematic review of pedicle screw placement in the thoracic and lumbar spine noted breach rates of 6-31% using free-hand methods, compared to 15-72% using fluoroscopy, 0-11% using CT navigation and 8-19% using fluoroscopic navigation in posterior fusions [90]. A systematic review focused on adolescent thoracic scoliosis revealed a 4.2% malposition rate out of 14570 screws, though studies confirming screw malposition with CT scans noted a malposition rate of 15.7% [9]. However, the most important clinical

endpoint for screw insertion is the risk of complications, with breaches only being a potential predictor of complications. Screw-related complications from this study included twelve re-operations from misplaced or loosened screws, one pulmonary effusion from intrathoracic malposition, four dural leaks and one temporary neurologic deficit to a total of 18 complications from 1666 patients (1.08%) [9].

An analysis of the Scoliosis Research Society Morbidity and Mortality (SRS M&M) data in 2006 on 6716 AIS patients showed a 0.32% screw-related neurological complication rate with incomplete spinal cord injury in 0.21% of patients and an implant-related complication rate of 0.64% in posterior-only surgeries for AIS compared to an overall complication rate of 5.1% [91]. Updated data on 11227 patients with idiopathic scoliosis showed new neurologic deficit in 0.7% of patients, divided into 0.3% with nerve root deficit and 0.4% with incomplete spinal cord deficit, with 0.15% which did not have full neurologic recovery [7]. The most recent update on the SRS M&M showed neurologic deficits ranged from 0.23-0.37% from 2009-2012 [92]. A separate analysis on the Spinal Deformity Study Group data from 1301 surgical cases noted a 0.69% neural complication rate [93]. Aortic puncture has also been reported in posterior spinal fusion surgeries in general, which could potentially cause life-threatening bleeding [94]. Overall, while complication rates remain low, the potentially catastrophic consequences warrant further investigation into how to reduce breaches.

#### 2.2.8. Free-hand vs Image Guidance Comparison

The primary purpose of image guidance is to improve screw insertion accuracy. A systematic review on 8539 screws comparing navigation and free-hand methods for any-cause spine surgery revealed a risk ratio of 0.39 favoring navigation with moderate heterogeneity with an  $I^2$  of 49% [95]. Reduced breach rates were found at cervical, thoracic and lumbar levels individually. Another meta-analysis on pedicle screw accuracy focused on scoliosis surgery noted a pooled odds ratio of 0.44 in favour of image guidance vs free-hand methods, though with high heterogeneity ( $I^2=82.6%$ ) with similar correction rates [96]. One of the purposes of this thesis project will be to systematically review breach rates and complication rates specifically for AIS surgery.

The improved accuracy of image guidance does come at a cost however, as guidance systems are large, expensive and heavy, require longer operating room times and can interrupt the flow of the operation [80]. Both C-arm fluoroscopy and O-arm CT scanners are positioned to surround the patient on the operating table, requiring careful maneuvering to prevent disturbance of the sterile surgical field and interruption of the surgical flow. Multiple scans are often needed in the case of the O-arm due to the

short length of the CT scanner itself. Navigation methods require time-consuming manual registration processes prior to surgery to localize anatomy when using pre-operative CT scans [96].

Current guidance methods also expose patients and operative staff to ionizing radiation. The doses of radiation are generally higher for CT or fluoroscopy, particularly when generating a 3D spine, compared with free-hand methods which may only use plain X-rays to confirm screw placement [12,97,98]. Radiation exposure is more concerning for pediatric patients. One estimate showed that a typical abdominal CT examination resulted in an estimated lifetime risk of fatal cancer of 1 in 1000 [13–16,99,100]. Radiation scatter in the operating room is concern for staff as well when using fluoroscopy that requires staff to operate the machine in the room though the actual cancer risk remains unknown[100,101].

The cost effectiveness of image guidance has been reviewed, revealing that there are insufficient studies to accurately conclude on whether it is worthwhile [102]. Cost reduction primarily takes the form of lower re-operation rates with a ‘break-even’ point considered to be 8 patients prevented from being re-operated. A prospective study of 100 patients undergoing thoracolumbar image guidance surgery noted the cost savings for image guidance was \$71286 per 100 cases from a reduction of revision surgeries from 3% to 0% and was particularly useful for difficult or long cases [103].

Although guidance methods reduce pedicle screw breach rates, their usage remains controversial within the orthopedic and neurosurgical world. A non-ionizing guidance system would be useful to provide the same added accuracy while minimizing the excess bulk, cost, time and radiation that conventional guidance offers.

#### 2.2.9. Non-Ionizing Technologies to Improve Pedicle Screw Insertion Safety

Non-ionizing methods to assess pedicle screw impingement on nerves include neuromonitoring technologies, electrical conductivity devices and ultrasound imaging.

Spinal neuromonitoring is widely accepted as standard of care in optimal surgical treatment of scoliosis to detect screw impingement on nerves [3]. Electrodes are placed peripherally on the patient’s arms and legs, as well as on the motor cortex on their head. A neurophysiologist can then either stimulate sensory or motor nerves and determine the time of conduction from limb to brain to detect damage to a nerve [104]. Neuromonitoring has been shown to be highly sensitive and specific in detecting physical impingement of the screw on the spinal cord or nerve roots that may lead to neural injury. However,

neuromonitoring requires extra personnel and equipment to monitor neural signals and is only able to prevent neural injury when damage is detected.

A handheld electrical conductivity device has been developed and is commercially available to determine if a breach has occurred. By inserting this device into a reamed hole through the pedicle [105,106], a breach can be detected by using the difference in conductivity in bone versus soft tissues while the guide hole is being reamed, potentially preventing impingement of a nerve. However, this method has not been widely adopted due to the higher sensitivity and specificity of neuromonitoring in detecting nerve damage.

A similar device that physically detects breaches uses cylindrical ultrasound transducer inserted into the reamed hole in the pedicle. The device images and detects if it is contacting soft tissue rather than bone, similar to the electrical conductivity device [18]. However, this method neither provides guidance for screw insertion, nor does it functionally determine if a breach has damaged a nerve.

Conventional ultrasound imaging has also been explored as a potential guidance method to visualize the path through the pedicle in real-time during insertion. Phased array ultrasound was evaluated to determine the optimal frequency to provide adequate resolution to determine the thickness of cortical bone at the pedicle [107]. The difference in cortical thickness measurements between micro-CT and ultrasound was found to be 0.4-0.5mm, with the 5 MHz ultrasound probe. However, the deep internal structures still could not be adequately visualized for pedicle screw insertion.

Another study on using surface ultrasound -CT registration methods for spinal fusion shows promise in overlaying spinal ultrasound images on top of CT scans with the eventual goal of providing image guidance [17,108]. However, an integrated system combining conventional motion capture systems with handheld ultrasound along with visualization of screw trajectories has not been completed. Specifically, the accuracy of screw insertion in such a system has not been evaluated.

### 2.3. Technical Background for Image Guidance for Scoliosis Surgery

The technologies required to provide image guidance include motion capture and imaging techniques including ultrasound, CT or MRI. From a software perspective, the critical components of a navigation system include reliable position and orientation tracking of the ultrasound transducer and surgical tools, image processing techniques to enhance images, image registration and a 3D visual display environment. These topics will be discussed in this section.



### 2.3.1. Motion Capture Hardware

One of the key technologies used in navigation guidance is 3D tracking. Three common methods of tracking objects in 3D space include mechanical, electromagnetic and optical methods [109]. Mechanical methods involve attaching the tracked object to a physical arm with encoders that can determine the location of the object. Accuracy can be very high, though hysteresis errors can result due to the mechanical nature of the encoders and usage is cumbersome due to being attached to a mechanical arm. Electromagnetic methods involve mounting an electromagnetic receiver on a tracked object that measures induced electrical currents in a magnetic field generated from a stationary transmitter. However metallic objects in proximity to tracked object can distort the field resulting in tracking inaccuracies, and accuracies are generally not as high as optical tracking [110,111].

Lastly, optical methods use multiple cameras that record the position markers mounted to the tracked object to determine their position [109]. Optical tracking has been the prevailing modality for 3D tracking in the surgical suite because of its high accuracy, low invasiveness and compatibility with metallic equipment, though it does require line-of-sight and false markers can be captured from objects with high reflectivity.

Motion capture technology involves four main components: a capture volume, at least two cameras, motion tracking markers, and an acquisition system. The capture volume must be large enough for adequate distance for multiple cameras to visualize the markers. In a surgical suite, cameras are often ceiling mounted to provide a birds' eye view of the surgical field. The cameras emit infrared light into the capture area which reflects off spherical reflective markers back to each camera. The markers are detected as circular reflections in each camera. The size and location of each marker in each 2-dimensional field of view is used to project the 3-dimensional position of the markers in 3D space by synchronizing the images from each camera together [112–114]. To track orientation, three or more markers need to be mounted to an object and be tracked as a single object. There are also active markers which emit infrared light to minimize false markers being tracked.

The quality and accuracy of motion capture is affected by the type and position of the cameras, the size of volume that is being tracked, size of markers being tracked, and the quality of the calibration process of the cameras [112,114–116].

### 2.3.2. 3D Position and Orientation Mathematics

Optical motion capture technology is part of a subset of stereophotogrammetry and computer vision technologies, to make 3D measurements from 2D images. While other technologies may capture all the visible structures in a field of view, motion capture maximizes real-time accuracy by only allowing infrared light reflected off or emitted by markers mounted on a tracked object minimizing the density of spatial information returning to the cameras. Spherical markers are used as an easily detectable shape (a circle) in each camera. However, before markers can be tracked accurately, the position and orientation of the cameras relative to each other must first be determined.

This is done by tracking a rigid body that includes three markers that are mounted at a known distance from each other, known as a calibration wand. Each camera uses the size of the markers to estimate the depth position or distance the cameras are from the markers, and the relative position of the markers to determine camera orientation, lateral and vertical position. The 3D point can be projected onto the 2D planes of each camera using a projection matrix that includes information about the camera position and orientation, as well as intrinsic properties including focal length, image center, aspect ratio and lens distortion [117,118]. Mathematically, the transformation follows Equation 2-1[118]:

#### ***Equation 2-1: Motion Capture Camera Transforms***

$$P_I = T_{Int} * T_{Ext} * P_W$$

Where:

- $P_I$  is the coordinates of the image points (x,y,1)
- $P_W$  is the real-world location in three dimensions (X,Y,Z, 1)
- $T_{Int}$  is the transformation matrix for the intrinsic properties of the cameras
- $T_{Ext}$  is the transformation matrix for the extrinsic properties of the cameras (position and orientation of the cameras)

For the intrinsic properties, all points on the 2D plane of the cameras are linearized into projections in the 3D space and the 2D-to-3D transform is inherent to the camera. The extrinsic properties need to be calibrated with every change in camera position. Accuracy is enhanced by using more than one camera to provide improved depth perception and to compare the 3D projection of tracked markers between cameras. Based on a series of these images being recorded together, the camera position accuracy is refined. Once the position and orientation of each camera has been established, motion capture of a variety of capture markers can be undertaken.

A calibration square needs to be placed in the capture volume to define the X, Y and Z axes. The markers themselves are labeled to allow motion tracking of the positions of each marker. If a marker is occluded in the field of view of one camera, the extra cameras can continue tracking the marker.

Orientation of an object can only be tracked when three or more markers are placed on the object to form a plane. Orientation in three dimensions are represented by Euler angles, orientation matrices, and orientation quaternions. Euler angles determine orientation as a series of three rotations that are orthogonal to each other: roll, pitch and yaw (Figure 2-8: Euler angle representation of orientation with  $\alpha$  as the angle between X and N (reference) axis,  $\beta$  as the angle between z and Z axis, and  $\gamma$  between the N and X axes). This is an intuitive and readily visualized method of representing orientation. However, their robustness as a measure of orientation runs into issues when the rotations are large enough to overlap orthogonal planes, an issue known as Gimbal lock [119]. Combining multiple changes in orientation is cumbersome when using Euler angles because of changing coordinate systems with each rotation.

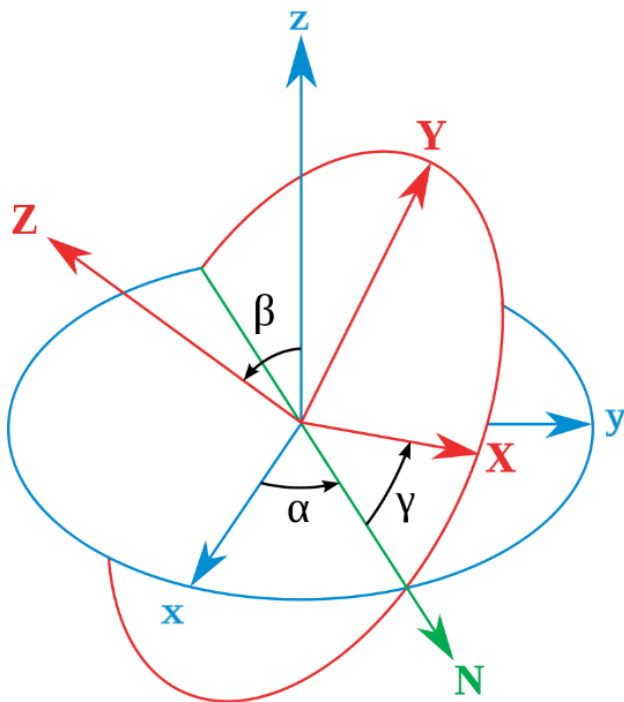


**Figure 2-8: Euler angle representation of orientation with  $\alpha$  as the angle between X and N (reference) axis,  $\beta$  as the angle between z and Z axis, and  $\gamma$  between the N and X axes**

Rotation matrices are a subset of transformation matrices which may include translation, reflection, scaling and shear. In the case of rigid bodies in the three-dimensional world, the four matrices in Equation 2-2 may be used to translate and rotate any given position column vector:

**Equation 2-2: Transformation Matrix Multiplication**

$$\begin{bmatrix} 1 & 0 & 0 & 0 \\ 0 & \cos \theta_x & -\sin \theta_x & 0 \\ 0 & \sin \theta_x & \cos \theta_x & 0 \\ 0 & 0 & 0 & 1 \end{bmatrix} \begin{bmatrix} \cos \theta_y & 0 & \sin \theta_y & 0 \\ 0 & 1 & 0 & 0 \\ -\sin \theta_y & 0 & \cos \theta_y & 0 \\ 0 & 0 & 0 & 1 \end{bmatrix} \begin{bmatrix} \cos \theta_z & -\sin \theta_z & 0 & 0 \\ \sin \theta_z & \cos \theta_z & 0 & 0 \\ 0 & 0 & 1 & 0 \\ 0 & 0 & 0 & 1 \end{bmatrix} \begin{bmatrix} 1 & 0 & 0 & x \\ 0 & 1 & 0 & y \\ 0 & 0 & 1 & z \\ 0 & 0 & 0 & 1 \end{bmatrix}$$

**Rotation in X**
**Rotation in Y**
**Rotation in Z**
**Translation**

Multiplying the rotation matrices in series is representative of multiple Euler angle transformations, allowing for ease of transformation of column vectors. However, the same ambiguities in rotation that are present in Euler angle representation are found in rotation matrices. Rotation matrices are also difficult to visualize.

The last and most robust form of representing rotations take the form of a quaternion. Because any sequence of rotations can be considered equivalent to a single rotation, quaternions represent orientation using a single angle and a single unit vector. Orientation quaternions take the form of Equation 2-3:

**Equation 2-3: Quaternion Rotation Notation**

$$q = \cos \frac{\theta}{2} + (u_x \mathbf{i} + u_y \mathbf{j} + u_z \mathbf{k}) \sin \frac{\theta}{2}$$

Where:

- $q$  is the quaternion
- $\theta$  is the angle of rotation
- $u_x, u_y, u_z$  are the coefficients for the unit vector axis of rotation.

A detailed analysis of quaternions is beyond the scope of this thesis. In short, the  $u_x, u_y$  and  $u_z$  terms can be used to represent a direction vector, while the fourth term in the quaternion equation describes the roll of the vector about that direction vector, similar to an axis-angle representation of direction. The additional term allows quaternions to be more robust in representing specific orientations than either Euler angles or rotation matrices, while also being more efficient to calculate and interpolate, having only four terms vs nine in a rotation matrix. However, although calculation of a quaternion is simple, the numerical values of quaternions are difficult to visualize in the real world when compared with Euler angles [120]. Conversion between Euler angles, rotation matrices and quaternions can be done readily, so a combination of the three will be used throughout this project [121].

### 2.3.3. Motion Capture Accuracy

Motion capture systems have been used extensively in gait analysis, providing accuracy of within 1% error for 120 mm translations [122]. Optical navigators on passive markers for surgery have been evaluated to have errors of between 0.2-1.9mm through a variety of methodologies including in industrially verified phantoms and electrode positioning for deep brain stimulation [111,123,124]. Angular accuracies of screw insertion from navigation systems were  $<3^\circ$  in two *in-vivo* studies using post-operative CT scans to confirm screw position [11,125]. Active markers have also been tested, with translational error calculated as 0.06 mm and rotational at  $5.05^\circ$ [126]. Navigation using optical tracking compared with image registration of CT scans found registration errors of 0.5-3mm in cadaver and human studies [127,128].

Since the positional accuracies vary widely depending on the setup [113,114], it is important to optimize and evaluate conventional motion capture in the surgical suite in developing an image guidance system. The required theoretical accuracy of navigation systems was found to be less than 1mm and  $5^\circ$  by Rampersaud et al., when considering screw trajectories in 3D space [129]. While good accuracy has been achieved by commercially available navigation systems, the question remains whether more inexpensive and flexible motion capture camera systems can be used in navigation with equivalent or better accuracy.

### 2.3.4. Ultrasound Physics

Medical ultrasound uses high frequency sound waves above 20 kHz to generate images of internal organs in human anatomy [130]. Applications range from echocardiography to obstetrical assessment to abdominal diagnoses.

Ultrasound scanners usually involve four components: a transmitter or pulser to energize the transducer, an ultrasound transducer, a receiver to detect the reflected signal from the transducer, and a display that can present the images [131]. Transmitters send an alternating electrical signal to the transducer which has an array of piezoelectric crystals that expand or contract according to the voltage of the signal. The high frequency vibrations of the crystal are transmitted into the tissue being imaged by direct contact. Typically, an ultrasound transducer is placed on a patient's skin with acoustic coupling gel to ensure good contact between the transducer and skin. Sound waves are transmitted through the patient's soft tissues and reflected back to the transducer when there are different acoustic impedances between media. Depth is mapped according to the time at which signals are received by the transducer, with signals that require longer to return being deeper [131]. Medical ultrasound assumes a constant speed of sound to calculate distances, requiring adjustment when imaging in a water-based medium (1480 m/s) compared with a soft tissue medium (1540 m/s).

As the vibrations move through the medium, the reflected signals that return to the transducer are detected by the crystals as small amplitude vibrations. The signals are converted into an electrical signal and amplified. An array of crystals can be combined across the transducer surface to generate a 2-dimensional “brightness mode” (B-mode) image that converts the amplitude (A-mode) depth-map of each transducer, into a gray-scale image (Figure 2-9: Sample B-mode 2-dimensional image of a vertebral phantom and corresponding landmarks on plastic phantom)

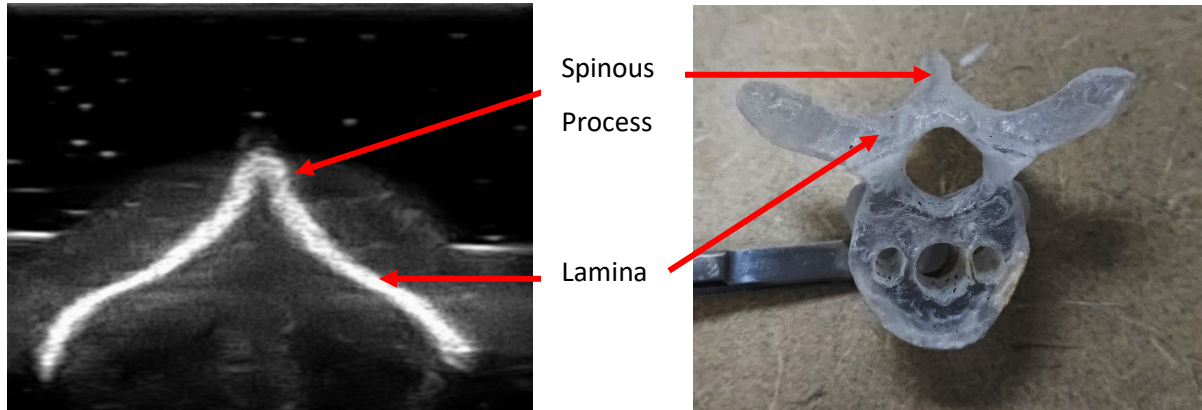


**Figure 2-9: Sample B-mode 2-dimensional image of a vertebral phantom and corresponding landmarks on plastic phantom**

Because multiple piezoelectric elements are used to generate and detect signals, the focal point of this beam can be changed by controlling the timing of firing piezoelectric elements, which can affect the lateral resolution of images captured by the transducer [131]. Axial resolution on the other hand, is affected by the frequency of ultrasound being used, with higher frequencies allowing for higher resolutions, but being attenuated more readily.

The amplitude of the reflected signal is stronger when the acoustic impedance between two different media is greater, under Equation 2-4:

**Equation 2-4: Reflectivity from Acoustic Impedance**

$$R = \left[ \frac{Z_1 - Z_2}{Z_1 + Z_2} \right]^2$$

Where:

- R is the proportion of incident sound waves that are reflected,
- $Z_1$  is the acoustic impedance of the first medium (Rayls) and
- $Z_2$  is the acoustic impedance of the second medium (Rayls)

Bone has a high acoustic impedance of  $7.8 \times 10^6$  Rayls compared to soft tissues at  $1.34\text{-}1.71 \times 10^6$  Rayls, and water at  $1.65 \times 10^6$  Rayls resulting in a strong contrast at soft tissue-bone or fluid-bone interfaces[132]. The reflection from these interfaces is called specular reflection [133]. In contrast, diffuse reflection typically come from reflections throughout the structures within a soft tissue such as liver or kidneys resulting in greyscale reflections rather than the strong white reflections from a specular reflection. The incident angle also affects reflection strength, with ultrasound signals ideally being perpendicular to the reflecting surface [131]. Interfaces that are not perpendicular may reflect the ultrasound signal away from the transducer. While medical ultrasound imaging is usually used to image soft tissues, bone imaging resulting in specular reflections has recently become a greater topic of interest [17,108,134].

One of the key challenges in obtaining measurements from ultrasound is that the acquisition of ultrasound is user dependent. Unlike X-rays or CT scans which give a static snapshot of what is being imaged, ultrasound is often taken as a video, as a different position and orientation results in variations in the imaged geometry and different artifacts. In the case of imaging bony surfaces, the sharpness of the reflected surface varies, resulting in different reflection intensities coming from the same surface when performing reconstructions.

### 2.3.5. 3D Ultrasound

Ultrasound can be extended into the third dimension through two methods: conversion of 2D images into 3D images using position and orientation information, or using a 2-dimensional ultrasound probe [135]. The first method involves using the same motion capture technologies mentioned previously to track the ultrasound transducer in 3D space. 3D ultrasound also includes image-based sensing, determining the relative position of the probe by analyzing the features on the images themselves, though this method is not highly accurate [135].

Two-dimensional arrays have transducer elements axially and laterally to obtain a volumetric scan [136]. However, significant challenges remain in acoustic impedance matching to minimize reflection of received signals and building arrays with a large enough field of view to be useable clinically. As a result, 2D image conversion to 3D volumes using motion tracking remains the more common form of 3D ultrasound imaging [135].

Volumes need to be reconstructed in an accurate and timely manner to be used clinically. Voxels can be reconstructed using voxel-based methods, pixel-based methods, and function-based methods [135,137].

Voxel-based methods traverse each voxel in the image volume and fill the voxels based on the pixels whose positions are calculated from the trajectory and position of 2D ultrasound image slices. Interpolation can be done by estimating the trajectory and position of regions between 2D slices and populating the voxels based on these estimates. Redundant samples of a voxel can either be averaged together or the higher intensity sample being used for the voxel.

Pixel-based methods are the most common, traversing pixels in the B-scan 2D images and filling their corresponding voxels. The pixel value is transferred to the nearest voxel in the volume, while if multiple pixels run through one voxel, its average, maximum or most recent value can be used. Kernel-based algorithms may introduce a local region around the pixel to then populate the nearby voxels [138,139].

Lastly, function-based methods choose a function and uses pixel values and relative positions of these pixels to determine the coefficients of the function to interpolate the volume [135]. The speed of the algorithm can be increased by dividing the volume into smaller sections (resulting in a sequence of functions) or by reducing the resolution of the voxel volume for initial function estimates and then increasing resolution on next iterations for fine-tuning.

Processing time is an important limiting factor for image reconstructions, with interpolation, usage of Kernels or functional methods using more computational power than the nearest-neighbor method [135]. Reconstruction speed also depends on the number of images and the size of the volume being processed. Lastly processing speed plays a role in reconstruction time, with speeds of 0.03s per image having been achieved for pixel nearest-neighbor method on computers 10 years ago [135]. Optimized Kernel-based methods can achieve similar speeds on modern multi-core GPUs with better smoothing and interpolation between frames [135,140].

Calibration of 3D ultrasound is the process of finding the transform between the tracking marker's pivot point to the transducer surface itself. While the translational transform can be readily acquired by simply measuring the pivot position to the transducer surface, more precise transforms can be found by scanning calibration blocks including cross-wires, Z-fiducials or wall phantoms [109,141,142]. Cross-wires and Z-fiducials involve scanning thin wires that appear as points on the ultrasound image. The distance of the points is known, allowing for back-calculation of the position and orientation of the transducer. Wall-phantoms involve scanning a wall to produce a line on the ultrasound image to calculate the position and orientation of the transducer. With automated calibration, errors can be reduced to sub-millimetre levels



[143]. Temporal calibration is also an important aspect to consider, aligning motion capture data with ultrasound imaged frames [109].

### 2.3.6. 3D Ultrasound Imaging Accuracy

Most of the accuracy evaluation of 3D ultrasound involves determining the dimensional accuracy of volumes or structures. Mechanical encoders were the first 3D ultrasound machines to be evaluated, providing accuracies within 13% error [144]. Using a mechanical fanning encoder, Partik et al. found mean absolute volumetric deviations of 18.5% or 31 mL on a 168 mL kidney, equivalent to a 31mm linear error [145]. Ioannou studied the surface area of phantom fetal fontanelles using a mechanical 3D transducer showing a median percent error of 0.6-12.1%, or 2-3.4mm [146]. The volumetric accuracy of an optical surface encoder on a 2cm agar rod showed a volumetric error of 181mm<sup>3</sup>, or 5.65mm linearly in a study by Poulsen et al. [147]. Inaccuracies in these studies were attributed to limitations in the positional encoder degrees of freedom and potential inaccuracies in the 3D rendering algorithms

In these cases, the equivalent linear accuracies would be distributed throughout the entire volume or surface, thus the linear error may be smaller. In surgical registration, the actual position of the tissues being imaged is more important than the surface area or volume being reconstructed. Processing time, image accuracy and image quality need to be balanced for each given application [137]. Bony surfaces can be readily segmented from soft tissues within the saline bath to reduce processing times. However, accuracy of such a system still needs to be explored.

### 2.3.7. CT and MRI Tomographic Imaging

While a detailed overview of CT and MRI imaging is beyond the scope of this project, the basic acquisition and segmentation of images from these modalities is important to understand for image registration.

Both Computed Tomography and Magnetic Resonance Imaging are considered tomographic imaging modalities, meaning the 3D anatomy is sliced into sections [148]. Computed Tomography (CT) scans use an X-ray scanner mounted on a rotating gantry that images the patient from multiple angles to reconstruct anatomy. A 3D image is obtained by translating the gantry axially to produce multiple slices that represent the patient. Contrast depends on the amount of X-ray absorption, with highly dense materials like bone absorbing the most, contrasting strongly with neighboring soft tissue.

Magnetic resonance imaging (MRI) involves subjecting the body to strong magnetic fields to align hydrogen atoms in the body and then release the alignment. The different rates of decay resulting from unalignment of these atoms of different tissues allows for tissue contrast. This allows for excellent soft

tissue contrast to identify structures. While segmentation of bony vertebral bodies has been completed, developing an automated, fast and reliable method to isolate vertebrae from MRI continues to be a challenge being studied [149]. Detailed image processing and segmentation of either CT or MRI spines is outside the scope of this thesis. Pre-segmented 3D images will be registered to the 3DUS surfaces.

### 2.3.8. Image Processing

While the CT scans used in the present study will be pre-segmented and processed, the ultrasound scans require image processing including noise removal and image segmentation of bone to convert ultrasound images into useable formats for registration [150]. Two major sets of image processing methods were tested for this thesis project: image filters and morphological image processing.

Image filters are used to emphasize or filter out features from images. Contrast enhancement, median filtering, averaging blurring, and binarization were tested and applied in this project. Additional filters including edge detection and morphological image processing were tested, though these would not be used in the final system, as outlined in Chapter 5: .

Median and averaging filters reduce noise and smooth edges for improved edge detection [151]. Median filtering involves analyzing small regions of interest of a pre-determined pixel size and replacing the center value with the median of that region. Median filtering removes noise while retaining the original image edges. Averaging blurring is the simplest of the smoothing filters, taking a certain pixel region and replacing the center value with the average, resulting in less noise but more ambiguity on image edges.

Contrast enhancement is a form of gray-level mapping, where the original gray-level values are mapped to a new gray-level map [151]. For this project, contrast stretching is performed, where the dynamic range of the image is reduced, resulting in full saturation for high saturation pixels, no image for low saturation pixels, and a more dramatic contrast for the regions between the upper and lower thresholds. Binarization is an extreme form of contrast enhancement, where a threshold is set to determine which saturation of pixels will be mapped to maximum and which to zero saturation. Mapping pixels to zero saturation can be applied early to reduce the number of pixels that need to be transformed during reconstruction.

Morphological processing alters images based on the other shapes neighboring region. Basic operators include erosion, dilation, opening and closing (Figure 2-10: Morphological processing (a) erosion, (b) dilation, (c) opening, and (d) closing using a circular structural element. Dark blue represents original shape while light blue represents the borders of the new shape. Closing shows union of two squares. (Renatokeshet, 2008)) [152]. In all cases, a small structuring element is used to probe the image. Erosion

reduces the size of image features while dilation expands the size of image features, according to the shape of the structuring element. Different shapes can be used, though circles are most used to evenly erode or dilate the image in all directions. Opening involves an erosion, followed by a dilation while closing involves a dilation followed by an erosion which allows retention of shape size, while smoothing or connecting edges.

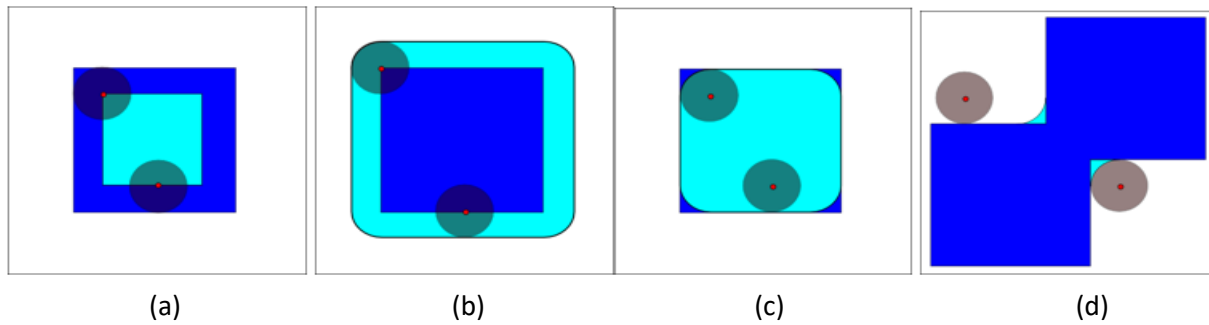


**Figure 2-10: Morphological processing (a) erosion, (b) dilation, (c) opening, and (d) closing using a circular structural element. Dark blue represents original shape while light blue represents the borders of the new shape. Closing shows union of two squares. (Renatokeshet, 2008)**

Another common morphological technique is the top-hat filter. The filter is used to equalize nonuniformity in intensities of background regions due to different angles of reflections coming from the vertebral surface. The difference between the input image and the morphologically “opened” image, resulting in patterned background noise being filtered out. Surface reflections become brighter throughout the entire image rather than only near the ultrasound beam focal point, providing a better source image for contrast thresholds to be enacted. A sample image is shown in Figure 2-11: Top-hat filter removing background artifact on ultrasound image, (a) shows the original while (b) is the filtered image..

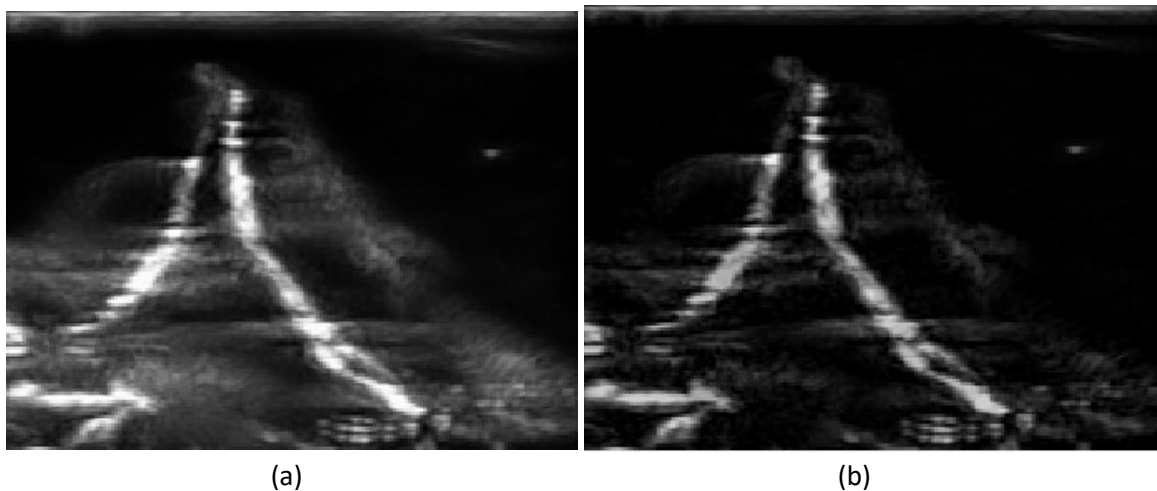


**Figure 2-11: Top-hat filter removing background artifact on ultrasound image, (a) shows the original while (b) is the filtered image.**

Edge detection identifies points in an image where the image intensity changes significantly in order to identify structures. The Canny edge detection involves applying a Gaussian filter to the image to reduce noise and smooth the image, finds intensity gradients in an image to determine regions, thins the resulting edges, filters remaining edge pixels that may represent a weak gradient value, and then tracks the edge connections to produce a smooth and continuous surface.

For all these filters, the order of operations is important, as each sequential step alters the effects of the next operation. After image processing, the binarized ultrasound scans would be used for image registration to minimize file size and processing times.

#### 2.3.9. Volumetric Image Registration

Image registration is the process of spatially aligning two different images of the same scene [153]. In the medical field, images from different modalities can be overlapped to provide additional clinical information [154]. The most prominent example of this is registration of functional imaging modalities such as Positron Emission Tomography (PET) and Single-Photon Emission Computed Tomography (SPECT) with anatomically accurate tomographic modalities including MRI and CT scans, allowing localization functional information to high resolution anatomical images [155–158]. An example is shown in Figure 2-12: Image Registration of CT and PET Scan (Myohan, 2009).

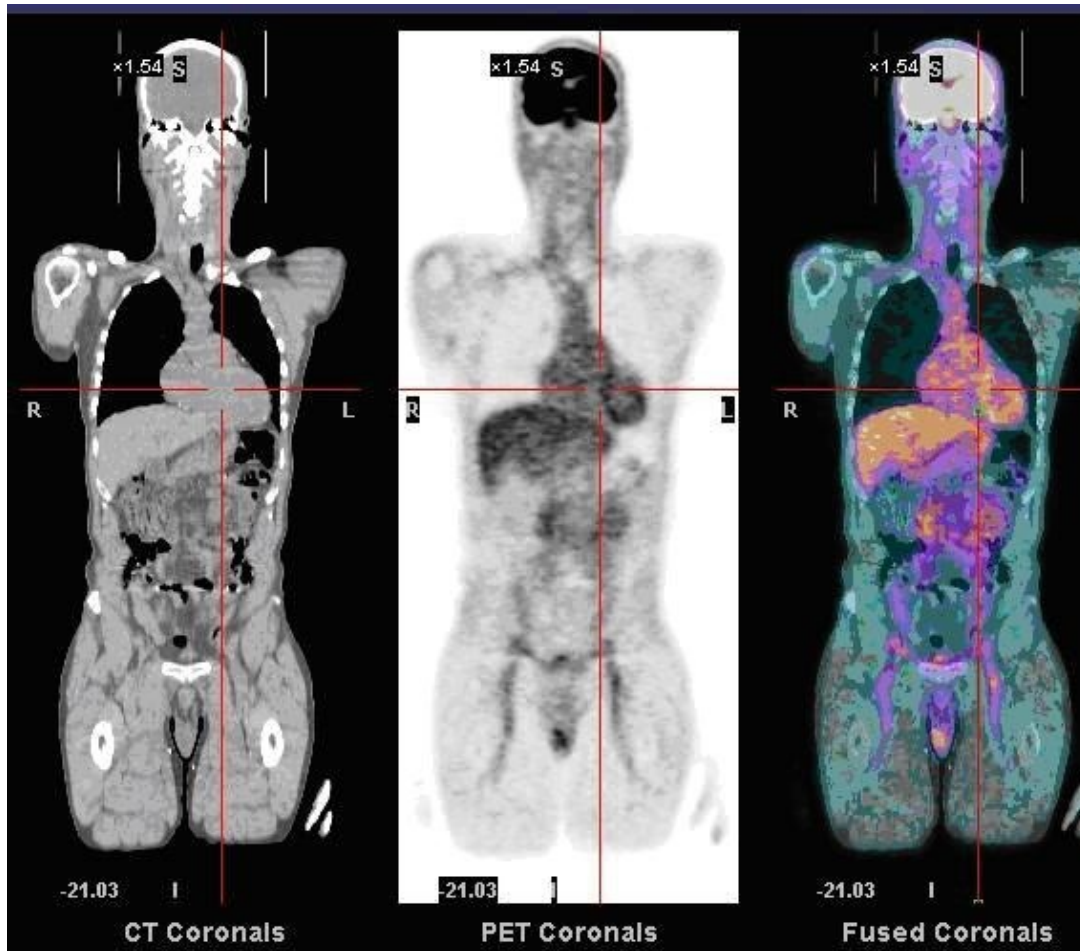


*Figure 2-12: Image Registration of CT and PET Scan (Myohan, 2009)*

Image registrations differ from surgical registrations. While image registration refers to the accuracy of registering two images, surgical registration refers to the accuracy of registering virtual anatomy to the real-world surgical field. Both are important in this project, though a good surgical registration would not be possible without an accurate image registration.

Registering CT images to ultrasound images presents a unique challenge, because ultrasound scans are performed in different orientations, whereas CT images are regularly spaced and uniformly aligned. Ultrasound images are also scan-dependent, with images changing between scans. However, ultrasound images of bony surfaces typically have high contrast, as do CT scans, allowing them to be registered together more easily as binary images.

The two main methods in image registration for grayscale images include landmark-based registration and intensity-based registration [159]. Landmark-based registration requires detection of features in the image to act as anchor points to register. The landmarks in the two images are then used to find the best

geometrical transformation to align these landmarks. Features can be automatically detected or manually probed [127,154,160]. Intensity-based registration is an iterative process where images are transformed and an image similarity metric is used to determine how similar the overlapping images are [161].

The type of transformation is an important factor in image registration speed. Linear transformations are the most basic type, involving transforming the entire volume in rotation, translation, scaling, reflection or shearing. A sample of these transformations in two-dimensions is shown in Figure 2-13.

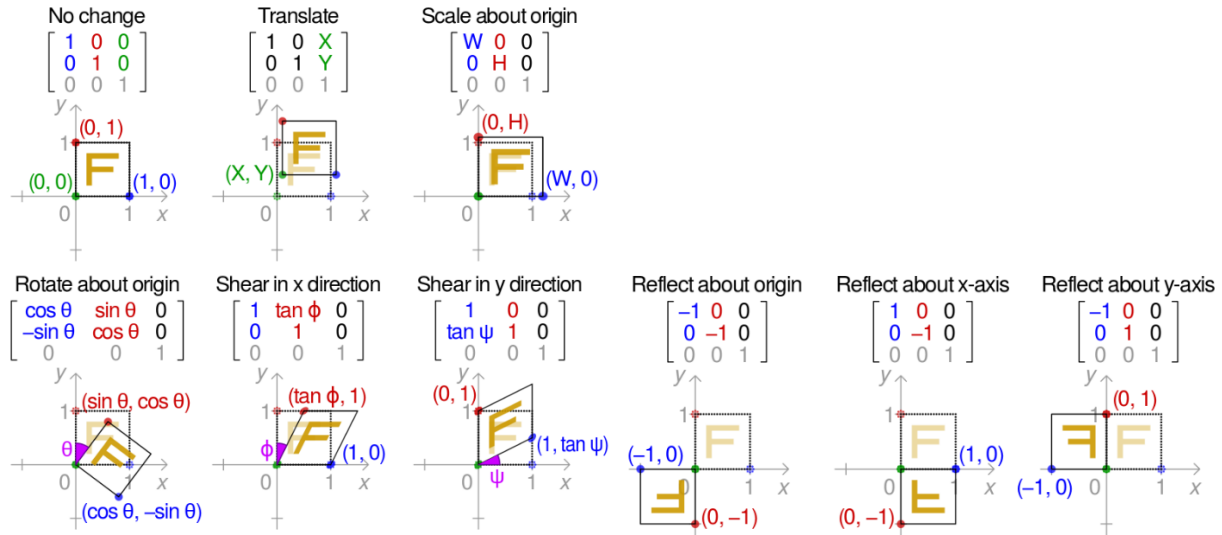


**Figure 2-13: Translation, scaling, rotation, shear and reflection transformations for 2D images (Cmglee, 2016)**

Non-rigid transformations can locally warp regions for a better match. Many non-rigid transformation tools exist for different purposes which are beyond the scope of this thesis [162]. A simpler form of linear registration is rigid registration which only includes rotation and translation in the transform by assuming that the object is non-deformable [163].

After each iterative transformation, the similarity between images needs to be evaluated. Common methods include the sum of squared error of intensity differences, mutual information and structural similarity index. Sum of squared error of intensity differences involves overlapping the two images and calculating the error in intensity between each overlapping pixel and then calculating the sum of all the errors over the image. It is the simplest optimization metric, with a smaller number indicating better registration. Mutual information is a measure of the dependence between two variables, determining how knowing one variable may reduce uncertainty about the other [164]. In image registration, a greater mutual information means that the pixels in the two images are highly dependent on each other,

indicating a good registration. The structural similarity index was historically used to predict the quality of output television images compared to original uncompressed images as a replacement for mean-squared error [165]. The similarity of the images is analyzed in a windowed approach according to luminance, contrast and structure of the images, with ideal similarity giving a score of one and no structural similarity yielding a score of zero. Each metric would be tested during the image registration evaluation portion of the thesis project.

#### 2.3.10. Surface Image Registration

In addition to more traditional volumetric image registration algorithms, surface registration algorithms have also been developed, the most common one being the Iterative Closest Point (ICP) registration algorithm [166].

Rather than volumetric data, the ICP algorithm uses point clouds of the two volumes. The vertices of the moving point cloud are mapped to the vertices of their nearest neighbors on the fixed volume and the transformation that minimizes the mean-squared distance between the vertices is calculated. The algorithm is iterated to determine if a better transformation could be applied which further minimizes the mean-squared distance. The algorithm stops when the difference in error levels reaches a certain threshold. [167,168].

As part of the ICP algorithm, the data needs to be down-sampled to improve the speed of registrations. Grid averaging is often used, which divides the volume into a grid of known size and averaging the positions and normal vectors of the points within that grid. Outliers can also be removed to prevent them from skewing the registration mean squared error results.

Importantly, the ICP algorithm converges to the nearest local minimum, requiring that the initial estimate be somewhat close to the optimized position [169]. A combination between volumetric and surface registrations would be needed to quickly and reliably register the CT and 3D ultrasound surface images. Volumetric registrations could pre-align the images, according to the features and geometry of the vertebrae, and surface registration could fine-tune the registrations.

#### 2.3.11. Image Registration Speed and Accuracy

Three factors in spinal 3DUS facilitate the speed of registration. First, the high acoustic contrast between bony surfaces and the saline medium allows for binary images to be registered rather than grayscale images, significantly reducing the number of pixels needed to be transformed. Secondly, because images are binary, interpolation in grayscale is not required to facilitate the registration. Lastly, bony surfaces are

rigid, allowing for just rotation and translation to be performed to transform the moving image [154]. However, because of the sparse dataset that arises from these binary images that only contain a thin surface, a custom transformation algorithm needed to be developed to allow a global minimum to be reached during registration.

Image registration accuracy of bony tissues has been evaluated in the past. Registration of the ultrasound spinal scans onto CT scans have been able to achieve accuracies of within 2.5mm with calculation times of less than five seconds [170]. Penney et al. registered ultrasound to CT scanned femurs, finding a mean RMS errors of less than 2.3mm on most registrations [171]. Yan et al. developed a spinal ultrasound-CT registration method achieving median registration errors of 0.66mm on phantoms and 1.65mm on a porcine model for 4 minute registrations, showing that soft tissues may complicate the usage of 3D ultrasound for spine surgery [17]. Koo et al. studied ultrasound to MRI registration of human lumbar dry bone specimens and porcine specimens, finding accuracies of 1.22mm on the human bone and 2.57mm on porcine cadavers [172].

For surgical registration accuracy, a study by Holly et al. revealed a navigation error of 1.3-1.4mm and a computed registration error of 0.5-1.2mm on embalmed human spinal specimens when using the spinous process, laminae and already inserted screws as landmarks [127]. Another study on cadaveric dry bone lumbar spines found an accuracy of 0.96mm and 0.91° when using fiducials to register the spine [173].

In summary, image registration has been used between ultrasound images and CT images. However, while some studies may have a high registration speed, their accuracies were not adequate for surgical use. Other studies may have higher accuracies but their speed remains outside the useful range for surgery. A system that satisfies both criteria is needed.

#### 2.3.12. 3D Environment Display

The final component of the system is the 3D visual display for the navigation system. A variety of tools are available to display 3D models of anatomy and motion captured tools in a virtual environment. The primary driving factor in selecting the environment was compatibility with the motion capture cameras. The position and orientation data from motion captured tools are streamed directly to the environment and attached to objects created in the environment to represent those tools. Similarly, the registered position and orientation of the vertebra would be applied to the 3D model of the vertebra in the virtual space to place it in the correct position.



Ease of programming and minimal streaming latency were additional factors in selecting the environment. Matlab's Virtual Reality environment, Unreal Engine and Unity were all potential display candidates. The process in selecting the environment will be outlined in Chapter 7: .

#### 2.4. Section 2.4: Conclusion

Any biomedical engineering project involves the intersection between the medical context and the technical requirements of the application. For this thesis project, an understanding of the strongest medical evidence related to screw misplacement and image guidance is required to justify the development of any surgical guidance system. A systematic review with meta-analysis is undertaken in Chapter 3: to produce this justification. Each subsequent section will then build upon the next in ensuring an accurate and fast guidance system. Motion capture accuracy will be evaluated in Chapter 4: , followed by 3D ultrasound reconstruction and localization accuracy in Chapter 5: , and then image registration accuracy in Chapter 6: . Further justifications for the motion capture configurations, 3D ultrasound reconstruction algorithms, image registration algorithms and registration evaluation metrics will be given in these sections. Chapter 7: will bring the errors in each step together to determine if the combined errors (and combined processing times) of each technical component of the system are low enough to be applied in the surgical suite.

## Chapter 3: Systematic Review and Meta-Analysis of Image Guidance in Pedicle Screw Insertion<sup>1,2</sup>

### 3.1. Overview

This chapter reports the results of two systematic review searches and a meta-analysis of breach and screw-related complication rates in AIS surgery comparing free-hand methods and image guidance methods. Section 3.2 outlines the objectives of both systematic reviews. Section 3.3 provides the methodology of the two systematic reviews while Section 3.4 presents the results which summarizes the most recent systematic review. Section 3.5 is a discussion on the clinical relevance of the evidence and lastly, Section 3.6 summarizes the results, makes recommendations for future study and outlines how the clinical evidence motivates the current study.

The starting point of determining the need for new medical technology must include an assessment of the current evidence of standard practice. When assessing standard practice, expert opinion articles or mechanistic studies form the base of the evidence hierarchy as the highest risk of bias group, followed by case studies and cross-sectional studies. Cohort studies and randomized controlled trials are higher on the hierarchy by selecting a representative sample population, controlling for confounding factors and then comparing a baseline treatment with a new treatment. Systematic reviews and meta-analyses are generally considered the highest quality of evidence as the compilation of the best studies that are focused on a specific question that can eventually be formed into clinical practice guidelines [174].

A systematic review was undertaken to ascertain if image guidance has any benefit in surgical treatment of adolescent idiopathic scoliosis. If image guidance was found to have no benefit in reducing breaches and complications, then a new guidance system would not have been worth pursuing.

---

<sup>1</sup>Chan A, Parent E, Wong J, Narvacan K, San C, Lou E: Does image guidance decrease pedicle screw-related complications in surgical treatment of adolescent idiopathic scoliosis: a systematic review update and meta-analysis. *Eur Spine J* 29, 694–716 (2020). <https://doi.org/10.1007/s00586-019-06219-3>

<sup>2</sup>Chan A, Parent E, San C, Narvacan K, Lou E: Intraoperative Image Guidance and Navigation in Adolescent Idiopathic Scoliosis Posterior surgery: A systematic Review on Screw-Related Complications and Breach rates, *The Spine Journal*, doi:<http://dx.doi.org/10.1016/j.spinee.2017.04.001>, 17(9):1215-1229, (2017).

## 3.2. Objectives

The goal of both systematic reviews was to compare image guidance and free-hand methods for posterior spinal fusion and instrumentation for patients with AIS. The first review included articles prior to October 2015 and was a qualitative review of the evidence while the second review included articles published prior to October 2017 and included a meta-analysis on pedicle screw breaches. The primary objective of these reviews was to study pedicle breach rates and screw-related complication rates. Secondary objectives in the meta-analysis included comparing clinically significant breaches, breaches at thoracic compared to lumbar vertebral levels, and surgical time. The combined results of both systematic reviews are presented here.

## 3.3. Methods

### 3.3.1. Search Strategy

Two systematic reviews were completed. The second systematic review search strategy was the same as the first but completed two years after the first review. The systematic review protocol was registered with the International Prospective Register of Systematic Reviews (CRD42016030088). The methodology of the Preferred Reporting Items for Systematic Review and Meta-Analysis Protocols (PRISMA) was followed [175]. The PICO (Population, Intervention, Comparison, Outcome) question developed involved the following:

- Population: Adolescent idiopathic scoliosis patients, eligible for surgery, 10-25 years old, undergoing posterior spinal fusion and instrumentation, usage of pedicle screws in surgery
- Intervention: Image guidance or navigation for screw insertion
- Comparison: Free-hand (non-guidance) methods for pedicle screw insertion
- Outcomes: Screw-related complications, pedicle breaches

Search terms were brainstormed between the Edmonton Scoliosis research team and clinicians and a medical librarian (LD) at University of Alberta. The search included terms related to idiopathic scoliosis as both indexed and free-text terms, while excluding adult and infantile deformities, degenerative diseases and traumatic spinal diseases. Search terms related to screws, hooks, wires and rods were added as well. Search terms related to spinal fusion, pedicle screw usage, imaging methods, screw-insertion methods and complications were not included. When consulting with the research librarian, it was felt that their inclusion would reduce the sensitivity of the search. As a result, the search focused purely on the population and did not include search terms related to the intervention, comparison, or outcomes. The full search can be found in Appendix 1: Search Strategy

A medical librarian was consulted to design the search. Ovid was used to search MEDLINE, EMBASE, and CENTRAL databases, EBSCO for CINAHL database and Thomson Reuters for the Web of Science database. Search terms were grouped in three themes: scoliosis, adolescence and instrumentation.

Non-clinical studies and case studies were excluded, and the search was limited to English literature. Only studies published after 1970 were included, when pedicle screws were becoming more widely used. Animal studies, editorials and conference abstracts were also excluded. Study designs up to Level 4 evidence according to the Center for Evidence-Based Medicine Levels of Evidence were included: randomized trials, observational studies with dramatic effect, controlled-cohort studies and case series with more than ten patients [174]. The first search was completed October 23, 2015 while the second search was completed on October 26, 2017.

Citations were imported into Zotero reference manager and the de-duplication function was used after merging articles. The de-duplication function involves displaying two likely duplicated articles, based on title, authors and publication date, and then manually merging or selecting which article to keep. A single reviewer performed de-duplication and confirmed that each article had an associated abstract. Articles without abstracts were manually searched and added. The full article list was then exported into Excel, including the authors, article title, bibliographic information and the abstract.

### 3.3.2. Study Screening

Because many studies were anticipated after the search, abstract and full-text screening were completed separately. For the first systematic review, I reviewed all the articles, while five additional co-reviewers were recruited as secondary reviewers through the University of Alberta Undergraduate Research Initiative or were colleagues from the lab. Each article was classified as 'Include', 'Exclude' or 'Unclear' according to the inclusion criteria as shown in Table 3-1. For each criterion, the minimum proportion of patients that needed to meet that criteria were set at 80% (denoted as an asterisk in the categories in the table).

**Table 3-1: Study inclusion and exclusion criteria**

<b>Abstract Inclusion Criteria</b>	<b>Full-Text Inclusion Criteria</b>	<b>Exclusion Criteria</b>
Randomized controlled trials, prospective/retrospective cohort studies	All Abstract Inclusion Criteria	Adults (>25) or pediatrics (<10)
Adolescents*		Non-idiopathic Scoliosis
Idiopathic Scoliosis*		Anterior Fusion only
Posterior Fusion and instrumentation*		Hooks and Wires only
Screw Usage*		Obsolete instrumentation (Harrington/Luque)
Sample size >10	Complications or Breaches reported	Non-clinical studies (cadaver, simulation, animal)
	Free-hand or image guidance specified	

\*Asterisk denotes minimum proportion of patients that needed to meet that criteria were set at 80%

Training for abstract screening involved in-person review of 25 calibration abstracts, where each screening decision and the reasoning behind each screening was discussed between the reviewers. Screening was then performed independently by each reviewer, with discrepancies screened a second time by each reviewer. If agreement was not met after the second round of screening, a consensus was reached between both reviewers through discussion.

Full-text screening was completed by me as one reviewer and three other co-reviewers as the second reviewer. Full-text screening had additional criteria also listed in Table 3-1. Full-text review training involved a two-hour in-person session reviewing three articles, followed by screening 25 calibration articles. Each remaining article was then independently screened for up to two rounds. If agreement was not found after two rounds, the article was discussed until a consensus was reached.

For the update of the first systematic review, all three secondary co-reviewers had been involved in the first systematic review. A more thorough de-duplication process was undertaken to identify duplicate patient populations. Articles from the same center with the same sample size and recruitment period were excluded, while for articles from the same center with overlapping recruitment periods, the authors were contacted to confirm if the patient populations overlapped. The article with the larger sample size

and more comprehensive breach or complications reporting was selected if no response was received from the authors. De-duplication was conducted by both me and a biomedical trainee.

### 3.3.3. Study Extraction and Quality Appraisal

Data extraction was completed by me and five co-reviewers. Training involved working through one extraction with each reviewer in detail, followed by 3-5 calibration articles for each co-reviewer. Extraction was categorized as: study design, study population, surgical details, imaging usage, complications and breaches (shown in Table 3-2). Extractions were completed in Excel. Each extraction was compared and in the case of discrepancies, the primary investigator referred to the original article with the co-reviewer confirming any corrections.

**Table 3-2: Extraction categories**

<b>Study Design</b>	<b>Study Population</b>	<b>Surgical Information</b>	<b>Image-Guidance Method</b>	<b>Complications and Breaches</b>
Study Period	Number of Subjects	Surgical Approach	Image-Guidance or Free-hand	Definitions of Breach
Timeline	Age	Hybrid or Screws	Pre-op Imaging	Definitions of Complication
Type of Study	Gender Ratio	Number of Screws	Intra-op Imaging	Follow-up Period
Inclusion Criteria	Skeletal Maturity	Instrumentation Type	Post-op Imaging	Number of Breaches
Exclusion Criteria	Curve Type	Curve Correction	Neuro-monitoring	Type of Complications
	Curve Severity	Surgical Blood Loss		Number of Complications
		Surgical Time		

While we originally intended to use the Cochrane Risk of Bias Assessment to evaluate study quality, there was only one randomized controlled trial, making comparability with the other cohort studies and case studies challenging. The Quality in Prognostic Studies (QUIPS) tool was used to evaluate the quality of studies instead [176]. The criteria presented in the QUIPS tool included study participation, study attrition, the prognostic factor being assessed, outcome measures, confounding factors, and statistical assessment. These generalized criteria were tailored for this study to ensure specific, objective and repeatable criteria were used between reviewers for quality assessment, shown in Appendix 2: Quality Appraisals. Each domain was rated as a high, moderate or low risk of bias according to 3-7 sub-criteria. To ensure consistency between reviewers, five calibration articles were used to compare repeatability of these criteria prior to continuing the study.

Importantly, the study attrition category was altered from the first systematic review. Studies that failed to report drop-out rates and potential impacts of patients that were lost to follow-up were classified as high risk of bias for the second review.

#### 3.3.4. Inter-Rater Reliability Assessment

Agreement between reviewers on abstract screening, full-text screening and quality appraisal was evaluated using percent agreement and the Kappa statistic [177]. A percent agreement above 75% was considered good while a Kappa of greater than 0.60 was considered moderately strong.

#### 3.3.5. Summary Tables

The results from each extraction were compiled by one reviewer. In cases of discrepancies between reviewers in data extraction, the original article was referenced, and the most accurate value was used. A summary table covering the study design, surgical details, and imaging used in screw placement decision-making was constructed from this data. For breach and complication rates and definitions, any discrepancies were evaluated and confirmed by two reviewers, with separate summary tables included for breaches, breach definitions, and screw-related complications.

#### 3.3.6. Meta-Analysis

A meta-analysis was performed using Review Manager 5.3 (Nordic Cochrane Center, Copenhagen) on breach rates using a random-effects model to quantify the effect of image guidance compared with free-hand methods on breach rates. Head-to-head comparisons of free-hand and image guidance methods were reported as odds ratio (OR). Breach proportions were reported for individual groups reporting of breach rates from either method. Surgical times were reported as absolute differences for comparative studies, and surgical time for single groups. The percentage of variability was estimated with the  $I^2$  statistic, with articles with  $>75\%$  being considered to have high heterogeneity, though this was not specified as affecting quality assessment on an a priori basis [178].

A subgroup analysis on breach rates for only high-risk breaches (breaches  $> 4\text{mm}$ , or  $> \frac{1}{2}$  screw diameter), as well as breaches according to vertebral level were completed. Surgical time was also meta-analyzed to determine if image guided surgeries were longer than free-hand. Meta-analyses were completed using only the moderate risk-of-bias or better articles. For articles which reported that there were no breaches, a value of 0.01% was used in the meta-analysis to allow inclusion in the table.

Due to the low incidence and high heterogeneity of studies reporting screw-related complications, a meta-analysis could not be completed.

### 3.3.7. Summary Statements

Each objective was answered using the Levels of Evidence summary statement strategy, using consistency of findings and quality of studies to formulate statements as per criteria in Table 3-3. Studies of excellent methodological quality would include low risk of bias randomized controlled trials, while cohort studies of low risk of bias were considered studies of good methodological quality. Moderate risk of bias studies was considered to have fair methodological quality, while high risk of bias studies were considered as having poor methodological quality. The definition of “multiple studies” was having more than two studies with >75% agreement in studies.

**Table 3-3: Levels of evidence**

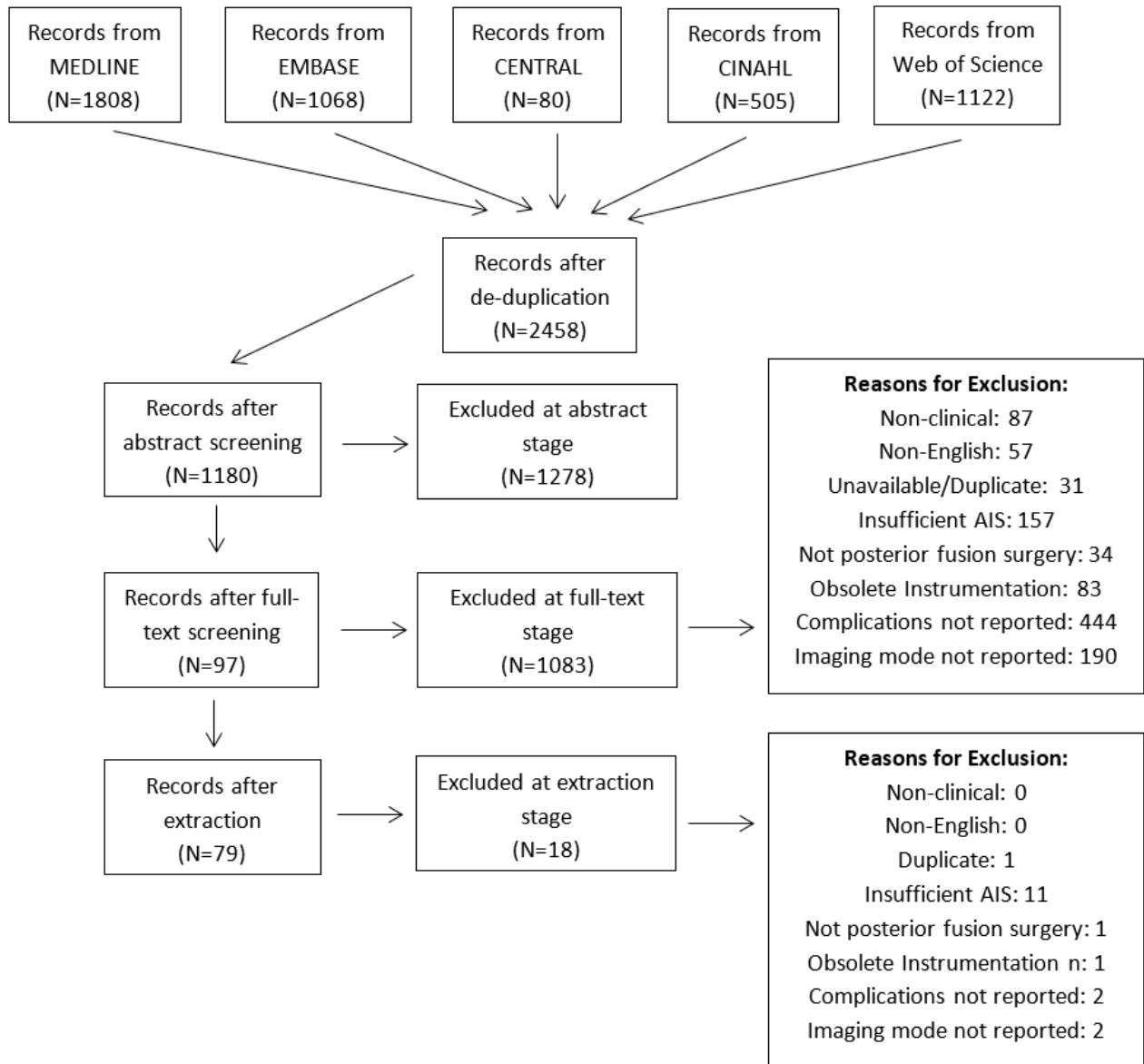
<b>Level</b>	<b>Criteria</b>
Strong	Consistent findings in multiple studies of good methodological quality OR in one study of excellent methodological quality
Moderate	Consistent findings in multiple studies of fair methodological quality OR in one study of good methodological quality
Limited	One study of fair methodological quality
Conflicting	Conflicting findings
Unknown	Only studies of poor methodological quality

## 3.4. Results

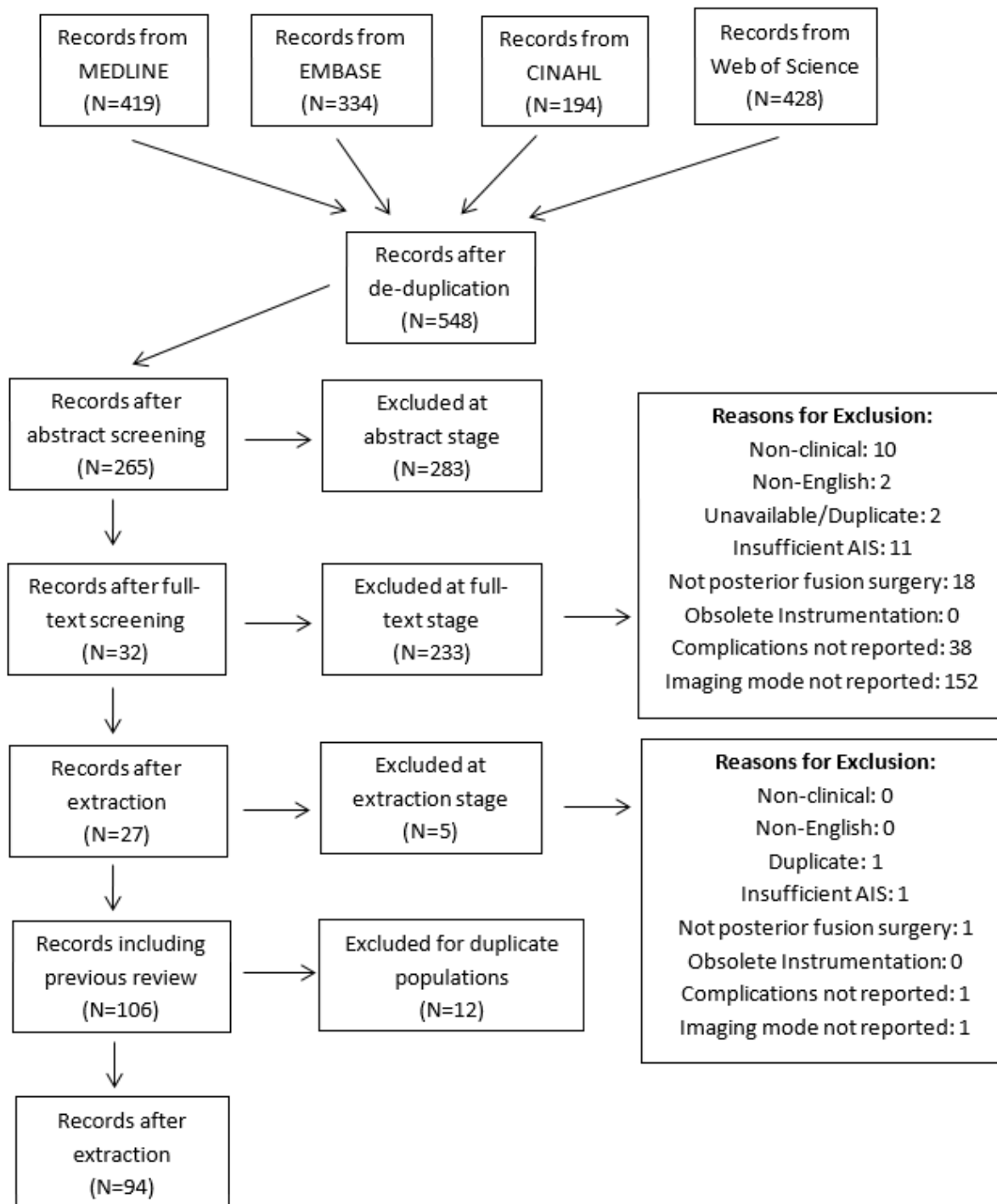
### 3.4.1. Article Screening and Extraction

The PRISMA selection flowcharts from each of the reviews is shown in Figure 3-1. The first systematic review included 2458 abstracts. An additional 548 articles were screened in the second review and 27 papers were added to the original 79 papers for a total of 106 included papers. After screening for duplicate populations, 12 articles were excluded, six articles with confirmed identical patient samples and six for which authors did not respond. The full reference list can be found in Appendix 3: Systematic Review List. Refer to the journal article for an appendix with the full extractions.





(a)



(b)

**Figure 3-1: Preferred Reporting Items for Systematic Reviews and Meta-Analyses flow diagram for (a) 1st systematic review (2017) and (b) 2nd systematic review and meta-analysis (2019)**

In the first review, 48.0% of abstracts were included while the second review included 48.4% of abstracts. For full-text screening, 91.8% of full-text articles were excluded in the first review while 87.9% of full-texts were excluded in the second, the most common reasons being:

- Imaging mode/free-hand method not reported (485 articles, 33.6%)
- Complications of breaches not reported (345 articles, 23.9%)
- Insufficient number of patients with AIS (180 articles, 12.5%)

The second set of articles had more articles excluded for lack of complications reporting (57.4%) while the first set had more articles that did not report imaging modes or free-hand methods (37.8%). This shift was likely due to free-hand methods being widely reported only in the mid-2000s, while 292 articles were from prior to 2003.

For the first review, first-round percent agreement and Kappa coefficient after abstract screening were 74.7% and 0.49. Corresponding first-round values were 76.0% and 0.47 for full-text screening and 72% and 0.56 for the quality assessment. For the second review, first-round percent agreement for abstract screening was 82% with a kappa of 0.78. Full-text was at 91% agreement with a kappa of 0.59 while quality assessment was at 78% agreement with a kappa of 0.75. The improvement in reviewer agreement from the first review to the second review was likely due to the second-round reviewers being well-trained from the previous review and greater clarity on what would likely be reported.

### 3.4.2. Study Characteristics

From 94 articles, 144 individual cohorts (groups) were found. Six head-to-head CT guidance vs free-hand studies including one randomized study were found, along with one CT-navigation vs fluoroscopic guidance comparative study (Table 3-4) [86,179–184]. Four studies used CT-navigation [87,185–187] and seven used fluoroscopy [188–194]. Most free-hand studies used fluoroscopy for screw confirmation or planning (69.3%, 52/75) with the remaining studies not reporting any imaging intra-operatively, no imaging or using 3D printed templates for screw insertion (Table 3-5).

Most articles were retrospective studies (67.0%, 63/94). Recruitment was randomized in six studies (9.2%,6/94). Most studies were case series (67.0%, 63/94) while cohort studies were second most common (29.8%, 28/94). The average number of participants ranged from 10 to 481 per group, while the average age of participants ranged from 11 to 18.3 years old depending on the group. Most patients were females in most studies.

Most patients had Lenke 1 curve type (53.1%, 2040/3843) with 16 studies that focused only on Lenke 1 curves (23.3%, 894/2040). Lenke 2 and Lenke 3 were the next most common classifications. King classification was used in only two studies, both of them published prior to 2010 [195,196].

**Table 3-4: Patient characteristics for head-to-head studies and image guidance studies**

Category	Categories	Head-to-Head			Head-to-Head			Image Guidance				
		*	CT-Navi	Free-Hand	*	CT-Navi	Fluoro Guided	*	CT-Navigation	*	Fluoroscopy	
Recruitment Timeline	Retrospective	6/6	5 [2]		1/1	1 [1]		4/4	4 [2]		7/7	5 [3]
	Prospective		1			0			0			2
	Ambispective		1			0			0			0
Type of Recruitment	Randomized	4/6	1		1/1	0		2/4	0		5/7	0
	Consecutive		3 [1]			0			2 [1]			5 [1]
	Convenience		0			1 [1]			0			0
Type of Study	Randomized	6/6	1		1/1	0		4/4	0		7/7	0
	Cohort		4 [1]			0			3 [1]			3 [2]
	Matched Cohort		1 [1]			1 [1]			0			0
	Case-Control		0			0			0			0
	Case Series		0			0			1 [1]			4 [1]
Number of Participants		12/12	25 (10-46)	32.5 (10-92)	2/2	12	12	5/5	40.6 (19-62)	7/7	52.4 (21-140)	
Number of Screws		12/12	322 (145-710)	347.5 (169-712)	0/2	x	x	5/5	611.6 (265-865)	4/7	819 (138-2020)	
Age (years)		8/12	14.2-17.2	15.1-16.4	2/2	11-18	11-18	5/5	13.9-16.2	6/7	14.5-15.8	
% Males		8/12	10-40%	10-30%	0/2	x	x	5/5	5.3-16.4%	5/7	9.4-54.2%	
Curve Types	Lenke 1	4/12	34 (70%)	74 (73%)	0/2	x	x	3/5	82 (60.3%)		5/7	77 (38.3%)
	Lenke 2		9 (16%)	17 (17%)		x	x		33 (24.3%)			18 (9.0%)
	Lenke 3		7 (13%)	10 (10%)		x	x		7 (5.1%)			19 (9.4%)
	Lenke 4		0 (0%)	0 (0%)		x	x		4 (2.9%)			2 (1.0%)
	Lenke 5		1 (2%)	1 (10%)		x	x		0 (0.0%)			65 (32.3%)
	Lenke 6		0 (0%)	0 (0%)		x	x		10 (7.4%)			20 (10.0%)
	Lenke 1 Only											32
	King I											
	King II											
	King III											
	King IV											
	King V											

Abbreviations: Navi – Navigation, Fluoro – Fluoroscopy. \*Denotes number of articles reporting this item over the number of articles in this category. Square brackets [] denote articles from the second systematic review search. For number of participants and screws, brackets denote the range. For curve type, number in brackets denotes percentage of patients of that curve type overall

**Table 3-5: Patient characteristics for all types of free-hand studies**

Category	Categories	*	Imaging Not Reported	*	No Imaging	*	Post-screw Fluoro	*	Pre-screw Fluoro	*	3D Printed Templates
Recruitment Timeline	Retrospective	19/19	13 [4]	4/4	2 [1]	38/43	25 [6]	8/9	8 [1]	1/1	0
	Prospective		5 [1]		2 [0]		12 [1]		0		1
	Ambispective		1 [1]		0		1 [0]		0		0
Type of Recruitment	Randomized	11/19	1 [0]	3/4	0	24/43	4	6/9	0	1/1	0
	Consecutive		9 [2]		3 [1]		20 [4]		5		1
	Convenience		1 [1]		0		0		1 [1]		0
Type of Study	Randomized	19/19	0	4/4	0	43/43	0	9/9	0	1/1	0
	Cohort		3 [1]		1 [0]		9 [1]		4 [0]		1
	Matched Cohort		0		0		0		0		0
	Case-Control		0		0		0		0		0
	Case Series		16 [5]		3 [1]		34 [6]		5 [1]		0
Number of Participants		33/33	43.0 (10-195)	6/6	29.2 (11-62)	68/68	34.6 (11-161)	10/10	98.5 (15-481)	1/1	16
Number of Screws		10/33	388.2 (89-1036)	1/6	88	22/68	532.5 (34-1400)	9/10	1670.1 (238-5923)	1/1	168
Age (Years)		32/33	12.1-16.5	5/6	14-16.8	65/68	13.1-16.9	8/10	13.8-18.3	1/1	5-18
% Males		27/33	10.0-50.0%	6/6	12.9-29.0%	58/68	5.0-100.0%	8/10	13.3-30.8%	1/1	25%
Curve Types	Lenke 1	33/33	238 (32.2%)	5/6	71 (65.7%)	52/68	510 (46.2%)	3/10	60 (55.0%)	0/1	0
	Lenke 2		163 (22.0%)		15 (13.9%)		199 (18.0%)		7 (6.4%)		0
	Lenke 3		154 (20.8%)		4 (3.7%)		202 (18.3%)		19 (17.4%)		0
	Lenke 4		69 (9.3%)		2 (1.9%)		62 (5.6%)		5 (4.6%)		0
	Lenke 5		82 (11.1%)		12 (11.1%)		89 (8.1%)		15 (13.8%)		0
	Lenke 6		34 (4.6%)		4 (3.7%)		43 (3.9%)		3 (2.8%)		0
	Lenke 1 Only		481				381				
	King I		0 (0.0%)						5 (2.2%)		
	King II		44 (26.2%)						131 (57.2%)		
	King III		61 (36.3%)						33 (14.4%)		
	King IV		31 (18.5%)						20 (8.7%)		
	King V		32 (19.0%)						40 (17.5%)		

Abbreviations: Fluoro – Fluoroscopy, \*Denotes number of articles reporting this item over the number of articles in this category. Square brackets [] denote articles from the second systematic review search. For number of participants and screws, brackets denote the range. For curve type, number in brackets denotes percentage of patients of that curve type overall.

**Table 3-6: Surgical and imaging characteristics for head-to-head studies and image guidance studies**

Category	Categories	Head-to-Head			Head-to-Head			Image Guidance			
		*	CT-Navi	Free-Hand	*	CT-Navi	Fluoro Guided	*	CT-Navigation	*	Fluoroscopy
Cobb Angle	Pre-op	10/12	48.3-70.0°	50.9-79.8°	0/2	x	x	5/5	52.7-62.4°	6/7	48.5-74.0°
	Post-op	6/12	10.4-31.3°	11.0-37.2°	0/2	x	x	5/5	17.9-22.0°	4/7	10.0-17.6°
	Change	6/12	32.5-50.8°	24.3-42.3°	0/2	x	x	5/5	31.8-42.3°	4/7	34.8-51.1°
Type of Surgery	Posterior	12/12	6 [2]	6 [2]	2/2	1	1	5/5	5 [3]	7/7	7 [3]
	ARPF		0	0		0	0		0		0
	MIS		0	0		0	0		0		0
Type of Fixation	Screw	12/12	6 [2]	6 [2]	2/2	1	1	5/5	4 [2]	7/7	6 [2]
	Hybrid		0	0		0	0		1 [1]		1 [1]
Surgical Blood Loss (mL)		4/12	153-1013	418-787	0/2	x	x	2/4	1060-1138	3/7	523-1030
Operative Time (min)		6/12	210-443	192-412	0/2	x	x	2/5	242-310	2/7	274-310
Pre-op Imaging	X-ray	10/12	1	3 [1]	0/2	x	x	5/5	3 [2]	6/7	2 [1]
	CT		4 [1]	2 [1]		x	x		2 [1]		2 [1]
	X-ray + MRI		0	0		x	x		0		1 [0]
	X-ray + CT		0	0		x	x		0		1 [0]
Intra-op Imaging	Fluoroscopy	10/12		4 [2]	2/2	0	1	5/5	0	7/7	7 [3]
	CT		5 [2]			1	0		4 [2]		0
	CT-Navi +Fluoro		1						0		0
	None								1 [1]		0
Post-op Imaging	X-ray	12/12	2	2	2/2			5/5	0	7/7	3 [1]
	CT		3 [1]	3 [1]		1	1		3 [2]		3 [2]
	MRI		0	0					0		0
	X-ray + MRI		0	0					0		0
	X-ray + CT		1 [1]	1 [1]					2 [1]		1 [0]
	None		0	0					0		0
Post-op Screw Imaging	All CT (%)	12/12	5 (83%)	5 (83%)	2/2	1 (100%)	1 (100%)	5/5	5 (3)	4/7	3 (2)
	Some CT (%)		0 (0%)	0(0%)					0		0
	X-ray/Fluoro		1 (17%)	1 (17%)					0		1
Neuro-monitoring	Yes	10/12	5 [2]	5 [2]	2/2	x	x	3/5	3 [2]	4/7	3 [1]

Abbreviations: Navi – Navigation, Fluoro – Fluoroscopy, ARPF – Anterior release, posterior fusion, MIS – Minimally invasive surgery. Square brackets denote articles from the second systematic review search. For number of participants and screws, brackets denote the range. For curve type, number in brackets denotes percentage of patients of that curve type overall.

**Table 3-7: Surgical and imaging characteristics for all types of free-hand studies**

Category	Categories	*	Imaging Not Reported	*	No Imaging	*	Post-screw Fluoro	*	Pre-screw Fluoro	*	3D Printed Templates
Cobb Angle	Pre-op	32/33	38.2-90.0°	6/6	51.0-66.0°	61/68	42.0-102.2°	8/10	45.5-60.6°	1/1	54.2°
	Post-op	30/33	6.6-28.8°	6/6	15.6-23.9°	55/68	6.0-53.1°	8/10	15.3-18.4°	1/1	15.3°
	Change	30/33	29.0-57.0°	6/6	32.8-44.3°	55/68	28.8-72.3°	8/10	27.0-42.8°	1/1	38.9°
Type of Surgery	Posterior	33/33	32 [10]	6/6	5 [2]	67/68	63 [13]	10/10	10 [1]	1/1	1
	ARPF		1		0		4		0		0
	MIS		0		1: MIS		0		0		0
Type of Fixation	Screw	33/33	28 [10]	6/6	3 [0]	68/68	46 [8]	10/10	9 [1]	1/1	1
	Hybrid		5		3 [2]		22 [5]		1		0
Surgical Blood Loss (mL)		20/33	270-1120	3/6	261-712	32/68	305-1813	1/10	1870	1/1	700
Operative Time (min)		16/33	183-560	4/6	182-475	37/68	136-380	4/10	132-424	0/1	x
Pre-op Imaging	X-ray	32/33	24 [8]	5/6	3 [0]	60/68	49 [13]	8/10	6	1/1	0
	CT		2		0		2		2 [1]		1
	X-ray + MRI		2		2 [0]		8		0		0
	X-ray + CT		4 [2]		0		1		0		0
Intra-op Imaging	Fluoroscopy	0/33	0	6/6	0	68/68	68 [13]	10/10	10 [1]	0/1	0
	CT		0		0		0		0		0
	CT-Navi +Fluoro		0		0		0		0		0
	None		0		6 [2]		0		0		0
Post-op Imaging	X-ray	33/33	24 [8]	6/6	5 [2]	68/68	48 [8]	10/10	4	1/1	0
	CT		7		1		10 [0]		3 [1]		1
	MRI		0		0		0		0		0
	X-ray + MRI		0		0		0		0		0
	X-ray + CT		2 [2]		0		8 [4]		3		0
	None		0		0		2 [2]		0		0
Post-op Screw Imaging	All CT (%)	9/33	7 (2)	1/6	1 (1)	18/68	10 (1)	6/10	3	0/1	0
	Some CT (%)				0		8 (3)		3		0
	X-ray/Fluoro		2		0		0				0
Neuro-monitoring	Yes	14/33	14 [6]	2/6	2 [2]	51/68	48 [10]	5/10	4	0/1	0
	No		0		0		3		1		0

Abbreviations: Navi – Navigation, Fluoro – Fluoroscopy, ARPF – Anterior release, posterior fusion, MIS – Minimally invasive surgery. Square brackets denote articles from the second systematic review search. For number of participants and screws, brackets denote the range. For curve type, number in brackets denotes percentage of patients of that curve type overall.

Posterior-only surgeries comprised 95.1% of the cohorts (137/144 groups), with only screws used in 77.1% of cohorts (111/144) (Table 3-6 and Table 3-7). All studies from the new systematic review search used posterior-only surgery, and screws-only were present in 19/24 (79.2%) of the new groups. Average curve size was 58.9° with the median at 58° and average correction of 40.2° and median of 39.9°.

Plain X-ray was used in 86.6% (110/127) of groups that reported pre-operative imaging, with 71.6% (91/127) of groups using X-rays exclusively (Table 3-6 and Table 3-7). The remaining articles that did not use X-rays, used CT exclusively (16/127, 12.5%), with an additional 17 articles that did not report on pre-operative imaging. Post-operatively, X-rays were used in 63.9% (92/144) of studies, exclusively in 61.1% (88/144). Intraoperatively, 83.3% (90/108) of patients had fluoroscopy and CT scans in 10.2% (11/108) in articles reporting intraoperative imaging. Of articles that reported post-operative screw assessment, CT scans were used for all patients in 71.9% (41/57) of groups, with all new studies that reported breach rates also using post-operative CT scans. Neuromonitoring was used in 92.3% (84/91) of studies that reported if they used neuro-monitoring.

Of the 46 studies that reported pedicle breaches, there were 15 breach definitions (Table 3-8 and Table 3-9). The most common definition, found in eight studies, was the Gertzbein definition which uses four grades: no breach, <2mm, 2-4mm and >4mm [197]. The definition by Abul-Kasim et al. was the most comprehensive, defining three grades for medial and lateral breaches, and two grades for anterior, foraminal and endplate breaches [198]. Any breach by any definition was counted as a breach for the meta-analysis.



**Table 3-8: Breach definitions from head-to-head and image guidance studies**

Breach Type	Breach Definition	Head-to-Head		Image Guidance	
		CT-Navi vs Free-Hand	CT-Navi vs Fluoroscopy	CT-Navigation	Fluoroscopy
Screw Axis, 2 Grades	Central axis outside the cortex	1 (1)		1 (1)	
Screw Axis, 2 Grades, Clinical	Central axis outside the cortex; additional grades for suboptimal, unsafe or removed screws	1 (1)			
Screw Axis, 3 Grades	Breach with central axis within cortex or outside the cortex				1
Screw Depth, 2 Grades, Clinical	Greater than 2mm breach; additional grades for removed and cancelled insertions			1	
Screw Depth, 4 Grades	Four grades: no breach, less than 2mm breach, less than 4mm breach and greater than 4mm breach	3		2 (1)	
Screw Depth, 4 Grades, Directional	Four grades, no breach, less than 2mm, more than 2mm, more than 4mm breach, medial vs anterior				1 (1)
Screw Depth, 5 Grades	Five grades: no breach, less than 2mm breach, less than 4mm breach, less than 6mm breach and greater than 6mm breach				1
Clinical	Any breach, divided into lateral, antero-lateral, medial or inferior breaches, and vascular damage				
None	Not pre-defined	1			1
Total		6 (2)	0	4 (2)	4 (1)

Number in each column denotes number of articles with that breach definition. Number in brackets denotes articles from the second review with that breach definition

**Table 3-9: Breach definitions from all types of free-hand studies**

Breach Type	Breach Definition	Unreported Imaging	No Imaging	Post-screw Fluoroscopy	Pre-screw Fluoroscopy	3D Printed Templates
Screw Axis, 2 Grades	Central axis outside the cortex	1		1	1	
Directional Screw Axis System	Central axis outside the cortex for medial and lateral; any cortical breach for anterior, endplate or foraminal breach	1		1	2 (2)	
Neuro-monitor Alarm	Neuro-monitoring alarm			1		
Screw Depth, 2 Grades	Any breach greater than 2mm	1		2		
Screw Depth, 2 Grades, Directional	Greater than 2mm medial or greater than 4mm lateral breach	1		2		
Screw Depth, 4 Grades	Four grades: no breach, <2mm breach, < 4mm breach >4mm breach			2 (1)		1
Screw Depth, 4 Grades, Anatomical	Four grades: no breach, <2mm breach, >2mm breach and >2mm breach through costovertebral joint	1				
Screw Depth, 4 Grades, Clinical	Four grades: no breach, cortical breach, <2mm breach and in-out-in breach, unacceptable placement and neurovascular injury			1		
Screw Depth, 5 Grades	Five grades: no breach, <2mm breach, < 4mm breach, <6mm breach and > 6mm breach			2 (1)	1	
Clinical	Any breach, divided into lateral, antero-lateral, medial or inferior breaches, and vascular damage		1 (1)			
None	Not pre-defined	1		4 (1)	4	
Total		6	1 (1)	16 (3)	8 (2)	1

Number in each column denotes number of articles with that breach definition. Number in brackets denotes articles from the second review with that breach definition

### 3.4.3. Quality Assessments

Only one of 94 studies had a low ROB overall as shown in Figure 3-2[199]. There were 18 studies of moderate ROB with two head-to-head studies, three image guidance and thirteen free-hand studies. Study attrition, measurement of complications/breaches and study confounding were the three quality domains that had the < largest number of high ROB studies at 86.2%, 63.8% and 48.9%, respectively. Most articles had moderate quality in study participation at 68.1%. The categories where most articles had low ROB ratings were statistical analysis/presentation (92.6%) and image guidance definition (59.6%) of papers. All studies that reported breach rates that achieved moderate or low overall risk of bias used CT scans to confirm screw placement (Appendix 3: Systematic Review List).

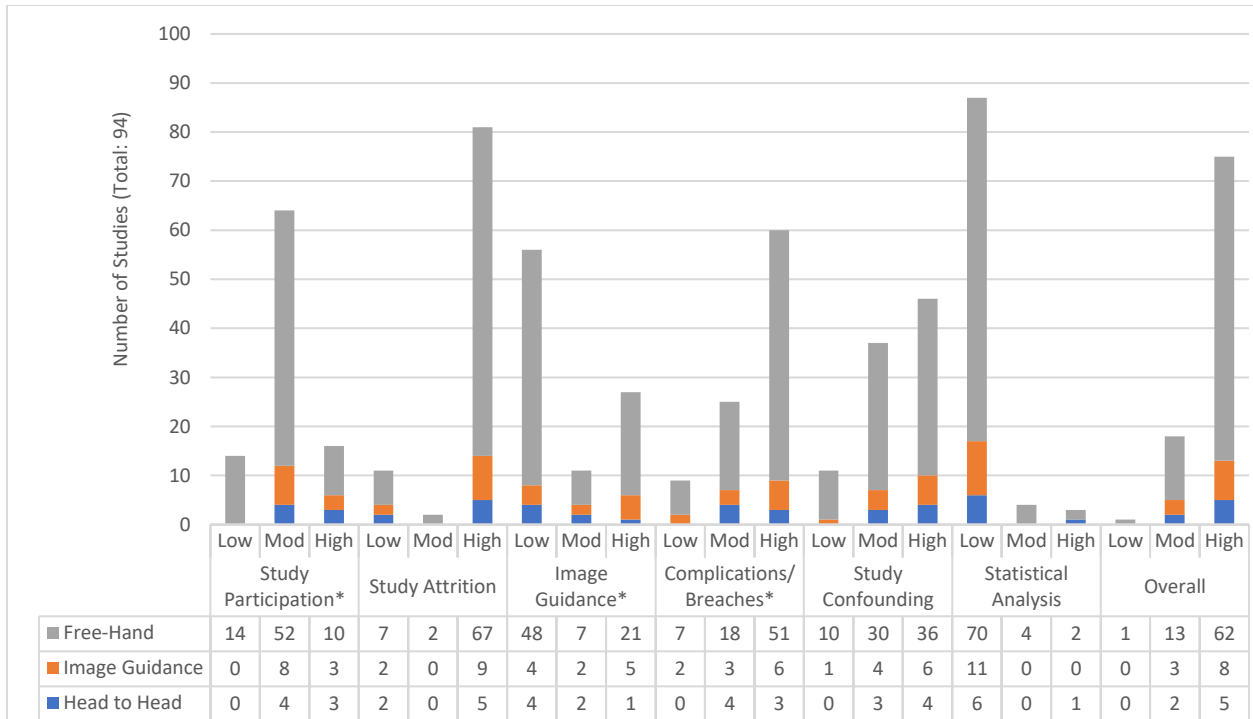


**Figure 3-2: Quality assessments in each category for head-to-head, image guidance and free-hand studies. \*Denotes categories used to assess overall quality. Abbreviations: Mod denotes moderate risk of bias**

### 3.4.4. Breaches and Complications

Table 3-10, Table 3-11, Table 3-12 and Table 3-13 show breach rates for the studies that reported pedicle breaches, with more clinically relevant magnitude breaches (>4mm, >1/2 screw width) and directions reported independently. There were only two moderate risk-of-bias or better head-to-head studies comparing CT guidance with free-hand methods, one of which reported breaches greater than 1/2 screw width at 57.8% vs 26% for free-hand vs image guidance, and medial breaches at 8.3% vs 3.0% in favour of image guidance [184]. No CT-navigation cohort study of moderate risk-of-bias or better reported medial or large magnitude breaches, while one fluoroscopy study reported breach rates of 9.2% >4mm and 4.6% medial breaches [192]. Three moderate quality free-hand groups reported breaches >4mm at 0% [85,88], one reported >1/2 screw width breaches at 14.2% [200] and four reported medial breaches at 0.0-6.2% [85,200-202].

**Table 3-10: Breaches in head-to-head comparison studies**

		Head to Head					
Breaches	Risk of Bias	CT Guidance (6 Studies, 6 Groups)			Free-Hand (6 Studies, 6 Groups)		
		Number of Groups	Number of Screws	Breach Rates	Number of Groups	Number of Screws	Breach Rates
Any Breach	Low						
	Moderate	2/2	469	5.9-26.0%	2/2	354	13.6-57.8%
	High	4/4	1463	1.5-26.5%	4/4	1731	5.1-46.3%
Breach >4mm	Low						
	Moderate	0/2	x	x	0/2	x	x
	High	1/2	264	1.1%	1/2	214	20.1%
Breach >1/2 Screw	Low						
	Moderate	1/2	300	26.0%	1/2	185	57.8%
	High	0/2	x	x	0/2	x	x
Medial	Low						
	Moderate	1/2	169	3.0%	1/2	169	8.3%
	High	1/2	264	2.7%	1/2	214	7.5%
Lateral	Low						
	Moderate	1/2	169	3%	1/2	169	5.3%
	High	1/2	264	8.7%	1/2	214	20.6%
Superior	Low						
	Moderate	0/2	x	x	0/2	x	x
	High	0/2	x	x	0/2	x	x
Inferior	Low						
	Moderate	0/2	x	x	0/2	x	x
	High	0/2	x	x	0/2	x	x
Anterior	Low						
	Moderate	0/2	x	x	0/2	x	x
	High	0/2	x	x	0/2	x	x

Number of groups column denotes number of articles that reported breaches of that type, out of the total number of groups in that category. The 'x' denotes no articles of that category tracked the respective complication in that row.

**Table 3-11: Breaches in image guidance studies (CT-navigation and fluoroscopy)**

		Image Guidance					
Breaches	Risk of Bias	CT-Navigation (4 Studies, 5 Groups)			Fluoroscopy (7 Studies, 7 Groups)		
		Number of Groups	Number of Screws	Breach Rates	Number of Groups	Number of Screws	Breach Rates
Any Breach	Low						
	Moderate	2/2	1130	6.9-7.9%	1/1	2020	20.2%
	High	3/3	1928	7.9-15.7%	3/6	1256	0.0-50.7%
Breach >4mm	Low						
	Moderate	0/2	x	x	1/1	2020	9.2%
	High	3/5	1383	0.2-0.7%	3/6	1118	0-2.7%
Breach >1/2 Screw	Low						
	Moderate	0/2	x	x	0/1	x	x
	High	0/5	x	x	3/6	138	2.9%
Medial	Low						
	Moderate	0/2	x	x	1/1	2020	4.6%
	High	2/5	1529	0.6-2.8%	3/6	800	2.9-24.6%
Lateral	Low						
	Moderate	0/2	x	x	1/1	2020	13.4%
	High	2/5	1529	3.0-4.3%	3/6	800	4.1-24.6%
Superior	Low						
	Moderate	0/2	x	x	1/1	2020	0.0%
	High	0/5	x	x	3/6	662	0.2%
Inferior	Low						
	Moderate	0/2	x	x	1/1	2020	0.0%
	High	0/5	x	x	3/6	662	0.0%
Anterior	Low						
	Moderate	0/2	x	x	1/1	2020	0.3%
	High	2/5	1529	0.0%	3/6	800	0.3-1.4%

Number of groups column denotes number of articles that reported breaches of that type, out of the total number of groups in that category. The 'x' denotes no articles of that category tracked the respective complication in that row.

**Table 3-12: Breaches in free-hand methods for articles with unreported imaging and no imaging in surgery**

		Free-Hand					
Breach	Risk of Bias	Unreported Imaging (19 Studies, 33 Groups)			No Imaging (4 Studies, 6 Groups)		
		Number of Groups	Number of Screws	Breach Rates	Number of Groups	Number of Screws	Breach Rates
Any Breach	Low						
	Moderate				1/1	88	13.6%
	High	8/33	4151	1.8-29.2%	0/5	x	x
Breach >4mm	Low						
	Moderate				0/1	x	x
	High	0/33	x	x	0/5	x	x
Breach >1/2 Screw	Low						
	Moderate				0/1	x	x
	High	2/33	1746	16.9-18.8%	0/5	x	x
Medial	Low						
	Moderate				1/1	88	0.0%
	High	6/33	2334	1.0-10.8%	0/5	x	x
Lateral	Low						
	Moderate				1/1	88	13.6%
	High	4/33	2334	1.5-18.4%	0/5	x	x
Superior	Low						
	Moderate				0/1	x	x
	High	5/33	2334	0.5-9.0%	0/5	x	x
Inferior	Low						
	Moderate				0/1	x	x
	High	2/33	1931	1.1-2.1%	0/5	x	x
Anterior	Low						
	Moderate				0/1	x	x
	High	0/33	x	x	0/5	x	x

Number of groups column denotes number of articles that reported breaches of that type, out of the total number of groups in that category. The 'x' denotes no articles of that category tracked the respective complication in that row.

**Table 3-13: Breaches in free-hand methods for articles reporting screw placement with fluoroscopic confirmation or using 3D printed templates**

		Free-Hand								
Breach	Risk of Bias	Post-screw Fluoroscopy (43 Studies, 68 Groups)			Pre-screw Fluoroscopy (9 Studies, 10 Groups)			3D Printed Templates (1 Study, 1 Group)		
		# of Groups	# of Screws	Breach Rates	# of Groups	# of Screws	Breach Rates	# of Groups	# of Screws	Breach Rates
Any Breach	Low				1/1	2201	14.3%			
	Mod	4/16	904	9.7-32.4%	1/1	873	17.1%			
	High	16/52	9215	0.1-66.8%	7/8	12488	0.1-33.9%	1/1	168	6.50%
Breach >4mm	Low				0/1	x	x			
	Mod	3/16	678	0.0%	0/3	x	x			
	High	15/52	1485	0.0-2.7%	1/10	448	7.8%	1/1	168	0.00%
Breach >1/2 Screw	Low				1/1	2201	14.3%			
	Mod	0/16	x	x	1/1	873	14.2%			
	High	2/52	1218	0-30.6%	1/10	238	9.2%	0/1	x	x
Medial	Low				1/1	2201	5.0%			
	Mod	2/16	833	2.7-5.4%	1/1	873	6.2%			
	High	9/52	4536	0.3-16.0%	4/10	9476	0.1-10.7%	1/1	168	6.50%
Lateral	Low				1/1	2201	7.1%			
	Mod	2/16	833	7.1%	1/1	873	8.0%			
	High	10/52	4664	0.8-14.6%	3/10	3553	0.4-21.9%	1/1	168	6.50%
Superior	Low				1/1	2201	0.5%			
	Mod	1/16	720	0.0%	1/1	873	0.9%			
	High	5/52	1464	0.0-4.8%	2/10	3105	0.3-3.8%	0/1	x	x
Inferior	Low				1/1	2201	1.0%			
	Mod	1/16	720	0.0%	1/1	873	0.5%			
	High	5/52	1464	1.1-17.1%	2/10	3105	0.0-1.0%	0/1	x	x
Anterior	Low				0/1	x	x			
	Mod	1/16	720	1.5%	1/1	873	1.5%			
	High	3/52	1531	0.9-2.7%	1/10	448	2.5%	0/1	x	x

Number of groups column denotes number of articles that reported breaches of that type, out of the total number of groups in that category. The 'x' denotes no articles of that category tracked the respective complication in that row.

Table 3-14, Table 3-15 and Table 3-16 show screw-related complication rates for the included studies of all quality. There were no complications observed in any head-to-head studies. Complications in CT-navigation studies ranged from 0-1.8%, all of which were dural lesions. For fluoroscopy, complications ranged from 0-8.3%, all of which were nerve root injuries. Screw-related complications from free-hand methods included dural lesions (0-16%), nerve root injuries (0-5.9%), spinal cord injury (0-4%) and re-operations related to screw misplacement (0-21.1%) for an overall screw-related complication rate of 0-21.1%. There were no complications observed in the 3D-printed templates study.

**Table 3-14: Complications in head-to-head studies**

		Head to Head				Head to Head			
		CT-Navigation		Free-Hand		CT-Navigation		Fluoroscopic Guidance	
		Patients	Groups	Patients	Groups	Patients	Groups	Patients	Groups
<b>Number of Groups</b>	<b>Risk of Bias</b>								
	<b>Low</b>								
	<b>Moderate</b>	39	2/2	23	2/2				
	<b>High</b>	116	4/4	172	4/4	12	1/1	12	1/1
<b>Complications</b>		Total	Rates	Total	Rates	Total	Rates	Total	Rates
<b>Screw-Related</b>	<b>Low</b>								
	<b>Moderate</b>	0	0.0%	0	0.0%				
	<b>High</b>	0	0.0%	0	0.0%	0	0.0%	0	0.0%
<b>Nerve Root</b>	<b>Low</b>								
	<b>Moderate</b>	0	0.0%	0	0.0%				
	<b>High</b>	0	0.0%	0	0.0%	0	0.0%	0	0.0%
<b>Dural Lesion</b>	<b>Low</b>								
	<b>Moderate</b>	x	x	x	x				
	<b>High</b>	x	x	x	x	x	x	x	x
<b>Spinal Cord Injury</b>	<b>Low</b>								
	<b>Moderate</b>	0	0.0%	0	0.0%				
	<b>High</b>	0	0.0%	0	0.0%	0	0.0%	0	0.0%
<b>Reoperation</b>	<b>Low</b>								
	<b>Moderate</b>	x	x	x	x				
	<b>High</b>	x	x	x	x	x	x	x	x
<b>Pneumothorax</b>	<b>Low</b>								
	<b>Moderate</b>	x	x	x	x				
	<b>High</b>	x	x	x	x	x	x	x	x

Groups column denotes number of articles that reported complications of that type, out of the total number of groups in that category. The 'x' denotes no articles of that category tracked the respective complication in that row.



**Table 3-15: Complications in image guidance (CT-navigation and fluoroscopy) and free-hand methods (unreported imaging)**

	Risk of Bias	Image Guidance				Free-hand	
		CT-Navigation		Fluoroscopy		Unreported Imaging	
		Patients	Groups	Patients	Groups	Patients	Groups
<b>Number of Groups</b>	<b>Low</b>						
	<b>Moderate</b>	81	2/2	140	1/1	191	1/1
	<b>High</b>	122	3/3	139	4/6	1195	30/32
<b>Complications</b>		Total	Rates	Total	Rates	Total	Rates
<b>Screw-Related</b>	<b>Low</b>						
	<b>Moderate</b>	0	0.0%	2	1.4%	0	0.0%
	<b>High</b>	1	0.0-1.8%	2	0-8.3%	13	0-21.1%
<b>Nerve Root</b>	<b>Low</b>						
	<b>Moderate</b>	0	0.0%	2	1.4%	0	0.0%
	<b>High</b>	0	0.0%	2	0-8.3%	7	0-5.9%
<b>Dural Lesion</b>	<b>Low</b>						
	<b>Moderate</b>	x	x	0	0.0%	x	x
	<b>High</b>	1	1.8%	0	0.0%	0	0.0%
<b>Spinal Cord Injury</b>	<b>Low</b>						
	<b>Moderate</b>	0	0.0%	0	0.0%	0	0.0%
	<b>High</b>	0	0.0%	0	0.0%	2	0-1.0%
<b>Reoperation</b>	<b>Low</b>						
	<b>Moderate</b>	x	x	0	0.0%	0	0.0%
	<b>High</b>	0	0.0%	0	0.0%	4	0-21.1%
<b>Pneumothorax</b>	<b>Low</b>						
	<b>Moderate</b>	x	x	0	0.0%	x	x
	<b>High</b>	0	0.0%	0	0.0%	0	0.0%

Groups column denotes number of articles that reported complications of that type, out of the total number of groups in that category. The 'x' denotes no articles of that category tracked the respective complication in that row.

**Table 3-16: Complications in free-hand methods (no imaging, fluoroscopic confirmation, 3D printed templates)**

	Risk of Bias	No Imaging		Post-screw Fluoroscopy		Pre-screw Fluoroscopy		3D Printed Templates	
		Patients	Groups	Patients	Groups	Patients	Groups	Patients	Groups
Number of Groups	Low					116	1/1		
	Moderate	11	1/1	760	16/16	49	1/1		
	High	164	5/5	1718	52/52	805	8/8	0	0/1
<b>Complications</b>		<b>Total</b>	<b>Rates</b>	<b>Total</b>	<b>Rates</b>	<b>Total</b>	<b>Rates</b>	<b>Total</b>	<b>Rates</b>
Screw-Related	Low					2	1.7%		
	Moderate	0	0.0%	0	0.0%	0	0.0%		
	High	0	0.0%	5	0-16.0%	7	0-4.8%		
Nerve Root	Low					0	0.0%		
	Moderate	0	0.0%	0	0.0%	0	0.0%		
	High	0	0.0%	0	0.0%	2	0-0.4%		
Dural Lesion	Low					0	0.0%		
	Moderate	x	x	x	x	x	x		
	High	0	0.0%	4	0-16.0%	1	0-6.7%		
Spinal Cord Injury	Low					0	0.0%		
	Moderate	0	0.0%	0	0.0%	0	0.0%		
	High	0	0.0%	1	0-4.0%	0	0.0%		
Reoperation	Low					2	1.7%		
	Moderate	x	x	x	x	x	x		
	High	0	0.0%	0	0-7.7%	3	0.0%		
Pneumo-thorax	Low					0	0.0%		
	Moderate	x	x	x	x	x	x		
	High	0	0.0%	0	0-12.5%	1	0.0%		

Groups column denotes number of articles that reported complications of that type, out of the total number of groups in that category. The 'x' denotes no articles of that category tracked the respective complication in that row. Grey shading denotes no articles were available in that risk of bias category.

### 3.4.5. Meta-Analysis

Only moderate quality studies or better were included in the meta-analysis. The moderate quality studies that were meta-analyzed had seven different breach definitions (Table 3-8) which were combined into a breach or no-breach definition.

The odds ratio meta-analyzed from head-to-head studies comparing image guidance (all using CT-navigation) and free-hand methods was 0.28 [0.20-0.40,  $I^2=1\%$ ] from two studies favoring navigation (Figure 3-3).

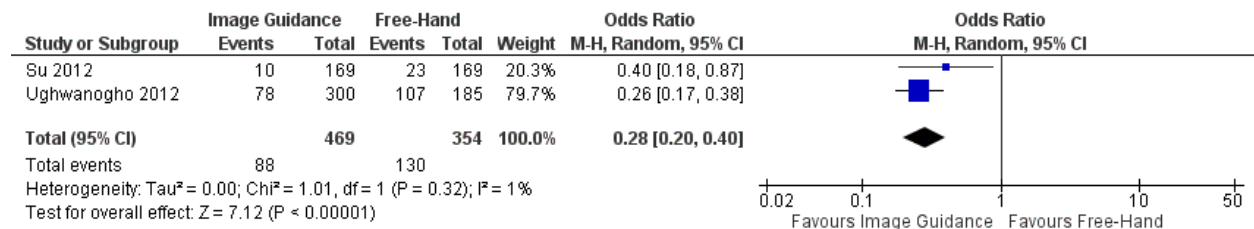


**Figure 3-3: Overall breach rates for moderate quality or better head-to-head studies**

For breaches from single-arm groups, the per-screw breach rate for free-hand methods was 20% [14-25%,  $I^2=95\%$ ] compared with 13% [6-21%,  $I^2=98\%$ ] for image guidance overall, not reaching statistical significance ( $p=0.18$ ) (Figure 3-4). Not shown in the figures, the breach rates for CT studies alone was 11% (5-18%,  $I^2=94\%$ ), and fluoroscopy alone was 20% (19-22%, single study), neither of which reached statistical significance in comparison to free-hand ( $p=0.06$  and  $p=0.85$  respectively).

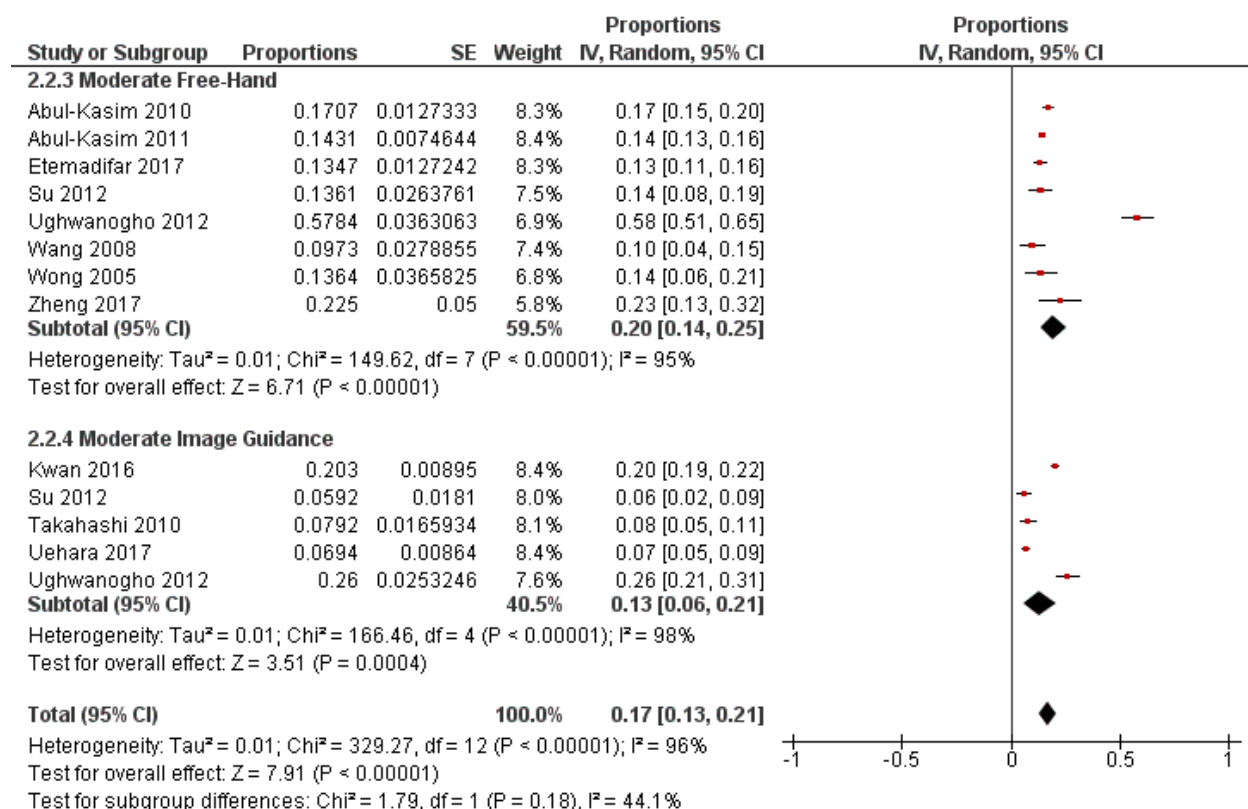


**Figure 3-4: Breach rates for moderate quality single-arm groups comparing image guidance vs free-hand methods**

Considering head-to-head studies whose definitions involved greater risk of complications (>4mm, >1/2 screw width), only Ughwanogho et al. was rated as a moderate risk of bias or better and reported an odds ratio of 0.26 [17-38%, one study] favoring image guidance which can be seen in Figure 3-3. For single-arm cohort studies, the free hand breach rate was 21% [9%-32%, I<sup>2</sup>=100%] compared to 11% [3%-19%, I<sup>2</sup>=99%] for image guidance but the difference did not reach significance with p=0.19 (Figure 3-5).

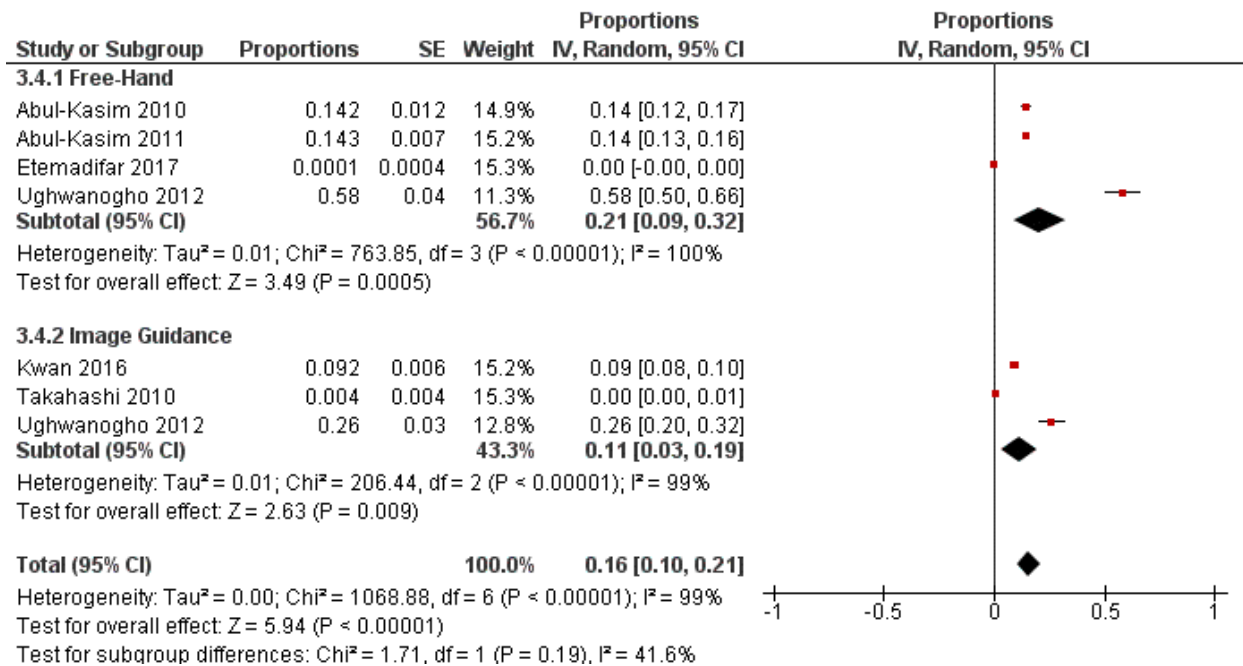


**Figure 3-5: Breach rates for moderate quality or better single-arm groups comparing high risk breaches from image guidance vs free-hand methods**

Only one image guidance vs free-hand study reported breaches according to levels, with Su et al. reporting a free-hand OR of 3.07 [0.87-10.84] and an image guidance OR of 1.83 [0.38-8.95], both having lower lumbar than thoracic breaches, though more dramatically for free-hand patients (Figure 3-6) [184]. For articles reporting both lumbar and thoracic breaches, the odds ratio for lumbar vs thoracic breaches was 1.72 [1.36-2.18, I<sup>2</sup>=0%] for free-hand and 1.83 [0.38-8.95, I<sup>2</sup>=0%] for image guidance studies with no statistical difference between groups ( $p=0.94$ ) (Figure 3-6).

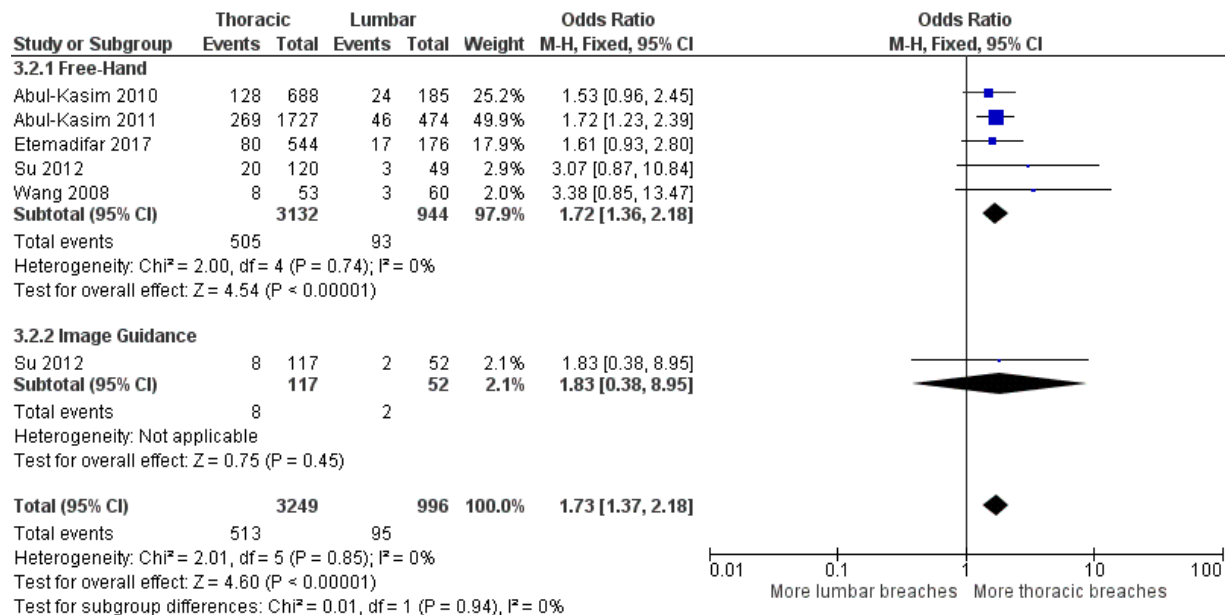


**Figure 3-6: Breaches for moderate quality or better studies reporting both thoracic and lumbar breaches for free-hand and image guidance studies**

Figure 3-7 and Figure 3-8 display results from moderate-quality or better cohorts that report thoracic and/or lumbar levels. Thoracic breach rates for free-hand methods were 16% [15-17%, I<sup>2</sup>=3%] compared with 7% [2-11%, single study only] for image guidance (Figure 3-7) with statistically significant difference between subgroups (p<0.01). Lumbar breach rates for free-hand methods were 9% [7-12%, I<sup>2</sup>=27%] compared with 4% [0-9%, single study only] for image guidance (Figure 3-8) with no statistically significant difference between subgroups (p=0.07).

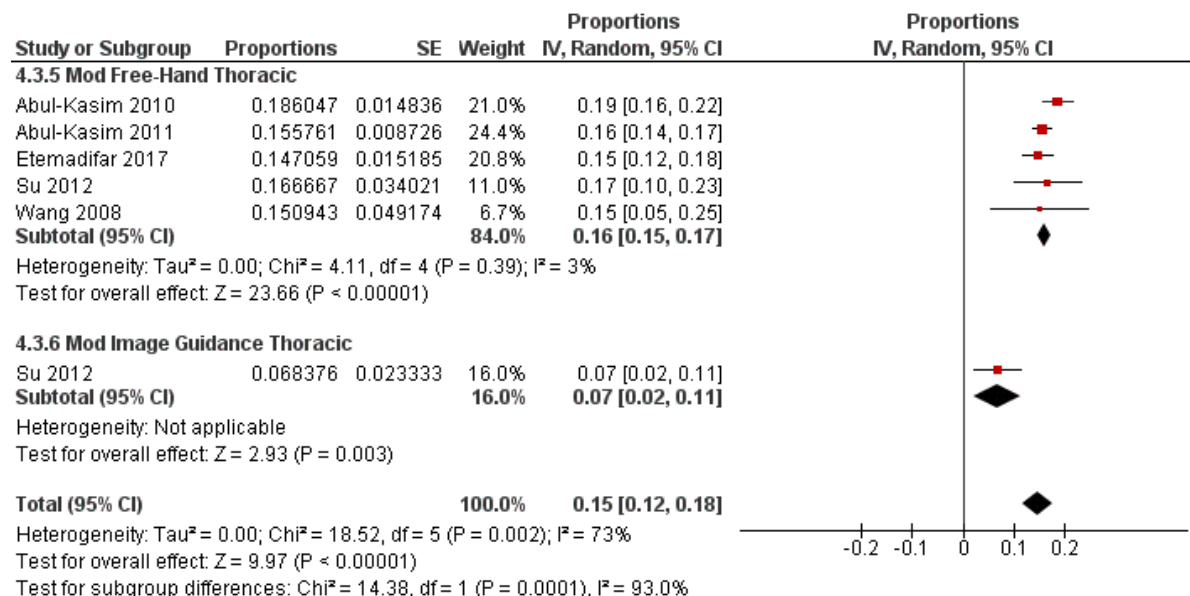


**Figure 3-7: Thoracic breaches for moderate quality or better single-arm groups**

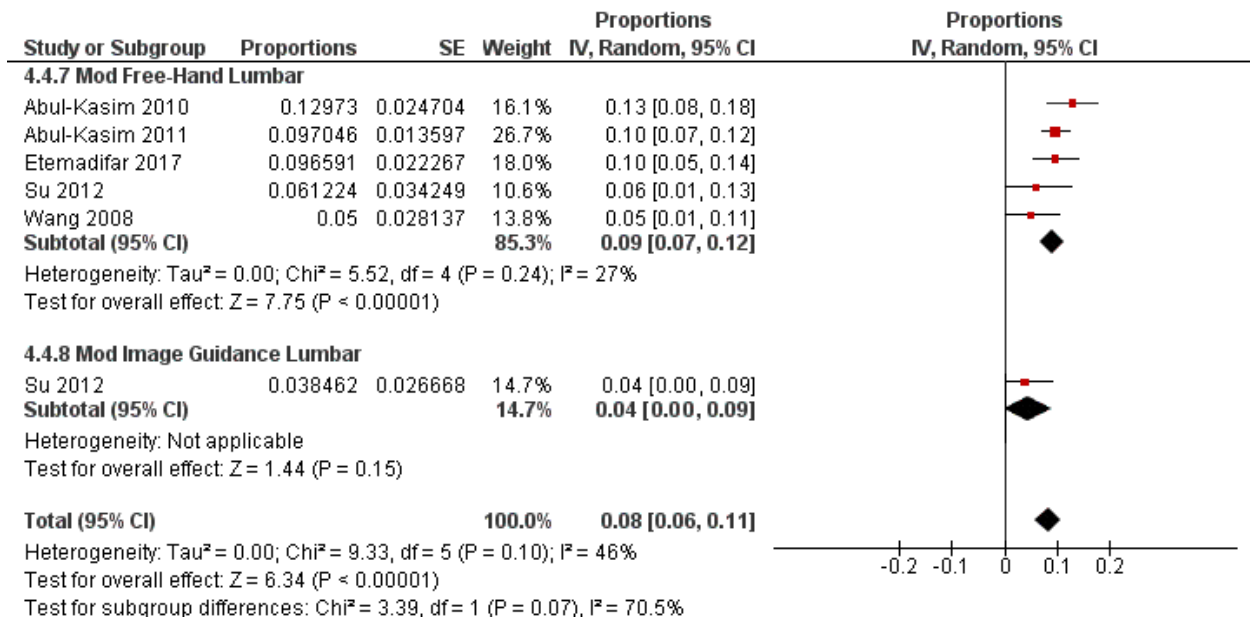


**Figure 3-8: Lumbar breaches for moderate quality or better single-arm groups**

Figure 3-9 displays surgical time for head-to-head studies of any quality comparing image guidance vs free-hand, with the mean difference favouring free-hand methods at 41.6 minutes [6.2-77.1min, I<sup>2</sup>=0%]. No moderate quality or better head-to-head studies reported surgical times. Figure 3-10 displays surgical times from moderate risk of bias single group studies, with free-hand methods at 226 minutes [219.6-234.0 min, I<sup>2</sup>=98%] compared with 258 minutes [240.6-274.7 min, I<sup>2</sup>=91%] for image guidance from two studies with significantly shorter times for free-hand (p<0.01).

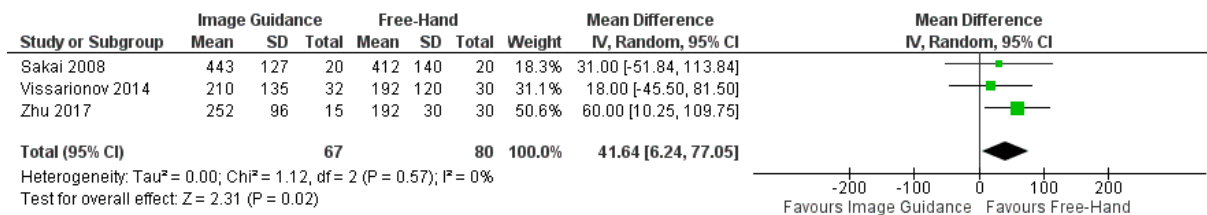


**Figure 3-9: Surgical time for any quality head-to-head studies**

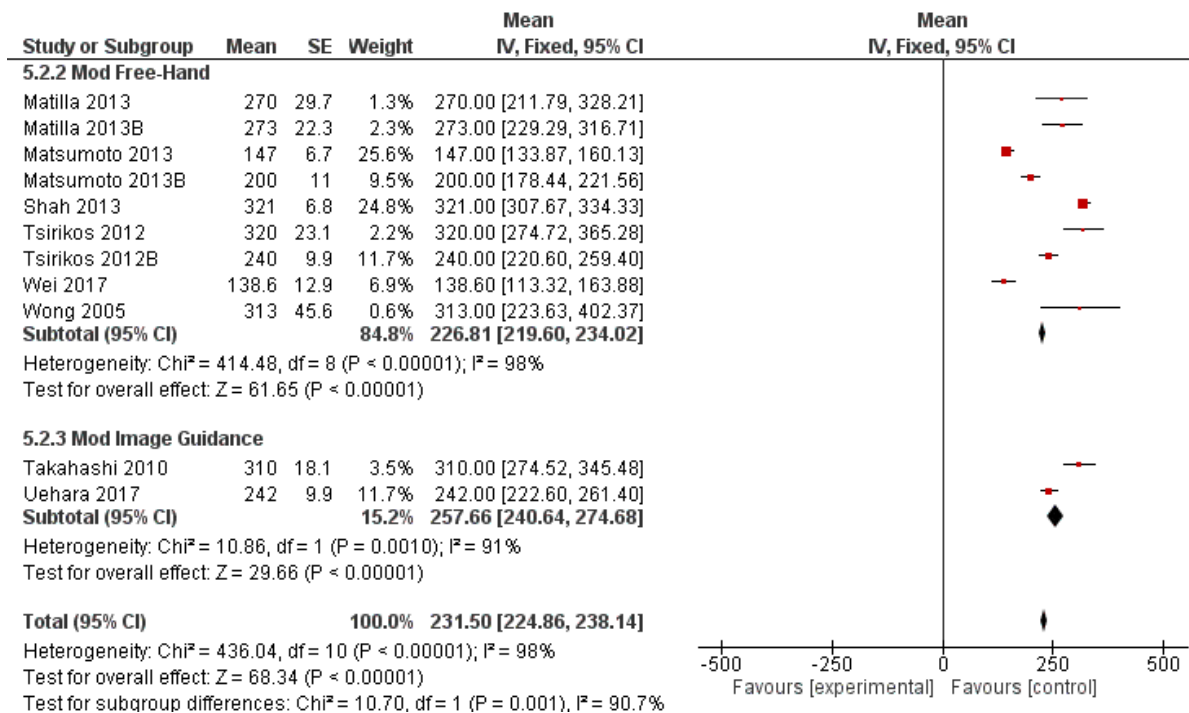


**Figure 3-10: Surgical time for moderate quality or better single arm groups comparing image guidance vs free-hand**

### 3.4.6. Summary Statements

Summary statements can be found in Table 3-17, including head-to-head studies comparing free-hand vs image guidance studies, single-arm groups reporting breach rates and complication rates from free-hand and image guidance studies, breach rates comparing thoracic vs lumbar levels, and surgical times comparing free-hand and image guidance.



**Table 3-17: Summary statements**

Strength of Evidence	Type of Study	Outcome Measure	Number and quality of Groups	Finding	Heterogeneity
<b>A: Head-to-head breaches and complications</b>					
Moderate	Head-to-head studies	Breaches	Two moderate ROB (Figure 3-3)	<b>OR:</b> 0.28 [0.20-0.40] [180,184] Favors image guidance	Low (I <sup>2</sup> =1%)
Limited	Head-to-head studies	Breaches, <1/2 screw width	One moderate ROB (No Figure)	<b>OR:</b> 0.26 [0.17-0.38] [180] Favors image guidance	One group
Limited	Head-to-head studies	Breaches, medial-only	One moderate ROB (No Figure)	<b>OR:</b> 0.34 [0.12-0.96] [184] Favors image guidance	One group
Moderate	Head-to-head studies	Screw-related complications	Two moderate ROB (Table 3-14)	<b>No complications in any groups</b> [180,184]	N/A
<b>B: Single-arm groups breaches and complications</b>					
Moderate	Single-arm studies	Breaches, Free-hand vs Image Guidance	Seven moderate-ROB, one low ROB free-hand Five moderate-ROB image guidance (Figure 3-4)	<b>Free-hand:</b> 20% [14-25%] [85,88,180,184,199-202] <b>Image Guidance:</b> 13% [6-21%] [87,180,184,185,192] No difference (p=0.18)	<b>Free-hand:</b> High (I <sup>2</sup> =95%) <b>Image Guidance:</b> High (I <sup>2</sup> =98%)
Moderate	Single-arm studies	Breaches, Free-hand vs CT Navigation	Seven moderate-ROB, one low ROB free-hand Four moderate-ROB image guidance (No Figure)	<b>Free-hand:</b> 20% [14-25%] [85,88,180,184,199-202] <b>CT Navigation:</b> 11% [5-18%] [87,180,184,185] No difference (p=0.06)	<b>Free-hand:</b> High (I <sup>2</sup> =95%) <b>CT Navigation:</b> High (I <sup>2</sup> =94%)
Moderate	Single-arm studies	Breaches, Free-hand vs Fluoroscopy	Seven moderate-ROB, one low ROB free-hand One moderate-ROB image guidance (No Figure)	<b>Free-hand:</b> 20% [14-25%] [85,88,180,184,199-202] <b>Fluoroscopy:</b> 20% [19-22%] [192] No difference (p=0.85)	<b>Free-hand:</b> High (I <sup>2</sup> =95%) <b>Fluoroscopy:</b> One group
Moderate	Single-arm studies	High-risk breaches, Free-hand vs Image Guidance	Three moderate-ROB, one low ROB free-hand Three moderate-ROB image guidance (Figure 3-5)	<b>Free-hand:</b> 21% [9-32%] [85,180,199,200] <b>Image Guidance:</b> 11% [3-19%] [180,185,192] No difference (p=0.19)	<b>Free-hand:</b> High (I <sup>2</sup> =100%) <b>Image Guidance:</b> High (I <sup>2</sup> =99%)
Moderate	Single-arm studies	High-risk breaches, Free-hand vs CT Navigation	Three moderate-ROB, one low ROB free-hand Two moderate-ROB CT navigation (No Figure)	<b>Free-hand:</b> 21% [9-32%] [85,180,199,200] <b>CT Navigation:</b> 13% [0-38%] [180,185] No difference (p=0.59)	<b>Free-hand:</b> High (I <sup>2</sup> =100%) <b>CT Navigation:</b> High (I <sup>2</sup> =99%)
Limited	Single-arm studies	High-risk breaches, Free-hand vs Fluoroscopy	Three moderate-ROB, one low ROB free-hand One moderate-ROB fluoroscopy (No Figure)	<b>Free-hand:</b> 21% [9-32%] [85,180,199,200] <b>Fluoroscopy:</b> 9% [8-10%][192] No difference (p=0.05)	<b>Free-hand:</b> High (I <sup>2</sup> =95%) <b>Fluoroscopy:</b> One group
Conflicting	Single-arm studies	Screw-related Complications	Two moderate-ROB CT-navigation One moderate-ROB no imaging (Table 3-15) One moderate-ROB pre-screw fluoroscopy One low-ROB pre-screw fluoroscopy 16 moderate-ROB pre-screw fluoroscopy (Table 3-16)	CT Navigation: 0-1.6% <b>Free-hand, no imaging:</b> 0% [180,184] <b>Free-hand, pre-screw fluoroscopy, mod-ROB:</b> 0% [202] <b>Free-hand, pre-screw fluoroscopy, low-ROB:</b> 1.7% [200] <b>Free-hand, post-screw fluoroscopy:</b> 0% [85,88,201,203-209]	N/A

Unknown	Single-arm studies	Screw-related Complications	Unspecified imaging Template-assisted (Table 3-16)	No moderate risk of bias groups or better.	N/A
<b>C: Thoracic and lumbar breach levels</b>					
Limited	Head-to-head studies	Thoracic vs lumbar breaches, Image guidance	One moderate ROB (Figure 3-6)	<b>OR:</b> 1.83 [0.38-8.95] [184] Favors lumbar levels	One group
Moderate	Head-to-head studies	Thoracic vs lumbar breaches, Free-hand	One low ROB Four moderate ROB (Figure 3-6)	<b>OR:</b> 1.72 [1.36-2.18] [85,184,199–201] Favors lumbar levels	Low I <sup>2</sup> =0%
Limited	Single-arm studies	Thoracic breaches, free-hand vs image guidance	One low ROB free-hand Four moderate ROB free-hand One moderate ROB image guidance (Figure 3-7)	<b>Free-hand:</b> 16% [15-17%] [85,184,199–201] <b>Image Guidance:</b> 7% [2-11%] [184] Significant ( $p<0.01$ ) Favors image guidance	<b>Free-hand:</b> Low (I <sup>2</sup> =3%) Image Guidance: One group
Limited	Single-arm studies	Lumbar breaches, free-hand vs image guidance	One low ROB free-hand Four moderate ROB free-hand One moderate ROB image guidance (Figure 3-8)	<b>Free-hand:</b> 9% [7-12%] [85,184,199–201] <b>Image Guidance:</b> 4% [0-9%][184] No difference ( $p=0.07$ )	<b>Free-hand:</b> Low (I <sup>2</sup> =27%) Image Guidance: One group
<b>D: Surgical time</b>					
Unknown	Head-to-head	Surgical times	Three high ROB head-to-head groups (Figure 3-9)	<b>Mean Difference:</b> 41.6 mins (6.2-77.1 mins) Favoring free-hand ( $p<0.05$ ) [181–183]	Low I <sup>2</sup> =0%
Moderate	Single-arm studies	Surgical times	Nine moderate ROB free-hand Two moderate ROB image guidance (Figure 3-10)	<b>Free-hand:</b> 226.8 mins (219.6-234.0 mins) [202,204,205,207–209] <b>Image Guidance:</b> 257.7 mins [240.6-274.7 mins] [87,185] Significant ( $p<0.01$ ) Favors free-hand	<b>Free-hand:</b> High (I <sup>2</sup> =98%) Image Guidance: High (I <sup>2</sup> =91%)

### 3.5. Discussion

#### 3.5.1. Review Update Improvements

The results of the systematic review update benefited from being a repeated process, allowing for improvements to be made to the methodology, though the overall structure remained the same. The comprehensiveness of the search strategy and high sensitivity in screening criteria allowed for inclusion of as many relevant articles as possible in this study [210]. The more experienced reviewers from the 1<sup>st</sup> systematic review were also brought back, allowing for a high agreement for abstract, full-text and quality assessment at 82%, 91% and 78% respectively, and kappas of 0.78, 0.59 and 0.68. Since the objective criteria for quality assessments had already been determined from the 1<sup>st</sup> study, the agreement in quality assessments was higher in the 2<sup>nd</sup> study.

Some changes were made to a few aspects of the study. First, the complications from full-text screening was focused on screw-related complications. While bleeding, infections and re-operations were tracked, complications that may have resulted from screw insertion were the focus. To differentiate complications that were recorded by the article and those that were not, studies that reported no complications in specific categories were marked as 'zeroes' in those categories, while the remaining categories were left blank to indicate these were unknown.

With regards to quality assessment, study attrition was changed so that authors needed to report that no patients were lost to follow-up, resulting in a larger group of studies having a high risk of bias. However, this category was not used in the final determination of risk of bias. Because of this change, the articles from the first systematic review had quality assessments repeated, using an automated points system to ensure consistency of assessments between the two studies.

Lastly, based on the findings from the previous review, a meta-analysis was planned for the breach rates, though still not for complication rates due to the small sample sizes and rarity of screw-related complications occurring. The addition of a meta-analysis strengthened the quantitative basis for current evidence on breach rates, both in general, and for thoracic vs lumbar levels.

Some post-hoc analysis was undertaken to ensure a more accurate perspective coming from these articles. First, a second round of de-duplication was performed, focused on removing overlapping patient populations. Studies from the same center were screened for inclusion dates, number of patients and study characteristics, with identical study populations being removed and questionable populations resulting in an inquiry to the authors. Only one author responded to our inquiries, confirming the populations were different [211]. From this process, two articles that had moderate risk of bias were excluded, one fluoroscopic guidance study [212] and one free-hand study [213].

Second, the study type was re-assessed to be classified according to the purposes of the systematic review (breach rates or complication rates) rather than the study's purpose, as many studies would report breach rates or complication rates without it being a primary outcome for their study. For example, while some studies may have been reported to be randomized controlled trials, their purpose may have been to assess surgical details rather than complications or breaches; classifying this as a randomized controlled trial may exaggerate the study quality. As a result, although all the moderate risk of bias studies were originally considered by the authors as randomized or cohort studies, the two head-to-head studies included one

cohort studies and one randomized study, while the remaining single-arm studies were coded as ten case series and seven cohort studies.

Lastly, further analysis into surgical times and infection rates related to those surgical times was not originally planned for this meta-analysis, though these were both extracted. While surgical time had enough data to be meta-analyzed, there was not enough data from moderate quality studies or better on infection rates to justify meta-analysis.

### 3.5.2. Population Applicability

Studies were generally smaller than 100 patients, one of the study quality assessment criteria with an average of 41 patients and median of 25.5. Number of screws was not included in the quality assessment, though there were 640 on average, with a median of 370 screw from the 60 studies that report breaches.

The patient population from this systematic review matched the typical surgical candidate. The average age was 14.1 years old with a range of 12.1 to 18.6 years old [214]. Gender ratio involved more male patients than the commonly reported ratio at 4:1 or 20.5% males to 79.5% female, compared to the typical gender ratio of 7.2:1 but was still in favour of females [28]. Both curve size and curve correction were within the typical surgical range, with an average initial Cobb angle of 58.9° and average correction 40.2°. Lastly, curve types matched the prevalence as originally studied when the Lenke classification system was developed with Lenke Type 1 main thoracic curves being the most common, followed by Lenke Type 2 double thoracic curves, Type 3 double major curves and Type 5 thoracolumbar curves being less prevalent, and Type 4 triple major curves and Type 6 thoracolumbar/lumbar main thoracic curves being rare [215]. The search and screen successfully identified the target patients that would be relevant in this review.

### 3.5.3. Key Findings

The first systematic review concluded that while point estimates for breaches were reduced in image guidance compared with free-hand methods, complications were still unknown. The goal of the update was to quantitatively assess the difference in breach rates, as well as determine if further larger studies in complication rates had been completed under the new article search.

Despite finding 23 new studies there was not a significant change to current evidence regarding breach rates and complication rates, though current evidence on breaches has been made clearer. The meta-analysis of moderate risk of bias head-to-head studies showed decreased breach rates with CT navigation, while analysis of cohort studies showed no statistically significant difference between image guidance and free-hand methods (Figure 3-3). Interestingly, removing the Ughwanogho et al. study which appears to

be an outlier with higher breach rates in both groups, resulted in a more homogeneous dataset for both freehand (15% [13-16%,  $I^2=43\%$ ) and CT-guidance (7% [7-8%,  $I^2=0\%$ ) and a statistically significant difference between groups ( $p<0.01$ ). A methodological cause for the higher breach rates in this particular study could not be found; the patient population of this study was not different, nor was the screw insertional method noticeably different. Breaches were defined as having 50% of the shank outside the central axis of the pedicle like other studies in the meta-analysis. High risk breach rates do not appear to have a significant difference between free-hand and image guidance methods, though the high heterogeneity among available studies to date still makes this difficult to assess.

This systematic review included a meta-analysis of breach rates comparing lumbar and thoracic levels, including articles that specified if screws were inserted in thoracic or lumbar levels. This study showed that breaches were higher for thoracic levels than lumbar with a pooled OR of 1.73 [1.37, 2.18,  $I^2=0\%$ ], confirming the results of previous studies showing that thoracic levels are at higher risk of breach [216,217]. Breach rates in the thoracic spine using free-hand methods had low heterogeneity ( $I^2=3\%$ ) and were statistically increased, compared to the lone image guidance study that reported thoracic breaches. However, image guidance did not have a statistically significant effect on breach rates in lumbar levels. Image guidance can be an important tool for narrow thoracic pedicles but may not be needed for the larger lumbar pedicles.

Complications were not meta-analyzed, both because there were too few image guidance studies to compare, and because complication rates were so low with head-to-head studies all at 0%, CT-navigation at 0%, fluoroscopy at 1.4% and free-hand at 0-1.7%. Neurologic deficits have been reported to range from 0.2-0.8% from the Scoliosis Research Society Morbidity and Mortality Database (SRSMMMD) [92,218]. Further information on neurologic complication rates based on the usage of image guidance or free-hand methods would be useful to record to better determine the usefulness of navigation systems in AIS surgery, though the voluntary nature of the database may bias results.

As navigation systems often require extra steps to insert screws, a meta-analysis of surgical time was completed [79], showing increased surgical times of 42 minutes in all-quality head-to-head studies with low heterogeneity ( $I^2=0\%$ ), and an increase of 31 minutes from moderate-quality cohort studies, though heterogeneity was high in the cohort studies ( $I^2>90\%$  for both groups). Navigation may prolong surgeries which may increase the risk of infection. A systematic review of surgical site infections reported a 17% increase in likelihood of infection for every 30 minutes of surgery [219]. However, as these surgical times

are not comparing the actual screw insertion time or even incision time, it is important not to draw too broad a conclusion on the increased surgical time.

#### 3.5.4. Study Quality Assessment

In the second systematic review, six articles had moderate quality or 26% of studies, compared with only 16% from the first review indicating an improvement in study quality. Although the study attrition category was changed to require studies to explicitly state information on follow-ups, this category was not included when assessing the overall quality of studies. The study population category had 81% of studies reaching moderate risk-of-bias or better, unchanged from the previous study. Study size remains a challenge, with an average size of 43 patients, up from 41 from the previous review. Unfortunately for determining complication rates, assuming a 1% free-hand complication rate, reducing complications to 0.5% when using image guidance would require a study to include almost 1500 patients in each arm using a one-tailed proportions inequality test assuming a 5% type 1 error and one-tailed proportions comparisons. However, breach rates are much more feasible to measure, with a 20% breach rate reduced to 10% requiring only 70 patients to detect as significant under similar power conditions.

Defining image guidance was significantly worse with 50% of studies being at moderate ROB or better compared with 80% from the previous study. It was mostly due to a lack of defining what free-hand method was used, likely because of how commonplace free-hand methods have become. However, it is important for the usage of fluoroscopy to be reported to ensure an accurate classification of the method of screw insertion.

The complications and breaches measurement category improved by the most, with 60% of articles having a moderate risk-of-bias or better, compared with only 27% from the previous study. Of the breach studies, all the new studies used the Gertzbein or modified Gertzbein definition [197]. All the new studies also used CT to confirm some of the patients' screw placements, with 96% of the screws in these studies being confirmed by CT compared to 56% from the previous study. Out of the 27 groups that reported breaches at different vertebral levels, only four were from the new studies.

#### 3.5.5. Limitations on Findings

Any breach that was reported was noted as a breach, regardless of direction or magnitude. A subgroup analysis on only breaches that were >4mm or >1/2 screw width to represent the most clinically relevant breaches was attempted, but there was a lack of moderate risk-of-bias evidence reporting these breaches.

As a result, the 2<sup>nd</sup> study could still only report on breaches in general, including breaches that may be deliberately placed laterally or small breaches that are unlikely to lead to complications.

Perhaps the most important limitation of the meta-analysis results was the high heterogeneity between reported breach rates. This could be from the different breach definitions used, different training of surgeons at centers around the world or different methods of confirming breaches. All breaches from moderate quality studies used the 2mm grading system the central axis-outside-cortex definition, or a clinical breach system, except Wang et al., which still had comparable breach rates to the other articles [201]. The 2mm breach definition was the most common breach definition as systematically reviewed by Aoude et al. [89]. Certain articles may have focused on specific techniques such as minimally invasive navigation [183], focused on dysplastic or smaller pedicles [86,192], or used robotic assistance [194]. No method such as GRADE was used to downgrade quality of evidence due to heterogeneity. The odds ratio favoring image guidance may not be exact, but the trend in having decreased breach rates with image guidance is evident from these studies.

#### 3.5.6. Recommendations on Future Study Reporting

Additional randomized controlled trials would be useful in determining the usefulness of image guidance for breach rates. A minimum sample size of 70 for each group would be recommended to detect neurologic complications, in addition to reporting screw-related complications, infection rates and surgical times to better delineate the potential advantages and drawbacks of image guidance. However, for actual assessment of complications, the SRS Morbidity and Mortality Database appears to be the best source, as their dataset is large enough to report complication rates accurately. It would be important to report if image guidance or free-hand methods were used for surgeries in this database, and systematically include all surgeries completed at the center in reporting.

It is encouraging to see that defining breaches using 2mm increments and usage of CT scans to confirm breaches has largely become the standard for studies assessing breach rates in AIS surgery, as recommended in the first systematic review.

### 3.6. Conclusion

There is moderate evidence that image guidance reduces breach rates in AIS surgery from head-to-head studies (OR= 0.28 [0.20-0.40, I<sup>2</sup>=1%]), moderate evidence of no difference in breach rates from cohort studies with high heterogeneity, limited evidence of reduced thoracic breaches with image guidance (7% vs 15%  $p<0.01$ ) and limited evidence of no difference in lumbar breaches with image guidance (4% vs 9%,

$p=0.07$ ). There is moderate evidence that complications are no different between the two methodologies, both at 0% from head-to-head studies and conflicting evidence from cohort studies that there is no change in complication rates with navigation (0-1.6%) compared with free-hand methods (0-1.7%). There is moderate evidence that image guidance increases surgical times (257 mins vs 227 mins,  $p<0.01$ ).

Further randomized controlled trials comparing complication and breach rates between image guidance and free-hand methods with clearly defined breach and complications definitions are recommended to improve the current body of evidence on this question. However, given the current benefits of image guidance to reduce breach rates, it would be sensible to continue development on an image guidance system that did not include the main drawbacks of current navigation systems, specifically ionizing radiation, bulk, and interruption to surgical flow.



## Chapter 4: Evaluation of Accuracy and Precision of Motion Capture Cameras<sup>3</sup>

### 4.1. Summary

Surgical navigation requires translation of the real-world space into the virtual world, both for tracking surgical tools and for localizing patient anatomy. Motion capture camera technology is promising for accurately tracking position and orientation. As a result, the accuracy of the motion capture cameras is fundamentally the most important aspect in ensuring accuracy and precision of the overall navigation system. This chapter outlines the process for evaluating the motion capture camera accuracy. Section 4.2 outlines the setup and calibration of the system for usage in the operating room. Section 4.3 presents results from testing cameras when recording static objects. Section 4.4 presents results from testing different motion camera factors including rigid body types, marker sizes, calibration wand style, number of cameras and position of cameras. Section 4.5 presents dynamic testing, specifically translation and rotation of rigid bodies. Lastly, Section 4.6 discusses the proposed system and compares it with the current clinical data.

### 4.2. System Setup

#### 4.2.1. Motion Capture Camera Setup

Motion capture technology includes four components, the capture volume, motion capture cameras, motion tracking markers and an acquisition system. For a spine surgical field, the capture volume is composed of a region that is 0.6m in width, 0.8m in length and 0.6m in height surrounding the thoracic vertebrae which would typically be 15cm in width and 30cm in length. Because surgeons are typically standing on either side of the patient, cameras need to be mounted above the patient either by the patient's head or their feet. Mounting near the head was selected because of the closer proximity to the thoracic spine which is where the smallest pedicles tend to be and to avoid workflow obstruction by the patient's feet.

Optitrack 13W cameras (Prime 13W, NaturalPoint, United States) were selected because of their small size at 69x69x22mm, their wide field of view angle 82° x 70°, their high level of accuracy at within

---

<sup>3</sup>Chan A, Aguilon J, Hill D, Lou E (2017) Precision and Accuracy of Motion Tracking System for Pedicle Screw Placement in Adolescent Idiopathic Scoliosis. Med Eng Phys 46:33-43

0.2mm[220] and their compatibility with many other programs including Python, Matlab and Unity to stream position and orientation data. The cameras record at 120 to 240Hz, and they emit and capture 850nm infrared light to minimize interference from visible light. Three to four cameras would be used.

The cameras were connected to a switch through ethernet cables which in turn were connected to a computer via ethernet. Data from the cameras stream into the tracking software, Motive (Tracker v.1.10.0, NaturalPoint, United States) which displays the position of reflected markers on-screen as shown in Figure 4-1. The cameras need to be calibrated so that the relative positions of the cameras can be identified, and a 3D virtual capture volume that covers the camera field of view can be displayed

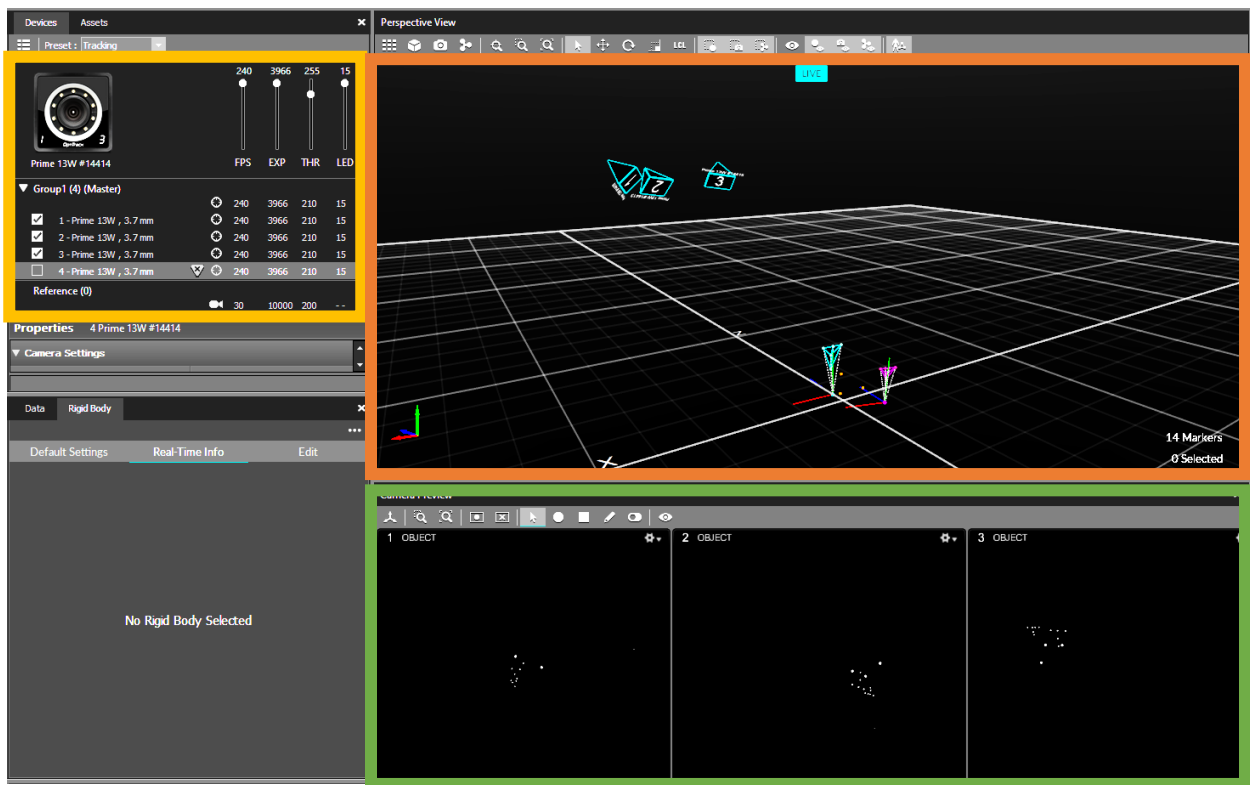


**Figure 4-1: Software view of motion capture cameras tracking objects. The yellow box outlines camera settings. The orange box shows the 3D view including cameras (labeled 1, 2 and 3 in the upper left corner) and motion tracked objects (teal and purple). The green box displays reflective markers as they appear in the view of each camera**

#### 4.2.2. Motion Capture Camera Calibration

Camera calibration was completed using the Optitrack CW-250 Calibration wand as shown in Figure 4-2. The wand has three motion capture markers at known distances from each other (250mm total width). By moving the wand throughout the capture volume, the cameras can back-project their relative positions and create the capture volume. The wand process would typically take less than a minute, with a

reprojection error (error of the 3D position of a point projected onto the 2D camera face) and recommended ray length (distance of markers from the cameras) displayed after wand. The target reprojection error for this study was 0.15mm and the recommended maximum ray length was at least 1.7m to ensure the spine would be within the optimal range. After calibration, the Optitrack CS-200 calibration square was placed in the center of the volume to set the origin of the capture volume (Figure 4-2).

The standard Optitrack markers used for the entire thesis study were 7.9mm reflective markers mounted on the M3 size bases (9mm circular diameter base). Larger sized markers on the calibration wand and square were not tested due to their higher risk of overlap in the camera field of views. While a single marker is sufficient to evaluate positional accuracy of the system, mounting three or more markers on a single object allows creation of a rigid body to evaluate orientation accuracy. The Motive system displays XYZ translational coordinates and Pitch, Yaw and Roll rotational angles using the XYZ Euler rotation sequence, but natively uses quaternion to determine orientation of rigid bodies.

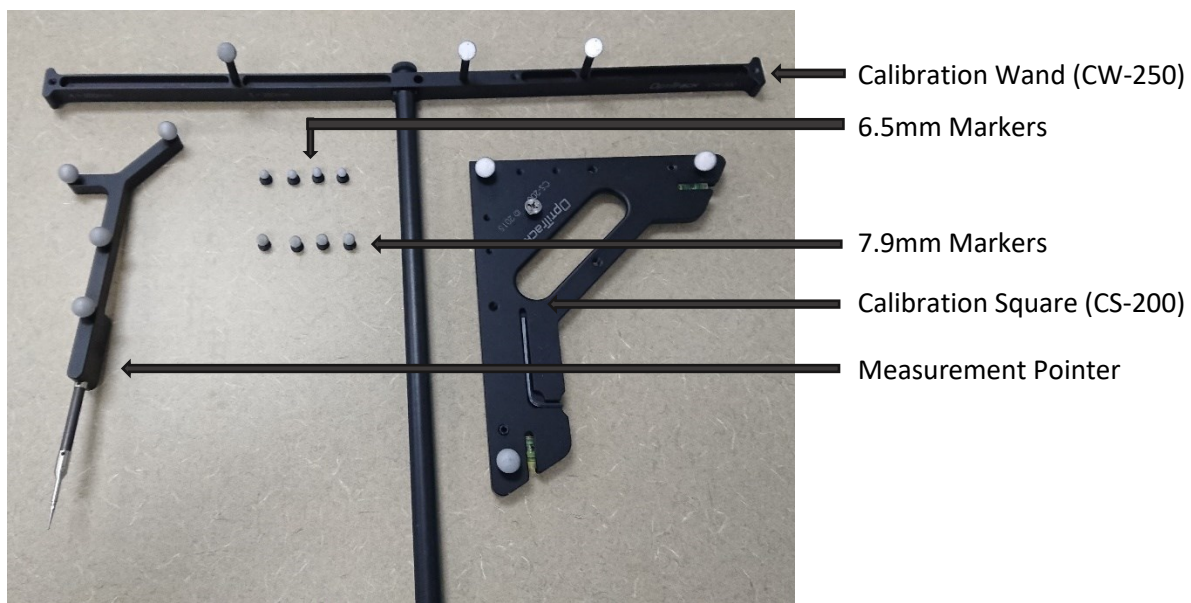


**Figure 4-2: Optitrack calibration equipment and reflective markers**

#### 4.2.3. Operating Room Compatibility

Most of the surgical navigators use the same reflective markers as the Optitrack system. However, as this system was not designed for the operating room, we needed to test the system compatibility with surgical tools in the operating room which could reflect infrared light emitted from these cameras, resulting in extra marker artifacts that may confuse tracking algorithms. The camera software includes three settings

to adjust compatibility with different spaces: exposure, threshold and LED. The exposure determines the amount of light exposure to each camera during capture; higher exposure results in brighter images. The threshold setting changes the light intensity level that must be met before the cameras start tracking an object when in marker-tracking mode; a higher threshold filters out more intensities of reflections. Lastly, the LED setting changes the number of LEDs that are actively emitting during recording. For this thesis project, the exposure was set to the highest setting while threshold was adjusted until only the markers could be visualized consistently. LED always maximized the number of LEDs emitting light.

The main objective of this compatibility test was to determine the effects of surgical lighting on the reflectivity of surgical tools and water. The motion cameras were brought to a surgical suite and a capture volume on the surgical table was calibrated and centered with the calibration square. A rigid body was created by mounting reflective markers on a periosteal elevator. Additional surgical implements (pedicle screws and rods) and a water bath were placed in the surgical field. Two surgical lights were placed in three different positions: directly above the capture volume at 1.5m height, directly above the volume at a 1m height, and lights angled, with one placed cranially and aimed caudally and the other placed caudally and aimed cranially, both at around 20° from vertical. The rigid body (Figure 4-3) was then moved throughout the capture volume and recorded for 1 minute. Each recording was screened for artifacts and disturbances in motion capture. Figure 4-3 shows the surgical bed, lights, and camera positions for the first configuration. Note that the configuration of the cameras had not been decided or tested at this point.

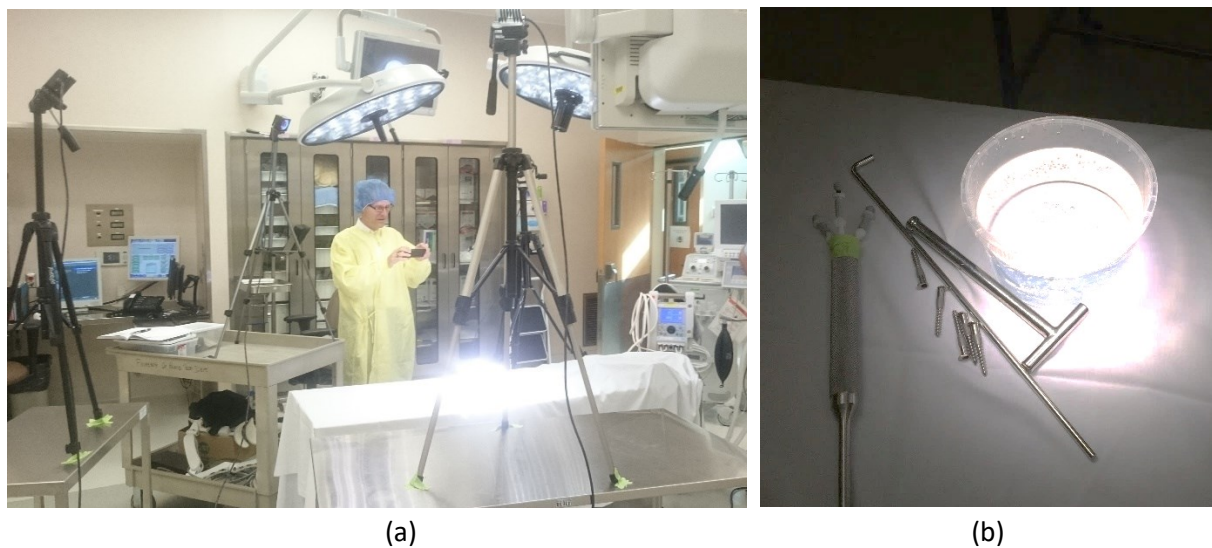


**Figure 4-3: Surgical suite showing setup of cameras with surgical lights turned on (left), surgical tools, dish of water and markers mounted on periosteal elevator (right)**

From this test no artifacts or disturbances were found.

The final configurations in term of the number and position of cameras were determined based on experiments discussed in Section 4.4.3. In the interim, the setup of the cameras involved three cameras mounted on tripods at 0.8-1.2m above the surgical bed (Y-direction) and 1.0-1.2m cranial to the capture volume (Z-direction) with a 1.0m width between the outermost cameras (X-direction) as shown in Figure 4-4. Cameras were placed at different heights and angles to cover multiple viewing angles for tracking objects. This setup was based on the minimum number of required cameras and dimensions of an operating room.

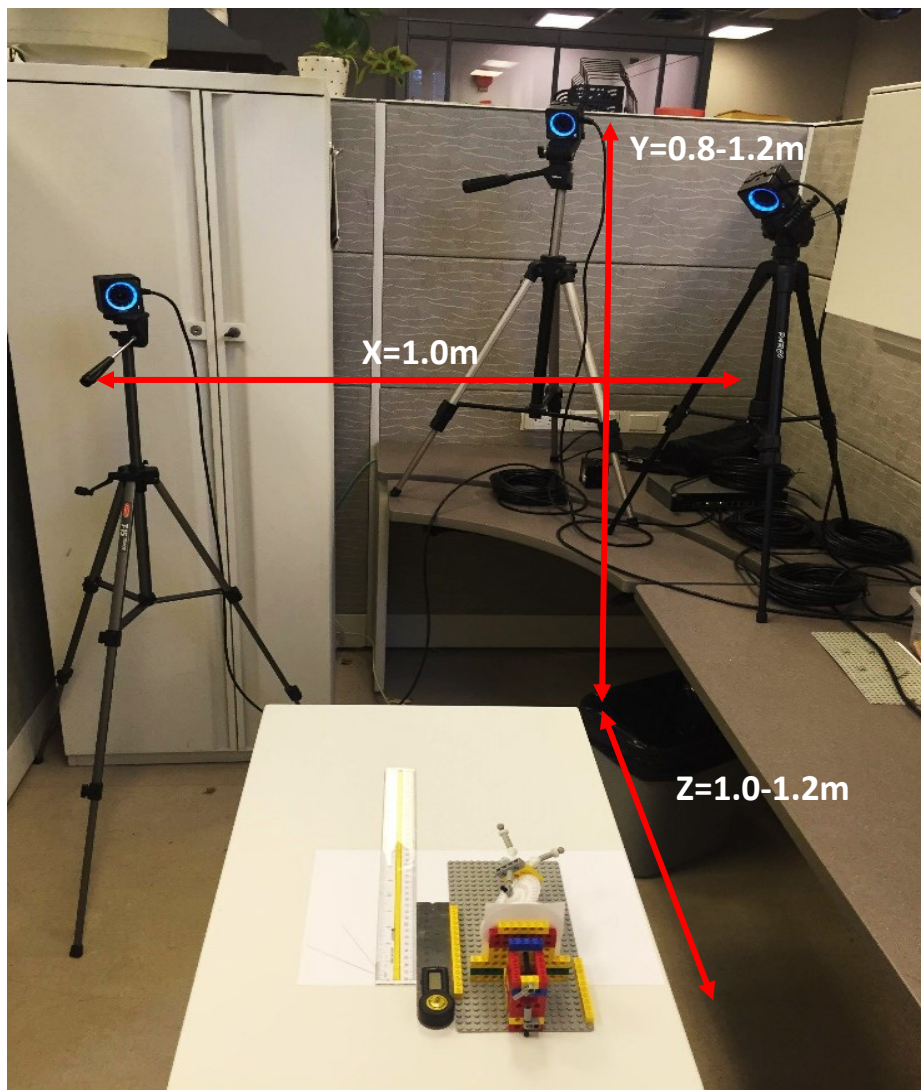


*Figure 4-4: Lab-based initial motion capture setup*

## 4.3. Static Testing

### 4.3.1. Static Testing Methodology

The first experiment was to determine the stability of static recording of markers to obtain a baseline of camera performance. A right triangle with 90mm x 120mm x 150mm was 3D printed with a fused-deposition modeling 3D printer (Makerbot Replicator 2X, Stratasys, Eden Prairie, Minnesota, USA) to hold three markers in a stationary position to generate a rigid body for static testing (Figure 4-5). The camera setup in Figure 4-4 was used and the 7.9mm markers were tested.

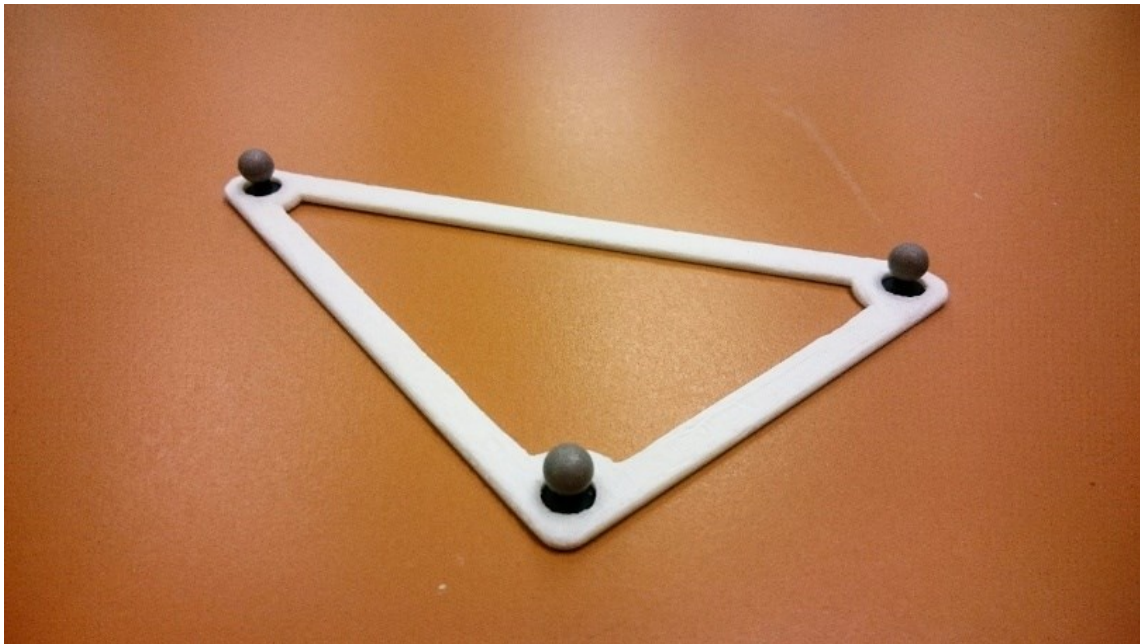


***Figure 4-5: 3D printed right triangle used for holding markers in place for static testing.***

Two experiments were completed to determine the precision of the markers: a set of three ten-minute trials and three six-hour trials. The ten-minute trials involved recording the position and orientation of the rigid body at 120 frames per second with samples taken at every 30 seconds for 1.5 seconds (180 frames) over a 10-minute period. To determine if cameras required a warm-up time, two sets of trials were completed: the first with cameras recording data within five minutes of being turned on from ambient room temperature (20°C) and the second with cameras being turned on for one hour prior to recording. The six-hour trial involved turning on the cameras from cold and then recording positional and rotational data every five minutes, acquiring data at 120 frames per second over two seconds (240 frames). Six hours was chosen to mimic the length of a spinal surgery. Cameras and markers were not moved between each of the three six-hour trials over three days. The mean difference from origin from their corresponding

time samples was calculated to compare the two trials. Each cold-start test was started on a different day with the pre-heat test completed on the same day, to allow for cameras to fully cool down.

The Motive Tracker position and orientation data was exported for the rigid body and data was post-processed by filling gaps with linear interpolation since the position and orientation should be unchanged when recording. The precision was quantified by calculating the 95% confidence interval of the standard deviation of position or rotation data for the sampled recording.

#### 4.3.2. Static Testing Findings

Figure 4-6 presents the mean difference from origin of rotation and position values for the ten-minute trials and the six-hour trials. The ten-minute trials showed precisions of 0.25mm and 0.06° from cold start, and 0.01mm and 0.01° from one hour preheat. For the six-hour trial data, standard deviation of all six hours is compared to hours two to six in Figure 4-6, showing a dramatic decrease in standard deviation when only including hours 2-6. The Y position (vertical) was the least accurate position, while roll (rotation about the Z-axis pointing away from the camera faces) was the least accurate rotation.

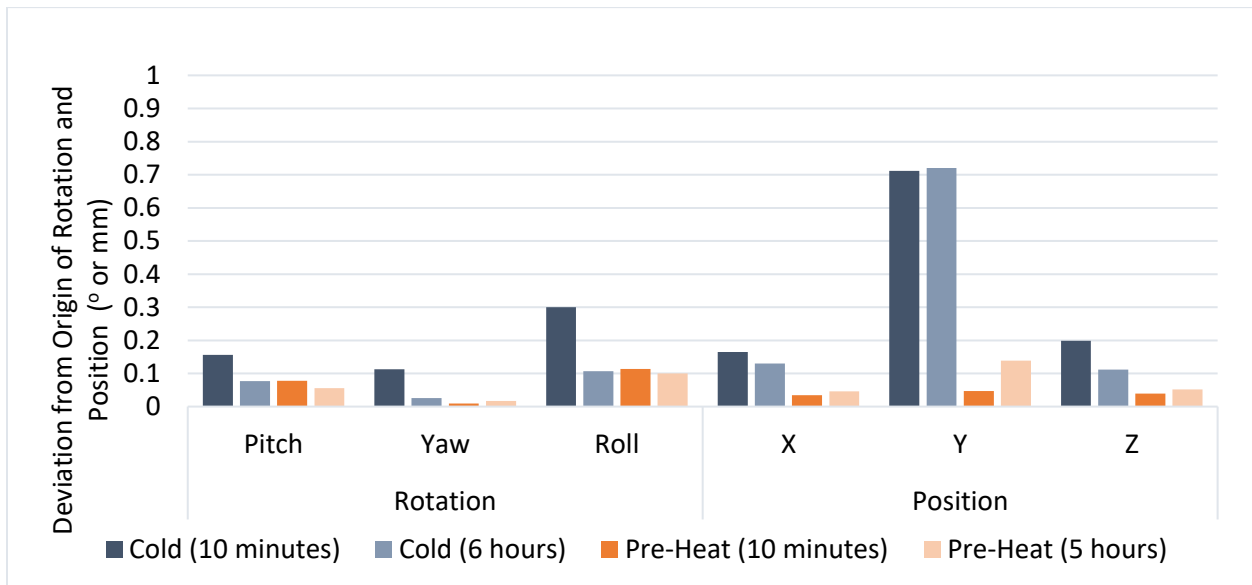


**Figure 4-6: Rotational and translational deviation over 95% confidence interval for cold-start over 10 minutes, cold-start over 6 hours, pre-heat over 10 minutes, and omitting the first hour of the cold-start 6-hour trial as pre-heat over five hours.**

A six-hour timeline of static position and rotation from the initial position is shown in Figure 4-7. A decrease in position of more than 2mm was noted in the Y direction, while a decrease of more than 0.3mm was found in both X and Z directions. Rotational precision was more consistent over six hours, varying

between  $-0.15^\circ$  to  $0.05^\circ$  throughout the recording time with no obvious time period at which the values settle to an equilibrium level.

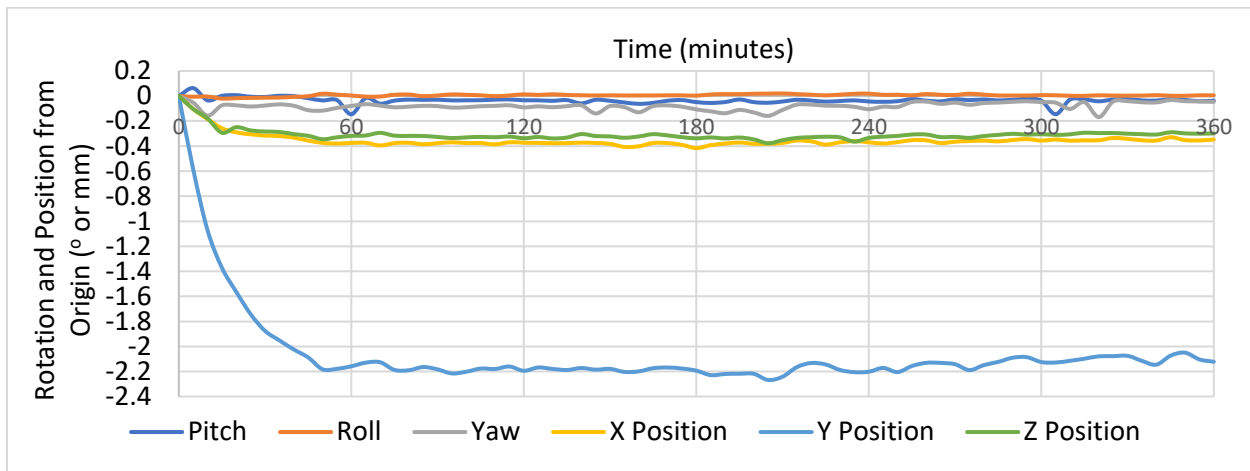


**Figure 4-7: Positional and rotational value deviation from initial value over six hours, sampled every five minutes from cold start.**

Overall, the mean difference from the origin greatly improved with a one-hour pre-heat period. The ten-minute tests showed a mean difference of 0.25mm and  $0.05^\circ$  without pre-heat and 0.01mm and  $0.01^\circ$  with pre-heat. Similarly, the six-hour tests showed improved precisions from 0.77mm and  $0.04^\circ$  over the first hour to 0.03mm and  $0.02^\circ$  over hours two to six, showing that the cameras are highly repeatable even over a long period of time, provided they have enough of a warm-up time.

Focusing on the 2mm deviation in the Y-direction, the position consistently decreased in the same direction in all tests, despite no movement of cameras or markers between each test. Cameras were locked in place and the rigid body was taped securely to the rigid capture surface. Slight but gradual movement of the cameras was considered, but any downward camera motion due to gravity would have shifted entire frame of reference downwards, resulting in a relative upward motion of markers rather than down in this study. The drift settled at the same time in all directions. Therefore, all subsequent testing was completed with a one-hour pre-heat period.

#### 4.4. Auxiliary Testing

##### 4.4.1. Statistical Methodology for Motion Capture Evaluation

Accuracy for the remaining motion capture tests was tested by recording the initial position of rigid bodies, translating them or rotating them to their final position, and then measuring their displacement linearly or rotationally. Translations and rotations were performed by mounting the rigid body onto digital



calipers (Mitutoyo, Japan) or a 3D-printed Lego rotation device shown in Figure 4-13 and then performing the displacement. The rigid body shown was created with a polyjet 3D printer (Objet30 Pro, Stratasys, United States). The displacement measured on the cameras was compared to either the linear calipers or 3D-printed rotating device. The 3D-printed protractor would rotate following the YZX Euler convention and the cameras were set to the same configuration (Figure 4-10). The precision of Lego block placement was found to be within 0.05mm by making 10 measurements after removing and re-placing the protractor on the Lego pegboard which would result in a potential error of 0.1° and deemed to be adequate for this application.

Accuracy was calculated as a root-mean-square (RMS) error using Equation 4-1:

**Equation 4-1: RMS Accuracy Equation**

$$RMS\ Accuracy = \sqrt{\frac{\sum_{N=1}^n (X_N - X_o)^2}{N}}$$

Where:

- $X_N$  represents the position value being measured
- $X_o$  is the theoretical value
- $N$  is the number of samples taken.

The confidence interval of the mean value of the position was calculated in Equation 4-2:

**Equation 4-2: Confidence Interval of Mean:**

$$Confidence\ Interval\ of\ Mean\ Value = X \pm t \frac{s}{\sqrt{N}}$$

Where:

- $X$  is the mean value of the position
- $s$  is the standard deviation of the sampled position values
- $N$  is the number of position values
- $t$  value for that number of position values at a 95% confidence interval.

4.4.2. Markers, Rigid Body and Calibration Wand Evaluation

The various accessories that would be used for motion capture were evaluated next, studying the optimal marker sizes, rigid body configuration, and calibration wand size (Figure 4-8). The markers were placed on the triangular rigid body (markers placed 25mm apart) in Figure 4-8b, and then translated within the X-Z plane by 40mm, ten times each (five along the X-axis, five along the Z-axis), to test the repeatability of measurements. Next, 6.4mm markers were tested with the same configuration. Third, a linear rigid body

configuration (markers placed 24mm and 16mm apart) was compared to a triangular configuration and translated in the same manner (Figure 4-8a).

Lastly, the accuracy of tracking the standard rigid body after performing calibration wand with a smaller 96mm calibration wand (markers 56mm and 40mm apart) was compared to the standard Optitrack CW-250 wand (markers 100mm and 150mm apart) that was used previously to determine if using a small calibration wand at comparable size to the rigid body would affect accuracy. The triangular rigid body with 7.9mm markers was used as the standard rigid body in this case and translated in the same manner as above.

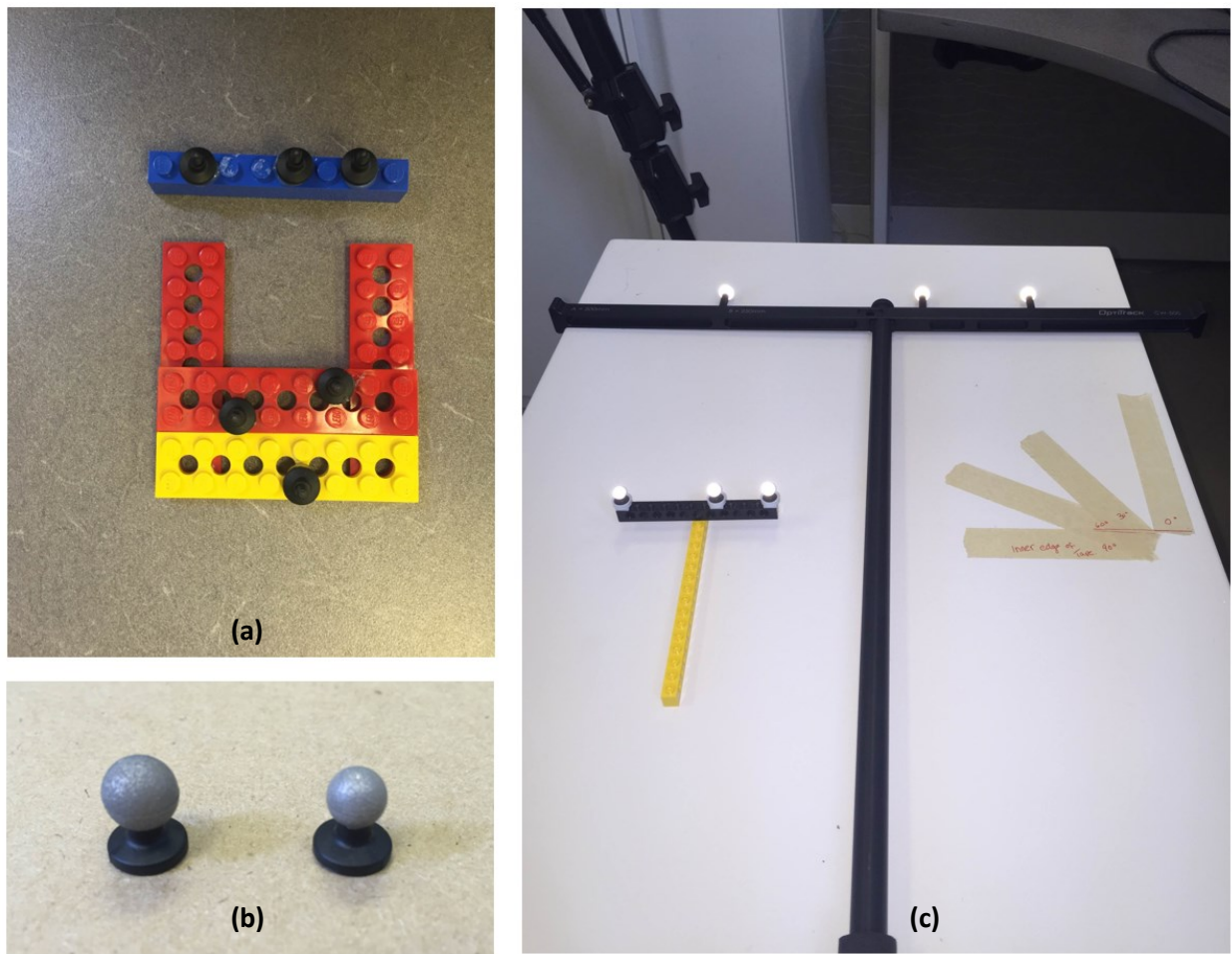


**Figure 4-8: Motion capture accessories: (a), linear rigid body and triangular rigid body; (b), 7.9mm vs 6.4mm markers; (c), Standard calibration wand vs custom small calibration wand.**

Figure 4-9 compares the positional RMS accuracy and standard error of the four tests: the triangular rigid body with 7.9mm, triangular rigid body with 6.4mm markers, the linear rigid body with 7.9 mm markers, and the custom 96mm wand for calibration. The RMS accuracy was 0.20mm for the standard triangular

rigid body, 0.20mm for smaller markers, 0.50mm for the linear rigid body and 0.30mm for the custom wand.

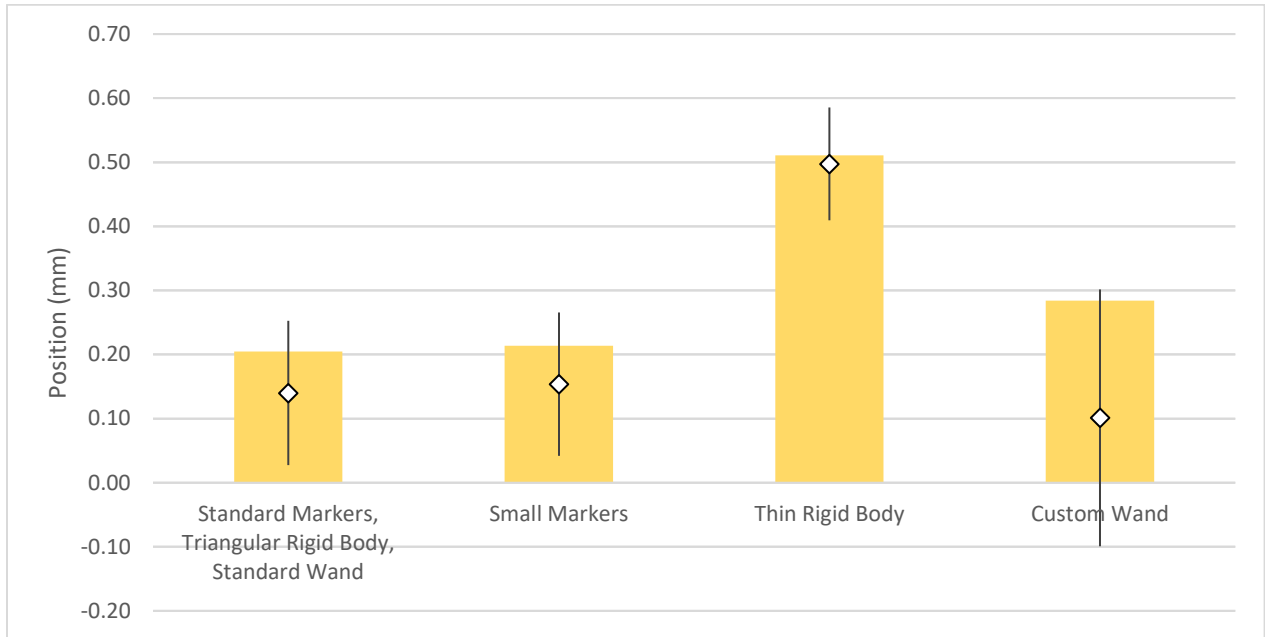


**Figure 4-9: Positional RMS accuracy (bar chart) and 95% standard error (diamond with error bars) from different rigid bodies and wands. The 7.9mm marker rigid body compared with 6.4mm markers, linear rigid body (standard markers and wand) and custom 9.6cm wand for calibration (standard triangular rigid body and marker size)**

The 7.9mm triangular rigid body had similar accuracy to the 6.4mm markers. This contrasts with Windolf et al. who found that larger reflective markers yielded improved accuracy [114]. The triangular rigid body had superior accuracy to the linear rigid body. The superiority of the triangular rigid body was expected since having markers along two dimensions of the three-marker plane would provide more spatial information for tracking than along a single dimension. In particular, the Z direction had a significantly worse accuracy, likely due to the linear rigid body being aligned to the Z direction during placement. The custom wand had inferior accuracy compared with the large wand which was likely because even small errors in tracking the small wand or placement of markers on the wand would result in errors propagating when calibrating camera positions. As a result, a standard wand with triangular rigid bodies and any sized markers would be used in future experiments.

#### 4.4.3. Camera Configuration Evaluation

The number and positions of cameras was the next attribute tested. Three variables were tested: Number of cameras (3 or 4), height alignment (staggered or aligned), and depth alignment (staggered or aligned),

resulting in a total of eight combinations. Height staggering ranged from  $\pm 15\text{cm}$ , and depth staggering ranged from  $\pm 20\text{cm}$  as shown in Figure 4-10.

To assess accuracy, the three-marker rigid body (Figure 4-13 **Error! Reference source not found.**) was used. The accuracy of the caliper was within  $0.01\text{mm}$ . The rigid body was translated ten times by  $40\text{mm}$  for each of the eight camera configurations.

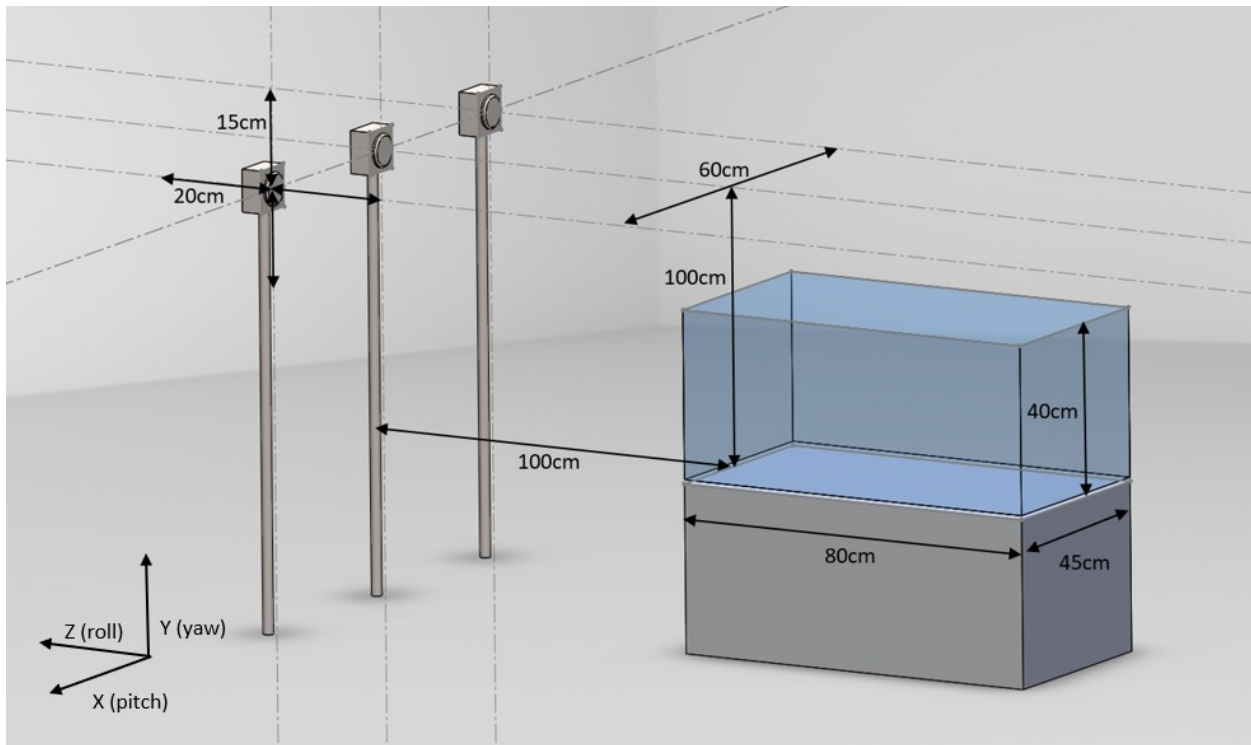


**Figure 4-10: Schematic of camera position relative to capture volume. Blue (translucent) region shows capture volume. For camera configuration testing, depth was varied by 20cm in either direction and height by 15cm in either direction while overall width was kept constant at 60cm due to surgical space constraints.**

Figure 4-11 compares the position RMS accuracy and standard error between the eight configurations. The configuration with best accuracy used three cameras with staggered height (side cameras at  $+15\text{cm}$  and  $-15\text{cm}$  with center camera at  $0\text{cm}$ ) and aligned depth at  $100\text{cm}$ , with an accuracy of  $0.15\text{mm}$  while the poorest used four cameras with aligned heights and staggered depth at  $0.55\text{mm}$ .

The configuration with best repeatability (shown in the error bars in Figure 4-11) used three cameras with both staggered heights (side cameras at  $+15\text{cm}$  and  $-15\text{cm}$  with center camera at  $0\text{cm}$ ) and staggered depths (side cameras at  $+20\text{cm}$  and  $-20\text{cm}$  and center camera at  $0\text{cm}$ ) of cameras, with repeatability at  $0.05\text{mm}$ . The poorest used four cameras with staggered height and aligned depth at  $0.10\text{mm}$ . On average,

three cameras were superior to four cameras at 0.10mm vs 0.20mm, staggered height was similar to aligned height at 0.15mm vs 0.15mm and aligned depth superior to staggered depth at 0.10mm vs 0.20mm.

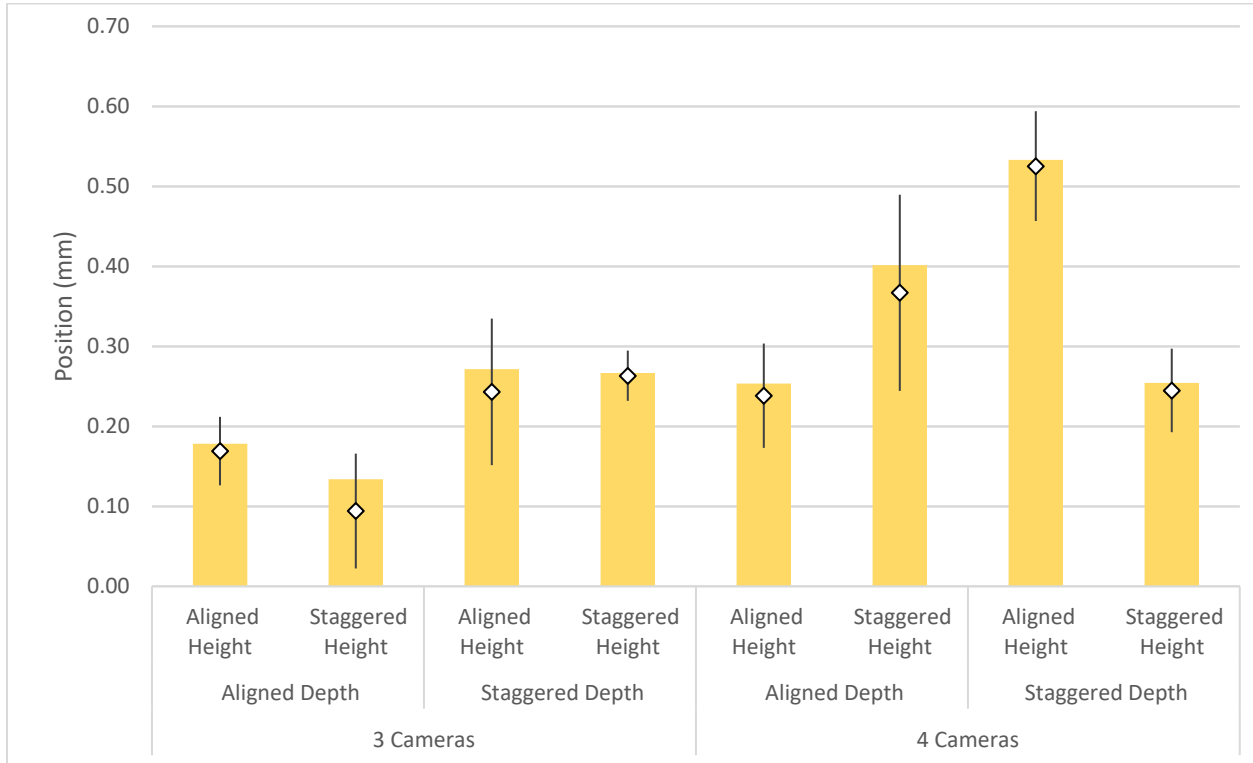


**Figure 4-11: Positional RMS accuracy (bar chart) and 95% standard error (diamond with error bars) comparing eight camera configurations: three to four cameras, aligned or staggered heights, aligned or staggered depths, in X, Z and Y directions.**

Camera configuration also had surprising results, with three cameras superior to four cameras in both accuracy and standard error. While it was expected that increasing the number of overlapping fields would improve accuracy, it is possible that three overlapping perspectives is already adequate to maximize accuracy in those fields. Adding a redundant image did not contribute new information. Instead, it hampered the accuracy, potentially due to imprecise matching of camera properties like gain, focal length and spectral response. Considering previous research, Eichelberger et al. found that eight cameras were superior to six, but ten was no different from eight cameras [221]. Windolf et al. compared a three camera setups in arbitrary positions with two four camera setups, showing it to be superior to one four camera setup and inferior to the other, all camera setups being arbitrary[114]. This study showed that increasing number cameras was no guarantee of improved accuracy.

#### 4.4.4. Auxiliary Evaluation Summary

In future experiments, the rigid body would have an added marker to ensure proper orientation tracking by providing more than one plane to be reconstructed from the marker positions. This is in-line with current industry navigation systems that use four markers or more in a plane. Calibration would be completed using the 250-CW configuration of the calibration wand.

For the cameras, a three-camera system staggered height and aligned depth was selected as the superior configuration. Typical navigation setups in the operating room involve two- or three-camera systems mounted on a moveable ceiling mount. As surgeons typically stand on either side of the operating table, cameras are usually mounted above the head of the patient to minimize occlusion of camera views. Although tripods were used in this study for ease of adjustment of the cameras, a rigid motion capture frame was fabricated for testing in the operating room.

#### 4.4.5. Navigation Camera Frame Setup

The motion capture frame was designed by two teams of mechanical engineers in their Capstone Project to allow mounting of up to four cameras to allow for a higher number of perspectives to prevent marker occlusion. A full design report was submitted by both teams but only a summary of the results is presented here. The primary purpose of the frame was to rigidly mount four cameras above the operating space at a height of 1.5-2.0m and width of 0.6m to fit around a typical operating table. Cameras were mounted on double socket arms that could be re-oriented and re-positioned within a range of 0.2m about a center of rotation. For ease of mobility and setup, the frame was mounted on two separate wheeled bases that lift-lock in place. The two halves of the frame could be fixed together to improve rigidity during usage. The selected wheeled bases were heavy and wide to tipping. An integrated ethernet cable management system and mount for the ethernet switch was included. Figure 4-12 shows the labelled components on the final motion capture frame design.

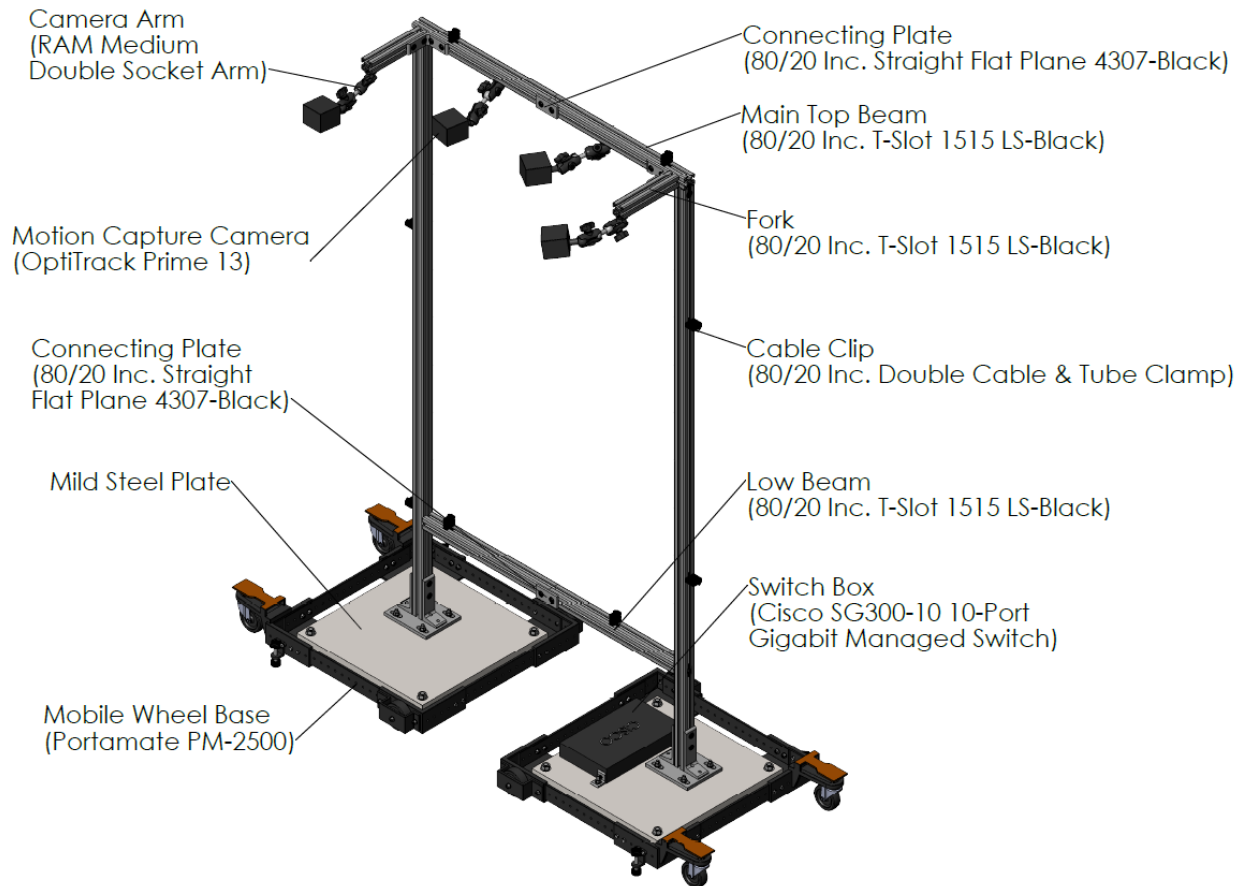


**Figure 4-12: 3D rendering of motion capture frame**

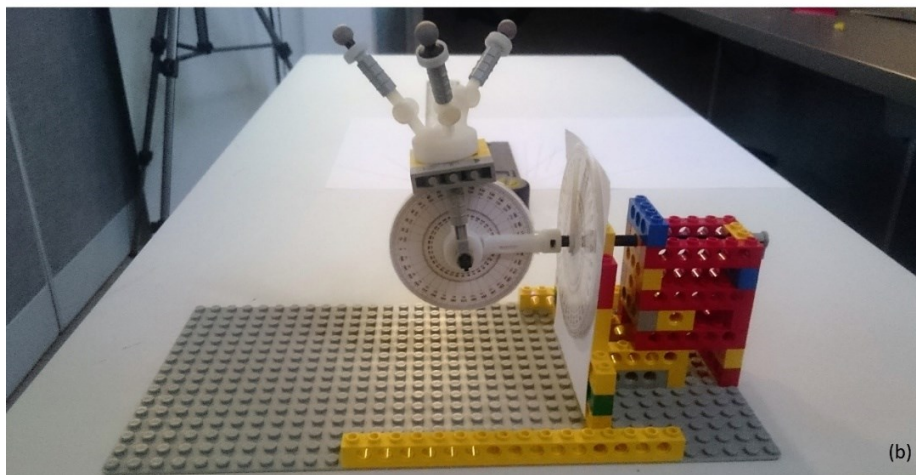
## 4.5. Displacement Testing

### 4.5.1. Displacement Testing Methodology

The final set of testing for motion capture cameras involved recording translations and rotations of rigid bodies. Translation magnitude was tested by mounting the rigid body onto digital calipers (Figure 4-13a) and translating three times by 10mm, 20mm, 40mm, 80mm and 150mm in X, Y and Z directions separately. The magnitude of these movements was chosen based on the translations required to move across the dimensions of the T4 to T9 region of a standardized phantom spine model. To test the accuracy of rotation, a set of rotation variables (summarized in Table 4-1) were tested by mounting on the rotational device in Figure 4-13. Testing was completed over a single day. With each variable, each combination was tested three times. Angle values were selected to cover the range of motions of pedicle screw placement.



(a)



(b)

**Figure 4-13: Motion capture measurements: a) Rigid body mounted on a digital caliper for translational testing, (b) Mounting of rigid body on a three-directional protractor for rotational testing.**

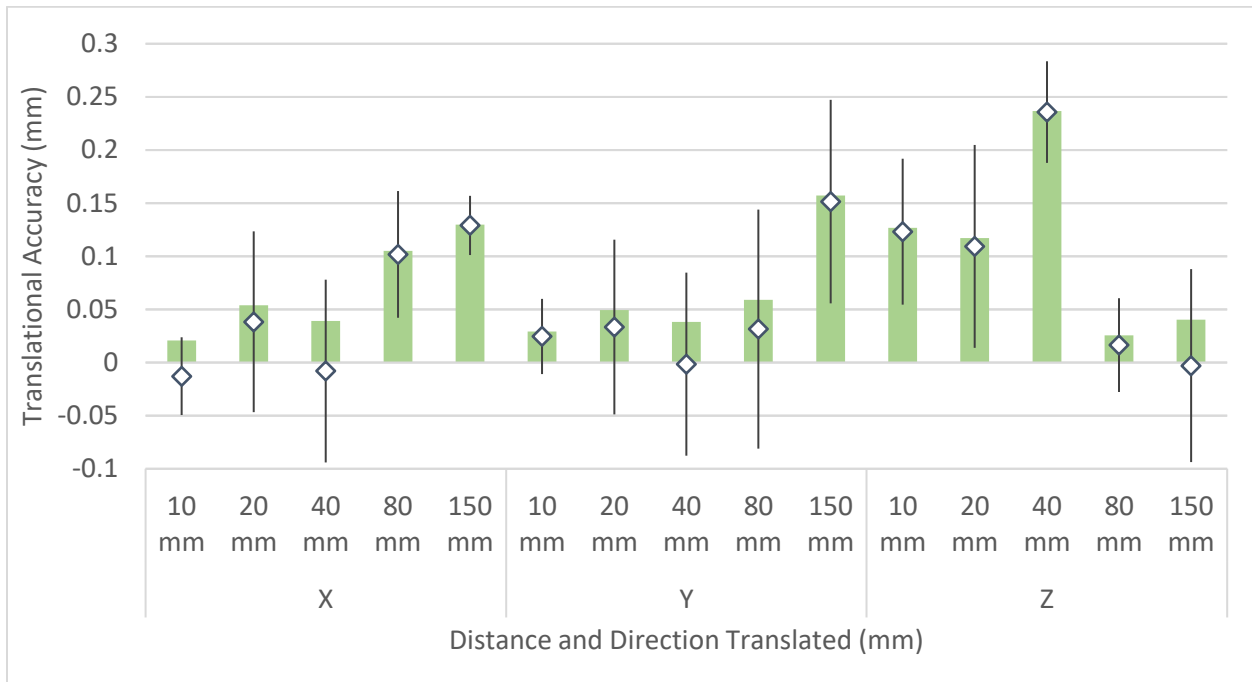
**Table 4-1: Rotational variables tested in the motion capture system**

Variable Changed	Description of Variable
<b>Single Direction</b>	30° and -60° rotations about each axis individually. 30°, 0° and 0°    0°, 30° and 0°    0°, 0° and 30° 60°, 0° and 0°    0°, 60° and 0°    0°, 0° and 60°
<b>Three Directions</b>	Combinations of three rotations along three axes: -30°, 45° and -60°    45°, -30° and -60°    -60°, 45° and -30° -30°, -60° and 45°    45°, -60° and -30°    -60°, -30° and 45°
<b>Small Angles</b>	Combinations of three rotations along three axes: 5°, 10° and 5°    10°, 10° and 5° 5°, 5° and 10°    10°, 5° and 10°
<b>Large Angles</b>	Combinations of two rotations along three axes: 60°, 60° and 0°    60°, 0° and 60°    0°, 60° and 60° 65°, 65° and 0°    65°, 0° and 65°    0°, 65° and 65° 70°, 70° and 0°    70°, 0° and 70°    0°, 70° and 70° 75°, 75° and 0°    75°, 0° and 75°    0°, 75° and 75°



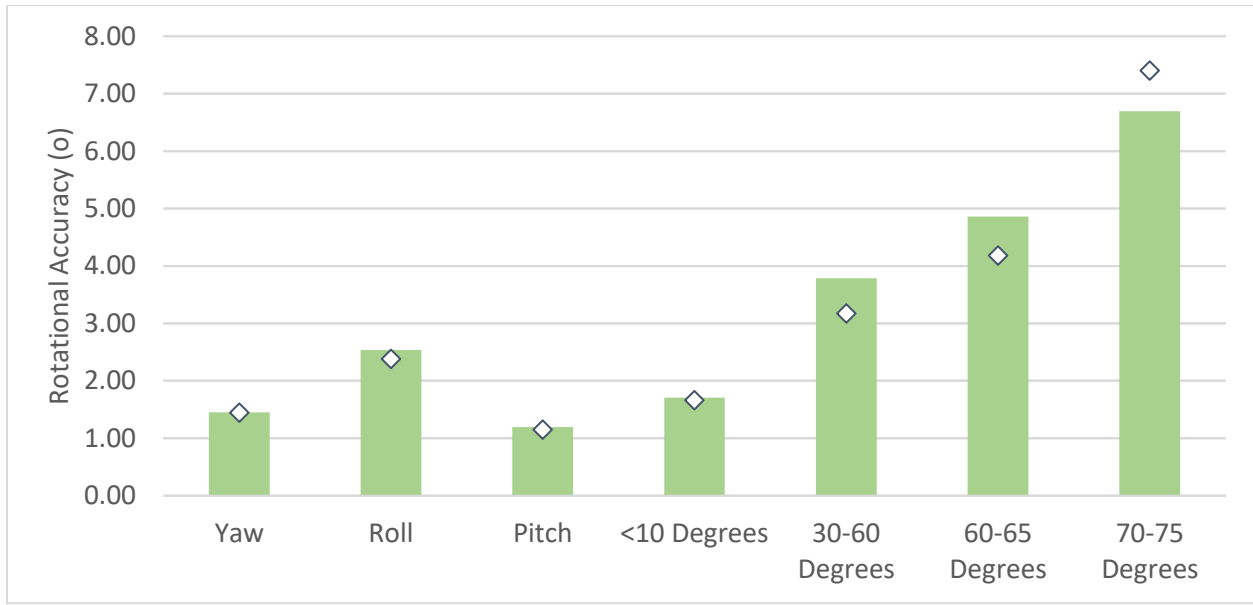
#### 4.5.2. Dynamic Testing Results

Figure 4-14 displays the RMS accuracy and 95% standard error of 10-150mm movements in each direction. The RMS accuracy when translating 10mm, 20mm, 40mm, 80mm and 150mm was 0.15mm, 0.15mm, 0.25mm, 0.10mm and 0.20mm while the standard errors were 0.10mm, 0.15mm, 0.15mm, 0.15mm and 0.15mm, respectively.



**Figure 4-14: Positional RMS accuracy (bar chart) and 95% confidence interval of standard error from the actual mean (diamond with error bars) at 10mm, 20mm, 40mm, 80mm and 150mm in X, Z and Y directions. . Diamond represents the standard error from the actual mean value while bar chart represents RMS error.**

Figure 4-15 compares the rotational RMS accuracy and standard error of the rotations from Table 4-1. The roll accuracy (rotation about the Z-axis) was least accurate, while yaw and pitch (rotations about the Y and X axis respectively) were more accurate. The accuracies were: from two rotations less than 10° at 1.7°, three rotations less than 60° at 3.8°, two rotations between 60° and 65° at 4.9° and two rotations greater than 70° at 6.7°. The standard error was less than 0.05° for all rotational tests.



**Figure 4-15: Rotational RMS accuracy (bar chart) and 95% confidence interval of standard error from the actual mean (diamond with error bars) comparing rotation in only X, Y and Z directions, two angle combinations at <math><10^\circ</math> degrees, three angle combinations at <math>30^\circ</math>, <math>45^\circ</math> and <math>60^\circ</math>, two angles combinations at <math>>60^\circ</math> degrees and two angle combinations at <math>>70^\circ</math>. Error bars are too small to be visualized on the figure as they were less than <math>0.05^\circ</math>.**

Translational accuracy and standard error were superior in the X direction. Translational accuracy was larger in the Z and standard error was poorer in the Y direction, though overall accuracy and standard error remained below 0.10mm for both. Accuracy travelling 40mm in the Z direction appeared to be an outlier since it did not follow a consistent trend with the other translation magnitudes, with errors spiking higher than the other results. There was no identifiable reason for this, though it did appear to be repeatable.

Because the X direction is orthogonal to all three cameras it has greatest redundancy in the motion capture field of view. However, the Z direction is at an angle with respect to the three cameras with motion that is mostly parallel to the camera's orientation which explains its larger errors. From these translational results, the RMS accuracy of the system was deemed as 0.25mm, equivalent to the worst RMS accuracy from the translational tests. The standard error of the measurements was 0.1mm which was comparable to the ten-minute static precision value of 0.10mm over a 95% confidence interval.

Regarding rotation, the worst accuracy was for angles greater than <math>70^\circ</math> at <math>6.9^\circ</math> which was expected. The standard error was small (worst at <math>0.05^\circ</math> for angles greater than <math>70^\circ</math>) Angles greater than <math>70^\circ</math> would be too inaccurate for clinical use given the poorest accuracy value of <math>9.1^\circ</math> compared with the required accuracy

of 5.0°. The large angular errors are likely due to angles in one direction being detected in a different direction due to the large magnitude of the rotations. These angles would be unlikely in a clinical setting, as the screws would be inserted virtually parallel to the surgical table.

#### 4.5.3. Pegboard Pilot Test

An additional displacement test using a LEGO pegboard to act as a frame of reference was also completed. Firstly, the repeatability of distances between LEGO pegs was determined by making caliper measurements throughout the pegboard. From 30 measurements, a 95% confidence interval of 14 micrometers was found. Secondly, a pilot test on motion capture accuracy from different displacements was completed. Three distances were tested: (a) 8mm lateral and 9.6mm vertical displacement, (b) 24mm lateral and 19.2 vertical displacement, and (c) 120mm lateral and 115.2mm vertical displacement. The distances were determined according to the dimensions of the LEGO blocks themselves. Two sets of 12 measurements were completed for each distance, the first moving laterally in the X direction and the second moving vertically in the Y direction.

Results in Table 4-2 found a distance dependence to the error value, with larger displacements having larger errors, which aligns with the caliper findings. Further evaluation of pegboard positional accuracy would be done with the 3D ultrasound phantoms.

**Table 4-2: Displacement accuracy and standard deviation for pegboard**

	<b>8mm Lateral, 9.6mm Vertical</b>	<b>24mm Lateral, 19.2mm Vertical</b>	<b>120mm Lateral, 115.2mm Vertical</b>
<b>Accuracy (mm)</b>	0.15	0.20	0.30
<b>SD (mm)</b>	0.20	0.30	0.35

## 4.6. Clinical Relevance

### 4.6.1. Phantom Studies on Motion Capture Accuracy

The aim of this study was to determine if commercial-grade motion capture systems had adequate accuracy for surgical application. The lower cost and greater flexibility in using multiple cameras at different areas in the operating room make these systems attractive to use for navigation systems, for this 3D ultrasound system. However, their accuracy needs to be comparable to current navigators.

In the surgical field, measurement error of surgical optical navigators have a range from 0.2-1.9 mm, whether for placement of surgical instruments or measurements of landmarks [111,123,124]. The most precise evaluation of motion capture was completed by Koivukangas et al. on the StealthStation S7 system (Medtronic, Louisville, CO, USA) and was tested on an industrially verified phantom, resulting in an

accuracy of  $0.2\pm 0.1\text{mm}$  for up to 120mm translations. A head phantom was tested using the Polaris Vicra (NDI, Waterloo, Canada) navigation camera resulting in errors of 0.3-0.6mm for registration. Comparing to current results from the Optitrack 13W system, these accuracies are comparable with the reported studies.

#### 4.6.2. In-Vivo Navigation Accuracy

Holloway et al. evaluated the O-arm for both measurement error and accuracy of lead positioning in deep brain stimulation procedures, finding an accuracy of 0.7mm and 2.1mm respectively. Navigation in human cadavers and in patients have found registration errors of 0.5-3mm [127,128]. Papadopoulos et al. reports the mean registration error as estimated by the computer which depends on the cameras to measure error instead of an external validating device. Holly et al. used a more accurate measure by calculating the distance between the actual probe position and the virtual probe position, measuring surgical registration accuracy. This study uses digital calipers or a 3D protractor to determine accuracy of position and rotation. Translating these engineering measures directly into screw trajectories remains a shortcoming of this thesis chapter.

Further in vivo studies have compared intra-operative predicted screw trajectories with post-operative screw placement. Oertel et al. found that predicted screw trajectories differed from post-operative trajectories by  $2.8^\circ$  [11]. Scheufler et al. had similar findings, with trajectories differing by less than  $2^\circ$  in 98% of patients [125]. Because these were in vivo studies, usage of post-operative CT to confirm screw position is likely the best method to validate placement, though these studies did not consider positional accuracies. From this study, accuracies ranged from  $1.7^\circ$  to  $3.8^\circ$  for rotations less than  $60^\circ$  and  $4.9^\circ$  for rotations between  $60-65^\circ$ . While numerical accuracies are inferior in this system, further study in measuring screw trajectories would be needed to ensure comparability. Also, the error in our study considered all three dimensions while current in vivo studies compared axial scans of screws on single planes, potentially underestimating the actual angular error. Still, the desired standard of  $5^\circ$  was achieved for rotations less than  $65^\circ$ .

It is expected that screw trajectories will be less than  $45^\circ$  during screw insertion. In an adult cadaver study by Chung et al., the maximum required transverse and sagittal screw angles ranged from  $9.4$  to  $29.5^\circ$  and  $5.2$  to  $25.4^\circ$  respectively [222]. Pedicle angles in a skeletal study of pediatrics patients by Zindrick et al. found transverse pedicle angle ranges from  $-4.2$  to  $35.3^\circ$  and sagittal angles from  $1.8$  to  $23.3^\circ$  [20]. By calibrating the orientation of the motion capture system according to the spinal coordinate system, the range of angles of screw insertion can be kept similar to the transverse and sagittal pedicle angles reported

in the two studies above, though a wider range would be ideal to maintain robustness of the system. Given the maximum angles of 23.3° and 35.3° the 3.9° accuracy level achieved in rotations less than 60° meet the required accuracies.

Focusing on the final application, accuracy of pedicle screw placement has typically been presented as a breach rate, with breaches defined as either a magnitude in millimetres, or according to the proportion of the screw penetrating the cortex of the pedicle [186,199]. Both medio-lateral translation and transverse trajectory can affect the extent of a breach. However, a recent study by Guha et al. suggested that clinical accuracy and engineering accuracy are often not well correlated and recommended that absolute navigation accuracy be reported for true evaluation and navigation system accuracy [223]. For this study, the engineering accuracies relative to a static flat surface, have been confirmed to be adequate for screw placement. However, further study into evaluating accuracies relative actual anatomy needs to be completed.

#### 4.7. Conclusion

The Optitrack Prime 13W system was evaluated for its accuracy in usage for pedicle screw placement in spinal surgery. The system exceeded translational accuracy requirements at 0.25mm compared to the required 2mm clinical standard. However, rotational accuracy met the 5° requirement only in rotations less than 65° at 4.9°. A three-camera configuration with each camera aligned at the same depth while having varying heights to cover the camera area had the best accuracy. The system also has comparable accuracy to conventional CT-navigation systems, showing that mid-range motion capture has similar capabilities to current navigation technologies.

## Chapter 5: Development of 3D Ultrasound for Surface Reconstruction and Positioning of Vertebrae<sup>4,5</sup>

### 5.1. Summary

Ultrasound is an inexpensive, handheld, and radiation-free imaging modality that uses echoes from high frequency mechanical vibrations to generate images. The advent of 3D ultrasound to reconstruct human anatomy has allowed for more readily interpretable images, but the accuracy of these images is still in question due to the user-dependence of generating these images. For navigation surgery, it is critical to generate images with high anatomical accuracy which are localized in the correct position for navigation. This chapter outlines the process used in developing and testing a new 3D ultrasound system that was designed specifically for reconstructing and localizing spinal surfaces. Section 5.2 outlines the motion capture and ultrasound settings, and preliminary streaming testing of the system. Section 5.3 describes the software development process and the image processing that was used. Section 5.4 reports the calibration process for this 3D ultrasound system. Section 5.5 outlines the reconstruction accuracy of the system on phantoms while Section 5.6 describes the accuracy of 3D ultrasound to localize the placement of these phantoms throughout the space. Section 5.7 presents evaluates the position and orientation of vertebrae-like phantoms and probes placed through pedicle holes phantoms Section 5.8 presents a discussion of the strengths and weaknesses of this study, and a comparison with other current technologies while concluding remarks are given in Section 5.9.

---

<sup>4</sup>Chan A, Parent E, Lou E (2018) Reconstruction and positional accuracy of 3D ultrasound on vertebral phantoms for adolescent idiopathic scoliosis spinal surgery. *Int J Comput Assist Radiol Surg.* 14(3): 427-439

<sup>5</sup>Ottacher D, Chan A, Parent E, Lou E (2020) Positional and Orientational Accuracy of 3D Ultrasound Navigation System on Spinal Phantoms for Scoliosis Surgery. *IEEE: Trans Instr. Meas.* – Accepted Jan 20, 2020

## 5.2. System Setup

### 5.2.1. Motion Capture Setup

The previous chapter outlines the basic setup of the motion capture system. To re-iterate, three- Optitrack Prime 13W cameras (NaturalPoint, United States) were placed on tripods 0.8-1.2m above and 1.0-1.2m cranial to the capture volume with 1.0m width between the two outermost cameras. Cameras were set to capture at 240 Hz and calibration was completed with an Optitrack CW-250 Calibration wand to obtain over 10000 data points over 1 minute until an estimated error of less than 0.15mm was achieved. The capture volume origin was set by placing the Optitrack CS-200 Calibration Square on a pegboard in the center of the volume.

### 5.2.2. Ultrasound Settings

The ultrasound scanner used in this study was an Ultrasonix SonixTablet (BK Ultrasound, Peabody, MA, United States) which includes a 128 elements transducer and 40 MHz sampling rate. Initially, two transducers were tested, first an L14-5/38 linear array with 38mm width and the second a C5-2/60 curved array with 60mm width. Tests with the curved array transducer showed a significant amount of artifact when imaging phantoms due to reverberations from the surrounding container walls. While the linear array was narrower than a typical vertebra would be, it was selected for its higher frequencies offering higher resolution and better reflections on the bone. Figure 5-1 shows the software user interface for the Ultrasonix system, including the three sets of potential settings.

The relevant settings that were changed included: Focus #, Focus, Focus Span, Sector, Persist, FrRate, Freq, Depth and Map. The 'Focus #' changes the number of ultrasound focal points in the image, 'Focus' changes the position of the focal point and 'Focus Span' changes the distance between each focal point if multiple are present. The 'Sector' determines the size of the lateral window of the transducer. The 'Persist' setting determines the number of frames that will be smoothed with the current frame during display. The 'FrRate' changes the image acquisition frame rate while 'Freq' changes the transducer frequency between 5 MHz, 6.67MHz and 13.3 MHz. The 'Depth' determines the maximum imaging depth of the transducer, while 'Map' determines the contrast profile for imaging out of 17 presets.

For proper sizing of the window, a 100% 'Focus Span' was selected, using the full-width of the transducer, while 'Depth' was set to 3.0cm to minimize reverberation artifacts while ensuring adequate imaging depth. Two focal points were included with a window of 1.5cm centered at a depth of 1.5cm. Because the ultrasound is used to image the bony surface, there were no attenuation concerns for transducer

frequency, allowing the frequency to be set at the highest level (13.3MHz) resulting in high resolution images. Lastly, the frame rate was set to medium at 31Hz, to ensure minimal lag when streaming to the computer. 'Persist' was turned down to zero to reduce smoothing between frames and 'Map' was changed to #17 to maximize contrast between bone and the water medium.

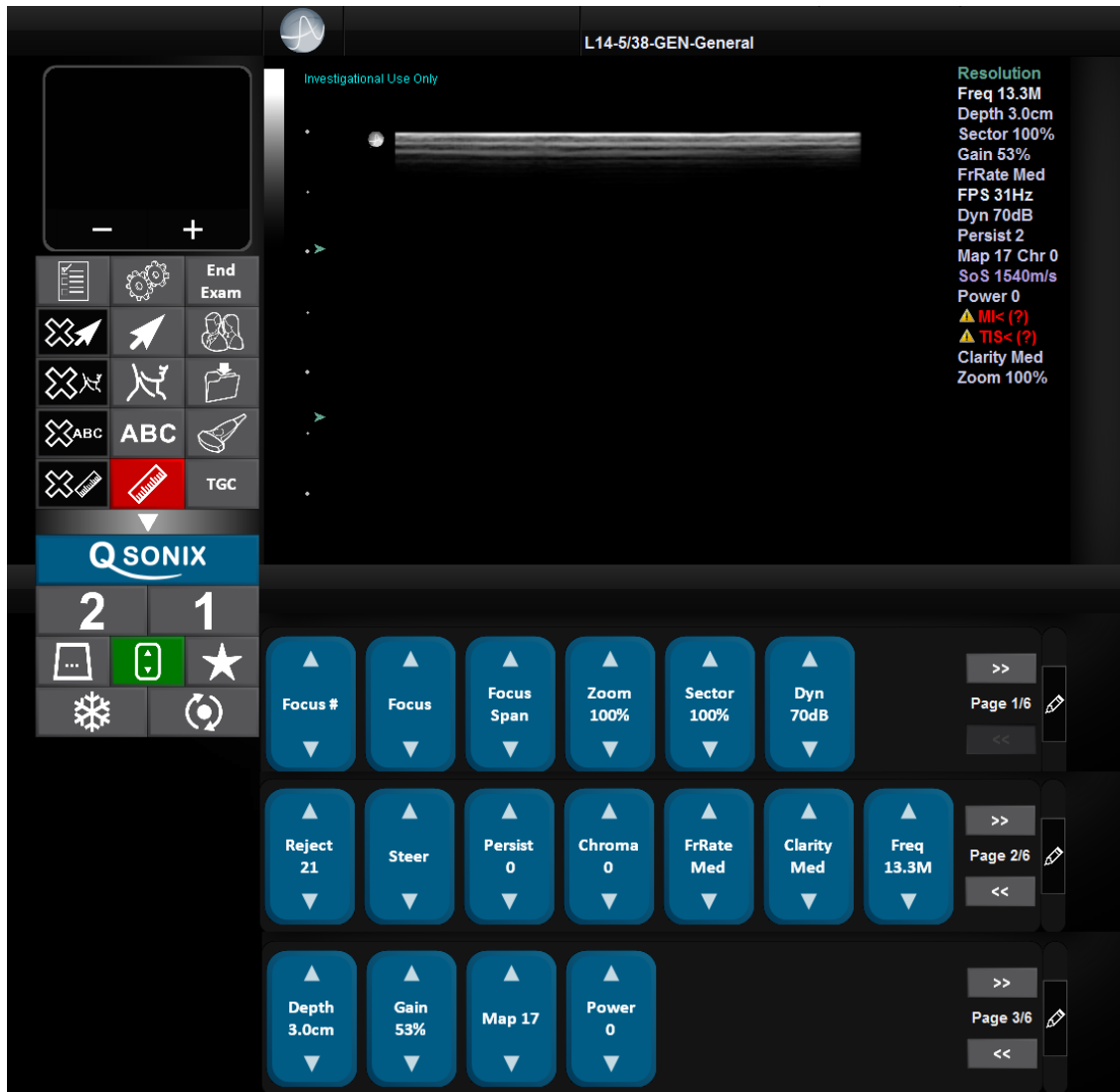


**Figure 5-1: User interface display for Ultrasonix SonixTablet System**

Other settings that were not changed included Clarity (which increases the sharpness of images but did not have an effect on surface reflections), Time-Gain Compensation (which is not relevant in water due to its low attenuation), SOS or Speed of Sound (which was accounted for in Matlab software), Steer (which would change the beam direction from straight-downwards to angled), Chroma (which changes the color



of the grayscale image) and Reject, Gain and Dyn (which would change image contrast but would be adjusted in Matlab software)

In order to generate 3D ultrasound images, motion capture markers were mounted onto the ultrasound transducer to provide position and orientation information for 3D reconstructions. A custom 3D printed marker holder was designed using Solidworks (Dassault Systemes, Velizy-Villacoublay, France) and produced from an Objet30 Pro (Stratasys, Eden Prairie, MN, United States) polyjet 3D printer with 0.1mm accuracy (Figure 5-2). The holder was rigidly attached to the ultrasound transducer and allowed for different reflective marker configurations by using attachments that are compatible with LEGO (The Lego Group, Billund, Denmark). The usage of LEGO components allowed for fast and secure re-configuration of reflective markers. Five markers were mounted onto the ultrasound transducer in an asymmetric pattern to create a unique rigid body configuration. The marker holder was designed to keep the position of the center marker consistent for calibration purposes, while allowing the other markers to be reconfigured. The center marker was placed at the following coordinates:  $X=0\text{mm}$  relative to the medio-lateral line of symmetry of the transducer,  $Y=107\text{mm}$  directly above the transducer surface and  $Z=38\text{mm}$  in front of the center of the transducer surface. The marker holder has two halves that are held in place using sliding locking keys on either side. Double-sided sponge tape was placed on the marker holder-transducer interface for a tight friction fit which could result in a small amount of deformation during scans but prevent slippage of the housing relative to the transducer. The probe itself was not modified.

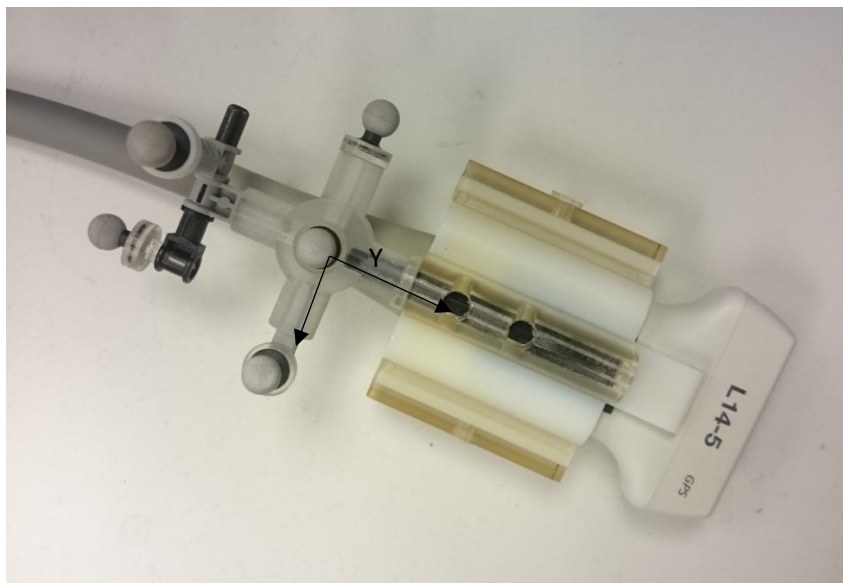


**Figure 5-2: Ultrasound marker holder mounted onto linear transducer**

### 5.2.3. Preliminary Streaming Testing

The Motive software and the Ultrasonix software both come with software development kits that allow streaming of data to Matlab. Motive streams the frame number, XYZ position data and quaternion orientation data, while Ultrasonix streams 480x640 resolution images and frame data to Matlab but is only compatible with the 32-bit version of Matlab due to legacy issues with the software development kit. Although it would have been possible to develop using other coding languages including Python, it was decided that due to its ability to work quickly with matrices and personal familiarity with the language, it would be better to continue with Matlab.

Both the ultrasound and motion capture cameras streamed data to a computer through a 1000 Mbps ethernet connection to minimize lag. The cameras and ultrasound unit were connected to a Cisco SG300-28 Switch which was then connected to a laptop. Data streaming was activated in Motive software. The Ultrasonix software required the Microsoft Windows firewall to be deactivated, media sharing to be allowed, and software data streaming settings to be activated to stream to the laptop. A static IP address was setup to ensure compatibility with the switch and multiple computers. An ultrasound frequency of 31Hz was found to be the highest output frequency without lag, while the motion capture cameras could output at their maximum 240 Hz without issues.

The capture volume was setup so that the positive X-direction ran across the field of view of the cameras (left side being positive when facing the cameras), the positive Y-direction was vertically upwards, and the positive Z-direction was away from the camera faces.

## 5.3. Software Development for 3D Ultrasound Reconstruction

### 5.3.1. 3D Ultrasound Reconstruction Schematic

The basic process from data streaming to 3D ultrasound reconstruction is shown in Figure 5-3. The ultrasound and motion camera data streamed through Matlab into a combined graphical user interface (GUI) which allowed the user to record the ultrasound image sequence into a 3D image volume or Portable Network Graphics (PNG) image stack, and the motion capture data and ultrasound frame data into a data table. The GUI allowed users to connect to the ultrasound and motion capture systems, start and stop recording, and rename saved files. The data was then imported into an image processing program that performed image processing to enhance the vertebral surface image and then paired each ultrasound image with the associated motion capture data and to realign the frame into the motion capture coordinate system.

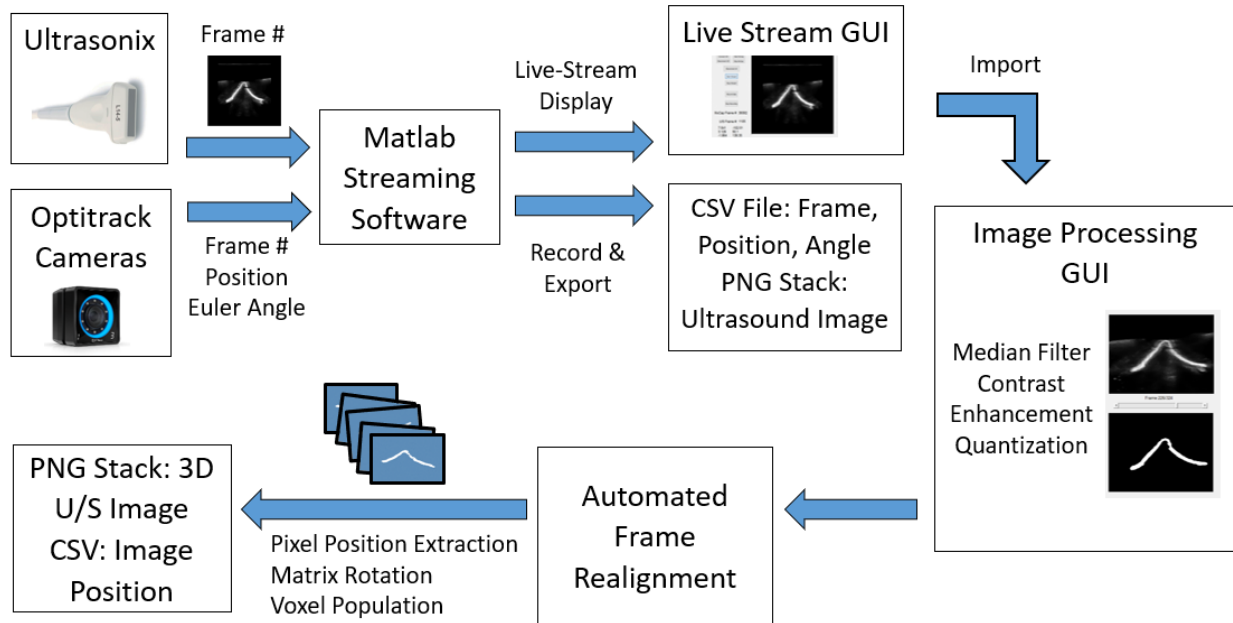


**Figure 5-3: Schema of the 3D ultrasound reconstruction process. PNG: Portable Network Graphics, CSV: Comma-Separated File**

### 5.3.2. Data Acquisition Graphical User Interface

A data streaming graphical user interface (GUI) was created in Matlab to connect to both the motion capture cameras and the ultrasound machine. Figure 5-4 shows the developed GUI. After connecting to the ultrasound and motion capture cameras, the image streamed to the main display alongside the motion capture frame number, ultrasound frame number, the rotation of the ultrasound transducer in XYZ Euler angles (converted from quaternion in Matlab), and the XYZ Cartesian position of the ultrasound transducer relative to the capture volume coordinate system. Also included in the GUI was the ability to name the file that will contain the combined output datasets.

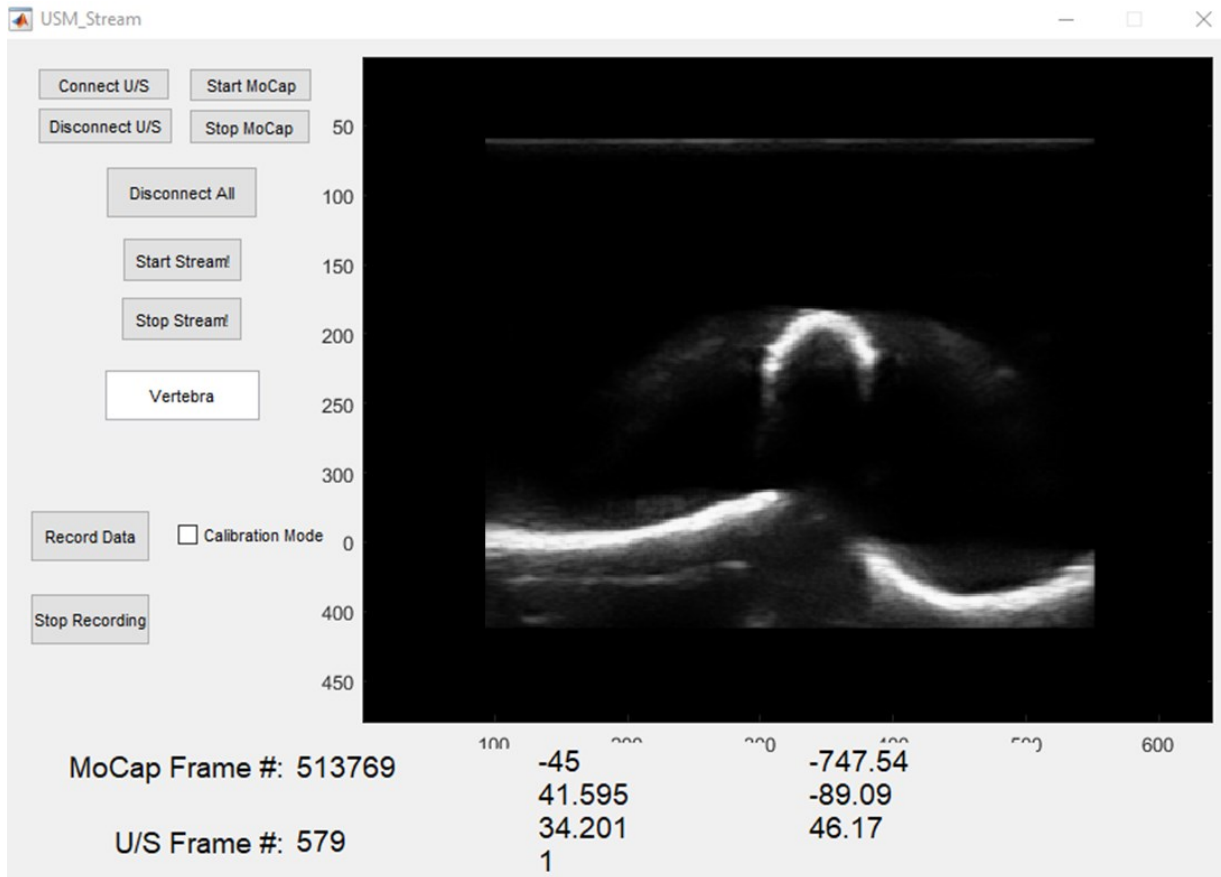


**Figure 5-4: Screenshot of ultrasound and motion capture streaming user interface: Screenshot of ultrasound and motion capture streaming user interface**

The streaming software would collect frames for reconstruction only after hitting the record button. The program immediately would record the motion capture and ultrasound data upon hitting 'Record Data', allowing for 40 seconds of data to be collected at 30 frames per second. Upon clicking 'Stop Recording', the software collected the data into two arrays: a three-dimensional volume containing all the raw 2D images from the ultrasound scan, and a list containing all the motion capture data and ultrasound frame data in chronological order. Because the ultrasound was captured at around 31Hz while motion capture was at 240Hz, there was one ultrasound frame number per eight motion capture frames in this list. Image processing and reconstruction were completed using subsequent programs.

### 5.3.3. Image Filtering Evaluation

Matlab was used to import the raw image and motion capture files and apply image processing. The full resolution images were cropped and resized to 190x150 pixels, equivalent to a 0.2mm resolution per pixel, to increase processing speeds. For evaluation purposes, a GUI was first developed to process the images to allow a variety of filters to be applied and to provide immediate feedback on the image being processed

to aid in the selection of filtering types and levels. Four pre-processing filters were tested: median filtering, averaging filtering, top-hat filtering, contrast filtering and binarization filtering. A description of how these filters work is in Chapter 2: . A sample of the GUI used is shown in Figure 5-5.

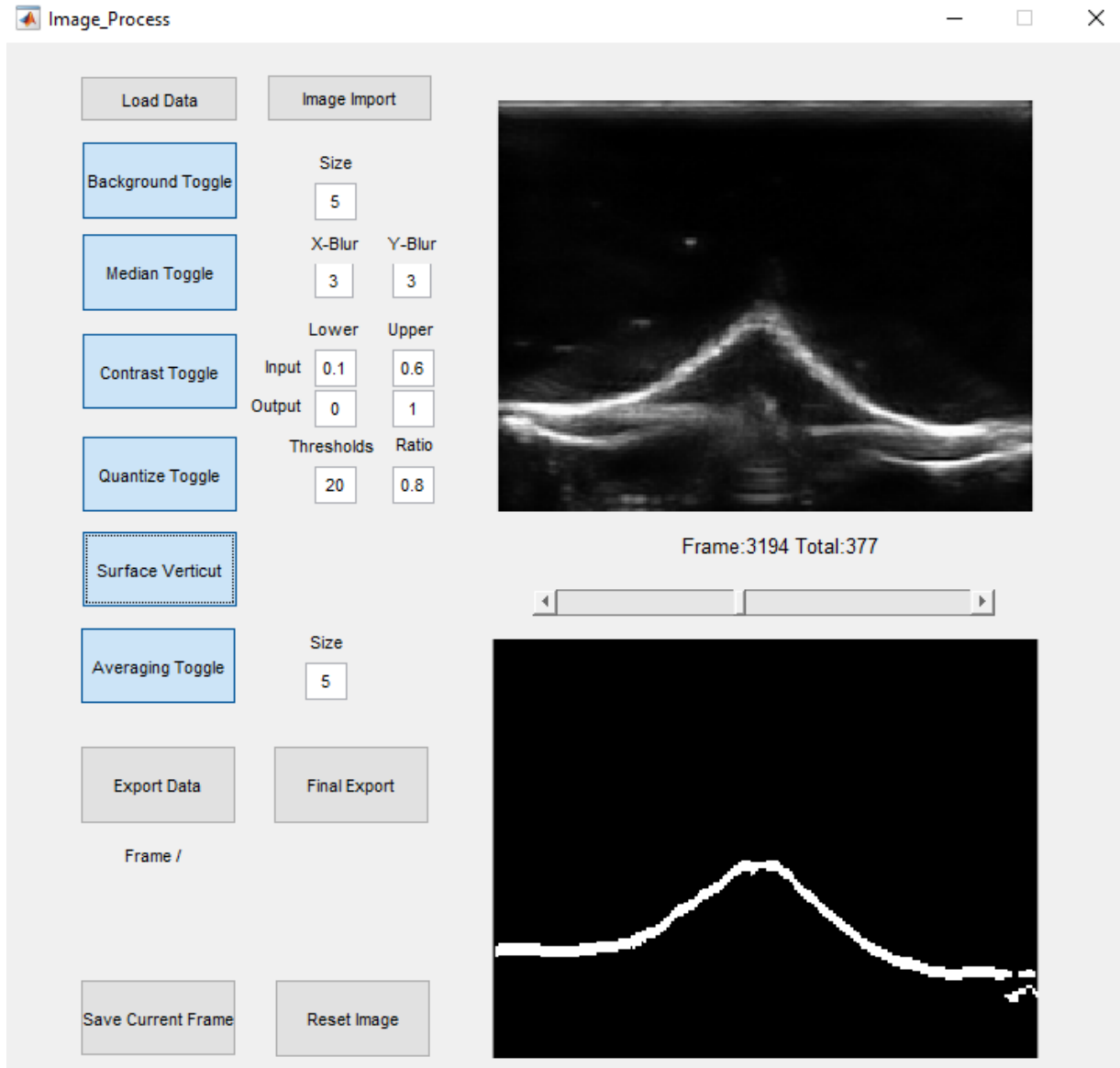


**Figure 5-5:** Screenshot of image processing graphical user interface showing the original image (top) and filtered image (bottom). The ‘Background’ Filter is the Top-Hat filter, the “Surface Verticut” filter removes regions below the top 5 pixels of the surface, the other filters correspond to the other previously described filters.

When testing the filters, the goal was to ensure that the vertebral surface could be reconstructed into a continuous surface and converted into a binary image for registration. Because ultrasound depends on reflected signals, the angle of incidence and depth can dramatically affect images. Vertebral regions that

are outside the focal point, or at angles that are not orthogonal to the transducer have weaker reflections, despite having the same high acoustic impedance difference as orthogonal surfaces at the ultrasound focal point. Furthermore, ultrasound signals are inherently noisy with a large amount of salt and pepper noise from particles that may be in the medium, or the uneven phantom surfaces. As a result, even when applying blurring filters to the images, edge detection filters would often result in a large amount of edges being detected throughout the images that were not from the vertebra.

The ultrasound images also had significant amounts of artifact, due to the transducer being designed for use in soft tissues where there would be a natural amount of attenuation, rather than in water where there is virtually no attenuation. Reverberations from the container itself were common, resulting in large regions of low-to-moderate intensity reflections to appear where there should have been no reflections. Reverberation artifacts (where ultrasound signals reflect back and forth between surfaces and the transducer) were also present due to the low attenuation of the water medium. These artifacts needed to be filtered out.

To speed up processing time in the pixel-by-pixel reconstruction, image processing was applied prior to reconstruction to minimize the number of pixels that would be reconstructed. Blurring filters were applied first to remove salt-and-pepper noise and these dim regions would be removed afterwards using contrast filters to reduce the pixel counts.

Initial evaluation of filters involved imaging a variety of plastic phantoms that were designed using Solidworks and 3D printed using an Objet30 Pro polyjet printer, mentioned previously. Figure 5-6 shows a sample of the phantoms that were used for initial filter evaluation. Two wide angle prisms were printed to represent the angles coming from the transverse processes (top row). Two narrow phantoms, one with a point and one with a squared slope, represent the spinous process (middle row). Lastly, two phantoms with paired structures were included to represent the tips of the transverse process: one with paired conical ends and paired triangular prism ends; one with paired pointed ends laterally and paired pointed ends medially (bottom row). Initial evaluations involved capturing the raw images and then applying filters to determine if a continuous surface could be consistently reconstructed.

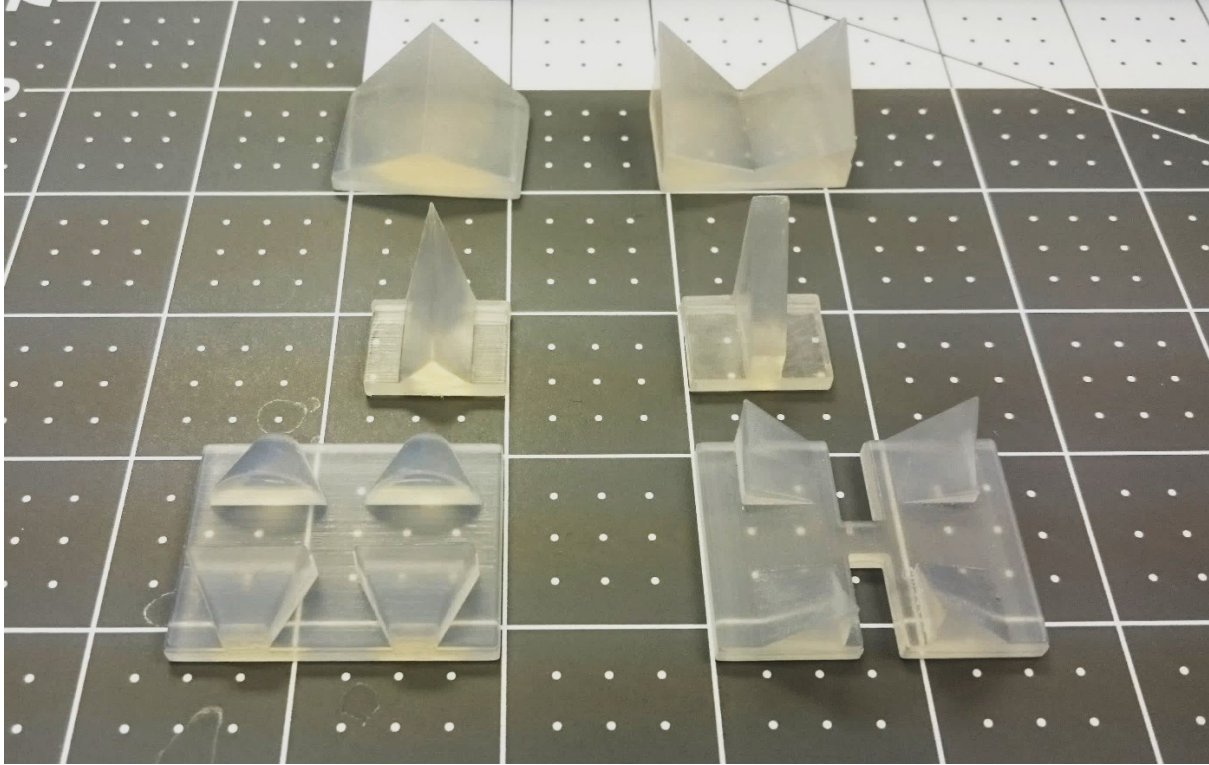


**Figure 5-6: Sample of the phantoms used for filter evaluation. Each square has 1-inch dimensions, with dots denoting quarter inches.**

From these experiments, median (size of 2x2 pixels) and averaging (size of 3x3 pixels) were applied to remove salt-and-pepper noise while a top-hat filter using a disc diameter of 10 pixel was applied to remove background artifacts from reverberations. Contrast filters were set to remove the bottom 25% of pixel intensities to maximize phantom surface reflections. Lastly, because ultrasound is linearly emitted and then reflected, any artifacts that appeared deep to the surface of the phantom were removed using a custom filter (Surface Verticut Filter on Figure 5-5) that detected the first bright set of pixels in each pixel column of the image. A sample of the resulting filtered surface is shown in Figure 5-5.

#### 5.3.4. Ultrasound Volume Reconstruction

The filtered images were then inputted into a program that combined the motion capture data with their corresponding ultrasound 2D images (Figure 5-3). The center of rotation of the ultrasound transducer was set to the top, left-most pixel of the image, with all pixel coordinates being measured relative to this point. The positive X direction would move across the transducer in the lateral direction towards the right, while the positive Y direction was down along the depth of the image.

The coordinates of each pixel in each image were extracted and transformed according to the position and orientation obtained from motion capture cameras. The 3D volume was then generated by converting every coordinate into an active voxel in the 3D volume according to the nearest-neighbor pixel method. The position of the reconstructed volume relative to the motion capture volume coordinate system was recorded so that every pixel would be localized according to the motion capture 3D volume coordinate system. Source code can be found in Appendix 4: Ultrasound Reconstruction Code.

No averaging interpolation was used due to the binary nature of the imported images. However, to fill gaps in between frames, the thickness of each 2D frame was tripled during reconstruction. The 0.6mm thickness of the resulting frames were well within the 6mm elevation aperture of the elements on the transducer and would not add artifactual thickness to the image erroneously. Voxels with overlapping pixels were simply considered active pixels. To further minimize the gaps that formed between frames and to smooth out the vertebral surface into a continuous structure, the volume was sliced on the Y-Z plane (sagittal plane) and an averaging filter with a pixel size of 2x2 was used to fill the gaps, followed by binarization of the image.

Lastly, a connectivity filter was applied, which detected which voxels were connected and removed all but the largest 20 groups of connected pixels. If the vertebra would contain the largest connected set of voxels, any remaining artifacts at the edges of the volume would be removed.

While the reconstruction process was simple, the calibration of the transducer would be important to retain dimensional and positional accuracy of the vertebrae. First, the time difference between the motion capture data stream and the ultrasound image stream needed to be calibrated. Second, the transform from the center reflective marker mounted on the ultrasound, to the transducer surface needed to be accurately measured and calibrated. Lastly, the filters needed to be adjusted to balance having accurate dimensions being reconstructed with ensuring a continuous surface was recorded for reconstruction.

## 5.4. Calibration of 3D Ultrasound

### 5.4.1. Temporal Calibration

Initial calibration of the 3D ultrasound system involved mounting the transducer to T-slotted aluminum OpenBeam framing, an open-source extruded aluminum framing system. The framing system restricted the motion of the transducer to three degrees of translation (along each axis) and one degree of rotation (rotating about the X-axis). An image of the OpenBeam mount is shown in Figure 5-7. The transducer



holder included screw holes that allowed it to be rigidly attached to the frame while Teflon tape was added to sliding surfaces to allow smooth motion.

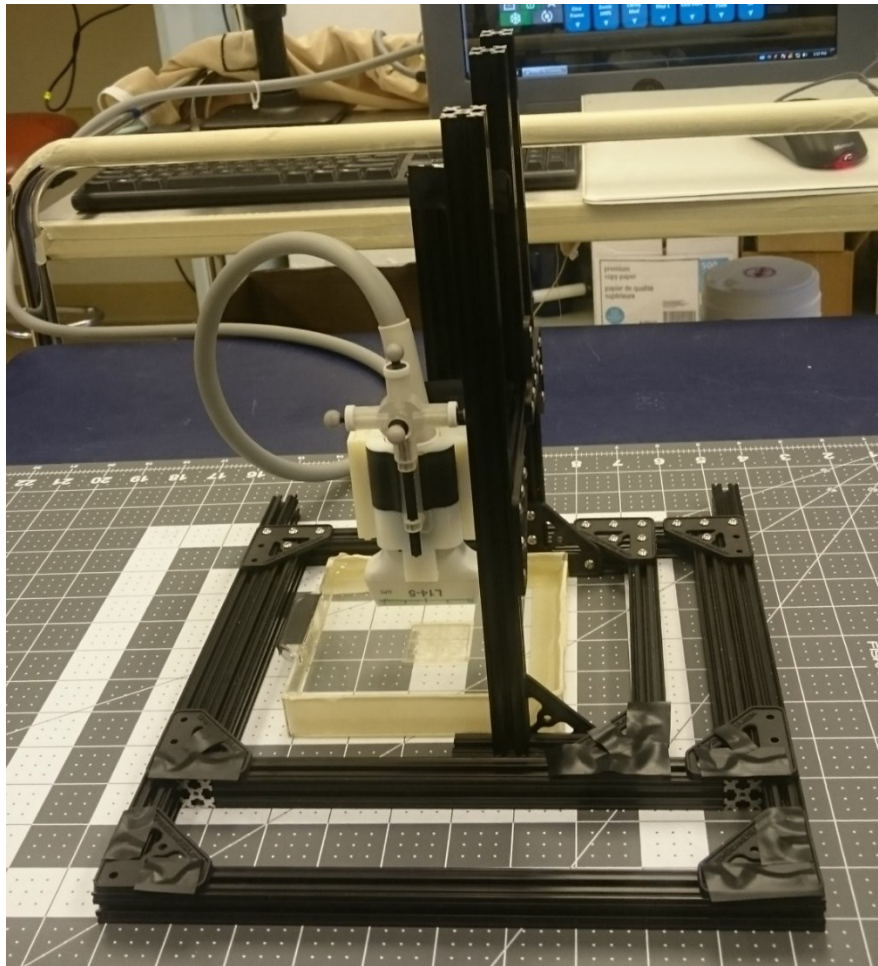


**Figure 5-7: Ultrasound transducer mounted to OpenBeam translating frame**

Temporal calibration involved ensuring the captured ultrasound frames match with their corresponding motion capture frame. With poor synchronization, the ultrasound frame pixels would be placed in the incorrect position and orientation, resulting in a faulty 3D reconstruction.

Temporal calibration was performed by moving the transducer away and towards the floor of the water bath (Figure 5-7) in the Y direction at 3-5mm/s using the OpenBeam frame. A slow and controlled speed was used to minimize inaccuracies due to latency. The distance between the transducer surface and the floor was extracted for each frame and then plotted against time. The motion capture Y position was then also plotted against time and the root mean squared error was calculated between the motion capture Y-position and the ultrasound transducer-to-floor distance. The time shift with the smallest RMS error was

determined as the optimal frame shift that would account for time delays between the two systems. Temporal calibration was repeated ten times. Both the ultrasound and motion capture frame shifts were tested.

The temporal calibration results are shown in Figure 5-8. The root mean square error was minimized when shifting ultrasound images two frames or 67ms earlier to match with motion capture data, showing an RMS error of  $0.7 \pm 0.1$ mm compared with  $0.9 \pm 0.3$ mm when no frame shift is added.

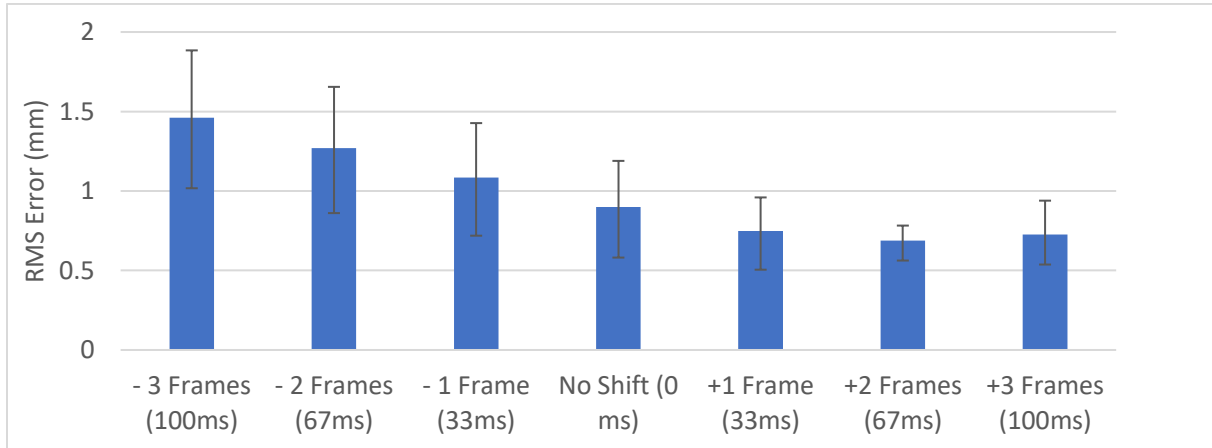


**Figure 5-8: Temporal calibration shifting ultrasound frames**

Shifting the motion capture frames is shown in Figure 5-9. Shifting resulted in no appreciable difference, with shifting one frame up resulting in the same error as no shift, with values all within 0.03mm which is below the resolution of the motion capture system.

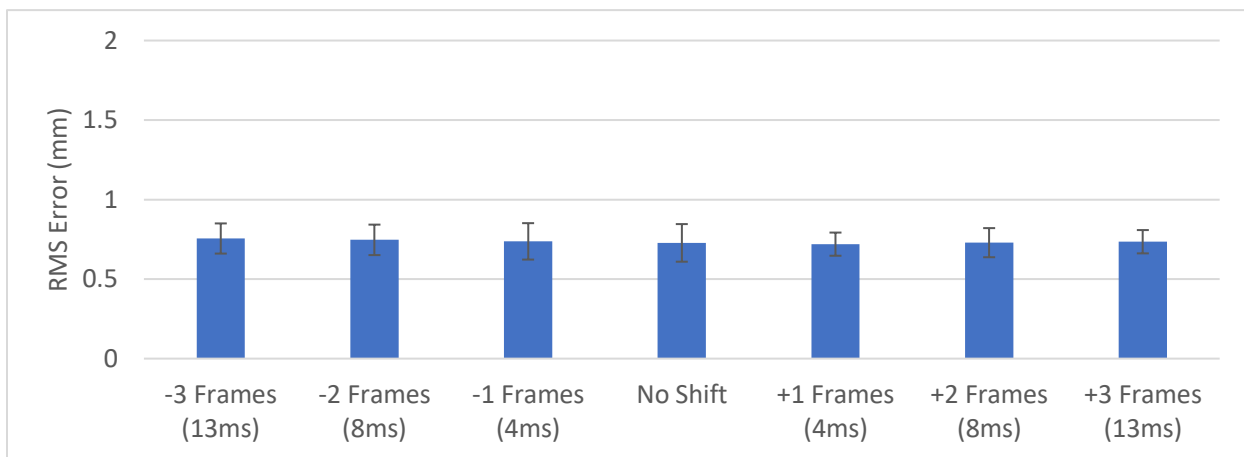


**Figure 5-9: Temporal calibration shifting motion capture frames**

Because the motion capture frame rate is eight times higher than the ultrasound capture frame rate, it was sensible that shifting ultrasound frames has a larger effect on accuracy. The high frame rate at 240 fps makes shifts in motion capture position unappreciable when less than 3 frames whereas ultrasound frames at 30fps are more significant. However, the motion capture data was found to be quite noisy. The two frames before and after the ultrasound frame were averaged together to be paired with the ultrasound frame.

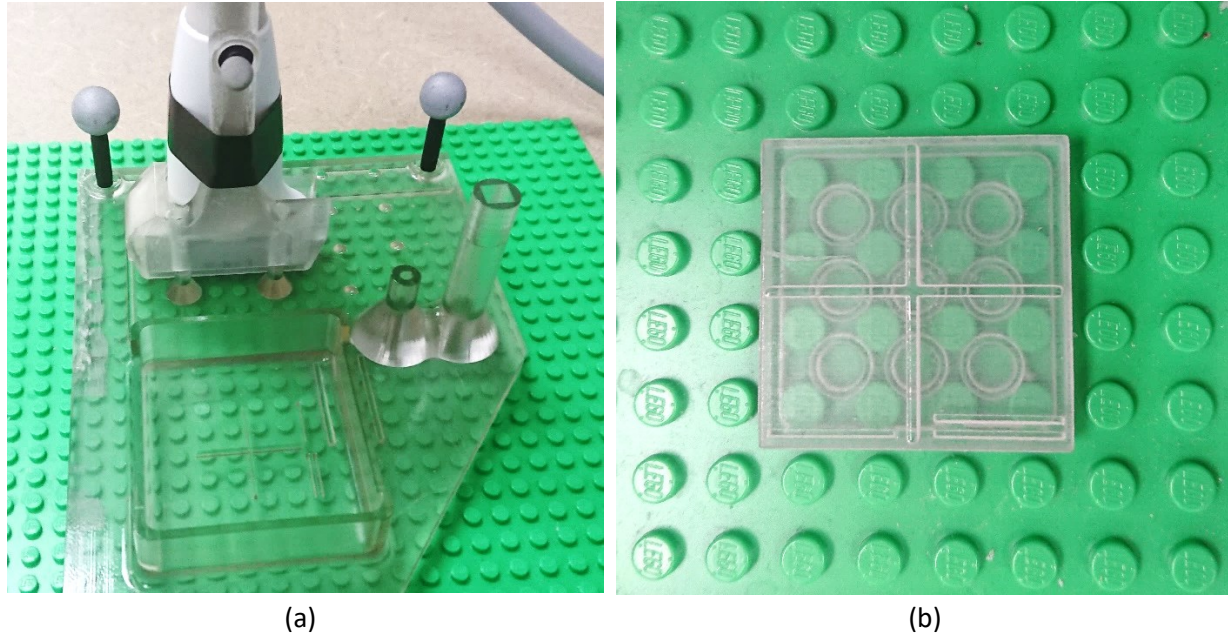
Other temporal calibration methods include synchronization hardware modules to send ultrasound information to tracking device upon image acquisition to measure an offset [224]. This study followed a similar methodology as Treece et al. by imaging a flat phantom and moving the transducer vertically and then matching the distance measurements between the tracker and ultrasound [225]. This method provided an empirical offset between tracker and ultrasound which is adequate for this current system. However, with different ethernet setups and speeds, the ultrasound frame lag could differ slightly, though repeating the calibration process on two different computers found no difference. Still, usage of a synchronization module could improve transferability of calibration results and provide greater reassurance on temporal calibration adequacy.

#### 5.4.2. Spatial Calibration

Spatial calibration is required to determine the rigid transformation between the motion capture markers and the location of the transducer surface. Depending on where the centroid of the rigid body is placed, the position and rotations of each pixel in the ultrasound frame could be positioned incorrectly, particularly in rotating about the wrong axis. Prior to calculating the spatial transformation, the orientation of the transducer needed to be set. The ultrasound marker holder was designed to include a mounting bracket to allow it to be rigidly placed on a calibration mount aligned to the motion capture coordinate system. The mounting square is shown in Figure 5-10.

The transformation was first measured directly using digital calipers. The spatial transformation between the rigid body pivot to the far-left corner of the transducer surface (transducer origin) was [19.5, -107.0, 38.0] mm for the [X,Y,Z] directions. To refine the accuracy of this measured transformation, a spatial calibration experiment was performed. A crosshair phantom (Figure 5-10) was placed at the origin of the capture volume and imaged. The position of the center of the crosshair from the resulting image was compared with the motion-capture based center. The difference between these two values were used to adjust the transformation matrix until the difference was less than 0.25mm in each dimension, typically requiring 3-4 calibration scans. The final calibrated transformation was compared to the transformation

as measured by calipers. The precision of calibration was then evaluated by scanning the cross-hairs phantom an additional five times with the given spatial transformation. The standard deviation of the position of the ultrasound transducer when rigidly placed at the capture volume origin was also recorded.



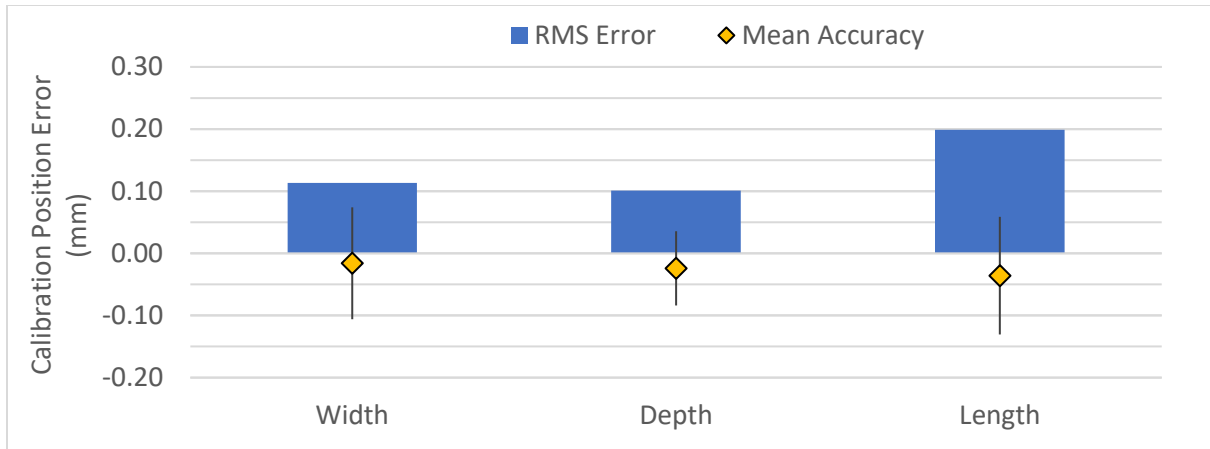
**Figure 5-10: Calibration Setup, (a) Mounting bracket to set ultrasound orientation. (b) Crosshairs phantom for calibration**

Table 5-1 presents manual calibration results. The mean transformation matrix from five separate calibrations is displayed as well as the standard deviation of the transformation matrix. The standard deviation of the position of the ultrasound transducer surface when placed at the capture volume origin is also displayed.

**Table 5-1: Transformation matrix mean and standard deviation and ultrasound transducer surface position standard deviation**

Direction	Mean Transformation Matrix	Transformation Matrix SD	Ultrasound Origin Position SD
X	19.5mm	0.1mm	0.2mm
Y	-107.0mm	0.0mm	0.2mm
Z	38.1mm	0.7mm	0.1mm

The average RMS accuracy and precision of the position from five scans after selecting the transformation matrix are shown in Figure 5-11. The root mean squared errors in [X,Y,Z] directions were [0.1, 0.1, 0.2] mm with standard deviations of [0.1, 0.1, 0.1] mm.



**Figure 5-11: Spatial calibration, RMS errors of X (width), Y(depth) and Z (length) position of origin (bar graph), and precision of measurements (diamond with standard error bars)**

The precision and RMS accuracy of rotation from five scans of the phantom after selecting the transformation matrix are shown in Figure 5-12. The root mean squared errors about [X,Y,Z] axes were [0.3, 0.5, 0.5]<sup>o</sup> with standard deviations of [0.2, 0.3, 0.1]<sup>o</sup>.

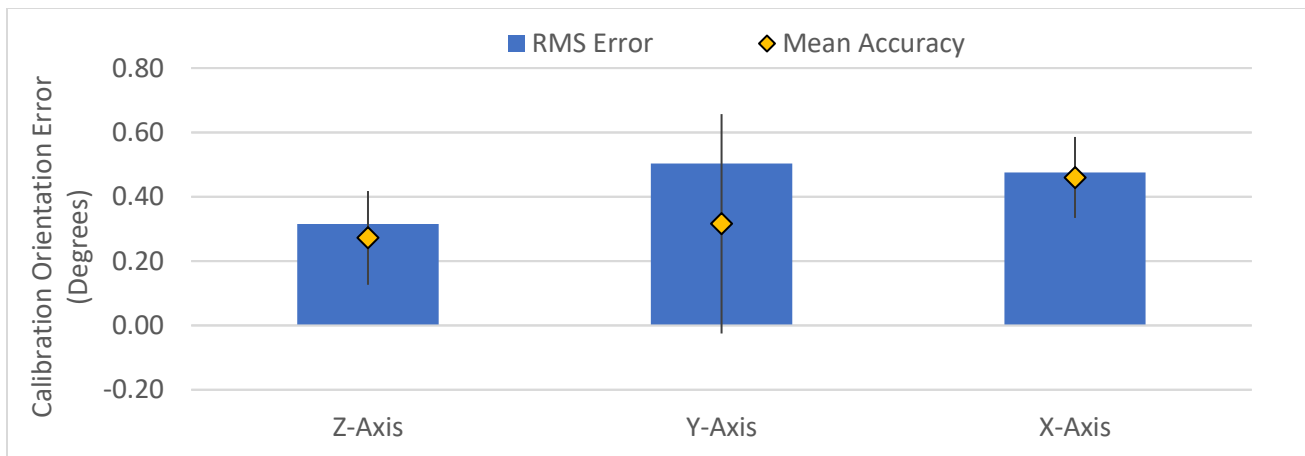


**Figure 5-12: Spatial calibration, RMS rotation errors about each axis of rotation at the origin (bar graph), and precision of measurements (diamond with standard error bars)**

The manual measurement only differed from the calibrated value by 0.1mm. The standard deviation of the transformation matrix was significantly higher in the Z direction at 0.7mm compared to X at 0.1mm and the Y remained unchanged. When accounting for deviations from the zero position during initial rigid body placement, the standard deviation improved to 0.1mm in the Z (length) direction. Because all the cameras face the Z direction, there may be reduced repeatability for position measurements in that direction. The elevation thickness of the ultrasound would also contribute to this increased error, as the resolution in the elevation direction would be up to 4mm, making measurements in the Z-direction less

precise than other dimensions. Still, the accuracy and repeatability values remain within the technical 1mm standard [73].

Spatial calibration in other studies has been automated by imaging predetermined points within a volume, cross-wires, wall phantoms and Z-fiducials [109,141,142]. Each of these use a different physical structure, whether wires strung within the volume, walls that act as a flat surface, or linear structures in the shape of a Z respectively, that can be imaged to determine the spatial calibration of the transducer. This study used a process like wall calibration as a simple and easily automated method. It could be useful to calibrate the current system with other commonly used calibration methods to verify repeatability of results across different calibration methods.

#### 5.4.3. Filter Calibration

After calibration was completed, the filters used for ultrasound scans were calibrated on the phantoms shown in Figure 5-6, to ensure dimensional accuracy of scanned objects. The user-dependent nature of the ultrasound scans made filter calibration particularly challenging, as different scans with the same filter settings would often have slightly different reconstruction accuracy results. Rather than performing quantitative measurements of dimensions resulting from scans of different filters, a qualitative approach was undertaken to determine which set of filters would most consistently provide reconstructions with similar results. The effects of each filter in general terms is described in Chapter 2: , but the effects on the vertebral images themselves will be outlined below.

Top-hat filtering, which is effective at removing patterned background noise, was able to remove reverberation artifacts while retaining most of the vertebral surface outline. However, when scanning at wider angles, the decreased sharpness of the surface resulted in a reduced intensity in these regions as well, resulting in an inconsistent vertebral surface being reconstructed. This filter was not used in the final system because of these inconsistent results.

Both averaging and median filtering were able to remove most of the salt-and-pepper noise in both the background and on the vertebral surface. However, median filtering depended on the size of the element used to perform filtering, with larger elements dramatically increasing the processing time. Averaging filtering had similar results to the median filter but was faster and was favored in this system. The final averaging filter used a 3x3 pixel size to balance noise reduction effects with image clarity.

Contrast was the most important filter in this system. By applying averaging filtering and then a contrast filter, background artifacts and salt-and-pepper noise were consistently removed. The final minimum

threshold was set at 50% of maximum intensity while the maximum intensity was set at 80% with all values below 50% being set to zero intensity, all values between 50-80% being scaled to 0-100%, had all values above 80% being set to maximum intensity. Increasing the minimum threshold would result in removal of more pixels, while decreasing the maximum threshold would result in more pixels being assigned the maximum intensity value.

Lastly, a custom surface filter that found the first bright pixel in each column and kept the next five bright pixels was applied. This was applied to reduce the number of extraneous pixels being applied for reconstruction. A sample of the combined effects of the averaging, contrast and surface filter is in Figure 5-13. The averaging filter helps to remove some of the artifact and clarify the surface, while contrast filters out extraneous pixels. The surface filter removes pixels that are below the surface. In soft tissue, there would be significantly decreased artifacts due to the higher attenuation of signal in soft tissues.

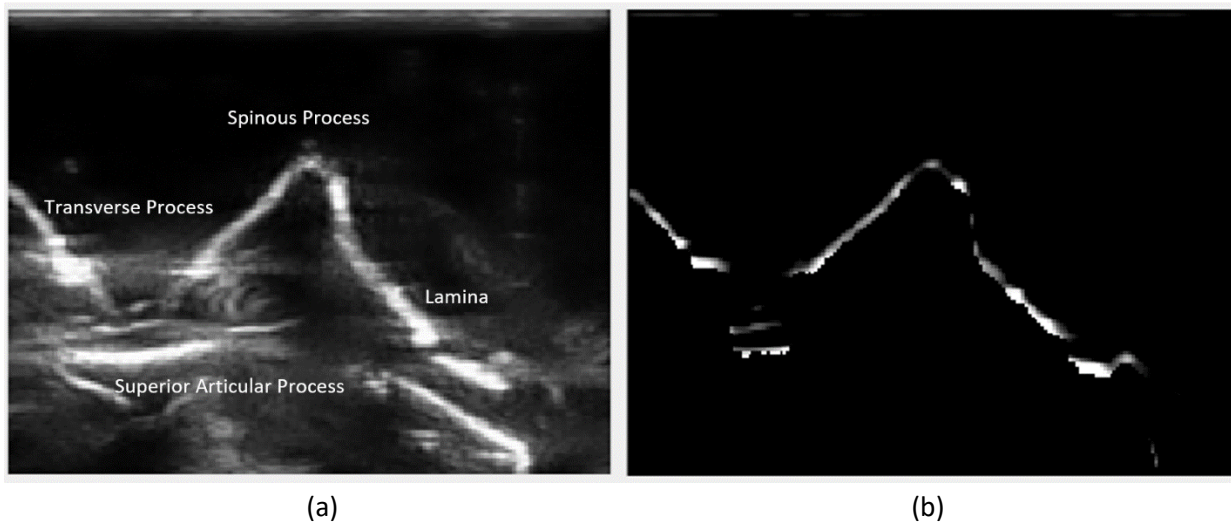


**Figure 5-13: Sample of averaging, contrast and surface filter applied to a scan of a phantom vertebra along the X-Y (transverse) plane. From (a) original image to (b) filtered image.**

As mentioned previously, a second set of filters was applied after re-orienting the volume along the Y-Z (sagittal) plane to smooth the surface. A 2x2 sized averaging filter was applied, followed by a quantization filter removing the pixels with intensities in the lowest 20%. A sample of the combined filters is shown in Figure 5-14. While the original image contains thin slices of the vertebra, the averaging filter (3x3 pixel size) blends the surface together as the quantization filter converts the greyscale picture to a binary image.

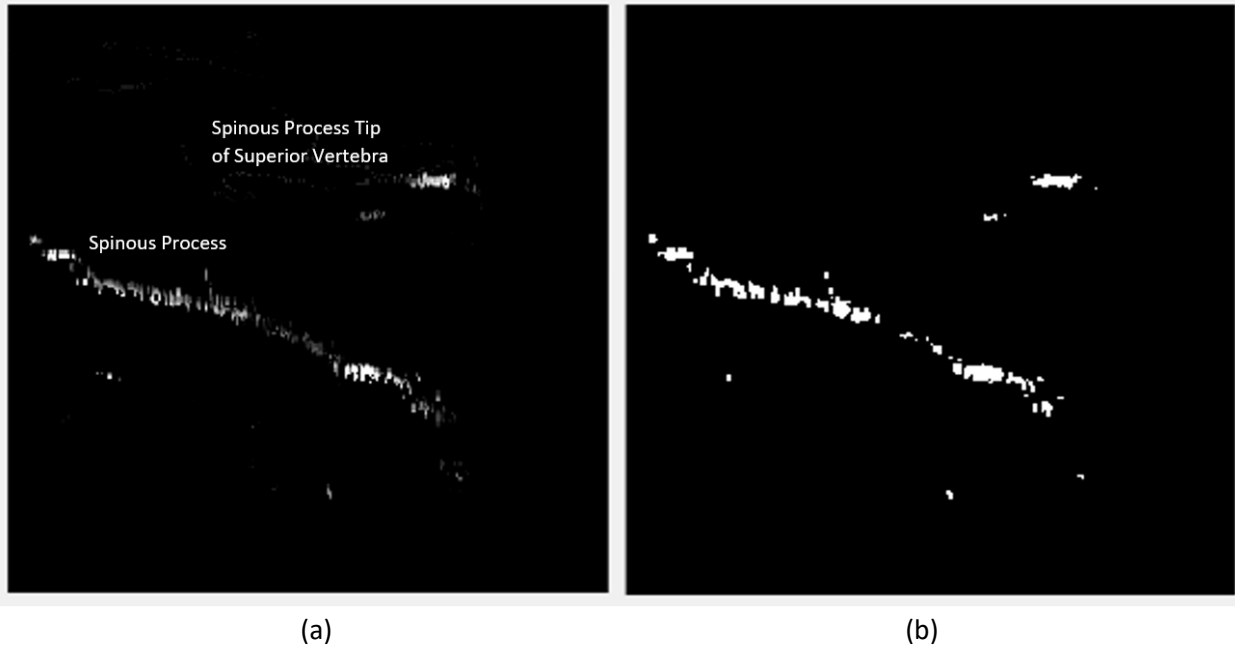


**Figure 5-14: Sample of averaging and quantization filter applied to a US scan of a phantom vertebra along the Y-Z (sagittal) plane. From (a) original image to (b) filtered image.**

These filters were adopted for the rest of the reconstruction and positional accuracy experiments performed in this chapter. The exact values of the filters would be changeable for different tissues and anatomies if needed in a real situation.

## 5.5. Reconstruction of Vertebral Phantoms

### 5.5.1. Phantom Modeling and Experimental Design

The first set of phantom experiments involved evaluating reconstruction accuracy. Seven plastic 3D-printed phantoms were mounted onto a LEGO peg board and immersed in a 500x500x70mm<sup>3</sup> water bath (Figure 5-15A) and scanned using the 3D ultrasound system. Again, the X-axis was defined as the direction across the camera faces, the Y-axis was vertically upwards, and the Z-axis was away from the cameras. Five of the scanned phantoms were newly designed, two for measuring linear dimensions (Figure 5-15B,II) and two for measuring angular dimensions (Figure 5-15B,III). For the linear dimension phantoms, one had successively larger circles while the other had successively larger squares. For both, the diameter of each successive ring was 10mm larger than the next, with each ring being 2.5mm in width with 2.5mm gaps between each ring. The height of the rings was 2mm. For the angular dimension, two were used to measure angles in the XY (transverse) or ZY (sagittal) plane and one for angles in the XZ (coronal) plane (horizontal measurements). The first vertical angular phantom had a minimum angle of 7.5° and maximum angle of 22.5° with 2.5° angle increments while the second had a minimum angle of 5° and maximum



angle of  $35^\circ$  with  $5^\circ$  increments in between. For the horizontal phantom, the minimum angle was  $5^\circ$  and maximum at  $95^\circ$  with increments of  $5^\circ$  in between each. The wide-angle concave and convex phantoms from before were also scanned. The phantoms were designed with a  $90^\circ$  angle in the center of the tall side of the phantom, and a  $120^\circ$  angle in the center of the short side of the phantoms.

Phantoms were scanned three times in the same inferior-to-superior direction and measured three times on each dimension. The flat phantoms (Figure 5-15ii) were used to only measure linear dimensions while the angular phantoms (Figure 5-15Biii) were used only for angular dimensions. The vertebrae-mimicking phantoms had both angular and linear dimension measurements. The reconstructed image stack was imported into ImageJ (NIH, Bethesda, Maryland, USA) and then exported as an STL file that could be measured in Netfabb (Autodesk, San Rafael, California, USA) for three dimensional measurements.

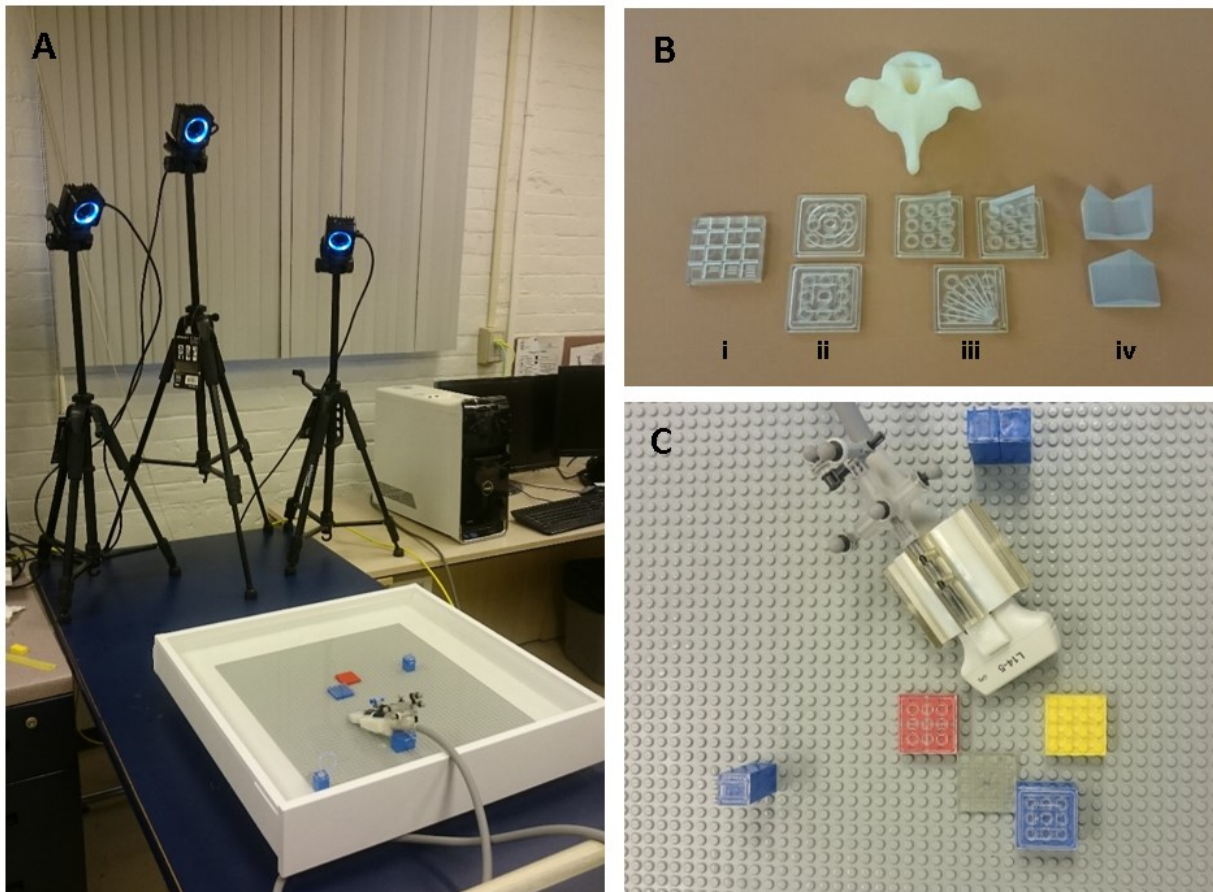


**Figure 5-15: Ultrasound scan setup, (A) Motion capture cameras with capture space, (B) a 3D printed vertebra (top) and 3D printed phantoms for ultrasound imaging (I) calibration phantom, (II) linear dimension phantom, (III) angular dimension phantom, (IV) vertebrae mimicking phantom, (C) LEGO pegboard in ultrasound water bath.**

### 5.5.2. Linear and Angular Reconstruction Results

The accuracy of linear reconstructions on flat phantoms is displayed in Figure 5-16. The accuracies for [X, Y, Z] directions were [0.6, 0.1, 0.6]mm with repeatabilities of [0.1, 0.2, 0.1]mm for 5-25mm linear measurements. There was no trend between measurement error and size of dimensions.

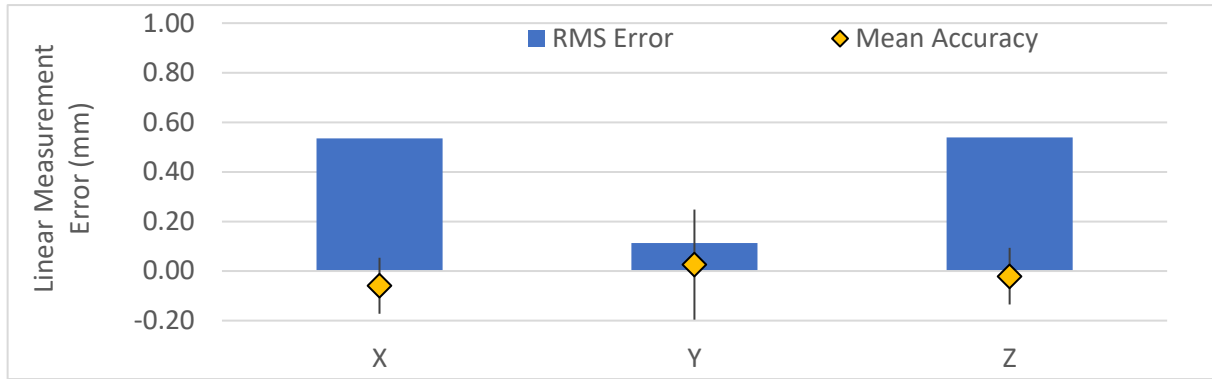


**Figure 5-16: Linear reconstruction RMS error (bar graph) and precision (diamond with standard error bars) on flat square and flat circle phantoms**

The accuracy of angular reconstructions on angular phantoms is displayed in Figure 5-17. The accuracies about the [X, Y, Z] axes were [0.8, 0.7, 0.7] $^{\circ}$  with repeatabilities of [0.3, 0.2, 0.3] $^{\circ}$  for measurements from 2.5-35 $^{\circ}$ . There was no trend between measurement error and size of dimensions.

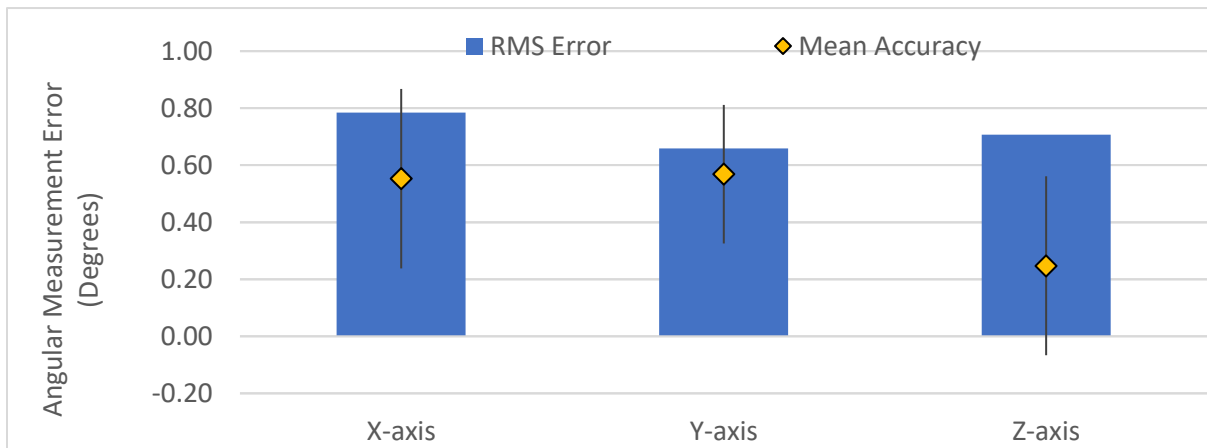


**Figure 5-17: Angular reconstruction RMS error (bar graph) and precision (diamond with standard error bars) on angled phantoms**

Figure 5-18 displays a sample of the linear and angular 3D ultrasound reconstructions.

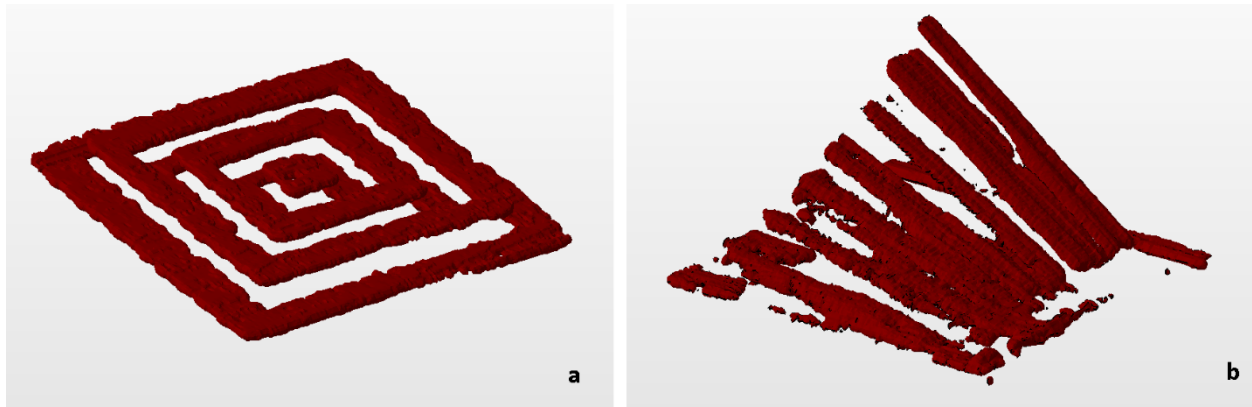


**Figure 5-18: Sample 3D ultrasound reconstructions of linear (a) and angular (b) phantoms**

### 5.5.3. Vertebrae-Like Reconstruction Results

The reconstruction accuracy of vertebrae-mimicking phantoms is displayed in Figure 5-19. The linear accuracies across the width, length and depth dimensions of the vertebrae-like phantoms were [0.3, 0.5, 0.4] mm in the [X,Y,Z] directions with repeatabilities of [0.4, 0.5, 0.4]mm. The angular accuracies on surfaces at a convex angle towards or concave angle away from the transducer was 1.2° and 1.9° respectively with standard deviations of 1.2° and 1.8°.

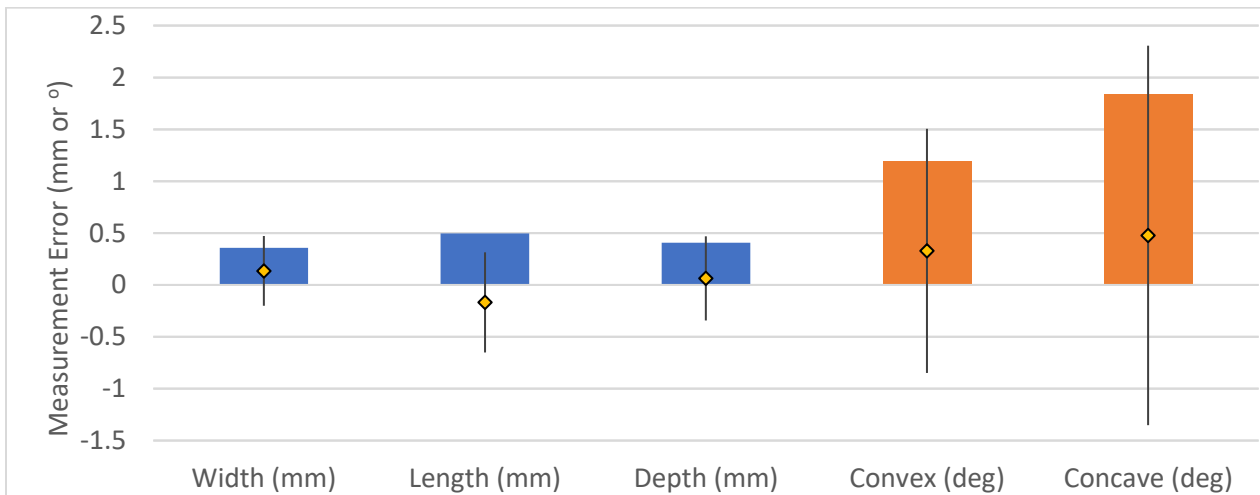


**Figure 5-19: Reconstruction accuracies on concave and convex vertebrae-mimicking phantoms along width, length and depth directions and angles on concave and convex surfaces.**

### 5.5.4. Reconstruction Accuracy Experiment Discussion

The linear reconstruction accuracies on the flat phantoms were [0.6, 0.1, 0.5] mm compared to the vertebrae-like phantom at [0.4, 0.5, 0.4]mm in the X, Y and Z directions, respectively. The ultrasound transducer itself has a theoretical axial (Y) resolution of 0.3mm and lateral (X) resolution of 0.3mm,

comparing favorably with the accuracies in this study. The elevation (Z) aperture of the transducers is 4mm which is difficult to compare with actual resolution.

The slightly better accuracies in the X and Z dimensions (along transverse and axial directions) on vertebrae-like phantoms are likely due to the broader contours and larger dimensions being measured. The flat phantoms were designed to be a series of nested shapes. Because of the small 2.5mm gap between each nested shape, there was increased reflection intensity in the gap between the shapes, resulting in thicker than expected measurements for dimensions. The worsening of accuracies in the Y direction is likely due to the increased variation in depths and inclusion of oblique dimensions on the vertebrae-like phantoms.

Repeatability worsened slightly from flat phantoms compared with vertebrae-like phantoms, at [0.1, 0.2, 0.1] vs [0.4, 0.5, 0.4]mm in the X (transverse), Y(depth) and Z(axial) directions respectively. The slightly worsened repeatability can again be explained by the oblique and curved surfaces on the vertebrae-like phantoms that result in a greater variation in reflected ultrasound signal.

Angular accuracies were 0.7-0.8° on the angled phantoms, and 1.2-1.9 ° on vertebrae-like phantoms. Repeatability was 0.3° on angled phantoms compared with 1.2-1.8° on vertebrae-like phantoms. Accuracies and repeatabilities worsened in both cases when measuring vertebrae-like phantoms. Again, the irregular contours on the vertebrae-like phantoms slightly worsen the angular measurements. The reference plane was also not always clear on the vertebrae-like phantoms. Still, the accuracies are well within the required 5° set as the standard for pedicle screw insertion [73].

Because the 3D ultrasound system will be used to determine the location of screw placements and trajectories, linear and angular measurements were used to evaluate the accuracy of the system, rather than target registration error or feature-based accuracy measurement metrics. A potential shortcoming to dimensional measurements is that the edges of these dimensions have a gradual contour, usually resulting in an over-estimation of how large scanned objects were. As a result of this over-estimation in size, it would not be ideal to use surface edges as a landmark for the purpose of image registration. Instead, landmarks within the structure of the vertebra, whether it is the spinous process or peaks on the transverse process, would be more useful. Another limitation of this study is that all sweeps were done along the Z-axis (axial direction), which could change accuracy if performed in another direction.

The challenge in generating reconstructions was balancing dimensional accuracy with acquiring fully connected reconstructed images. Because ultrasound image contrast varies significantly depending on

the incident angle of ultrasound, filters needed to be selected to provide robust image reconstructions in a variety of conditions. However, for the final navigation system, it will not be reconstruction accuracy that will determine navigational accuracy, but the relative locations of landmarks. A vertebra reconstruction that is slightly wider or narrower than the original can still provide accurate localization if it is placed in the correct position. The next set of experiments sought to determine this accuracy.

## 5.6. Localization of Phantom Position and Orientation

### 5.6.1. Localization Accuracy Experimental Design

The second set of tests involved determining the accuracy of the localization ability of the 3D ultrasound system. The calibration crosshair phantom (Figure 5-15Bi) was used for position accuracy testing. The phantom was placed at the capture volume origin and then moved to 28 different pre-determined positions covering a  $300 \times 100 \times 30 \text{ mm}^3$  volume (Figure 5-20), similar to the volume of 6-8 vertebrae in an open posterior spinal surgery. Positions were selected to cover the full range of a typical thoracic spine, with different heights distributed evenly amongst the grid positions. The position of the phantom was physically measured on the pegboard grid based on its known dimensions and then compared with the position as recorded by the system.

The orientation of the phantom at each position was also measured. The rotation about the X and Z axes (pitch and roll) were measured in ImageJ (National Institutes of Health, Bethesda, MD, USA) by drawing a line along the top surface of the crosshairs in sagittal and transverse views respectively in the 3D reconstruction and measuring the angle between the line and a horizontal line. The rotation about the Y axis (yaw) was measured by drawing a line along the crosshairs in the coronal view and measuring the angle between the line and a vertical line.

Three scans were completed per position. Root mean squared error and standard error to a 95% confidence interval were calculated on the positional and orientation differences.

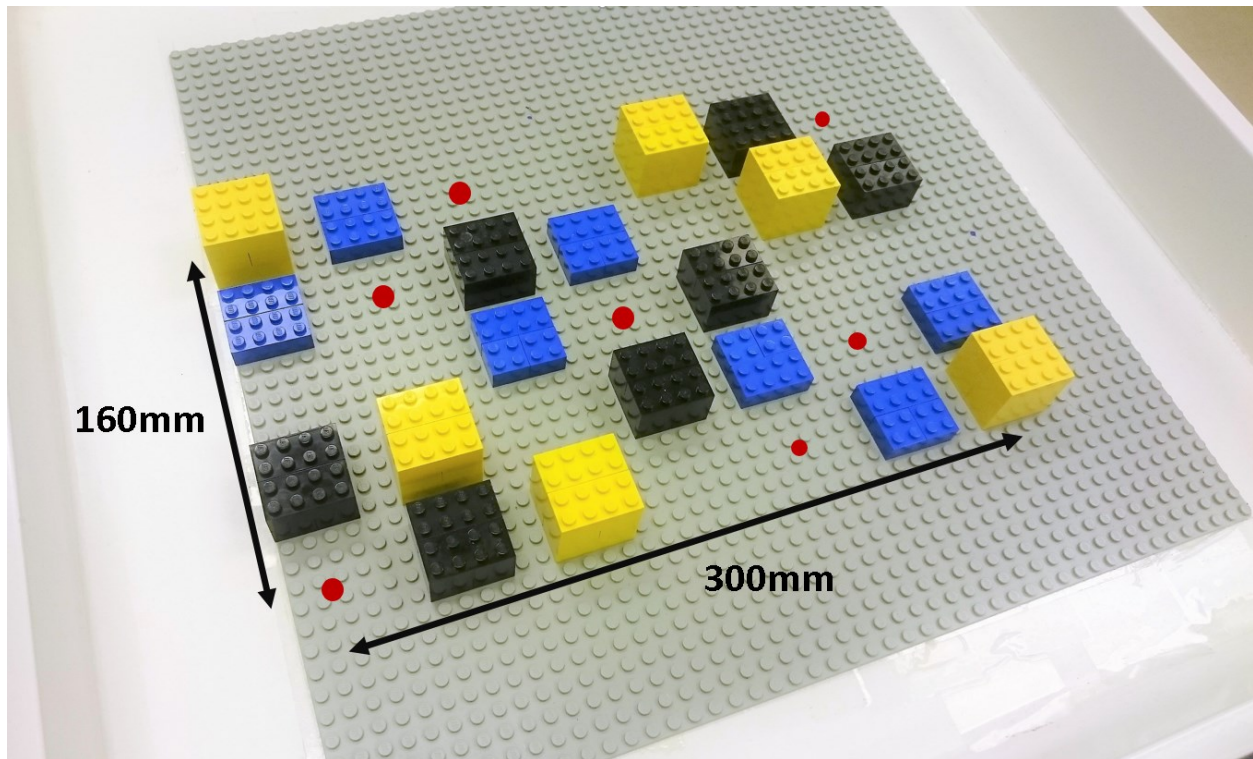


**Figure 5-20: Positional pegboard setup including the 28 placement locations. Dots denote where the phantom was placed directly on the pegboard. Phantom was placed on raised blocks at heights of 8mm, 16mm and 24mm**

#### 5.6.2. Localization Positional Accuracy Result

The mean and range of accuracy and repeatability of phantom position in X, Y and Z directions are shown in Table 5-2. Accuracy was the RMS error of the measurements, while repeatability was the 95% confidence interval standard error of the three measurements.

**Table 5-2: Positional RMS accuracy and repeatability in X, Y and Z directions**

Direction	Mean±SD Accuracy	Accuracy Range	Mean±SD Repeatability	Repeatability Range
X	0.4±0.2mm	0.1-0.8mm	0.1±0.1mm	0.00-0.3mm
Y	0.4±0.4mm	0.0-1.4mm	0.1±0.1mm	0.00-0.4mm
Z	0.3±0.2mm	0.0-0.7mm	0.1±0.0mm	0.00-0.2mm

A histogram of positional RMS errors is shown in Figure 5-21, with 73 (87%) within 0.6mm.

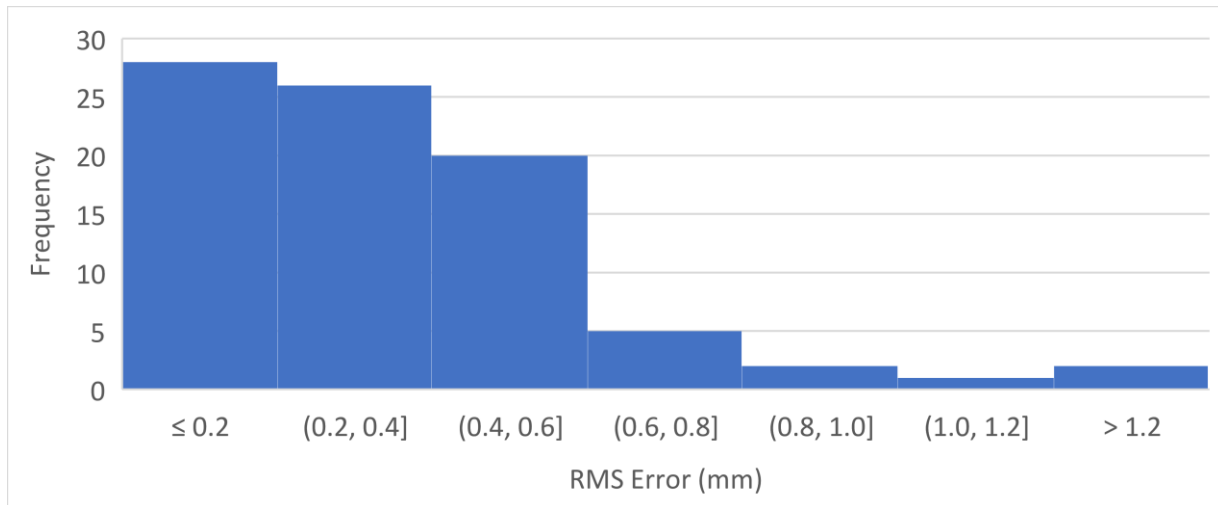


**Figure 5-21: Histogram of the frequency distribution of positional RMS error values in each dimension throughout the volume**

A chart displaying the average positional error at each position is shown in Figure 5-22. All measurements that were greater than 0.8mm of error (6% of measurements) were clustered at the edge nearest to the cameras.

	Z: -144mm	Z: -96mm	Z: -48mm	Z: 0mm	Z: 48mm	Z: 96mm	Z: 144mm
X: -80mm	● 1.27	● 0.83	● 0.41	● 0.84	● 0.59	● 0.40	● 0.40
X: -40mm	● 0.79	● 0.69	● 0.58	● 0.60	● 0.18	● 0.55	● 0.55
X: 0mm	● 0.63	● 0.49	● 0.28	● 0.66	● 0.66	● 0.66	● 0.66
X: 40mm	● 1.50	● 0.98	● 0.55	● 0.60	● 0.41	● 0.56	● 0.56
X: 80mm	● 1.51	● 1.07	● 0.94	● 0.56	● 0.53	● 0.92	● 0.92

Legend:	Y: 0mm	Y: 9.6mm	Y: 19.2mm	Y: 28.8mm
	●	●	●	●

**Figure 5-22: Positional error values at the 28 positions in mm. Position on the Z-axis is represented by each column while position on X-axis is represented by each row. Position on Y-axis is represented by the grayscale shade of the cell. Cells with the dotted pattern denote no measurements taken at that location. Up-arrows represent errors <0.5mm, no arrow represents errors <1.0mm and down-arrows represent errors >1.0mm**

The positional accuracy of each direction varied depending on the capture location. Moving along the Z-direction, errors along the Z-axis were higher when far from the cameras while errors along X and Y axes were higher when on the proximal side of the origin vs the distal side [0.5,0.7,0.1] vs [0.3,0.2,0.4] mm. Errors worsened from [0.3,0.2,0.2] to [0.4,0.5,0.3] mm when moving from the origin to the lateral edges of the capture volume. Errors also worsened slightly when moving in the Y-direction up from the baseplate [0.4,0.4,0.2] to an elevated position at [0.5,0.5,0.3].

While the trend of higher accuracy at the origin is expected, the accuracies limit the range in which this system could be used. The range of usage within the spinal cavity would likely be 100x30x150mm, considering the width of the spinal incision, the variation in depth of the vertebrae and usage in the highest risk pedicles from T4 to T9. Within this range, the mean position accuracy would be [0.3, 0.2, 0.3] mm in each direction with worst accuracies of [0.6, 0.4, 0.4] mm. However, if the full range of capture from this study was used (160x30x300mm) some areas at the edges of the capture volume could reach accuracies of up to 0.9mm.

The average repeatability of measurements was within 0.1mm in each direction while the worst repeatabilities were within 0.4mm. This high level of repeatability was expected, given that the motion capture cameras were originally determined to have an average repeatability of within 0.2mm. The worse repeatabilities compared with motion capture were expected, since small angular changes in scanning direction could result in ultrasound reflection intensities changing significantly, resulting in variation in thresholding of the phantom edges.

### 5.6.3. Localization Orientation Accuracy Result

The mean and range accuracy and repeatability of phantom orientation about the X, Y and Z axes is shown in Table 5-3.

**Table 5-3: Orientation RMS accuracy and repeatability in X, Y and Z directions**

Direction	Mean±SD Accuracy	Accuracy Range	Mean±SD Repeatability	Repeatability Range
X (pitch)	0.1±0.2°	0.1-0.5°	0.2±0.1°	0.0-0.5°
Y (yaw)	0.5±0.3°	0.2-1.1°	0.4±0.3°	0.1-0.7°
Z (roll)	0.5±0.3°	0.1-1.2°	0.2±0.3°	0.1-0.7°

A histogram of orientation RMS error values in all directions is shown in Figure 5-23. All 84 measurements were within 1.3° error, well within the required 5° accuracy. A chart displaying the average orientation error at each position is shown in Figure 5-24. The magnitude of orientation error was not associated with position within the testing volume.



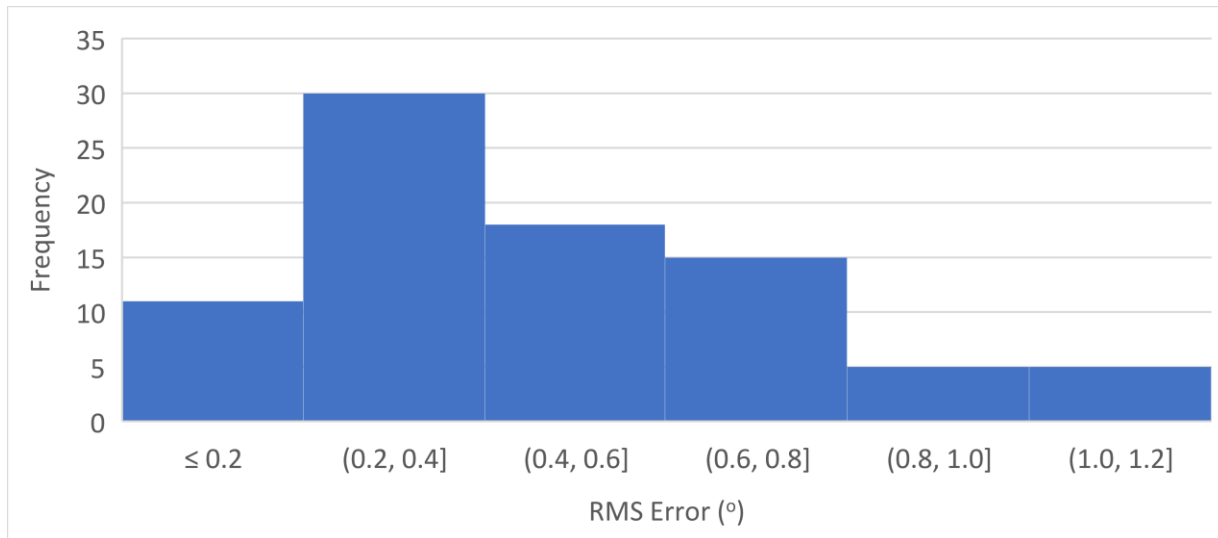


**Figure 5-23: Histogram of the frequency distribution of orientation RMS error values in each dimension throughout the volume**

	Z: -144mm	Z: -96mm	Z: -48mm	Z: 0mm	Z: 48mm	Z: 96mm	Z: 144mm
X: -80mm	▲ 0.63	▲ 0.79	▬ 1.42		▲ 0.89	▲ 0.76	▲ 0.79
X: -40mm	▬ 1.17	▬ 1.37	▲ 1.00	▲ 0.79		▲ 0.76	▲ 0.70
X: 0mm			▲ 0.99	▲ 0.69	▲ 0.77	▬ 1.27	
X: 40mm		▬ 1.21		▲ 0.87	▲ 0.85	▲ 0.68	▲ 0.73
X: 80mm	▲ 0.93	▲ 0.95	▲ 0.51		▲ 0.89	▬ 1.23	▲ 0.81

Legend:	Y: 0mm	Y: 9.6mm	Y: 19.2mm	Y: 28.8mm

**Figure 5-24: Orientation error values at the 28 positions, in degrees. Position on the Z-axis is represented by each column. Position on X-axis is represented by each row. Position on Y-axis is represented by the grayscale shade of the cell. Cells with the dotted pattern denote no measurements taken at that location. Up-arrows represent errors <1.0°, no arrow represents errors >1.0°. No values were greater than 5.0° requiring down arrows.**

The mean orientation accuracy about each axis was within 0.6°. The orientation was again most accurate near the origin of the capture volume. The RMS error changed by less than the mean repeatability of 0.35° in all directions. No clear trend could be found in orientation accuracy throughout the capture volume. The average repeatability of orientation measurements in each direction was within 0.35° with the maximum error being less than 0.75°, meeting the requirements [73].

#### 5.6.4. Localization Sources of Error

Sources of error in position and orientation can be traced to three major sources: ultrasound-space setup, camera position and orientation, and rigid body orientation. First, the setup itself involved mounting the

pegboard onto a flat surface. There may be slight variation in thickness in the mounting adhesive throughout the capture volume, or the water tub floor may not be perfectly flat. However, when the water bath was rotated to different orientations, the same errors were found in captured position. Accuracy varying according to position has been documented previously, though typically accuracy improves in the regions proximal to the cameras [39, 40]. Both lens distortion and thermal drift are potential causes for these inaccuracies, though the cameras were pre-heated for one hour already.

The Y direction was most strongly affected by outliers with a mean of 0.4mm vs median of 0.3mm. When removing outlier values that were clustered proximally to the cameras in the Z-direction, the mean and median were reduced to 0.2mm and 0.2mm, respectively. Surprisingly, the X position had the poorest accuracy, despite that direction being across the field-of-view of the cameras. Some of this reduction in accuracy could be from marker overlap on the rigid body. However, all accuracies were still well within the required accuracy of 1mm for usage in spine surgery. Usage of active markers could reduce marker overlap issues since the LEDs are smaller and can strobe at different frequencies.

Rigid body orientation is an important potential source of error when evaluating orientation. The orientation of the ultrasound transducer relative to the capture volume was initialized by mounting the transducer onto the calibration square. Variations in this mounting process would result in inaccuracies in the orientation. Still, most accuracies were less than 1°, which would be acceptable in this application.

## 5.7. Vertebral Position and Orientation Experiments

### 5.7.1. Capture Volume, Phantom Vertebra and Probe Design

So far, the experiments only tested the reconstruction accuracy on regular objects, as well as the positional accuracy of a single crosshairs phantom placed throughout the capture volume in the same orientation. The next set of experiments focused on localizing a vertebra-like phantom that was placed throughout the capture volume in different orientations. The accuracy of a motion capture probe being inserted into the vertebra was also evaluated to represent the accuracy of surgical tools being used in the operating room.

The same experimental setup with three motion capture cameras, ultrasound scanner and peg board water bath were used. A 12.4cm x 30.4cm area on the LEGO baseplate was considered the test area as shown in Figure 5-25. A smaller area as well was defined as the critical region that would require the highest level of accuracy in surgery as a 12.4cm x 20.8cm area. Two heights were tested: one on the baseplate surface and the second raised using a 9.6cm LEGO block.

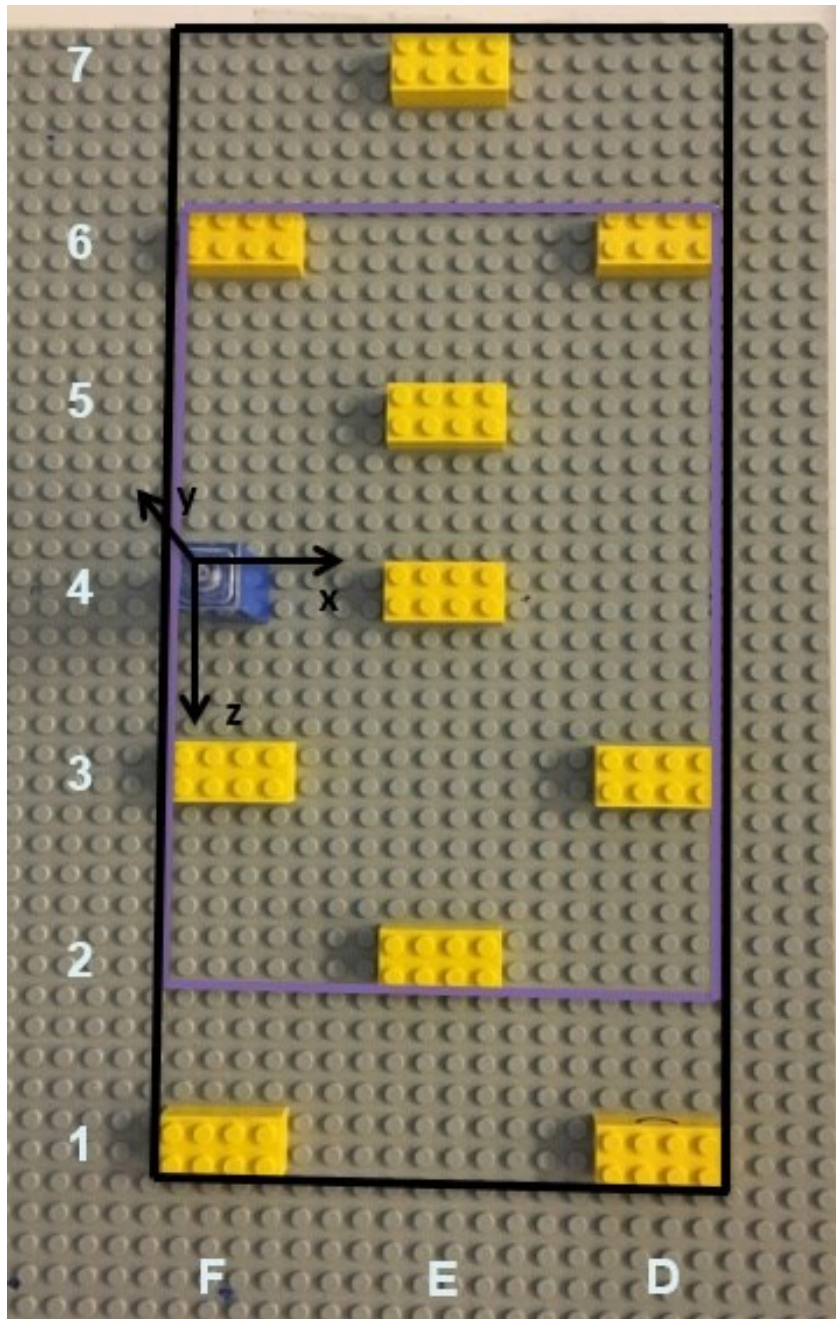


**Figure 5-25: Test area on LEGO pegboard. Black rectangle includes full test region while purple region is the critical region. Yellow bricks indicate raised heights**

Four new 3D printed phantoms were used (Figure 5-26a). Three vertebrae (i-iii) had pairs of pre-printed holes: (i) two vertical holes (neutral vertebra), (ii) left hole pitched  $15^\circ$  caudally and right hole pitched  $-30^\circ$  cranially (pitch vertebra) and (iii) left hole rolled  $30^\circ$  medially and right hole rolled  $-15^\circ$  medially (roll vertebra). Pitch was defined as rotations about the x-axis (transverse direction), yaw about the y-axis (posterior-anterior direction) and roll about the z-axis (axial direction). The dimensions and features of

the phantoms themselves were based on a T6 vertebra, and included the spinous process, two transverse processes, the lamina and the superior articular processes. A fourth vertebra (Fig. 2iv) was printed with four small divots in the place of holes to evaluate the accuracy of a Micron Series Digitizing Probe (Figure 5-27ii), (Optitrack, Corvallis, OR, USA) as a comparative reference.

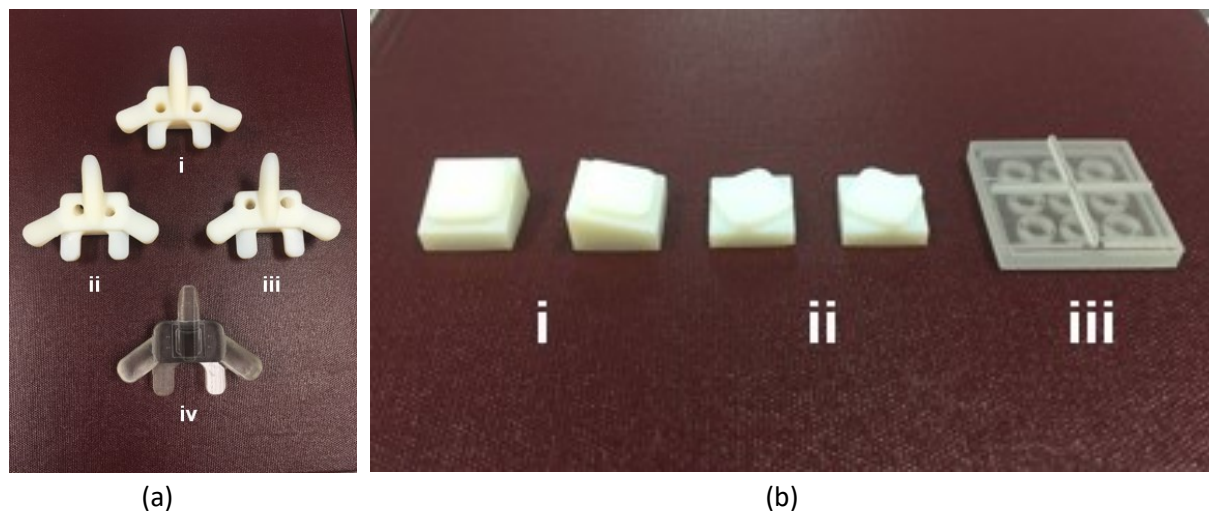


**Figure 5-26: Phantoms and tilters, (a) 3D-printed phantom vertebrae used in experimentation, i) Neutral, ii) Pitch, iii) Roll, and iv) Divots. (b) Custom printed tilters for pitch or roll (i), yaw (ii) and calibration square (iii).**

To evaluate the effect of changing vertebral orientation, four tilters were 3D printed: two for providing rotations in pitch or roll at 15 and 30° (Figure 5-26b,i), and two for yaw rotations to 30° (ii), all of which were also 3D printed.

Two localization accuracies were tested in this experiment. First, the 3D ultrasound reconstruction localization was tested by measuring the hole positions reconstructed in ImageJ (National Institutes of Health, Bethesda, MD, USA). The reconstructed volumes are positioned relative to the motion capture system's coordinate system. The position was compared with the theoretical position calculated by their pegboard position and the tilter orientation magnitude and direction.

Second, the accuracy of placement of surgical tools into these holes was evaluated using a custom 3D-printed device (Figure 5-27a). The device was screwed into the holes and the motion capture recorded position and orientation of the device were recorded. These were compared with the theoretical position and orientation which were calculated by the pegboard position, tilter orientation and hole orientation. The holes were threaded with a 1/4"-20 thread to ensure that it could remain stationary while inserted for measurement of orientations. The probe was kept small to reduce errors in transforming the center of rotation from the markers to the tip of the probe. This device was used in the three vertebrae with large

holes. The 3D printed probe was compared to an industrially manufactured Micron Series Digitizing Probe (Figure 5-27b) which could only measure position, not orientation. The fourth vertebra with the divots was used to measure accuracy of this device.

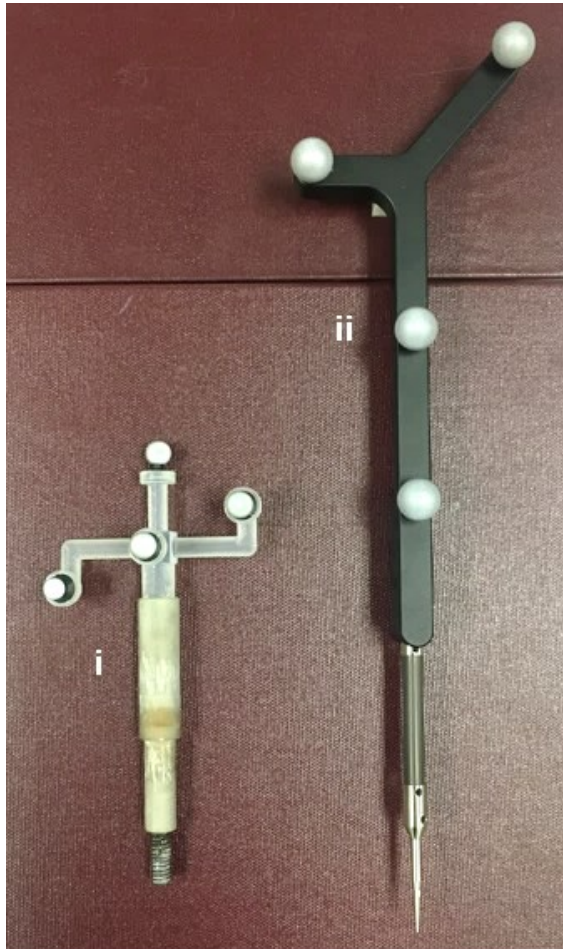


**Figure 5-27: Motion capture devices used, i) 3D-printed pointer device with threaded tip and ii) Micron Series Digitizing Probe.**

### 5.7.2. Experimental Design

Two sets of experiments were completed to assess accuracy of motion capture and 3DUS systems. First, individual variables were tested including vertebra position, orientation, and which of the three types of vertebrae were used:

- Position Test: The neutral vertebra was placed at 22 measurement locations throughout the 3x7 grid including two heights at the origin. Figure 5-25 show the heights at each location.

- Orientation Test: The neutral phantom was mounted on tilters in seven orientations: neutral, pitched  $\pm 15^\circ$ , rolled  $\pm 15^\circ$ , and yawed  $\pm 30^\circ$ . This test was only performed for the 3D-printed device and 3DUS as the Probe did not measure orientations.
- Vertebra Test: The three vertebrae with the uniquely oriented holes for the 3D-printed device and the 3DUS were tested at the neutral position. The Probe did not measure orientations and was not evaluated in this portion.

Three measurements were taken of each hole for each phantom.

Secondly, an experiment was conducted which involved combining the above variables for the 3D-printed device, Probe and 3DUS. Each location in the 3x7 grid was assigned a height, orientation, and vertebra which randomized each variable while retaining a balanced distribution of each variable throughout the capture volume. A full factorial experiment was not completed because of the large number of scans that would be required (three vertebrae, 42 positions, six orientations repeated 3 times resulting in 2268 scans). For the 3D-printed device and the 3DUS, combinations of these allowed for orientations of holes with up to two rotations with maximum  $45^\circ$  for rotational measurements. The Probe used the unique vertebra at all locations.

The capture volume origin was assigned the neutral vertebra and tested at both heights to ensure the system was calibrated. There were 22 unique combinations of position, orientation and vertebra, with three measurements taken of both holes, for a total of 132 measurements. The experiment was conducted three times for the 3D-printed device and 3DUS for a total of 396 measurements and conducted once for the Probe for comparison.

### 5.7.3. Individual Experiment Results

Figure 5-28 shows a sample rendering of the 3D ultrasound reconstruction. The 3D ultrasound reconstruction accuracy was  $0.6 \pm 0.5$  mm for the full range and  $0.5 \pm 0.4$  mm for critical region for the position test,  $0.4 \pm 0.1$  mm in the neutral orientation and  $0.5 \pm 0.2$  mm,  $0.5 \pm 0.2$  mm, and  $0.5 \pm 0.3$  mm for rotations of pitch, roll and yaw respectively, and of  $0.3 \pm 0.1$  mm,  $0.7 \pm 0.3$  mm, and  $0.4 \pm 0.1$  mm for the neutral, pitch, and roll vertebrae respectively, shown in Figure 5-29.

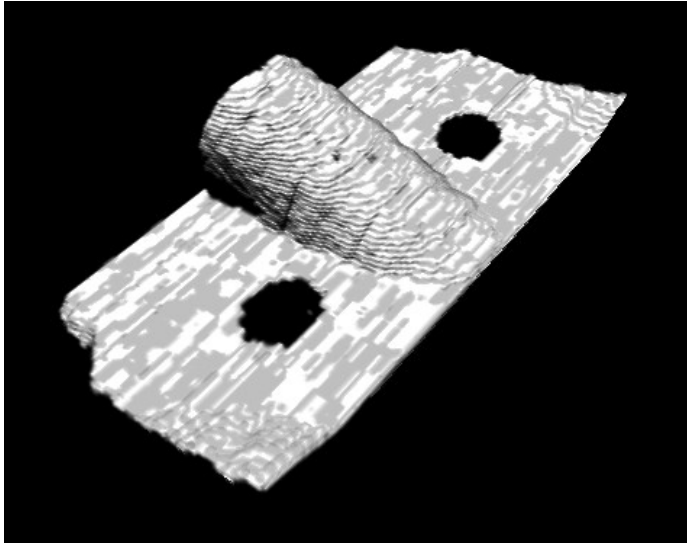


**Figure 5-28:** A 3D rendering using ImageJ of a sample reconstruction of a phantom vertebra that was analyzed in ImageJ.

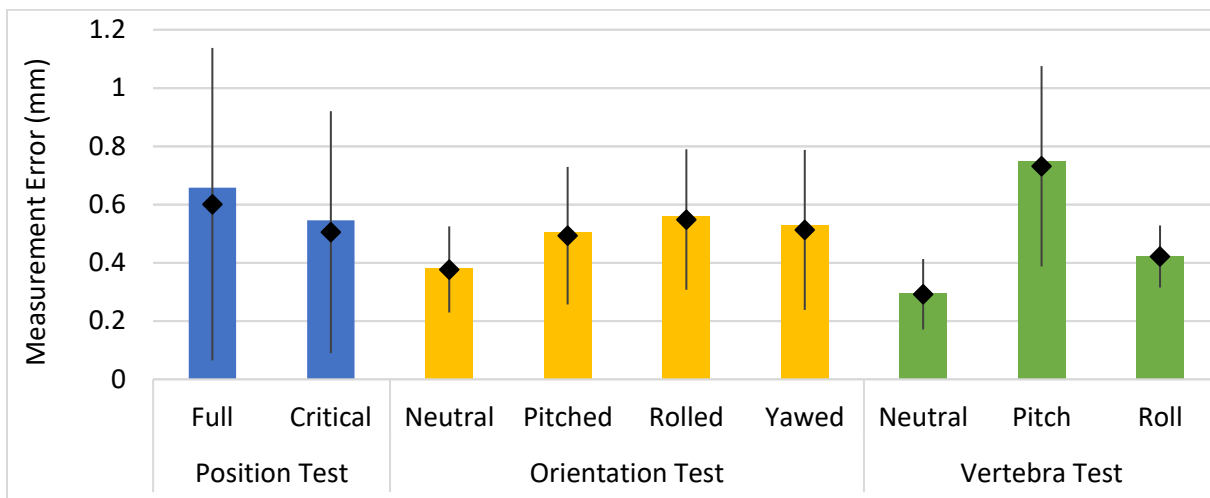


**Figure 5-29:** 3D Ultrasound individual experiments results. Full and critical indicate the full range and the critical region respectively. Diamond represents mean, bar chart represents RMS error, and whiskers represent 95% confidence interval of standard error.

The accuracy and precision of the 3D-printed device are shown in Figure 5-30. The position test found accuracy of  $0.6 \pm 1.0$  mm for the full range and  $0.4 \pm 0.3$  mm for critical region. The orientation test showed accuracy of  $0.4 \pm 0.0$  mm for the neutral orientation of the vertebra and  $0.3 \pm 0.2$  mm,  $0.6 \pm 0.2$ , and  $0.5 \pm 0.1$  mm for rotations of the vertebra in pitch, roll and yaw respectively. The vertebra test found accuracies of  $0.5 \pm 0.2$  mm,  $0.8 \pm 0.7$  mm, and  $1.2 \pm 0.6$  mm for the neutral, pitch and roll vertebrae respectively. Rotational accuracy throughout the individual experiments was  $0.3 \pm 0.7^\circ$ .

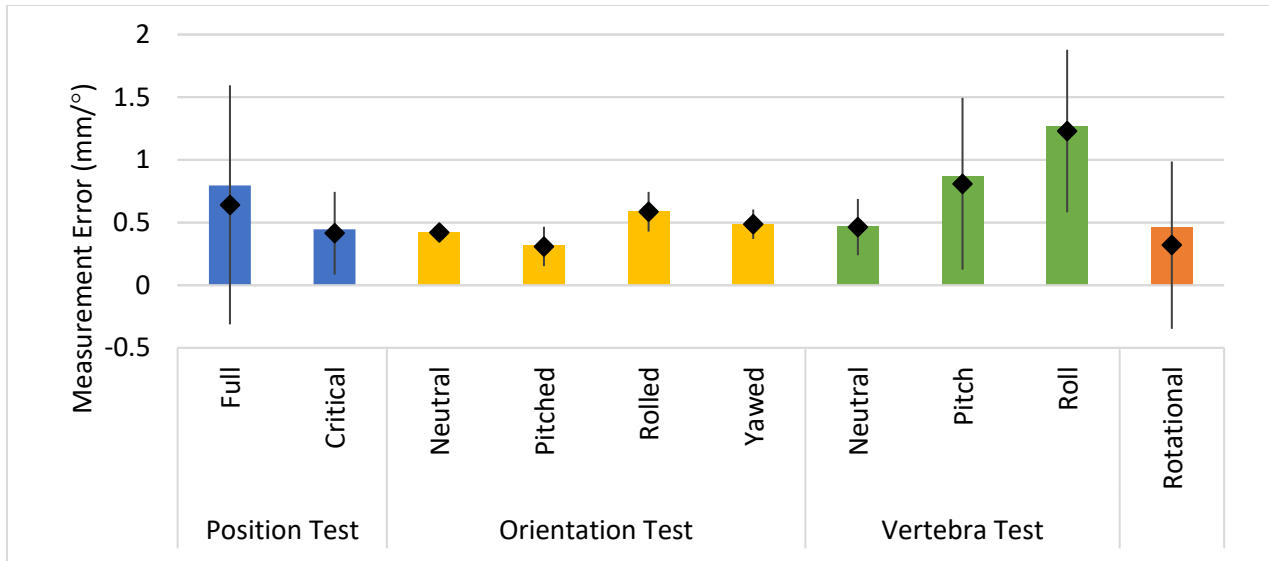


**Figure 5-30: 3D-printed device individual experiments results. Full and critical indicate the full range and the critical region respectively. Diamond represents mean, bar chart RMS error, and whiskers represent 95% confidence interval of standard error.**

For the Probe device, only the position was measured, with accuracies of  $0.6 \pm 0.4$  mm for the full range and  $0.5 \pm 0.4$  mm for the critical region (Figure 5-31)

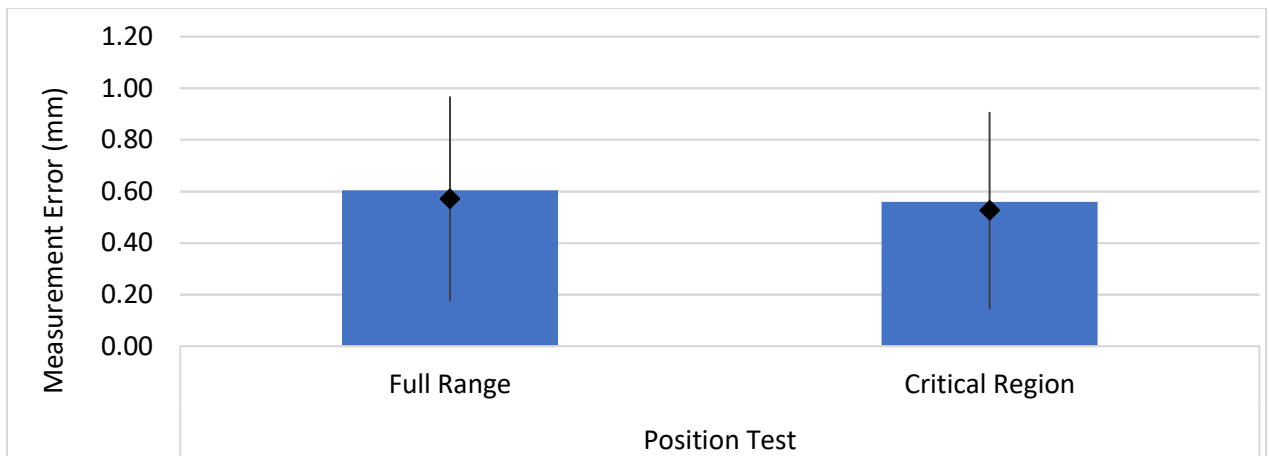


**Figure 5-31: Probe position test results. Diamond represents mean, bar chart represents RMS error, and whiskers represent 95% confidence interval of standard error.**

Position seemed to play a substantial role in the measurement accuracy of the devices, with higher accuracies in the central regions and lower accuracies at the edges. For orientation, the application of the tilter mounts resulted in lower accuracy by several tenths of a millimeter compared to the neutral. Part of this error was likely from tolerances between meshing 3D-printed parts with Lego components. Additionally, applying the tilters changed the angle at which the 3D-printed device and 3D ultrasound



were performing measurements, resulting in these orientation errors to be propagated in both positional and rotational inaccuracies. The vertebrae test also revealed systematic errors for the 3D-printed device and 3D reconstructions. For the 3D-printed device, both the pitch and roll phantoms produced repeatable results that were outside of the target positional accuracy. Manufacturing issues would likely play a role in these errors, as the phantom vertebrae were manually threaded into the relatively soft plastic material. Also, because the holes were tilted, the shape of the holes and positions of the threads themselves could slightly alter the 3D ultrasound images. It was also difficult to thread these vertebrae at the exact designed angle. While the increased complexity and potential sources of error did show a worsening trend for accuracy, the accuracies were still within the clinically accepted limits of 2mm, even for the most extreme cases. The full experiment would clarify the effects of combining all these variables.

#### 5.7.4. Full Experiment Results

The full experiment combined all three variables, with Table 5-4 showing the accuracy values found in this experiment and Figure 5-32 showing the results from the 3D ultrasound reconstruction, the 3D-printed pointer device and the professional probe device in one graph.

**Table 5-4: Full experiment positional and rotational accuracy**

Device	Full Test Area (mm)	Critical Region (mm)	Rotational Accuracy (°)
<b>3D-printed Device</b>	1.1±1.1	1.0±1.0	0.0±1.7°
<b>Probe</b>	0.7±0.4	0.8±0.3	N/A
<b>3D Ultrasound</b>	0.8±0.6	0.7±0.5	N/A

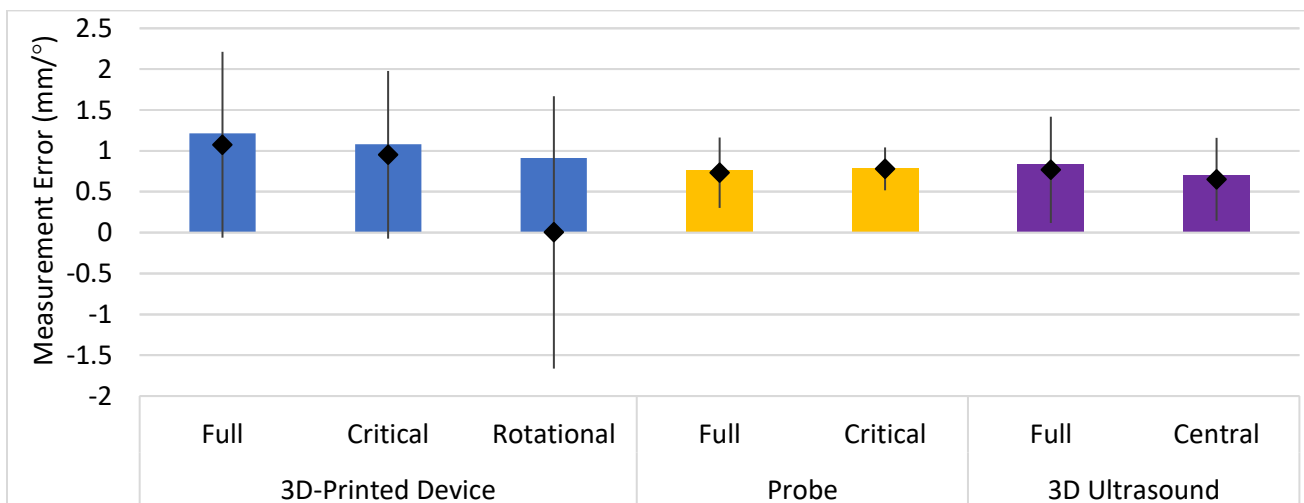


**Figure 5-32: Full experiment test results for all three devices. Full and critical indicate the full range and the critical region respectively. Diamond represents mean, bar chart represents RMS error, and whiskers represent 95% confidence interval of standard error.**

The full experiments showed that accuracies were improved in the critical region compared with the full capture volume for both the pointers and for the 3D ultrasound, even when combining different combinations of rotations and vertebra types. The probe out-performed the 3D-printed device, having higher accuracies for both full and critical regions, likely due to its higher quality fabrication. Most importantly, the accuracy of the 3D ultrasound and probe were within the clinically accepted limit of 2mm, both being within 1.2mm errors, but not within the technical target of 1mm.

## 5.8. Discussion on 3D Ultrasound Results

### 5.8.1. Technical Comments

Three major experiments were conducted in this thesis project during the development of the 3D ultrasound system: Calibration of the 3D ultrasound timing, evaluation of the reconstruction and positional accuracy on generic phantoms, and evaluation of the positional accuracy on vertebrae-like phantoms throughout the capture volume in different orientations. Because high accuracies are required for this project, the main challenge in all three experiments was ensuring the experimental designs had high precision to allow for accuracy to be evaluated. Sources of error included the 3D-printed polyjet fabricated components, the water tank construction, the motion capture camera hardware, and the ultrasound images.

The primary source of error throughout these experiments was likely the fabrication of the 3D-printed components. Lego components are typically constructed from Acrylonitrile butadiene styrene which has a high Shore Hardness (100 on Scale D) and are dimensionally stable when exposed to water. Their high accuracies have already been mentioned previously. However, the Veroclear material is somewhat softer (Shore Hardness D of 83-86) and dimensions can change by 1% in water, resulting in components slowly fitting more poorly as experiments moved forward, resulting in less accurate results. Particularly when inserting probes into the phantoms, there would be increased wear with screwing the probe into the hole, resulting in greater inaccuracies. Using another 3D printer could potentially have better dimensional stability but would have had poorer accuracy in the prints themselves. Future studies on determining localization accuracy (or surgical registration accuracy) would not use threaded holes to reduce potential for wear. There would also be an attempt to reduce the dependence of measurements on physical alignment of the phantoms so that poorly fitting phantoms would not affect results. Probe placement at pitch and roll angles had a particularly large effect on positional accuracy and would require further investigation.

Evaluation of the motion capture cameras was already performed in Chapter 4: . However, that evaluation focused on displacement accuracy of the system, rather than the positional accuracy. The motion capture system was able to measure distances between points accurately and reliably (within 0.25mm), but questions remained as to whether it could measure exact locations accurately, particularly at the edges of the capture volume. This result seems to imply that regions that are far from the capture volume origin may have distortions in the measurements being made. There could be systematic errors in the base plate. However, the repeatability of the LEGO pegboard was extremely high when measured with calipers and rotating the baseplate did not seem to change the trends in errors, suggesting that it was a camera issue, not the water tank issue. It may be that higher quality (and thus higher cost) cameras would have reduced distortion. Still, the accuracies were within the clinically accepted accuracies surgical usage, although they failed the 1mm goals of the study.

The ultrasound images themselves would likely contribute some degree of error as well. However, given the high resolution of the images, and their usage in measuring submillimeter masses in clinical applications, it would be unlikely that the images themselves are contributing a large portion of the errors found in this study.

### 5.8.2. Clinical Relevance

Several studies have previously investigated the use of 3DUS for a variety of purposes with tracked, freehand probes [226–230]. These systems were generally used for in vivo measurements and visualization of sub-surface landmarks, including determining the location of needle tips and reconstructing spinal vertebrae. Concerns for these types of systems are needle tip visibility [227,231] as well as the retention of true form of reconstructed structures [232,233]. Given that the application of the system in this study is with a water/saline bath, reconstruction quality was not an issue when compared with soft tissue reconstructions. These studies found reconstruction accuracies within 1mm and angular accuracies within 5° between two needle tips.

As mentioned in Section 2.3.6, Poulsen et al. studied volumetric accuracy on a 2cm agar rod within an agar and graphite medium, erring by 181mm<sup>3</sup>, a 5.65mm linear accuracy [147]. The poorer accuracy is likely due to the phantom being deformable when scanned and the usage of an optical surface scanner for motion tracking. Loannou et al. studied surface area measurements of fetal fontanelle phantoms with surface areas ranging from 95mm<sup>2</sup> to 654mm<sup>2</sup>[146]. The median percent error ranged from 0.6-12.1%, or 2-3.4mm. The larger errors could be explained by the fontanelles being scanned at greater depth than our study.

Studies in ultrasound registration techniques have also been used to determine accuracy of ultrasound reconstructions. A study by Zenbutsu et al. used 3D ultrasound in water-based laparoscopic surgery, projecting blood vessel images onto 2D laparoscopic images, finding vessel depth error at 1.88mm [234]. Penney et al. registered ultrasound to CT scanned femurs, finding mean RMS errors of less than 2.3mm on most registrations [235]. Yan et al. developed a spinal ultrasound-CT registration method achieving median registration errors of 0.66mm on phantoms and 1.65mm on a porcine model, showing that while submillimeter accuracies are possible, soft tissues may complicate the usage of 3D ultrasound for spine surgery [17]. Koo et al. studied ultrasound to MRI registration of human lumbar dry bone specimens and porcine specimens, finding accuracies of 1.22mm on the human bone and 2.57mm on porcine cadavers. In all these cases, soft tissues were included in the registration process which would worsen errors. As soft tissues will likely lie around and on top of parts of the bony structures, the edges and the depth of the bony surface may be altered, though the surface will remain visible. Further study of the effects of soft tissue on image registration accuracy from these reconstructed vertebrae would be investigated [236].

## 5.9. Conclusion

The 3D ultrasound system was evaluated for its accuracy in usage for pedicle screw placement in spinal surgery. The full 3D ultrasound experiment showed accuracies of  $0.8\pm 0.6\text{mm}$  for 3D ultrasound,  $0.7\pm 0.4\text{mm}$  for a high-quality motion capture probe, and  $0.0\pm 1.7^\circ$  for rotational accuracy from a custom-made probe. The system has comparable accuracies to current 3D ultrasound systems for reconstruction accuracy and has similar accuracies to registration technologies for spine surgery. The application of this system as a localization tool for image-guidance surgery appears feasible. Next steps would focus on accurate image registration of CT vertebrae to the 3D ultrasound surface scan.

## Chapter 6: Image Registration of Intraoperative Ultrasound to Pre-operative 3D Imaging

### 6.1. Summary

Image registration is the alignment of the coordinate systems of two different images into the same coordinate system. In the medical field, it usually involves the registration of images from two different modalities. In this case, the need to localize anatomy using the ultrasound surface while visualizing the internal anatomy of the bone requires registration of either a CT or MRI of the vertebra to the ultrasound surface image. This chapter describes the development process in adapting image registration techniques to this unique application. Section 6.2 describes the software development process in using registration techniques. Section 6.3 presents the development of a pre-registration process by aligning the volumes in a roughly correct position. Section 6.4 describes two registration sequences that were tested: an iterative transformation-based sequence, and an iterative-closest-point sequence. Section 6.5 presents the results from a phantom experiment involving registering vertebrae and localizing them in the capture volume space. Section 6.6 includes preliminary experiments on a porcine spine on the feasibility of registration of real bone that includes soft tissue. Lastly, Section 6.7 is a discussion on the strengths and limitations of the system and a comparison of other systems.

### 6.2. Initial Registration Testing

#### 6.2.1. Phantom Volume Generation

The vertebrae-like phantoms from Figure 5-26 were used for preliminary evaluation. The models needed to be converted into a 3D binary volume. Phantom models are typically in stereolithography (STL) format which converts solid objects into thousands of triangular faces. The vertices of every triangle and the direction of the resulting faces of every triangle are described in the STL file. Using the face information as a shell, the model was converted into a 3D volume of the vertebra using a custom Matlab converter. This volume would be used for image registration in the next set of experiments.

For all registrations, the 3D ultrasound was considered the stationary volume while the CT was the moving volume. Because the 3D ultrasound is localized by the motion capture cameras, its coordinates needed to be kept absolute, while the CT scan coordinates are arbitrary, making it more logical to transform and move the CT coordinates to register onto the 3DUS image.

### 6.2.2. Pre-built Software Algorithms

Two pre-built image registration programs were tested on the dataset: image registration in the open-source and free 3DSlicer (Version 4.3.1, Boston, Massachusetts, USA) medical image visualization software, and the native registration program in Matlab (Mathworks, Natick, Massachusetts, USA) [237].

The 3DSlicer software has a variety of different types of registration methods available. First, the interactive landmark-based registration was tested. An ultrasound scan was performed on the 3D-printed vertebra, and the surface scan was uploaded into slicer. The center of the upper-most tip of the spinous process and the center of the upper-most tips of the transverse processes were selected on both images and then registered to each other. This preliminary test showed that the scaling between the two images was correct and that the surfaces could be registered using these clear landmarks (Figure 6-1). However, because the goal of this system is to have an automated registration system, a manually-selected landmark-based system would not be appropriate.

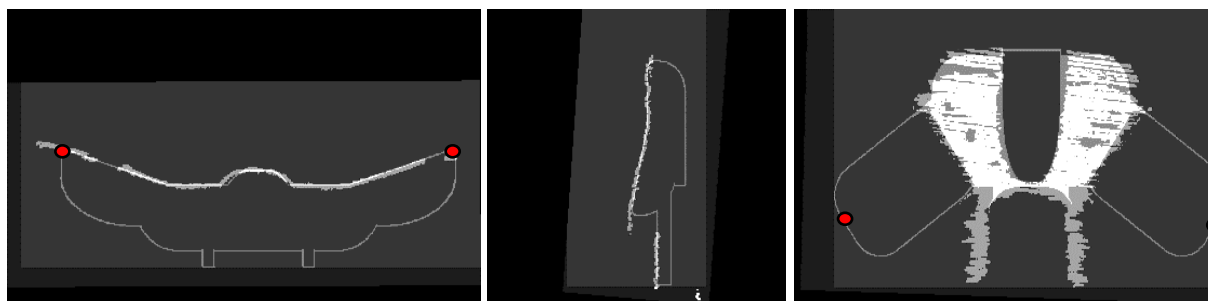


**Figure 6-1: Sample manual landmark registration showing grayscale model (thin outline) registered to grayscale ultrasound surface (thick line) on transverse, sagittal and coronal views respectively. Red dots denote transverse process landmark locations (spinous process landmark is out of frame).**

The fast-rigid registration on 3DSlicer was tested next, which is an intensity-based registration that registers the volume by evaluating voxel signal intensity. A rigid (6 degree-of-freedom) transformation was applied to the test volumes. To increase the chances of successful registration in this initial test, the orientation of the ultrasound was pre-aligned to the CT scan. The position was left unchanged. Registration took over 45 minutes and was not successful after testing three different ultrasound scans. This was fully understandable because the dataset is binary and sparse (most of the volume has empty pixels), while the registration algorithm would usually be used on volumes in which every voxel included image data. Given the need for automation and high speed, 3DSlicer was not further tested for image registration.

The native image registration program in Matlab was tested next, with a rigid transformation being performed on the test volumes. A mean squares optimization metric was used for the transformations and the orientations were pre-aligned. Again, registration was not successful after requiring 30 minutes of processing time and testing on three different ultrasound volumes. Again, this failure was expected, since this algorithm is used to register full volumes, rather than sparse surface data. It was decided that it would be best to develop a custom algorithm to speed up registrations, improve the success rate and gain an understanding of how to register these volumes.

### 6.2.3. Registration Process

Intensity-based registration is an iterative process. The volumes are overlapped, and an optimization metric is used to compare the overlap. The most basic metric is the mean-squared error, calculated between pixel intensities between the two volumes using Equation 6-1: Mean-squared Error for Image Registration:

**Equation 6-1: Mean-squared Error for Image Registration:**

$$MSE = \frac{1}{n} \sum_{i=1}^n (Y_{i,1} - Y_{i,2})^2$$

Where:

- $n$  is the total number of voxels in each volume
- $Y_{i,1}$  is the pixel value in the first volume (CT)
- $Y_{i,2}$  is the pixel value in the second volume (3DUS)

The mean-squared error would therefore be minimized if all the bright CT pixels were aligned with all the bright 3DUS pixels, indicating a good registration. The process is repeated by transforming one of the volumes (the moving volume), then re-overlapping the volumes and calculating the error. The transformations are iterated multiple times, and the transformation with the lowest mean-squared error would be selected as the best registration. Iterations are repeated until a change in error threshold is met or are repeated through a specific range at a certain increment that is deemed adequate for the application. The latter approach was selected to reduce the chance of local minima being reached rather than global minima.

Volumes were represented as two data types: a full reconstructed binary volume that contained the surface or model; and a list of coordinates or point cloud of every white pixel in the binary volumes. The binary volumes are used for calculating the mean-squared errors between the two volumes and for user

display. The point cloud is used for the transformations, with every coordinate being transformed individually. Transforming individual pixels was found to be much faster than attempting to transform the entire volume. The point cloud would also be used for the iterative closest point surface registrations.

To increase speed of registrations, volumes were either scaled down (For pre-registration and the 6-degree-of-freedom registrations that will be described later) or re-sampled in the case of the iterative closest point registrations.

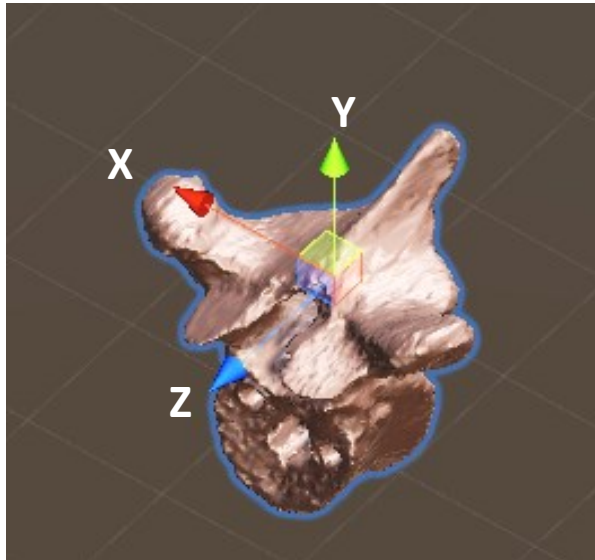


**Figure 6-2: Conventions relative to vertebrae showing X (lateral or transverse), Y (postero-anterior) and Z (cranio-caudal or axial) directions**

The conventions for rotations and translations for image registration involve the X axis pointing across the camera faces, the Y axis pointing vertically upwards and the Z axis pointing away from the camera faces. The alignment of these conventions relative to a typical vertebra placed in the surgical capture volume are shown in Figure 6-2. Rotationally, pitch is a rotation about the X-axis, yaw is a rotation about the Y-axis and roll is a rotation about the Z-axis.

#### 6.2.4. Registration Evaluation Metrics

As stated before, an intensity-based registration would be pursued rather than landmark based, due to the ability to automate this registration approach. However, many evaluation metrics exist for optimizing registrations, including mean-squared error, mutual information and structural similarity index as outlined in Section 2.3.9.

To test the speed of the evaluation metrics, a program that determines the most symmetric orientation of the phantom was developed. The phantom vertebrae shown in Figure 5-26 were used as the phantom



to be registered. The neutral phantom which was already symmetric and was set as the fixed volume. Then, a set of 121 volumes was generated by rotating the vertebra about its line of symmetry in  $1^\circ$  increments from  $-60^\circ$  to  $60^\circ$ . Because the vertebra is symmetric, the evaluation metric should show that overlap is the highest when not rotating the vertebra while any rotation would have less overlap.

In this preliminary test, mean-squared error, structural similarity index and mutual information were tested. Mean-squared error was ten times faster than structural similarity index and mutual information (2.2s vs 25.7s vs 28.9s respectively), all returning the same alignments of the phantom after overlapping the resulting images together. Because the mean-squared error was the fastest and yielded good results, it was selected as the evaluation metric going forward.

### 6.3. Pre-Registration Development

#### 6.3.1. Pre-Registration Concepts

Medical images typically have a certain orientation convention to allow for some pre-alignment of the images to reduce the range of orientations and positions that need to be assessed. However, for the 3DUS images compared with a pre-operative CT or MRI, the vertebrae may be in vastly different orientations and positions. The 3D ultrasound coordinate system is aligned with the motion capture system, while the CT coordinate system is aligned with the bore of the CT scanner itself. Also, because the patient is positioned differently and a surgical procedure is being conducted on the patient's spine, the vertebrae could be in very different orientations and positions when images are obtained. The first step of this registration process involved pre-registering the images by roughly aligning their orientations and their positions, using some of the inherent geometric features of the vertebrae to speed up the process. The code for this section can be found in Appendix 5: Image Pre-Registration Code

The typical orientation of both the CT and 3DUS surface scans involve the posterior surface of the spine facing up vertically, and the spinous process pointed away from the cameras since the cameras are cephalad to the spine. This restricts the orientation to a single quadrant in a 3D coordinate system. Two sets of iterative pre-registrations were completed to align the orientation of the two volumes (Figure 6-3). First, the symmetric nature of vertebrae was used to orient the yaw and roll of both the CT and the 3DUS surface images along the sagittal plane of symmetry. Second, the slope of the spinous processes and the laminae of the symmetric CT and 3DUS was aligned to calculate the transform that would orient the pitch.

Using the yaw and roll symmetry and the pitch slopes of the vertebrae, the CT could be pre-aligned to the 3DUS image. The CT was first transformed to its symmetric position, then to the 3DUS-slope-aligned

position. The inverse transform of the 3DUS was then applied to transform the CT to align with the original 3DUS surface.

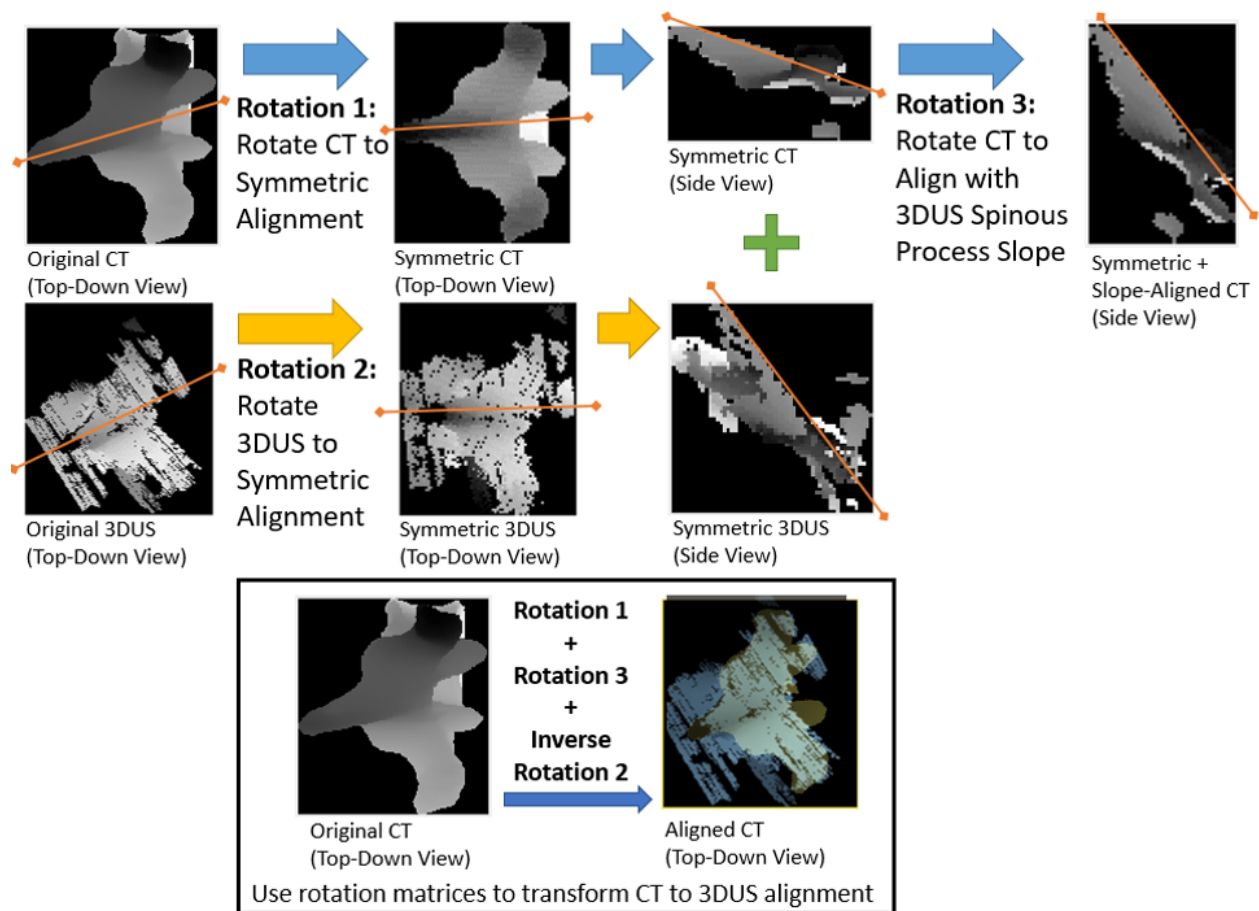


**Figure 6-3: Flowchart of required rotations to pre-orient CT with 3DUS scan in three steps**

The positional alignment was achieved by aligning the centroids of the two bodies. The centroid of the bodies was calculated using the point cloud data, using the Equation 6-2:

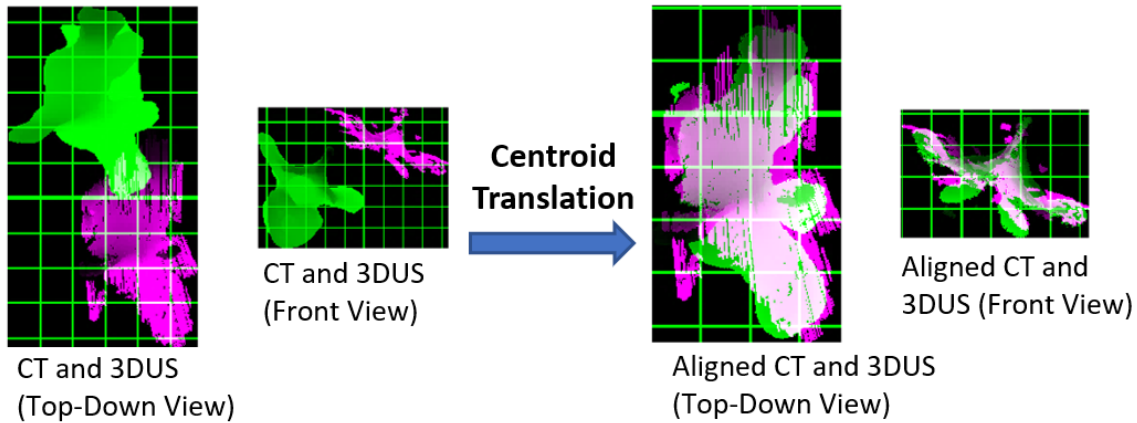
**Equation 6-2: Centroid of CT or 3DUS Bodies**

$$x_c = \frac{x_1 + x_2 + \dots + x_k}{k}$$

Where:

- $x_c$  is the centroid in the x-direction
- $x_{1-k}$  are the x-coordinates of each point in the volume
- $k$  is the total number of points

The posterior surface of the CT vertebra was extracted and then the centroid for all three coordinates (x, y and z) from both images was calculated (Figure 6-4). The CT was then translated by the difference between the centroid positions of the 3DUS and the CT.



### Calculate CT and 3DUS centroids and translate to align surfaces

*Figure 6-4: Sample of CT and 3DUS centroid translational alignment (CT in green and 3DUS in pink)*

The resulting transformed CT volume would be then used for full registration. The details of testing the symmetry, slope, and centroid iterative pre-registrations are presented in the next section.

#### 6.3.2. Pre-Registration Robustness Testing

Throughout the process of pre-registration, the robustness and speed of the iterations needed to be evaluated to ensure a reliable process that would still be fast enough to be used in the surgical suite. The symmetry and slope algorithms needed to function reliably for a wide range of orientations for the CT and 3DUS images.

To evaluate this process, a more realistic phantom needed to be used. A plastic phantom spine was CT-scanned and segmented using 3DSlicer to extract the vertebrae of the phantom. Figure 6-5 shows the phantom as a 3D model and the extracted T6 vertebra. This phantom was 3D-printed and then ultrasound scanned throughout the registration testing phase.

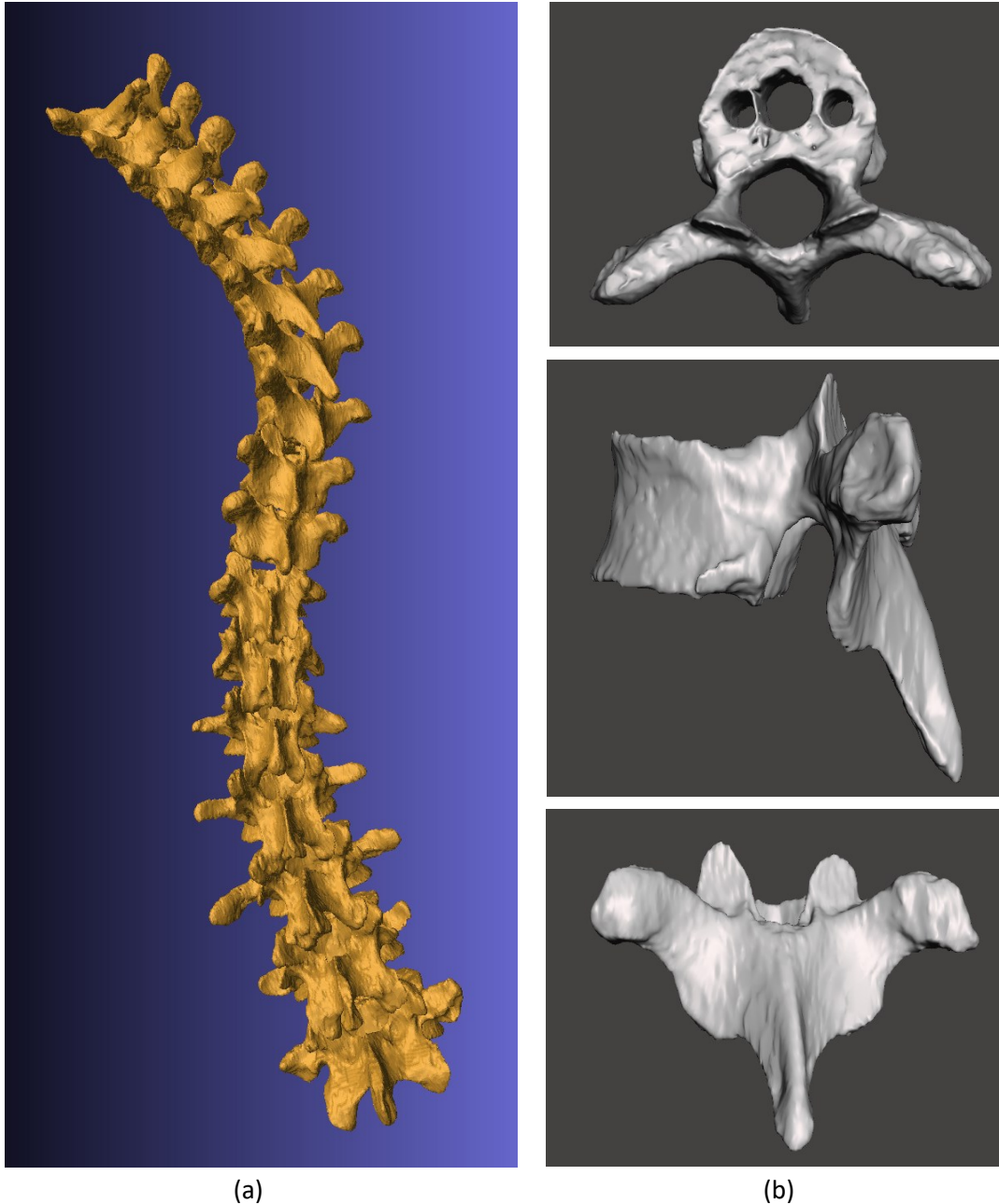


**Figure 6-5: Phantom spinal model (a), Segmented T6 vertebra in different views (b) including transverse view (top), sagittal view (middle) and coronal view (bottom) shown as a sample.**

### 6.3.3. CT Symmetry Pre-Registration

Both the CT and the 3DUS vertebrae are symmetric about the sagittal plane, meaning that only the roll and the yaw of the vertebrae would affect the symmetry of the vertebra in the volume's coordinate system. The remaining factors that would need to be determined include: (1) the optimal scaling factor for images when performing registrations, (2) the sequence and combination of yaw and roll rotations being applied to the images, and (3) the range and increment between rotations that would be applied to

the images. The goal was to minimize processing time (scaling images more, having fewer combinations and smaller ranges with wider increments), while ensuring adequate accuracy.

The T3 to T8 vertebrae were extracted from the spine and used for this set of experiments since they represent the most likely vertebrae that would require guidance in screw placement [73]. Each vertebra was aligned to its symmetric position and then rotated in 14 different orientations as shown in Table 6-1.

**Table 6-1: List of orientations in degrees (pitch, yaw, roll)**

Small Rotations		Large Rotations	
(0,0,-26)	(0,8,-13)	(0,-14,42)	(0,-49,0)
(0,33,0)	(0,-21,15)	(0,-38,-18)	(0,0,47)
(0,-14,7)		(0,-23,-35)	(0,48,54)
(0,-15,27)		(0,36,24)	(0,-41,-43)

A two-step scaling system was applied, iterating a wide range of rotations on images with a larger scaling factor, then using the output rotation from that step to iterate a smaller range of rotations with a smaller scaling factor. This method would reduce the risk of the algorithm finding a local minimum by ensuring the full range of orientations were assessed.

The first evaluation test on the symmetry algorithm involved putting the vertebral volume through the symmetry algorithm at different scaling values shown in Table 6-2. The vertebrae were rotated through a range of  $\pm 90^\circ$  (to cover  $180^\circ$  of vertebral rotation) and  $10^\circ$  increments for the first step of iterations. The vertebrae were rotated through the full range in yaw first. The best yaw orientation was selected and then that yaw rotation was rotated through the full range of roll rotations. The best orientation from the yaw and roll combination from the first scaling factor was then selected and then a new set of rotations (range of  $\pm 20^\circ$  at  $2^\circ$  increments) were applied on a second volume that was scaled down less. This was called the alternating method since yaw rotations are applied, followed by roll at one scale resulting in 19 rotations for each set (total 38), followed by yaw and then roll at the second scale resulting in 21 rotations for each set (total 42). This compares to the combined method which performs all rolls and yaws in combination with each other which would result in  $19 \times 19$  rotations (361 total) at the first scale and  $21 \times 21$  rotations at the second scale (441 total).

The scaling rates were chosen to be multiples of either two, five or ten for simplicity. The algorithm was then applied on each vertebra (T3 to T8), each rotated to one of the small rotations listed in Table 6-1. The final outputted transformation angle was compared to its respective pre-determined orientation angles. A 3.6 GHz 4<sup>th</sup> generation Core i7 with 16GB of RAM computer was used for all registrations. The

success rate was judged as being within 5° of rotation from the symmetric orientation while the processing time is reported on the T6 vertebra (rotated to (0,-15,27)) as a sample of the relative processing times. The success rates and times are displayed in Table 6-2.

**Table 6-2: Success rate at different scaling values**

<b>Two-Step Scaling Set</b>	<b>Success Rate</b>	<b>Processing Time</b>
1:40 and 1:20	0%	0.6s
1:25 and 1:10	33%	2.4s
1:20 and 1:10	67%	2.6s
1:15 and 1:10	67%	2.9s
1:16 and 1:8	100%	3.5s
1:20 and 1:5	100%	4.7s
1:15 and 1:5	100%	4.8s
1:10 and 1:5	100%	6.6s

From these results, it was clear that scaling the images too much would result in poorer success rates. The 1:16 and 1:8 scaling levels were selected for further testing.

The second factor that was tested was comparing the alternating method with the combined method. Each of the T3 to T8 vertebrae were rotated by each of the 14 different orientations in Table 6-1 resulting in 84 symmetry evaluations. The same range and increment were applied.

For the alternating method when rotating yaw and then roll, the success rate was only 52.3%, with 25/84 (29.8%) having errors larger than 10° and 15/84 (17.9%) having errors larger than 5°. Rotating by roll first and then yaw fared better but the success rate was still only 63.0%, with 15/84 (17.9%) having errors larger than 10° while 16/84 (19.0%) had errors larger than 5°.

The combined method had no rotational errors greater than 10° and only 11/84 (13.1%) greater than 5° resulting in an 86.9% success rate. Five of these errors came from largest combination of rotations (48° in pitch and, 54° in yaw), showing that large rotations off the symmetric orientation could hamper performance of the algorithm. Part of the error also could be from Euler angles being used to represent rotations which depends on the order of operations. However, the processing time increased by ten times (30s). Still, the combined method was selected because of its superior accuracy, especially in reducing 10° errors, but time savings would need to be found by changing the range and increments.

The final factor that needed to be decided on was the range and increment of rotations was selected. The range for the first step of registration was set to ±70° which would be greater than the angles of the most tilted vertebrae at the top or bottom of a curve for yaw rotations, while axial vertebral rotation relative

to the neutral vertebra would rarely be larger than  $60^\circ$ . The increment was kept at  $10^\circ$  to provide good coverage over the full range of rotations. The range of the second step was set at  $\pm 20^\circ$  while the increment was increased to  $4^\circ$ . The  $20^\circ$  range overlaps reduces the chances of reaching a local minimum, while the  $4^\circ$  increment is small enough to yield an adequate initial estimate for the registration algorithm. As a result, 15 rotations in each direction (225 total, from 361) were applied in the first stage and 11 rotations in each direction (121 total, from 441) in the second stage.

The resulting yaw and roll transform would be applied in the final pre-registration process. The same experiment was applied (six vertebrae, 14 orientations, 84 total tests). Again, 11/84 (13.1%) had error greater than  $5^\circ$  with none larger than  $10^\circ$ . Processing time was decreased to the 15s range which was considered adequate for this application. More definitive experiments would be completed once all the components of registration were developed and combined.

#### 6.3.4. 3DUS Symmetry Pre-Registration

The 3DUS symmetry algorithm differs from the CT algorithm because only a surface image is available which contains extraneous surface reflections from neighboring vertebrae or soft tissue. The 3D surface volume was converted to a 2D surface map (scaled at a 1:16 ratio) with the intensity of pixels representing the depth (depth in the Y direction). First, the plane that was most parallel to the surface was found to align the roll orientation by simply counting the number of non-zero pixels in the 2D image. The image with the most non-zero pixels reliably had the roll orientation correctly aligned since surfaces that were oriented off-angle would have regions that could be occluded by other more superficial pixels on the 2D surface map, resulting in fewer pixels appearing on the 2D projection.

To improve the effectiveness of the algorithm, the initial transformation was set to be the average orientation of the ultrasound transducer itself since the ultrasound transducer would usually be orthogonal to the surface in order to capture a higher quality image. Second, the yaw orientation was aligned by cropping the outer  $\frac{1}{4}$  of the 2D image and then calculating the symmetry on the cropped image to reduce the effects of extraneous surfaces. Surface orientation yaw was iterated from  $\pm 70^\circ$  with increments of  $10^\circ$ , like the CT images.

From the resulting transform, the 2D surface map of the vertebra was created and then scaled 1:8. An iterative symmetric algorithm like the CT symmetry algorithm was applied to determine the most symmetric orientation about the sagittal plane, with yaw ranging from  $-20^\circ$  to  $20^\circ$  with  $5^\circ$  increments, and roll ranging from  $-30^\circ$  to  $30^\circ$  with  $5^\circ$  increments, resulting in a total of 117 combinations of orientations.

The orientation with the most symmetric 2D map was selected and the resulting yaw and roll transform was extracted. Processing times were less than 1s because 2D volumes were being used.

### 6.3.5. Slope Pre-registration

With both the CT and the 3DUS oriented in a roughly symmetric position, the final orientation that needed to be aligned was the pitch. The slope of the spinous processes and laminae would provide slope alignment information for this stage. First, the centroids of the two 1:8 scaled and symmetric surface volumes were calculated, and the CT surface was translated by the difference between the two centroid positions. Second, the pitch of the CT surface was iterated through a range and the amount of overlap between the CT surface and the 3DUS surface was calculated with mean-squared error, much like the symmetry algorithms from before.

While the centroids worked well to align the surfaces in the X and Z direction, the Y direction was often misaligned so that rotating the pitch failed to result in any overlap. Therefore, in addition to iterating through pitch rotations, translations in the Y direction were also applied to increase overlap. Again, a two-stage method of iterations were applied to increase the speed of registrations. First, the surface was rotated in pitch from  $\pm 40^\circ$  in  $5^\circ$  increments were applied. These were combined with translations in the Y direction at 1.6 mm increments over a range of 16mm to ensure overlap between the CT and 3DUS surface, resulting in 357 combinations (17 rotations x 21 translations). Second, pitches from  $\pm 10^\circ$  in  $2^\circ$  increments were applied, combined with the same translational range and increment in the Y, resulting in 231 combinations (11 rotations x 21 translations) The resulting pitch transformation from the slope algorithm would be used for the final pre-registration.

A summary of the ranges and increments of the pre-registration iterative algorithms are shown in Table 6.4. Angles are for both yaw and roll rotations.

**Table 6-3: Pre-registration algorithm summary**

<b>Algorithm</b>	<b>Range</b>	<b>Increment</b>	<b>Evaluation Metric</b>
CT Symmetry: 1:16	$\pm 70^\circ$	$10^\circ$	3D Symmetry Mean-Squared Error
CT Symmetry: 1:8	$\pm 20^\circ$	$4^\circ$	3D Symmetry Mean-Squared Error
3DUS Plane Alignment 1:16	$\pm 70^\circ$	$5^\circ$	2D Number of Pixels
3DUS Symmetry 1:8	$\pm 30^\circ$	$5^\circ$	2D Symmetry Mean-Squared Error
Wide Range Slope 1:8	$\pm 40^\circ$	$5^\circ$	Slope Overlap Mean-Squared Error
Narrow Range Slope 1:8	$\pm 10^\circ$	$2^\circ$	Slope Overlap Mean-Squared Error



### 6.3.6. Centroid Pre-registration

After the three orientation transformations were applied, the centroids of the 3DUS and CT surfaces were calculated using Equation 6-2. The CT centroid was then translated by the difference between the 3DUS and the CT centroid. The translational transform was used for the pre-registration transformation process.

### 6.3.7. Ultrasound Scanning Variability

An important factor that needed to be considered throughout the process was the variability in ultrasound scans. Because the ultrasound is free-hand, every scan is slightly different, resulting in different surface images that needed to be registered each time. Common scanning defects were noted:

1. Scanning areas that were not relevant to the vertebrae would result in the 3DUS symmetry algorithm to function less effectively, as it depended on cropping out the outer  $\frac{1}{4}$  of the image. A non-centered scan could result in extraneous surfaces to be included in the cropped image.
2. The transverse processes were sometimes not completely visualized. The unique shape and structure of the transverse processes facilitated pre-registration greatly.
3. The reflectivity was not always consistent, due either to mis-orientation of the transducer, or keeping the transducer too close or too far from vertebrae during scans.

A standardized method of scanning was developed to remedy these issues. The vertebra was scanned longitudinally along the right side of the vertebrae including the spinous process while tilting slightly medially along the laminae, and then tilting slightly laterally when reaching the transverse processes. The transducer then crossed the midline and returned from the transverse process to the laminae and then spinous process along the left side, while tilting progressively more medially. A scan speed of 4-6mm/s was kept ensuring the volume was captured fully. The transducer was kept 1-1.5cm above the vertebrae in the water. The scan process and sample 3DUS scan are shown in Figure 6-6: Scan direction and quality, (a) Vertebrae scanning direction moving cephalad then caudal; (b-c) sample raw ultrasound images, with transducer at the top of the image: (I) laminae, (II) spinous processes, (III) left transverse process and (IV) superior articular processes.

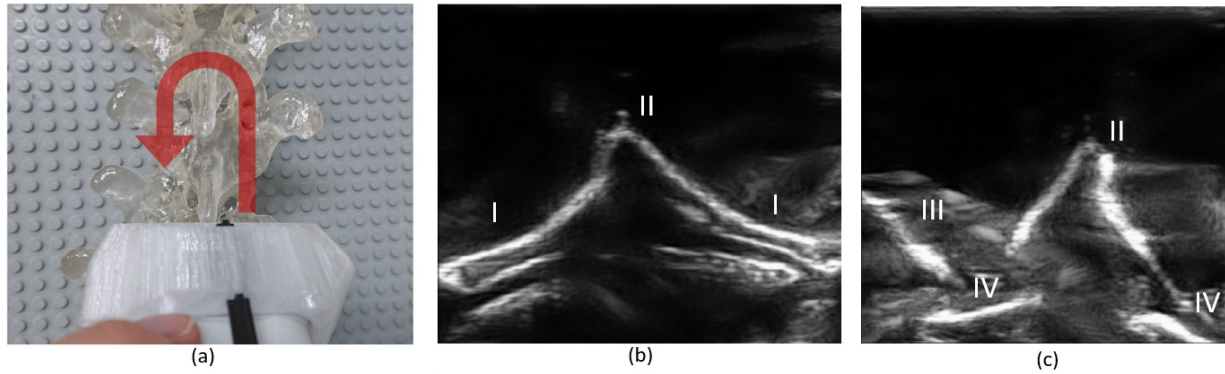


**Figure 6-6: Scan direction and quality, (a) Vertebrae scanning direction moving cephalad then caudal; (b-c) sample raw ultrasound images, with transducer at the top of the image: (I) laminae, (II) spinous processes, (III) left transverse process and (IV) superior articular processes**

## 6.4. Registration Development

### 6.4.1. Conventional Registration Process

Following pre-registration to orient and position the vertebra in approximately the correct position, the CT and 3DUS volumes would be inputted into the full registration algorithm. A conventional volumetric intensity-based registration was developed, which iterated through different transformations to determine which registration has the best overlap. The six-degrees-of-freedom (6DOF) include three in translation (along X, Y and Z axes) and rotation (about X, Y and Z axes, or pitch, yaw and roll respectively).

As part of the registration algorithm, a sequential scaling method was used to speed up registrations. The volumes were first scaled down 1:16 to perform initial 6DOF transformations through a pre-specified range and increment (Table 6-4: List of transformation sequences). The 1:8, 1:4 and 1:2 scaled versions of the original were used in subsequent transformation iterations using three-degree-of-freedom translations (3DOF,T), followed by rotations (3DOF,R) at each stage. The translations were separated from rotations to reduce the number of combinations. Translations were completed first as they had a larger impact on overlap. Source code can be found in Appendix 6: Image Registration Code.

**Table 6-4: List of transformation sequences**

Transform	Scale	Range	Increment
6 DOF	1:16 (3.2mm/pixel)	$\pm 9.6\text{mm}, \pm 20^\circ$	3.2mm, $5^\circ$
3DOF,T+3DOF,R	1:8 (1.6mm/pixel)	$\pm 6.4\text{mm}, \pm 5^\circ$	1.6mm, $1^\circ$
3DOF,T+3DOF,R	1:4 (0.8mm/pixel)	$\pm 1.6\text{mm}, \pm 2^\circ$	0.8mm, $1^\circ$
3DOF,T+3DOF,R	1:2 (0.4mm/pixel)	$\pm 0.4\text{mm}, \pm 1^\circ$	0.4mm, $1^\circ$
3DOF,T+3DOF,R	1:1 (0.2mm/pixel)	$\pm 0.2\text{mm}, \pm 1^\circ$	0.2mm, $1^\circ$

The ranges of translations and rotations were dynamic, with each subsequent stage's range being based on the best five registrations from the previous stage, plus the additional range shown in Table 6-4: List of transformation sequences. The increments of transformations were kept constant through each individual stage.

Three sets of experiments were performed to evaluate this image registration algorithm: i) a single-vertebra image registration experiment, ii) a multi-vertebrae image registration experiment, and iii) a multi-vertebrae image and surgical registration experiment. The image registration experiments would evaluate the accuracy of CT-to-3DUS matching while the surgical registration experiment would evaluate the accuracy of localization of the CT scan compared to the real-world. In each experiment, a phantom vertebra would be scanned and registered to its respective CT vertebral model.

To evaluate image registration accuracy, the final position and orientation of the registered CT surface was further transformed manually to determine if a superior registration could be achieved with additional transformations by both visual inspection and the mean-squared error of the registrations. Rigid transformations were performed in increments 0.2mm and 1°. When a superior registration was found, the translation and rotation required to achieve that superior registration was used to calculate the RMS error of registration in Equation 6-3:

***Equation 6-3: RMS error for position and orientation***

$$RMS\ Error = \sqrt{e_x^2 + e_y^2 + e_z^2}$$

where:

$e_x$ ,  $e_y$  and  $e_z$  were either the positional (mm) or rotational (degrees) error values in their respective directions from the superior manual registration.

#### 6.4.2. Single Vertebra Registration Evaluation

The first evaluation experiment involved using ultrasound to scan the single T6 vertebra in its neutral orientation to generate a 3DUS volume image. Figure 6-7 shows the single T6 phantom used for ultrasound scans. The 14 CT orientations from Table 6-1 were each registered to 14 different 3DUS scans of arbitrary orientation (less than 30° in two directions) with the vertebra placed at the capture volume origin, resulting in a total of 196 registrations.



**Figure 6-7: 3D-printed T6 phantom for ultrasound scans**

Out of the 196 registrations, seven failed accuracy criteria, all having large angular errors (5.8-38.7°). Figure 6-8 and Figure 6-9 display histograms of the translational and rotational errors. Most RMS errors were within the technical accuracy criteria of 1mm (182/196, 93.8%) and 5° (190/196, 96.9%).

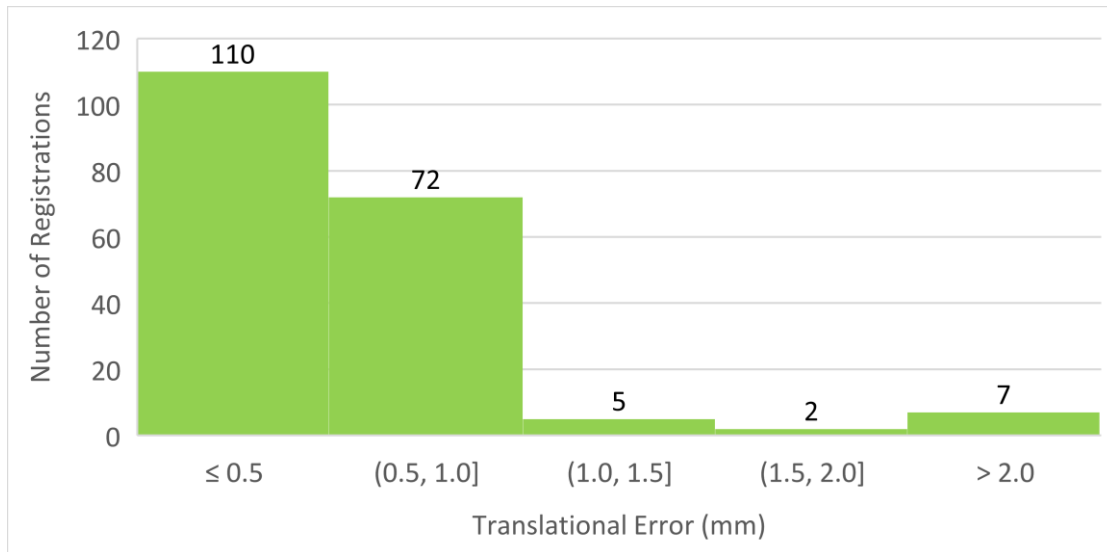


**Figure 6-8: Histogram of single-vertebrae registration translational accuracy. Target: <1.0mm. Square bracket denotes the bin is inclusive of the value.**

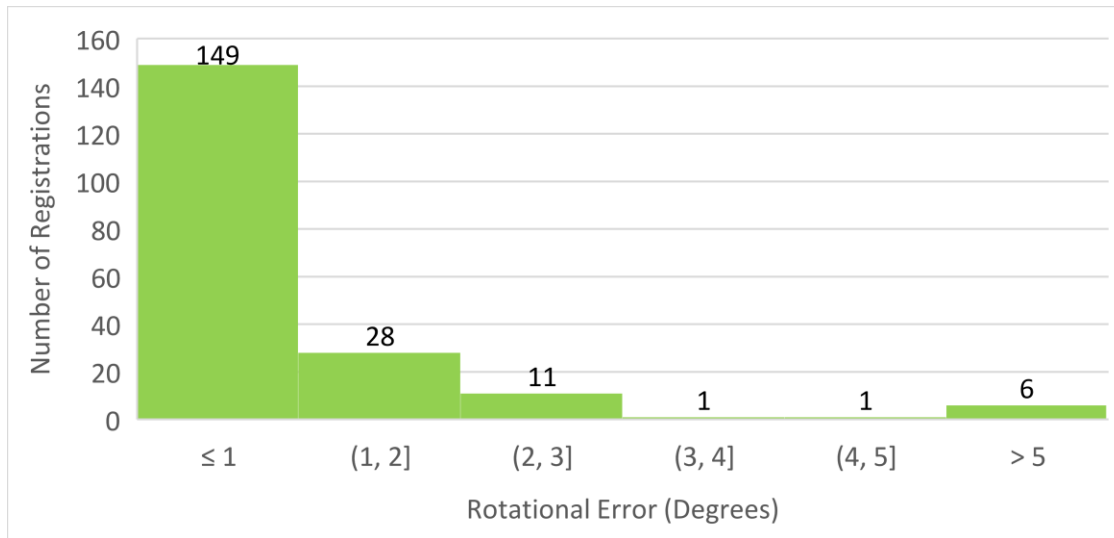


**Figure 6-9: Histogram of single-vertebrae registration rotational accuracy. Target: <math><5.0^\circ</math>. Square bracket denotes the bin is inclusive of the value.**

The average accuracy from the successful registrations with 95% confidence interval for positions was  $0.0 \pm 0.5\text{mm}$ ,  $0.0 \pm 0.7\text{mm}$  and  $0.0 \pm 0.8\text{mm}$  in the X, Y, and Z directions, respectively (Figure 6-10). Unsuccessful registrations were excluded since they were easily identifiable visually with the spinous processes being completely misaligned between the CT and 3DUS scan. Rotationally, average accuracies from the successful registrations were  $0.2 \pm 1.5^\circ$ ,  $0.0 \pm 1.0^\circ$  and  $0.1 \pm 0.7^\circ$  about the X, Y and Z axes. The combined RMS error was  $0.5 \pm 0.6\text{mm}$  for translation, and  $0.6 \pm 1.5^\circ$  for rotation. Average registration time was  $20.8 \pm 3.6\text{s}$ .

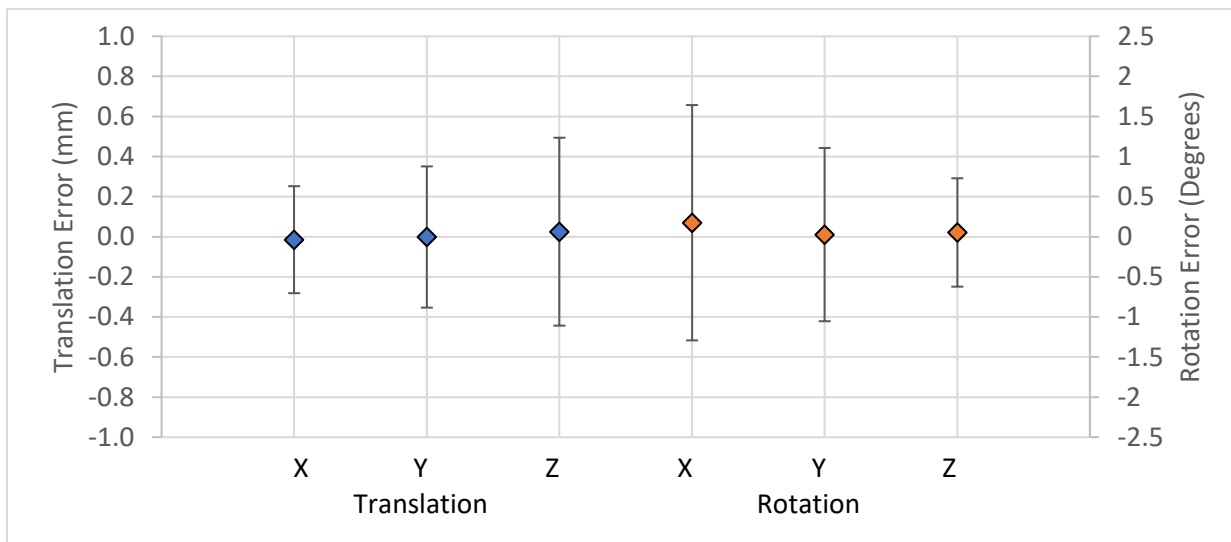


**Figure 6-10: Average positional and rotational error in each direction from successful registrations including 95% confidence interval**

Although there was a 92.8% success rate for these registrations, the failures were large, at  $4.6 \pm 7.6\text{mm}$  and  $11.9 \pm 24.1^\circ$ . Failures were apparent already at the pre-registration preview stage, with the orientations being more than  $10^\circ$  different from the optimal orientations. The poor registrations were largely from poor or strongly angled ultrasound scans.

Some changes were made before moving onto multi-vertebra testing. The center of the laminae was cropped by removing the outer 30% during the slope-matching pre-registration phase to further reduce the effects of extraneous artifacts on slope registration between CT and ultrasound scans. Second, the lower threshold for binarization in the 3D ultrasound was reduced from 50% to 45% to increase the number of surface pixels available for registration.

#### 6.4.3. Multi-Vertebra Phantom Registration Evaluation

The second experiment was a multi-vertebrae model experiment to determine the effects of neighboring vertebrae above and below the vertebra being registered. A new model was mounted to the LEGO pegboard shown in Figure 6-11.



**Figure 6-11: Multi-vertebra phantom with LEGO mount.**

The vertebra was oriented in nine different orientations: neutral, yaw-left, yaw-right, pitch-up, pitch-down, roll-left, roll-right all at  $15^\circ$  and two combination orientations randomly selected, covering either roll and pitch, roll and yaw or yaw and pitch. The orientations were achieved by mounting the vertebra onto tilters shown in Figure 6-12. Each of the T5 to T8 vertebrae were scanned three times in each orientation for a total of 108 registrations (4 vertebrae x 3 scans x 9 orientation).

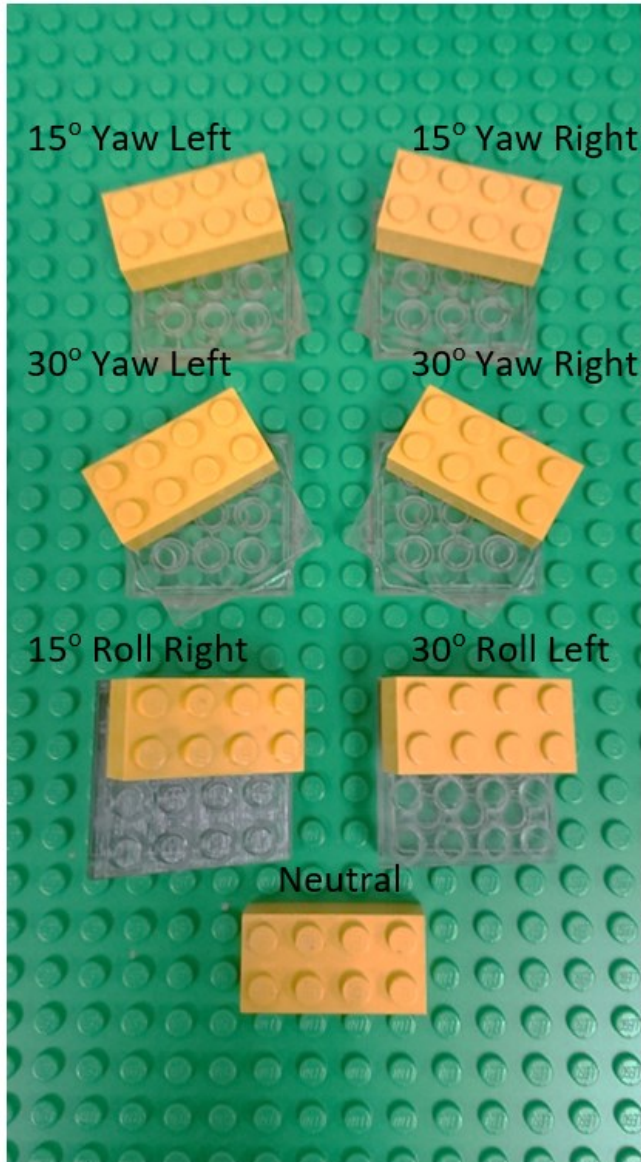


**Figure 6-12: Tilting mounts. Four yaw mounts were included (15° and 30° yaw to the left and right), and two roll and pitch mounts (15° and 30° which could be rotated 90° to allow for roll in either direction and pitch in either direction)**

From 108 registrations on the T5-T8 vertebrae, the average RMS error was  $0.3 \pm 0.2$  mm and  $1.2 \pm 1.2^\circ$ , with only two registrations failing the 1 mm and  $5^\circ$  criteria (98.2% success rate). A histogram of the accuracies of each registration is shown in Figure 6-13 and Figure 6-14. The two failures were from rotations being larger than  $5^\circ$ , one at  $5.0^\circ$  and the other at  $5.1^\circ$ . All translations were within 1 mm.

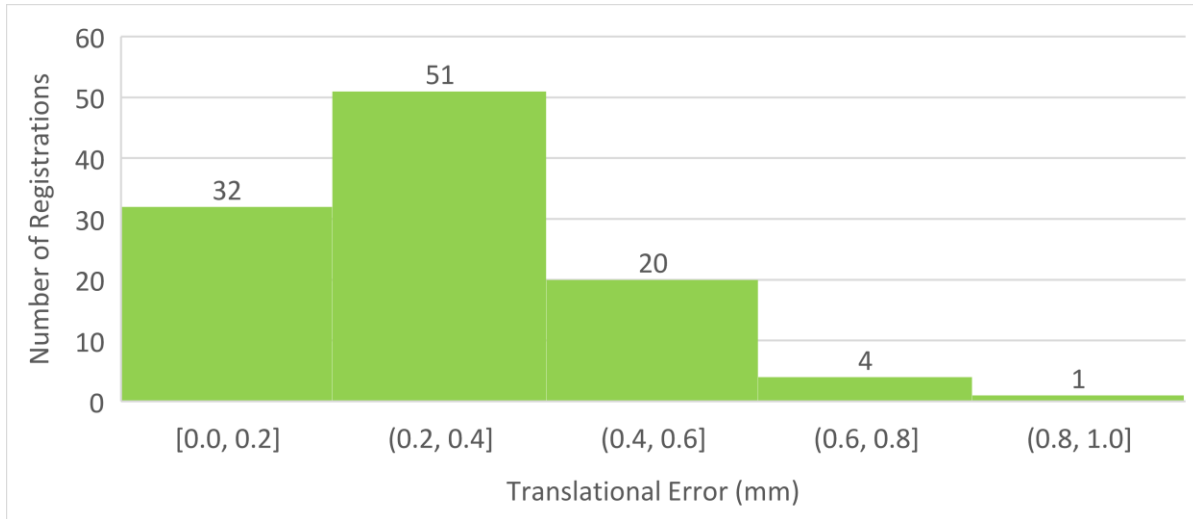


**Figure 6-13: Histogram of the translational registration accuracy from the multi-vertebrae model. Target: <1.0mm. Square bracket denotes the bin is inclusive of that value.**

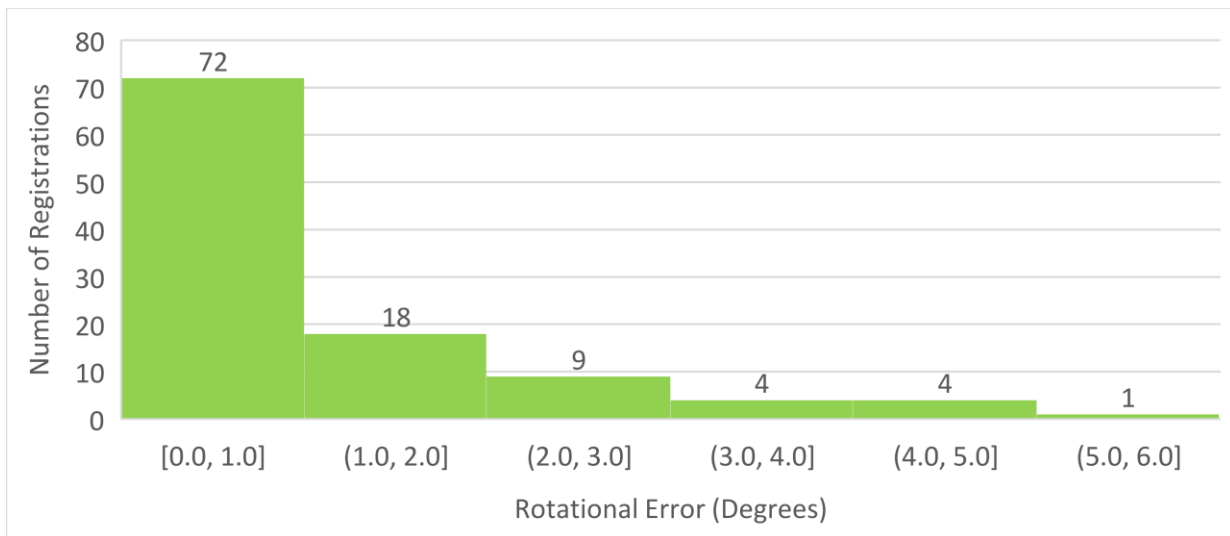


**Figure 6-14: Histogram of the rotational registration accuracy from the multi-vertebrae model. Target: <5.0°. Square bracket denotes that the bin is inclusive of that value.**

The average accuracy of registrations including a 95% confidence interval are shown in Figure 6-15. The average registration time was  $24.6 \pm 4.1$ s.



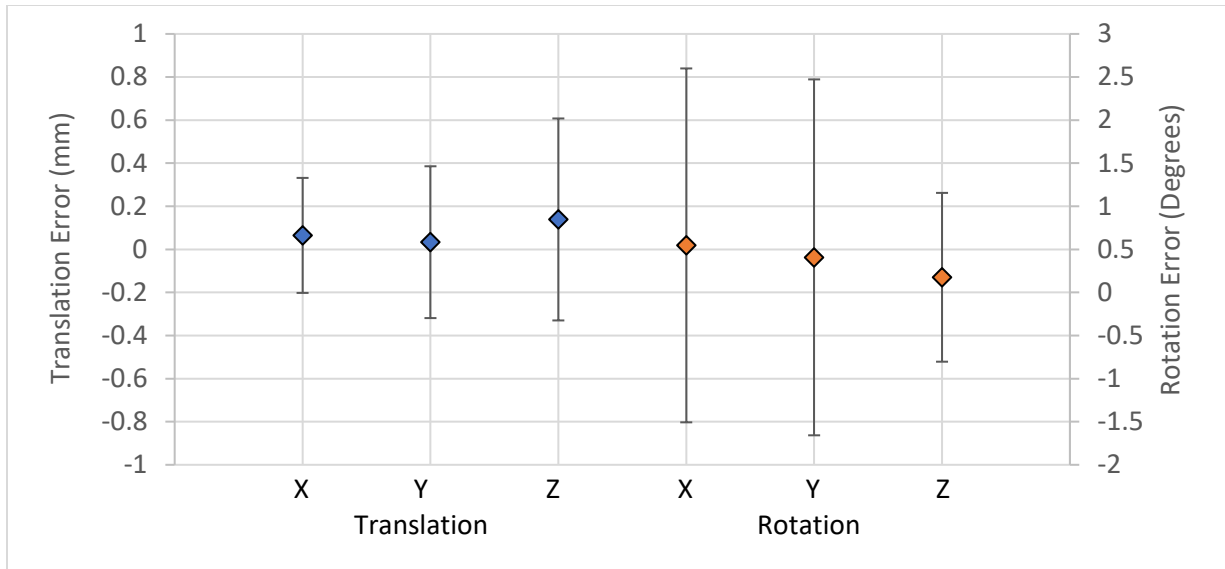


**Figure 6-15: Average positional and rotational error in each direction from multi-vertebrae registrations including 95% confidence interval**

Registrations from the multi-vertebrae model met the criteria in all but two registrations (98.1% success rate), with an accuracy that was comparable to the single-vertebrae ( $0.3 \pm 0.2 \text{mm}$  and  $1.2 \pm 1.2^\circ$ ) and a registration time that was also comparable at 24.6s vs 20.8s. The failures resulted from poor 3DUS scan quality, with transverse process or laminae missing large regions after image processing. Again, it was evident at the pre-registration phase that orientations were not properly aligned. Image quality was an issue that would need further testing. Real bone would likely have better reflectivity than the phantoms.

While positional accuracy remained mostly constant, rotation worsened from  $0.7\text{-}1.7^\circ$  to  $1.2\text{-}2.1^\circ$ . The worsened rotational accuracy was likely due to the presence of vertebrae above and below the vertebra, resulting in extra regions that may bias the registration away from the ground truth. The Z translation and the X and Y rotations (pitch and yaw) tended to be the poorest performing dimensions, likely because the camera positions were all on one side of the capture volume to save space in the operating room.

The 3D ultrasound contrast filter was altered to increase the number of pixels that would be retained (reduced lower bound from 45% to 40%) maximize the surface that would be present in the final image. Refinement to scanning technique was also made to keep the transducer surface orthogonal to phantom surfaces. At this stage, parallel processing was added using Matlab's Parallel Computing Toolbox to speed up the process of registration allowing registration iterations to be run simultaneously.

#### 6.4.4. Surgical Registration Evaluation

The final experiment using the conventional registration process involved testing both the image registration accuracy (error between the CT surface and the 3DUS surface) and the surgical registration accuracy (error between the CT model from the image registration and the actual position of the phantom).

For this set of experiments, the multi-vertebrae phantom was mounted to tilters (Figure 6-12) in seven orientations: neutral, yaw-left, yaw-right, pitch-up, pitch-down, roll-left and roll-right. Each orientation included 15° and 30° magnitudes for 13 potential orientations. The tilters and phantom were shown previously in Figure 6-11 and Figure 6-12. Each of the T5-T8 vertebrae were individually scanned three times for the neutral orientation to a total of 12 scans. Two of the four vertebrae were then scanned three times for each of the 12 tilted orientations to a total of 72 scans at non-neutral orientations. The two vertebrae that were scanned was randomized while ensuring each vertebra was scanned the same number of times.

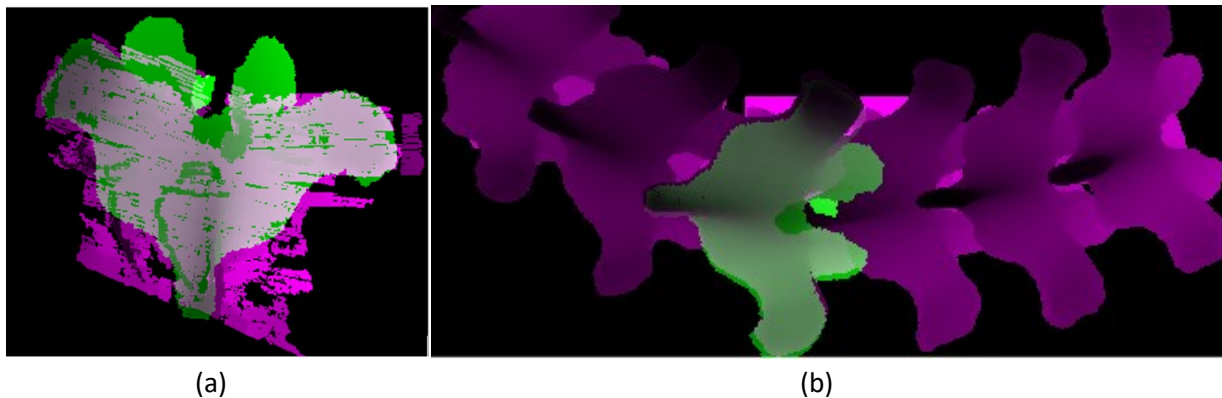


**Figure 6-16: Image and surgical registrations, (a) Sample image registration, CT in green and 3DUS in pink with overlapped regions in light pink (b) Sample surgical registration with registered phantom (green) overlaid on theoretical position of spinal segment (pink). Registered region is where green and pink overlap (light pink)**

In this experiment both the image registration (Figure 6-16a) and the surgical registration (Figure 6-16b) were evaluated. Image registration compared the registered CT surface to the 3DUS scan to determine where the optimal registration would be placed, while surgical registration involved comparing the true position of the vertebrae with the registered position of the CT vertebra. To perform surgical registration, the phantom model was converted to a 3D volume image file with known coordinates for each pixel (pink phantom in Figure 6-16b). The phantom was then transformed according to the dimensions and orientation of the tilting mounts to provide the true position of the vertebrae.

For the final experiment, intra-rater reliability evaluation was performed on the image mean-squared error by the same evaluator two weeks apart and intraclass correlation coefficient (ICC(3,1), two-way mixed, absolute agreement) was calculated to ensure manual evaluation was repeatable.

The results of the 84 registrations resulted in a 96.4% success rate and one failure. Figure 6-17 and Figure 6-18 show the histogram of accuracy for image registration, not including the obvious failure but including two registrations that exceeded the 1mm target (Figure 6-20). The image registration accuracy was  $0.3\pm 0.2\text{mm}$  and  $0.9\pm 0.8^\circ$ . The average accuracies and standard deviations are shown in Figure 6-19. The lone failure had a clear misalignment between spinous processes. The results from the first measurements are reported here. The intraclass correlation coefficient (ICC (3,1)) was 0.76 for the registration mean-squared error indicating good reliability in these manual accuracy evaluations.

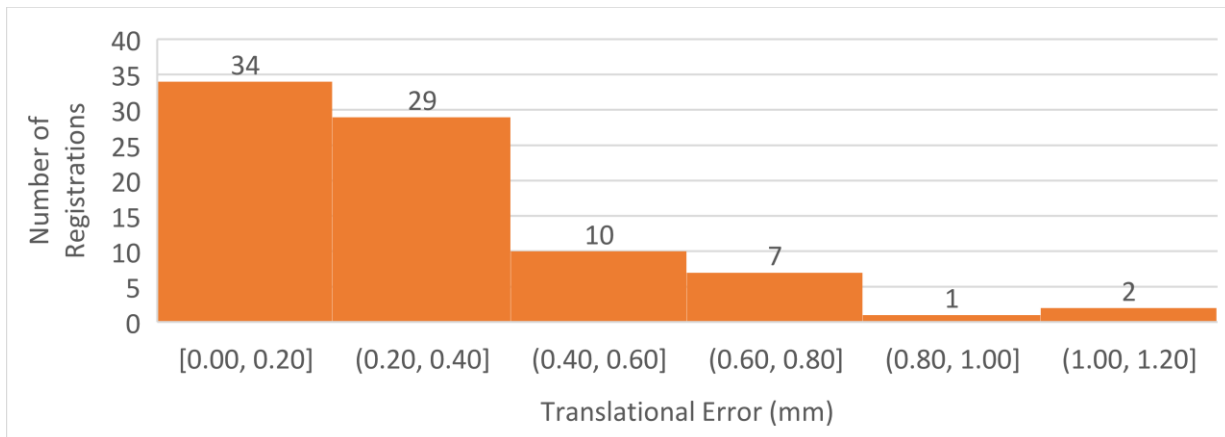


**Figure 6-17: Histogram of image registration translation accuracy from multi-vertebrae model in surgical simulation experiment. Target <1.0mm. Square bracket denotes bin is inclusive of that value.**

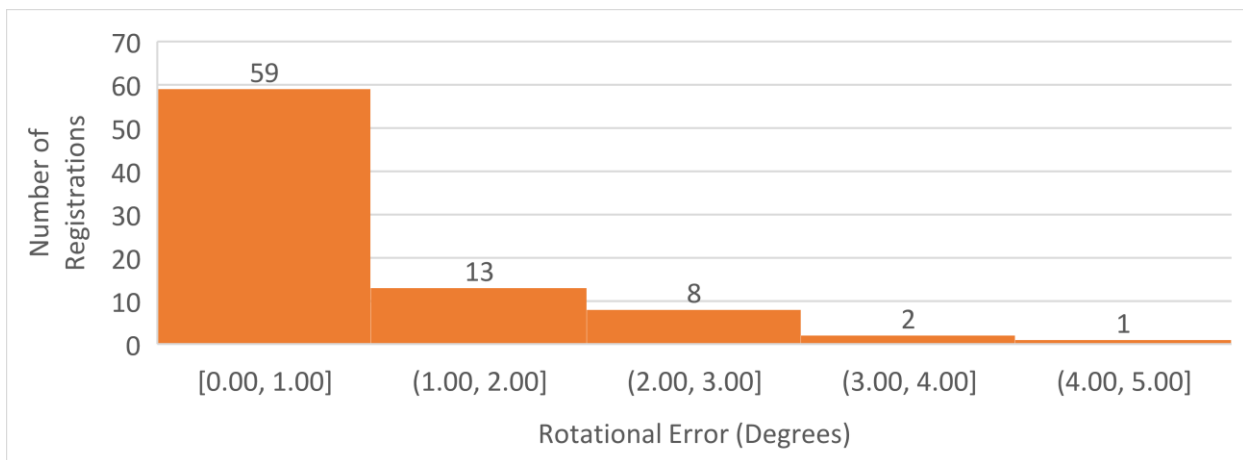


**Figure 6-18: Histogram of image registration rotational accuracy from multi-vertebrae model in surgical simulation experiment. Target: <5.0°. Square bracket denotes bin is inclusive of that value.**

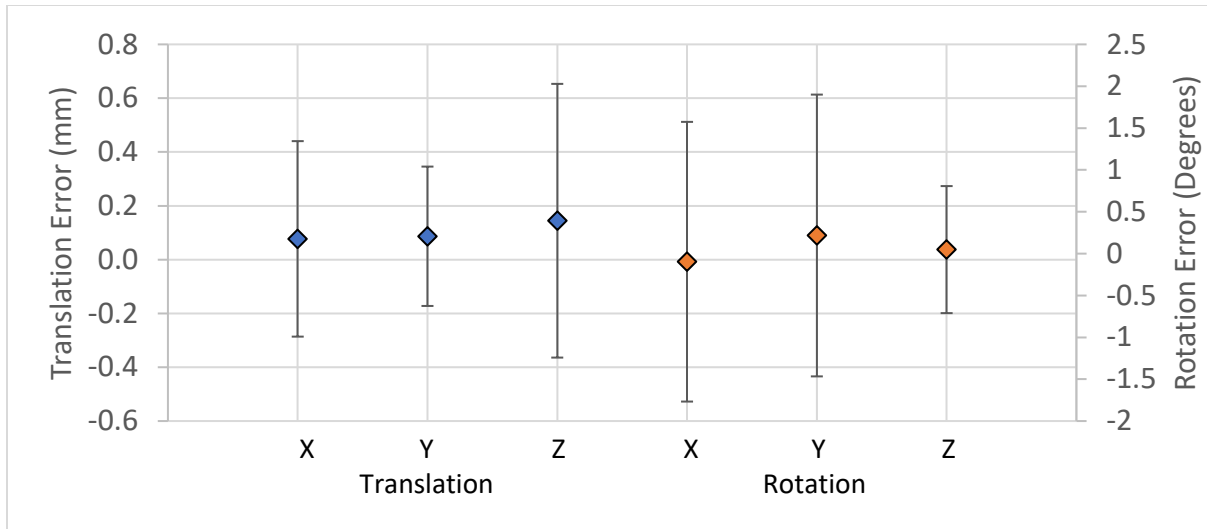


**Figure 6-19: Average positional and rotational error in each direction from image registrations including 95% confidence interval**

Previous experiments illustrated that poor scan quality and off-center scans (2-3cm) resulted in a poorer registration. Average accuracies were in line with the multi-vertebra experiment at  $0.3 \pm 0.2 \text{mm}$  and  $0.9 \pm 0.8^\circ$ . The average registration time was  $13.3 \pm 2.3 \text{s}$  and total processing time was  $16.2 \pm 3.0 \text{s}$  for the surgical registrations. Registration time was improved with parallel processing. Most registrations had excellent errors, meeting the 1mm and  $5^\circ$  targets.

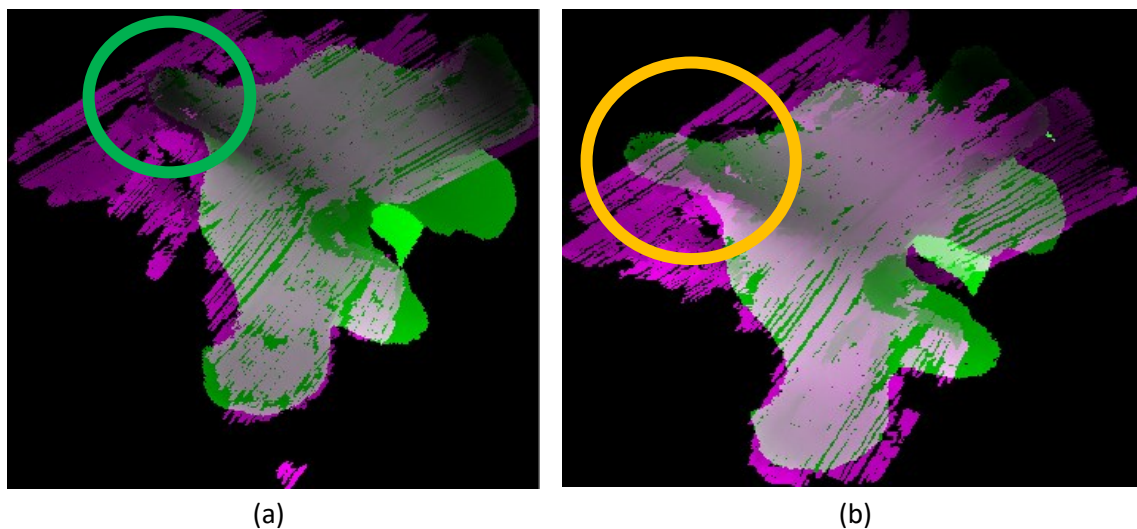


**Figure 6-20: Example of image registration (a) successful registration and (b) lone failure showing misalignment between ultrasound and CT image at the spinous process**

The surgical registration accuracy testing was performed on the same 84 registrations as above. Figure 6-21 and Figure 6-22 show histograms of the translational and rotational accuracies of the surgical registration. The success rate was only 32.1% (27/84) meeting the 1mm technical criteria and 89.3%

(75/84 registrations) meeting the clinical <2mm criteria. One failed the 5° rotational criteria. The ICC(3,1) was 0.631 for surgical registration mean-squared errors, indicating moderate reliability in these manual evaluations.

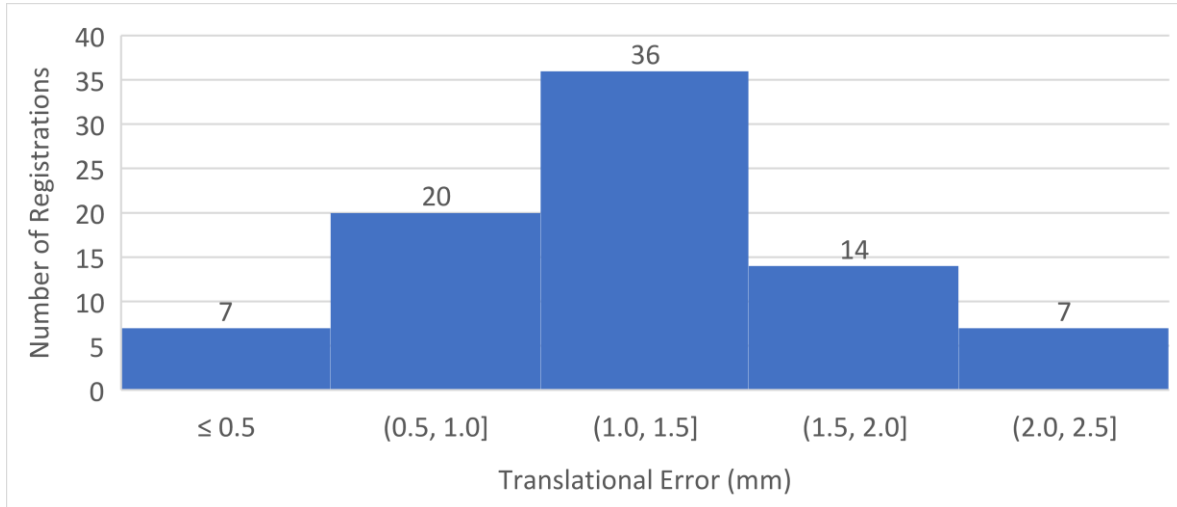


**Figure 6-21: Histogram of surgical registration translational accuracy from multi-vertebrae model. Target accuracy <1.0mm. Square bracket denotes that the bin is inclusive of that value.**

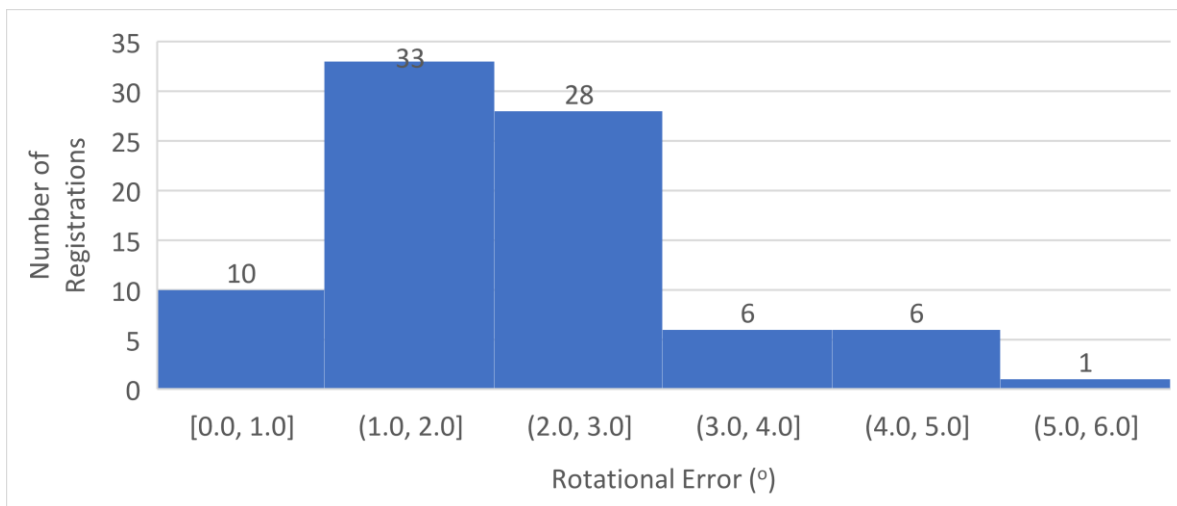


**Figure 6-22: Histogram of surgical registration rotational accuracy from multi-vertebrae model. Target accuracy <5.0°. Square bracket denotes that the bin is inclusive of that value.**

The overall average surgical registration accuracy was 1.2±0.5mm and 2.2±2.0°. The translational and rotational component accuracies are displayed in Figure 6-23.

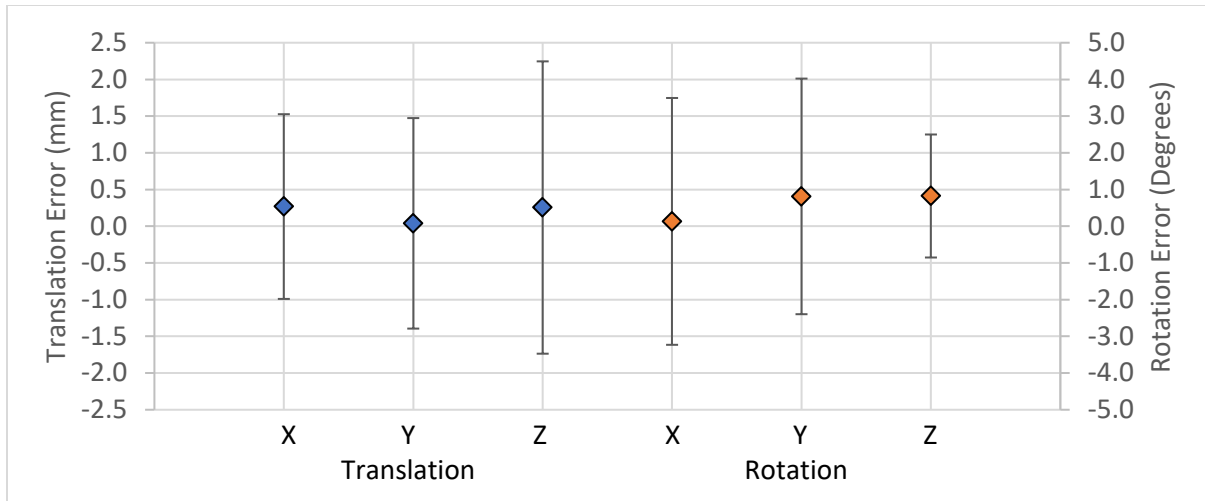


**Figure 6-23: Average positional and rotational error in each direction from surgical registrations including 95% confidence interval**

For the surgical registrations, the success rate was 32.11% for the 1mm criteria and 89.3% for the 2mm criteria with translational accuracy worsening by 4 times ( $1.2 \pm 0.5\text{mm}$ ) and rotational worsening by two times ( $2.2 \pm 2.0^\circ$ ). Positional accuracies were worst on in the Z-direction while rotational accuracies were worst about X and Y axes which corresponded to previous experiments.

The excellent image registration accuracy compared with the poorer surgical registration accuracies show that the 3DUS and motion capture system are the main sources of error in surgical registration.

#### 6.4.5. Iterative Closest Point Evaluation

The second registration method that was tested was the iterative closest point (ICP) surface registration algorithm. As stated previously, rather than performing a volumetric intensity-based image registration, this algorithm uses point-matching between two point-clouds that represent surfaces in order to perform registrations. The main requirement of this method is that the point clouds need to be somewhat aligned prior to registration for the registration to be successful. Because the pre-registration process aligns the 3DUS and CT surfaces in proximity and orientation, the ICP registration was a natural fit for this process. Source code can be found in Appendix 6: Image Registration Code.

Two data processing settings were evaluated prior to performing registrations: data down-sampling and inlier ratio. As mentioned in Section 2.3.10, the grid averaging method of down-sampling involves dividing the volume into boxes of a pre-specified grid size, then averaging the pixel positions and normal vectors of those surfaces. The appropriate degree of down-sampling needed to be determined. Secondly, the

inlier ratio, which determines the proportion of data that would be considered an outlier, needed to be determined. Both would affect the accuracy and the speed of registrations.

To evaluate the effectiveness of each set of grid size and inlier ratio, the pre-registrations from the surgical registration evaluation experiment were extracted and inputted into the ICP registration algorithm using different sets of grid sizes and inlier ratios. Grid sizes (number of pixels within the 3D box) ranged from 2 to 15 in increments of one, while inlier ratio ranged from 20% to 80% with increments of 20%.

Accuracy was determined by comparing the mean-squared-error of the resulting registration with the manual registration mean-squared errors from the previous experiment. Table 6-5 shows the processing speeds from varying down-sampling and inlier ratios on a T6 vertebral registration at neutral position while Table 6-6 shows the effects on mean-squared error as a sample.

**Table 6-5: Processing time (s) for completing registration when varying inlier ratio and down-sampling grid size on T6 vertebra**

Down-Sampling Grid Size (pixels)	Inlier Ratio						
	20%	30%	40%	50%	60%	70%	80%
2	2.56	5.35	3.96	5.35	4.79	4.92	4.25
4	1.24	0.79	0.72	0.63	0.86	0.61	0.69
6	0.44	0.29	0.31	0.49	0.36	0.50	0.30
8	0.16	0.28	0.35	0.19	0.13	0.12	0.35
10	0.13	0.11	0.15	0.07	0.08	0.05	0.06
12	0.06	0.05	0.06	0.05	0.03	0.03	0.04
14	0.03	0.06	0.15	0.03	0.03	0.03	0.03

**Table 6-6: Mean-squared error for varying inlier ratio and down-sampling grid size on T6 vertebra (lowest five errors in bold)**

Down-Sampling Grid Size (pixels)	Inlier Ratio						
	20%	30%	40%	50%	60%	70%	80%
2	4.634	3.577	3.265	3.141	2.905	2.714	2.684
4	3.569	3.091	3.072	3.027	2.788	2.749	2.711
6	3.386	3.331	3.218	2.738	2.723	2.682	2.745
8	3.566	2.885	2.856	2.786	2.762	2.720	2.707
10	3.761	3.544	2.800	2.719	2.712	2.693	2.743
12	4.054	3.320	2.763	2.747	2.735	2.708	2.698
14	2.843	2.699	2.709	2.752	2.751	2.791	2.858

The slowest processing times were from low down-sampling (2-4 grid size). The combination of low inlier ratio and low down-sampling grid size resulted in poorer mean-squared errors. However, having a low

down-sampling (2-4 grid size) did not yield results that were significantly better than the faster results from higher down-sampling (6-14 grid size). All the results from grid sizes of >4 were faster than 0.5s.

When repeating this process on the 84 different registrations, there was no clear inlier ratio or grid size that outperformed the others when testing on the full set of registrations. Therefore, instead of selecting the best combination to perform registrations, multiple combinations of both would be applied at the same time for each registration and the best registration would be selected from those. The slowest down-sampling grid size and the lower inlier ratios which yielded poorer accuracy results (<0.4) were not included to as they did not yield better results.

The optimal range that balanced accuracy and speed needed to be determined to allow multiple grid sampling levels and inlier ratios to be processed at the same time. A full range from 3 to 15 grid size and 0.5 to 0.8 inlier ratio was tested first, resulting in an average registration time of  $23.0 \pm 6.5s$ . This was deemed too long for surgical usage. Reducing the grid size range to 5-9 and inlier ratio to 0.6-0.8 resulted in average registration times of  $5.7 \pm 1.5s$  which would be useable in the operating room. Figure 6-24 shows the error differences between these two sets of ranges.

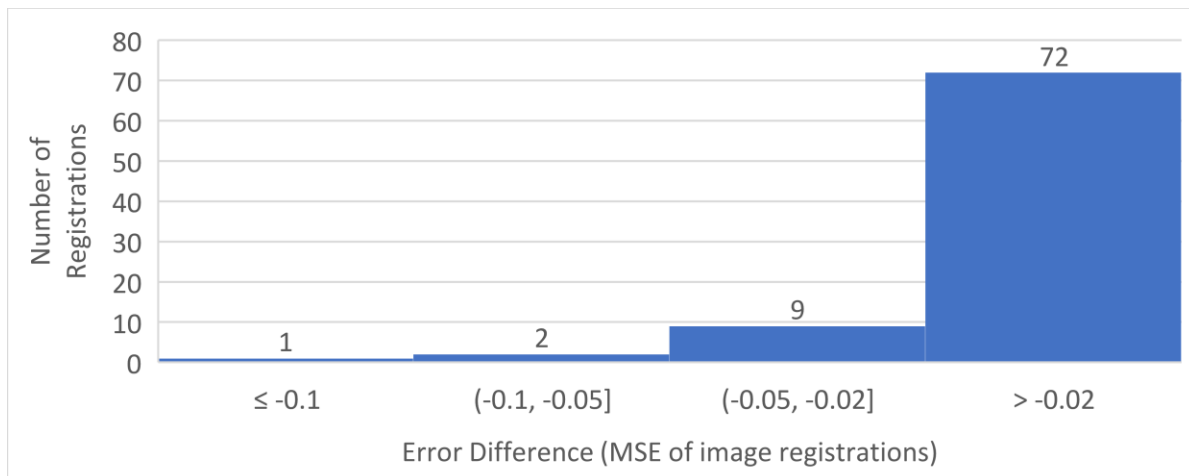


**Figure 6-24: Histogram of the difference in MSE of pixel intensities between full-range and reduced-range ICP registrations. Error of zero indicates the same grid sampling and inlier ratio was selected for both full and reduced range registrations. Square brackets denote value is inclusive to that bin**

Of the 84 registrations completed, 48.8% of the reduced-range set of registrations were the optimal registrations in the full-range set as well, having the same errors. An additional 30.9% had MSE of more than 0.02 in pixel intensity than the optimal registrations in the full-range set. Only 4 registration had errors that were more than 0.05 units larger than the full-range set. By comparison, a 1-degree rotation or translation from the manual registration would result in a 0.05 error unit change for the smallest error



changes. These errors were considered small enough and the speed gain was large enough to use the reduced-range ICP registration algorithm.

Comparing the accuracy of this set of ICP registrations to the conventional registration process showed that the ICP registration outperformed the conventional registration in all but six registrations (92.8%) with an average improvement of 7.1%.

The results of the 84 registrations using the ICP algorithm are shown in Figure 6-25 with two failures not displayed. Both failures were visually detectable. The image registration accuracy was  $0.2 \pm 0.1\text{mm}$  and  $0.2 \pm 0.4^\circ$ . Translational accuracy was  $0.0 \pm 0.1\text{mm}$ ,  $0.0 \pm 0.1\text{mm}$  and  $0.1 \pm 0.1\text{mm}$  in the X, Y and Z directions respectively while the rotational accuracy was  $0.0 \pm 0.1^\circ$ ,  $0.0 \pm 0.0^\circ$  and  $0.1 \pm 0.1^\circ$  about the X, Y and Z axes respectively. The total processing time was  $9.9 \pm 1.8\text{s}$  for the iterative closest point registration method.

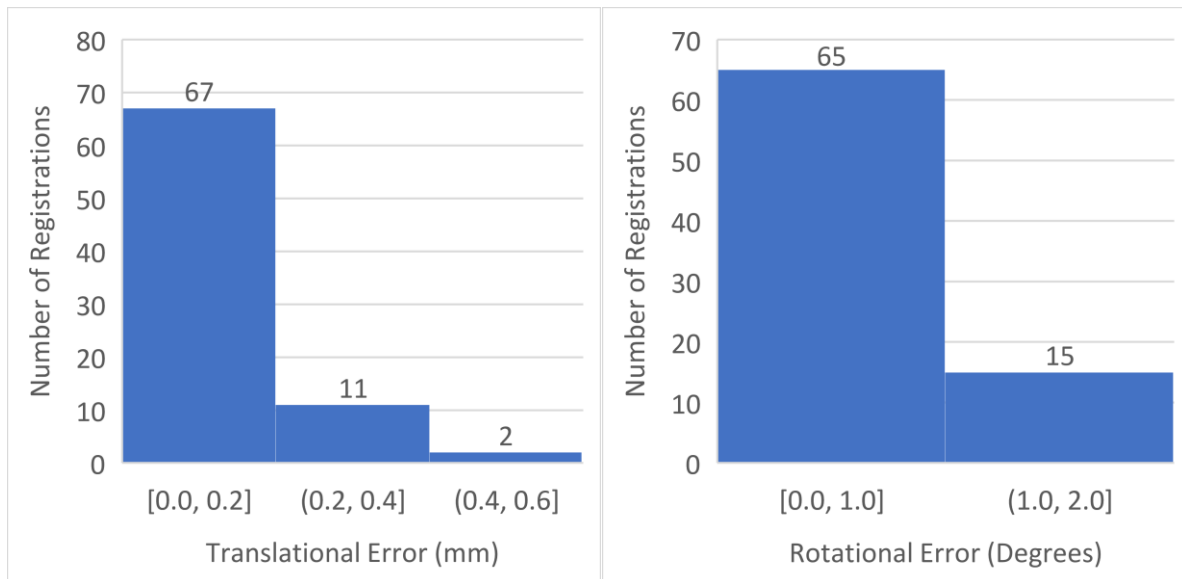


**Figure 6-25: Histogram of image registration translational and rotational accuracy from multi-vertebrae model in surgical simulation experiment using iterative closest point registration. Target <math><1.0\text{mm}</math>,**

The ICP registration algorithm was superior to the conventional registration algorithm both in time and in accuracy. A pilot test was conducted to determine if it could be used without any pre-registration. Testing the 12 neutral vertebral scans, only 8 of them resulted in a successful registration, requiring ICP registration times that ranged in the 9-11s range, rather than the more typical 2-4s range. It was decided that the incremental time cost of the pre-registration (typically 3-5s) was worth the higher robustness of the ICP registration on pre-oriented and pre-aligned vertebrae. The combination of pre-registration with ICP registration would be used in the final system.

## 6.5. Phantom Registration Discussion

### 6.5.1. Technical Evaluation of Registration Experiments

One of the main limitations of this study was that registration error evaluation was based on manually inputted transformations to determine the optimal position and orientation of the vertebra. While it would have been more ideal to use the original vertebral orientation rather than registered orientation to form the ground truth registration, the processing time for completing this manually or automatically was found to be unfeasible while not reliably providing a more accurate ground truth registration. The manual method was faster and more reliable than using an automated method because the combination of mean-squared error and visually inspected landmarks aided helped the evaluator to find a global minimum more readily. The 3DUS images were high enough quality that it was easy to identify transformations that would improve or worsen registrations. The intra-evaluator reliability was also calculated to show that the manual registrations were reproducible in judging the registration system.

Secondly, because phantom spines were used in this experiment, it was unknown how soft tissues would interact with the ultrasound reconstruction. A porcine spine feasibility study was undertaken in the next section to determine if registrations could be successful with soft tissue present. Another problem that would be explored was determining if the anatomy as segmented and extracted from a CT scan was similar to an ultrasound scan in displaying bony anatomy. The problem is further compounded with an MRI image, as the lower resolution and more challenging segmentation could result in reduced registration accuracies. On the surgical side, since the segmentation of the CT or MRI must include only bone, the bony surfaces of the spine would need to be cleanly exposed with soft tissues absent from the top surface to maximize registration. The study in Section 6.6 explored if soft tissues in between vertebrae resulted in poorer registration accuracies.

As for the experimental design itself, although the build plate was mounted rigidly to the base of the tank, there might have been slight deformation of the base due to the weight of the water pushing down on the base resulting in poorer Y-translation values. There also might have been errors in the mounting process. The tolerances on the 3D-printed parts were 0.1mm, resulting in fits that were not as tight as LEGO-on-LEGO connections. For the polyjet 3D printer used in this experiment, any regions with angled overhangs would require additional filler material to be added to act as a structural support for those overhangs. As a result, the surface finish of the pitch and roll angled tilter blocks was uneven, being glossy and smooth on the exposed side, and matte and indented on the overhanging side the required supports.

These parts needed to be sanded to smooth out these imperfections. These errors combined could result in an overall error of less than 0.5mm.

Chapter 4: outlined the evaluation of the motion tracking camera system, noting accuracies of 0.25mm for translations up to 15cm and  $3.8^\circ$  for rotations less than  $45^\circ$  in two directions (any combination of X, Y or Z). However, these were displacements, not actual positions within the capture volume. The positional accuracies of  $0.7\pm 0.5\text{mm}$  and orientation accuracies  $0.0\pm 1.7^\circ$  noted in Chapter 5: were comparable to the surgical registration accuracies of  $1.2\pm 0.5\text{mm}$  and  $2.2\pm 2.0^\circ$  found in this section. Notably, the repeatabilities were similar, though the accuracies, both in position and orientation worsened when adding registration to the evaluation.

The main source of error appeared to be the motion capture calibration of the 3D ultrasound system. From Figure 6-23, there was a 0.3mm systematic error in both X and Z positions, and a  $1^\circ$  systematic error in both Y and Z rotations. However, a pattern between certain positions or orientations with accuracy was not found. Additional evaluation into the relationship between orientation and position could clarify if there are systematic errors present.

#### 6.5.2. Clinical Comparison of Registration Experiments

When comparing with literature, the image registration accuracies were superior or comparable to previous registration studies. For bony registration, errors have ranged from 0.66 to 2.3mm, ranging from CT scanned femurs, CT registration of dry phantom spines, and MRI registration of dry bone [17,172,235]. However, when using porcine models, the registration accuracy was 1.65mm and 2.57mm, likely due to increased soft tissue on the surfaces [17,172]. These studies used target registration error that were based on fiducial marker errors to determine accuracy of the system.

This study uses actual transformations of the CT surface to determine errors and includes both rotation and translation to match surfaces as a more direct measure of error. The  $0.3\pm 0.2\text{mm}$  and  $1.3\pm 1.0^\circ$  accuracies outperform the target registration errors from other studies, though it would be assumed that some of the rotational errors were translated into positional errors in the other studies.

Surgical registration accuracy studies in the past have shown errors of 0.5-1.2mm on embalmed human spines using CT navigation [127]. Another cadaveric study on surgical registration of CT scans of the lumbar spine using fiducial markers found accuracies of 0.96mm and  $0.91^\circ$  [173]. These surgical registration values are based on CT scans in the operating room but are still comparable with this ultrasound-based navigation system.

## 6.6. Porcine Spine Pilot Feasibility Study

### 6.6.1. Experimental Setup

To determine if the registration algorithm functioned on real tissues, a pilot test using a porcine spine was undertaken. The evaluation had two goals: (a) to determine if there was an appreciable difference between soft tissue reflections and bone reflections; and (b) to determine if the registration algorithm was able to register the ultrasound to CT images.

A 40-50kg pig was obtained from the Surgical Medical Research Institute after ethical approval for usage of porcine tissues for ultrasound scans was obtained. The pig was dissected by removing the T10 to L2 vertebrae including a 6cm perimeter soft tissues remaining on the spine. These levels were selected as being the most similar to the human thoracic spine, having smaller spinous processes than higher levels, and having smaller transverse processes than the lumbar levels. The pig spine was then CT scanned in a 64 mA and 120kV CT scanner with the contrast set at the bone window level.

The CT scan was segmented using Seg3D2, and each vertebral level was separated from each other by simply cutting the volume to be inclusive of the entire vertebra, regardless of inclusion of adjacent vertebrae. This method of separating vertebrae was selected because the ultrasound scan also includes adjacent vertebrae in the scan, potentially aiding in the registration process.

The pig spine was then dissected in a similar fashion to a posterior spinal fusion, starting with a longitudinal incision down to the spinous process, then incision of the periosteum on the spinous processes and removal of the periosteum out to the transverse processes. Subperiosteal dissection was completed up to the facets and transverse processes until each individual vertebra was isolated and posterior surface was exposed. Figure 6-26 shows a picture of the exposed posterior surfaces of the pig spine, with this pig having 14 thoracic levels (T10-T14 shown here along with L1-L2)



**Figure 6-26: Exposed pig spine with T10 on the left and L2 on the right (five thoracic levels and two lumbar levels were exposed)**

The pig spine was placed in a water bath and each level from T10 to L2 (seven levels) was ultrasound scanned three times, according to the usual with a forward scan on the right side of the spine followed by a return scan along the left side of the spine. The pig spine was then registered using the ICP registration algorithm.

#### 6.6.2. Image Intensity Evaluation

The intensity of recorded ultrasound signal depends heavily on the reflectivity of the surface and the incident angle of the ultrasound. As a result, a quantitative comparison of the bone compared with the soft tissue was not undertaken because of the varied angles of the vertebral surface and the soft tissue regions. Instead, a qualitative assessment was made on each ultrasound scan, to identify the features that would distinguish bone from soft tissues. Figure 6-27 to Figure 6-29 show three sample pictures from T11 from these qualitative evaluations.



*Figure 6-27: Raw ultrasound image from a pig spine scan showing spinous process on the left (I), lamina in the middle (II), and soft tissue on the right (III).*

From Figure 6-27, the effects of the incident angle are obvious, with the lamina (region II) showing a clear ultrasound reflection in the central region of the image, while the spinous process fades out as the angle increases in region I. The soft tissue below region III contains a significant degree of speckling throughout the region. If a simple contrast filter was applied, region II would be readily segmented for registration, region III would be appropriately removed, but region A would be also be removed despite being bone.

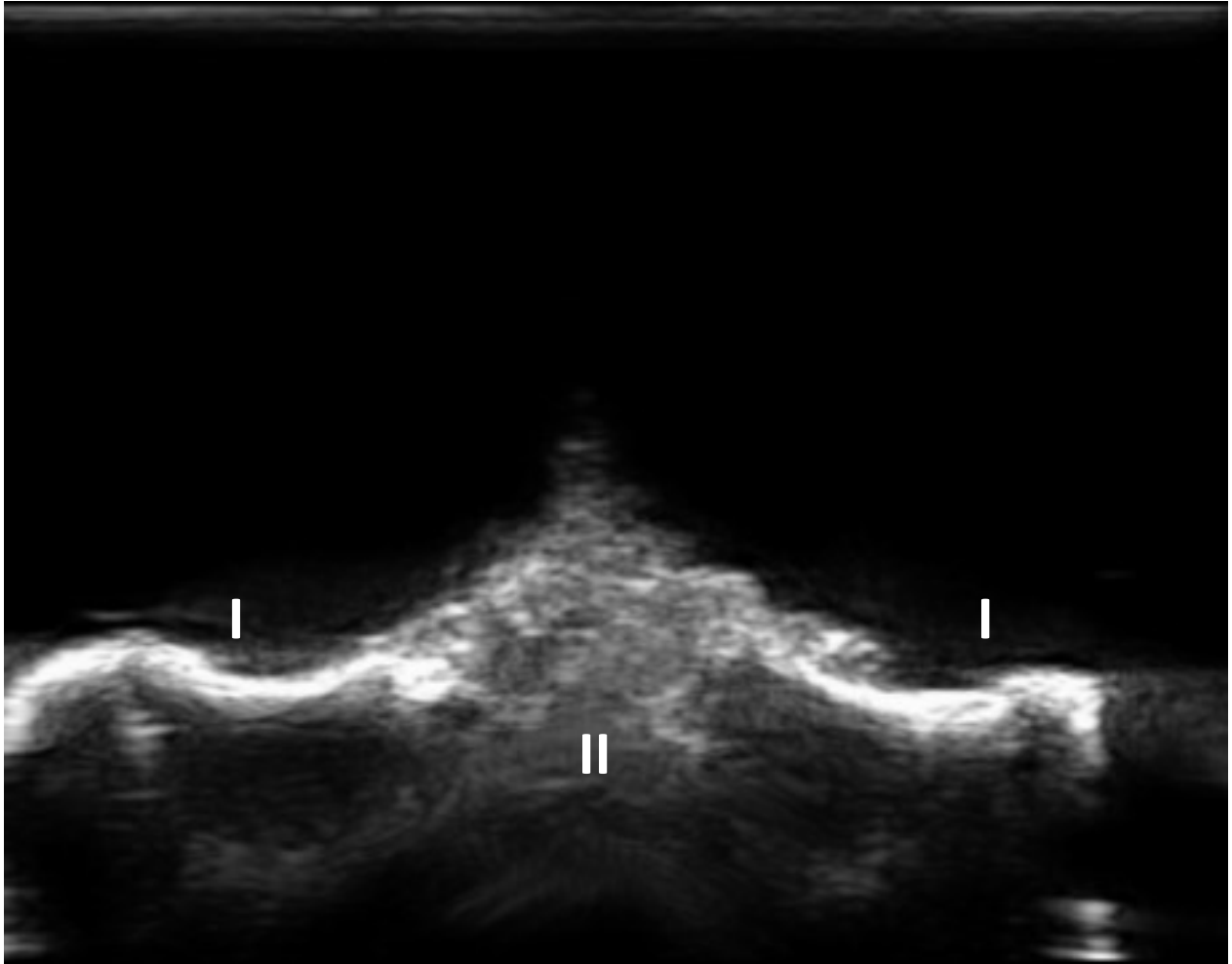


*Figure 6-28: Raw ultrasound image from a pig spine scan showing the inferior articular processes (region I), with the soft tissue region inferior to the spinous process (II)*

Figure 6-28 shows a region where incident angles were similar between bony surfaces and soft tissue surfaces. The large area of speckling in region II is indicative of soft tissue, while the clear white outline and the black shadowing deep to the surfaces in regions I clearly indicate a bony reflection. Again, a simple contrast filter would allow segmentation between the bony regions from the soft tissue region in the center. An additional filter could be applied that detects that region II has a much deeper region that is imaged that would be absent if it was bony tissue.

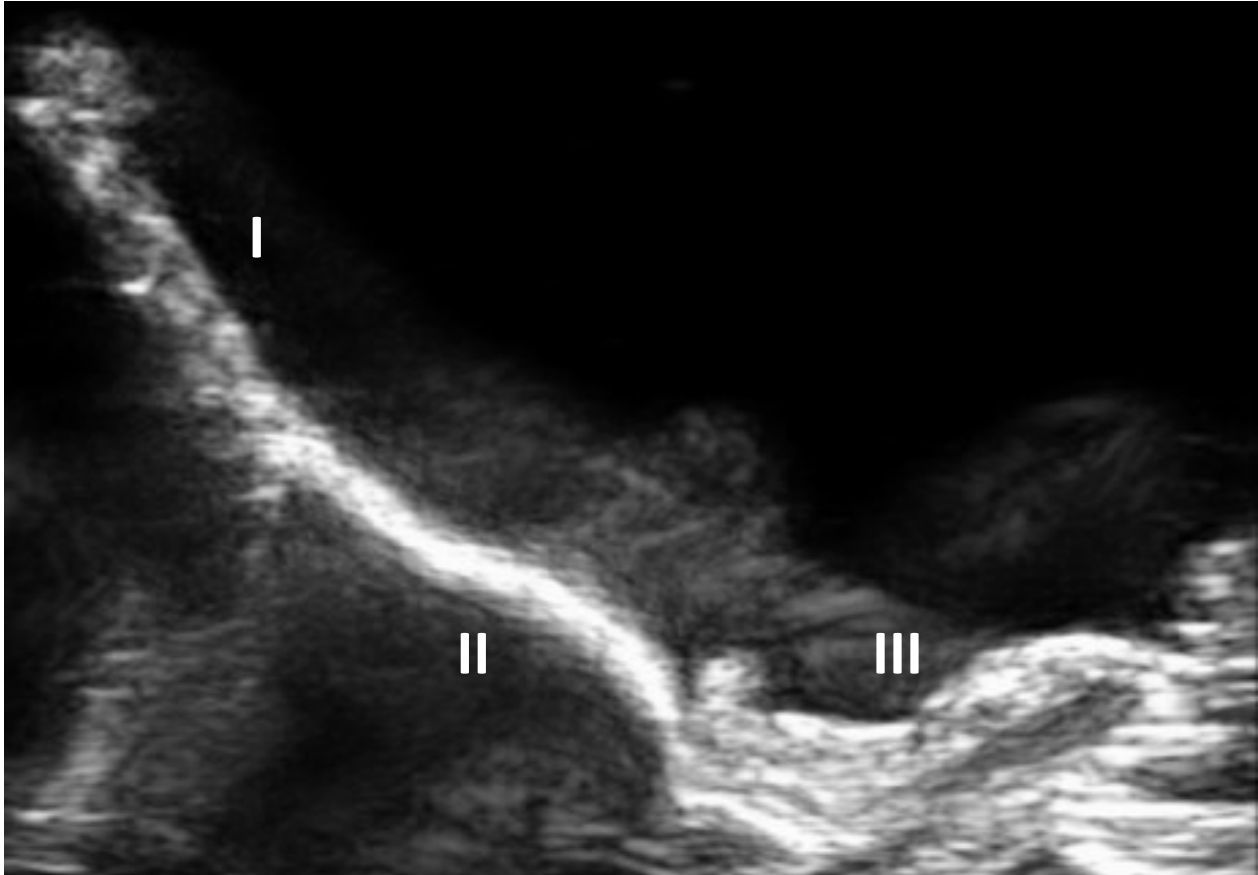


*Figure 6-29: Raw ultrasound image from a pig spine scan showing the spinous process (I), lamina (II), and soft tissue (III)*

The final sample image in Figure 6-29 shows a more equivocal case, where it is more difficult to distinguish between soft tissue and bony tissue. Again, the spinous process in region I is at a high incident angle to the ultrasound, but the shadowing below the region distinguishes it as bone. Region II is clearly bone, with both shadowing and a clear reflected surface. However, region III has strong reflections along the surface, but also significant speckling throughout the region deep to the surface. In this case, a contrast filter would remove region I despite it being bone, while region III would be kept alongside region II, despite being soft tissue.

It would be helpful to test additional algorithms to distinguish region III from region II in future studies. However, the bony surfaces can be readily captured, segmented, and reconstructed, similar to the phantom surfaces from previous studies. There may be some additional soft tissue regions that may be captured as well, but the important bony regions are present for registration.



### 6.6.3. Pig Spine Registration Feasibility

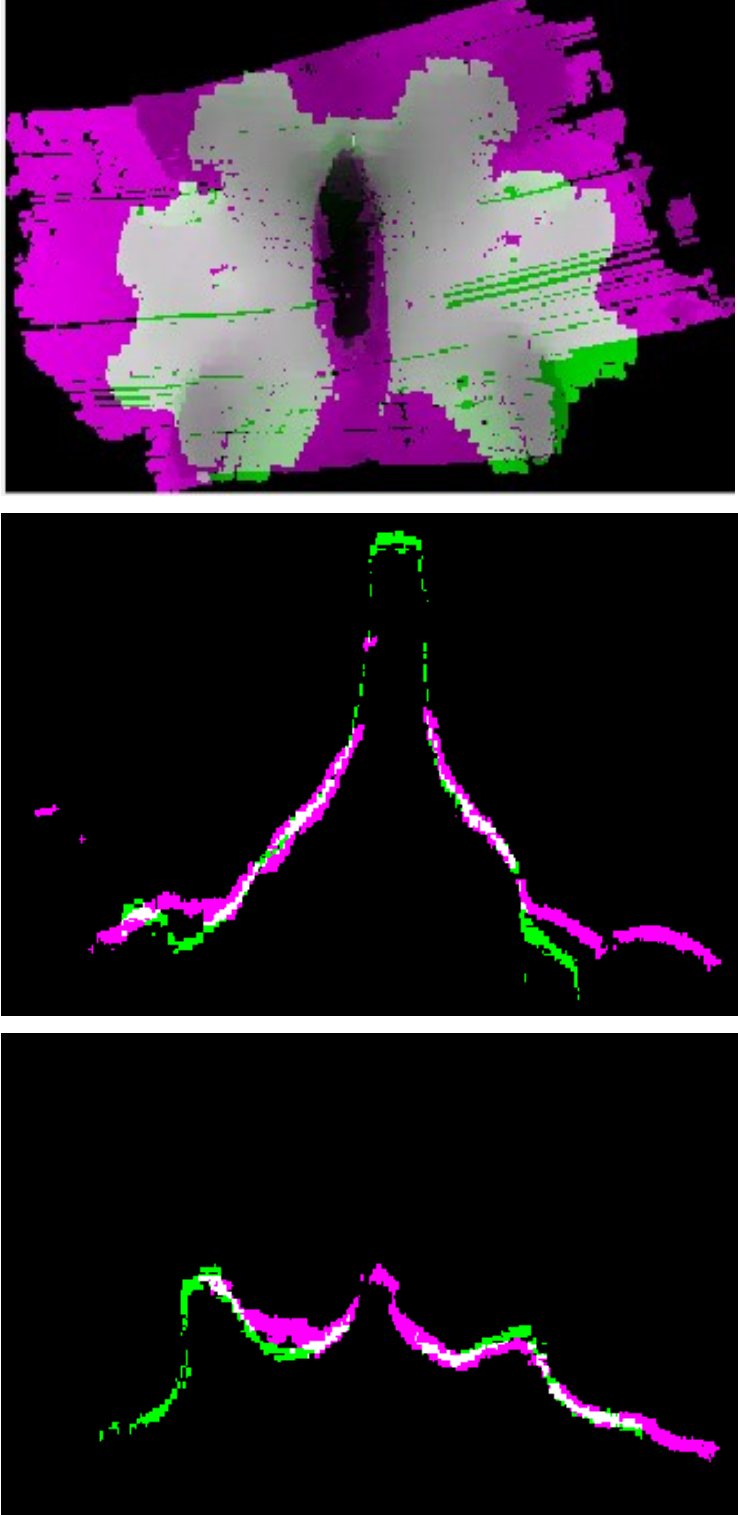
The more important analysis on the pig spine 3D ultrasound scans and registrations was determining if registration could be successful on real tissue. However, because of the large amount of remaining soft tissue on the spines, particularly at the articular process regions, it was not feasible to quantitatively determine if the best registration was selected like in the previous phantom studies. Instead, this study qualitatively determined if the algorithm was able to register the pig spine consistently and reveal potential factors that may complicate registrations, particularly with the addition of soft tissue artifacts and more variable surface depths from the pig spine relative to a typical thoracic human spine.

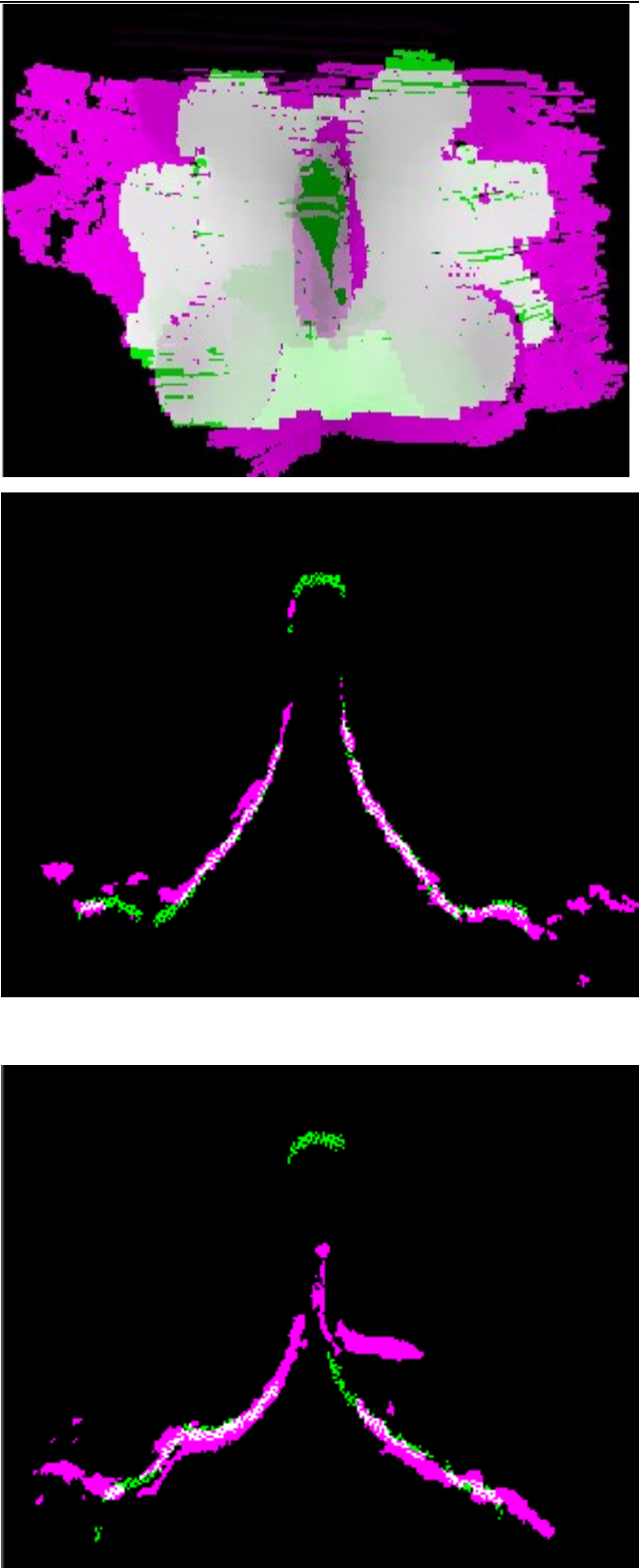
Each of the seven vertebrae were registered three times each. When registering the pig spines, the 3D ultrasound image processing filters, and procedure were not changed from the phantom spine settings. The final image processing settings used a contrast filter lower bound of 40% and upper bound of 80% and averaging filter of 3x3 pixels for the first step, and an averaging filter of 2x2 pixels and quantization level of 80% for the second step.

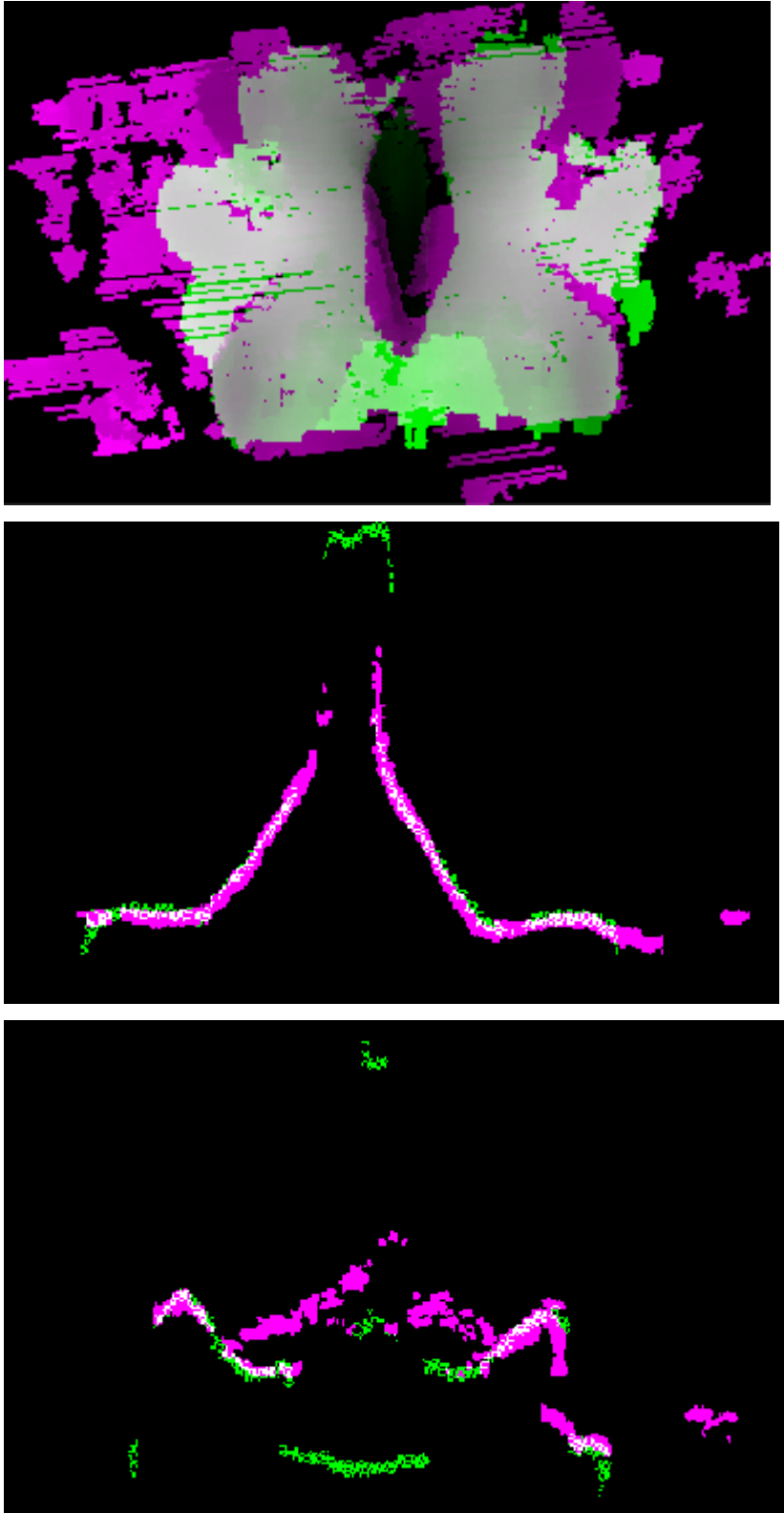
Table 6-7 displays the success rates of registration of each pig spine level, along with sample images of the top-down view and slices from two cross-sections of the registration. One of the cross-sections is at the spinous process, while the second cross-section is at the region just inferior to the spinous process at the inferior articular process. Pink regions denote unregistered ultrasound surfaces, green denote unregistered CT surfaces, while white regions denote registered ultrasound and CT surfaces together. A registration was considered a success if there was alignment of the spinous process, articular processes and, where relevant, transverse processes between the CT and the 3DUS surface image.

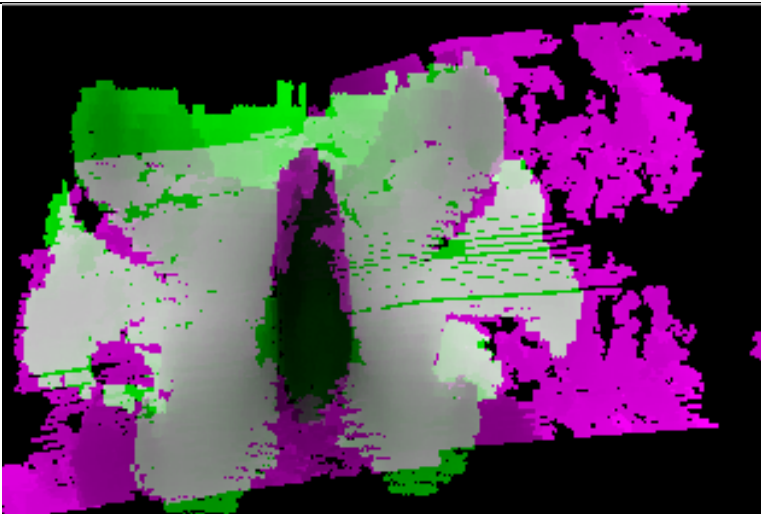
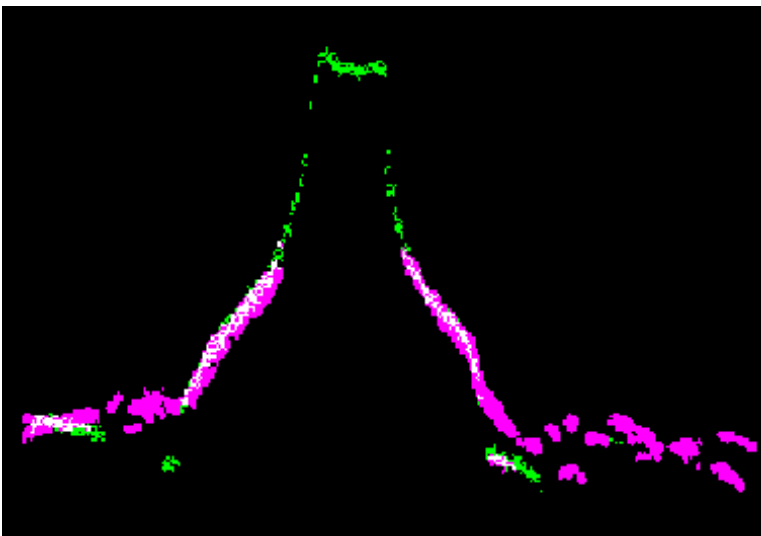
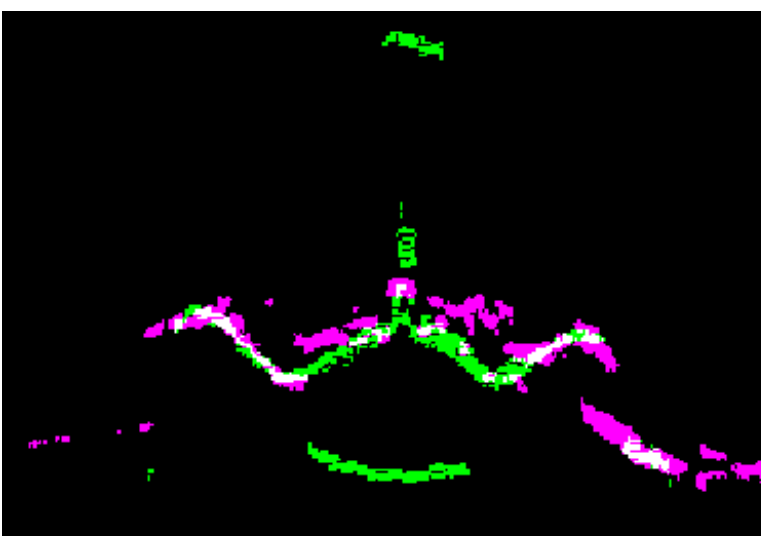
From Table 6-7, 19/21 registrations were successful, with all the failures coming from the T10 registration. Both the failures were from the same T10 vertebra, with pre-registration being unsuccessful due to the scan being off-center, resulting in an inaccurate ultrasound symmetry alignment.

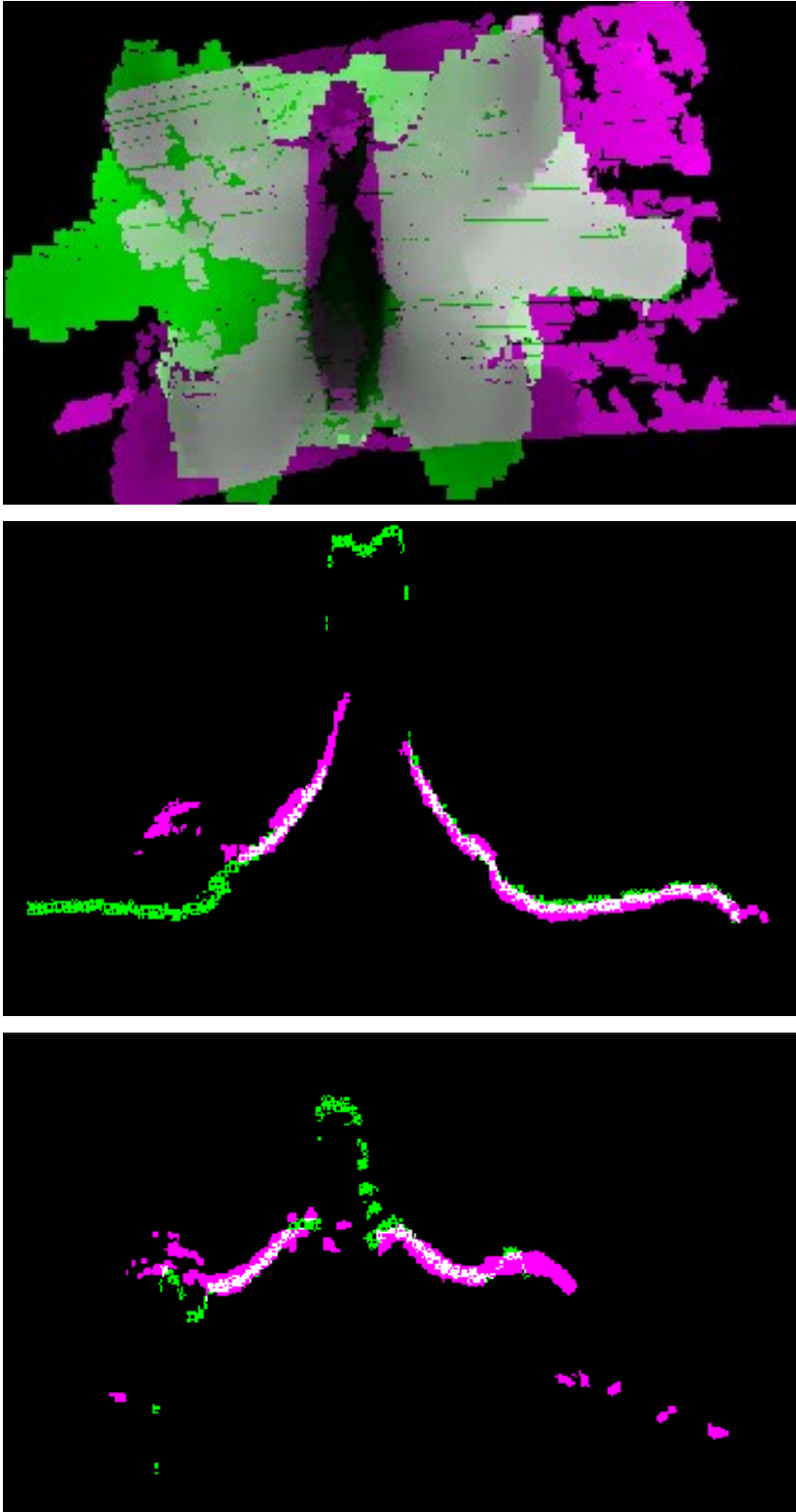
**Table 6-7: Pig spine registration success rate and sample images**

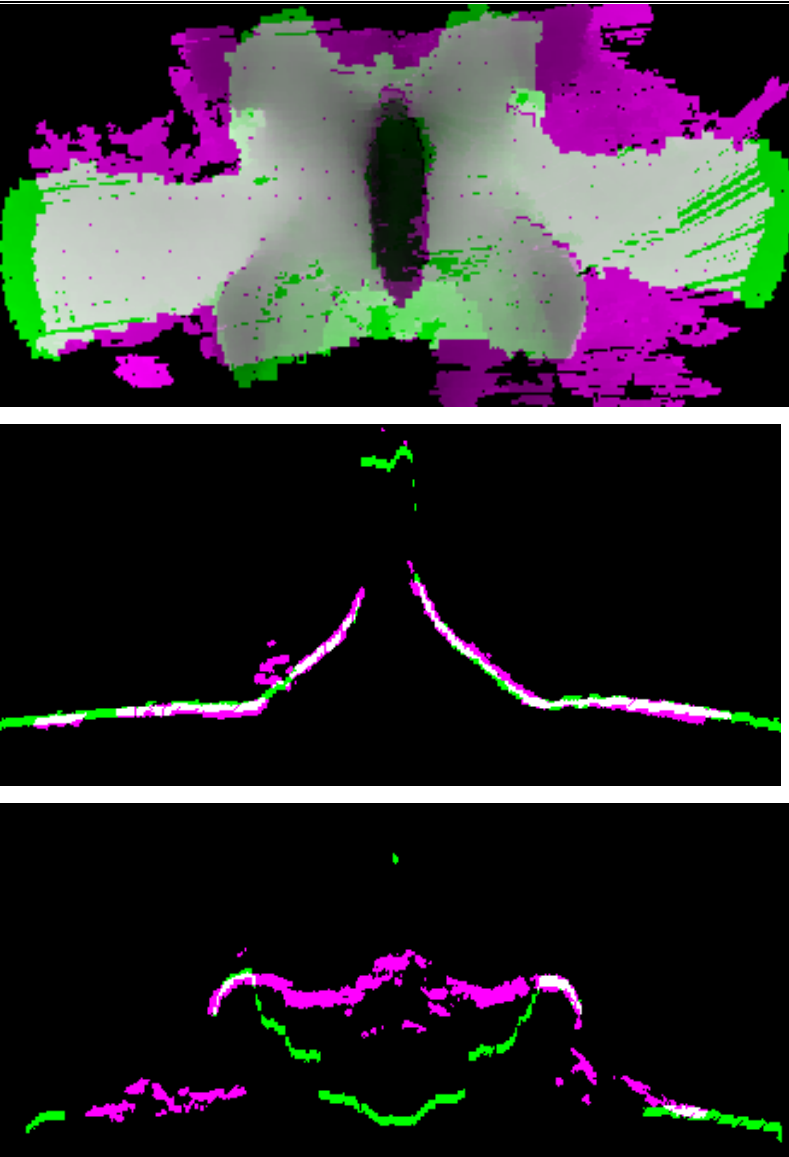
Level	Success Rate	Images
T10	1/3 Successful	
<p><b>Notes</b></p> <p>The successful registration is shown here. The unsuccessful registrations had complete misalignment to the proper alignment.</p> <p>For this registration, the spinous process is aligned vertically in the top-down view as expected.</p> <p>However, from the second figure, most of the spinous process is not visualized, particularly the upper tip, due to the high incident angle of ultrasound in those regions. Still, the rest of the spinous process is well aligned.</p> <p>The final figure shows that there may be some soft tissue obscuring the bone on the left side of the image where the pink ultrasound region is superficial to the green CT region. This is a repeated finding in the other images as well.</p>		

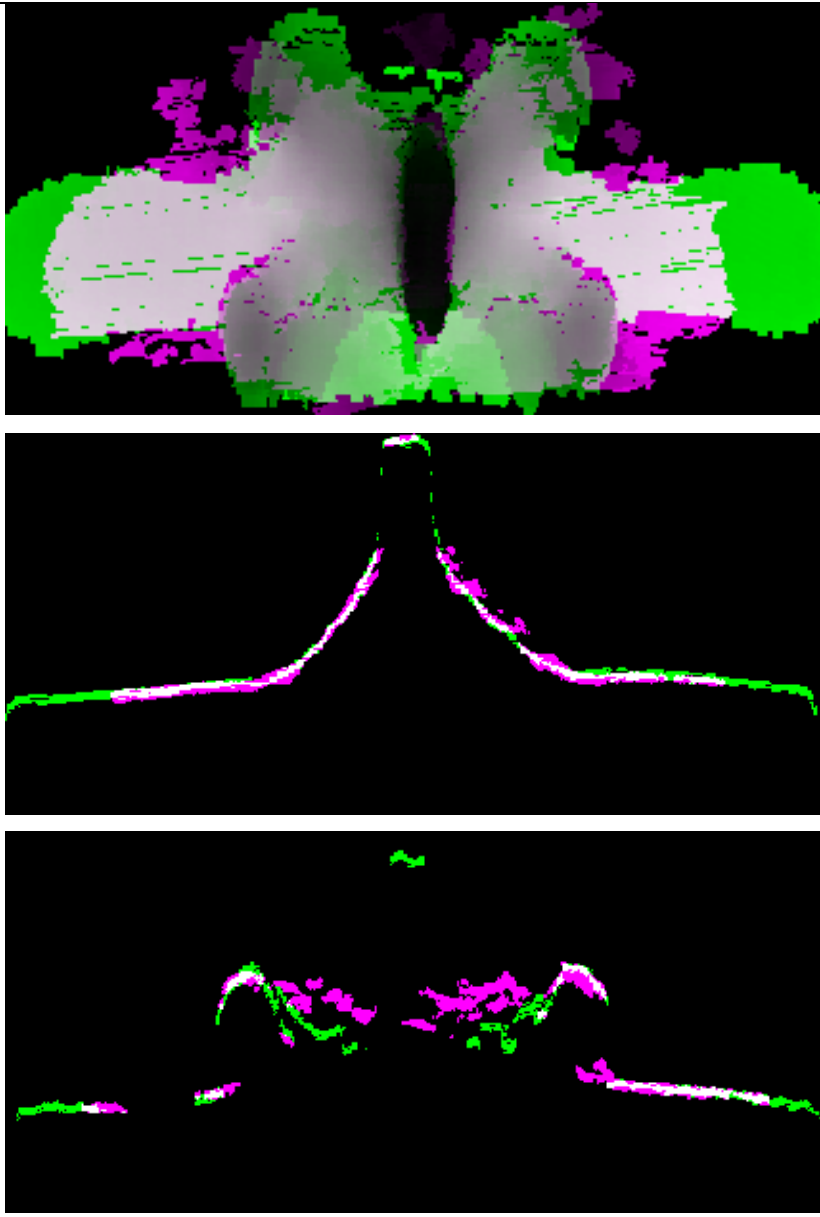
Level	Success Rate	Images
T11	3/3 Successful	 <p data-bbox="201 327 626 716"><b>Notes</b> All these registrations were successful. As with the previous set of registrations, the upper regions of the spinous process were not segmented and retained on the 3D ultrasound image, shown in both cross-sectional images. However, the remaining regions followed the contour accurately.</p> <p data-bbox="201 772 626 961">Soft tissue reflections can be seen on the second image, lateral to the bony regions on the right, and superficial to bony regions on the left side.</p> <p data-bbox="201 1018 626 1291">A sidelobe artifact can be seen in the third image to the right of the spinous process peak. Stray ultrasound signals contacting the spinous process at an angle reflect to the transducer resulting in a 'wing-like' structure.</p>

Level	Success Rate	Images
T12	3/3 Successful	 <p data-bbox="201 327 578 514"><b>Notes</b> All these registrations were successful, with spinous process tips not being retained again.</p> <p data-bbox="201 569 578 919">The final image cross section demonstrates a region where soft tissue has high enough intensity reflections to be retained (pink speckling in the center) while the actual bone lies underneath along a second set of reflections from the bone structures.</p>

Level	Success Rate	Images
T13	3/3 Successful	  
<p><b>Notes</b></p> <p>All these registrations were successful, with spinous process tips not being retained but the bottom regions following the spinous process contours.</p> <p>Similar to the T12 image, the final image cross section demonstrates a region where soft tissue has high enough intensity reflections to be retained (pink speckling in the center) while the actual bone lies underneath. The bony reflections are filtered out of the 3DUS image in this case, so the green CT bony region does not seem to be registered to any 3DUS surface reflections near the middle of the image despite good registration laterally.</p>		

Level	Success Rate	Images
T14	3/3 Successful	 <p data-bbox="201 325 555 596"><b>Notes</b> All these registrations were successful, with spinous process tips not being retained but the bottom regions following the spinous process contours.</p> <p data-bbox="201 646 555 961">There may be a slight misalignment shifted to the right in this image, as the green CT is aligned with the interior side of the pink line on the left, and the exterior side of the pink line on the right.</p> <p data-bbox="201 1012 555 1285">Soft tissues are visible on the right side of the top-down view throughout. Soft tissues can also be seen in the second image on the right, with a pink region that is superficial to the flat green bony CT region.</p>

Level	Success Rate	Images
L1	3/3 Successful	
<p><b>Notes</b></p> <p>All these registrations were successful. It was obvious that the registration was aligned properly with the clear outline of the lumbar transverse process having excellent overlap. Again, the spinous process is not visualized.</p> <p>In the final image, there is a large amount of soft tissue (pink speckling) blocking the bony CT surface below at the center of the image</p>		

Level	Success Rate	Images
L2	3/3 Successful	
<p><b>Notes</b>  All these registrations were successful. Again, the good registration alignment can be seen with the clear outline of the lumbar transverse process overlapping between the CT and 3DUS image. In this case, the tip of the spinous process is visualized.</p> <p>In the final image, there is a large amount of soft tissue (pink speckling) blocking the bony CT surface below at the center of the image.</p>		

#### 6.6.4. Pig Spine Registration Discussion

The pig spine experiment was a feasibility study in exploring the reflectivity of bone compared with soft tissue, and to determine if the current registration algorithm could successfully align the porcine vertebrae between the CT and 3DUS surfaces. This study showed that registration was possible, even with a significant amount of soft tissue in the joint regions. Furthermore, this study showed that the bony surface as extracted from a CT scan aligned closely with the bony surface imaged from a 3D ultrasound machine, as demonstrated in the close alignment between the two surfaces in all the images that did not



have significant areas of soft tissue. However, there is significant work left to be done to improve robustness of registrations.

Firstly, image processing needs to be evaluated further. To differentiate between soft tissues and bony regions, both intensity and shadowing could be used together to identify regions of interest. From Figure 6-27 and Figure 6-29, there is a clear distinction between the three types of reflections: orthogonal bone (bright and clear bony demarcations and shadowing), oblique bone (low intensity reflections but with clear demarcations and shadowing), and soft tissue (variable reflections but without clear demarcations nor shadowing). Further work in morphological image processing or variable image contrast levels need to be explored to extract the bone from ultrasound images more clearly. The spinous process is a particularly unique feature that would aid registration significantly if it could be visualized.

Second, a mechanism to automatically detect the relevant anatomy and crop out extraneous regions is needed for the pre-registration process. Figure 6-30 shows top-down views of the uncropped and the cropped images of one of the failed T10 vertebra registrations. The region was cropped by estimating the number of pixels that would need to be removed to make the vertebra centered in the image (approximately 1cm or 50 pixels). The first image shows that the scan was performed off-center resulting in extra artifact on the right side of the image resulting in the ultrasound symmetry algorithm failing to properly align the ultrasound. The extraneous regions tend to be flat and could potentially be cropped out automatically through image processing.

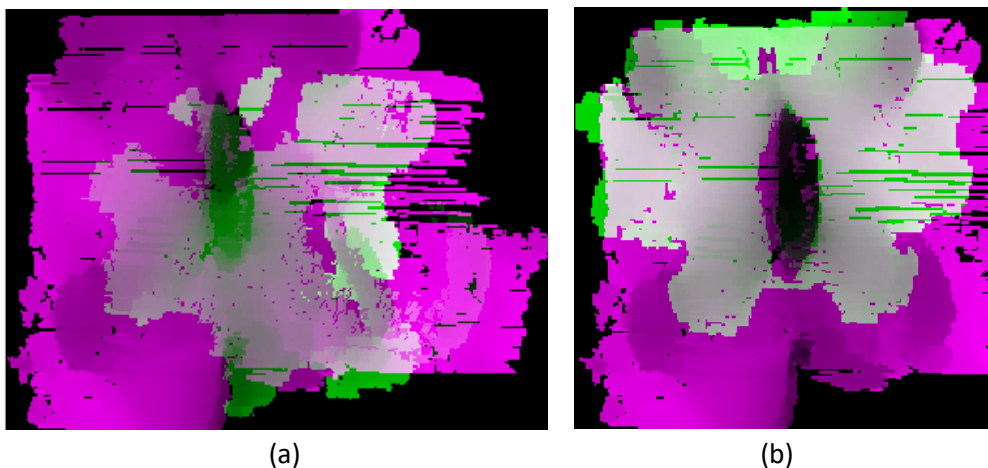


**Figure 6-30: Failed porcine registration, (a) Uncropped image resulting in failed registration due to ultrasound symmetry misalignment and (b) cropped image resulting in successful registration**

Lastly, the feasibility appraisal was solely qualitative in nature. To better quantitatively evaluate the system, it would be important to either compare the overlap between particular features or landmarks

on the images themselves, or to use the motion capture system to track a surgical probe to determine if the vertebra has been positioned correctly. The latter evaluation will be used to determine the surgical registration accuracy in the final chapter of this thesis, but it would be important to do the same experiments on porcine spines to ensure transferability from phantoms to live tissue.

## 6.7. Conclusion

A custom algorithm to pre-align CT and 3DUS vertebrae and then register the two images was developed and evaluated on phantom spines quantitatively. These results showed that a two-step method, pre-registration along with an iterative closest point registration, could accurately perform image registration on phantom vertebrae. The porcine spine feasibility study qualitatively showed that registrations between CT scans and ultrasound scans on a porcine spine could successfully be registered together, though the accuracy is still unknown. While improvements can continue to be made to the algorithm, the basic framework of the registration process is promising for clinical use.

However, surgical registration continues to be a challenge. The surgical registration accuracies were four times poorer than the image registration accuracies, indicating that the motion capture and 3D ultrasound system itself needs to be investigated further to determine where the surgical registration errors are coming from. The next experiment will outline the navigational accuracies of the first prototype of the navigation system.

## Chapter 7: Navigation

### 7.1. Summary

This chapter reports the navigation accuracy results of the 3D ultrasound guidance system on human vertebral phantoms. Section 7.1 outlines the 3D environment development process and the methodology used to measure navigation accuracy. Section 7.2 describes the methodology used to calibrate the navigation system. Section 7.3 describes the CT and MRI segmentation process. Section 7.4 presents the results from preliminary experiments on the previously used phantoms and the results from a fractional factorial experiment conducted on new phantoms extracted from an adolescent spine. Section 7.5 presents the comments and qualitative evaluation from an orthopedic surgeon. Lastly, section 7.6 presents a discussion on the state of the current system.

### 7.2. Navigation User-Interface Development

#### 7.2.1. Environment Selection

As mentioned in Section 2.3.12, a variety of software environments are available for displaying objects in a 3D space. These include Matlab Virtual Reality (Mathworks, Natick, Massachusetts, USA), Unreal Engine (Epic Games, Cary, North Carolina, USA), and Unity (San Francisco, California, USA), the latter two are typically used for designing video games. All three of these tools are compatible with the Optitrack camera streaming system.

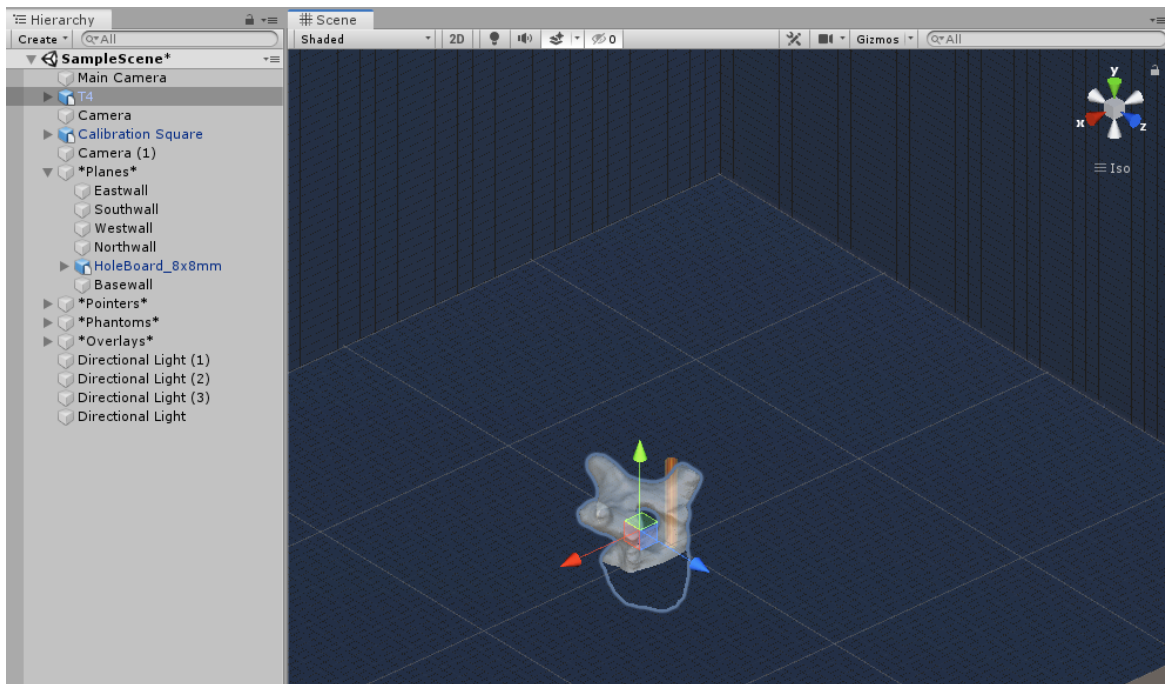
To decide which software environment should be used, two criteria were considered. First, the system could display surgical tools and vertebral anatomy without temporal latency. It is important that when moving objects in the physical world, the virtual objects move at the same time in the virtual world. Second, the quality of rendering is critical. To allow surgeons to see where they are placing the screws, the vertebrae need to be translucent so that the pedicle boundaries can be seen while the screw is being inserted. The details of the pedicle anatomy need to be seen clearly.

Since most of the software functions were already developed in Matlab, the Matlab Virtual Reality platform would have been a good fit for this software package. However, the environment platform was found to be better suited for simulations, rather than displaying anatomical information. The rendering engine struggled with the large number of faces on the vertebral model and the user interface was cumbersome to use, making other platforms more advantageous.

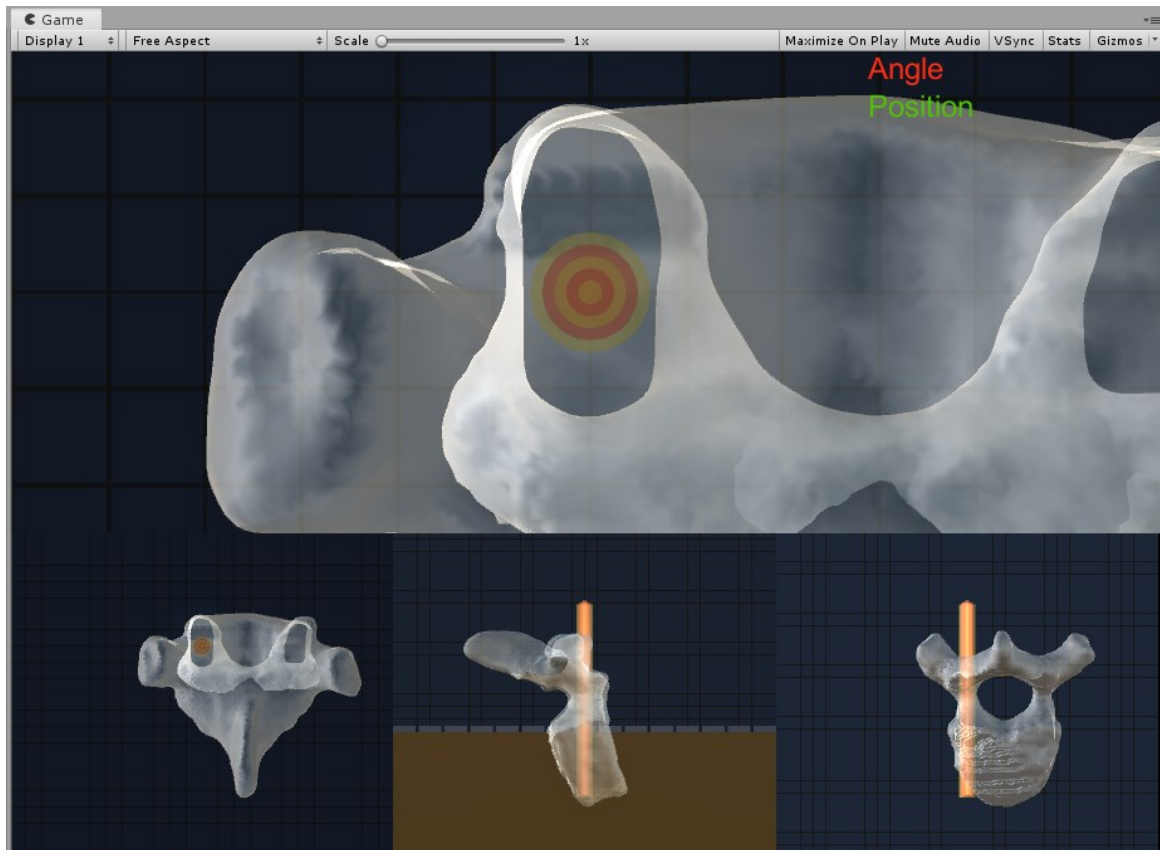
Between Unreal Engine and Unity software, both have been used to create high quality video games with low latency inputs. Being unfamiliar with either software engine, I consulted a software developer who was familiar with both engines. The Unity engine was selected due to its lower barrier of entry in coding and development, while providing excellent visual fidelity. Unity software was considered easier to develop using C# rather than C++ for the purposes of prototyping, and provided ample libraries of tutorials and sample code to aid in the development process.[238,239]

### 7.2.2. Navigation Setup

At its base, Unity is a game engine that includes a 3-dimensional environment in which objects can be placed at different positions and orientations. The objects in this project included the various vertebrae being registered, the screw probe with motion capture markers mounted to it, flat surfaces that acted as a floor or walls, cameras that provide different perspectives of the 3D space, and various forms of lighting that allow for different visualization effects on the vertebra that can provide better contrast for viewing the pedicles. Figure 7-1 shows a screenshot of the software environment, including a panel showing all the available objects on the left, a “Scene View” with a freely controllable camera to view the environment from any perspective in the middle, and a “Game View” which shows what would be displayed in the finalized exported and compiled software.



(a)



(b)

*Figure 7-1: Screenshot of (a) Unity object panel and scene view and (b) game view including the motion capture probe (orange/yellow cylinder), vertebra (white bony object) and capture volume floor and walls (blue background). Center image is the screw-camera while the bottom displays the coronal, sagittal and transverse views of the vertebra*

In this navigation environment, there are three objects displayed: the probe (yellow and orange cylinder in Figure 7-1b), which moves according to the motion capture position and orientation of a 3D-printed probe (Figure 7-2), the vertebra (shown in white in Figure 7-1) which would be placed and oriented according to the image registration software from Chapter 6: , and the walls and floor of the motion capture environment (shown in blue) which includes a grid to allow for calibration experiments to be conducted. The vertebra is made translucent to allow for visualization of the pedicle from multiple angles. The grid was sized to have 8mm squares to match the distance between pegs on a Lego pegboard.

Objects that cannot be seen on screen include cameras and lighting sources. There are four cameras, one that is aligned with the long axis of the motion capture probe to provide an axial view that is parallel to the probe, and three cameras that are aligned to coronal, sagittal and axial views of the vertebra. The primary camera is the axial probe camera, as it provides the best view of the pedicle. A directional light is

placed at each cardinal direction around the vertebra to enhance the contrast of the edges of the pedicles and the rest of the vertebrae.

### 7.2.3. Vertebral Placement

The registered vertebra must be placed in the correct position according to the image registration information. This requires proper translation from the image volume coordinate system to the 3D vertebral model coordinate system so that the transformations (are applied correctly. The positive and negative directional conventions of the images and the model files needed to be standardized.

The model coordinate system is set according to the motion capture system coordinate system, where the left transverse process pointed in the positive X direction, the posterior surface of the vertebra faced upwards in the positive Y direction, and the spinous process pointed away from the cameras in the negative Z direction. The image coordinate system conventionally involves the (0,0) coordinate on an image being top-left most pixel, increasing when moving to the right or moving downwards. As a result, in the image coordinate system, the left transverse process is in the negative X direction and the posterior surface of the vertebra facing upward in the negative Y direction, while the spinous process points in the negative Z direction, similar to the 3D model. A Matlab program was created to translate the transformations from image coordinate system to the model coordinate system.

Positionally, the coordinates of vertices in the model file (in stereolithography or STL format) are set according to their original position in the CT scan. The coordinates were translated so that the minimum coordinate was (0, 0, 0) and all other vertices were in the positive quadrants. The image itself was windowed to remove any extraneous black space so that the minimum coordinate was also (0,0,0) in the volume coordinate system.

Six transformations are calculated from the image registration program and applied to the 3D model. The pre-registration includes three rotations, one from the CT symmetry algorithm, one from the 3DUS symmetry algorithm, and one from the CT-3DUS slope algorithm. The pre-registration also includes the CT centroid to 3DUS centroid transformation. The ICP registration includes one rotation and one translation. Each of these transformations are applied sequentially, similar to the image registration algorithm. Because the transforms are applied on a single rigid body, it has no significant effect on processing time compared with applying them to an image volume where each pixel is transformed.

#### 7.2.4. User Interface

Because this is a proof-of-concept, the workflow of performing registrations has not been completely streamlined yet. Three sets of software programs are required to go from ultrasound scan to vertebral display. The ultrasound streaming and recording software uses Matlab 2015 32-bit version because the Ultrasonix hardware is only able to stream to the 32-bit version of Matlab. The 3DUS user interface is shown in Figure 5-4, including a 2D live-stream of ultrasound data, and controls for activating the stream and recording data. This software outputs the raw ultrasound 2D images and their corresponding motion capture data.

The image registration software is an automated text-based software that uses Matlab 2019, 64-bit version. The updated Matlab version is used to increase the speed of registrations, both because of the ability to use more memory for calculations, and the ability to perform parallel processing on registrations. The raw ultrasound and motion capture data is inputted into the software, alongside a 3D volume of the CT model of the corresponding vertebra. The image registration is performed automatically, displaying the CT and 3DUS raw volumes, the overlapped volumes in posterior-anterior view and transverse views after pre-registration, and the overlapped volumes in posterior-anterior and transverse views after registration to allow for quality control. The software applies the translations and rotations to the corresponding 3D model file (OBJ file) for the vertebra.

Lastly, the software shown in Figure 7-1, developed in Unity, displays the vertebrae. The program requires the modified 3D model file which is then displayed in its appropriate position. Open-source code for importing .OBJ files and for a file-select user interface was downloaded and modified to allow compatibility with this system [240,241]. The motion captured position and orientation of a surgical probe is streamed to the virtual probe, allowing to move in real-time on the screen. The source code is shown in Appendix 7: Navigation Code

While the final goal would be to simply have one user interface that includes the ultrasound streaming interface, the automated registration software, and the vertebral display, that is beyond the scope of this thesis project. The code can be converted into Python in the future which would be compatible with the ultrasound hardware, provide parallel processing for image registrations and can interact with Unity.

## 7.3. Navigation Calibration

### 7.3.1. Motion Capture Probe Calibration

The motion capture cameras appeared to be a significant source of error from previous studies. with 3D ultrasound positional accuracies at  $0.7\pm 0.4\text{mm}$  and probe placement at  $1.1\pm 1.1\text{mm}$  and  $0.0\pm 1.7^\circ$  in Chapter 5: and surgical registrations being at  $1.2\pm 0.5\text{mm}$  and  $2.2\pm 2.0^\circ$  in Chapter 6: Because these measurements were made by analyzing static images, it was difficult to ascertain the source of error. With the 3D Unity display though, an experiment measuring the accuracy of probed positions using motion capture could be conducted live, allowing for quick and intuitive measurements to be taken.

The probe (Figure 7-2b) was calibrated by placing it onto a 3D printed calibration square that includes a stand for both the 3D ultrasound transducer and a motion capture probe. The drawing and corresponding picture for this stand is shown in Figure 7-2. At each of the squared-off corners of the stand, large markers were mounted to set the coordinate system of the motion capture system. The ultrasound transducer was calibrated by mounting it on the circular mounts forming a triangle above the square in the drawing. A water dish with a crosshairs wall phantom is also included for 3D ultrasound calibration if required. To the right of the water dish are two cylindrical mounts for the motion capture probe. Lastly, a set of 4.5mm and 1.0mm divots are placed along the top of the square to allow for dynamic calibration of the 3D-printed probe (4.5mm) and the Digitizing Probe from Chapter 5: if needed.

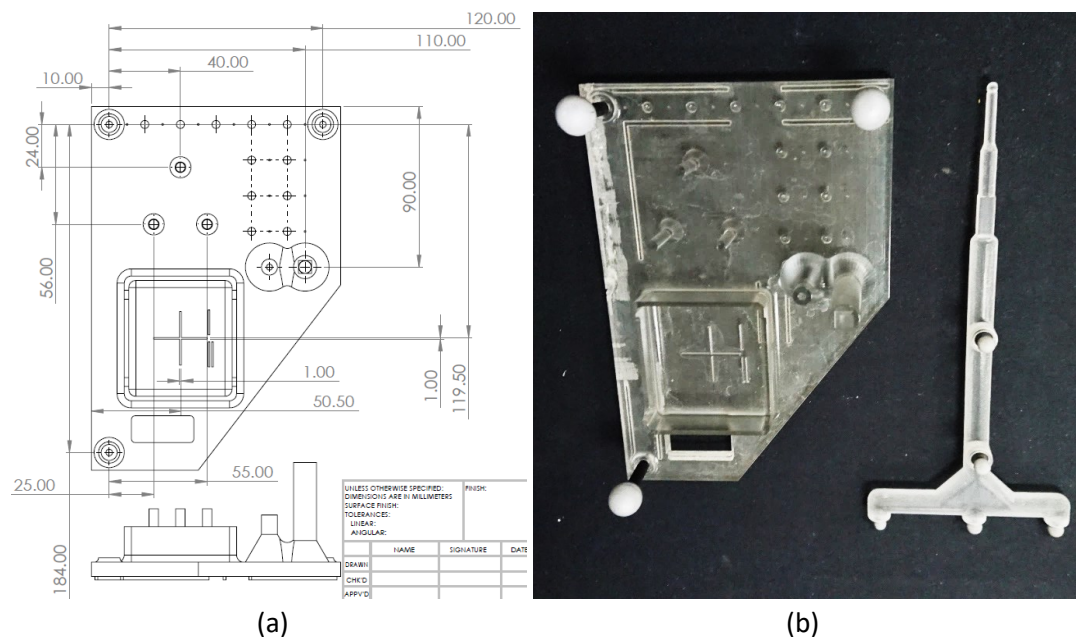


**Figure 7-2: Drawing of calibration square(a) All dimensions in mm. Picture of calibration square (b) including the three reflective markers at each corner, triangular-pillar ultrasound stand (top left), water dish with calibration crosshairs (bottom left), and 3D probe calibration stand (center right)**



First, the repeatability of removing and replacing the ultrasound transducer and 3D probe into the fixed calibration stands was tested, because all other measurements would be based on this location. Both were removed and replaced ten times and their positions were recorded using the motion capture system. From this test, none of the positions differed by more than 0.1mm in any direction for either rigid body and the angle varying by 0.2° at most from the average value.

Next, the 3D probe positional calibration was evaluated. The motion capture software includes an automated probe calibration program, involving placing the probe in a half-sphere divot and then rotating it in different positions to find the position of the probe tip. This dynamic calibration method was compared with a static method which involved simply measuring the X, Y and Z displacements from the central probe marker to the tip of the probe using a ruler, and using that as the transform when creating the rigid body. Both methods were repeated nine times and standard deviation was calculated to determine repeatability of each method.

The standard deviation using the dynamic method was 0.3mm, compared with the static method which was 0.1mm. The static method allowed the probe to be placed in the same position repeatably, while there was some variation in the probe position when using the dynamic method. However, when the probe is rotated axially along its axis, the probe position would wander in a circle with a 2-3mm radius, depending on the roll rotation of the probe. Yaw and pitch did not seem to have a similar effect. It was decided that the static method would be used for probe calibration, as it allowed for highly repeatable measurements to be taken between calibrations, with the caveat that the probe face would be aligned directly with the cameras within 2 degrees. Further study in minimizing the amount of probe wandering during rotation would be warranted.

### 7.3.2. Grid Accuracy Testing

With the probe calibrated, the accuracy of the motion capture system relative to the LEGO pegboard could be evaluated. The pegboard was first compared with digital calipers and rulers. The LEGO pegboard was then compared with the motion capture system by placing the probe at various locations on the pegboard. The first experiment would validate the dimensions of the entire LEGO pegboard setup, while the second would determine if motion capture aligned with the validated setup.

First, individual LEGO bricks were measured using digital calipers and the repeatability was recorded. A single 4x2 brick theoretically measured 16mm by 32mm. However, to allow for tolerances to fit bricks

together, the actual measurements were found to be  $15.84 \pm 0.02\text{mm}$  by  $31.73 \pm 0.02\text{mm}$  after performing five repeated measurements.

To determine if this tolerancing was repeatable over long distances on a pegboard, a set of 4x2 bricks were placed on a pegboard at increasing spacing from 6 pegs to 18 pegs (48mm to 144mm) and measured using digital calipers, with five repeats per measurement. Longer distances of up to 30 pegs (240mm) were measured with a ruler with 1mm increments, allowing for tolerance measurements of 0.5mm. Figure 7-3 shows the results from the caliper measurements.

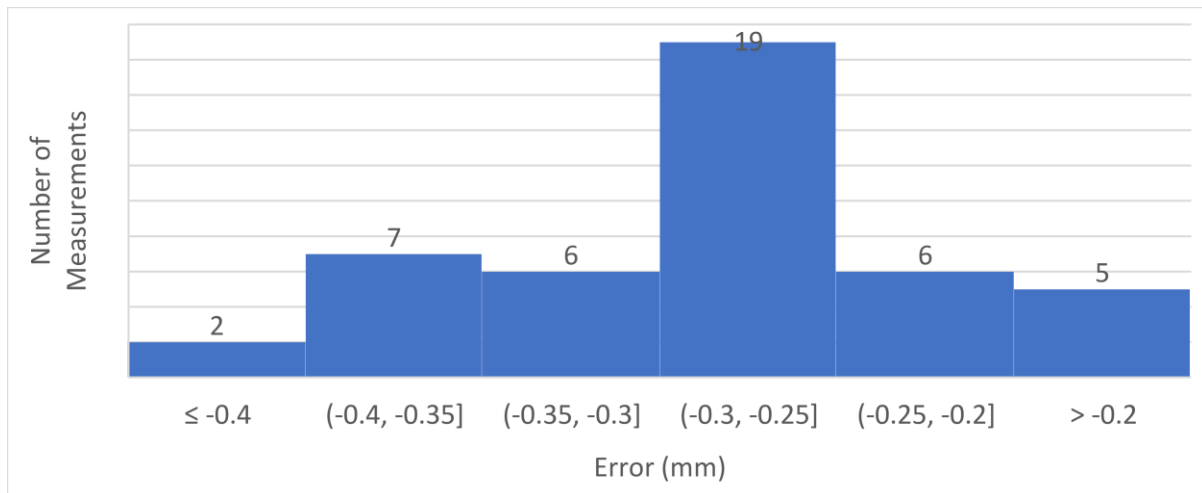


**Figure 7-3: Histogram of difference between actual and theoretical width of LEGO bricks.**

Figure 7-3 shows that the average tolerance is typically between 0.2 and 0.4mm, with the majority being close to 0.3mm. The standard deviation of all the measurements together was 0.07mm, showing that the LEGO pegboard has a high repeatability. The repeatability of any given single measurement was 0.05mm. When measuring longer distances than the calipers, the ruler measurements were found to be the same as the theoretical dimensions of the brick. Tolerances less than 0.5mm could not be resolved given the 1mm increments on the ruler. These results show that the LEGO would be unlikely to be the source of 3D ultrasound and surgical registration errors from previous studies.

The vertical direction was also tested with blocks were stacked on top of each other. A single brick is theoretically 9.6mm in height but with tolerancing, the height was found to be typically  $9.48 \pm 0.03\text{mm}$ . Heights of one to four bricks were then measured with calipers, five times. Figure 7-4 shows a histogram of the errors from these measurements.

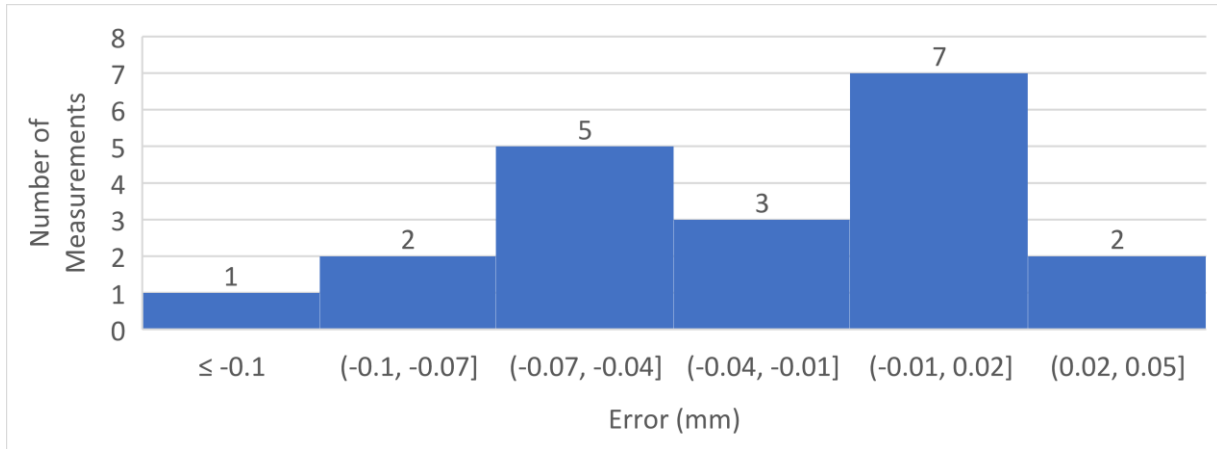


**Figure 7-4: Histogram of difference between actual and theoretical height of LEGO bricks.**

In this case, the average tolerance was typically within  $\pm 0.1\text{mm}$ , again showing a high degree of repeatability in measurements. It would be unlikely for the LEGO bricks themselves to be causing errors in the motion capture measurements, especially in the magnitude of 1mm as found in the 3D ultrasound and surgical registration tests in Chapters 5 and 6.

### 7.3.3. Motion Capture Live Accuracy Testing

The next test compared the positions on the LEGO pegboard with the motion capture live display. The pegboard was modeled and recreated in Unity, replacing each peg with a 1mm diameter circle. The tip of the probe was modeled with five concentric circles, alternating in color, each being 1mm larger than the next to a maximum diameter of 5mm. Figure 7-5 shows the probe on the pegboard. The amount of overlap between the probe and the pegs was used to measure the error in probe placement. The average error in distance and the standard deviation of these errors were calculated.

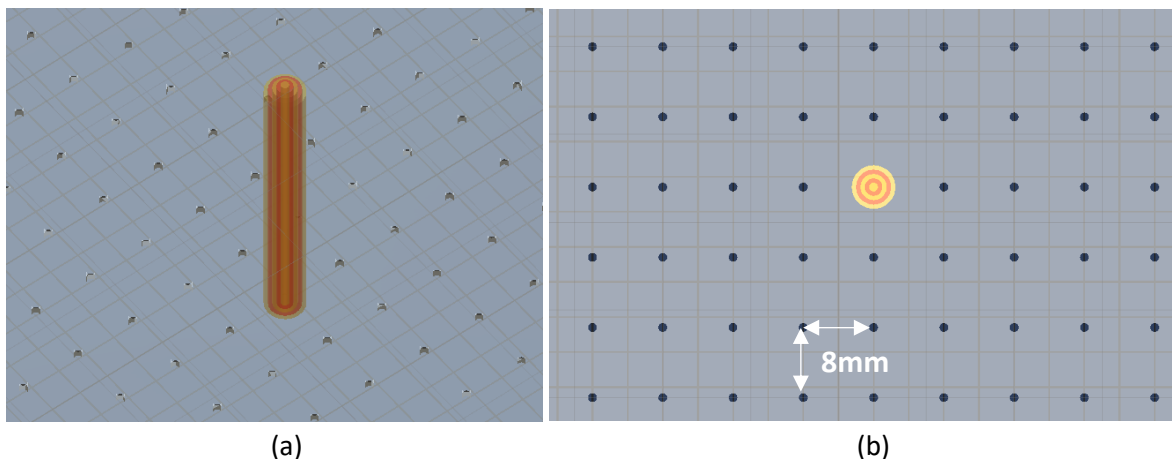


**Figure 7-5: Probe views, (a) 3D view of the yellow and red probe on the pegboard and (b) top-down view of the probe on the pegboard.**

The physical probe and pegboard are shown in Figure 7-6. The grid marked by the black dots in the figure are four pegs apart from each other in the X and Z directions. Bricks were added throughout the volume to take measurements at different heights, with blue and black bricks being one brick height, red bricks denote two brick heights, and yellow bricks denote three brick heights. The full dimensions tested were 160mm by 224mm with a 28.8mm height. The probe was placed at each location four times at the center of the four pegs. The Y positional error (height) itself was not measured because the entry-point on a lamina would typically be within the XZ plane, while the screw would be inserted through along the Y plane.

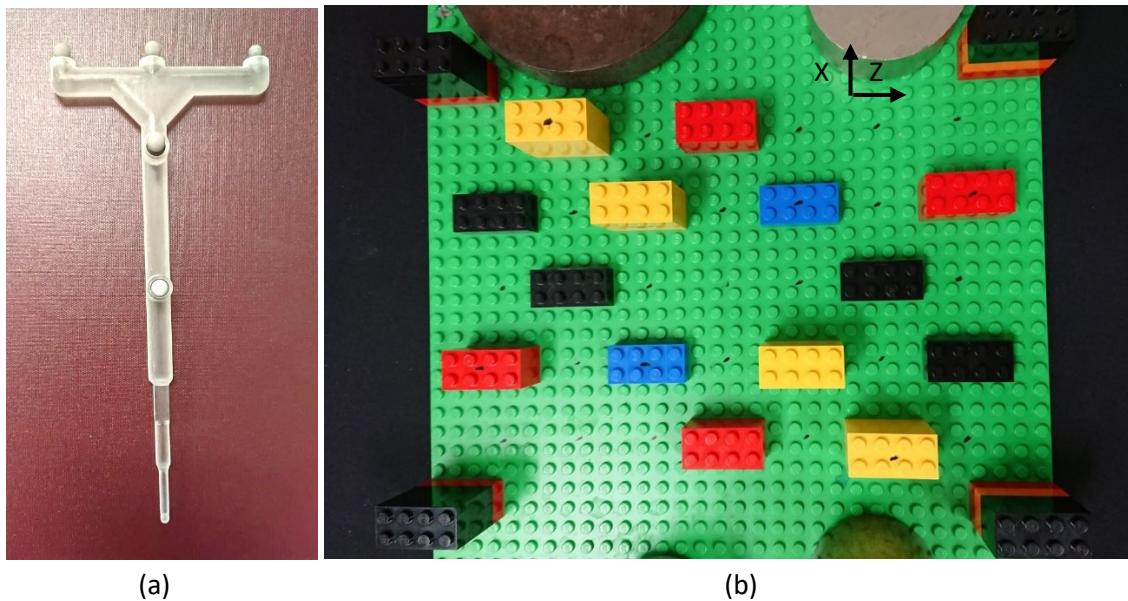


**Figure 7-6: Probe with motion capture markers (a) and pegboard grid (b)**

Figure 7-7 shows a histogram of the results from this motion capture accuracy test. The RMS error of the positional error from live measurements was  $0.7 \pm 0.5$ mm with the worst error at 1.5mm. Errors were larger when on higher bricks, with the 3-brick height having an RMS error of  $1.0 \pm 1.0$ mm compared with the base height having an RMS error of  $0.6 \pm 0.3$ mm. Errors were marginally higher in the outer rim of the plate with RMS error at  $0.6 \pm 0.2$ mm compared with and RMS of  $0.4 \pm 0.2$ mm in the core regions.

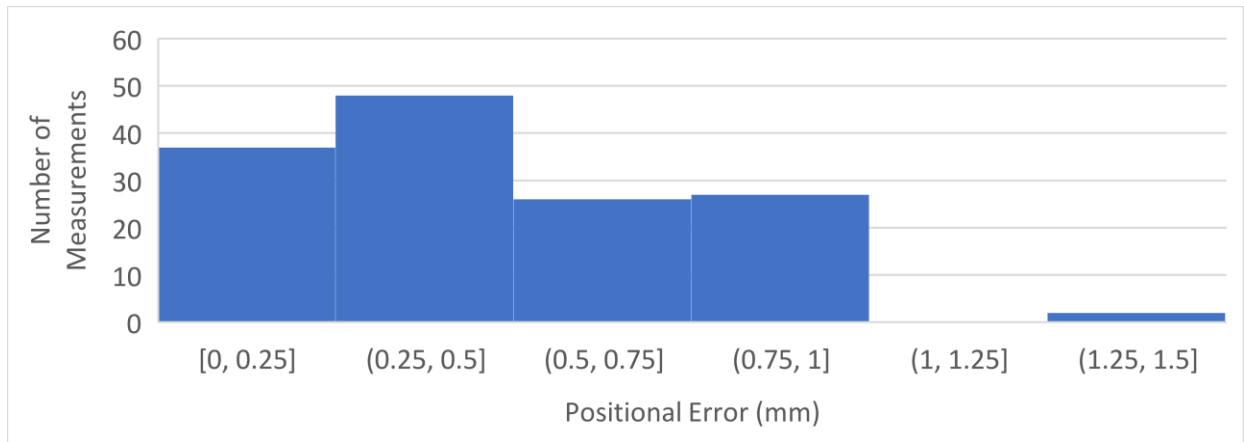


**Figure 7-7: Histogram of motion capture positional error throughout all positions (square brackets denote that value is inclusive)**

The motion capture errors from this live experiment corresponded closely with the 3D ultrasound positional accuracies at  $0.7 \pm 0.4$  mm. With image registrations accuracies being at  $0.2 \pm 0.1$  mm for ICP registration, the combination of these errors approaches the surgical registration errors of  $1.2 \pm 0.5$  mm. However, some of the errors found in this study could be from human errors in probe placement, as the probe was centered on its location by visual inspection.

All the errors measured in the experiments so far have involved comparing the motion capture system to a ground truth like calipers or the Lego pegboard. However, for this navigation system, it is more important that the 3D ultrasound is calibrated properly relative to 3D probe. This remove the build plate construction or unsteady human hands as sources of error to allow evaluation of whether there is a systematic error in the camera system relative to the real world that is not present when measuring 3D ultrasound relative to the probes.

#### 7.3.4. Repeatability of 3D Ultrasound

The basic 3D ultrasound calibration has already been outlined in Section 5.4, involving scanning a cross-hairs phantom and then re-adjusting the transformation between the markers to the transducer surface, according to where the center of the crosshairs appears in the volume.

The repeatability of the 3D ultrasound calibration was tested again, similar to Section 5.4 by performing five calibration scans on the built-in calibration square shown in Figure 7-2. The standard deviation of the calibration square position measured by the 3D ultrasound was 0.2 mm in the X (transverse) direction, 0.1 mm in the Y (vertical) direction and 0.5 mm in the Z (axial) direction. This confirmed the previous findings that the Z-direction would be the least accurate.

## 7.4. Image Segmentation and Modeling

### 7.4.1. Patient Screening

So far, only the phantom human spine (Figure 7-5) and a cadaveric pig spine (Figure 6-26) have been scanned. Extracting a human spine from a CT scan, 3D printing it and using it for scans to test the accuracy of the 3D ultrasound image guidance system would be more indicative of the real case. The gaps between vertebrae in a true patient are smaller than on the phantom, and the size of the vertebrae themselves would be smaller than the adult-sized phantom. The phantom human spine approach was selected over the pig spines because of the anatomical differences between humans and pigs, making results from pig registrations less applicable to human spines. Ethics approval for retrieving patients' CT scans was obtained and a nurse practitioner from the Edmonton scoliosis clinic was consulted to obtain MRI or CT images of patients who underwent AIS surgery.

The first few sets of data were extracted from patients who underwent an O-arm CT scan during their surgery, because they were the most readily available patient CT scans. Scans from three such patients were provided by the nurse practitioner for image segmentation. However, the variability in bony contrast between each image slice and the high amount of noise in the images, made it complicated to perform image segmentation accurately and efficiently. In addition, the O-arm scans were performed at only 4-5 levels, which limited the usefulness of the resulting 3D-printed spine, as many phantoms would need to be printed to scan just two levels. It was decided that using a pre-operative CT or MRI would be more appropriate for this project.

A list of all pediatric posterior fusion surgeries from 2019-2020 was screened for pre-op CT or MRI images of patient spines. A total of 20 MRI images from patients with AIS and eight CT scans were extracted and exported for segmentation. For these images, the reason for imaging was an important aspect to consider. MRI images were typically obtained to rule out neurologic causes or processes that could be related to the scoliotic curvature. As a result, most of the MRI images were of the full spine and included multiple views at 1mm resolution.

The CT scans were primarily not ordered for children with idiopathic scoliosis, but for other causes that required a CT scan. However, most scans only had a small section of the spine, had congenital abnormalities, or had bony translucencies or lesions that were not suitable for segmentation. Only one thoracic spine had more than 2 levels between T3 to T11 available for segmentation and was used for CT segmentation. The CT scan had a slice thickness of 1.0mm and resolution of 0.4x0.4mm pixels.

### 7.4.2. MRI Segmentation

Segmentation of MRI images was tested first, as it would be ideal to use MRI imaging pre-operatively because of its lack of radiation. A literature review was conducted to determine if there were readily available MRI bone segmentation algorithms. Unfortunately, automated algorithms were found to be only useable on the vertebral body itself and lacked detail on the spinous process and transverse processes [149,242]. Manual segmentation was attempted instead. Seg3D2 (Scientific Computing and Imaging Institute, University of Utah, Salt Lake City, Utah, USA) software was used to perform segmentation of the bony vertebrae (including transverse processes, spinous processes, laminae, pedicles and vertebral bodies) because of its low cost, ease of use, speed, and flexibility.

The segmentation process involved cropping the relevant spinal region and then performing histogram equalization filtering on the image to improve image contrast by spreading out the intensity range of the image. The images were median filtered to reduce noise, particularly in the vertebra, and a threshold binary filter was applied to remove surrounding soft tissues from the image while keeping the bony vertebra. The volume was then manually inspected slice-by-slice to ensure the correct pixels were being kept (bony regions). A sample image of a single segmented MRI vertebra is shown in Figure 7-8.

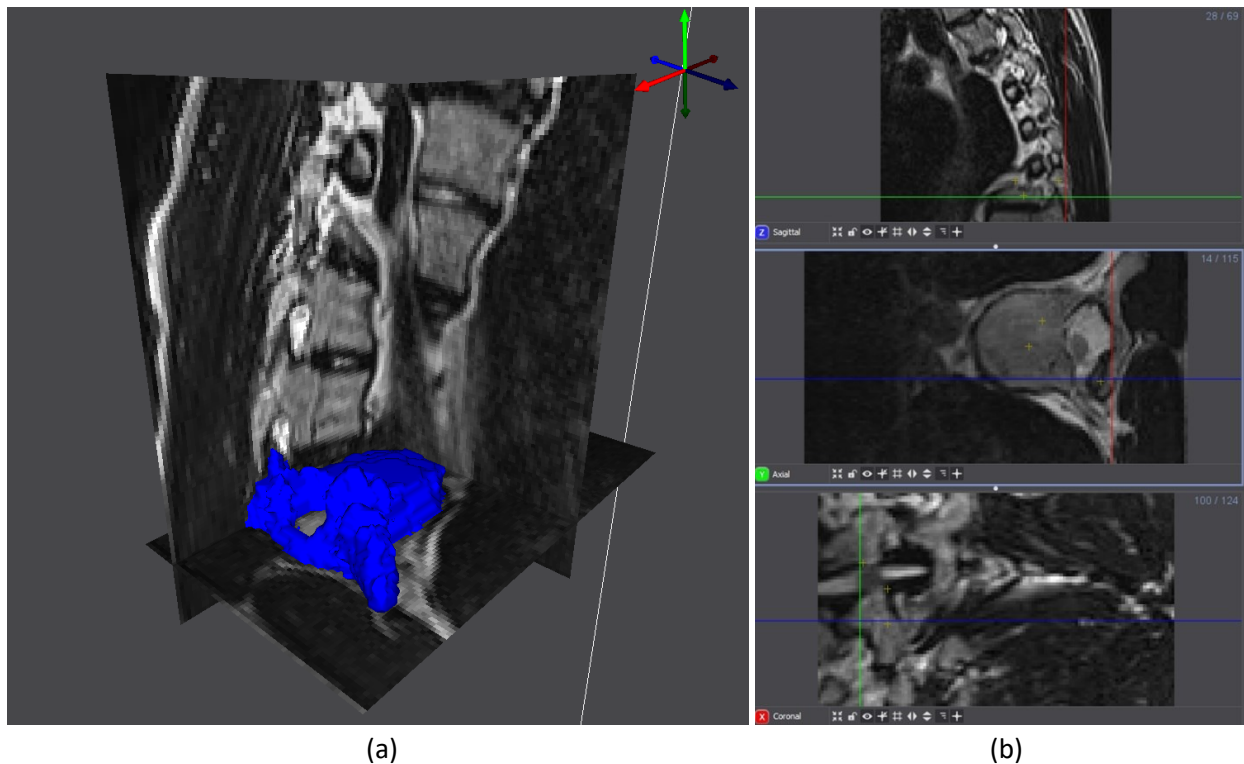


**Figure 7-8: Sample of MRI segmentation of the T9 vertebra showing (a) 3D view and (b) and cross sections of vertebra with sagittal, transverse and coronal views.**

The process of extracting even one vertebra was found to be highly variable and unreliable. First, the contrast was somewhat inconsistent between slices; especially the posterior elements in which the laminae and spinous process tip are relatively thin and have poor contrast relative to surrounding muscles. The low resolution of MRI images and the low contrast between laminae and soft tissues made segmentation challenging. Even performing segmentation on one vertebra took more than two hours of iterative reassessments from multiple directions to ensure the correct pixel was being labeled. It was then decided to move onto using CT images as it is easier to perform bone segmentation on CT images since MRI segmentation was not meant to be the focus of this study.

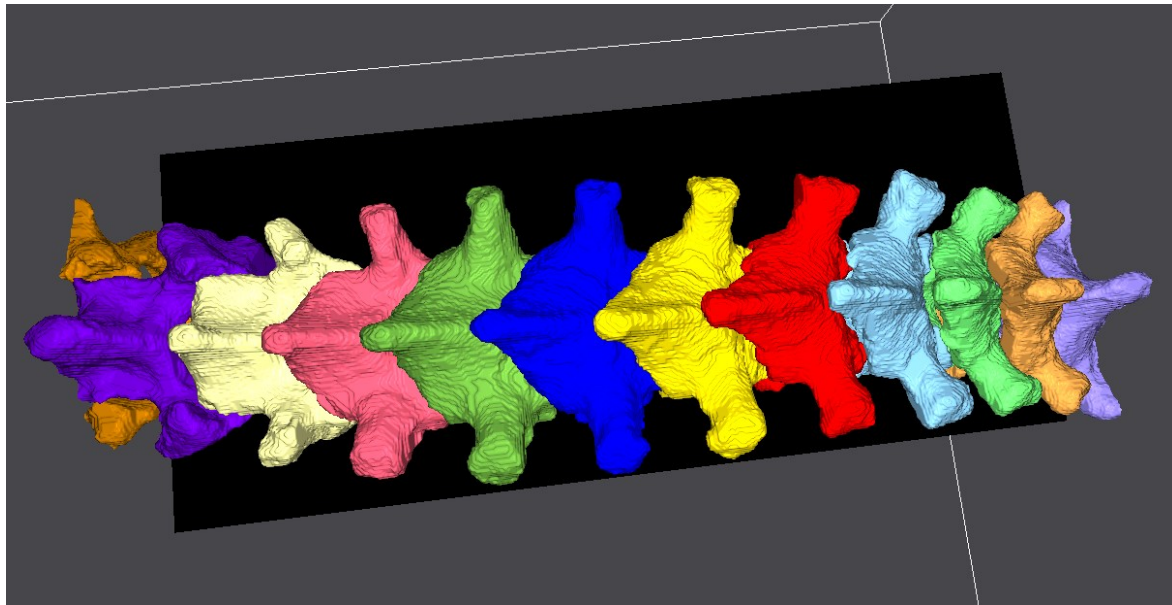
#### 7.4.3. CT Segmentation

For CT segmentation, a patient with visible T2-to-L1 spines was selected, though there was no curvature on this spine. Segmentation was performed in three major phases: contrast enhancement, binary thresholding, and volume filling. The contrast was enhanced by reducing noise and applying histogram equalization to maximize the effectiveness of the binary thresholding. The volume was thresholded, and then the surfaces were smoothed, and holes were filled to provide a solid bony volume. The detailed segmentation process was as follows:

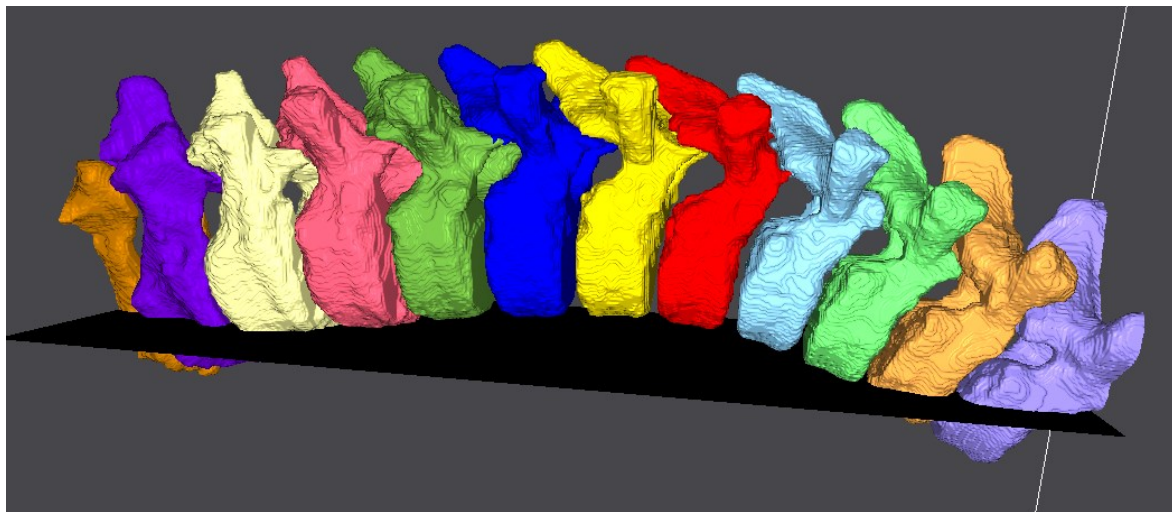
1. The volume was cropped to fit only the spine.
2. A 2x2 median filter was applied to reduce noise in the volume.
3. Histogram equalization was applied to improve the intensity spread for better thresholding.
4. The volume was binary thresholded to isolate the bony regions. Thresholds were selected based on visual inspection.
5. The volume was then eroded and dilated by 2 pixels to remove extraneous noise and to smooth bony surfaces.
6. A hole-filling filter was applied to fill holes within the bony regions.
7. A manual assessment of the spine was conducted to ensure bony areas were labelled properly.
8. Lastly, the vertebrae were manually separated at the articular facet joints arbitrarily. These would not be visible on ultrasound scan and so the exact separation point was not important.

The entire process required 2-3 hours for the twelve vertebrae included in the volume. The segmented volume is shown in Figure 7-9.





(a)



(b)

***Figure 7-9: Sample of segmentation of the CT scan including coronal view (a) and sagittal view (b) with rightmost vertebra as T1 and leftmost vertebra as T12***

The most time-consuming part of image segmentation was the manual separation of each individual vertebra. However, this process could be automated and has been automated by other groups in the past [243]. An automated segmentation process is out of the scope of this project but would be useful to streamline the guidance system.

For the purposes of the navigation experiment, the segmented spine was then up-sampled to the same resolution as an ultrasound scan (0.2mm resolution) then converted to a 3D model file (OBJ file) using Seg3D2. This model file would be used for 3D printing the phantom that would be scanned with the 3D

ultrasound navigation system, be the source for the CT image volume for image registration and be the model that would be displayed on the navigation screen in Unity.

## 7.5. Navigation Pilot Study

### 7.5.1. Navigation Pilot Study on Original Phantom

The accuracy of the navigation system was pilot tested using the same phantom spine from Chapter 6. The phantom includes T4 to T9 vertebrae but only T5 to T8 were scanned to ensure that there was a vertebra above and below each vertebral level. The model included a LEGO stand but also had the addition of holes through the pedicles with a pre-determined trajectory. The pedicle hole trajectories are shown in Table 7.1, where pitch about the X-axis rotating in the cranial-caudal direction while yaw is about the Y-axis rotating in the medio-lateral direction. Entry-points were selected using free-hand method landmarks and trajectories were selected in such a way to prevent pedicle breaches. The hole diameter was 4.5mm to fit the 4.5mm tip of the probe shown in Figure 7-6. The rotational error target was  $<5^\circ$  while the positional error target was 2mm clinically, but 1mm as a technical target [73].

**Table 7-1: Original phantom pedicle hole trajectories**

	Left		Right	
Vertebra	Pitch	Yaw	Pitch	Yaw
<b>T5</b>	9° Inferior	15° Medial	10° Inferior	0°
<b>T6</b>	8° Inferior	6° Medial	16° Inferior	12° Medial
<b>T7</b>	4° Inferior	5° Medial	0°	10° Medial
<b>T8</b>	0°	10° Medial	0°	8° Superior

Two studies were completed. First a repeatability study was completed with the phantom at the capture volume origin. Three scans were completed for each vertebra, to a total of 12 vertebrae scans and 24 probe insertions. Second, the effect of altering orientation and position were tested independently. The orientation of the phantom was kept at the origin in neutral and then placed in roll, pitch and yaw at  $15^\circ$  in both directions, to a total of 28 vertebrae scans (7 orientation x 4 vertebrae) and 56 probe insertions. The phantom was then repositioned in each of the four cardinal directions, 9.6cm from the origin to a total of 16 vertebrae scans (4 position x 4 vertebrae) and 32 probes insertion. There were 88 probes placed in total in the accuracy test. Placement positions are shown in Figure 7-10.

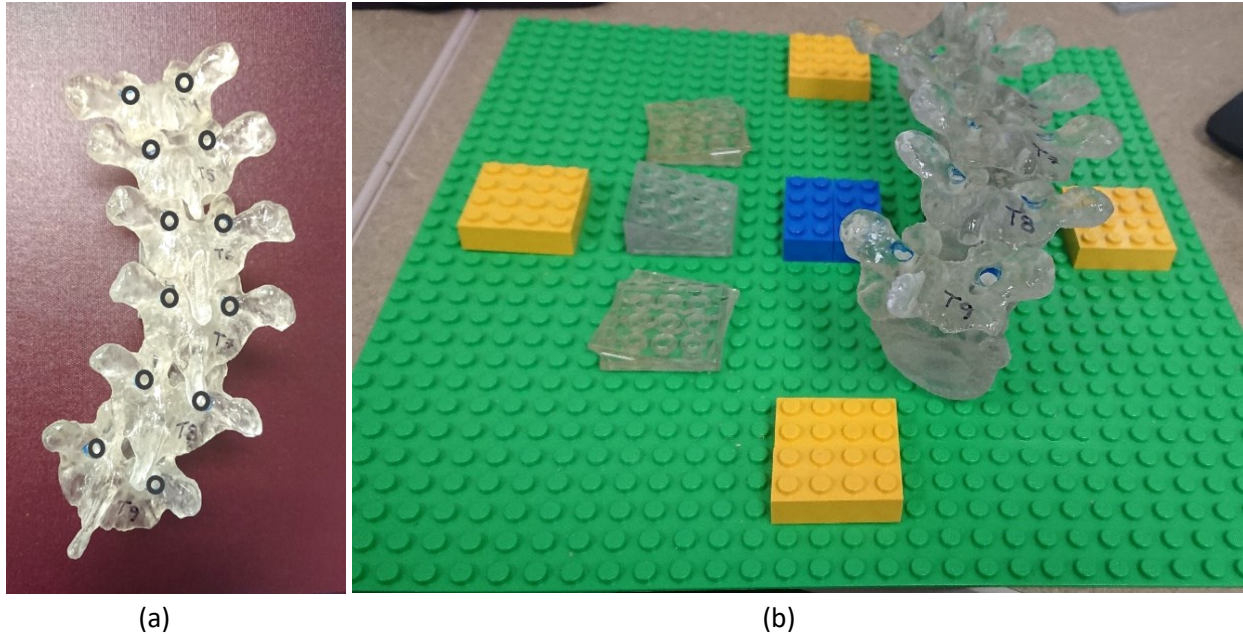


**Figure 7-10: Navigation setup: (a) Phantom vertebra with pedicle holes, (b) Capture volume including the origin (blue), the four cardinal directions (yellow) and the three tilting stands (clear) with yaw-left at the top, pitch and roll in the middle and yaw-right at the bottom.**

The phantom was placed in the water bath and then was scanned with the 3D ultrasound system. The 3D model of the phantom was then registered to the 3D ultrasound image and the transform from the image registration program was applied to the 3D model (OBJ model) which was then loaded in Unity and displayed on the program screen.

Entrypoint error was determined by measuring the amount of overlap between the probe and the pedicle hole on the screen. As mentioned previously, the simulated probe tip in the software has multiple concentric rings which are 1mm larger than the next. Therefore, the width of each ring represents an error of 0.5mm on each side, allowing for increments of 0.25mm to be measurable (half-way between the edges of each ring). The amount of overlap between the rings and the edge of the hole determined the amount of error. The direction of the error was not recorded in this experiment but would be added in subsequent testing. Figure 7-11 shows the probe overlapping with the pedicle hole.

Orientation or trajectory error was measured by the on-screen trajectory of the probe when the probe was aligned to the pedicle hole on screen. The on-screen trajectory was compared to the designed hole trajectory, including the modifications that come from mounting the vertebra on the tilting stands. Figure 7-11 shows the trajectory values displayed on the screen during the experiment. One of the complications in measuring angles in Euler angles is that when three angles are measured at the same time, there are multiple possible combinations of angles that can represent the same 3D rotation. In our case, the axial

(roll) rotation about the axis of the probe is not important since it does not contribute to the probe trajectory. The main drawback though, was that the roll angle would need to be zero, aligned to the cameras, which would allow for the more repeatable static calibration method in Section 7.3.3 to be used, at the expense of needing to be more careful with roll rotations.

For both position and orientation, the average entry-point and trajectory error and standard deviation were calculated for probe placements in each of the vertebrae. The scan time, user-action time and processing time were also recorded. A 3.6 GHz 4<sup>th</sup> generation Core i7 with 16GB of RAM computer was used. User-action time included activating the 3DUS stream and opening the navigation software.

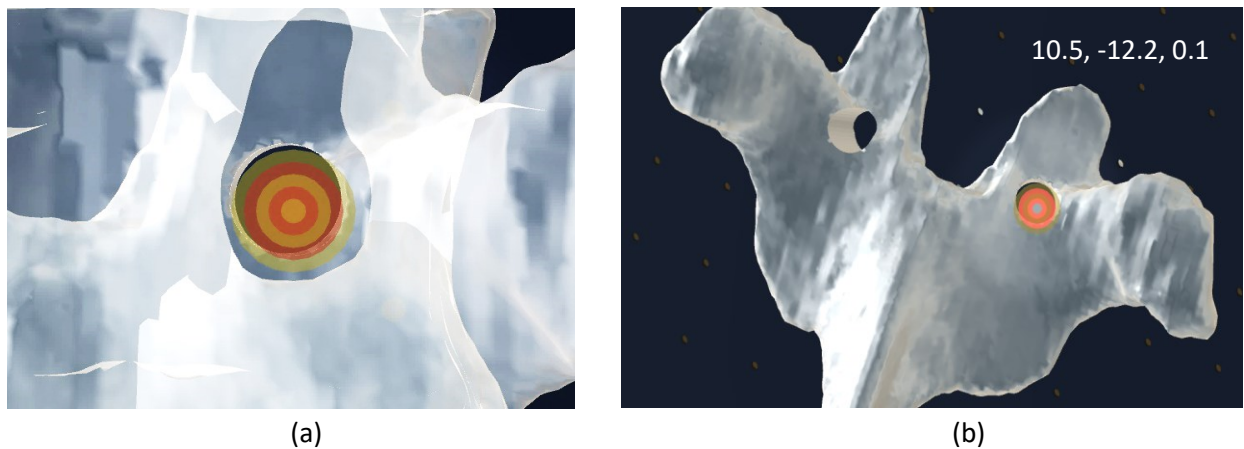


**Figure 7-11: Virtual display of translucent vertebra including the probe (red and yellow concentric circles) placed into pedicle hole (a), and the Euler angles of the probe displayed (b)**

The results of the repeatability experiment are shown in Figure 7-12. The overall average entry-point repeatability was  $0.3 \pm 0.1$  mm ( $n = 24$ ), with 0.5 mm being the worst repeatability (T6 vertebra). The average trajectory repeatability was  $0.3 \pm 0.1^\circ$  ( $n = 24$ ), worst at  $0.4^\circ$  (T6 vertebra). The repeatabilities of both were high for all the vertebrae.

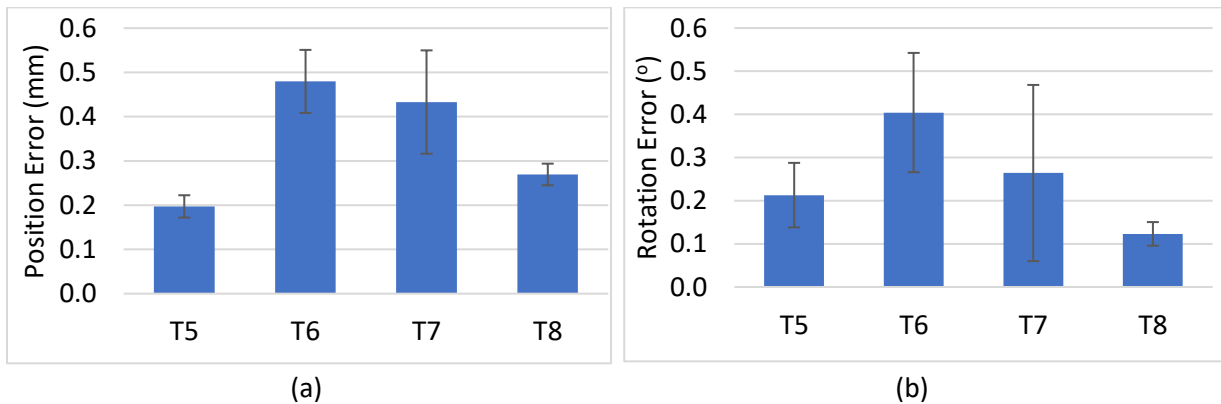


**Figure 7-12: Entry-point (a) and trajectory error (b) from repeatability test: three measurements in each hole for each vertebra at the capture volume origin**

The result of the accuracy experiment is shown in Figure 7-13. Of the 88 placements, one probe placement was outside the 2mm clinical standard, while all the trajectory errors were within the 5-degree target. The average entry point error was  $1.3 \pm 0.4$ mm while the average trajectory error was  $1.3 \pm 0.7^\circ$ . Surprisingly, the T6 vertebra had the highest error, potentially because the pitch angle was largest.

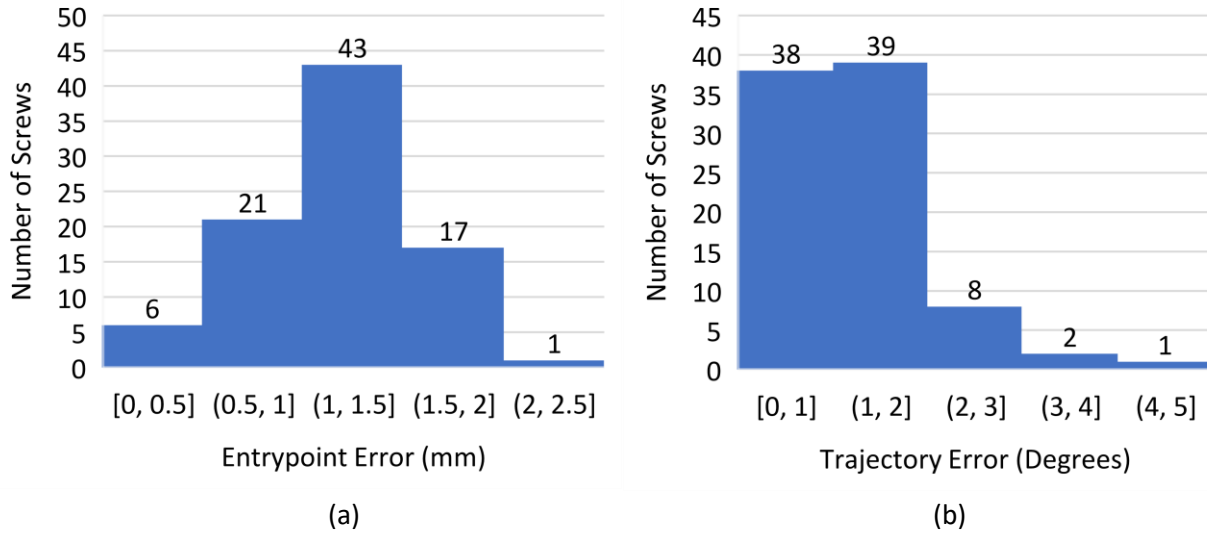


**Figure 7-13: Histograms of (a) entry-point and (b) trajectory errors from pilot test**

The entry-point errors were in line with the surgical registration errors found in Chapter 6 of  $1.2 \pm 0.5$ mm. The trajectory error improved from  $2.2 \pm 2.0^\circ$  from Chapter 6, likely due to the different standards being used between the two studies. The image registration orientation was compared to the theoretically perfect case, while the navigation hole trajectory compared the 3D ultrasound with the motion capture probe which are calibrated with the Lego pegboard's alignment. This would be more realistic, as the more important error for the surgeon is between 3D ultrasound and probe insertion.

The average ultrasound scanning time was  $14.5 \pm 1.8$ s. The registration processing time was  $15.5 \pm 2.1$ s. The user action time required  $16.0 \pm 2.6$ s. The total time per scan was  $46.0 \pm 4.7$ s. It would be expected that the final system would have a more streamlined user-interface that would reduce the user-action time by at least 10 seconds, as the only user-actions would be to activate the function to record an ultrasound scan.

However, further investigation in the image registration process found a programming error that led to the optimal registration not being selected. Rather than the best registration, the last ICP registration that was being processed being selected in the program. This would involve the ICP algorithm with the largest inlier ratio (0.8) and largest grid size (9) being applied to the registration, which would typically be one of the better registrations out of the fifteen being applied, due to its high inlier ratio. This error would be

corrected in subsequent navigation experiments. Overall, while the accuracies were promising, they could potentially be even higher if the correct registration was selected and used.

#### 7.5.2. Navigation Pilot Study on Large CT Spine Phantom

The next navigation experiment involved the 3D spine model created from CT images described in Section 7.3. The 3D model and the 3D image volume were oriented according to the standard outlined in Section 7.1.3. The spine itself was then 3D printed in two different sections, one with T2 to T8 (shown in Figure 7-14 on the left) and one from T7 to T12. The pedicle hole trajectories were again selected by using free-hand probe insertion landmarks to select the entry-point and then using a trajectory that would not breach the pedicle. The list of trajectories is shown in Table 7-2 with T3 to T7 being on the first phantom and T8 to T11 being on the second. T2 and T12 were not included as they were the end vertebrae and would not have a vertebra above or below them, which could bias their error results.

**Table 7-2: Pedicle hole trajectories for pilot study**

	Left		Right	
Vertebra	Pitch	Yaw	Pitch	Yaw
T3	6° Inferior	5° Medial	7° Inferior	4° Medial
T4	8° Inferior	4° Medial	5° Inferior	5° Medial
T5	0°	7° Medial	0°	4° Medial
T6	8° Superior	7° Medial	7° Superior	5° Medial
T7	4° Superior	0°	9° Superior	0°
T8	15° Inferior	0°	10° Inferior	0°
T9	7° Inferior	0°	0°	0°
T10	4° Superior	0°	6° Superior	0°
T11	0°	0°	4° Inferior	0°

The spine was mistakenly scaled to a larger size during the conversion process from image to solid model (1.25x the original size). Each spine was also mistakenly printed in different surface finishes, with the T2-T8 being matte and the T7-T12 being glossy like the previous spines. The previous spines (from Chapter 6: and in Figure 7-10) were printed in glossy as it was thought that they would result in better reflections to represent bony reflections. Even with these unexpected changes, the experiment was conducted as an opportunity to determine if a larger spine would result in poorer registrations due to the increased scanning surface area resulting in larger artifacts and more pronounced calibration errors from longer scans, and to compare the effect of the surface finish of the spines on scan quality. Figure 7-14 shows the two phantoms used in this study.

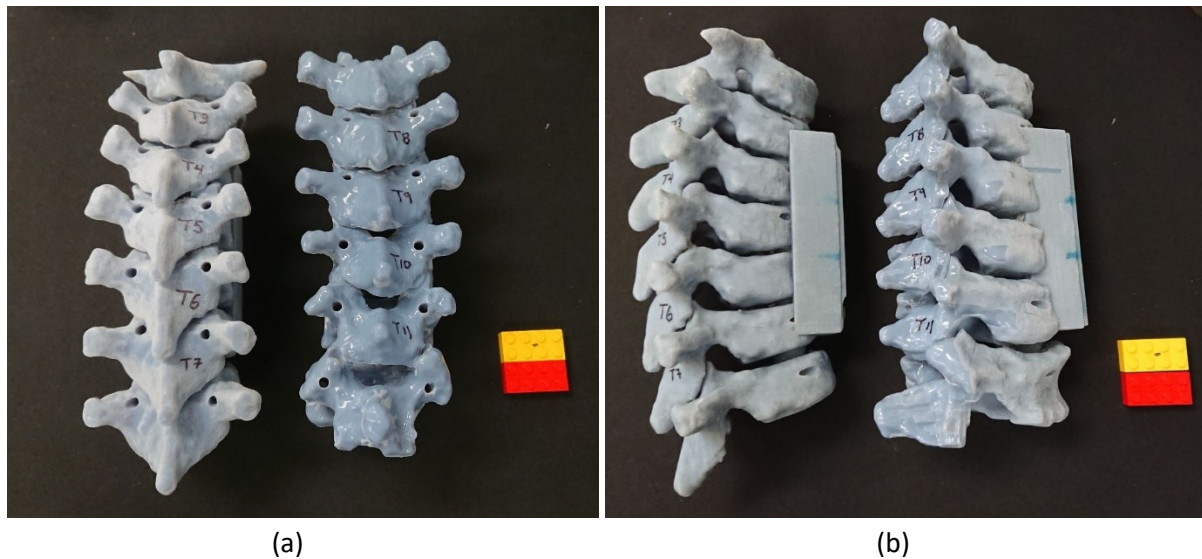


**Figure 7-14: Oversized phantoms in (a) coronal view and (b) sagittal view. In each figure, the surface finish of the left spine is matte and glossy on the right. Lego blocks for scale are 32x16mm.**

A similar experimental design to Section 7.5.1 was undertaken for this second pilot study on the 1:1.25 scaled CT spine. A repeatability study on the nine levels (T3 to T11) was completed (9 vertebral levels x 3 scans = 27 scans), followed by accuracy testing by re-orienting the phantom at the origin to  $\pm 15^\circ$  in roll, pitch and yaw (6 orientations x 2 vertebral levels x 2 scans = 24 scans), and by re-positioning the phantom, this time at the corners of a 25.6x12.8cm (32 pegs long by 16 pegs wide) capture area (4 corners x 2 vertebral levels x 2 scans=8 scans). An additional accuracy test was completed, combining positions at the corners with orientations (4 positions x 3 orientations x 2 scans=24 scans), with vertebrae were randomized amongst the positions and orientations, using a fractional factorial approach to balance the distribution of position, orientation and vertebrae. A total of 83 scans were completed and therefore 166 pedicle holes were probed.

The repeatability of the measurements at the origin are displayed in Figure 7-15. The average entry-point repeatability was  $0.3 \pm 0.1$ mm while the average trajectory repeatability was  $0.5 \pm 0.2^\circ$ . These values remain in line with those from the pilot study, though trajectory repeatability worsened slightly from  $0.3 \pm 0.1^\circ$ .

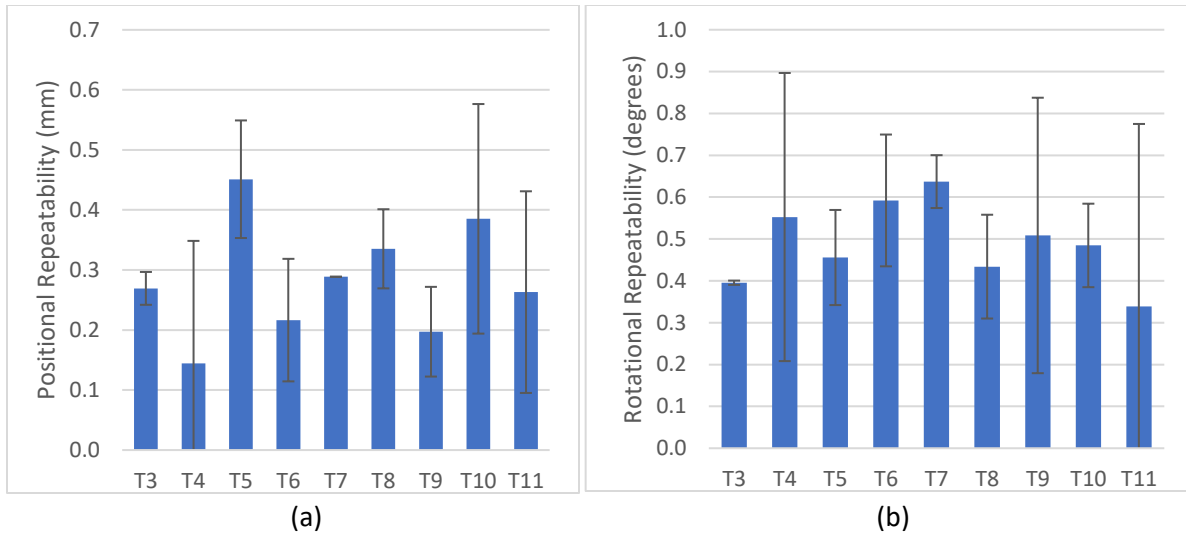


**Figure 7-15: Histograms of (a) entry-point and (b) trajectory error from repeatability test: three measurements in each hole for each vertebra at the capture volume origin**

For the orientation test (comparing roll, pitch and yaw in each direction), the entry-point error was  $0.5 \pm 0.4\text{mm}$  (Range:0.0-1.3mm) while the trajectory error was  $1.4 \pm 0.9^\circ$  (Range:0.1-4.5°). For the position test (comparing placement at each of the cardinal directions), the entry-point error was  $0.3 \pm 0.3\text{mm}$  (Range:0.0-0.8mm) while the trajectory error was  $1.4 \pm 0.8^\circ$  (Range:0.1-2.8°). Figure 7-16 and Figure 7-17 show histograms of the error distribution observed in the orientation and position tests, respectively.

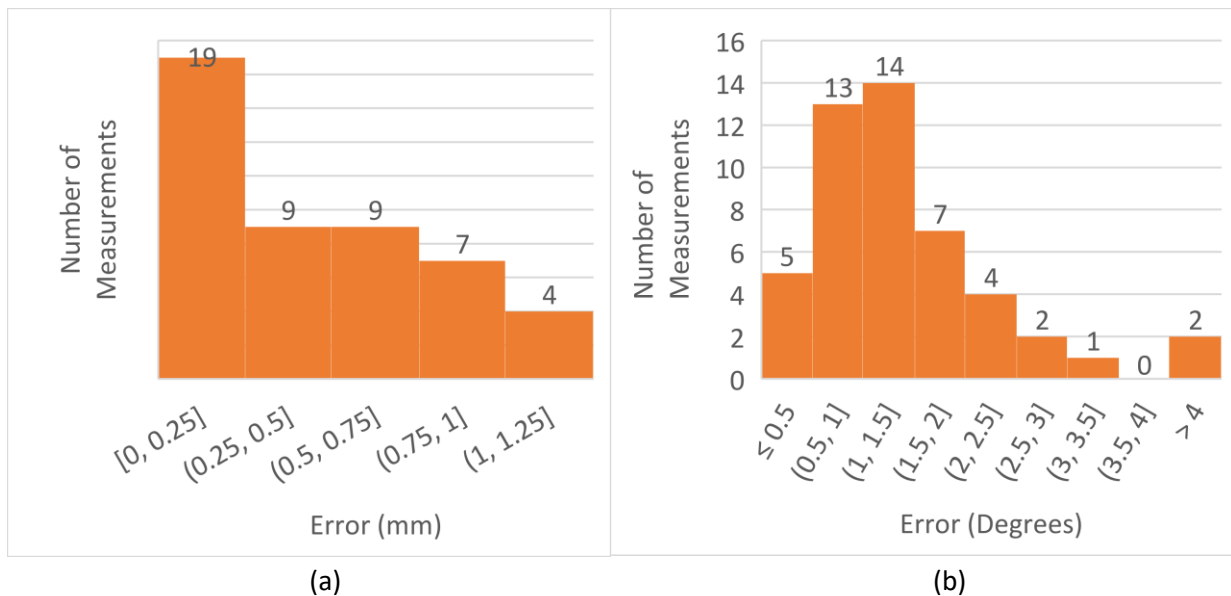


**Figure 7-16: Histograms of (a) entry-point and (b) trajectory error of the probe placement from the orientation test (phantom rotated in roll, pitch and yaw varied in both directions)**



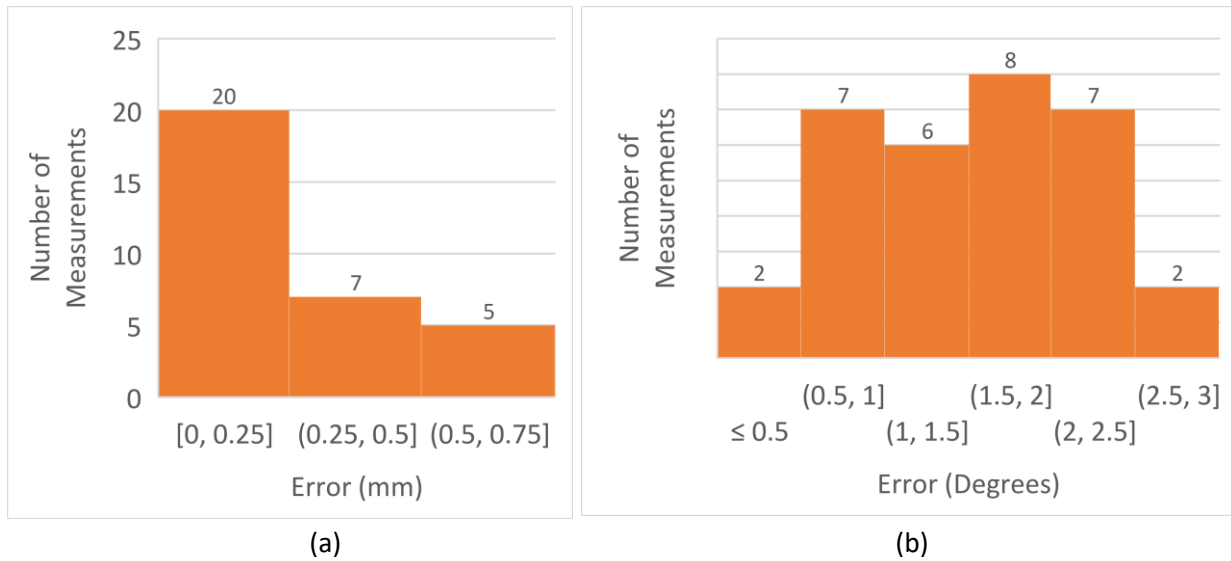


**Figure 7-17: Histograms of (a) entry-point and (b) trajectory error of the probe placement from the position test (phantom placed at each cardinal direction)**

The entry-point error was lower in the position test than the orientation test (0.3 vs 0.5mm), suggesting that changing position may have a smaller effect on entry-point than changing orientation. The trajectory accuracies were similar at 1.4°, though the orientation test had two results with angles greater than four degrees. The reduced accuracy on both vertebrae is likely due to the holes being pitched towards the cameras resulting in marker occlusion in this orientation. The vertebrae on the cranial side of the spine tend to follow a kyphotic angle relative to the neutral plane, resulting in the probe pointing towards the cameras and markers potentially being partially occluded. Part of the challenge was also the 32 x 16 peg rectangle of the capture volume, with measurements taken at the regions closest to the cameras having markers occluded by the tank itself for twelve measurements.

For the mixed orientation and position test (combining different orientations with different cardinal positions), the average entry-point error was 0.5±0.5mm (Range:0.0-1.5mm) while the average trajectory error was 2.0±0.8° (Range:0.4-3.8°). Figure 7-18 shows a histogram of these results. The angular error was larger for the mixed test when compared with position or orientation test alone. The average was within the 1mm and 5° error technical standard (83.3% success rate) and all probe placements were well within the 2mm clinical standard.

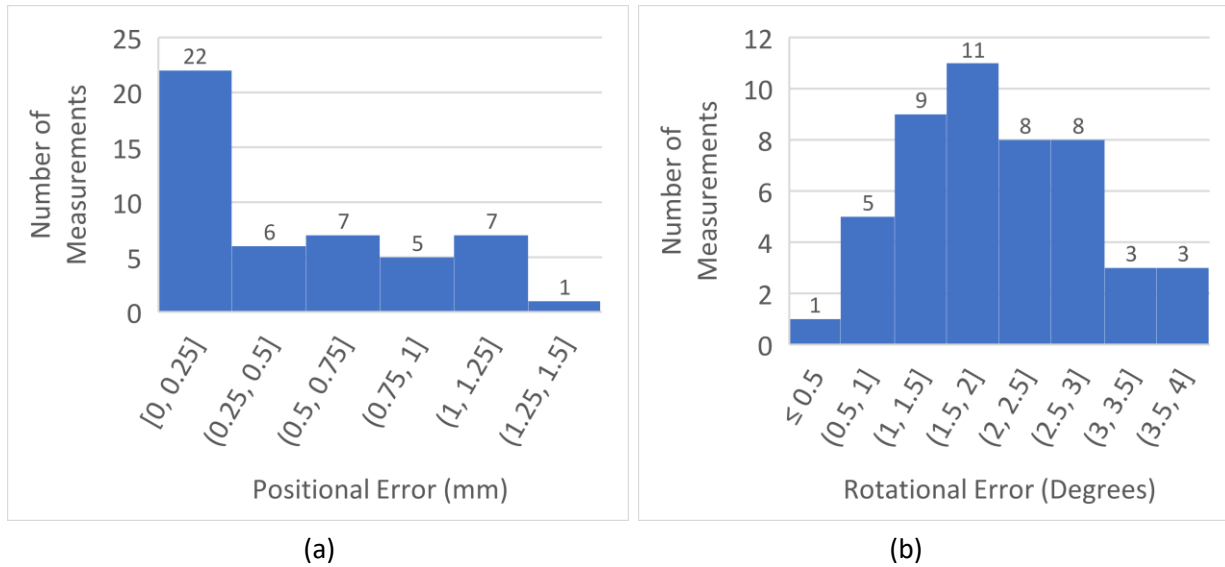


**Figure 7-18: Histograms of (a) entry-point and (b) trajectory accuracy from mixed orientation and position test**

Compared with the first pilot test which used sub-optimal ICP registration parameters, the entry-point errors were dramatically improved from  $1.3 \pm 0.4 \text{ mm}$  to  $0.5 \pm 0.5 \text{ mm}$  using the optimized registration. When comparing only the separated results, the trajectory error from the original study was  $1.3 \pm 0.7^\circ$  compared with  $1.4 \pm 0.8^\circ$  for the orientation and  $1.4 \pm 0.9^\circ$  for the position test, both being almost identical to the previous study. Selecting the best ICP registration had a larger effect on positional error than rotational error.

Importantly, the entry-point errors were smaller than the surgical registration errors which were  $1.2 \pm 0.5 \text{ mm}$  and  $2.2 \pm 2.0^\circ$ . While the surgical registrations compared the vertebral position to the ideal case, where the cameras are aligned perfectly to the Lego pegboard and mounts are perfectly mated together, this experiment used the probe position to determine the accuracy of the 3D ultrasound position. This indicated that with proper calibration between the 3D ultrasound and probe, the motion capture accuracies could be improved.

The average processing time for registrations was  $18.9 \pm 3.1 \text{ s}$ , longer than the  $15.5 \pm 2.1 \text{ s}$  from the previous study which had smaller vertebrae. The vertebrae in this study would likely apply to patients with the largest spines. Comparing with anthropometric studies, the transverse process left-to-right distance in the T12 vertebra was  $65 \text{ mm}$  compared with  $53.1 \pm 4.7 \text{ mm}$ , and the spinous process height was  $20 \text{ mm}$  compared with  $18.0 \pm 1.5$  in one study, making this in the 75-95<sup>th</sup> percentile of adult size [244].

Lastly, the scan quality of the matte-printed spine (T3-T7 levels) was superior to the glossy-printed spine (T8-T11 levels) (shown in Figure 7-19). However, the effect on navigation accuracy is unclear. While the matte spine did have better overall accuracies ( $0.4\pm0.4\text{mm}$  and  $1.7\pm0.8^\circ$  compared with  $0.6\pm0.6\text{mm}$  and  $2.2^\circ\pm0.8^\circ$ ), it is unknown if it was because of the vertebral shape of the more cranial levels, or actually because of surface finish. However, the matte spines had similar reflectivity and clarity in contrast as the pig spines when visually comparing them. The matte finish may have increased the surface area with the water due to the textured surface, resulting in a larger proportion of surfaces that would be orthogonal to the transducer to reflect sound signals back. This texturing would be found in bone as well, making the matte finish more realistic. The final experiment would use matte-printed spines rather than glossy spines.

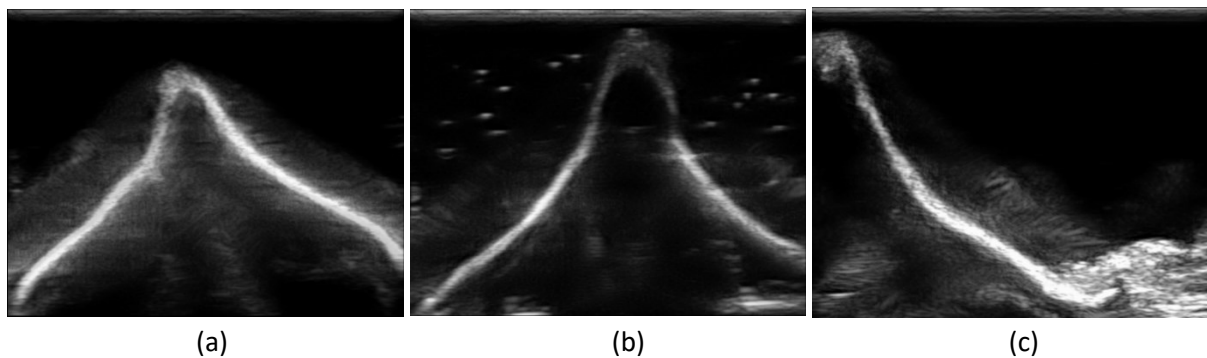


**Figure 7-19: Sample ultrasound images from (a) matte spine, (b) glossy spine and (c) pig spine at the spinous process**

## 7.6. Navigation Study

### 7.6.1. Experimental Design

The final experiment in the navigation accuracy evaluation attempted to provide a much larger dataset to determine the effects of orientation, position and vertebral level on the accuracy of scans. A total of 684 probes, or 342 scans were completed. The details of the factors being tested are outlined below.

The CT-scanned phantoms were scaled to the correct size and printed in matte. Figure 7-20 shows coronal and sagittal views of these phantoms which include T2 to T8 levels on the first phantom (scan T3 to T7) and includes T7 to T12 on the second phantom (scanned T8 to T11).

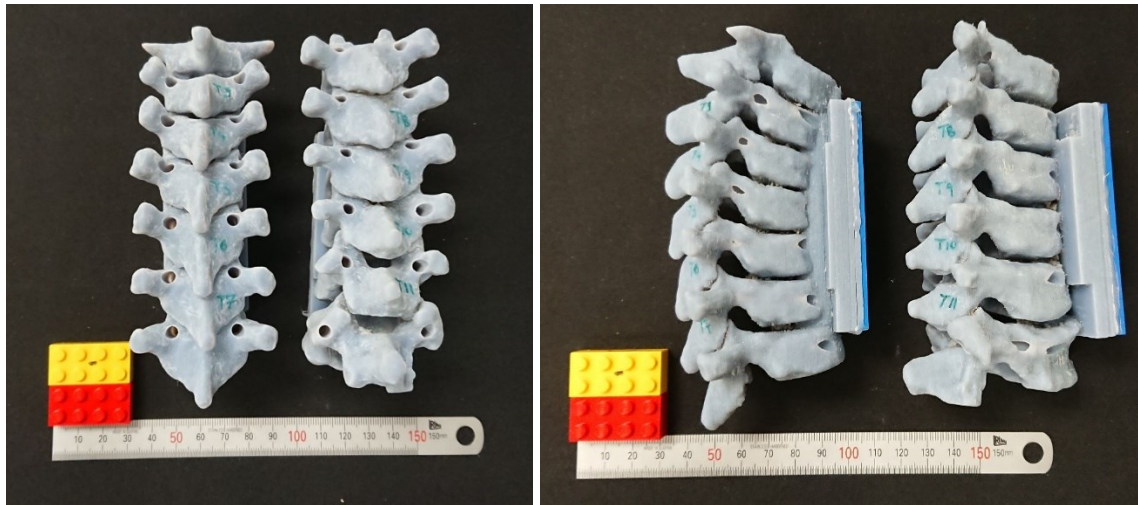


**Figure 7-20: Coronal and sagittal views of the two 3D printed phantoms**

Again, the phantoms included a Lego mount and holes with known trajectory going into the spine. The trajectories are shown in Table 7-3 with T3 to T7 on the first phantom and T8 to T11 on the second phantom.

**Table 7-3: Pedicle hole trajectories for navigation study**

	Left		Right	
Vertebra	Pitch	Yaw	Pitch	Yaw
T3	18° Inferior	10° Medial	18° Inferior	8° Medial
T4	13° Inferior	11° Medial	14° Inferior	13° Medial
T5	10° Inferior	14° Medial	12° Inferior	11° Medial
T6	0°	8° Medial	2° Inferior	5° Medial
T7	2° Inferior	7° Medial	5° Inferior	3° Medial
T8	11° Inferior	10° Medial	10° Inferior	5° Medial
T9	10° Inferior	5° Medial	14° Inferior	3° Medial
T10	4° Inferior	4° Medial	5° Inferior	7° Medial
T11	5° Inferior	0°	3° Inferior	2° Medial

The experimental setup was similar to the pilot test, with the capture volume origin set using the calibration square and then placing one of the phantoms at the origin or at each corner of a 19.2x12.8cm rectangle (24 pegs long by 16 pegs). A smaller length was used to prevent occlusion of markers from the tank walls, which hampered the ability to take reliable measurements for some of the conditions near the boundaries in the previous pilot test. Figure 7-21: Top-down view of pegboard, showing the scale of the calibration square (left) and the T7-T12 vertebra mounted in yaw-negative (left) at center, and T2-T8 vertebra mounted in pitch-negative (up) on the north-east corner shows the experimental setup.

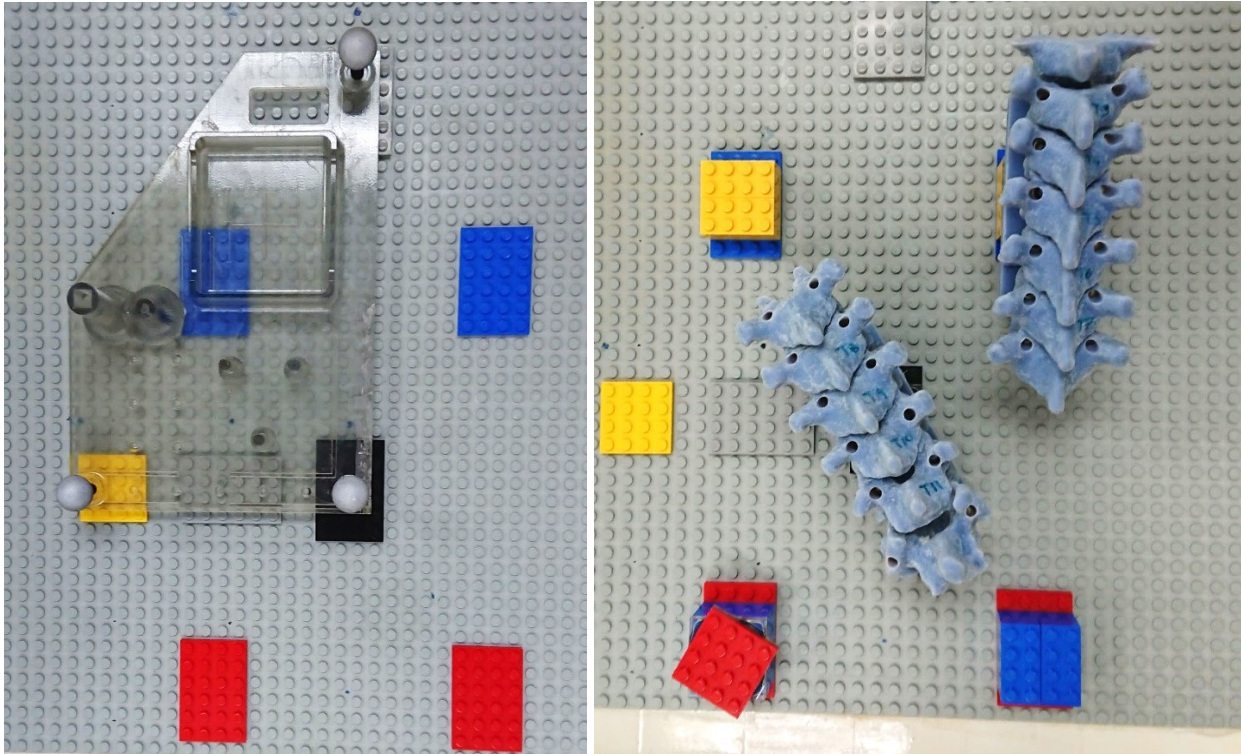


**Figure 7-21: Top-down view of pegboard, showing the scale of the calibration square (left) and the T7-T12 vertebra mounted in yaw-negative (left) at center, and T2-T8 vertebra mounted in pitch-negative (up) on the north-east corner**

Two experiments were undertaken. In the first, the phantom was placed at the capture volume origin then oriented in neutral, and yaw, pitch and roll in both directions. The orientations were altered in this experiment, increasing yaw to  $30^\circ$  in both directions to better represent the potential angles being captured in surgery. Pitch and roll were kept at  $15^\circ$  because the tank was not deep enough to allow for a  $30^\circ$  pitch or roll. The orientation test was repeated due to the previous studies finding that orientation had a larger effect on errors than position. All vertebrae and orientation combinations were completed, with two scans each (9 vertebrae x 7 orientations x 2 scans = 126 scans, 252 probes).

Second, the phantom was placed at each of the four corners of the capture volume in one of the six tilted orientations, and at either the base-plate height or a height of two bricks (19.2mm high). The full set of vertebrae, orientations, positions and heights were not scanned as it would result in a huge number of scans needing to be undertaken (864 scans). Instead, 108 combinations were randomized (for 216 scans), using a balanced approach to ensure that each vertebra, each position, each height and each orientation was represented an equal number of times. The randomized but balanced combinations selected in this experiment are shown in Table 7-4.

**Table 7-4: Vertebra, position, height and orientation combinations**

	Positions								
Orientation	NW-U	NW-D	SW-U	SW-D	SE-U	SE-D	NE-U	NE-D	Extra
Y+	T6	T4	T3	T5	T3	T5	T4	T7	T10A
Y+	T9	T7	T11	T8	T11	T10	T8	T9	T6
Y-	T6	T9	T7	T4	T8	T7	T5	T6	T11
Y-	T3	T5	T8	T10	T9	T11	T10	T3	T4
R+	T8	T10	T5	T4	T4	T3	T6	T5	T3A
R+	T11	T9	T6	T7	T7	T9	T11	T8	T10B
R-	T8	T4	T7	T3	T5	T4	T9	T11	T5
R-	T10	T6	T9	T11	T6	T8	T7	T10	T3B
P+	T3	T11	T4	T6	T11	T3	T10	T5	T7
P+	T5	T8	T9	T10	T7	T8	T6	T4	T9B
P-	T4	T3	T5	T6	T4	T5	T3	T9	T9A
P-	T7	T11	T10	T8	T10	T6	T7	T11	T8
Extra	T10A	T5 T7	T11 T3A	T9A	T9B	T6 T10B	T4 T8	T3B	
NW: Northwest, NE: Northeast, SW: Southwest, SE: Southeast U: Up (2 bricks/19.2mm), D: Down (Baseplate) Y+: Yaw Right, Y-: Yaw Left, R+: Roll Left, R- Roll Right, P+: Pitch Down, P- Pitch Up Extra: Additional vertebra in that position or orientation category									

For both origin and corner experiments, ANOVA analysis was completed to determine if there was a significant difference in entry-point and trajectory errors between the different categories being analyzed. Levene’s test was applied to determine if a conventional ANOVA or a Welch’s ANOVA would be used, with the latter used if variances were not homogeneous. Games-Howell testing was applied post-hoc if there were significant differences between means.

### 7.6.2. Origin Experiment Results

A histogram of the trajectory and entry-point errors are given in Figure 7-22. When combining the trajectory angles and entry-point positional errors together, the average entry-point error was  $0.4 \pm 0.4\text{mm}$  while the average trajectory error was  $2.2 \pm 1.0^\circ$ . One rotational error was larger than the  $5^\circ$  (T5 pitch+) while 12 entry-points were larger than the 1mm technical goal (95.3% success rate) and none were above the 2mm clinical standard[73].

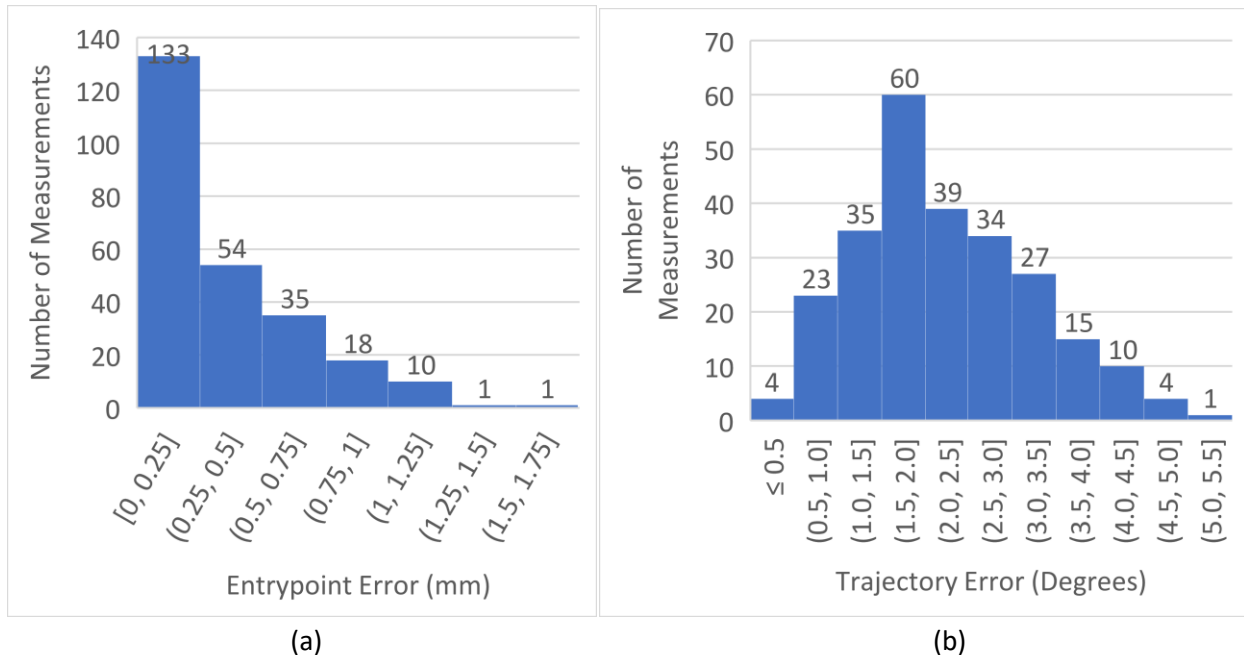


**Figure 7-22: Histograms of (a) entry-point and (b) trajectory accuracy from origin experiment.**

To gain a better understanding of how orientation and vertebral level may have affected results, the individual pitch and yaw trajectories and X and Z entry-point errors were compared using ANOVA analysis.

First, comparing the left hole and the right hole, the mean and standard deviation of each error is given in Table 7-5. A paired t-test showed significant differences for all errors except Z errors, indicating that their mean errors are different. Having holes on the same vertebral body results in their mean errors being similar, but not enough to justify simply measuring one hole's accuracy to represent the other hole's accuracy.

**Table 7-5: Probe insertion errors comparing left and right holes in origin test**

Hole	Pitch Error (°)	Yaw Error (°)	X Error (mm)	Z Error (mm)
Left	0.6±1.5	-1.5±1.3	0.1±0.4	-0.1±0.4
Right	0.4±1.4	-1.5±1.2	-0.1±0.4	-0.1±0.4
P-values	$p < 0.01$	$p < 0.01$	$p < 0.01$	$p = 0.76$

The accuracies according to orientation of vertebrae are shown in Figure 7-23. Overall, the average pitch error was  $0.5 \pm 1.6^\circ$  and the error for yaw was  $-1.5 \pm 1.3^\circ$ . The average X (medio-lateral) error was  $0 \pm 0.4\text{mm}$  and  $-0.1 \pm 0.4\text{mm}$  for Z (cephal-caudal) error.

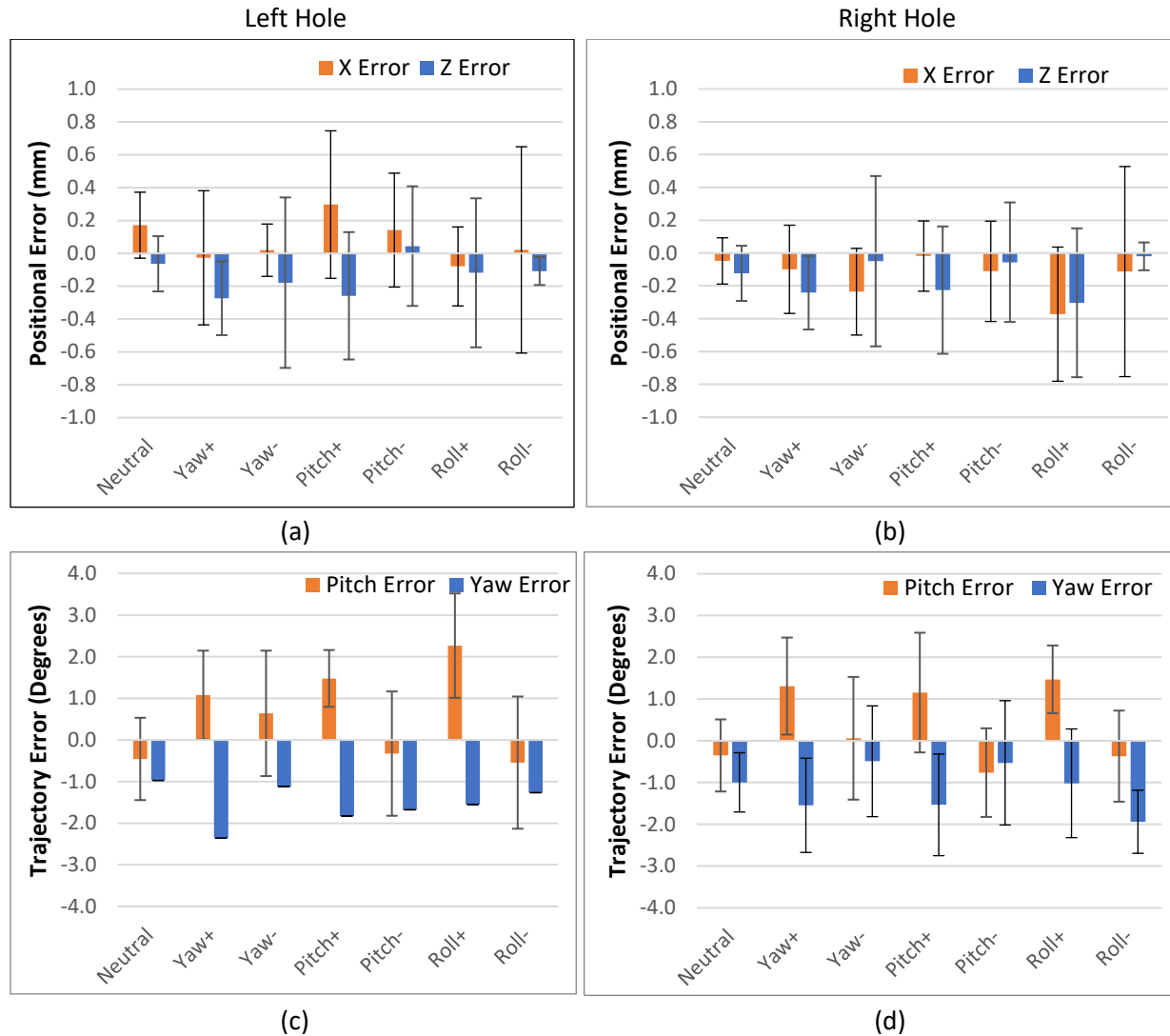


**Figure 7-23: Mean error and standard deviation of entry-point (a,b) and trajectory (c,d) errors from probing the left hole (a,c) and the right hole (b,d), analyzed according to orientation.**

The graphs show a few important results. First, the neutral orientation tends to have the most repeatable results, having the smallest standard deviation (except Z-error in Roll-). This is likely due to the orientation being aligned to the calibration square. Second, there is a systematic error in both pitch and yaw rotations, with all the yaw errors being negative (average  $-1.5^\circ$ , range  $-1.1$  to  $-2.4^\circ$ ), and most of the pitch errors being positive (average  $1.5^\circ$ , range  $-0.5$  to  $2.3^\circ$ ). The rotational calibration of the system may need to account for these systematic errors.

Levene's tests for homogeneity of variances showed significant differences in entry-point and trajectory variances and so Welch's ANOVA was applied. Significant differences were found for entry-point and trajectory errors except Z-position errors in the left hole. All p-values from all the ANOVA analyses are



shown in Table 7-7: Mean, standard deviation, range of means of entrypoint and trajectory errors in each category and ANOVA results from origin and corner tests.

Post-hoc testing showed no statistically significant differences in entry-point error for either X errors or Z errors in either left or right holes, regardless of the orientation. For pitch trajectory error for both holes, orientations in neutral, pitch- and roll- were statistically different from yaw+, pitch+ and roll+. The yaw- orientation was not different between orientations in the left hole but was different from the second group in the right hole. For yaw error, only the neutral and yaw+ orientations were statistically different in the left hole. Larger errors are found in the yaw+, pitch+ and roll+ in Figure 7-23. An obvious experimental reason for these errors being increased could not be identified. Further investigation into the source of these errors, the effect of camera position and marker position on these orientations could be warranted.

There were systematic errors in the positional errors in the left hole, all of which were negative. However, their magnitude was small, with average errors within 0.1mm for both right and left holes in both the X and Z directions. Although it is good to know that positional errors do not vary significantly depending on the orientation of the vertebra, the positional errors approaching the 2mm mark remain a concern for position variations.

Figure 7-24 shows the mean and standard deviation of entry-point and trajectory errors, organizing according to which vertebra was scanned.

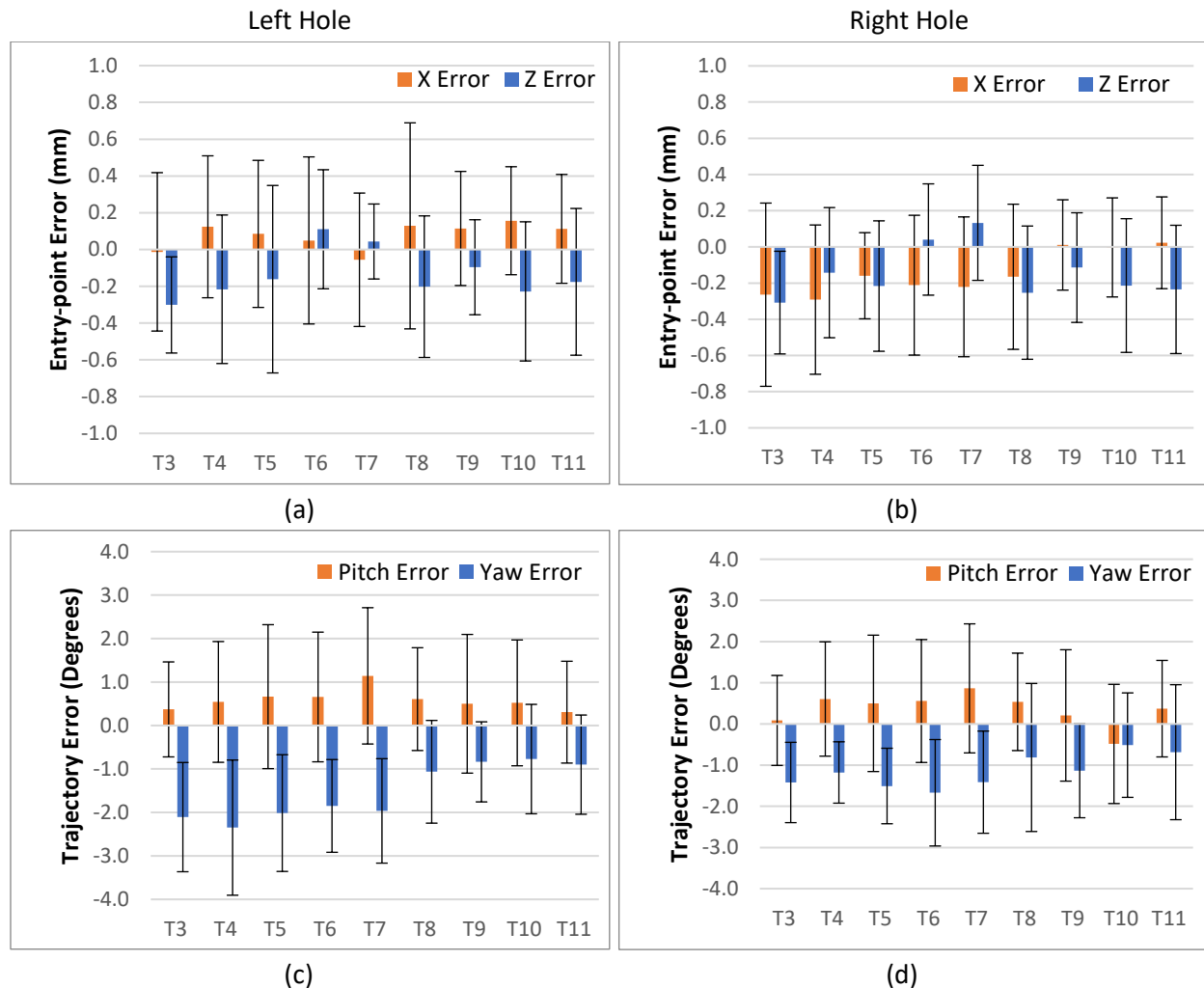


**Figure 7-24: Mean error and standard deviation of entry-point (a,b) and trajectory (c,d) errors from probing the left hole (a,c) and the right hole (b,d), analyzed according to vertebra.**

For this test, the variances were found to be homogeneous. ANOVA analysis only found a difference in errors for yaw in the left hole, and Z-errors in the right hole. For Z-errors in the right hole, post-hoc testing showed that only T3 error differed from T6 and T7 statistically. The small errors in T6 and T7 could be due to the algorithm originally using the T6 vertebra as the template for image registration.

Post-hoc testing showed that for yaw error in the left hole, T4 was different from T9 and T10. From Figure 7-24c, the vertebrae on the first phantom (T3 to T7) have a larger error at close to  $-2.0^{\circ}$  compared to the second T8 to T11 phantom at  $-1.0^{\circ}$ . While the exact cause is unknown, the first phantom's mount may have had a slight tilt resulting in larger yaw rotations than expected. Overall, the fact that there were only two statistically significant differences (differing by 1-1.5°, within clinical significance) showed that vertebral level had a minimal impact on entry-point and trajectory errors.

### 7.6.3. Corner Experiment Overall Errors

A histogram of the entry-point and trajectory errors from the corner experiment is shown in Figure 7-25: Histograms of (a) entry-point and (b) trajectory accuracy from corner experiment. None of these errors exceeded 2mm or 5° while 19/432 exceeded the 1mm technical target (95.6% success rate). The average positional error was  $0.5 \pm 0.3$ mm while the average trajectory error was  $2.0 \pm 0.8^\circ$ . These results are promising in providing adequate accuracy for surgery. The average processing time was  $8.9 \pm 1.4$ s which would also be adequate for surgery.

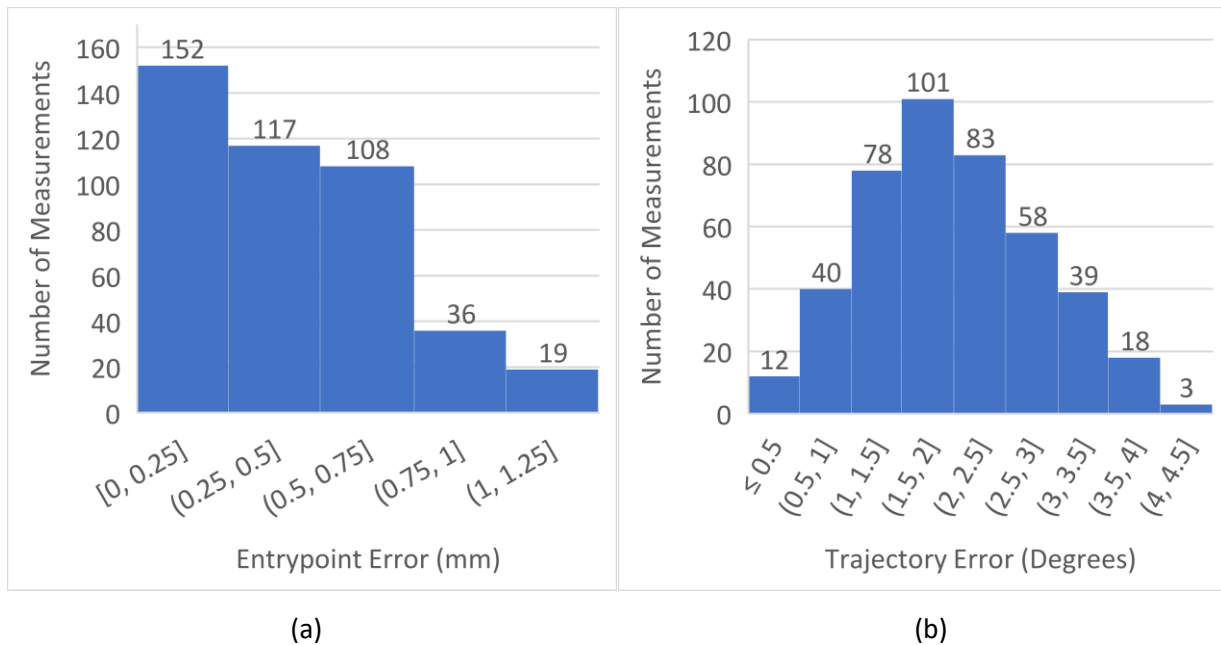


**Figure 7-25: Histograms of (a) entry-point and (b) trajectory accuracy from corner experiment**

Although these values are within the desired range, it would be useful to determine if there may have been a relationship between scan position, vertebral orientation or vertebral level on results. Analysis was performed to determine the effect of left vs right holes, position on the X and Z plane, the height of the vertebra, the orientation of the vertebra and the vertebral level. The average pitch error was  $0.4 \pm 1.5^\circ$  while the average yaw error was  $-0.8 \pm 1.3^\circ$ . The average X-error (transverse) was  $0.1 \pm 0.3$ mm while the average Z-error (axial) was  $-0.1 \pm 0.5$ mm. These values corresponded closely with the origin test errors.

### 7.6.4. Corner Experiment: Left vs Right Holes

Table 7-6 shows the average errors in each dimension for the left vs right holes. Comparing the accuracy when inserting into the left vs right holes, the paired t-test showed that both trajectory errors were statistically significant, as well as the Z (cephal-caudal) entry-point errors. This was opposite to the origin experiment. The Z-error standard deviation was larger than the X-error standard deviation though this

was still within clinical accuracy. This result aligned with the 3D ultrasound calibration results showing poorer repeatability in the Z-direction, due this being the camera depth direction, and due to it being the ultrasound transducer elevation direction.

**Table 7-6: Probe insertion errors comparing left and right holes in corner test**

Hole	Pitch Error (°)	Yaw Error (°)	X Error (mm)	Z Error (mm)
Left	0.4±1.5	-0.9±1.4	0.1±0.3	0.0±0.5
Right	0.3±1.4	-0.7±1.3	0.1±0.3	-0.2±0.5
P-values	$p < 0.05$	$p < 0.05$	$p = 0.45$	$p < 0.05$

7.6.5. Corner Experiment: Errors vs Position (Cardinal Directions)

Figure 7-26 displays the pitch, yaw, X (transverse) position and Z (axial) position errors, analyzed according to their position on the pegboard.

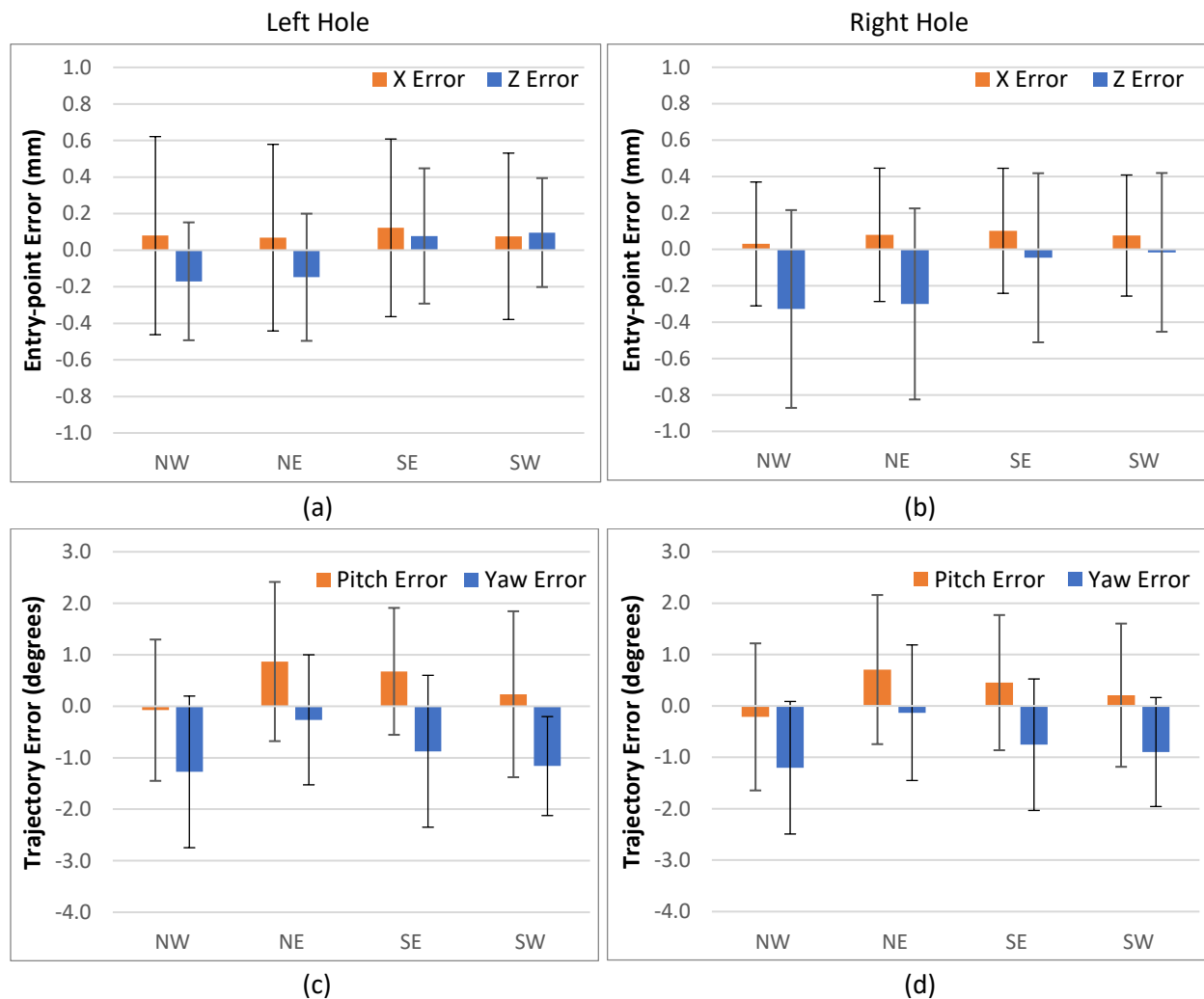


**Figure 7-26: Mean error and standard deviation of entry-point (a,b) and trajectory (c,d) errors from probing the left hole (a,c) and the right hole (b,d), analyzed according to position on pegboard**

From Welch's ANOVA analysis the X position was not statistically significant for either hole ( $p=0.88$  for left and  $p=0.74$  for right) while the Z-error and both trajectory errors had statistically significant differences. From the post-hoc analysis for Z-positional errors, there were differences in the NW and SW errors in the left hole while in the right hole, both NW and NE errors differed from SE and SW errors. There appeared to be a position-dependence in errors with the north positions being closer to the cameras and having larger errors than the south positions.

For pitch errors, the NW and SW corners differed from the NE corner for pitch error, while the NW corner differed from the SE only in the left hole. For yaw errors, the NW and SW errors only differed from the NE positions for both holes. The SE corner had no difference from any other position. Trajectory error seemed affected by where the measurements were being recorded. This could be explained by the cameras being at a sharper angle to the probe in the closer regions, resulting in more marker overlap. These results aligned with the positional accuracy findings in Section 5.6.

### 7.6.6. Corner Experiment: Errors vs Height

Figure 7-27 compares errors in pitch, yaw, X-position, and Z-position according to testing height.

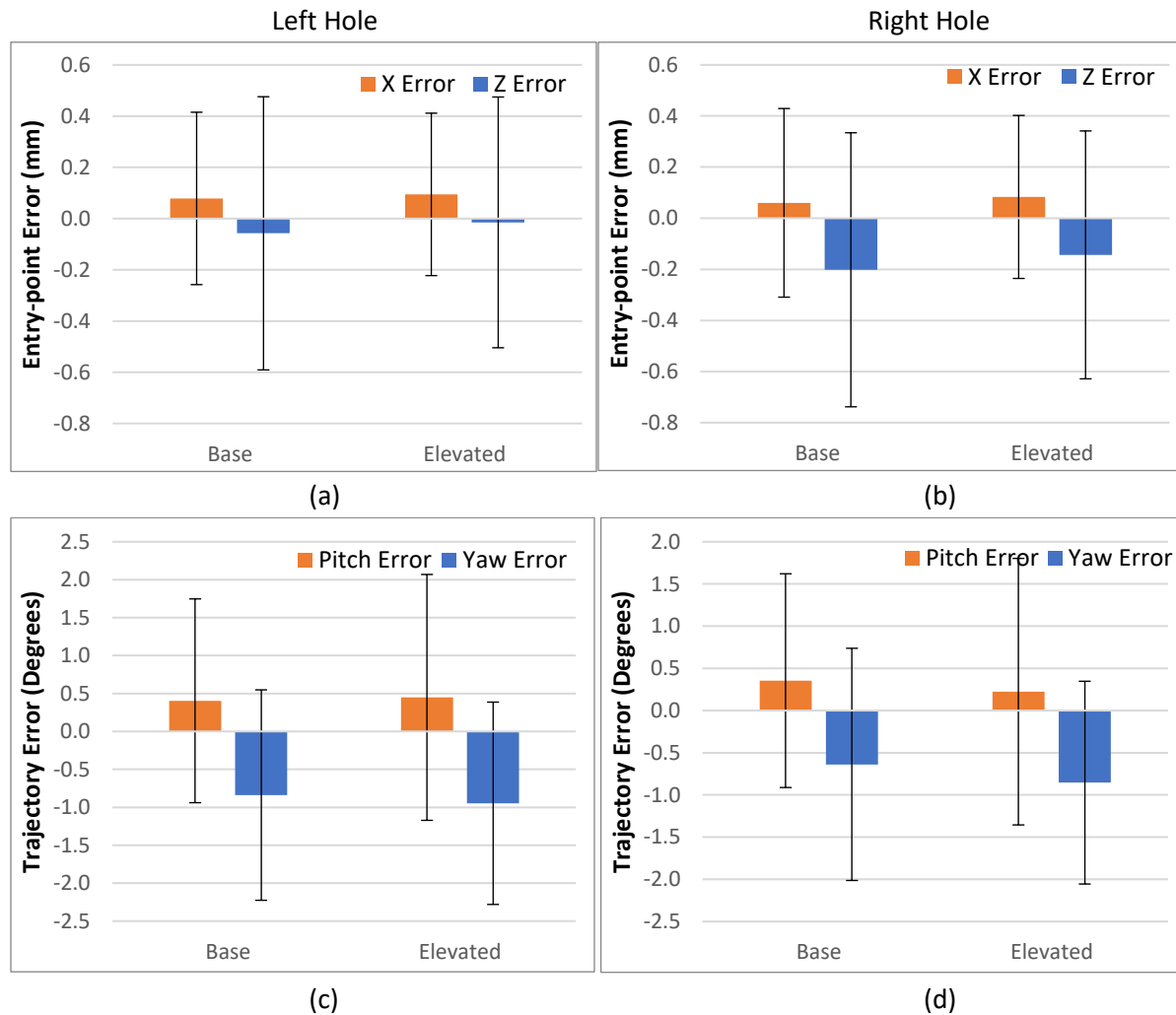


**Figure 7-27: Mean error and standard deviation of entry-point (a,b) and trajectory (c,d) errors from probing the left hole (a,c) and the right hole (b,d), analyzed according to height on pegboard (0mm and 19.2mm heights)**

There was no difference between base and elevated positions for any of the accuracies, indicating that the height variations did not influence placement errors.

### 7.6.7. Corner Experiment: Errors vs Orientation

Figure 7-28 compare the accuracies of pitch, yaw, X-position and Z-position according to the orientation of the vertebral placement.

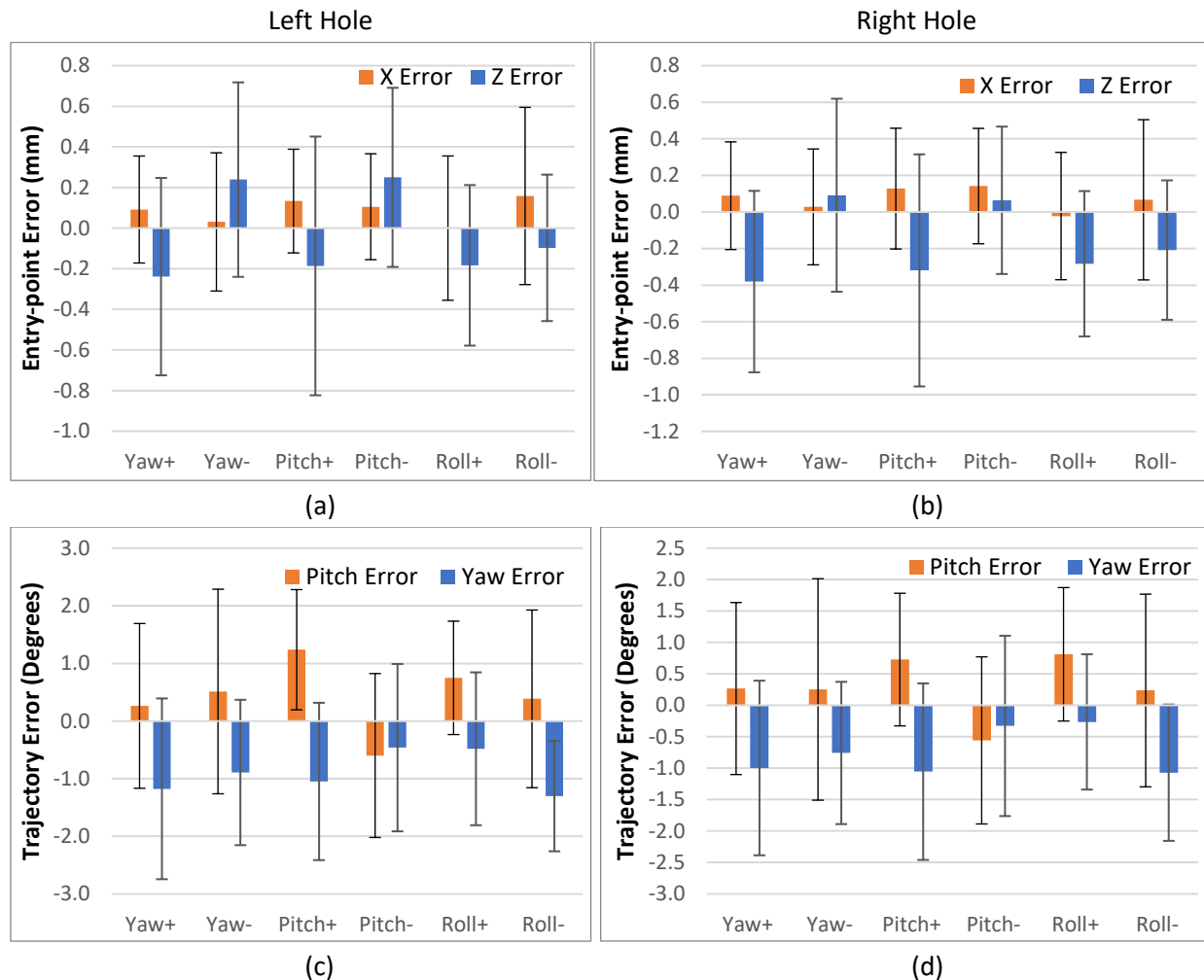


**Figure 7-28: Mean error and standard deviation of entry-point (a,b) and trajectory (c,d) errors from probing the left hole (a,c) and the right hole (b,d), analyzed according to six vertebral orientations**

From the Welch's ANOVA analysis of positional errors, the X-position errors in both holes were not significantly different ( $p=0.29$  for left and  $p=0.33$  for right) but Z-position errors were different for both ( $p<0.05$ ). From post-hoc testing, the Z-errors from tilting the vertebra in Yaw+, Pitch+, Roll+ and Roll- were statistically different from Yaw- and Pitch- in both left and right holes. Comparing with the origin tests in Section 7.6.2, a similar pattern was found where the Z-errors in the Yaw+, Pitch+, Roll+ and Roll- orientations were more negative than the Yaw- and Pitch- errors. However, the in the origin test were not statistically significant.

The trajectory error differences were significant for both pitch and yaw orientations in both holes ( $p < 0.05$ ). From post-hoc testing, the pitch trajectory error from tilting the vertebra in Pitch- differed from Pitch+ and Roll+ for both holes. For the left hole, Pitch- differed from Yaw- and Roll- as well, though all these errors were close to zero. The pitch error was worse for the Pitch+ orientation, which corresponds with the probe being tilted towards the cameras resulting in potential marker occlusion. For yaw trajectory error, there were no statistically significant differences between different orientations from post-hoc testing.

Comparing with the origin test in Section 7.5.2, for pitch trajectory error, the Pitch+ and Roll+ errors performed the worst in both origin and corner tests. For yaw trajectory errors, orientations with the worst performance Yaw+, Pitch+ and Roll- had the worst performance in both tests as well. In both tests, the error was negative, which suggests there is a systematic error present across the orientations. This consistent trend indicates that there are systematic errors that could be accounted for with further investigation. Further investigation into these errors may allow the navigation errors to be improved.



### 7.6.8. Corner Experiment: Errors vs Vertebral Level

Figure 7-29 compares the errors in pitch, yaw, X-position and Z-position according to the vertebral level.

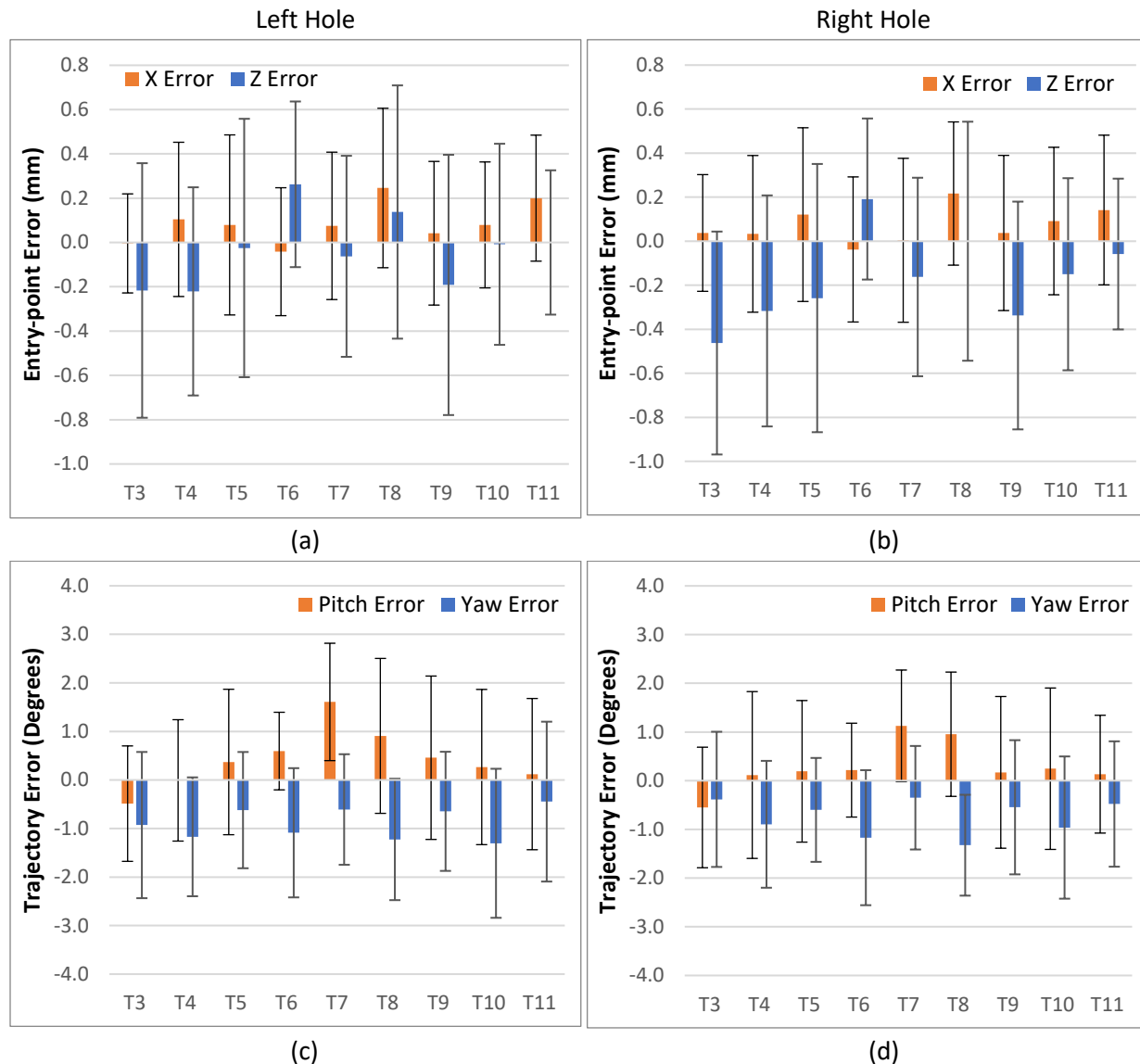


**Figure 7-29: Mean error and standard deviation of entry-point (a,b) and trajectory (c,d) errors from probing the left hole (a,c) and the right hole (b,d), analyzed according to vertebral level**

From the Welch's ANOVA analysis of entry-point errors, the Z-errors were statistically significant between levels ( $p < 0.05$ ) while the X-errors were only different for the left hole, not the right ( $p = 0.28$ ). In post-hoc testing, for the Z-direction, the only statistically significant difference was the T6 from T3, T4 and T9 in both holes. The Z-errors had larger variations, though errors remained below 0.5mm. The larger negative errors in the T3-T5 levels and the positive errors in T6 corresponded with the origin test, though the T6

errors in the origin test were closer to zero. The X-direction had no significant difference in entry-point errors between vertebrae from post-hoc testing.

For trajectory, the pitch errors were statistically significantly different between vertebral levels ( $p < 0.05$ ). Yaws were not significant for either hole. From post-hoc testing, the T7 vertebra in the left hole was significantly different from the T3, T4, T10 and T11 levels for pitch while T8 was different from only T3. The peak in pitch errors in the T7 vertebra also corresponded with the origin test. For the right hole, both T7 and T8 differed only from T3. There appeared to be some increase in errors from the T7 and T8 vertebrae from this study, perhaps because these were the end vertebrae on their respective phantoms.

A summary of the ANOVA findings from both the origin and the corner tests is displayed in Table 7.7. The mean and standard deviation of each error is shown. The range of means within each category is also shown (eg: the range of means for each orientation).

Probe placement accuracies are affected the most by position on the build plate and orientation of the vertebra. Varying height did not affect accuracy results. The T6 vertebra had different and worse errors than the other vertebrae in the Z-direction entry-point, while the T7 and T8 vertebrae had different and worse errors than the others the pitch trajectory. Importantly though, all the mean errors were within the 5° and 2mm accuracy targets, while more than 95% of the positional errors within 1mm. These results help direct where further investigation may be required which will be discussed in the next section.

**Table 7-7: Mean, standard deviation, range of means of entypoint and trajectory errors in each category and ANOVA results from origin and corner tests**

<b>Origin Test</b>					
<b>Hole</b>	<b>Error Mean±SD</b>	<b>Position</b>	<b>Height</b>	<b>Orientation</b>	<b>Vertebra Level</b>
<b>Left</b>	Pitch (°) 0.4±1.4			-0.5 to 1.9 p<0.05	-0.5 to 0.9 p=0.96
	Yaw (°) -1.2±1.2			-2.0 to -0.8 p<0.05	-1.7 to -0.5 p<0.05
	X (mm) -0.1±0.4			-0.4 to 0.0 p<0.05	-0.3 to 0.0 p=0.89
	Z (mm) -0.2±0.4			-0.3 to 0.0 p=0.09	-0.3 to 0.1 p=0.06
<b>Right</b>	Pitch (°) 0.7±1.8			-0.5 to 2.1 p<0.05	0.2 to 1.1 p=0.39
	Yaw (°) -1.6±1.4			-1.1 to 2.3 p<0.05	-2.4 to -0.9 p=0.17
	X (mm) 0.1±0.3			-0.2 to 0.3 p<0.05	-0.1 to 0.2 p=0.12
	Z (mm) 0.1±0.5			-0.2 to 0.0 p<0.05	-0.2 to 0.3 p<0.05
<b>Corner Test</b>					
<b>Hole</b>	<b>Error Mean±SD</b>	<b>Position</b>	<b>Height</b>	<b>Orientation</b>	<b>Vertebra Level</b>
<b>Left</b>	Pitch (°) 0.4±1.5	-0.1 to 0.9 p<0.05	0.4 to 0.4 p=0.83	-0.6 to 0.8 p<0.05	0.0 to 1.6 p<0.05
	Yaw (°) -0.9±1.4	-1.2 to -0.3 p<0.05	-0.9 to -0.8 p=0.56	-1.3 to -0.5 p<0.05	-1.2 to -0.4 p=0.27
	X (mm) 0.1±0.3	0.1 to 0.1 p=0.88	0.1 to 0.1 p=0.72	0.0 to 0.2 p=0.39	0.0 to 0.2 p<0.05
	Z (mm) 0.0±0.5	-0.2 to 0.0 p<0.05	-0.1 to 0.0 p=0.54	-0.2 to 0.3 p<0.05	-0.2 to 0.3 p<0.05
<b>Right</b>	Pitch (°) 0.3±1.4	-0.2 to 0.7 p<0.05	0.2 to 0.4 p=0.50	-0.6 to 0.7 p<0.05	-0.6 to 1.1 p<0.05
	Yaw (°) -1.6±1.4	-1.2 to -0.1 p<0.05	-0.9 to -0.6 p=0.22	-1.1 to -0.3 p<0.05	-1.2 to -0.4 p<0.05
	X (mm) 0.1±0.3	0.0 to 0.1 p=0.74	0.1 to 0.1 p=0.62	0.0 to 0.1 p=0.31	0.0 to 0.2 p=0.28
	Z (mm) -0.2±0.5	-0.3 to 0.0 p<0.05	-0.2 to -0.1 p=0.40	-0.4 to 0.1 p<0.05	-0.5 to 0.2 p<0.05

### 7.6.9. Discussion

Out of a total of 252 origin probe placements and 432 corner probe placements, there was one probing that failed accuracy criteria due to a rotation  $>5^\circ$ , no placements that failed accuracy criteria due to  $>2\text{mm}$  placement, and 31 placements that failed technical criteria of 1mm (4.5%). While the results are promising, continued work needs to be undertaken to reduce systematic errors in rotation and determine the conditions for which accuracy is likely to worsen.

As mentioned previously, there were systematic errors present in the trajectory results in this experiment, noted by the average pitch error being  $0.4 \pm 1.5^\circ$  and the average yaw error at  $-0.8 \pm 1.3^\circ$ . Further work in evaluation orientation error repeatability likely need to be completed to determine if these errors can be further reduced. The current method of calibrating the ultrasound and probe involves mounting the two devices on mounts that are on the calibration square. There may be a correction factor that can be applied after mounting the devices to account for this error.

Additional improvements could include creating a more robust 3D ultrasound calibration system, performing orientation repeatability tests, or making more detailed measurements on the experimental design itself. In particular, since the trajectory errors are based on comparing the Euler angles displayed on-screen and then compared to the ideal orientation of the holes, there may be real-world errors that appear, including warping in pegboard when weighed down with water, or the vertebra not sitting perfectly flush against the pegboard. In this scenario, the quantified errors from this experiment would exceed the real-life errors.

For entry-point error, there were minimal systematic errors as the average errors were close to zero with the X-error (transverse) at  $0.1 \pm 0.3\text{mm}$  and the Z-error (axial) at  $-0.1 \pm 0.5\text{mm}$ . Importantly, all measurements were made with the probe facing the cameras at the same roll angle (roll about the axis of the probe), to ensure consistency of results. As mentioned previously, when rotating the probe while it was in the hole, the on-screen probe would erroneously translate, indicating that the transform between the markers and the probe was not perfect. To alleviate this issue, either a mechanical system would need to be a designed that allows screw rotation without moving the probes (common in navigation systems), or a more detailed calibration process would need to be developed.

In the ideal case, none of the variables tested here (position, height, vertebral orientation and vertebral level) would affect accuracy results. While this was true of height, this was not true for position and orientation which both influenced placement accuracy. For position, the worsened positional accuracy

when closer to the cameras was also found in previous 3D ultrasound tests (Section 5.6). Having worsened yaw trajectory accuracy on the west side of the capture volume and worse pitch trajectory accuracy on the east side was new. It would be best to determine the optimal working range of the cameras to ensure they could fit in the confines of the operating room. The camera frame was designed to allow 30cm adjustments in any direction which could be enough to reduce marker occlusion issues. A re-designed marker arrangement would be another improvement.

Regarding vertebral level, both the pitch angle and the Z-error had statistically significant differences between different levels. From both origin and corner tests, pitch angle for T7 and T8 are more problematic in their errors. Z-errors were increased in the T3 and T4 vertebrae which could be from their relatively kyphotic angle or because they are closer to the cameras when mounted.

It is also interesting that it is the vertebral levels that are near the ends of their phantoms that had greater errors. There may have been a small amount of warping in the phantoms, or the Lego attachment may have loosened slightly, resulting in some tilting of the phantom when inserting the probe. One of the key problems is that trajectory errors are measured against ideal values, unlike the entry-point where the probe is physically inserted into the vertebral hole and the error is measured against the visualized probe position versus the virtual phantom. It would be ideal to include a virtual protractor on the displayed probe to directly measure the angle between the probe and the vertebral hole to remove any potentially experimental design errors.

Compared to the current literature, older studies have found CT surgical registration accuracies in the spine close to  $1.3 \pm 0.1$ mm when using navigation probes to evaluate screw placements[127]. Surgical registration studies on the skull have found target registration errors of between 0.7 to 1.2mm [245–247] when performing CT surgical registrations and then measuring fiducial markers or key landmarks. Accuracies in the submillimeter range remain the best of what navigation systems can offer. Trajectory accuracies have not been reported for these systems, likely due to the different application of surgical registration in the otolaryngology field.

One of the key challenges in this field is that while numerical accuracy is useful, the most important and widely used clinical marker of navigation accuracy is the presence of a breach. Most clinical studies report breaches in 2mm increments on a post-operative CT and do not report how accurate navigation systems are. As a result, it is difficult to compare this 3D ultrasound navigation system to the wide array of screw

insertion accuracy studies. Further study in using the system to insert screws in porcine or cadaver spines would allow comparison of this navigation system with those studies.

## 7.7. Surgeon Demonstration

### 7.7.1. Demonstration Setup

The final portion of this thesis project involved showing the ultrasound navigation system to an orthopedic surgeon. The navigation equipment was packed and transported to a separate room to test the setup time for navigation. The setup process required approximately 30 minutes to connect the cameras and 3D ultrasound, as well as create the capture volume space with the wanding process. Calibration of the probe and 3D ultrasound required an additional 5 minutes. The surgeon had an opportunity to test out the ultrasound scanning process, shown in Figure 7-30.

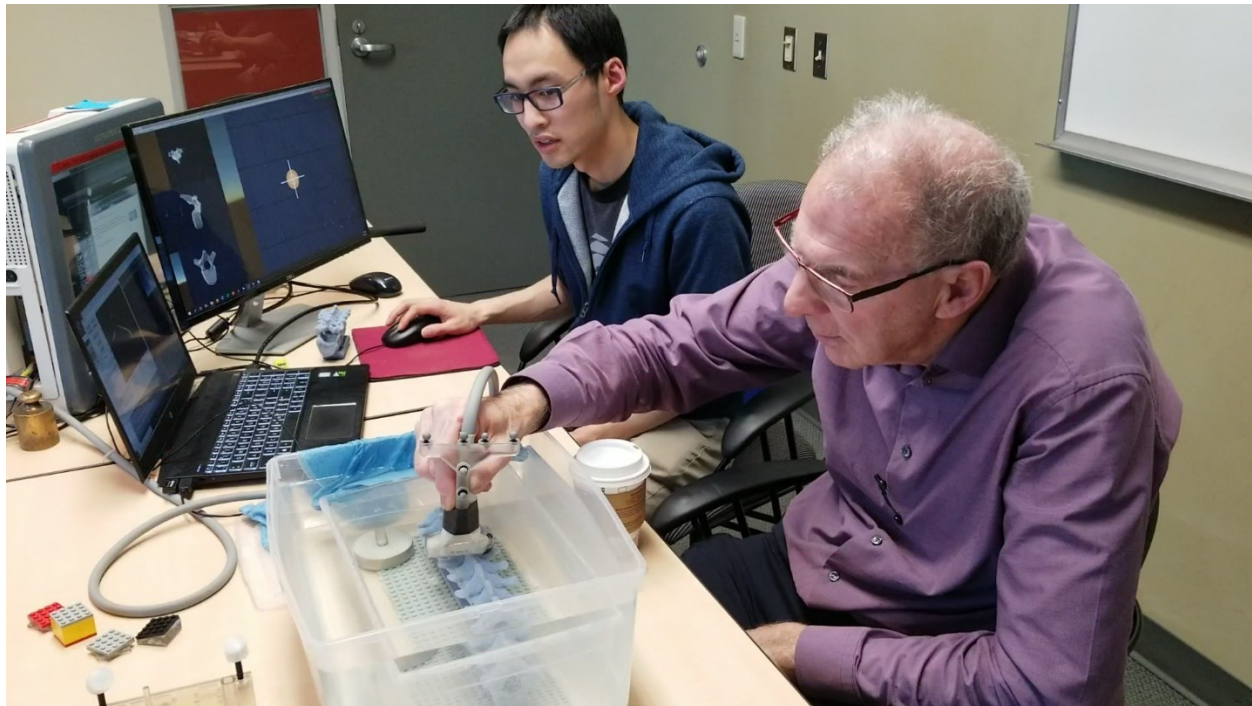


**Figure 7-30: Surgeon performing 3D ultrasound scan on a phantom spine.**

Scans were demonstrated on two phantoms. First, the phantom from the Figure 7-20 experiment including pedicle holes was scanned. From these scans, the accuracy of the system was demonstrated, with the probe being within 1mm of the required entry-point during insertion. Second, the same phantom without pedicle holes was scanned once by the orthopedic surgeon and the probe was placed in the position that the orthopedic surgeon expected to place the screw if inserting it free hand. The navigation display showed no pedicle breach based on this position.

### 7.7.2. Surgeon Feedback

The main strengths of this system as described by the surgeon were the ionizing radiation-free nature of the navigation system and the high speed of the registration algorithm allowing feedback on screw placement to return very quickly. The spine cavity could be easily filled with saline during surgery and an ultrasound machine could be made readily available for ultrasound scanning. With a scan requiring only 10-15s and processing times in the 10s range, this system could quickly give surgeons visual feedback on where their screws are being placed.

The motion capture calibration process and the usage of probing tools is already accepted in orthopedic surgery, making the learning curve less daunting for first-time users of this US system. As for the display only showing a model rather than orthogonal views on a CT scan, the surgeon saw no disadvantage to simply using the model. Having the model instead of slices allowed for the probe to be more intuitively localized and placed into the pedicle. This would be particularly useful when probing the pedicle hole to ensure that the hole was not medially breaching the pedicle.

The primary weakness that was revealed was that any movement in the cameras could cause the motion capture system to lose their calibration. During the demonstration, one or more of the cameras lost their calibration. Whether it was due to the pre-heat time being too short, or due to accidental bumping the frame, the probe could no longer be reliably tracked, and the system needed to be re-calibrated. While the motion capture frame was designed to minimize movement, it would be better to have cameras mounted on an overhead gantry, out of reach of the surgery activities. In addition, a simplified calibration process in setting up the capture volume and squaring the ultrasound probe and the pointer probe to the capture volume would improve the acceptability of the system in the event of camera disturbance.

The actual views displayed on the navigation screen were also areas that needed further improvement. Figure 7-31 shows the navigation screen on the right monitor, with the screw-axial view as the largest window on the display (right) and the orthogonal views as smaller views on the left.



**Figure 7-31: Navigation display showing pedicle probe (yellow/red cylinders) placed into pedicle holes**

It was difficult for the surgeon to get proper orientation from the main screen alone because the camera moved with the screw, rather than remaining stationary while the probe moved within the camera view. The orthogonal views were also found to be too small. Fine-tuning of the display for the surgeon's preferences would need to be undertaken prior to further experimentation with the surgeons. Overall, the reception to this navigation was positive in offering a flexible, fast, and radiation-free method of pedicle screw insertion.

## 7.8. Conclusion

A custom navigation 3D environment was developed to validate measurements from the 3D ultrasound image registration guidance system. A segmented spine from a CT scan of a real patient was used to create the phantom and perform registrations, and the surgical registration accuracy of the system was found. While the results were largely successful (95.5% within 1mm and 5° from 684 probe placements, display time at <20s) there remain improvements that could be made to orientation measurements, and minimizing systematic sources of error (camera positioning, and orientation measurement changes)

The next steps to improving this system will be presented in Chapter 8:



## Chapter 8: Conclusion

### 8.1. Summary

This chapter reports the status of the navigation system as designed and evaluated in this thesis report. Section 8.2 summarizes the final results from this navigation system. Section 8.2.2 outlines potential challenges and future work to bring this system to clinical usage.

### 8.2. Summary of Thesis Work

#### 8.2.1. Current Status of the Navigation System

This thesis has outlined the process of developing a novel 3D ultrasound-based navigation system for spine surgery from basic technological components (motion capture cameras, conventional medical ultrasound, image registration algorithms, 3D virtual display) to an integrated system that could be used in the operating room. The system requires a pre-segmented model of the vertebrae and the model in a 3D volume image format. At its base level, the system only requires motion capture information (positions and rotations) that are calibrated to an ultrasound machine that displays individual frames.

From a software perspective, the system currently uses Matlab to perform image processing and image registration which is then outputted directly to the model file. Unity is then used to import the vertebral model file and to display streamed data from the motion capture cameras.

This project has demonstrated that the navigation software is feasible for surgical use. The accuracy of the system is  $0.5 \pm 0.3$ mm and  $2.0 \pm 0.8^\circ$  and with an average processing time of  $8.9 \pm 1.4$ s, based on 216 ultrasound scans and 432 screw placements, comparable to current CT navigation systems at 1mm [127,245]. The system is accurate for rotations at up to  $30^\circ$  yaw and  $15^\circ$  pitch and roll, within a  $19.2 \times 12.8 \times 1.92$ cm range centered around the capture volume origin, with accurate results from T3 to T11 vertebrae for both adult and child sized phantoms. While the orientation and positional range would cover the majority of spinal positions, it would be important to expand the range further to ensure robustness of the system.

In a more general sense, this thesis has taken the approach of using available technology and experimental techniques and has combined them to achieve these successful results. Commercial-grade motion capture cameras were found to have submillimeter accuracies relative to the real-world from Chapter 4 but had even better accuracies when different rigid bodies are calibrated within that space and measured relative to each other as shown in Chapter 7. For 3D ultrasound reconstruction, the basic nearest-neighbor pixel-

based reconstruction was fast enough and provided enough information about ultrasound surfaces for registrations to be successful from Chapter 5. Registrations could be fast and successful by simply scaling the images and using the symmetry of the vertebrae to pre-register, and surface registration to fine-tune the registrations from Chapter 6. The ability to add different calibration tools virtually to a 3D environment connected to the motion capture system was invaluable in evaluating the accuracy of this system in Chapter 7.

Throughout this thesis, Lego was used as a surprisingly useful and powerful tool to conduct positional measurements, allowing for high flexibility and highly repeatable measurements to be made. Polyjet 3D printing using the Stratasys Objet 30 printer was another important technology, in printing calibration blocks, spinal phantoms, and calibration probes. The speed at which new iterations of these highly accurate tools could be produced would not have been possible even fifteen years ago.

The innovations in this project have not been in the development of completely novel techniques or algorithms to perform image registration. Instead, the innovation has been the integration of all of these technologies in a unique way that was able to provide an accurate, radiation-free and fast navigation tool that can help give peace of mind to surgeons and potentially reduce the risk of life-debilitating injuries to scoliosis patients. Key to the system is the usage of ultrasound for navigation, which has been used for spinal registration but not for spinal navigation thus far. Keeping things simple and empirical has allowed the results to speak for themselves, with the probe placement results directly demonstrating the accuracy of this system. While there is still significant work to be done before this system is robust enough and streamlined enough for clinical testing, the results show great promise in providing radiation-free image guidance.

### 8.2.2. Original Contributions

The following are the main original contributions of this thesis project

1. Systematic review of key clinical evidence in favour of guidance to reduce pedicle breaches.
2. Evaluation of commercial-grade motion capture system for surgical navigation
3. Development of a bone-surface 3D ultrasound imaging system for bone localization
4. Development of a two-step automated registration method for 3D ultrasound and CT images of the vertebrae
5. Validation of guidance system in providing accurate pedicle screw entry-point and trajectory information

## 8.3. Challenges and Future Works

### 8.3.1. Hardware Improvements

Further improvements and investigation take the form of hardware updates, software streamlining, clinical evaluation and advancing display technology. From a hardware perspective, there are multiple areas that should be upgraded or changed to maximize usability in the operating room.

Regarding the motion capture system, the cameras themselves are likely adequate for surgery, though comparison with more conventional medical-grade cameras could be useful to determine if there is marked improvement. However, the main area of improvement for the capture system is in the calibration process.

All motion capture systems require a wanding process. Because this can be completed prior to the surgery itself and can be done in a relatively short period of time (<5 minutes), it would not be a barrier to usage. However, the calibration of the capture volume, the screw-driver probe and the ultrasound itself needs to be streamlined. The data presented in this chapter showed that there were systematic errors in the orientation of the probe.

A fully fleshed-out calibration process for the probe and the ultrasound needs to be undertaken to minimize these systematic errors. This study used a static system where the ultrasound and the probe were rigidly mounted to the calibration square itself to calibrate their orientations and positions. It may be that a dynamic system that uses a calibration ultrasound scan alongside dynamic movement and probing with the pedicle probe would be more robust in providing accurate calibrations. In this thesis, the static calibration method was chosen because of its simplicity and speed, but further improvements in accuracy may require a more robust method. Similarly, further evaluation of temporal calibration, particularly when moving at different speeds, needs to be completed to ensure reconstructions remain accurate when moving faster than the 3-5mm/s speed outlined in the thesis.

The motion capture markers need to be added to surgical hardware, similar to current navigation systems. For the screwdriver itself, it may be necessary to design a device that allows the markers to stay in one position while the screwdriver itself is turning to allow for more accurate screw placement. Designing more robust and permanent methods to fix the markers on the ultrasound transducer also need to be designed, by using tighter friction fits or directly screwing markers onto the transducer. Lastly, sterilization of these tools needs to be fully fleshed out.

The ultrasound system likely needs to be upgraded to a higher resolution system that has better compatibility with current software. Given that the ultrasound images need to be displayed in the navigation software itself, a screen-less handheld ultrasound unit would be an ideal candidate for usage with this system such as the Clarius system (Clarius Mobile Health, Burnaby, BC, Canada) so that the large ultrasound machine and screen would not need to be wheeled into the operating room [248]. This would allow the entire scanner to be encased in a sterile bag or be sterilized entirely since it would be independent from a separate machine. Evaluation of ultrasound quality and the visibility of motion capture markers through the bag would need to be considered.

### 8.3.2. Software Improvements

The current software regimen of using Matlab 2015 (Mathworks, Natick, Massachusetts, USA) for ultrasound streaming due to compatibility requirements from the Ultrasonix system, then Matlab 2019 (Mathworks, Natick, Massachusetts, USA) for image registration and processing, followed by Unity for final display is too cumbersome. The Ultrasonix transducer in this thesis is compatible with the Python programming language, one of the most common programming languages currently in use. Porting the current software to Python would be largely a matter of ensuring the image processing and image registration libraries that were used in Matlab are also available in Python. More importantly though, Python does have compatibility with Unity and with Unreal Engine, the two leading 3D virtual environment development kits currently in use. This would allow all components including the ultrasound stream, image registration and 3D display to be put into a single package and could minimize the need for the user to interact with the software.

Regarding the software itself, further work in image processing would need to be undertaken when the system is used on real tissue. As mentioned in Chapter 6, there are various features in soft tissue that make them distinct from bony prominences when scanning the spine. One of the key differences is the presence of reflections deep to the surface of the soft tissue. Additional filters to differentiate these soft tissue regions from bony regions would help minimize the extraneous data in the 3D ultrasound images that are used for image registration. Refinement to the current image processing filters also needs to be undertaken to be specific for bony anatomy.

Image registration speed could also be increased. Firstly, the symmetry alignment of the CT scanned vertebrae could be pre-processed since this step does not require comparison with the ultrasound, reducing the processing time by 1-2s. Additional evaluation on the range of angles for the ultrasound symmetry alignment could be completed, as well as evaluating the range of inlier ratio and downsampling

for the iterative closest point algorithm could be completed to further reduce registration time. Lastly, the image registration software displays the pre-registered and registered images, which could be downsampled to further reduce registration times.

### 8.3.3. Clinical Considerations

This thesis has demonstrated the technical feasibility of using 3D ultrasound for registrations of pre-operatively segmented CT images on phantoms. The next step is to demonstrate that the system is accurate in more realistic cases. These phantoms did not have a scoliotic curvature, did not have deformed vertebrae due to the deformity, and did not include the presence of soft tissue. While a porcine model was qualitatively evaluated in this thesis, the entry-point and trajectory accuracies were not tested. A first intermediate step could be to add soft tissue mimicking surfaces to scoliotic phantom spines, whether it is blue phantom ultrasound gel, silicone sheets, or even blocks of pork placed underneath the plastic spine. The pre-printed holes could still be used to confirm the entry-point and trajectory accuracy with the same on-screen multi-ringed probe, with the addition of an on-screen protractor. This would provide the most intuitive and useful accuracy information about the navigation system.

The next step would be to use the system to insert pedicle screws into either a porcine or cadaver spine and then perform post-operative CT-scans to determine if there were pedicle breaches present. In addition to simply determining if there was a breach, the on-screen position and trajectory could be compared to the CT position and trajectory relative to key landmarks. Extensive cadaver tests where the spine is exposed in the same way as a spine surgery would be needed to ensure safety and reliability of this system.

One of the important questions that arose in this project was how to source the pre-operative model. As previously mentioned, MRI would be more ideal due to its lack of ionization radiation. However, bony anatomy is difficult to segment from MRI images. Whether the solution was training a machine learning algorithm to segment MRI images after manual segmentation, using a template-vertebra approach to mask of the MRI images, or creating a new MRI sequence to isolate the bone, there would need to be significant work to adequately segment the bony MRI spine. However, it would be difficult to justify using CT scans due to their ionizing radiation. An alternative option would be to use an EOS X-ray scan, a low dose X-ray that acquires both posterior-anterior and lateral views at the same time to allow for a manual reconstruction of the spine to be created [249]. The model based on this reconstruction could potentially be used as a 3D model for the registration process. Extensive evaluation of the accuracy of EOS

reconstructions of the pedicles would need to be done to ensure reconstructed pedicles are representing true anatomy.

It cannot be understated how important it will be to receive regular feedback from orthopedic surgeons for continued development of the system. Whether it is in providing guidance on how screws are typically inserted, how best to display the motion capture information or how best to fit navigation into the usual surgical workflow, the experience and knowledge of the surgeons would be invaluable in guiding the technical design of the system.

#### 8.3.4. Technological Advancement

Current navigation systems typically use a monitor to display navigation information. The need to look at the monitor and back down at the surgical space remains a barrier to navigation usage. There is a learning curve that needs to be overcome to translate data on a navigation screen to the real world.

One of the potential solutions to this problem is the usage of augmented reality. Augmented reality in the surgical suite involves using either a high intensity projector, a glass surface or a vizor to overlay a virtual image on top of the a physical object to add or 'augment' the visualized information in the real world [250]. Augmented reality has already been used in navigation surgery with promising results, outperforming free-hand methods in one comparative trial when evaluating breaches (<2mm breaches in 93.9% vs 89.6% in free-hand with  $p < 0.05$ ) [251,252]. Adding a 3D ultrasound system would be a natural fit with an augmented reality system, as the model or even simply the optimal screw trajectory could be overlaid on top of anatomy to give visual information on how to place pedicle screws. Furthermore, this could be readily compatible with a robotic surgical system that scans the spine, decides on the optimal trajectory and inserts the screw. The combination of non-ionizing imaging and augmented reality can truly bring navigation surgery into the future.

#### 8.4. Final Remarks

In summary, there is great potential for radiation-free navigation to dramatically change how spinal surgery is conducted. Motion capture and ultrasound are readily available for the operating room. This thesis has outlined the feasibility of this technology on phantom spines. However, further study in stream-lining the image processing and registration, settling on an appropriate pre-operative imaging modality to obtain the full 3D model, and testing on real tissues on a cadaver spine need to be conducted. It is only after these three key factors have been settled that further clinical study and medical device approvals should be pursued.

## References

- [1] Weinstein SL, Dolan LA, Cheng JC, Danielsson A, Morcuende JA. Adolescent idiopathic scoliosis. *Lancet* (London, England) 2008;371:1527–37.
- [2] Weinstein SL, Dolan LA, Wright JG, Dobbs MB. Effects of Bracing in Adolescents with Idiopathic Scoliosis. *New England Journal of Medicine* 2013;369:1512–21. <https://doi.org/10.1056/NEJMoa1307337>.
- [3] de Kleuver M, Lewis SJ, Gerscheid NM, Kamper SJ, Alanay A, Berven SH, et al. Optimal surgical care for adolescent idiopathic scoliosis: an international consensus. *Eur Spine J* 2014;23:2603–18. <https://doi.org/10.1007/s00586-014-3356-1>.
- [4] Westrick ER, Ward WT. Adolescent idiopathic scoliosis: 5-year to 20-year evidence-based surgical results. *J Pediatr Orthop* 2011;31:S61–68. <https://doi.org/10.1097/BPO.0b013e3181fd87d5>.
- [5] Maruyama T, Takeshita K. Surgical treatment of scoliosis: a review of techniques currently applied. *Scoliosis* 2008;3:6. <https://doi.org/10.1186/1748-7161-3-6>.
- [6] Cuartas E, Rasouli A, O'Brien M, Shufflebarger HL. Use of all-pedicle-screw constructs in the treatment of adolescent idiopathic scoliosis. *J Am Acad Orthop Surg* 2009;17:550–61.
- [7] Reames DL, Smith JS, Fu K-MG, Polly DW, Ames CP, Berven SH, et al. Complications in the surgical treatment of 19,360 cases of pediatric scoliosis: a review of the Scoliosis Research Society Morbidity and Mortality database. *Spine* 2011;36:1484–91. <https://doi.org/10.1097/BRS.0b013e3181f3a326>.
- [8] Ledonio CGT, Polly DW, Vitale MG, Wang Q, Richards BS. Pediatric pedicle screws: comparative effectiveness and safety: a systematic literature review from the Scoliosis Research Society and the Pediatric Orthopaedic Society of North America task force. *J Bone Joint Surg Am* 2011;93:1227–34. <https://doi.org/10.2106/JBJS.J.00678>.
- [9] Hicks J, Singla A, Shen F, Arlet V. Complications of Pedicle Screw Fixation in Scoliosis Surgery. *Spine* n.d.;35:E465–470.
- [10] Mezger U, Jendrewski C, Bartels M. Navigation in surgery. *Langenbecks Arch Surg* 2013;398:501–14. <https://doi.org/10.1007/s00423-013-1059-4>.
- [11] Oertel MF, Hobart J, Stein M, Schreiber V, Scharbrodt W. Clinical and methodological precision of spinal navigation assisted by 3D intraoperative O-arm radiographic imaging. *Journal of Neurosurgery: Spine* 2011;14:532–6. <https://doi.org/10.3171/2010.10.SPINE091032>.
- [12] Helm PA, Teichman R, Hartmann SL, Simon D. Spinal Navigation and Imaging: History, Trends, and Future. *IEEE Transactions on Medical Imaging* 2015;34:1738–46. <https://doi.org/10.1109/TMI.2015.2391200>.
- [13] Walker CT, Turner JD. Radiation Exposure in Scoliosis Surgery: Freehand Technique versus Image Guidance. *World Neurosurgery* 2015;83:282–4. <https://doi.org/10.1016/j.wneu.2015.01.004>.
- [14] Ul-Haque M, Shufflebarger HL, O'Brien M, Macagno A. Radiation Exposure During Pedicle Screw Placement in Adolescent Idiopathic Scoliosis: Is Fluoroscopy Safe?: *Spine* 2006;31:2516–20. <https://doi.org/10.1097/01.brs.0000238675.91612.2f>.
- [15] Brenner DJ. Estimating cancer risks from pediatric CT: going from the qualitative to the quantitative. *Pediatr Radiol* 2002;32:228–221; discussion 242–244. <https://doi.org/10.1007/s00247-002-0671-1>.
- [16] Pearce MS, Salotti JA, Little MP, McHugh K, Lee C, Kim KP, et al. Radiation exposure from CT scans in childhood and subsequent risk of leukaemia and brain tumours: a retrospective cohort study. *Lancet* 2012;380:499–505. [https://doi.org/10.1016/S0140-6736\(12\)60815-0](https://doi.org/10.1016/S0140-6736(12)60815-0).
- [17] Yan CXB, Goulet B, Tampieri D, Collins DL. Ultrasound-CT registration of vertebrae without reconstruction. *Int J CARS* 2012;7:901–9. <https://doi.org/10.1007/s11548-012-0771-9>.

- [18] Mujagić M, Ginsberg HJ, Cobbold RSC. Development of a method for ultrasound-guided placement of pedicle screws. *IEEE Trans Ultrason Ferroelectr Freq Control* 2008;55:1267–76. <https://doi.org/10.1109/TUFFC.2008.789>.
- [19] Gardocki R. Spinal Anatomy and Surgical Approaches. *Campbell's Operative Orthopedics*. 2nd ed., n.d., p. 1571–609.
- [20] Zindrick MR, Knight GW, Sartori MJ, Carnevale TJ, Patwardhan AG, Lorenz MA. Pedicle morphology of the immature thoracolumbar spine. *Spine* 2000;25:2726–35.
- [21] Moussazadeh N, Fu GK-M. Spinal Anatomy. *Youmans and Winn Neurological Surgery*. 7th ed., n.d., p. 2259–70.
- [22] Hattori T, Sakaura H, Iwasaki M, Nagamoto Y, Yoshikawa H, Sugamoto K. In vivo three-dimensional segmental analysis of adolescent idiopathic scoliosis. *European Spine Journal : Official Publication of the European Spine Society, the European Spinal Deformity Society, and the European Section of the Cervical Spine Research Society* 2011;20:1745–50.
- [23] Donzelli S, Poma S, Balzarini L, Borboni A, Respizzi S, Villafane JH, et al. State of the art of current 3-D scoliosis classifications: a systematic review from a clinical perspective. *J Neuroeng Rehabil* 2015;12. <https://doi.org/10.1186/s12984-015-0083-8>.
- [24] Hedequist D, Emans J. Congenital scoliosis. *J Am Acad Orthop Surg* 2004;12:266–75.
- [25] Vialle R, Thévenin-Lemoine C, Mary P. Neuromuscular scoliosis. *Orthopaedics & Traumatology: Surgery & Research* 2013;99:S124–39. <https://doi.org/10.1016/j.otsr.2012.11.002>.
- [26] Arlet V, Odent Th, Aebi M. Congenital scoliosis. *Eur Spine J* 2003;12:456–63. <https://doi.org/10.1007/s00586-003-0555-6>.
- [27] Canavese F, Rousset M, Le Gledic B, Samba A, Dimeglio A. Surgical advances in the treatment of neuromuscular scoliosis. *World J Orthop* 2014;5:124–33. <https://doi.org/10.5312/wjo.v5.i2.124>.
- [28] Konieczny MR, Senyurt H, Krauspe R. Epidemiology of adolescent idiopathic scoliosis. *Journal of Children's Orthopaedics* 2013;7:3–9.
- [29] Janicki JA, Alman B. Scoliosis: Review of diagnosis and treatment. *Paediatr Child Health* 2007;12:771–6.
- [30] Kesling KL, Reinker KA. Scoliosis in twins. A meta-analysis of the literature and report of six cases. *Spine* 1997;22:2009–14.
- [31] Grauers A, Einarsdottir E, Gerdhem P. Genetics and pathogenesis of idiopathic scoliosis. *Scoliosis Spinal Disord* 2016;11. <https://doi.org/10.1186/s13013-016-0105-8>.
- [32] Katz D. The Etiology and Natural History of Idiopathic Scoliosis. *Journal of Prosthetics and Orthotics* 2003;15:3–10.
- [33] Ogilvie J. Adolescent idiopathic scoliosis and genetic testing. *Curr Opin Pediatr* 2010;22:67–70. <https://doi.org/10.1097/MOP.0b013e32833419ac>.
- [34] Lowe T, Lawellin D, Smith D, Price C, Maher T, Merola A, et al. Platelet calmodulin levels in adolescent idiopathic scoliosis: do the levels correlate with curve progression and severity? *Spine* 2002;27:768–75.
- [35] Yu J, Fairbank JCT, Roberts S, Urban JPG. The elastic fiber network of the anulus fibrosus of the normal and scoliotic human intervertebral disc. *Spine* 2005;30:1815–20.
- [36] Kouwenhoven J-WM, Castelein RM. The pathogenesis of adolescent idiopathic scoliosis: review of the literature. *Spine* 2008;33:2898–908. <https://doi.org/10.1097/BRS.0b013e3181891751>.
- [37] Burwell RG, Dangerfield PH, Moulton A, Grivas TB. Adolescent idiopathic scoliosis (AIS), environment, exposome and epigenetics: a molecular perspective of postnatal normal spinal growth and the etiopathogenesis of AIS with consideration of a network approach and possible implications for medical therapy. *Scoliosis* 2011;6:26. <https://doi.org/10.1186/1748-7161-6-26>.
- [38] Shaw M, Adam CJ, Izatt MT, Licina P, Askin GN. Use of the iPhone for Cobb angle measurement in scoliosis. *Eur Spine J* 2012;21:1062–8. <https://doi.org/10.1007/s00586-011-2059-0>.



- [39] Kotwicki T. Evaluation of scoliosis today: Examination, X-rays and beyond. *Disability and Rehabilitation* 2008;30:742–51. <https://doi.org/10.1080/09638280801889519>.
- [40] Langensiepen S, Semler O, Sobottke R, Fricke O, Franklin J, Schönau E, et al. Measuring procedures to determine the Cobb angle in idiopathic scoliosis: a systematic review. *Eur Spine J* 2013;22:2360–71. <https://doi.org/10.1007/s00586-013-2693-9>.
- [41] Jada A, Mackel CE, Hwang SW, Samdani AF, Stephen JH, Bennett JT, et al. Evaluation and management of adolescent idiopathic scoliosis: a review. *Neurosurgical Focus* 2017;43:E2. <https://doi.org/10.3171/2017.7.FOCUS17297>.
- [42] Escalada F, Marco E, Duarte E, Muniesa JM, Belmonte R, Tejero M, et al. Growth and curve stabilization in girls with adolescent idiopathic scoliosis. *Spine* 2005;30:411–7.
- [43] Escalada F, Marco E, Duarte E, Muniesa JM, Boza R, Tejero M, et al. Assessment of angle velocity in girls with adolescent idiopathic scoliosis. *Scoliosis* 2009;4:20-7161-4–20.
- [44] Lonstein JE, Carlson JM. The prediction of curve progression in untreated idiopathic scoliosis during growth. *The Journal of Bone and Joint Surgery American Volume* 1984;66:1061–71.
- [45] Bunnell WP. The natural history of idiopathic scoliosis before skeletal maturity. *Spine* 1986;11:773–6.
- [46] Hacquebord JH, Leopold SS. In Brief: The Risser Classification: A Classic Tool for the Clinician Treating Adolescent Idiopathic Scoliosis. *Clin Orthop Relat Res* 2012;470:2335–8. <https://doi.org/10.1007/s11999-012-2371-y>.
- [47] Ryan PM, Puttler EG, Stotler WM, Ferguson RL. Role of the triradiate cartilage in predicting curve progression in adolescent idiopathic scoliosis. *J Pediatr Orthop* 2007;27:671–6. <https://doi.org/10.1097/BPO.0b013e3181373ba8>.
- [48] Sanders JO, Browne RH, Cooney TE, Finegold DN, McConnell SJ, Margraf SA. Correlates of the peak height velocity in girls with idiopathic scoliosis. *Spine* 2006;31:2289–95. <https://doi.org/10.1097/01.brs.0000236844.41595.26>.
- [49] Noshchenko A, Hoffecker L, Lindley EM, Burger EL, Cain CM, Patel VV, et al. Predictors of spine deformity progression in adolescent idiopathic scoliosis: A systematic review with meta-analysis. *World J Orthop* 2015;6:537–58. <https://doi.org/10.5312/wjo.v6.i7.537>.
- [50] Asher MA, Burton DC. Adolescent idiopathic scoliosis: natural history and long term treatment effects. *Scoliosis and Spinal Disorders* 2006;1:1–10. <https://doi.org/10.1186/1748-7161-1-2>.
- [51] Weiss H-R. Adolescent idiopathic scoliosis (AIS) - an indication for surgery? A systematic review of the literature. *Disabil Rehabil* 2008;30:799–807. <https://doi.org/10.1080/09638280801889717>.
- [52] Reichel D, Schanz J. Developmental psychological aspects of scoliosis treatment. *Pediatr Rehabil* 2003;6:221–5. <https://doi.org/10.1080/13638490310001644593>.
- [53] Donnelly MJ, Dolan LA, Grande L, Weinstein SL. Patient and Parent Perspectives on Treatment for Adolescent Idiopathic Scoliosis. *Iowa Orthop J* 2004;24:76–83.
- [54] Kotwicki T, Chowanska J, Kinel E, Czaprowski D, Tomaszewski M, Janusz P. Optimal management of idiopathic scoliosis in adolescence. *Adolesc Health Med Ther* 2013;4:59–73. <https://doi.org/10.2147/AHMT.S32088>.
- [55] Richards BS, Bernstein RM, D’Amato CR, Thompson GH. Standardization of criteria for adolescent idiopathic scoliosis brace studies: SRS Committee on Bracing and Nonoperative Management. *Spine* 2005;30:2068–75; discussion 2076-2077.
- [56] Bridwell KH. Surgical treatment of idiopathic adolescent scoliosis. *Spine* 1999;24:2607–16.
- [57] Lenke LG, Betz RR, Haher TR, Lapp MA, Merola AA, Harms J, et al. Multisurgeon assessment of surgical decision-making in adolescent idiopathic scoliosis: curve classification, operative approach, and fusion levels. *Spine* 2001;26:2347–53.
- [58] Warner W, Sawyer J. *Scoliosis and Kyphosis*. Campbell’s Operative Orthopedics. 13th ed., Elsevier; n.d., p. 1897–2120.

- [59] Kirzner N, Hilliard L, Martin C, Quan G, Liew S, Humadi A. Bone graft in posterior spine fusion for adolescent idiopathic scoliosis: a meta-analysis. *ANZ J Surg* 2018;88:1247–52. <https://doi.org/10.1111/ans.14551>.
- [60] Helenius I. Anterior surgery for adolescent idiopathic scoliosis. *J Child Orthop* 2013;7:63–8. <https://doi.org/10.1007/s11832-012-0467-2>.
- [61] Gopinathan P. Anterior scoliosis surgery the state of art procedure. *J Orthop* 2015;12:63–5. <https://doi.org/10.1016/j.jor.2015.04.001>.
- [62] Lonner BS, Kondrachov D, Siddiqi F, Hayes V, Scharf C. Thoracoscopic spinal fusion compared with posterior spinal fusion for the treatment of thoracic adolescent idiopathic scoliosis. *Surgical technique. J Bone Joint Surg Am* 2007;89 Suppl 2 Pt.1:142–56. <https://doi.org/10.2106/JBJS.F.01389>.
- [63] Dobbs MB, Lenke LG, Kim YJ, Luhmann SJ, Bridwell KH. Anterior/posterior spinal instrumentation versus posterior instrumentation alone for the treatment of adolescent idiopathic scoliotic curves more than 90 degrees. *Spine* 2006;31:2386–91. <https://doi.org/10.1097/01.brs.0000238965.81013.c5>.
- [64] Luhmann SJ, Lenke LG, Kim YJ, Bridwell KH, Schootman M. Thoracic adolescent idiopathic scoliosis curves between 70 degrees and 100 degrees: is anterior release necessary? *Spine* 2005;30:2061–7.
- [65] Deniz Olgun Z, Yazici M. Posterior instrumentation and fusion. *J Child Orthop* 2013;7:69–76. <https://doi.org/10.1007/s11832-012-0456-5>.
- [66] Basques BA, Lukasiewicz AM, Samuel AM, Webb ML, Bohl DD, Smith BG, et al. Which Pediatric Orthopaedic Procedures Have the Greatest Risk of Adverse Outcomes? *Journal of Pediatric Orthopaedics* 2017;37:429–34. <https://doi.org/10.1097/BPO.0000000000000683>.
- [67] Steinmetz MP, Rajpal S, Trost G. Segmental spinal instrumentation in the management of scoliosis. *Neurosurgery* 2008;63:131–8. <https://doi.org/10.1227/01.NEU.0000325679.25152.EE>.
- [68] Lenke L, Kuklo T, Ondra S. Rationale behind the current state-of-the- art treatment of scoliosis. *Spine* 2008;33:1051–4.
- [69] Suk S-I. Pedicle Screw Instrumentation for Adolescent Idiopathic Scoliosis: The Insertion Technique, the Fusion Levels and Direct Vertebral Rotation. *Clin Orthop Surg* 2011;3:89–100. <https://doi.org/10.4055/cios.2011.3.2.89>.
- [70] Hasler CC. A brief overview of 100 years of history of surgical treatment for adolescent idiopathic scoliosis. *J Child Orthop* 2013;7:57–62. <https://doi.org/10.1007/s11832-012-0466-3>.
- [71] Kim YJ, Lenke LG, Bridwell KH, Cho YS, Riew KD. Free hand pedicle screw placement in the thoracic spine: is it safe? *Spine* 2004;29:333–42; discussion 342.
- [72] Lee C-S, Kim MJ, Ahn Y-J, Kim Y-T, Jeong K-I, Lee D-H. Thoracic pedicle screw insertion in scoliosis using posteroanterior C-arm rotation method. *J Spinal Disord Tech* 2007;20:66–71. <https://doi.org/10.1097/01.bsd.0000211248.75200.3f>.
- [73] Rampersaud YR, Simon DA, Foley KT. Accuracy Requirements for Image-Guided Spinal Pedicle Screw Placement. *Spine* 2001;26:352–9. <https://doi.org/10.1097/00007632-200102150-0001>.
- [74] Gao B, Gao W, Chen C, Wang Q, Lin S, Xu C, et al. What is the Difference in Morphologic Features of the Thoracic Pedicle Between Patients With Adolescent Idiopathic Scoliosis and Healthy Subjects? A CT-based Case-control Study. *Clin Orthop* 2017. <https://doi.org/10.1007/s11999-017-5448-9>.
- [75] Larson A.N., Lonner B.S. Comparative effectiveness of implant density. *Semin Spine Surg* 2015;27:45–51. <https://doi.org/10.1053/j.semss.2015.01.010>.
- [76] Shen M, Jiang H, Luo M, Wang W, Li N, Wang L, et al. Comparison of low density and high density pedicle screw instrumentation in Lenke 1 adolescent idiopathic scoliosis. *BMC Musculoskeletal Disord* 2017;18:336. <https://doi.org/10.1186/s12891-017-1695-x>.

- [77] Luo M, Wang W, Shen M, Luo X, Xia L. Does higher screw density improve radiographic and clinical outcomes in adolescent idiopathic scoliosis? A systematic review and pooled analysis. *J Neurosurg Pediatrics* 2017;19:448–57. <https://doi.org/10.3171/2016.11.PEDS16334>.
- [78] Perna F, Borghi R, Pilla F, Stefanini N, Mazzotti A, Chehrassan M. Pedicle screw insertion techniques: an update and review of the literature. *Musculoskelet Surg* 2016;100:165–9. <https://doi.org/10.1007/s12306-016-0438-8>.
- [79] Vasudeva V, Moses Z, Cole T, Gologorsky Y, Lu Y. Chapter 14 - Image Guidance for Spine Surgery. In: Golby AJ, editor. *Image-Guided Neurosurgery*, Boston: Academic Press; 2015, p. 325–64. <https://doi.org/10.1016/B978-0-12-800870-6.00014-5>.
- [80] Puvanesarajah V, Liauw JA, Lo S, Lina IA, Witham TF. Techniques and accuracy of thoracolumbar pedicle screw placement. *World J Orthop* 2014;5:112–23. <https://doi.org/10.5312/wjo.v5.i2.112>.
- [81] Patel AA, Whang PG, Vaccaro AR. Overview of Computer-Assisted Image-Guided Surgery of the Spine. *Seminars in Spine Surgery* 2008;20:186–94. <https://doi.org/10.1053/j.semss.2008.06.005>.
- [82] Kim JM, Bowers AL, Chin KR. Intraoperative Imaging Techniques in Spine Surgery. *Seminars in Spine Surgery* 2007;19:78–86. <https://doi.org/10.1053/j.semss.2007.04.003>.
- [83] Tjardes T, Shafizadeh S, Rixen D, Paffrath T, Bouillon B, Steinhausen ES, et al. Image-guided spine surgery: state of the art and future directions. *Eur Spine J* 2010;19:25–45. <https://doi.org/10.1007/s00586-009-1091-9>.
- [84] Fischer CR, Kim Y. Selective fusion for adolescent idiopathic scoliosis: a review of current operative strategy. *Eur Spine J* 2011;20:1048–57. <https://doi.org/10.1007/s00586-011-1730-9>.
- [85] Etemadifar M, Jamalaldini M. Evaluating Accuracy of Free-hand Pedicle Screw Insertion in Adolescent Idiopathic Scoliosis Using Postoperative Multi-Slice Computed Tomography Scan. *Adv Biomed Res* 2017;6:19. <https://doi.org/10.4103/2277-9175.201331>.
- [86] Liu Z, Jin M, Qiu Y, Yan H, Han X, Zhu Z. The Superiority of Intraoperative O-arm Navigation-assisted Surgery in Instrumenting Extremely Small Thoracic Pedicles of Adolescent Idiopathic Scoliosis: A Case-Control Study. *Medicine (Baltimore)* 2016;95:e3581. <https://doi.org/10.1097/MD.0000000000003581>.
- [87] Uehara M, Takahashi J, Kuraishi S, Shimizu M, Ikegami S, Futatsugi T, et al. Computer-assisted skip pedicle screw fixation for adolescent idiopathic scoliosis. *J Orthop Sci* 2017;22:218–23. <https://doi.org/10.1016/j.jos.2016.11.012>.
- [88] Zheng X, Qian B-P, Liu Z, Sun X, Zhu Z-Z, Wang B, et al. Screw Placement at the Apex Alters Surgical Outcomes of Moderate Lenke 1 Adolescent Idiopathic Scoliosis. *Clin Spine Surg* 2017;30:E883–91. <https://doi.org/10.1097/BSD.0000000000000435>.
- [89] Aoude AA, Fortin M, Figueiredo R, Jarzem P, Ouellet J, Weber MH. Methods to determine pedicle screw placement accuracy in spine surgery: a systematic review. *European Spine Journal* 2015;24:990–1004. <https://doi.org/10.1007/s00586-015-3853-x>.
- [90] Gelalis ID, Paschos NK, Pakos EE, Politis AN, Arnaoutoglou CM, Karageorgos AC, et al. Accuracy of pedicle screw placement: a systematic review of prospective in vivo studies comparing free hand, fluoroscopy guidance and navigation techniques. *Eur Spine J* 2012;21:247–55. <https://doi.org/10.1007/s00586-011-2011-3>.
- [91] Coe JD, Arlet V, Donaldson W, Berven S, Hanson DS, Mudiyaam R, et al. Complications in spinal fusion for adolescent idiopathic scoliosis in the new millennium. A report of the Scoliosis Research Society Morbidity and Mortality Committee. *Spine (Phila Pa 1976)* 2006;31:345–9. <https://doi.org/10.1097/01.brs.0000197188.76369.13>.
- [92] Burton DC, Carlson BB, Place HM, Fuller JE, Blanke K, Cho R, et al. Results of the Scoliosis Research Society Morbidity and Mortality Database 2009–2012: A Report From the Morbidity and Mortality Committee. *Spine Deformity* 2016;4:338–43. <https://doi.org/10.1016/j.jspd.2016.05.003>.

- [93] Diab M, Smith A, Kuklo T. Neural Complications in the Surgical Treatment of Adolescent Idiopathic Scoliosis. *Spine* 2007;32:2759–63. <https://doi.org/10.1097/BRS.0b013e31815a5970>.
- [94] Watanabe K, Yamazaki A, Hirano T, Izumi T, Sano A, Morita O, et al. Descending Aortic Injury by a Thoracic Pedicle Screw During Posterior Reconstructive Surgery: A Case Report. *Spine* 2010;35:E1064. <https://doi.org/10.1097/BRS.0b013e3181ed29c1>.
- [95] Shin BJ, James AR, Njoku IU, Härtl R. Pedicle screw navigation: a systematic review and meta-analysis of perforation risk for computer-navigated versus freehand insertion. *J Neurosurg Spine* 2012;17:113–22. <https://doi.org/10.3171/2012.5.SPINE11399>.
- [96] Tian N-F, Huang Q-S, Zhou P, Zhou Y, Wu R-K, Lou Y, et al. Pedicle screw insertion accuracy with different assisted methods: a systematic review and meta-analysis of comparative studies. *European Spine Journal* 2011;20:846–59. <https://doi.org/10.1007/s00586-010-1577-5>.
- [97] Fan Chiang C-Y, Tsai T-T, Chen L-H, Lai P-L, Fu T-S, Niu C-C, et al. Computed tomography-based navigation-assisted pedicle screw insertion for thoracic and lumbar spine fractures. *Chang Gung Med J* 2012;35:332–8.
- [98] Sud A, Tsirikos AI. Current concepts and controversies on adolescent idiopathic scoliosis: Part II. *Indian J Orthop* 2013;47:219–29. <https://doi.org/10.4103/0019-5413.111493>.
- [99] Frush DP, Applegate K. Computed tomography and radiation: understanding the issues. *J Am Coll Radiol* 2004;1:113–9. <https://doi.org/10.1016/j.jacr.2003.11.012>.
- [100] Nelson EM, Monazzam SM, Kim KD, Seibert JA, Klineberg EO. Intraoperative fluoroscopy, portable X-ray, and CT: patient and operating room personnel radiation exposure in spinal surgery. *Spine J* 2014;14:2985–91. <https://doi.org/10.1016/j.spinee.2014.06.003>.
- [101] Villard J, Ryang Y-M, Demetriades AK, Reinke A, Behr M, Preuss A, et al. Radiation Exposure to the Surgeon and the Patient During Posterior Lumbar Spinal Instrumentation: A Prospective Randomized Comparison of Navigated Versus Non-navigated Freehand Techniques. *Spine* 2014;39:1004. <https://doi.org/10.1097/BRS.0000000000000351>.
- [102] Al-Khouja L, Shweikeh F, Pashman R, Johnson JP, Kim TT, Drazin D. Economics of image guidance and navigation in spine surgery. *Surg Neurol Int* 2015;6:S323–6. <https://doi.org/10.4103/2152-7806.159381>.
- [103] Watkins RG, Gupta A, Watkins RG. Cost-Effectiveness of Image-Guided Spine Surgery. *Open Orthop J* 2010;4:228–33. <https://doi.org/10.2174/1874325001004010228>.
- [104] Stecker MM. A review of intraoperative monitoring for spinal surgery. *Surg Neurol Int* 2012;3:S174–87. <https://doi.org/10.4103/2152-7806.98579>.
- [105] Ovadia D, Korn A, Fishkin M, Steinberg DM, Wientroub S, Ofiram E. The contribution of an electronic conductivity device to the safety of pedicle screw insertion in scoliosis surgery. *Spine* 2011;36:E1314-1321. <https://doi.org/10.1097/BRS.0b013e31822a82ec>.
- [106] Bai Y-S, Niu Y-F, Chen Z-Q, Zhu X-D, Gabriel LKP, Wong HK, et al. Comparison of the pedicle screws placement between electronic conductivity device and normal pedicle finder in posterior surgery of scoliosis. *J Spinal Disord Tech* 2013;26:316–20. <https://doi.org/10.1097/BSD.0b013e318247f21d>.
- [107] Chen Z, Wu B, Zhai X, Bai Y, Zhu X, Luo B, et al. Basic study for ultrasound-based navigation for pedicle screw insertion using transmission and backscattered methods. *PLoS ONE* 2015;10:e0122392. <https://doi.org/10.1371/journal.pone.0122392>.
- [108] Yan CXB, Goulet B, Pelletier J, Chen SJ-S, Tampieri D, Collins DL. Towards accurate, robust and practical ultrasound-CT registration of vertebrae for image-guided spine surgery. *Int J Comput Assist Radiol Surg* 2011;6:523–37. <https://doi.org/10.1007/s11548-010-0536-2>.
- [109] Mercier L, Langø T, Lindseth F, Collins DL. A review of calibration techniques for freehand 3-D ultrasound systems. *Ultrasound Med Biol* 2005;31:449–71. <https://doi.org/10.1016/j.ultrasmedbio.2004.11.015>.

- [110] Kindratenko VV. A survey of electromagnetic position tracker calibration techniques. *Virtual Reality* 2000;5:169–82. <https://doi.org/10.1007/BF01409422>.
- [111] Koivukangas T, Katisko JP, Koivukangas JP. Technical accuracy of optical and the electromagnetic tracking systems. *Springerplus* 2013;2. <https://doi.org/10.1186/2193-1801-2-90>.
- [112] Richards JG. The measurement of human motion: A comparison of commercially available systems. *Human Movement Science* 1999;18:589–602. [https://doi.org/10.1016/S0167-9457\(99\)00023-8](https://doi.org/10.1016/S0167-9457(99)00023-8).
- [113] Yongqiang Feng, Max L. Accuracy and Precision of a Custom Camera-Based System for 2-D and 3-D Motion Tracking During Speech and Nonspeech Motor Tasks. *Journal of Speech, Language & Hearing Research* 2014;57:426-438 13p. [https://doi.org/10.1044/2014\\_JSLHR-S-13-0007](https://doi.org/10.1044/2014_JSLHR-S-13-0007).
- [114] Windolf M, Götzen N, Morlock M. Systematic accuracy and precision analysis of video motion capturing systems--exemplified on the Vicon-460 system. *J Biomech* 2008;41:2776–80. <https://doi.org/10.1016/j.jbiomech.2008.06.024>.
- [115] Wiles AD, Thompson DG, Frantz DD. Accuracy assessment and interpretation for optical tracking systems. vol. 5367, 2004, p. 421–32. <https://doi.org/10.1117/12.536128>.
- [116] Ehara Y, Fujimoto H, Miyazaki S, Tanaka S, Yamamoto S. Comparison of the performance of 3D camera systems. *Gait & Posture* 1995;3:166–9. [https://doi.org/10.1016/0966-6362\(95\)99067-U](https://doi.org/10.1016/0966-6362(95)99067-U).
- [117] Guerra-Filho GB. *Optical Motion Capture: Theory and Implementation* 2005:29.
- [118] Chong S-Y, Dorow B, Ramasamy E, Dennerlein F, Röhrle O. The Use of Collision Detection to Infer Multi-Camera Calibration Quality. *Front Bioeng Biotechnol* 2015;3. <https://doi.org/10.3389/fbioe.2015.00065>.
- [119] Mitchell EEL, Rogers AE. Quaternion Parameters in the Simulation of a Spinning Rigid Body. *SIMULATION* 1965;4:390–6. <https://doi.org/10.1177/003754976500400610>.
- [120] Kuipers J. *Quaternions and Rotation Sequences*. vol. 1. 1999.
- [121] Diebel J. *Representing Attitude: Euler Angles, Unit Quaternions, and Rotation Vectors* 2006.
- [122] Thewlis D, Bishop C, Daniell N, Paul G. Next generation low-cost motion capture systems can provide comparable spatial accuracy to high-end systems. *Journal of Applied Biomechanics* 2013;29:112–7.
- [123] Holloway K, Docef A. A quantitative assessment of the accuracy and reliability of O-arm images for deep brain stimulation surgery. *Neurosurgery* 2013;72:47–57. <https://doi.org/10.1227/NEU.0b013e318273a090>.
- [124] Wittmann W, Wenger T, Loewe E, Lueth TC. Official measurement protocol and accuracy results for an optical surgical navigation system (NPU). *Conf Proc IEEE Eng Med Biol Soc* 2011;2011:1237–40. <https://doi.org/10.1109/IEMBS.2011.6090291>.
- [125] Scheufler K-M, Franke J, Eckardt A, Dohmen H. Accuracy of Image-Guided Pedicle Screw Placement Using Intraoperative Computed Tomography-Based Navigation With Automated Referencing. Part II: Thoracolumbar Spine. *Neurosurgery* 2011;69:1307–16. <https://doi.org/10.1227/NEU.0b013e31822ba190>.
- [126] Janssen R, Lou E, Durdle N, Raso J, Hill D, Liggins AB, et al. Active markers in operative motion analysis (PDF) - Semantic Scholar. *IEEE TRANSACTIONS ON INSTRUMENTATION AND MEASUREMENT* n.d.;55:854–9.
- [127] Holly LT, Bloch O, Johnson JP. Evaluation of registration techniques for spinal image guidance. *J Neurosurg Spine* 2006;4:323–8. <https://doi.org/10.3171/spi.2006.4.4.323>.
- [128] Papadopoulos EC, Girardi FP, Sama A, Sandhu HS, Cammisa FP. Accuracy of single-time, multilevel registration in image-guided spinal surgery. *Spine J* 2005;5:263–7; discussion 268. <https://doi.org/10.1016/j.spinee.2004.10.048>.
- [129] Rampersaud YR, Simon DA, Foley KT. Accuracy Requirements for Image-Guided Spinal Pedicle Screw Placement. *Spine* 2001;26:352–9. <https://doi.org/10.1097/00007632-200102150-0001>.

- [130] The essential physics of medical imaging. 3rd ed. Philadelphia: Wolters Kluwer Health/Lippincott Williams & Wilkins; 2012.
- [131] Merritt C. Physics of Ultrasound. Diagnostic Ultrasound. 5th ed., Elsevier, Inc; n.d.
- [132] Atlas of ultrasound-guided procedures in interventional pain management [electronic resource]. New York: Springer; 2011.
- [133] Butts C. Ultrasound. Roberts and Hedges' Clinical Procedures in Emergency Medicine and Acute Care. 7th ed., n.d., p. 1434–41.
- [134] Yousefifard M, Baikpour M, Ghelichkhani P, Asady H, Darafarin A, Amini Esfahani MR, et al. Comparison of Ultrasonography and Radiography in Detection of Thoracic Bone Fractures; a Systematic Review and Meta-Analysis. *Emerg (Tehran)* 2016;4:55–64.
- [135] Huang Q, Zeng Z. A Review on Real-Time 3D Ultrasound Imaging Technology. *Biomed Res Int* 2017;2017. <https://doi.org/10.1155/2017/6027029>.
- [136] Yen JT, Steinberg JP, Smith SW. Sparse 2-D array design for real time rectilinear volumetric imaging. *IEEE Transactions on Ultrasonics, Ferroelectrics, and Frequency Control* 2000;47:93–110. <https://doi.org/10.1109/58.818752>.
- [137] Solberg OV, Lindseth F, Torp H, Blake RE, Nagelhus Hernes TA. Freehand 3D ultrasound reconstruction algorithms--a review. *Ultrasound Med Biol* 2007;33:991–1009. <https://doi.org/10.1016/j.ultrasmedbio.2007.02.015>.
- [138] Chen X, Wen T, Li X, Qin W, Lan D, Pan W, et al. Reconstruction of freehand 3D ultrasound based on kernel regression. *Biomed Eng Online* 2014;13:124. <https://doi.org/10.1186/1475-925X-13-124>.
- [139] Barry CD, Allott CP, John NW, Mellor PM, Arundel PA, Thomson DS, et al. Three-dimensional freehand ultrasound: image reconstruction and volume analysis. *Ultrasound Med Biol* 1997;23:1209–24.
- [140] Wen T, Li L, Zhu Q, Qin W, Gu J, Yang F, et al. GPU-accelerated Kernel Regression Reconstruction for Freehand 3D Ultrasound Imaging: *Ultrasonic Imaging* 2017. <https://doi.org/10.1177/0161734616689464>.
- [141] Hsu P-W, Prager RW, Gee AH, Treece GM. Freehand 3D Ultrasound Calibration: A Review. *Advanced Imaging in Biology and Medicine*, Springer, Berlin, Heidelberg; 2009, p. 47–84. [https://doi.org/10.1007/978-3-540-68993-5\\_3](https://doi.org/10.1007/978-3-540-68993-5_3).
- [142] Chen TK, Abolmaesumi P, Thurston AD, Ellis RE. Automated 3D freehand ultrasound calibration with real-time accuracy control. *Med Image Comput Comput Assist Interv* 2006;9:899–906.
- [143] De Lorenzo D, Vaccarella A, Khreis G, Moennich H, Ferrigno G, De Momi E. Accurate calibration method for 3D freehand ultrasound probe using virtual plane. *Med Phys* 2011;38:6710–20. <https://doi.org/10.1118/1.3663674>.
- [144] Riccabona M, Nelson TR, Pretorius DH. Three-dimensional ultrasound: accuracy of distance and volume measurements. *Ultrasound Obstet Gynecol* 1996;7:429–34. <https://doi.org/10.1046/j.1469-0705.1996.07060429.x>.
- [145] Partik BL, Stadler A, Schamp S, Koller A, Voracek M, Heinz G, et al. 3D versus 2D ultrasound: accuracy of volume measurement in human cadaver kidneys. *Invest Radiol* 2002;37:489–95. <https://doi.org/10.1097/01.RLI.0000023573.59066.43>.
- [146] Ioannou C, Sarris I, Yaqub MK, Noble JA, Javaid MK, Papageorghiou AT. Surface area measurement using rendered three-dimensional ultrasound imaging: an in-vitro phantom study. *Ultrasound Obstet Gynecol* 2011;38:445–9. <https://doi.org/10.1002/uog.8984>.
- [147] Poulsen C, Pedersen PC, Szabo TL. An optical registration method for 3D ultrasound freehand scanning. *IEEE Ultrasonics Symposium*, 2005., vol. 2, 2005, p. 1236–40. <https://doi.org/10.1109/ULTSYM.2005.1603075>.
- [148] Mettler F. Introduction. *Essentials of Radiology*. 3rd ed., Elsevier; n.d., p. 1–9.

- [149] Hille G, Saalfeld S, Serowy S, Tönnies K. Vertebral body segmentation in wide range clinical routine spine MRI data. *Computer Methods and Programs in Biomedicine* 2018;155:93–9. <https://doi.org/10.1016/j.cmpb.2017.12.013>.
- [150] Che C, Sudharshan Mathai T, Galeotti J. Ultrasound Registration: A Review. *Methods* 2016. <https://doi.org/10.1016/j.ymeth.2016.12.006>.
- [151] Zhang Y. *Image Processing*. vol. 1. Berlin, Boston: De Gruyter; 2017. <https://doi.org/10.1515/9783110524116>.
- [152] Dougherty ER, Lotufo RA. *Hands-on Morphological Image Processing*. SPIE; 2003. <https://doi.org/10.1117/3.501104>.
- [153] Zitová B, Flusser J. Image registration methods: a survey. *Image and Vision Computing* 2003;21:977–1000. [https://doi.org/10.1016/S0262-8856\(03\)00137-9](https://doi.org/10.1016/S0262-8856(03)00137-9).
- [154] HAWKES DJ. Algorithms for radiological image registration and their clinical application. *J Anat* 1998;193:347–61. <https://doi.org/10.1046/j.1469-7580.1998.19330347.x>.
- [155] Gong S, O'keefe G, Scott A. Comparison and Evaluation of PET/CT Image Registration. *Conf Proc IEEE Eng Med Biol Soc* 2005;2:1599–603. <https://doi.org/10.1109/IEMBS.2005.1616743>.
- [156] Sjögreen-Gleisner K, Rueckert D, Ljungberg M. Registration of serial SPECT/CT images for three-dimensional dosimetry in radionuclide therapy. *Phys Med Biol* 2009;54:6181. <https://doi.org/10.1088/0031-9155/54/20/010>.
- [157] Daftary A. PET-MRI: Challenges and new directions. *Indian J Nucl Med* 2010;25:3–5. <https://doi.org/10.4103/0972-3919.63590>.
- [158] Bouziotis P, Fiorini C. SPECT/MRI: dreams or reality? *Clin Transl Imaging* 2014;2:571–3. <https://doi.org/10.1007/s40336-014-0095-6>.
- [159] Song H, Qiu P. Intensity-based 3D local image registration. *Pattern Recognition Letters* 2017;94:15–21. <https://doi.org/10.1016/j.patrec.2017.04.021>.
- [160] Goshtasby A. *Theory and applications of image registration* /. n.d.
- [161] Brock KK. Image Registration in Intensity- Modulated, Image-Guided and Stereotactic Body Radiation Therapy. *IMRT, IGRT, SBRT - Advances in the Treatment Planning and Delivery of Radiotherapy* 2007;40:94–115. <https://doi.org/10.1159/000106030>.
- [162] Keszei AP, Berkels B, Deserno TM. Survey of Non-Rigid Registration Tools in Medicine. *J Digit Imaging* 2017;30:102–16. <https://doi.org/10.1007/s10278-016-9915-8>.
- [163] Kotsas P, Dodd T. Rigid Registration of Medical Images Using 1D and 2D Binary Projections. *J Digit Imaging* 2011;24:913–25. <https://doi.org/10.1007/s10278-010-9352-z>.
- [164] Maes F, Loecx D, Vandermeulen D, Suetens P. Image registration using mutual information. In: Paragios N, Duncan J, Ayache N, editors. *Handbook of Biomedical Imaging: Methodologies and Clinical Research*, Boston, MA: Springer US; 2015, p. 295–308. [https://doi.org/10.1007/978-0-387-09749-7\\_16](https://doi.org/10.1007/978-0-387-09749-7_16).
- [165] Zhou Wang, Bovik AC, Sheikh HR, Simoncelli EP. Image quality assessment: from error visibility to structural similarity. *IEEE Transactions on Image Processing* 2004;13:600–12. <https://doi.org/10.1109/TIP.2003.819861>.
- [166] Bærentzen JA, Gravesen J, Anton F, Aanæs H. *Guide to Computational Geometry Processing: Foundations, Algorithms, and Methods*. London: Springer-Verlag; 2012. <https://doi.org/10.1007/978-1-4471-4075-7>.
- [167] Chen Y, Medioni G. Object modelling by registration of multiple range images. *Image and Vision Computing* 1992;10:145–55. [https://doi.org/10.1016/0262-8856\(92\)90066-C](https://doi.org/10.1016/0262-8856(92)90066-C).
- [168] Low K. Linear least-squares optimization for point-to-plane ICP surface registration. 2004.
- [169] Besl PJ, McKay ND. A method for registration of 3-D shapes. *IEEE Transactions on Pattern Analysis and Machine Intelligence* 1992;14:239–56. <https://doi.org/10.1109/34.121791>.

- [170] Winter S, Pechlivanis I, Dekomien C, Igel C, Schmieder K. Toward registration of 3D ultrasound and CT images of the spine in clinical praxis: design and evaluation of a data acquisition protocol. *Ultrasound Med Biol* 2009;35:1773–82. <https://doi.org/10.1016/j.ultrasmedbio.2009.06.1089>.
- [171] Penney GP, Blackall JM, Hamady MS, Sabharwal T, Adam A, Hawkes DJ. Registration of freehand 3D ultrasound and magnetic resonance liver images. *Medical Image Analysis* 2004;8:81–91. <https://doi.org/10.1016/j.media.2003.07.003>.
- [172] Koo TK, Kwok WE. A non-ionizing technique for three-dimensional measurement of the lumbar spine. *Journal of Biomechanics* 2016;49:4073–9. <https://doi.org/10.1016/j.jbiomech.2016.10.048>.
- [173] Tamura Y, Sugano N, Sasama T, Sato Y, Tamura S, Yonenobu K, et al. Surface-based registration accuracy of CT-based image-guided spine surgery. *Eur Spine J* 2005;14:291–7. <https://doi.org/10.1007/s00586-004-0797-y>.
- [174] Howick J, Chalmers I, Glasziou P. The 2011 Oxford CEBM Levels of Evidence: Introductory Document n.d.
- [175] Moher D, Liberati A, Tetzlaff J, Altman DG. Preferred reporting items for systematic reviews and meta-analyses: the PRISMA statement. *BMJ* 2009;339:b2535. <https://doi.org/10.1136/bmj.b2535>.
- [176] Hayden JA, van der Windt DA, Cartwright JL, Côté P, Bombardier C. Assessing bias in studies of prognostic factors. *Ann Intern Med* 2013;158:280–6. <https://doi.org/10.7326/0003-4819-158-4-201302190-00009>.
- [177] McHugh ML. Interrater reliability: the kappa statistic. *Biochem Med (Zagreb)* 2012;22:276–82.
- [178] Higgins JPT, Thompson SG, Deeks JJ, Altman DG. Measuring inconsistency in meta-analyses. *BMJ* 2003;327:557–60.
- [179] Su AW, McIntosh AL, Schueler BA, Milbrandt TA, Winkler JA, Stans AA, et al. How Does Patient Radiation Exposure Compare With Low-dose O-arm Versus Fluoroscopy for Pedicle Screw Placement in Idiopathic Scoliosis?. *J Pediatr Orthop* 2017;37:171–7. <https://doi.org/10.1097/BPO.0000000000000608>.
- [180] Ughwanogho E, Patel NM, Baldwin KD, Sampson NR, Flynn JM. Computed tomography-guided navigation of thoracic pedicle screws for adolescent idiopathic scoliosis results in more accurate placement and less screw removal. *Spine* 2012;37:E473-478. <https://doi.org/10.1097/BRS.0b013e318238bbd9>.
- [181] Sakai Y, Matsuyama Y, Nakamura H, Katayama Y, Imagama S, Ito Z, et al. Segmental pedicle screwing for idiopathic scoliosis using computer-assisted surgery. *J Spinal Disord Tech* 2008;21:181–6. <https://doi.org/10.1097/BSD.0b013e318074d388>.
- [182] Vissarionov S, Schroeder JE, Novikov SN, Kokyshin D, Belanchikov S, Kaplan L. The Utility of 3-Dimensional-Navigation in the Surgical Treatment of Children With Idiopathic Scoliosis. *Spine Deformity* 2014;2:270–5. <https://doi.org/10.1016/j.jspd.2014.03.004>.
- [183] Zhu W, Sun W, Xu L, Sun X, Liu Z, Qiu Y, et al. Minimally invasive scoliosis surgery assisted by O-arm navigation for Lenke Type 5C adolescent idiopathic scoliosis: a comparison with standard open approach spinal instrumentation. *J Neurosurg Pediatrics* 2017;19:472–8. <https://doi.org/10.3171/2016.11.PEDS16412>.
- [184] Su P, Zhang W, Peng Y, Liang A, Du K, Huang D. Use of computed tomographic reconstruction to establish the ideal entry point for pedicle screws in idiopathic scoliosis. *Eur Spine J* 2012;21:23–30. <https://doi.org/10.1007/s00586-011-1962-8>.
- [185] Takahashi J, Hirabayashi H, Hashidate H, Ogihara N, Kato H. Accuracy of multilevel registration in image-guided pedicle screw insertion for adolescent idiopathic scoliosis. *Spine* 2010;35:347–52. <https://doi.org/10.1097/BRS.0b013e3181b77f0a>.
- [186] Akazawa T, Kotani T, Sakuma T, Minami S, Tsukamoto S, Ishige M. Evaluation of pedicle screw placement by pedicle channel grade in adolescent idiopathic scoliosis: should we challenge narrow pedicles? *J Orthop Sci* 2015;20:818–22. <https://doi.org/10.1007/s00776-015-0746-0>.



- [187] Zhang W, Takigawa T, Wu Y, Sugimoto Y, Tanaka M, Ozaki T. Accuracy of pedicle screw insertion in posterior scoliosis surgery: a comparison between intraoperative navigation and preoperative navigation techniques. *Eur Spine J* 2017;26:1756–64. <https://doi.org/10.1007/s00586-016-4930-5>.
- [188] Shufflebarger HL, Geck MJ, Clark CE. The posterior approach for lumbar and thoracolumbar adolescent idiopathic scoliosis: posterior shortening and pedicle screws. *Spine* 2004;29:269–76; discussion 276.
- [189] Chen J, Yang C, Ran B, Wang Y, Wang C, Zhu X, et al. Correction of Lenke 5 adolescent idiopathic scoliosis using pedicle screw instrumentation: does implant density influence the correction? *Spine* 2013;38:E946-951. <https://doi.org/10.1097/BRS.0b013e318297bfd4>.
- [190] Sudo H, Ito M, Abe Y, Abumi K, Takahata M, Nagahama K, et al. Surgical treatment of Lenke 1 thoracic adolescent idiopathic scoliosis with maintenance of kyphosis using the simultaneous double-rod rotation technique. *Spine* 2014;39:1163–9. <https://doi.org/10.1097/BRS.0000000000000364>.
- [191] Upendra BN, Meena D, Chowdhury B, Ahmad A, Jayaswal A. Outcome-based classification for assessment of thoracic pedicular screw placement. *Spine* 2008;33:384–90. <https://doi.org/10.1097/BRS.0b013e3181646ba1>.
- [192] Kwan MK, Chiu CK, Gani SMA, Chan CYW. Accuracy and Safety of Pedicle Screw Placement in Adolescent Idiopathic Scoliosis (AIS) Patients: A Review of 2020 Screws Using Computed Tomography Assessment. *Spine* 2016. <https://doi.org/10.1097/BRS.0000000000001738>.
- [193] Sudo H, Abe Y, Abumi K, Iwasaki N, Ito M. Surgical treatment of double thoracic adolescent idiopathic scoliosis with a rigid proximal thoracic curve. *Eur Spine J* 2016;25:569–77. <https://doi.org/10.1007/s00586-015-4139-z>.
- [194] Macke JJ, Woo R, Varich L. Accuracy of robot-assisted pedicle screw placement for adolescent idiopathic scoliosis in the pediatric population. *J Robot Surg* 2016;10:145–50. <https://doi.org/10.1007/s11701-016-0587-7>.
- [195] Lee CS, Hwang CJ, Lee S-W, Chung JH, Ahn Y-J, Kim Y-T, et al. Changes of deformity due to the position and anesthesia in adolescent idiopathic scoliosis. *J Spinal Disord Tech* 2010;23:377–82. <https://doi.org/10.1097/BSD.0b013e3181bccec1>.
- [196] Suk S-I, Lee S-M, Chung E-R, Kim J-H, Kim S-S. Selective thoracic fusion with segmental pedicle screw fixation in the treatment of thoracic idiopathic scoliosis: more than 5-year follow-up. *Spine* 2005;30:1602–9.
- [197] Gertzbein SD, Robbins SE. Accuracy of pedicular screw placement in vivo. *Spine* 1990;15:11–4.
- [198] Abul-Kasim K, Strömbeck A, Ohlin A, Maly P, Sundgren PC. Reliability of low-radiation dose CT in the assessment of screw placement after posterior scoliosis surgery, evaluated with a new grading system. *Spine* 2009;34:941–8. <https://doi.org/10.1097/BRS.0b013e31819b22a4>.
- [199] Abul-Kasim K, Ohlin A. The rate of screw misplacement in segmental pedicle screw fixation in adolescent idiopathic scoliosis. *Acta Orthop* 2011;82:50–5. <https://doi.org/10.3109/17453674.2010.548032>.
- [200] Abul-Kasim K, Ohlin A, Strömbeck A, Maly P, Sundgren PC. Radiological and clinical outcome of screw placement in adolescent idiopathic scoliosis: evaluation with low-dose computed tomography. *Eur Spine J* 2010;19:96–104. <https://doi.org/10.1007/s00586-009-1203-6>.
- [201] Wang W, Zhu Z, Zhu F, Wang B, Chu WCW, Cheng JCY, et al. The changes of relative position of the thoracic aorta after anterior or posterior instrumentation of type I Lenke curve in adolescent idiopathic thoracic scoliosis. *Eur Spine J* 2008;17:1019–26. <https://doi.org/10.1007/s00586-008-0691-0>.
- [202] Wong CC, Ting F, Wong B, Lee PI. Accuracy of the funnel technique of thoracic pedicle screws insertion in scoliosis surgery--an evaluation by CT-scans. *Med J Malaysia* 2005;60 Suppl C:35–40.

- [203] Gotfryd AO, Avanzi O. Randomized Clinical Study on Surgical Techniques With Different Pedicle Screw Densities in the Treatment of Adolescent Idiopathic Scoliosis Types Lenke 1A and 1B. *Spine Deformity* 2013;1:272–9. <https://doi.org/10.1016/j.jspd.2013.05.004>.
- [204] Shah SA, Dhawale AA, Oda JE, Yorgova P, Neiss GI, Holmes Jr. L, et al. Ponte Osteotomies With Pedicle Screw Instrumentation in the Treatment of Adolescent Idiopathic Scoliosis. *Spine Deformity* 2013;1:196–204. <https://doi.org/10.1016/j.jspd.2013.03.002>.
- [205] Tsirikos AI, Subramanian AS. Posterior spinal arthrodesis for adolescent idiopathic scoliosis using pedicle screw instrumentation: does a bilateral or unilateral screw technique affect surgical outcome? *J Bone Joint Surg Br* 2012;94:1670–7. <https://doi.org/10.1302/0301-620X.94B12.29403>.
- [206] Lehman RA, Lenke LG, Keeler KA, Kim YJ, Buchowski JM, Cheh G, et al. Operative treatment of adolescent idiopathic scoliosis with posterior pedicle screw-only constructs: minimum three-year follow-up of one hundred fourteen cases. *Spine* 2008;33:1598–604. <https://doi.org/10.1097/BRS.0b013e318178872a>.
- [207] Mattila M, Jalanko T, Helenius I. En bloc vertebral column derotation provides spinal derotation but no additional effect on thoracic rib hump correction as compared with no derotation in adolescents undergoing surgery for idiopathic scoliosis with total pedicle screw instrumentation. *Spine* 2013;38:1576–83. <https://doi.org/10.1097/BRS.0b013e31829a6d37>.
- [208] Matsumoto M, Watanabe K, Ogura Y, Okada E, Hosogane N, Chiba K, et al. Short fusion strategy for Lenke type 1 thoracic curve using pedicle screw fixation. *J Spinal Disord Tech* 2013;26:93–7. <https://doi.org/10.1097/BSD.0b013e31823ac2e8>.
- [209] Wei X-Z, Zhou X-Y, Yang Y-L, Xu X-M, Li J-F, Bai Y-S, et al. Key Vertebral Pedicle Screw Strategy for the Correction of Flexible Lenke Type 1 Adolescent Idiopathic Scoliosis: A Preliminary Study of a 5-year Minimum Radiographic Follow-up. *Spine* 2017;42:1226–32. <https://doi.org/10.1097/BRS.0000000000002143>.
- [210] Chan A, Parent E, Narvacan K, San C, Lou E. Intraoperative image guidance compared with free-hand methods in adolescent idiopathic scoliosis posterior spinal surgery: a systematic review on screw-related complications and breach rates. *The Spine Journal* 2017;17:1215–29. <https://doi.org/10.1016/j.spinee.2017.04.001>.
- [211] Roberts SB, Tsirikos AI, Subramanian AS. Posterior spinal fusion for adolescent idiopathic thoracolumbar/lumbar scoliosis: clinical outcomes and predictive radiological factors for extension of fusion distal to caudal end vertebra. *Bone Joint J* 2014;96-B:1082–9. <https://doi.org/10.1302/0301-620X.96B8.33837>.
- [212] Lee CK, Chan CYW, Gani SMA, Kwan MK. Accuracy of cannulated pedicle screw versus conventional pedicle screw for extra-pedicular screw placement in dysplastic pedicles without cancellous channel in adolescent idiopathic scoliosis: a computerized tomography (CT) analysis. *Eur Spine J* 2017. <https://doi.org/10.1007/s00586-017-5266-5>.
- [213] Abul-Kasim K, Ohlin A. Evaluation of implant loosening following segmental pedicle screw fixation in adolescent idiopathic scoliosis: a 2 year follow-up with low-dose CT. *Scoliosis* 2014;9:13. <https://doi.org/10.1186/1748-7161-9-13>.
- [214] von Heideken J, Iversen MD, Gerdhem P. Rapidly increasing incidence in scoliosis surgery over 14 years in a nationwide sample. *Eur Spine J* 2017. <https://doi.org/10.1007/s00586-017-5346-6>.
- [215] Lenke LG, Betz RR, Clements D, Merola A, Haheer T, Lowe T, et al. Curve prevalence of a new classification of operative adolescent idiopathic scoliosis: does classification correlate with treatment? *Spine* 2002;27:604–11.
- [216] Parker SL, McGirt MJ, Farber SH, Amin AG, Rick A-M, Suk I, et al. Accuracy of free-hand pedicle screws in the thoracic and lumbar spine: analysis of 6816 consecutive screws. *Neurosurgery* 2011;68:170–8; discussion 178. <https://doi.org/10.1227/NEU.0b013e3181fdaf4>.

- [217] Modi H, Suh SW, Song H-R, Yang J-H. Accuracy of thoracic pedicle screw placement in scoliosis using the ideal pedicle entry point during the freehand technique. *Int Orthop* 2009;33:469–75. <https://doi.org/10.1007/s00264-008-0535-x>.
- [218] Reames D, Smith J, Fu K-M. Complications in the Surgical Treatment of 19,360 Cases of Pediatric Scoliosis. *Spine* 2011;36:1484–91.
- [219] Cheng H, Chen BP-H, Soleas IM, Ferko NC, Cameron CG, Hinoul P. Prolonged Operative Duration Increases Risk of Surgical Site Infections: A Systematic Review. *Surg Infect (Larchmt)* 2017;18:722–35. <https://doi.org/10.1089/sur.2017.089>.
- [220] Prime<sup>x</sup> 13W - In Depth. OptiTrack n.d. <http://www.optitrack.com/products/primex-13w/index.html> (accessed February 12, 2020).
- [221] Eichelberger P, Ferraro M, Minder U, Denton T, Blasimann A, Krause F, et al. Analysis of accuracy in optical motion capture - A protocol for laboratory setup evaluation. *J Biomech* 2016;49:2085–8. <https://doi.org/10.1016/j.jbiomech.2016.05.007>.
- [222] Chung KJ, Suh SW, Desai S, Song HR. Ideal entry point for the thoracic pedicle screw during the free hand technique. *Int Orthop* 2008;32:657–62. <https://doi.org/10.1007/s00264-007-0363-4>.
- [223] Guha D, Jakubovic R, Gupta S, Alotaibi NM, Cadotte D, da Costa LB, et al. Spinal intraoperative three-dimensional navigation: correlation between clinical and absolute engineering accuracy. *Spine J* 2016. <https://doi.org/10.1016/j.spinee.2016.10.020>.
- [224] Barratt DC, Davies AH, Hughes AD, Thom SA, Humphries KN. Optimisation and evaluation of an electromagnetic tracking device for high-accuracy three-dimensional ultrasound imaging of the carotid arteries. *Ultrasound Med Biol* 2001;27:957–68.
- [225] Treece GM, Gee AH, Prager RW, Cash CJC, Berman LH. High-definition freehand 3-D ultrasound. *Ultrasound Med Biol* 2003;29:529–46.
- [226] Huang Q, Zeng Z. A Review on Real-Time 3D Ultrasound Imaging Technology. *BioMed Research International* 2017. <https://doi.org/10.1155/2017/6027029>.
- [227] Neshat H, Cool DW, Barker K, Gardi L, Kakani N, Fenster A. A 3D ultrasound scanning system for image guided liver interventions. *Medical Physics* 2013;40:112903. <https://doi.org/10.1118/1.4824326>.
- [228] Fenster A, Bax J, Romagnoli C, Neshat H, Cool D, Kakani N. 3D Ultrasound Imaging in Image-Guided Intervention n.d.:4.
- [229] Welch JN, Johnson JA, Bax MR, Badr R, Shahidi R. A real-time freehand 3D ultrasound system for image-guided surgery. 2000 IEEE Ultrasonics Symposium. Proceedings. An International Symposium (Cat. No.00CH37121), vol. 2, 2000, p. 1601–4 vol.2. <https://doi.org/10.1109/ULTSYM.2000.921630>.
- [230] Sakuma I, Tanaka Y, Takai Y, Kobayashi E, Dohi T, Schorr O, et al. Three-dimensional digital ultrasound imaging system for surgical navigation. *International Congress Series* 2001;1230:117–22. [https://doi.org/10.1016/S0531-5131\(01\)00027-9](https://doi.org/10.1016/S0531-5131(01)00027-9).
- [231] Arif M, Moelker A, van Walsum T. Needle Tip Visibility in 3D Ultrasound Images. *Cardiovasc Intervent Radiol* 2018;41:145–52. <https://doi.org/10.1007/s00270-017-1798-7>.
- [232] Nguyen DV, Vo QN, Le LH, Lou EHM. Validation of 3D surface reconstruction of vertebrae and spinal column using 3D ultrasound data – A pilot study. *Medical Engineering & Physics* 2015;37:239–44. <https://doi.org/10.1016/j.medengphy.2014.11.007>.
- [233] Solberg OV, Lindseth F, Bø LE, Muller S, Bakeng JBL, Tangen GA, et al. 3D ultrasound reconstruction algorithms from analog and digital data. *Ultrasonics* 2011;51:405–19. <https://doi.org/10.1016/j.ultras.2010.11.007>.
- [234] Zenbutsu S, Igarashi T, Nakamura R, Nakaguchi T, Yamaguchi T. 3D ultrasound assisted laparoscopic liver surgery by visualization of blood vessels. 2013 IEEE International Ultrasonics Symposium (IUS), 2013, p. 840–3. <https://doi.org/10.1109/ULTSYM.2013.0216>.

- [235] Penney GP, Barratt DC, Chan CSK, Slomczykowski M, Carter TJ, Edwards PJ, et al. Cadaver validation of intensity-based ultrasound to CT registration. *Medical Image Analysis* 2006;10:385–95. <https://doi.org/10.1016/j.media.2006.01.003>.
- [236] Chan A, Aguilon J, Hill D, Lou E. Precision and accuracy of consumer-grade motion tracking system for pedicle screw placement in pediatric spinal fusion surgery. *Med Eng Phys* 2017;46:33–43. <https://doi.org/10.1016/j.medengphy.2017.05.003>.
- [237] Kikinis R, Pieper SD, Vosburgh KG. 3D Slicer: A Platform for Subject-Specific Image Analysis, Visualization, and Clinical Support. In: Jolesz FA, editor. *Intraoperative Imaging and Image-Guided Therapy*, New York, NY: Springer; 2014, p. 277–89. [https://doi.org/10.1007/978-1-4614-7657-3\\_19](https://doi.org/10.1007/978-1-4614-7657-3_19).
- [238] Unity, Learn n.d. <https://unity.com/learn> (accessed May 1, 2019).
- [239] Unity User Manual n.d. <https://docs.unity3d.com/Manual/index.html> (accessed May 1, 2019).
- [240] Dummiesman. Runtime OBJ Importer. Unity Asset Store: Runtime OBJ Importer 2019. <https://assetstore.unity.com/packages/tools/modeling/runtime-obj-importer-49547> (accessed May 10, 2019).
- [241] Suleyman Y Kula. Runtime File Browser. Unity Asset Store: Runtime OBJ Importer 2019. <https://assetstore.unity.com/packages/tools/gui/runtime-file-browser-113006> (accessed May 10, 2019).
- [242] Burian E, Rohrmeier A, Schlaeger S, Dieckmeyer M, Diefenbach MN, Syväri J, et al. Lumbar muscle and vertebral bodies segmentation of chemical shift encoding-based water-fat MRI: the reference database MyoSegmentUM spine. *BMC Musculoskeletal Disorders* 2019;20:152. <https://doi.org/10.1186/s12891-019-2528-x>.
- [243] Vania M, Mureja D, Lee D. Automatic Spine Segmentation using Convolutional Neural Network via Redundant Generation of Class Labels for 3D Spine Modeling. *ArXiv:171201640 [Cs]* 2017.
- [244] Badr El Dine FMM, El Shafei MM. Sex determination using anthropometric measurements from multi-slice computed tomography of the 12th thoracic and the first lumbar vertebrae among adult Egyptians. *Egyptian Journal of Forensic Sciences* 2015;5:82–9. <https://doi.org/10.1016/j.ejfs.2014.07.005>.
- [245] Runge A, Steinbichler T, Giotakis A, Schartinger V, Hörmann R, Riechelmann H, et al. Accuracy of surface registration in cranial electromagnetic navigation. *Otorhinolaryngol Head Neck Sur* 2018;3. <https://doi.org/10.15761/OHNS.1000169>.
- [246] Grauvogel TD, Engelskirchen P, Semper-Hogg W, Grauvogel J, Laszig R. Navigation accuracy after automatic- and hybrid-surface registration in sinus and skull base surgery. *PLOS ONE* 2017;12:e0180975. <https://doi.org/10.1371/journal.pone.0180975>.
- [247] Wei B, Sun G, Hu Q, Tang E. The Safety and Accuracy of Surgical Navigation Technology in the Treatment of Lesions Involving the Skull Base. *Journal of Craniofacial Surgery* 2017;28:1431–4. <https://doi.org/10.1097/SCS.00000000000003624>.
- [248] Portable Pocket Handheld Ultrasound Scanners - Clarius. Clarius Mobile Health n.d. <https://clarius.com/> (accessed March 19, 2020).
- [249] Rehm J, Germann T, Akbar M, Pepke W, Kauczor H-U, Weber M-A, et al. 3D-modeling of the spine using EOS imaging system: Inter-reader reproducibility and reliability. *PLOS ONE* 2017;12:e0171258. <https://doi.org/10.1371/journal.pone.0171258>.
- [250] Dey A, Billinghurst M, Lindeman RW, Swan JEI. A Systematic Review of 10 Years of Augmented Reality Usability Studies: 2005 to 2014. *Front Robot AI* 2018;5. <https://doi.org/10.3389/frobt.2018.00037>.
- [251] Elmi-Terander A, Burström G, Nachabé R, Fagerlund M, Ståhl F, Charalampidis A, et al. Augmented reality navigation with intraoperative 3D imaging vs fluoroscopy-assisted free-hand surgery for

spine fixation surgery: a matched-control study comparing accuracy. *Sci Rep* 2020;10:1–8. <https://doi.org/10.1038/s41598-020-57693-5>.

[252] Gibby JT, Swenson SA, Cvetko S, Rao R, Javan R. Head-mounted display augmented reality to guide pedicle screw placement utilizing computed tomography. *Int J CARS* 2018:1–11. <https://doi.org/10.1007/s11548-018-1814-7>.

## Figure References

The following figures were acquired according to Creative Commons Licenses that allow reuse and adaption of images, provided the original creation is credited.

Figure 2.1: Mikeingram1, 2017, Sagittal Spine Vector, digital image, viewed February 14, 2019, <<https://commons.wikimedia.org/wiki/File:SagittalSpineVector.svg>>, used with Creative Commons CC0 1.0 Universal Public Domain Dedication

Figure 2.2a: Anatomography, 2012, Thoracic vertebra 5 close-up superior surface, digital image, viewed February 14, 2019, <[https://commons.wikimedia.org/wiki/File:Thoracic\\_vertebra\\_5\\_close-up\\_superior\\_surface.png](https://commons.wikimedia.org/wiki/File:Thoracic_vertebra_5_close-up_superior_surface.png)>, used with Creative Commons Attribution-Share Alike 2.1 Japan License

Figure 2.2b: Anatomography, 2012, Thoracic vertebra 5 close-up posterior surface, digital image, viewed February 14, 2019, <[https://commons.wikimedia.org/wiki/File:Thoracic\\_vertebra\\_5\\_close-up\\_posterior\\_surface.png](https://commons.wikimedia.org/wiki/File:Thoracic_vertebra_5_close-up_posterior_surface.png)>, used with Creative Commons Attribution-Share Alike 2.1 Japan License

Figure 2.2c: Anatomography, 2012, Thoracic vertebra 5 close-up lateral surface, digital image, viewed February 14, 2019, <[https://commons.wikimedia.org/wiki/File:Thoracic\\_vertebra\\_5\\_close-up\\_lateral\\_surface.png](https://commons.wikimedia.org/wiki/File:Thoracic_vertebra_5_close-up_lateral_surface.png)>, used with Creative Commons Attribution-Share Alike 2.1 Japan License

Figure 2.3: Dailly Anthony, 2011, Moelle Epinière, viewed February 15, 2019, <[https://commons.wikimedia.org/wiki/File:Moelle\\_Epini%C3%A8re.png](https://commons.wikimedia.org/wiki/File:Moelle_Epini%C3%A8re.png)>, used with Creative Commons Attribution 3.0 Unported License

Figure 2.4: Skoliose-Info-Forum.de, 2005, Scoliosis cobb, viewed February 16, 2019, <[https://commons.wikimedia.org/wiki/File:Scoliosis\\_cobb.gif](https://commons.wikimedia.org/wiki/File:Scoliosis_cobb.gif)>, used with Creative Commons Attribution-Share Alike 3.0 Unported License

Figure 2.8: Lionel Brits, 2008, Euler Angles, viewed March 12, 2019, <[https://en.wikipedia.org/wiki/Euler\\_angles#/media/File:Eulerangles.svg](https://en.wikipedia.org/wiki/Euler_angles#/media/File:Eulerangles.svg)>, used with Creative Commons Attribution 3.0 Unported License

Figure 2.10a: Renatokeshet, 2008, Erosion, viewed March 12, 2019, < <https://commons.wikimedia.org/wiki/File:Erosion.png>>, used with Creative Commons Attribution-Share Alike 3.0 Unported License

Figure 2.10b: Renatokeshet, 2008, Dilation, viewed March 12, 2019, < <https://commons.wikimedia.org/wiki/File:Dilation.png>>, used with Creative Commons Attribution-Share Alike 3.0 Unported License

Figure 2.10c: Renatokeshet, 2008, Opening, viewed March 12, 2019, < <https://commons.wikimedia.org/wiki/File:Opening.png>>, used with Creative Commons Attribution-Share Alike 3.0 Unported License

Figure 2.10d: Renatokeshet, 2008, Closing, viewed March 12, 2019, < <https://commons.wikimedia.org/wiki/File:Closing.png>>, used with Creative Commons Attribution-Share Alike 3.0 Unported License

Figure 2.12: Myohan, 2009, viewed March 12, 2019, < [https://commons.wikimedia.org/wiki/File:NI\\_petct.jpg](https://commons.wikimedia.org/wiki/File:NI_petct.jpg)>, used with Creative Commons Attribution 3.0 Unported License

Figure 2.13: Cmglee, 2016, viewed March 15, 2019, < [https://en.wikipedia.org/wiki/Transformation\\_matrix#/media/File:2D\\_affine\\_transformation\\_matrix.svg](https://en.wikipedia.org/wiki/Transformation_matrix#/media/File:2D_affine_transformation_matrix.svg)>, used with Creative Commons Attribution-ShareAlike 3.0 Unported License

## Appendix 1: Search Strategy

### EMBASE, MEDLINE, CENTRAL

1. exp idiopathic scoliosis/
2. (idiopathic scoliosis or ais).mp.
3. 1 or 2
4. (((adult or infant\* or early onset) adj2 (deformity or degenerative or scoliosis)) or (degenerative adj2 scoliosis) or trauma\*).ti.
5. 3 not 4
6. (screw or screws or uniaxial or multiaxial or polyaxial or uni-axial or multi-axial or poly-axial).mp.
7. (((arthrodesis and (lumbar or spinal or spine or thoracic or sacral or sacrum or vertebra\*)) or spinal fusion) and (hook or hooks or rod or rods or wire or wires or instrumentation)).mp.
8. (spinal instrumentation or thoracic fusion or limited fusion or (posterior adj3 (fusion\* or correction\* or stabilisation or stabilization))).mp.
9. 6 or 7 or 8
10. 5 and 9
11. limit 10 to (conference abstract or conference proceeding or editorial or letter)
12. 10 not 11
13. case report/
14. ((case not (case control or case-control or case series or case-series or case-cohort or case cohort or case crossover)) adj4 (study or report\*)).tw.
15. ((year\* old or month\* old or day\* old or yr\* old or y old) adj3 (female or male or child or woman or man or girl or boy or baby)).tw.
16. 12 not (13 or 14 or 15)
17. limit 16 to (english language and yr="1970 -Current")
18. limit 17 to animals
19. 17 not 18
20. Scoliosis/
21. (idiopathic scoliosis or ais).mp.
22. 20 or 21

23. (((adult or infant\* or early onset) adj2 (deformity or degenerative or scoliosis)) or (degenerative adj2 scoliosis) or trauma\*).ti.
24. 22 not 23
25. (screw or screws or uniaxial or multiaxial or polyaxial or uni-axial or multi-axial or poly-axial).mp.
26. (((arthrodesis and (lumbar or spinal or spine or thoracic or sacral or sacrum or vertebra\*)) or spinal fusion) and (hook or hooks or rod or rods or wire or wires or instrumentation)).mp.
27. (spinal instrumentation or thoracic fusion or limited fusion or (posterior adj3 (fusion\* or correction\* or stabilisation or stabilization))).mp.
28. 25 or 26 or 27
29. 24 and 28
30. limit 29 to (comment or editorial or guideline or in vitro or letter or practice guideline)
31. 29 not 30
32. case reports/
33. ((case not (case control or case-control or case series or case-series or case-cohort or case cohort or case crossover)) adj4 (study or report\*)).tw.
34. ((year\* old or month\* old or day\* old or yr\* old or y old) adj3 (female or male or child or woman or man or girl or boy or baby)).tw.
35. case report\*.jw.
36. (or/32-35) and 31
37. 31 not 36
38. limit 37 to yr="1970 -Current"
39. limit 38 to english language
40. limit 39 to animals
41. 39 not 40
42. 19 use oomezd
43. 41 use prmz
44. 29 use cctr
45. 42 or 43 or 44
46. remove duplicates from 45



## CINAHL

S1: idiopathic scoliosis

S2: ais

S3: S1 OR S2

S4: TI (((adult or infant\* or early onset) n2 (deformity or degenerative or scoliosis)) or (degenerative n2 scoliosis) or trauma\*)

S5: S3 not S4

S6: (screw or screws or uniaxial or multiaxial or polyaxial or uni-axial or multi-axial or poly-axial)

S7: (((arthrodesis and (lumbar or spinal or spine or thoracic or sacral or sacrum or vertebra\*)) or spinal fusion) and (hook or hooks or rod or rods or wire or wires or instrumentation))

S8: (spinal instrumentation or thoracic fusion or limited fusion or (posterior n3 (fusion\* or correction\* or stabilisation or stabilization)))

S9: S6 or S7 or S8

S10: S5 and S9

S11: ((case not (case control or case-control or case series or case-series or case-cohort or case cohort or case crossover)) n4 (study or report\*))

S12: ((year\* old or month\* old or day\* old or yr\* old or y old) n3 (female or male or child or woman or man or girl or boy or baby))

S13: S10 not (s11 or s12)

S14: TI ( mouse or murine or rat or rats or sheep or chicken or pig or porcine or pigs or rabbit\* or zebra fish or zebra fish ) OR MW ( mouse or murine or rat or rats or sheep or chicken or pig or porcine or pigs or rabbit\* or zebra fish or zebra fish )

S15: S13 NOT S14

## Web of Science

**#1 TOPIC:** (screw or screws or uniaxial or multiaxial or polyaxial or uni-axial or multi-axial or poly-axial) *OR* **TOPIC:** ("spinal instrumentation" or "thoracic fusion" or "limited fusion" or "posterior spinal fusion\*" or (posterior SAME correction\*) or (posterior SAME stabilisation) or (posterior SAME stabilization))

*DocType=All document types; Language=All languages;*

**#2 TOPIC:** ("adolescent idiopathic scoliosis") *NOT* **TITLE:** ("adult scoliosis" or "infant\* scoliosis" or "early onset scoliosis" or "degenerative scoliosis" or trauma)

*DocType=All document types; Language=All languages;*

**#3 TOPIC:** ("adolescent idiopathic scoliosis") *NOT* **TITLE:** ("adult scoliosis" or "infant\* scoliosis" or "early onset scoliosis" or "degenerative scoliosis" or trauma)

Refined by: **[excluding]: DOCUMENT TYPES:** (EDITORIAL OR CASE REPORT OR LETTER)

*DocType=All document types; Language=All languages;*

#4 #3 AND #1

Refinedm by: **[excluding]: DOCUMENT TYPES:** (PATENT)

*DocType=All document types; Language=All languages;*

## Appendix 2: Quality Appraisals

<b>QUIPS 1</b>	Provide comments or text excerpts to facilitate the consensus process that will follow. Key Characteristics: Age, Gender, Curve Severity, Curve Type, Surgery Type	
<b>1. Study Participation</b>	<b>Goal: To judge the risk of selection bias: likelihood that relationship between PF and outcome is different for participants and eligible non-participants</b>	
Source of target population key characteristics:	The source population or population of interest is adequately described for key characteristics (LIST).	Must describe key characteristics in population.
Method used to identify population	The sampling frame and recruitment are adequately described, including methods to identify the sample sufficient to limit potential bias (number and type used, e.g., referral patterns in health care)	Must be randomized or consecutive and describe source of population (ex: database search, referral patterns). Partial if only one.
Recruitment period	Period of recruitment is adequately described	Must describe surgical dates in body of the article. No partial.
Place of recruitment	Place of recruitment (setting and geographic location) are adequately described	Must either mention hospital in body of text, or for single center, have single address in contacts. No partial.
Inclusion and exclusion criteria	Inclusion and exclusion criteria are adequately described (e.g., including explicit diagnostic criteria or “zero time” description).	Must include both inclusion and exclusion. Partial if only one.
Adequate study participation	There is adequate participation in the study by eligible individuals (>100 patients, multicenter)	Must have >100 patients in multicenter trial. Partial if only one.
Baseline characteristics: Age, Gender, Curve Severity, Curve Type, Surgery Type	The baseline study sample (i.e., individuals entering the study) is adequately described for key characteristics (LIST).	Must described 4/5 key characteristics. Partial if 2/5
<b>Summary Study participation</b>	<b>The study sample represents the population of interest on key characteristics, sufficient to limit potential bias of the observed relationship between PF and outcome:</b>	

<b>QUIPS 2</b>	Provide comments or text excerpts to facilitate the consensus process that will follow. Key Characteristics: Age, Gender, Curve Severity, Curve Type, Surgery Type	
<b>2. Study Attrition</b>	<b>Goal: To judge the risk of attrition bias: likelihood that relationship between PF and outcome are different for completing and non-completing participants</b>	
Proportion of baseline sample available for analysis	Response rate (i.e., proportion of study sample completing the study and providing outcome data) is adequate.	Must describe if patients are lost to follow-up after inclusion and exclusion criteria. If no attrition, all other boxes are N/A.
Attempts to collect information on participants who dropped out	Attempts to collect information on participants who dropped out of the study are described.	If lost to follow-up, must describe how follow-up was attempted.
Reasons and potential impact of subjects lost to follow-up	Reasons for loss to follow-up are provided.	If lost to follow-up, must give one reason for loss.
Outcome and prognostic factor information on those lost to follow-up	Participants lost to follow-up are adequately described for key characteristics (LIST).	If lost to follow-up, must describe 3/7 key characteristics for lost patients.
	There are no important differences between key characteristics (LIST) and outcomes in participants who completed the study and those who did not.	If lost to follow-up, must account for 3/7 key characteristics for lost patients.
<b>Study Attrition Summary</b>	<b>Loss to follow-up (baseline sample to study population analyzed) is not associated with key characteristics sufficient to limit potential bias to the observed relationship between PF and outcome:</b>	

<b>QUIPS 3</b>	Provide comments or text excerpts to facilitate the consensus process that will follow. Methods and Setting: Surgeon, Hospital	
<b>3. Prognostic Factor: Image Guidance/Free-Hand</b>	<b>Goal: To judge the risk of measurement bias related to how Image Guidance was measured</b>	
Definition of Image Guidance/Free-Hand	A clear definition or description of 'Image Guidance' is provided (e.g., including dose, level, duration of exposure, and clear specification of the method of measurement).	Must either cite article with full description (Kim et al/Watanabe et al) or give detailed description. No if only mentioned as free-hand or image-guidance with no description.
Valid and Reliable Measurement of Image Guidance	Method of Image Guidance measurement is adequately valid and reliable to limit misclassification bias (e.g., may include relevant outside sources of information on measurement properties, also characteristics, such as blind measurement and limited reliance on recall).	Not applicable for our variable.
	Continuous variables are reported or appropriate cut-points (i.e., not data-dependent) are used.	Not applicable for our variable.
Method and Setting of Image Guidance Usage	The method and setting of measurement of Image Guidance is the same for all study participants.	Must include description of both surgeon and hospital. Partial if only one.
Proportion of data on Image Guidance available for analysis	Adequate proportion of the study sample has complete data for Image Guidance variable.	Marked down only if unknown if certain patients had different method (free-hand or image guidance).
Method used for missing data	Appropriate methods of imputation are used for missing 'Image Guidance' data.	If unknown method patients, must describe how those patients were categorized. If no unknown method patients, N/A
<b>PF Measurement Summary</b>	<b>PF is adequately measured in study participants to sufficiently limit potential bias:</b>	

<b>QUIPS 4</b>	Provide comments or text excerpts to facilitate the consensus process that will follow. Methods and Setting: Surgeon, Hospital	
<b>4. Outcome Measurement: Complications and Breaches</b>	<b>Goal: To judge the risk of bias related to the measurement of outcome</b>	
Definition of the Complications and Breaches	A clear definition of outcome is provided, including duration of follow-up and level and extent of the outcome construct.	If complications or breaches mentioned, must pre-define both prior to results. For breach, must fully define what breach is. For complications, must list which complications were checked. Partial if complications were noted to be checked.
Valid and Reliable Measurement of Complications and Breaches	The method of outcome measurement used is adequately valid and reliable to limit misclassification bias (e.g., may include relevant outside sources of information on measurement properties, also characteristics, such as blind measurement and confirmation of outcome with valid and reliable test).	If breaches, must include reliability measures (multiple readers, blinded). Partial if only 1/2 reliability measures. If complications only, not applicable.
Method and Setting of Measurement of Complications and Breaches	The method and setting of outcome measurement is the same for all study participants.	Must include description of both surgeon and hospital. Partial if only one.
<b>Outcome Measurement Summary</b>	<b>Outcome of interest is adequately measured in study participants to sufficiently limit potential bias:</b>	

<b>QUIPS 5</b>	<p>Provide comments or text excerpts to facilitate the consensus process that will follow.</p> <p>Methods and Setting: Surgeon, OR, Hospital</p> <p>Key Confounders: Type of Screws, Type of Instrumentation, Levels of Fusion</p>	
<b>5. Study Confounding</b>	<b>Goal: To judge the risk of bias due to confounding by another factor</b>	
Important Confounders Measured	All important confounders, including treatments (key variables in conceptual model: LIST), are measured.	Must list 2/3 of: size of screws, uni/multiaxial screws, type of instrumentation. Must specify if thoracic/lumbar fusion measured. Partial if levels of fusion not measured, only mentioned.
Definition of the confounding factor	Clear definitions of the important confounders measured are provided (e.g., including dose, level, and duration of exposures).	Must define all key confounders that were listed previously. Partial if not all defined.
Valid and Reliable Measurement of Confounders	Measurement of all important confounders is adequately valid and reliable (e.g., relevant outside sources of information on measurement properties, blind measurement and limited reliance on recall).	Type of screws/instrumentation: Not applicable. Thoracic/lumbar fusion: blinded/multiple readers of X-ray information.
Method and Setting of Confounding Measurement	The method and setting of confounding measurement are the same for participants.	Must include description of both surgeon and hospital. Partial if only one.
Method used for missing data	Appropriate methods are used if imputation is used for missing confounder data.	If patients missing confounder data, must include methods of imputation. If no missing data, N/A.
Appropriate Accounting for Confounding	Important potential confounders are accounted for in study design (matching for key variables, stratification, or initial assembly of comparable groups).	For listed confounders, must either only include patients of those confounders, or separate patients in methods.
	Important potential confounders are accounted for in the analysis (i.e., appropriate adjustment).	For listed confounders, if not accounted in study design, must analyze patients of each confounder separately.
<b>Study Confounding Summary</b>	<b>Important potential confounders are appropriately accounted for, limiting potential bias with respect to the relationship between PF and outcome:</b>	

<b>QUIPS 6</b>	Provide comments or text excerpts to facilitate the consensus process that will follow. Methods and Setting: Surgeon, OR, Hospital Key Confounders: Type of Screws, Type of Instrumentation, Levels of Fusion	
<b>6. Statistical Analysis and Reporting</b>	<b>Goal: To judge the risk of bias related to the statistical analysis and presentation of results</b>	
Presentation of analytical strategy of complications/breaches related to image guidance	There is sufficient presentation of data to assess the adequacy of the analysis.	Must have appropriate stats: complication/breach rates for single variables, Kappa for reliability measures, comparative statistics for comparisons.
Model development strategy	The strategy for model building (i.e., inclusion of variables in the statistical model) is appropriate and is based on a conceptual framework or model.	If model is built (regression, correlation), must provide appropriate conceptual framework. Otherwise, N/A.
	The selected statistical model is adequate for the design of the study.	If model is built, must have appropriate statistics, otherwise N/A.
Reporting of results	There is no selective reporting of results.	If methods describe reporting of data related to complications, must report results.
<b>Statistical Analysis/Presentation Summary</b>	<b>The statistical analysis is appropriate for the design of the study, limiting potential for presentation of invalid or spurious results:</b>	



## Appendix 3: Systematic Review List of Extracted Articles

- [1] Abul-Kasim K, Ohlin A. The rate of screw misplacement in segmental pedicle screw fixation in adolescent idiopathic scoliosis. *Acta Orthop* 2011;82:50–5. doi:10.3109/17453674.2010.548032.
- [2] Abul-Kasim K, Ohlin A, Strömbeck A, Maly P, Sundgren PC. Radiological and clinical outcome of screw placement in adolescent idiopathic scoliosis: evaluation with low-dose computed tomography. *Eur Spine J* 2010;19:96–104. doi:10.1007/s00586-009-1203-6.
- [3] Akazawa T, Kotani T, Sakuma T, Minami S, Tsukamoto S, Ishige M. Evaluation of pedicle screw placement by pedicle channel grade in adolescent idiopathic scoliosis: should we challenge narrow pedicles? *J Orthop Sci* 2015;20:818–22. doi:10.1007/s00776-015-0746-0.
- [4] Anekstein Y, Mirovsky Y, Arnabitsky V, Gelfer Y, Zaltz I, Smorgick Y. Reversing the concept: correction of adolescent idiopathic scoliosis using the convex rod de-rotation maneuver. *Eur Spine J* 2012;21:1942–9. doi:10.1007/s00586-012-2355-3.
- [5] Bai Y-S, Niu Y-F, Chen Z-Q, Zhu X-D, Gabriel LKP, Wong HK, et al. Comparison of the pedicle screws placement between electronic conductivity device and normal pedicle finder in posterior surgery of scoliosis. *J Spinal Disord Tech* 2013;26:316–20. doi:10.1097/BSD.0b013e318247f21d.
- [6] Bosch L, Boan C, Falk M, White GR, Shrader MW. The Effect of Two Attending Surgeons on Patients With Large-Curve Adolescent Idiopathic Scoliosis Undergoing Posterior Spinal Fusion. *Spine Deform* 2017;5:392–5. doi:10.1016/j.jspd.2017.04.007.
- [7] Chaiyamongkol W, Klineberg EO, Gupta MC. Apical wiring technique in surgical treatment of adolescent idiopathic scoliosis: the intermediate outcomes between Lenke types. *J Spinal Disord Tech* 2013;26:E28-34. doi:10.1097/BSD.0b013e31827ada52.
- [8] Chen J, Yang C, Ran B, Wang Y, Wang C, Zhu X, et al. Correction of Lenke 5 adolescent idiopathic scoliosis using pedicle screw instrumentation: does implant density influence the correction? *Spine* 2013;38:E946-951. doi:10.1097/BRS.0b013e318297bfd4.
- [9] Christodoulou A, Ploumis A, Zidrou C, Terzidis J, Pournaras J. Idiopathic scoliosis. Segmental fusion with transpedicular screws. *Stud Health Technol Inform* 2002;91:433–7.
- [10] Clement J-L, Chau E, Geoffray A, Vallade M-J. Simultaneous translation on two rods to treat adolescent idiopathic scoliosis: radiographic results in coronal, sagittal, and transverse plane of a series of 62 patients with a minimum follow-up of two years. *Spine* 2012;37:184–92. doi:10.1097/BRS.0b013e3182155104.
- [11] Crostelli M, Mazza O, Mariani M. Free-hand pedicle screws insertion technique in the treatment of 120 consecutive scoliosis cases operated without use of intraoperative neurophysiological monitoring. *Eur Spine J* 2012;21 Suppl 1:S43-49. doi:10.1007/s00586-012-2218-y.
- [12] Crostelli M, Mazza O, Mariani M, Mascello D. Treatment of severe scoliosis with posterior-only approach arthrodesis and all-pedicle screw instrumentation. *Eur Spine J* 2013;22:808–14. doi:10.1007/s00586-013-3027-7.
- [13] Dede O, Ward WT, Bosch P, Bowles AJ, Roach JW. Using the freehand pedicle screw placement technique in adolescent idiopathic scoliosis surgery: what is the incidence of neurological symptoms secondary to misplaced screws? *Spine* 2014;39:286–90. doi:10.1097/BRS.000000000000127.
- [14] Di Silvestre M, Bakaloudis G, Lolli F, Vommaro F, Martikos K, Parisini P. Posterior fusion only for

- thoracic adolescent idiopathic scoliosis of more than 80 degrees: pedicle screws versus hybrid instrumentation. *Eur Spine J* 2008;17:1336–49. doi:10.1007/s00586-008-0731-9.
- [15] Ding R, Liang J, Qiu G, Shen J, Li Z. Evaluation of quality of life in adolescent idiopathic scoliosis with different distal fusion level: a comparison of L3 versus L4. *J Spinal Disord Tech* 2014;27:E155-161. doi:10.1097/BSD.000000000000073.
- [16] Dobbs MB, Lenke LG, Kim YJ, Luhmann SJ, Bridwell KH. Anterior/posterior spinal instrumentation versus posterior instrumentation alone for the treatment of adolescent idiopathic scoliotic curves more than 90 degrees. *Spine* 2006;31:2386–91. doi:10.1097/01.brs.0000238965.81013.c5.
- [17] Dobbs MB, Lenke LG, Kim YJ, Kamath G, Peelle MW, Bridwell KH. Selective posterior thoracic fusions for adolescent idiopathic scoliosis: comparison of hooks versus pedicle screws. *Spine* 2006;31:2400–4. doi:10.1097/01.brs.0000240212.31241.8e.
- [18] Ege T, Bilgic S, Koca K, Oguz E, Kilic E, Kose O, et al. Fluoroscopy for transpedicular screw placement in scoliosis: to what extent can radiation exposure be reduced by the freehand technique? *Turk Neurosurg* 2013;23:344–8. doi:10.5137/1019-5149.JTN.7016-12.1.
- [19] Etemadifar M, Jamalaldini M. Evaluating Accuracy of Free-hand Pedicle Screw Insertion in Adolescent Idiopathic Scoliosis Using Postoperative Multi-Slice Computed Tomography Scan. *Adv Biomed Res* 2017;6:19. doi:10.4103/2277-9175.201331.
- [20] Fiorillo P, Demonti HH. Postoperative radiographic control of instrumentation with thoracic pedicle screws in adolescent idiopathic scoliosis. *Coluna/Columna* 2013;12:282–4. doi:10.1590/S1808-18512013000400003.
- [21] Gavassi BM, Pratali R de R, Barsotti CEG, Ferreira RJR, Santos FPE dos, Oliveira CEAS de. Positioning of pedicle screws in adolescent idiopathic scoliosis using electromyography. *Coluna/Columna* 2015;14:97–100. doi:10.1590/S1808-185120151402142338.
- [22] Ghayem Hassankhani E, Omid-Kashani F, Moradkhani S, Ghayem Hassankhani G, Shakeri MT. Comparison of Clinical and Radiologic Outcome of Adolescent Idiopathic Scoliosis Treated with Hybrid Hook-Screw Instrumentation versus Universal Clamp System. *Adv Med* 2016;2016:7639727. doi:10.1155/2016/7639727.
- [23] Gómez H, Burgos J, Hevia E, Maruenda JI, Barrios C, Sanpera I. Immediate postoperative and long-term results of a minimally invasive approach for the correction of adolescent idiopathic scoliosis. *Coluna/Columna* 2013;12:291–5. doi:10.1590/S1808-18512013000400005.
- [24] Gotfryd AO, Avanzi O. Randomized Clinical Study on Surgical Techniques With Different Pedicle Screw Densities in the Treatment of Adolescent Idiopathic Scoliosis Types Lenke 1A and 1B. *Spine Deformity* 2013;1:272–9. doi:10.1016/j.jspd.2013.05.004.
- [25] Grabala P., Grabala M., Kossakowski D., Larysz D. Three-dimensional correction for idiopathic scoliosis with posterior spinal fusion and the risk of neurological complications. *Pol Ann Med* 2016;23:97–101. doi:10.1016/j.poamed.2016.02.004.
- [26] Haber LL, Hughes JD, Womack ED, Roberson RM, Wright PB. Screw Versus Hybrid Constructs for Flexible Thoracic Curves in Adolescent Idiopathic Scoliosis: A Prospective, Randomized Study. *Spine Deformity* 2014;2:367–73. doi:10.1016/j.jspd.2014.05.005.
- [27] Karatoprak O, Unay K, Tezer M, Ozturk C, Aydogan M, Mirzanli C. Comparative analysis of pedicle screw versus hybrid instrumentation in adolescent idiopathic scoliosis surgery. *Int Orthop* 2008;32:523–8. doi:10.1007/s00264-007-0359-0.

- [28] Kemppainen JW, Morscher MA, Gothard MD, Adamczyk MJ, Ritzman TF. Evaluation of Limited Screw Density Pedicle Screw Constructs in Posterior Fusions for Adolescent Idiopathic Scoliosis. *Spine Deform* 2016;4:33–9. doi:10.1016/j.jspd.2015.07.010.
- [29] Krallis P, Thoma S, Kosmidis I, Kyriakopoylos G, Hager I. Hybrid instrumentation for correction of adolescent idiopathic scoliosis. *Acta Orthop Belg* 2012;78:94–9.
- [30] Kwan MK, Chiu CK, Gani SMA, Chan CYW. Accuracy and Safety of Pedicle Screw Placement in Adolescent Idiopathic Scoliosis (AIS) Patients: A Review of 2020 Screws Using Computed Tomography Assessment. *Spine* 2016. doi:10.1097/BRS.0000000000001738.
- [31] Lee CS, Hwang CJ, Lee S-W, Chung JH, Ahn Y-J, Kim Y-T, et al. Changes of deformity due to the position and anesthesia in adolescent idiopathic scoliosis. *J Spinal Disord Tech* 2010;23:377–82. doi:10.1097/BSD.0b013e3181bccec1.
- [32] Lehman RA, Lenke LG, Keeler KA, Kim YJ, Buchowski JM, Cheh G, et al. Operative treatment of adolescent idiopathic scoliosis with posterior pedicle screw-only constructs: minimum three-year follow-up of one hundred fourteen cases. *Spine* 2008;33:1598–604. doi:10.1097/BRS.0b013e318178872a.
- [33] Li J, Cheung KMC, Samartzis D, Ganai-Antonio AKB, Zhu X, Li M, et al. Key-Vertebral Screws Strategy for Main Thoracic Curve Correction in Patients With Adolescent Idiopathic Scoliosis. *Clin Spine Surg* 2016;29:E434-41. doi:10.1097/BSD.0000000000000129.
- [34] Liu T, Hai Y. Sagittal plane analysis of selective posterior thoracic spinal fusion in adolescent idiopathic scoliosis: a comparison study of all pedicle screw and hybrid instrumentation. *J Spinal Disord Tech* 2014;27:277–82. doi:10.1097/01.bsd.0000451597.91287.a0.
- [35] Liu Z, Jin M, Qiu Y, Yan H, Han X, Zhu Z. The Superiority of Intraoperative O-arm Navigation-assisted Surgery in Instrumenting Extremely Small Thoracic Pedicles of Adolescent Idiopathic Scoliosis: A Case-Control Study. *Medicine (Baltimore)* 2016;95:e3581. doi:10.1097/MD.00000000000003581.
- [36] Lonner BS, Auerbach JD, Estreicher M, Milby AH, Kean KE. Video-assisted thoracoscopic spinal fusion compared with posterior spinal fusion with thoracic pedicle screws for thoracic adolescent idiopathic scoliosis. *J Bone Joint Surg Am* 2009;91:398–408. doi:10.2106/JBJS.G.01044.
- [37] Lonner BS, Auerbach JD, Estreicher MB, Kean KE. Thoracic pedicle screw instrumentation: the learning curve and evolution in technique in the treatment of adolescent idiopathic scoliosis. *Spine* 2009;34:2158–64. doi:10.1097/BRS.0b013e3181b4f7e8.
- [38] Lu S, Zhang YZ, Wang Z, Shi JH, Chen YB, Xu XM, et al. Accuracy and efficacy of thoracic pedicle screws in scoliosis with patient-specific drill template. *Med Biol Eng Comput* 2012;50:751–8. doi:10.1007/s11517-012-0900-1.
- [39] Luhmann SJ, Lenke LG, Kim YJ, Bridwell KH, Schootman M. Thoracic adolescent idiopathic scoliosis curves between 70 degrees and 100 degrees: is anterior release necessary? *Spine* 2005;30:2061–7.
- [40] Luo M, Shen M, Wang W, Xia L. Comparison of Consecutive, Interval, and Skipped Pedicle Screw Techniques in Moderate Lenke Type 1 Adolescent Idiopathic Scoliosis. *World Neurosurg* 2017;98:563–70. doi:10.1016/j.wneu.2016.11.064.
- [41] Macke JJ, Woo R, Varich L. Accuracy of robot-assisted pedicle screw placement for adolescent idiopathic scoliosis in the pediatric population. *J Robot Surg* 2016;10:145–50. doi:10.1007/s11701-016-0587-7.
- [42] Matsumoto M, Watanabe K, Ogura Y, Okada E, Hosogane N, Chiba K, et al. Short fusion strategy for

- Lenke type 1 thoracic curve using pedicle screw fixation. *J Spinal Disord Tech* 2013;26:93–7. doi:10.1097/BSD.0b013e31823ac2e8.
- [43] Mattila M, Jalanko T, Helenius I. En bloc vertebral column derotation provides spinal derotation but no additional effect on thoracic rib hump correction as compared with no derotation in adolescents undergoing surgery for idiopathic scoliosis with total pedicle screw instrumentation. *Spine* 2013;38:1576–83. doi:10.1097/BRS.0b013e31829a6d37.
- [44] Miyajima F, Desai S. Minimally invasive surgical options for adolescent idiopathic scoliosis. *Seminars in Spine Surgery* 2015;27:39–44. doi:10.1053/j.semss.2015.01.009.
- [45] Modi HN, Suh S-W, Hong J-Y, Yang J-H. Accuracy of Thoracic Pedicle Screw Using Ideal Pedicle Entry Point in Severe Scoliosis. *Clin Orthop Relat Res* 2010;468:1830–7. doi:10.1007/s11999-010-1280-1.
- [46] Okada E, Watanabe K, Hosogane N. Comparison of Stainless Steel and Titanium Alloy Instruments in Posterior Correction and Fusion Surgery for Adolescent Idiopathic Scoliosis-Prospective Cohort Study with Minimum 2-year Follow-Up. *Journal of Medical and Biological Engineering* 2013;33:325. doi:10.5405/jmbe.1052.
- [47] Ovadia D, Korn A, Fishkin M, Steinberg DM, Wientroub S, Ofiram E. The contribution of an electronic conductivity device to the safety of pedicle screw insertion in scoliosis surgery. *Spine* 2011;36:E1314-1321. doi:10.1097/BRS.0b013e31822a82ec.
- [48] O'Donnell C, Maertens A, Bompadre V, Wagner TA, Krengel W. Comparative radiation exposure using standard fluoroscopy versus cone-beam computed tomography for posterior instrumented fusion in adolescent idiopathic scoliosis. *Spine* 2014;39:E850-855. doi:10.1097/BRS.0000000000000363.
- [49] Privitera DM, Matsumoto H, Gomez JA, Roye Jr. DP, Hyman JE, Vitale MG. Are Breech Rates for Pedicle Screws Higher in the Upper Thoracic Spine? *Spine Deformity* 2013;1:189–95. doi:10.1016/j.jspd.2013.04.002.
- [50] Qi D, Wang J, Zhang Y, Zheng G, Zhang X, Wang Y. Positioning thoracic pedicle screw entry point using a new landmark: a study based on 3-dimensional computed tomographic scan. *Spine* 2014;39:E980-988. doi:10.1097/BRS.0000000000000398.
- [51] Qiu Y, Zhu F, Wang B, Yu Y, Zhu Z, Qian B, et al. Comparison of surgical outcomes of lenke type 1 idiopathic scoliosis: vertebral coplanar alignment versus derotation technique. *J Spinal Disord Tech* 2011;24:492–9. doi:10.1097/BSD.0b013e3182060337.
- [52] Quan GMY, Gibson MJ. Correction of main thoracic adolescent idiopathic scoliosis using pedicle screw instrumentation: does higher implant density improve correction? *Spine* 2010;35:562–7. doi:10.1097/BRS.0b013e3181b4af34.
- [53] Regidor I, de Blas G, Barrios C, Burgos J, Montes E, García-Urquiza S, et al. Recording triggered EMG thresholds from axillary chest wall electrodes: a new refined technique for accurate upper thoracic (T2-T6) pedicle screw placement. *Eur Spine J* 2011;20:1620–5. doi:10.1007/s00586-011-1800-z.
- [54] Roberts SB, Tsirikos AI, Subramanian AS. Posterior spinal fusion for adolescent idiopathic thoracolumbar/lumbar scoliosis: clinical outcomes and predictive radiological factors for extension of fusion distal to caudal end vertebra. *Bone Joint J* 2014;96-B:1082–9. doi:10.1302/0301-620X.96B8.33837.

- [55] Sabharwal S, Apazidis A, Zhao C, Hullinger H, Vives M. Comparison of intraoperative supine and postoperative standing radiographs after posterior instrumentation for adolescent idiopathic scoliosis. *J Pediatr Orthop B* 2011;20:389–96. doi:10.1097/BPB.0b013e328347c2bc.
- [56] Sakai Y, Matsuyama Y, Nakamura H, Katayama Y, Imagama S, Ito Z, et al. Segmental pedicle screwing for idiopathic scoliosis using computer-assisted surgery. *J Spinal Disord Tech* 2008;21:181–6. doi:10.1097/BSD.0b013e318074d388.
- [57] Sale de Gauzy J, Jouve J-L, Accadbled F, Blondel B, Bollini G. Use of the Universal Clamp in adolescent idiopathic scoliosis for deformity correction and as an adjunct to fusion: 2-year follow-up. *J Child Orthop* 2011;5:273–82. doi:10.1007/s11832-011-0357-z.
- [58] Samdani AF, Ranade A, Sciubba DM, Cahill PJ, Antonacci MD, Clements DH, et al. Accuracy of free-hand placement of thoracic pedicle screws in adolescent idiopathic scoliosis: how much of a difference does surgeon experience make? *Eur Spine J* 2010;19:91–5. doi:10.1007/s00586-009-1183-6.
- [59] Samdani AF, Tantorski M, Cahill PJ, Ranade A, Koch S, Clements DH, et al. Triggered electromyography for placement of thoracic pedicle screws: is it reliable? *Eur Spine J* 2011;20:869–74. doi:10.1007/s00586-010-1653-x.
- [60] Sánchez-Márquez JM, Sánchez Pérez-Grueso FJ, Pérez Martín-Buitrago M, Fernández-Baillo N, García-Fernández A, Quintáns-Rodríguez J. [Severe idiopathic scoliosis. Does the approach and the instruments used modify the results?]. *Rev Esp Cir Ortop Traumatol* 2014;58:144–51. doi:10.1016/j.recot.2013.11.010.
- [61] Şarlak AY, Tosun B, Atmaca H, Sarisoy HT, Buluç L. Evaluation of thoracic pedicle screw placement in adolescent idiopathic scoliosis. *Eur Spine J* 2009;18:1892–7. doi:10.1007/s00586-009-1065-y.
- [62] Sarwahi V, Horn JJ, Kulkarni PM, Wollowick AL, Lo Y, Gambassi M, et al. Minimally Invasive Surgery in Patients With Adolescent Idiopathic Scoliosis: Is it Better than the Standard Approach? A 2-Year Follow-up Study. *Clin Spine Surg* 2016;29:331–40. doi:10.1097/BSD.000000000000106.
- [63] Sensakovic WF, O’Dell MC, Agha A, Woo R, Varich L. CT Radiation Dose Reduction in Robot-assisted Pediatric Spinal Surgery. *Spine* 2017;42:E417–24. doi:10.1097/BRS.0000000000001846.
- [64] Shah SA, Dhawale AA, Oda JE, Yorgova P, Neiss GI, Holmes Jr. L, et al. Ponte Osteotomies With Pedicle Screw Instrumentation in the Treatment of Adolescent Idiopathic Scoliosis. *Spine Deformity* 2013;1:196–204. doi:10.1016/j.jspd.2013.03.002.
- [65] Shi Z, Chen J, Wang C, Li M, Li Q, Zhang Y, et al. Comparison of Thoracoscopic Anterior Release Combined With Posterior Spinal Fusion Versus Posterior-only Approach With an All-pedicle Screw Construct in the Treatment of Rigid Thoracic Adolescent Idiopathic Scoliosis. *J Spinal Disord Tech* 2015;28:E454-459. doi:10.1097/BSD.0b013e3182a2658a.
- [66] Shufflebarger HL, Geck MJ, Clark CE. The posterior approach for lumbar and thoracolumbar adolescent idiopathic scoliosis: posterior shortening and pedicle screws. *Spine* 2004;29:269–76; discussion 276.
- [67] Su AW, McIntosh AL, Schueler BA, Milbrandt TA, Winkler JA, Stans AA, et al. How Does Patient Radiation Exposure Compare With Low-dose O-arm Versus Fluoroscopy for Pedicle Screw Placement in Idiopathic Scoliosis?. *J Pediatr Orthop* 2017;37:171–7. doi:10.1097/BPO.0000000000000608.
- [68] Su P, Zhang W, Peng Y, Liang A, Du K, Huang D. Use of computed tomographic reconstruction to

- establish the ideal entry point for pedicle screws in idiopathic scoliosis. *Eur Spine J* 2012;21:23–30. doi:10.1007/s00586-011-1962-8.
- [69] Sudo H, Abe Y, Abumi K, Iwasaki N, Ito M. Surgical treatment of double thoracic adolescent idiopathic scoliosis with a rigid proximal thoracic curve. *Eur Spine J* 2016;25:569–77. doi:10.1007/s00586-015-4139-z.
- [70] Sudo H, Ito M, Abe Y, Abumi K, Takahata M, Nagahama K, et al. Surgical treatment of Lenke 1 thoracic adolescent idiopathic scoliosis with maintenance of kyphosis using the simultaneous double-rod rotation technique. *Spine* 2014;39:1163–9. doi:10.1097/BRS.0000000000000364.
- [71] Suk SI, Lee CK, Kim WJ, Chung YJ, Park YB. Segmental pedicle screw fixation in the treatment of thoracic idiopathic scoliosis. *Spine* 1995;20:1399–405.
- [72] Suk S-I, Lee S-M, Chung E-R, Kim J-H, Kim S-S. Selective thoracic fusion with segmental pedicle screw fixation in the treatment of thoracic idiopathic scoliosis: more than 5-year follow-up. *Spine* 2005;30:1602–9.
- [73] Takahashi J, Hirabayashi H, Hashidate H, Ogihara N, Kato H. Accuracy of multilevel registration in image-guided pedicle screw insertion for adolescent idiopathic scoliosis. *Spine* 2010;35:347–52. doi:10.1097/BRS.0b013e3181b77f0a.
- [74] Tsirikos AI, Mataliotakis G, Bounakis N. Posterior spinal fusion for adolescent idiopathic scoliosis using a convex pedicle screw technique: a novel concept of deformity correction. *Bone Joint J* 2017;99-B:1080–7. doi:10.1302/0301-620X.99B8.BJJ-2016-1351.R1.
- [75] Tsirikos AI, Subramanian AS. Posterior spinal arthrodesis for adolescent idiopathic scoliosis using pedicle screw instrumentation: does a bilateral or unilateral screw technique affect surgical outcome? *J Bone Joint Surg Br* 2012;94:1670–7. doi:10.1302/0301-620X.94B12.29403.
- [76] Uehara M, Takahashi J, Kuraishi S, Shimizu M, Ikegami S, Futatsugi T, et al. Computer-assisted skip pedicle screw fixation for adolescent idiopathic scoliosis. *J Orthop Sci* 2017;22:218–23. doi:10.1016/j.jos.2016.11.012.
- [77] Ughwanogho E, Patel NM, Baldwin KD, Sampson NR, Flynn JM. Computed tomography-guided navigation of thoracic pedicle screws for adolescent idiopathic scoliosis results in more accurate placement and less screw removal. *Spine* 2012;37:E473-478. doi:10.1097/BRS.0b013e318238bbd9.
- [78] Upendra BN, Meena D, Chowdhury B, Ahmad A, Jayaswal A. Outcome-based classification for assessment of thoracic pedicular screw placement. *Spine* 2008;33:384–90. doi:10.1097/BRS.0b013e3181646ba1.
- [79] Vallespir GP, Flores JB, Trigueros IS, Sierra EH, Fernández PD, Olaverri JCR, et al. Vertebral coplanar alignment: a standardized technique for three dimensional correction in scoliosis surgery: technical description and preliminary results in Lenke type 1 curves. *Spine* 2008;33:1588–97. doi:10.1097/BRS.0b013e3181788704.
- [80] Vissarionov S, Schroeder JE, Novikov SN, Kokyshin D, Belanchikov S, Kaplan L. The Utility of 3-Dimensional-Navigation in the Surgical Treatment of Children With Idiopathic Scoliosis. *Spine Deformity* 2014;2:270–5. doi:10.1016/j.jspd.2014.03.004.
- [81] Wang W, Zhu Z, Zhu F, Wang B, Chu WCW, Cheng JCY, et al. The changes of relative position of the thoracic aorta after anterior or posterior instrumentation of type I Lenke curve in adolescent idiopathic thoracic scoliosis. *Eur Spine J* 2008;17:1019–26. doi:10.1007/s00586-008-0691-0.
- [82] Wei X-Z, Zhou X-Y, Yang Y-L, Xu X-M, Li J-F, Bai Y-S, et al. Key Vertebral Pedicle Screw Strategy for

- the Correction of Flexible Lenke Type 1 Adolescent Idiopathic Scoliosis: A Preliminary Study of a 5-year Minimum Radiographic Follow-up. *Spine* 2017;42:1226–32. doi:10.1097/BRS.0000000000002143.
- [83] Wong CC, Ting F, Wong B, Lee PI. Accuracy of the funnel technique of thoracic pedicle screws insertion in scoliosis surgery--an evaluation by CT-scans. *Med J Malaysia* 2005;60 Suppl C:35–40.
- [84] Wu X, Yang S, Xu W, Yang C, Ye S, Liu X, et al. Comparative intermediate and long-term results of pedicle screw and hook instrumentation in posterior correction and fusion of idiopathic thoracic scoliosis. *J Spinal Disord Tech* 2010;23:467–73. doi:10.1097/BSD.0b013e3181bf6797.
- [85] Yang M, Li C, Li Y, Zhao Y, Wei X, Zhang G, et al. Application of 3D rapid prototyping technology in posterior corrective surgery for Lenke 1 adolescent idiopathic scoliosis patients. *Medicine (Baltimore)* 2015;94:e582. doi:10.1097/MD.0000000000000582.
- [86] Yang X, Xu H, Li M, Gu S, Fang X, Wang J, et al. Clinical and radiographic outcomes of the treatment of adolescent idiopathic scoliosis with segmental pedicle screws and combined local autograft and allograft bone for spinal fusion: a retrospective case series. *BMC Musculoskelet Disord* 2010;11:159. doi:10.1186/1471-2474-11-159.
- [87] Yeh Y-C, Niu C-C, Chen L-H, Chen W-J, Lai P-L. Comparison between harvesting and preserving the spinous process for adolescent idiopathic scoliosis. *BMC Musculoskelet Disord* 2016;17:366. doi:10.1186/s12891-016-1222-5.
- [88] Yilmaz G, Borkhuu B, Dhawale AA, Oto M, Littleton AG, Mason DE, et al. Comparative analysis of hook, hybrid, and pedicle screw instrumentation in the posterior treatment of adolescent idiopathic scoliosis. *J Pediatr Orthop* 2012;32:490–9. doi:10.1097/BPO.0b013e318250c629.
- [89] Zhang W, Takigawa T, Wu Y, Sugimoto Y, Tanaka M, Ozaki T. Accuracy of pedicle screw insertion in posterior scoliosis surgery: a comparison between intraoperative navigation and preoperative navigation techniques. *Eur Spine J* 2017;26:1756–64. doi:10.1007/s00586-016-4930-5.
- [90] Zhang Y, Lin G, Wang S, Zhang J, Shen J, Wang Y, et al. Higher Flexibility and Better Immediate Spontaneous Correction May Not Gain Better Results for Non-structural Thoracic Curve in Lenke 5C AIS Patients-risk Factors for its Correction Loss. *Spine* 2016. doi:10.1097/BRS.0000000000001760.
- [91] Zheng C-K, Kan W-S, Li P, Zhao Z-G, Li K. Treatment for severe idiopathic upper thoracic scoliosis in adolescence. *J Spinal Disord Tech* 2013;26:107–11. doi:10.1097/BSD.0b013e31824b7577.
- [92] Zheng X, Qian B-P, Liu Z, Sun X, Zhu Z-Z, Wang B, et al. Screw Placement at the Apex Alters Surgical Outcomes of Moderate Lenke 1 Adolescent Idiopathic Scoliosis. *Clin Spine Surg* 2017;30:E883–91. doi:10.1097/BSD.0000000000000435.
- [93] Zhu W, Sun W, Xu L, Sun X, Liu Z, Qiu Y, et al. Minimally invasive scoliosis surgery assisted by O-arm navigation for Lenke Type 5C adolescent idiopathic scoliosis: a comparison with standard open approach spinal instrumentation. *J Neurosurg Pediatrics* 2017;19:472–8. doi:10.3171/2016.11.PEDS16412.
- [94] Zifang H, Hengwei F, Yaolong D, Wenyuan S, Qifei W, Lei C, et al. Convex-Rod Derotation Maneuver on Lenke Type I Adolescent Idiopathic Scoliosis. *Neurosurgery* 2017. doi:10.1093/neuros/nyx102.

## Appendix 4: Ultrasound Reconstruction Code

```

function [US,Center,Y_Ang_Init]=A_Image_Processing(filename,pathname)
% A_Image_Processing
% Last Modified by A.Chan - Utter Matlab Noob, July 2019
%
% Purpose: Auto_Process takes images from US-Image Stack and CSV motion
% capture file and converts it to an image stack that is placed within the
% capture volume and aligned appropriately.
%
% Inputs to be updated:
% 1: Filters: More details are in the Filters.m file
%
% Inputs: User-selected CSV or MAT file
% Outputs: Volume: Image stack aligned to capture volume
%          Workspace: Location of capture volume
%%%%%%%%%%%%%%%%%%%%%%%%%%%%%%%%%%%%%%%%%%%%%%%%%%%%%%%%%%%%%%%%%%%%%%%%
display('A.1 Data Import')
[US_Raw, Mocap]=Import_Data(filename,pathname);
%% Phase 1: Surface Augmentation and Verticut
display('A.2 Surface Augmentation and Verticut')
Filt_Tog=struct('M',0,'C',1,...
               'H',0,'Q',0,...
               'V',1,'G',1);
Filt_Val=struct('M',[1,1],...           %Median Blur
               'C',[0.6,0.8,0,1],...   %Contrast Filter
               'H',[1],...           %Tophat Filter
               'Q',[5,0.6],...       %Quantization
               'G',[3]);             %Averaging

parfor k=1:size(Mocap,1)
    US_Raw(:,:,k)=Filters(US_Raw(:,:,k),Filt_Tog,Filt_Val);
end

[US, Center]=Realignment(US_Raw, Mocap);

Y_Ang_Init=round(mean(Mocap(:,7)),0);
%C=Center
US=permute(US,[1 3 2]); %Rotate to process in other direction (tried 2,3,1)

%% Phase 2: Surface Smoothing
[~, ~, N_Frames_A]=size(US);

display('A.3 Surface Smoothing')
Filt_Tog=struct('M',0,'C',0,...
               'H',0,'Q',1,...
               'V',0,'G',1);
Filt_Val=struct('M',[2,2],...           %Median Blur
               'C',[0.6,0.8,0,1],...   %Contrast Filter
               'H',[1],...           %Tophat Filter
               'Q',[5,0.8],...       %Quantization
               'G',[2]);             %Averaging
parfor k=1:N_Frames_A
    US(:,:,k)=Filters(US(:,:,k),Filt_Tog,Filt_Val);
end

```



```
display('A.4 Pixel Filter')
US=permute(US,[1 3 2]);
US=Vol_Pixel_Filter(US,20);
%US(:,230:end,:)=0; %Temp Cropper
display('(A) Image Processing Complete')
```

```

function [US_Stack, Mocap]=Import_Data(filename,pathname)
% Import_Data
% Last Modified by A.Chan - Utter Matlab Noob, October 2018
%
% Import Data from US-Image Stack and CSV motion capture file. Program
% allows you to select the Raw file, then automatically processes the rest
%
% Inputs to be updated:
% 1: MCshift: frameshift of motion capture frames at 240fps, based on
% temporal calibration
% 2: USshift: frameshift of ultrasound at 30fps, based on temporal
% calibration
% 3: Resolution: default is 0.2mm
%
% Other notes:
% 1: Code formerly rounded to nearest 0.05mm, deemed not necessary, but to
% do it, double the values, round to 0.1, then halve the values.
% 2: Previously did not process frames that had the same position, but this
% had a virtually non-existent effect on processing time and complicated
% the framing process. Just ignore it. Needs a while-loop to work.
%
% Inputs: User-selected CSV file
% Outputs:
% US_Final: Ultrasound Stack, cropped and resized at 0.2mm resolution
% Mocap: Eight columns: US Frames, MC Frames, correctly matched
%           MC Translation XYZ (x3)
%           MC Rotation XYZ (x3)
%%%%%%%%%%%%%%%%%%%%%%%%%%%%%%%%%%%%%%%%%%%%%%%%%%%%%%%%%%%%%%%%%%%%%%%%
file=strcat(pathname,filename);
displayfile=strcat('File: ',file);
disp(displayfile)
suffix=filename(end-3:end);
if suffix=='.csv'
    Mocap=csvread(file);
elseif suffix=='.mat'
    load(file);
    if exist('Vertebra','var')==1
        Mocap=Vertebra.MC;
    elseif exist('AAA','var')==1
        Mocap=AAA.MC;
    end
else
    display('Invalid file format')
    return
end
%User-defined inputs:
MCshift=1; %Frameshift Mocap Up 1 from calibration
USshift=2; %Frameshift U/S Up 2 from calibration
Res=0.2; %Resolution, default at 0.2mm

%% Remove Missing Images and Coordinates
%Mo-Cap 5-averaging and frameshift mocap
Frames=size(Mocap,1);
for k=3:Frames-3
    Mocap_ave(k,3:8)=mean(Mocap(k+MCshift-2:k+MCshift+2,3:8));
end

```

```

Mocap(3:Frames-3,3:8)=Mocap_ave(3:Frames-3,3:8); %Replace values

%Remove 0 frames from US
USzeros=find(Mocap(:,1)==0);
Mocap(USzeros,:)=[];
Frames=size(Mocap,1);

%Round to 0.1mm
Mocap(:,3:9)=round(Mocap(:,3:9),1); %Round decimal places to within 0.1
Mocap(:,3:5)=Mocap(:,3:5)*10; %Change from mm to 0.1mm

Mocap(:,3:5)=Mocap(:,3:5)/Res; %Round to 0.2mm but keep at real size
Mocap(:,3:5)=round(Mocap(:,3:5),0);
Mocap(:,3:5)=Mocap(:,3:5)*Res;
%% Extract Images Based on CSV Frame Numbers
US_Stack=zeros(150,195,Frames-USshift,'uint8'); %Test this out!
for k=(1+USshift):Frames %Frameshift according to USshift
    if suffix=='.csv'
        imgname=strcat(pathname,'Raw',num2str(Mocap(k,1)),'.png');
        US=imread(imgname);
        US_Stack(:,:,k-USshift)=imresize(US,[150,195]);
    elseif suffix=='.mat'
        if exist('Vertebra','var')==1
            US=uint8(Vertebra.US(:,:,k));
        elseif exist('AAA','var')==1
            US=uint8(AAA.US(:,:,k));
        end
        US(:,553:640)=[];
        US(:,1:90)=[];
        US(418:480,:)=[];
        US(1:60,:)=[];

        US_Stack(:,:,k-USshift)=imresize(US,[150,195]);
    end

end
Mocap(end-USshift:end,:)=[];
end

```

```

function [US] = Filters(US,Filt_Tog,Filt_Val)
% Filters.m
% Last Modified by A.Chan - Utter Matlab Noob, October 2018
%
% Filters takes US-Image Stacks and then processes them according to the
% image processing filters:
%
% Inputs:
% 1: US is the aligned or non-aligned ultrasound stack to be filtered
% 2: Filt_Tog: toggles whether or not the filter will be activated
%           H: Top-Hat Filter
%           G: Averaging filter or Gaussian filter if preferred
%           M: Median filter
%           C: Contrast filter
%           Q: Quantization filter
%           V: Verticut filter, cuts everything below first non-zero
% 3: Filt_Val: values of the filters being activated
%
% Inputs: US image stack, Processed motion capture data
% Outputs:
%   US: Ultrasound stack, filtered according to those chosen.
%%%%%%%%%%%%%%%%%%%%%%%%%%%%%%%%%%%%%%%%%%%%%%%%%%%%%%%%%%%%%%%%%%%%%%%%
warning off;
if Filt_Tog.H==1
    US=imtophat(US,strel('disk',Filt_Val.H));
end
if Filt_Tog.G==1
    h=ones(Filt_Val.G,Filt_Val.G)/(Filt_Val.G*Filt_Val.G);
    US=imfilter(US,h);
    %US=imgaussfilt(US,Filters(10));
end
if Filt_Tog.M==1
    US=medfilt2(US,Filt_Val.M);
end

if Filt_Tog.C==1
    US=imadjust(US,[Filt_Val.C(1);
Filt_Val.C(2)], [Filt_Val.C(3);Filt_Val.C(4)]);
end

US_max=max(max(US).');

if US_max<15
    [USX,USY]=size(US);
    US=zeros(USX,USY);
    IM_Q=0; IM_V=0;
end

if Filt_Tog.Q==1

    thresh=multithresh(US,Filt_Val.Q(1));
    Rng=Filt_Val.Q(1)+1;
    Ratios=zeros(1,Rng);
    N_zero=round(Filt_Val.Q(2)*(Rng),0);
    Ratios(1,(Rng-N_zero+1):Rng)=1;
    US=imquantize(US,thresh,Ratios);

```

```

    US=logical(US);
    US=US*256;
end

if Filt_Tog.V==1
    US_New=zeros(size(US),'uint16');
    Y_size=size(US,2);
    for j=1:Y_size
        %Find non-zero values
        if sum(US(:,j))>0 %Check if column has any non-zero values
            %Find location of all non-zero values
            Non_zeros=find(US(:,j));
            if size(Non_zeros,1)>6
                Surface=Non_zeros(6);
                US(Non_zeros(6):end,j)=0;
            end
        end
    end
end
end
end
end

```

```

function [US_Out, Dim_min]=Realignment(US_In,Mocap)
% Realignment.m
% Last Modified by A.Chan - Utter Matlab Noob, October 2018
%
% Realignment takes US-Image Stack and CSV motion capture file that have
% been processed by Import_Data and then realigns each frame to match the
% motion capture coordinate system
%
% Inputs to be updated:
% 1: R_vector: thickens the image, can make this variable but requires a
% bit of work to do so.
%
% Other notes:
% 1: Only runs efficiently if the images have already been processed, if
% running as a standalone without Import_Data and Filters, it will either
% not function or run very slowly.
%
% Inputs:
% US image stack - frames temporally calibrated
% Mocap: Eight columns: US Frames, MC Frames, correctly matched
%           MC Translation XYZ (x3) at 0.1mm resolution
%           MC Rotation XYZ (x3)
%
% Outputs:
% US_Out: Ultrasound Stack, aligned to the motion capture grid
% Dim_min: Motion capture alignment of the volume at 0.2mm resolution
%%%%%%%%%%%%%%%%%%%%%%%%%%%%%%%%%%%%%%%%%%%%%%%%%%%%%%%%%%%%%%%%%%%%%%%%
%Obtain coordinates of each point
Frames=size(Mocap,1);
Mocap(:,3:5)=Mocap(:,3:5)/2; %Reduces the resolution to 0.2mm
Frame=1;
%display('Finding Coordinates')
for j=1:Frames
    if sum(sum(US_In(:, :, j)))==0
    else
        %Obtain coordinates of non-zero values
        Ax_Pos=0; Lat_Pos=0; Val=0;
        [Ax_Pos, Lat_Pos]=find(US_In(:, :, j)); %Original position in frame is
YX

        %Obtain values at each of these coordinates
        for k=1:size(Lat_Pos,1)
            Val(k, :)=US_In(Ax_Pos(k), Lat_Pos(k), j);
        end
        Lat_Pos=Lat_Pos-1; Ax_Pos=Ax_Pos-1; %Shift Coordinates

        %All ultrasound frame values converted into vector form
        F_size=size(Lat_Pos,1);
        Frame_Pos=zeros(F_size,1);
        Quat_Pos=ones(F_size,1);
        R_vector=[Lat_Pos, Ax_Pos, Frame_Pos, Quat_Pos]; %This center is XYZ

        %Load motion capture data into transformer
        Lat_r = -Mocap(j,6); Ax_r = Mocap(j,7); Fr_r = -Mocap(j,8);
        Lat = -Mocap(j,3); Ax = -Mocap(j,4);Fr = Mocap(j,5);
        Transform=Transformer(Lat_r,Ax_r,Fr_r,Lat,Ax,Fr);
    end
end

```

```

        %Obtain transformed vectors for each frame
        R_new=R_vector*Transform;
        R_new(:,5)=Val;
        %Stack into all coordinates array
        Pixel_Value(Frame:Frame+F_size-1,:)=R_new;
        Frame=Frame+F_size;
    end
end
Pixel=round(Pixel_Value,0);
Pixel=unique(Pixel,'rows');

%Initialize blank volume based on range of values.
[MM,Dim_min,~,Pixel]=Vol_Sizing(Pixel);
[N_Pixels,~]=size(Pixel);
US_Out=zeros(MM(2,3)+1,MM(1,3)+1,MM(3,3)+1,'uint16');

%Populate volume
for k=1:N_Pixels
    US_Out(Pixel(k,2),Pixel(k,1),Pixel(k,3))=Pixel(k,5);
end

end

```

```

function Full_Rot=Transformer(rx,ry,rz,tx,ty,tz)
% Transformer.m
% Last Modified by A.Chan - Utter Matlab Noob, February 2019
%
% Transformer take the translations and rotations and converts it into a
% rotation matrix.
%
% Other notes:
% 1: Order matters, with translation performed last!
%
% Inputs: Translation and rotations
% Outputs:
%   Full_Rot: rotation matrix, (4x4)
%%%%%%%%%%%%%%%%%%%%%%%%%%%%%%%%%%%%%%%%%%%%%%%%%%%%%%%%%%%%%%%%%%%%%%%%
%Initial Coordinate
%Translation Matrix XYZ

Translation=...
[1, 0, 0, 0;...
0, 1, 0, 0;...
0, 0, 1, 0;...
tx, ty, tz, 1];

%Rotation Matrix XYZ
Xrot=...
[1, 0, 0, 0;...
0, cosd(rx), sind(rx), 0;...
0, -sind(rx), cosd(rx), 0;...
0, 0, 0, 1];

Yrot=...
[cosd(ry), 0, -sind(ry), 0;...
0, 1, 0, 0;...
sind(ry), 0, cosd(ry), 0;...
0, 0, 0, 1];

Zrot=...
[cosd(rz), sind(rz), 0, 0;...
-sind(rz), cosd(rz), 0, 0;...
0, 0, 1, 0;...
0, 0, 0, 1];

Full_Rot=Zrot*Yrot*Xrot*Translation;

```



## Appendix 5: Image Pre-Registration Code

```
function
[CT,US,List_Center,Transform,QC]=B_Preregistration(CT_A,US_A,Center,Y_Ang_Init)
%%%%%%%%%%%%%%%%%%%%%%%%%%%%%%%%%%%%%%%%%%%%%%%%%%%%%%%%%%%%%%%%%%%%%%%%
% B_Preregistration.m
% Last Modified by A.Chan - Utter Matlab Noob, July 2019
%
% Purpose: Registration of single CT vertebrae onto 3D ultrasound surface
% image of the same scale. Grouped with A_Image_Processing and
% C_Registration
%
% Inputs: CT volume and US volume from A_Image_Processed
% Outputs: CT aligned volume and US final volume
%
% 1: The volumes are imported and then scaled to speed up registration,
% with scaling at 0.2mm resolution rather than 0.1mm.
%
% 2: CT volume needs to be pre-rotated into symmetrical orientation.
% Ultrasound is also pre-rotated into symmetrical orientation so that the
% inverse rotation can be applied to the CT volume to align the two images.
% Symmetric rotations uses scaling factor 1 (currently at 8) to perform
% rotations. Ranges and increments are within the A_CT_Symmetry file.
%
% 3: Slope of the vertebrae is used to determine the optimal pitch rotation.
% Volume is re-surfaced and scaled by factor 2 (currently at 4),
% slope calculations are iterated, based on only the spinous process
% windowed with Vol_CropSpinous. The spinous process is displayed as a
% separate figure for quality control.
%
% 4: The full volume is rotated to align the two volumes at the 0.2mm
% resolution. Volume is surfaced, transformed, and then resized to be equa
%
% 5: The centroids of the volumes are aligned to speed up the translation
% registration process and reduce the range of translations required
%
% Volume Syntax:
% Vol_A - Original overlapped volumes
% Vol_B - Rotated volumes
% Vol_C - Rotated + centroid translated volumes - surface-only
% Vol_D - Rotated + centroid translated volumes - full body
%
% QC Syntax: A=Useful for all. B=Useful for me. C=Specific application
%%%%%%%%%%%%%%%%%%%%%%%%%%%%%%%%%%%%%%%%%%%%%%%%%%%%%%%%%%%%%%%%%%%%%%%%
%% Step B.1: Initialize Variables and Load Data
display('B.1 Initializing Variables and Loading Data')
Init_Ang=[0,0,0]; %Initial angle
Init_Pos=[0,0,0]; %Initial position
Scale=[8,4]; %Select scaling values for gross and fine symmetry
figure(3)
QC=1;

%Pre-process the Pixel Filter
US_A=Vol_Pixel_Filter(US_A,20);
```

```

%QC Check - Look at the CT and US images (A)
    QC=QC_Check(CT_A, US_A,1,QC);

%QC Check - Check the ultrasound grid (C)
    %Temp_Center=[size(US_A,2),size(US_A,1),size(US_A,3)];
    %Temp_Center(2,:)=Center(1,:);
    %QC=QC_Check(US_A, US_A,Temp_Center,QC);

%% Step B.2: Find Symmetric Transform for CT and US
disp('B.2 Re-orienting CT and US by Symmetry')
[CT_List_Sym,CT_Sym_Ang]=CT_Symmetry(CT_A,Scale);
[US_List_Sym,US_Sym_Ang]=US_Symmetry(US_A,Scale,Y_Ang_Init);
%QC Check - Determine if symmetry has been found (B)
    %QC=QC_Check(CT_List_Sym, US_List_Sym,1,QC);

%% Step B.3: Find the Spinous Process Slope
% Load new volumes for slope comparison.
disp('B.3 Re-orienting CT and US by Slope')

CT_Sym_Scaled=List2Vol(CT_List_Sym);
US_Sym_Scaled=List2Vol(US_List_Sym);

CT_Surf_Scaled=Vol_Surface(CT_Sym_Scaled,Scale(2));
%QC Check - See original slope (C)
%   CT_List_QC=Vol2List(CT_Surf_Scaled);
%   CT_List_QC(:,[1 2])=CT_List_QC(:,[2 1]);
%   US_List_Sym(:,[1 2])=US_List_Sym(:,[2 1]);
%   QC=QC_Check(CT_List_QC, US_List_Sym,1,QC);
%QC Check - Look at the cropping window for slopes (C)
%   Crop_Size=[10,0,0,3,6,2,6];
%   QC=QC_Check(Vol_Crop(CT_Surf_Scaled,Crop_Size),...
%       Vol_Crop(US_Sym_Scaled,Crop_Size),QC);

[CT_List_Slp,
US_List_Slp,CTUS_Slope_Ang]=CTUS_Slope(CT_Surf_Scaled,US_Sym_Scaled);
%QC Check - See if slope has made changes (C)
    %CT_List_Slp(:,[1 2])=CT_List_Slp(:,[2 1]);
    %US_List_Slp(:,[1 2])=US_List_Slp(:,[2 1]);
    %QC=QC_Check(CT_List_Slp, US_List_Slp,1,QC);

%% Step B.4: Rotate Full Symmetric Volumes, Reinitialize Variables
disp('B.4 Aligning Volumes and Performing Pre-Transforms')
% Initialize transforms
Transform(1,:)=CT_Sym_Ang(3,1:3)+CTUS_Slope_Ang(2,1:3);
Transform(2,:)=US_Sym_Ang(2,1:3);

% Shift the CT X and Y origin
CT_A_List=Vol2List(CT_A);
[~,~,Dim_max_Ori]=Vol_Sizing(CT_A_List);
CT_A_List(:,1:2)=CT_A_List(:,1:2)-Dim_max_Ori(:,1:2);

%Obtain the ultrasound origin
US.List=Vol2List(US_A);
US.List=US.List+Center; %This is the real world position of coordinates

```

```

%QC Check - Display original CT and US positions (B)
% [CT.Vol_A,US.Vol_A,~,~,Temp_Center]=Vol_Rewindow(CT_A_List,US.List);
% QC=QC_Check(CT.Vol_A,US.Vol_A,Temp_Center,QC);

% Transform the CT list
CT_Sym_List=Vol_AngPos_Origin(CT_A_List,Transform(1,:),Init_Pos);
[~,Dim_min_Sym,~]=Vol_Sizing(CT_Sym_List);

% Surface the volume
CT_Surf=List2Vol(CT_Sym_List);
CT_Surf=Vol_Surface(CT_Surf,1);
CT_Surf_List=Vol2List(CT_Surf);
CT.SurfList=CT_Surf_List+Dim_min_Sym;

% Transform ultrasound counter angle, these are the real-world coordinates
CT.FullList=Vol_AngPos_Origin(CT_Sym_List,Transform(2,:),Init_Pos);
CT.SurfList=Vol_AngPos_Origin(CT.SurfList,Transform(2,:),Init_Pos);

%QC Check - Display rotated CT and US positions (C)
%[CT.Vol_B,US.Vol_B,~,~,Temp_Center]=Vol_Rewindow(CT.SurfList,US.List);
%QC=QC_Check(CT.Vol_B,US.Vol_B,Temp_Center,QC);

%% Phase B.5: Translate Centroid of CT to Center of US
disp('B.5 Translating CT and US Centroids')
%Find the centroid of the CT volume and center of the US space to align.
%CT volume should be continuous. US center is unaffected by continuity
CT_Centroid=sum(CT.SurfList)/size(CT.SurfList,1);
US_Centroid=sum(US.List)/size(US.List,1);

%Translate centroids
Delta_Centroid=US_Centroid-CT_Centroid;
List_Center.Delta_Centroid=round(Delta_Centroid,0);
Transform(3,:)=Delta_Centroid*0.2;

[CT.SurfList,~]=Vol_AngPos(CT.SurfList,Init_Ang,Delta_Centroid);
[CT.FullList,~]=Vol_AngPos(CT.FullList,Init_Ang,Delta_Centroid);

%QC Check - Display centroid translated CT and US for surface (B)

[CT.Vol_C,US.Vol_C,~,~,List_Center.CSurf,MM]=Vol_Rewindow(CT.SurfList,US.List);
QC=QC_Check(CT.Vol_C,US.Vol_C,List_Center.CSurf,QC);

%QC Check - Display centroid translated CT and US for full, slower... (C)
%[CT.Vol_D,US.Vol_D,~,~,List_Center.DFull]=Vol_Rewindow(CT.FullList,US.List);
%QC=QC_Check(CT.Vol_D,US.Vol_D,List_Center.DFull,QC);

disp('(B) Pre-Registration Complete')
end

```

```

%%%%%%%%%%%%%%%%%%%%%%%%%%%%%%%%%%%%%%%%%%%%%%%%%%%%%%%%%%%%%%%%%%%%%%%%
% CT_Symmetry.m
%
% Paired with A_CT_Sym_Iterate. This function imports the volumes, scales
% them according to pre-determined rotations, and then initializes the
% range and increment of rotations for symmetry processing.
%
% Stage 1: The full volume is rotated grossly in large increments.
% Stage 2: The volume is trimmed to remove much of the vertebral body and
% the volume is rotated in smaller increments
% Stage 3: The volume is transformed according to the gross rotations then
% the fine rotations
%%%%%%%%%%%%%%%%%%%%%%%%%%%%%%%%%%%%%%%%%%%%%%%%%%%%%%%%%%%%%%%%%%%%%%%%
function [Sym_List,Ang]= CT_Symmetry(Ori_Vol,Scale)
%% Step 1: Initialize Volume and Variables
Init_Ang=[0,0,0]; %Initial angle
Init_Pos=[0,0,0]; %Initial position

Gross_Vol=Vol_Scale(Ori_Vol,Scale(1));
Gross_Vol=Vol_Fill(Gross_Vol);
Fine_Vol=Vol_Scale(Ori_Vol,Scale(2));

%% Step 2: Iterate Gross Volume Rotations
%Create Volume List
Gross_List=Vol2List(Gross_Vol);
Fine_List=Vol2List(Fine_Vol);

%Select range and increment for gross rotations
RngIncXZ1=[0,50,50;0,10,10]; %Range of 60 may be adequate
RngIncXZ2=[0,20,20;0,4,4]; %Range of 12 may be adequate

Ang(1,:)=CT_Sym_Iterate(Gross_List,RngIncXZ1,Init_Ang);

%Trim vertebral body to remove bias

[Trim_List,~]=Vol_AngPos(Gross_List,Ang(1,1:3),Init_Pos);
Trim=2/3; %Set proportion to keep
Trim_Vol=List2Vol(Trim_List);
Trim_Vol(ceil(size(Trim_Vol,1)*(Trim)):end,,:)=[];
Trim_List=Vol2List(Trim_Vol);

Ang(2,:)=CT_Sym_Iterate(Trim_List,RngIncXZ2,Init_Ang);
Ang(3,1:3)=Ang(1,1:3)+Ang(2,1:3);

%% Step 4: Obtain Transformation Matrix
[Sym_List,~]=Vol_AngPos(Fine_List,Ang(3,1:3),Init_Pos);

end

```

```

%%%%%%%%%%%%%%%%%%%%%%%%%%%%%%%%%%%%%%%%%%%%%%%%%%%%%%%%%%%%%%%%%%%%%%%%
% CT_Sym_Iterate.m
%
% Paired with A_CT_Symmetry. This function imports the volume coordinate
% list, range, increment and starting rotation angle and iterates rotations
% according to these angles. If both X and Z rotations are specified, it
% will rotate both at the same time.
% For error evaluation, this samples every other XY slice to calculate the
% mean-squared error for the volume.
%
% Input has three cases:
% 1 - Only Y rotation
% 2 - Only Z rotation
% 3 - Y-Z rotation combined
% The type is specified by the range-increment combined input
%%%%%%%%%%%%%%%%%%%%%%%%%%%%%%%%%%%%%%%%%%%%%%%%%%%%%%%%%%%%%%%%%%%%%%%%
function [AngFin]=CT_Sym_Iterate(List,RngInc,Angle)
%Initialize starting conditions
Angle_Ori=Angle;
Pos_Ori=[0,0,0];
Sample=2;
if RngInc(1,2)==0 %Y rotation only
    %Use values RngInc(1,1) and RngInc(2,1);
    for i=1:2*RngInc(1,2)/RngInc(2,2)+1
        Angle(2)=Angle_Ori(2)-RngInc(1,2)+((i-1)*RngInc(2,2));
        Err_Stack(i,1:3)=Angle;
        Ang_List=Vol_AngPos(List,Angle,Pos_Ori);
        Volume=List2Vol(Ang_List);
        Volume_Flip=fliplr(Volume);
        V_size=size(Volume);
        %Err=zeros(V_size(3),1);
        Err_Stack(i,4)=Error_Sampler(Volume,Volume_Flip,Sample);

    end
elseif RngInc(1,2)==0 %Z Rotation only
    %Use values RngInc(1,3) and RngInc(2,3);
    for i=1:2*RngInc(1,3)/RngInc(2,3)+1
        Angle(3)=Angle_Ori(3)-RngInc(1,3)+((i-1)*RngInc(2,3));
        Err_Stack(i,1:3)=Angle;
        Ang_List=Vol_AngPos(List,Angle,Pos_Ori);
        Volume=List2Vol(Ang_List);
        Volume_Flip=fliplr(Volume);
        V_size=size(Volume);
        %Err=zeros(V_size(3),1);
        Err_Stack(i,4)=Error_Sampler(Volume,Volume_Flip,Sample);

    end
else
    for i=1:2*RngInc(1,2)/RngInc(2,2)+1
        Angle(2)=Angle_Ori(2)-RngInc(1,2)+((i-1)*RngInc(2,2));
        i_ten=(i-1)*((RngInc(1,2)/RngInc(2,2))*2+1);
        for j=1:2*RngInc(1,3)/RngInc(2,3)+1
            Angle(3)=Angle_Ori(3)-RngInc(1,3)+((j-1)*RngInc(2,3));
            Err_Stack(i_ten+j,1:3)=Angle;
        end
    end
end

```

```

        Ang_List=Vol_AngPos(List,Angle,Pos_Ori);
        Volume=List2Vol(Ang_List);
        Volume_Flip=fliplr(Volume);
        V_size=size(Volume);
        %Err=zeros(V_size(3),1);
        Err_Stack(i_ten+j,4)=Error_Sampler(Volume,Volume_Flip,Sample);
    %{
    figure(4)
    Heat=Vol2Heat(Volume);
    Err_Stack
    imagesc(Heat)
    pause
    %}
    end
end
end

[Min_Val,Min_Row]=min(Err_Stack);
AngFin=Err_Stack(Min_Row(4),1:4);
Err_Stack;

end

```

```

%%%%%%%%%%%%%%%%%%%%%%%%%%%%%%%%%%%%%%%%%%%%%%%%%%%%%%%%%%%%%%%%%%%%%%%%
% US_Symmetry.m
% Paired with US_Sym_Iterate. This function imports the volumes, scales
% them according to pre-determined rotations, and then initializes the
% range and increment of rotations for symmetry processing.
% Stage 1: The full volume is rotated grossly in large increments.
% Stage 2: The volume is transformed according to the gross rotations then
% the fine rotations
%%%%%%%%%%%%%%%%%%%%%%%%%%%%%%%%%%%%%%%%%%%%%%%%%%%%%%%%%%%%%%%%%%%%%%%%
function [Sym_List,Ang,Err_S]= US_Symmetry( Ori_Vol,Scale,Y_Ang_Init)
%% Step 1: Initialize Volume and Variables

Init_Ang=[0,-Y_Ang_Init,0]; %Initial angle
Init_Pos=[0,0,0]; %Initial position

Gross_Vol=Vol_Scale( Ori_Vol,Scale(1) );
Gross_Vol=Vol_Fill( Gross_Vol );
Fine_Vol=Vol_Scale( Ori_Vol,Scale(2) );

%% Step 2: Iterate Gross Volume Rotations
%Create Volume List
Gross_List=Vol2List( Gross_Vol );
Fine_List=Vol2List( Fine_Vol );

%Select range and increment for gross rotations
RngIncXZ1=[0,0,70;0,0,5]; %Pixel count metric
RngIncXZ2=[0,20,30;0,5,5]; %Pixel-frame ratio
[Ang(1,:),Err_S.A]=US_Sym_Iterate( Gross_List,RngIncXZ1,Init_Ang );
[Ang(2,:),Err_S.B]=US_Sym_Iterate( Gross_List,RngIncXZ2,Ang(1,1:3) );

%% Step 4: Obtain Transformation Matrix
%Transform=Transform_Matrix_XYZT( Ang(2,1:3),Init_Pos ); %pick this one
%Transform=Transform_Matrix_ZYXT( Ang(2,1:3),Init_Pos ); %order matters..
[Sym_List,~]=Vol_AngPos( Fine_List,Ang(2,1:3),Init_Pos );
%Sym_List=Vol_AngPos( Fine_List,Ang(2,1:3),Init_Pos );

end

```

```

%%%%%%%%%%%%%%%%%%%%%%%%%%%%%%%%%%%%%%%%%%%%%%%%%%%%%%%%%%%%%%%%%%%%%%%%
% US_Sym_Iterate.m
% Paired with US_Symmetry. This function imports the volume coordinate
% list, range, increment and initial rotation angle and iterates rotations
% according to these angles. If both X and Z rotations are specified, it
% will rotate both at the same time.
% For error evaluation, the binarized heatmap is used to determine if
% the images are symmetrical.
% Input has three cases:
% 1 - Only X rotation
% 2 - Only Z rotation
% 3 - X-Z rotation combined
% The type is specified by the range-increment combined input
%%%%%%%%%%%%%%%%%%%%%%%%%%%%%%%%%%%%%%%%%%%%%%%%%%%%%%%%%%%%%%%%%%%%%%%%
function[AngFin,Err_Stack]=US_Sym_Iterate(List,RngInc,Angle)
%Initialize starting conditions

Angle_Ori=Angle;
Pos_Ori=[0,0,0];
Sample=2;
if RngInc(1,3)==0 %X rotation only
    %Use values RngInc(1,1) and RngInc(2,1). This set of code is not
    %currently active.
    for i=1:2*RngInc(1,2)/RngInc(2,2)+1
        Angle(2)=Angle_Ori(2)-RngInc(1,2)+((i-1)*RngInc(2,2));
        Err_Stack(i,1:3)=Angle;
        Ang_List=Vol_AngPos(List,Angle,Pos_Ori);
        New_Heat=List2Heat(Ang_List);
        Crop_Size=[4,1,3,1,3,0,0,0];
        Crop_Heat=Vol_Crop(New_Heat,Crop_Size);
        Err_Stack(i,4)=US_Sym_Error_Calcs(Crop_Heat);

    end
    [Min_Val,Min_Row]=min(Err_Stack);

elseif RngInc(1,2)==0 %Z Rotation only
    %Use values RngInc(1,3) and RngInc(2,3).
    for i=1:2*RngInc(1,3)/RngInc(2,3)+1
        Angle(3)=Angle_Ori(3)-RngInc(1,3)+((i-1)*RngInc(2,3));
        Err_Stack(i,1:3)=Angle;
        Ang_List=Vol_AngPos(List,Angle,Pos_Ori);
        New_Heat=List2Heat(Ang_List);
        Err_Stack(i,4)=size(find(New_Heat),1);
    end
    [Min_Val,Min_Row]=max(Err_Stack);

else
    for i=1:2*RngInc(1,2)/RngInc(2,2)+1
        Angle(2)=Angle_Ori(2)-RngInc(1,2)+((i-1)*RngInc(2,2));
        i_ten=(i-1)*((RngInc(1,3)/RngInc(2,3))*2+1);
        for j=1:2*RngInc(1,3)/RngInc(2,3)+1

            Angle(3)=Angle_Ori(3)-RngInc(1,3)+((j-1)*RngInc(2,3));
            Err_Stack(i_ten+j,1:3)=Angle;
            Ang_List=Vol_AngPos(List,Angle,Pos_Ori);
            New_Heat=List2Heat(Ang_List);

```



```

        Crop_Size=[4,1,3,1,3,0,0];
        Crop_Heat=Vol_Crop(New_Heat,Crop_Size);
        Err_Stack(i_ten+j,4)=US_Sym_Error_Calcs(Crop_Heat);

    end
end
[Min_Val,Min_Row]=min(Err_Stack);

end
AngFin=Err_Stack(Min_Row(4),1:4);
end

for j=1:2*RngInc(1,3)/RngInc(2,3)+1

    Angle(3)=Angle_Ori(3)-RngInc(1,3)+(j-1)*RngInc(2,3);
    Err_Stack(i_ten+j,1:3)=Angle;
    Ang_List=Vol_AngPos(List,Angle,Pos_Ori);
    New_Heat=List2Heat(Ang_List);

    Crop_Size=[4,1,3,1,3,0,0];
    Crop_Heat=Vol_Crop(New_Heat,Crop_Size);
    Err_Stack(i_ten+j,4)=US_Sym_Error_Calcs(Crop_Heat);

    %QC Check
    %{
    figure(9)
    subplot(2,1,1)
    imagesc(New_Heat)
    subplot(2,1,2)
    imagesc(Crop_Heat)
    Err_Stack
    pause
    %}
end
end
[Min_Val,Min_Row]=min(Err_Stack);

end
AngFin=Err_Stack(Min_Row(4),1:4);

End

```

```

%%%%%%%%%%%%%%%%%%%%%%%%%%%%%%%%%%%%%%%%%%%%%%%%%%%%%%%%%%%%%%%%%%%%%%%%
% CTUS_Slope.m
%
% Paired with A_CT_Slope_Iterate. This function imports both CT and US
% symmetric volumes and aligns the slope of the spinous process to
% initialize the pitch rotations
%
% Stage 1: The volume is cropped according to anatomic ratios, both for the
% CT and the US volumes
% Stage 2: Slopes are iterated on the cropped volumes at large range of
% angles, and then smaller angles, with the optimal pitch angle outputted.
% after the two sets of iterations
%%%%%%%%%%%%%%%%%%%%%%%%%%%%%%%%%%%%%%%%%%%%%%%%%%%%%%%%%%%%%%%%%%%%%%%%
function [CT_List,US_List,CTUS_Slope_Ang]=CTUS_Slope(CT_Vol,US_Vol)

%Initialize angles, ranges and increments
Init_Ang=[0,0,0]; %Initial angle
Init_Pos=[0,0,0]; %Initial position
RngIncY1=[40,0,0;5,0,0]; %Range of 40 vs 60?
RngIncY2=[10,0,0;2,0,0]; %Added to speed future steps

% Define CT Center and Width of Spinous Process
Crop_Size=[10,0,0,3,6,3,6];
CT_Vol_Crop=Vol_Crop(CT_Vol,Crop_Size);
US_Vol_Crop=Vol_Crop(US_Vol,Crop_Size);

CT_List=Vol2List(CT_Vol);
US_List=Vol2List(US_Vol); %This is unnecessary, but useful for evaluation

%Iterate rotations
Ang(1,:)=CTUS_Slope_Iterate(CT_Vol_Crop,US_Vol_Crop,RngIncY1,Init_Ang);
Ang(2,:)=CTUS_Slope_Iterate(CT_Vol_Crop,US_Vol_Crop,RngIncY2,Ang(1,1:3));

CTUS_Slope_Ang=Ang; %Output if you want to see CTUS Slope Angles
CT_List=Vol_AngPos(CT_List,Ang(2,1:3),Init_Pos);
%Transform=Transform_Matrix_XYZT(Ang(2,:),Init_Pos); %THE SIGN MATTERS
end

```

```

function[AngFin]=CTUS_Slope_Iterate(CT_Vol,US_Vol,RngInc,Angle)
%%%%%%%%%%%%%%%%%%%%%%%%%%%%%%%%%%%%%%%%%%%%%%%%%%%%%%%%%%%%%%%%%%%%%%%%
% CTUS_Slope_Iterate.m
%
% Paired with A_CT_Slope. This function iterates the slope comparisons

%%%%%%%%%%%%%%%%%%%%%%%%%%%%%%%%%%%%%%%%%%%%%%%%%%%%%%%%%%%%%%%%%%%%%%%%
% CTUS_Slope_Iterate.m
%
% Paired with A_CT_Slope. This function iterates the slope comparisons
% between the CT and US volumes
%
% Stage 1: The positions are aligned, first by aligning centroids, and then
% iterating position along the Y-direction to maximize overlap.
% Stage 2: Iteration of the slope angle and the amount of overlap is
% calculated with the optimal angle outputted.
%%%%%%%%%%%%%%%%%%%%%%%%%%%%%%%%%%%%%%%%%%%%%%%%%%%%%%%%%%%%%%%%%%%%%%%%
function[AngFin]=CTUS_Slope_Iterate(CT_Vol,US_Vol,RngInc,Angle)
%Initialize starting conditions
Angle_Ori=Angle;
Pos_Ori=[0,0,0];
Sample=2;
CT_List=Vol2List(CT_Vol);
US_List=Vol2List(US_Vol);

%Adjust centroid to maximize overlap
US_Centroid=sum(US_List)/size(US_List,1);%[size(US_Vol,2)/2,size(US_Vol,1)/2,
size(US_Vol,3)/2]
CT_Centroid=sum(CT_List)/size(CT_List,1);
CT_List(:,2)=CT_List(:,2)-round(CT_Centroid(2)-US_Centroid(2),0);

Pos=Pos_Ori;
Pos(1)=round((size(US_Vol,2)-size(CT_Vol,2))/2,0);
RngIncP=[0,10,0;0,1,0];

Position_Range=2*RngIncP(1,2)/RngIncP(2,2)+1;
Angle_Range=2*RngInc(1,1)/RngInc(2,1)+1;

for i=1:Position_Range
    Pos(2)=Pos_Ori(2)-RngIncP(1,2)+((i-1)*RngIncP(2,2));
    for j=1:Angle_Range
        Angle(1)=Angle_Ori(1)-RngInc(1,1)+((j-1)*RngInc(2,1));
        Err_Stack(j+(i-1)*(Angle_Range),1:3)=Angle;
        Ang_List=Vol_AngPos(CT_List,Angle,Pos);
        CT_NewVol=uint8(List2Vol_Presized(Ang_List,size(US_Vol)));
        Err_Stack(j+(i-
1)*(Angle_Range),4)=Error_Sampler(CT_NewVol,US_Vol,Sample)/...
            (sum(sum(sum(CT_NewVol)))+(sum(sum(sum(US_Vol)))))*1000;
        %QC CHECK, put into for loop if needed.
    end
end

end
[Min_Val,Min_Row]=min(Err_Stack);
AngFin=Err_Stack(Min_Row(4),1:4);
Err_Stack;

```

```

end
function [Heat_Error]=US_Sym_Error_Calcs(Heat)
%%%%%%%%%%%%%%%%%%%%%%%%%%%%%%%%%%%%%%%%%%%%%%%%%%%%%%%%%%%%%%%%%%%%%%%%
% US_Sym_Error_Calcs.m
%
% Used by US_Sym_Iterate. Calculates the symmetry of the ultrasound while
% ignoring pixels without data to compare the surfaces themselves, rather
% than just comparing the top half with the bottom half.
%
% Note: The optimization metric can be changed depending on which
% "Heat_Error" is commented out. The immse works in some cases but it less
% reliable than the custom system.
%%%%%%%%%%%%%%%%%%%%%%%%%%%%%%%%%%%%%%%%%%%%%%%%%%%%%%%%%%%%%%%%%%%%%%%%

HeatFlip=flipud(Heat);
Heat_Size=size(Heat,1)*size(Heat,2);
Heat_Err=0;
n=1;
for k=1:Heat_Size
    if or(Heat(k)==0,HeatFlip(k)==0)
    else
        Heat_Del=abs(Heat(k)-HeatFlip(k));
        Heat_Err=Heat_Err+Heat_Del;
        n=n+1;
    end
end
end
Heat_Error(1)=double(Heat_Err)/n;

%Heat_Error(2)=immse(Heat,HeatFlip); %This one second!
%Heat_Error(1)=double(Heat_Err);
%Heat_Error(1)=double(Heat_Err)/size(find(Heat),1);
%Heat_Error(1)=double(Heat_Err)/Heat_Size;
%Heat_Error(1)=size(find(Heat),1);
%Heat_Error(1)=n;
%Heat_Error(2)=Heat_Size;

%Heat_Error(1)=Heat_Size/size(find(Heat),1);
end

```

## Appendix 6: Image Registration Code

```
function [CT,US,EC,ET,Transform]=C_Registration(CT,US,Center,QC)
%%%%%%%%%%%%%%%%%%%%%%%%%%%%%%%%%%%%%%%%%%%%%%%%%%%%%%%%%%%%%%%%%%%%%%%%
% C_registration.m
% Last Modified by A.Chan - Utter Matlab Noob, December 2018
%
% Purpose: Registration of single CT vertebrae onto 3D ultrasound surface
% image of the same scale. Grouped with A_Image_Processing and
% B_Preregistration
%
% Inputs: CT volume and US volume from A_Image_Processing
% Outputs: CT aligned volume and US final volume
%%%%%%%%%%%%%%%%%%%%%%%%%%%%%%%%%%%%%%%%%%%%%%%%%%%%%%%%%%%%%%%%%%%%%%%%
Init_Ang=[0,0,0]; %Initial angle
Init_Pos=[0,0,0]; %Initial position
Scale=[16,8,4,2];
%QC Check - Display centroid translated CT and US for surface and full (B)
% QC=QC_Check(CT.Vol_D,US.Vol_D,Center.DFull,QC);

%% Phase C.1: Six Degree of Freedom Translations and Rotations
disp('C.1 Six Degree of Freedom Translations and Rotations')

[SixDOF_AngPos,ET.D,EC.D,~,~]=Transformation_6D(CT.Vol_C,US.Vol_C,Scale);

    Ang_PosD=SixDOF_AngPos; %Display error chart

[CT_D_List]=Vol_AngPos(CT.SurfList,SixDOF_AngPos(1,1:3),Scale(1)*SixDOF_AngPos(1,4:6));

%QC Check - Check 6DOF transformation
    [CT.Vol_D,US.Vol_D,~,~,Temp_Center]=Vol_Rewindow(CT_D_List,US.List);
    %QC=QC_Check(CT.Vol_C, US.Vol_C,Temp_Center,QC);

%% Phase C.2: Sequential Gross Translations-Rotations
disp('C.2 Translate and Rotate Gross Scaled Volumes')

[Gross_AngPos,ET.E,EC.E]=Gross_3D(CT.Vol_C,US.Vol_C,SixDOF_AngPos,Scale);

    Ang_PosE=Gross_AngPos; %Display error chart

CT_E_List=Vol_AngPos(CT.SurfList,Gross_AngPos(1,1:3),Scale(2)*Gross_AngPos(1,4:6));

%QC Check - Check Gross 3DOF
    % [CT.Vol_E,US.Vol_E,~,~,Temp_Center]=Vol_Rewindow(CT_E_List,US.List);
    %QC=QC_Check(CT.Vol_E, US.Vol_E,Temp_Center,QC);

%% Phase C.3: Sequential Fine Translations-Rotations
disp('C.3 Translate and Rotate Fine Scaled Volumes')

[Fine_AngPos,SFine_AngPos,Final_AngPos,ET.F,EC.F]=Fine_3D(CT.Vol_C,US.Vol_C,Gross_AngPos,Scale);
```

```

    Ang_PosF=Fine_AngPos; %Display error chart

CT_F_List=Vol_AngPos (CT.SurfList, SFine_AngPos (1,1:3), Scale (3)*Fine_AngPos (1,4
:6));

%QC Check - Check Fine 3DOF
    %[CT.Vol_F, US.Vol_F, ~, ~, Temp_Center]=Vol_Rewindow (CT_F_List, US.List);
    %QC=QC_Check (CT.Vol_F, US.Vol_F, Temp_Center, QC);

    Ang_PosG=SFine_AngPos; %Display error chart

[CT_G_List]=Vol_AngPos (CT.SurfList, SFine_AngPos (1,1:3), Scale (4)*SFine_AngPos (
1,4:6));

%QC Check - Check Superfine 3DOF
    %[CT.Vol_G, US.Vol_G, ~, ~, Temp_Center]=Vol_Rewindow (CT_G_List, US.List);
    %QC=QC_Check (CT.Vol_G, US.Vol_G, Temp_Center, QC);

    Ang_PosH=Final_AngPos; %Display error chart

[CT_H_List]=Vol_AngPos (CT.SurfList, Final_AngPos (1,1:3), Final_AngPos (1,4:6));

Fin_AngPos=[Final_AngPos (1,1:3); Final_AngPos (1,4:6)] %Displays final combined
recommended transformation

%% Phase C.4: Final Transformation of Full Volume
disp('C.4 Transform full CT Volume')

CT_Final_Centroid=round (sum (CT.SurfList) / size (CT.SurfList, 1), 0);
Origin_Rotate=Vol_AngPos_Origin (CT_Final_Centroid, Fin_AngPos (1,1:3), Init_Pos)
;
Origin_Translate=CT_Final_Centroid-Origin_Rotate;

CT.SurfList=Vol_AngPos_Origin (CT.SurfList, Fin_AngPos (1,1:3), Fin_AngPos (2,1:3)
+Origin_Translate);

Transform (1, :)=Fin_AngPos (1,1:3);
Transform (2, :)=(Fin_AngPos (2,1:3)+Origin_Translate)*0.2;
[CT.Vol_I, US.Vol_I, ~, ~, CT.Center]=Vol_Rewindow (CT.SurfList, US.List);
Error_Fin=Error_Sampler (CT.Vol_I, US.Vol_I, 1); %Display error chart
QC=QC_Check (CT.Vol_I, US.Vol_I, CT.Center, QC);

disp(' (C) Registration Complete')
end

```

```

function
[AngPos_Out,Error_Table,Error_Chart,ES1,ES2A]=Transformation_6D(CT,US,Scale)

Init_Ang=[0,0,0];    %Initial angle
Init_Pos=[0,0,0];    %Initial position
Scale=[16,8];

CT_6DOF=Vol_Scale(CT,Scale(1));
US_6DOF=Vol_Scale(US,Scale(1));

CT_List=Vol2List(CT_6DOF);

AngRngInc=[15,20,15;5,5,5];

AngN.X=(1+2*(AngRngInc(1,1)/AngRngInc(2,1)));
AngN.Y=(1+2*(AngRngInc(1,2)/AngRngInc(2,2)));
AngN.Z=(1+2*(AngRngInc(1,3)/AngRngInc(2,3)));

PosRngInc=[3,2,3;1,1,1];
PosN.X=(1+2*(PosRngInc(1,1)/PosRngInc(2,1)));
PosN.Y=(1+2*(PosRngInc(1,2)/PosRngInc(2,2)));
PosN.Z=(1+2*(PosRngInc(1,3)/PosRngInc(2,3)));

[Error_Table,Error_Chart,AngPos_6DOF]=Transformation_6D_Iterate(CT_List,US_6D
OF,AngRngInc,PosRngInc,AngN,PosN,Init_Ang,Init_Pos);
Error_Only=Error_Chart(4:end,4:end);

%Optimize according to largest-to-smallest difference
%Start with X position and Y angle
Grid=[PosN.Y*PosN.Z,AngN.Z*AngN.X];
[PosXAngY,ES1]=Mean_Min(Grid,[PosN.X,AngN.Y],Error_Only);

%Empirically, second is Y position and Z angle
Mini_ErrorA=Error_Only(1+(PosXAngY(1,1)-
1)*Grid(1):PosXAngY(1,1)*Grid(1),1+(PosXAngY(1,2)-
1)*Grid(2):PosXAngY(1,2)*Grid(2));
Mini_ErrorB=Error_Only(1+(PosXAngY(2,1)-
1)*Grid(1):PosXAngY(2,1)*Grid(1),1+(PosXAngY(2,2)-
1)*Grid(2):PosXAngY(2,2)*Grid(2));
Mini_ErrorC=Error_Only(1+(PosXAngY(3,1)-
1)*Grid(1):PosXAngY(3,1)*Grid(1),1+(PosXAngY(3,2)-
1)*Grid(2):PosXAngY(3,2)*Grid(2));

Mini_Grid=[PosN.Z,AngN.X];
[PosYAngZ(1:3,:),ES2A]=Mean_Min(Mini_Grid,[PosN.Y,AngN.Z],Mini_ErrorA);
[PosYAngZ(4:6,:),ES2B]=Mean_Min(Mini_Grid,[PosN.Y,AngN.Z],Mini_ErrorB);
[PosYAngZ(7:9,:),ES2C]=Mean_Min(Mini_Grid,[PosN.Y,AngN.Z],Mini_ErrorC);

%Lastly, Z position and X angle are calculated... these aren't that
%accurate necessarily

[PosZAngX(1,:)=Min_Error(Mini_Grid,PosYAngZ(1,:),Mini_ErrorA);
[PosZAngX(2,:)=Min_Error(Mini_Grid,PosYAngZ(2,:),Mini_ErrorA);
[PosZAngX(3,:)=Min_Error(Mini_Grid,PosYAngZ(3,:),Mini_ErrorA);

```

```

[PosZAngX(4,:)]=Min_Error(Mini_Grid,PosYAngZ(4,:),Mini_ErrorB);
[PosZAngX(5,:)]=Min_Error(Mini_Grid,PosYAngZ(5,:),Mini_ErrorB);
[PosZAngX(6,:)]=Min_Error(Mini_Grid,PosYAngZ(6,:),Mini_ErrorB);
[PosZAngX(7,:)]=Min_Error(Mini_Grid,PosYAngZ(7,:),Mini_ErrorC);
[PosZAngX(8,:)]=Min_Error(Mini_Grid,PosYAngZ(8,:),Mini_ErrorC);
[PosZAngX(9,:)]=Min_Error(Mini_Grid,PosYAngZ(9,:),Mini_ErrorC);

for k=1:3
    for j=1:3
        Angle=[-AngRngInc(1,1)+AngRngInc(2,1)*(PosZAngX(j+(k-1)*3,2)-1),...
            -AngRngInc(1,2)+AngRngInc(2,2)*(PosXAngY(k,2)-1),...
            -AngRngInc(1,3)+AngRngInc(2,3)*(PosYAngZ(j+(k-1)*3,2)-1)];

        Position=[-PosRngInc(1,1)+PosRngInc(2,1)*(PosXAngY(k,1)-1),...
            -PosRngInc(1,2)+PosRngInc(2,2)*(PosYAngZ(j+(k-1)*3,1)-1),...
            -PosRngInc(1,3)+PosRngInc(2,3)*(PosZAngX(j+(k-1)*3,1)-1)];
        AngPos(j+(k-1)*3,1:6)=[Angle,Position];
        AngPos(j+(k-1)*3,7)=PosZAngX(j+(k-1)*3,3);
    end
end
%QC Check
ErrList=Heat2List(Error_Only);
for k=1:size(ErrList,1)
    ErrList(k,3)=Error_Only(ErrList(k,1),ErrList(k,2));
end

ErrList=sortrows(ErrList,3);
Final_EList=ErrList(1:9,:);
for k=1:9
    Angle=[Error_Chart(1,3+Final_EList(k,2)),...
        Error_Chart(2,3+Final_EList(k,2)),...
        Error_Chart(3,3+Final_EList(k,2))];

    Position=[Error_Chart(3+Final_EList(k,1),1),...
        Error_Chart(3+Final_EList(k,1),2),...
        Error_Chart(3+Final_EList(k,1),3)];
    AngPos2(k,:)=[Angle,Position,1];
end
AngPos_Out(1,:)=AngPos(1,:);
AngPos_Out(2,:)=AngPos2(1,:);
end

```



```

function
[Error_Table,Error_Chart,AngPos]=Transformation_6D_Iterate(CT_List,US_6DOF,AngRngInc,PosRngInc,AngN,PosN,Init_Ang,Init_Pos)
Error_Chart_Columns=AngN.Y*AngN.Z*AngN.X;
Error_Chart_Rows=PosN.X*PosN.Y*PosN.Z;

Error_Chart=zeros(3+Error_Chart_Rows,3+Error_Chart_Columns);

Error_Chart(1,1)='1';
Error_Chart(2,2)='2';
Error_Chart(3,3)='3';

%Original ordered 6DOF method
for XR=1:AngN.X
    for YR=1:AngN.Y
        for ZR=1:AngN.Z
            for XP=1:PosN.X
                for YP=1:PosN.Y
                    for ZP=1:PosN.Z
                        Angle(1)=Init_Ang(1)-AngRngInc(1,1)+(XR-
1)*AngRngInc(2,1));
                        Angle(2)=Init_Ang(2)-AngRngInc(1,2)+(YR-
1)*AngRngInc(2,2));
                        Angle(3)=Init_Ang(3)-AngRngInc(1,3)+(ZR-
1)*AngRngInc(2,3));
                        Position(1)=Init_Pos(1)-PosRngInc(1,1)+(XP-
1)*PosRngInc(2,1));
                        Position(2)=Init_Pos(2)-PosRngInc(1,2)+(YP-
1)*PosRngInc(2,2));
                        Position(3)=Init_Pos(3)-PosRngInc(1,3)+(ZP-
1)*PosRngInc(2,3));
                        E_Col=3+1+(YR-1)*AngN.X*AngN.Z+(ZR-1)*AngN.X+(XR-
1);
                        E_Row=3+1+(XP-1)*PosN.Y*PosN.Z+(YP-1)*PosN.Z+(ZP-
1);

                        Error_Chart(1:3,E_Col)=Angle;
                        Error_Chart(E_Row,1:3)=Position';

                    end
                end
            end
        end
    end
end

parfor k=1:(size(Error_Chart,2)-3)
    Err_Col=Error_Chart(:,k+3);
    for j=1:(size(Error_Chart,1)-3)
        Angle=Error_Chart(1:3,k+3)';
        Position=Error_Chart(j+3,1:3);
        CT_New_List=Vol_AngPos(CT_List,Angle,Position);
        CT_New_Vol=List2Vol_Presized(CT_New_List,size(US_6DOF));
        Err_Col(j+3)=Error_Sampler(CT_New_Vol,US_6DOF,2);
    end
    Err_Chart(:,k+3)=Err_Col;
end

```

```

end
Error_Chart(4:end,4:end)=Err_Chart(4:end,4:end);
%}
%Construct Error Table for Top Min Errors
Top=5;
Error_Only=Error_Chart(4:end,4:end);
[Error_Val,Error_Row]=mink(Error_Only,Top);
Error_Locus=zeros(Top*size(Error_Only,2),3);
for j=1:size(Error_Only,2)
    for k=1:Top
        Error_Locus(k+5*(j-1),1)=Error_Val(k,j);
        Error_Locus(k+5*(j-1),2)=j;
        Error_Locus(k+5*(j-1),3)=Error_Row(k,j);
    end
end
Sort_Err_Min=sortrows(Error_Locus);

Error_Table=zeros(Top,7);
for k=1:Top
    Error_Table(k,1)=Sort_Err_Min(k,1);
    Error_Table(k,2:4)=Error_Chart(1:3,Sort_Err_Min(k,2)+3)';
    Error_Table(k,5:7)=Error_Chart(Sort_Err_Min(k,3)+3,1:3);
end
Error_Table(Top+1,:)=std(Error_Table);
Error_Table(Top+2,:)=ceil(size(Error_Only,1)/2),ceil(size(Error_Only,2)/2),Init_Ang,Init_Pos];
AngPos=Error_Table(1,:);
end

```

```

function [Gross_AngPos,Table,Chart]=Gross_3D(CT,US,AngPos,Scale)
%% Step 1: Initialize Volume and Variables
AngPos=sortrows(AngPos,7);
for m=1:2
    Init_Ang=AngPos(m,1:3);      %Initial angle
    Init_Pos=AngPos(m,4:6)*(Scale(1)/Scale(2)); %Initial position

    CT_Gross=Vol_Scale(CT,Scale(2));
    US_Gross=Vol_Scale(US,Scale(2));

    CT_List=Vol2List(CT_Gross);
    %% Step 2: Iterate Gross Volume Translations
    %OldRng[3,5,3,1,1,1];
    DynRng=[max(AngPos(:,4:6));min(AngPos(:,4:6))]*2;

    for k=1:3
        if abs(DynRng(1,k)-DynRng(2,k))<1
            DynRng(1,k)=DynRng(1,k)+4;
            DynRng(2,k)=DynRng(2,k)-4;
        elseif abs(DynRng(1,k)-DynRng(2,k))<3
            DynRng(1,k)=DynRng(1,k)+2;
            DynRng(2,k)=DynRng(2,k)-2;
        elseif abs(DynRng(1,k)-DynRng(2,k))<5
            DynRng(1,k)=DynRng(1,k)+1;
            DynRng(2,k)=DynRng(2,k)-1;
        end
    end

    Inc=[1,1,1];
    %OldRng[10,6,6,2,2,2];
    [Table.PosG,Chart.PosG]=Translation_3D_Iterate(CT_List,US_Gross,...
        DynRng,Inc,Init_Ang,Init_Pos);

    %% Step 3: Iterate Gross Volume Rotations
    DynRng=[max(AngPos(:,1:3));min(AngPos(:,1:3))];

    for k=1:3
        if abs(DynRng(1,k)-DynRng(2,k))<6
            DynRng(1,k)=DynRng(1,k)+5;
            DynRng(2,k)=DynRng(2,k)-5;
        end
    end

    Inc=[1,1,1];

    [Table.AngG1,Chart.AngG1]=Rotation_3D_Iterate(CT_List,US_Gross,DynRng,Inc,Ini
t_Ang,Table.PosG(1,1:3));

    [Table.AngG2,Chart.AngG2]=Rotation_3D_Iterate(CT_List,US_Gross,DynRng,Inc,Ini
t_Ang,Table.PosG(2,1:3));

    [Table.AngG3,Chart.AngG3]=Rotation_3D_Iterate(CT_List,US_Gross,DynRng,Inc,Ini
t_Ang,Table.PosG(3,1:3));

```

```
[Table.AngG4,Chart.AngG4]=Rotation_3D_Iterate (CT_List,US_Gross,DynRng,Inc,Ini  
t_Ang,Table.PosG(4,1:4));
```

```
[Table.AngG5,Chart.AngG5]=Rotation_3D_Iterate (CT_List,US_Gross,DynRng,Inc,Ini  
t_Ang,Table.PosG(5,1:3));
```

```
Table.TransG=[Table.AngG1;Table.AngG2;Table.AngG3;Table.AngG4;Table.AngG5];
```

```
for i=1:size(Table.AngG1,1)  
    for k=1:5  
        Table.TransG(i+(k-1)*size(Table.AngG1,1),5:7)=Table.PosG(k,1:3);  
    end  
end
```

```
TransG=[Table.TransG(:,1:3),Table.TransG(:,5:7),Table.TransG(:,4)];
```

```
TransG=sortrows(TransG,7);
```

```
if m==1
```

```
    Gross_AngPos=TransG(1:5,:);
```

```
else
```

```
    Gross_AngPos=[Gross_AngPos;TransG(1:5,:)];
```

```
end
```

```
Gross_AngPos=sortrows(Gross_AngPos,7);
```

```
end
```

```
end
```

```

function
[Fine_AngPos, SFine_AngPos, Fin_AngPos, Table, Chart]=Fine_3D(CT,US,AngPos,Scale)
%% Step 1: Initialize Fine Volume and Variables
Init_Ang=AngPos(1,1:3); %Initial angle
Init_Pos=AngPos(1,4:6)*(Scale(2)/Scale(3)); %Initial position

CT_Fine=Vol_Scale(CT,Scale(3));
US_Fine=Vol_Scale(US,Scale(3));
CT_List=Vol2List(CT_Fine);
%% Step 2: Iterate Fine Volume Transformations
%RngInc=[2,2,2;1,1,1];

DynRng=[max(AngPos(:,4:6));min(AngPos(:,4:6))]*2;
for k=1:3
    if abs(DynRng(1,k)-DynRng(2,k))<1
        DynRng(1,k)=DynRng(1,k)+2;
        DynRng(2,k)=DynRng(2,k)-2;
    elseif abs(DynRng(1,k)-DynRng(2,k))<3
        DynRng(1,k)=DynRng(1,k)+1;
        DynRng(2,k)=DynRng(2,k)-1;
    end
end

Inc=[1,1,1];
[Table.PosF,Chart.PosF]=Translation_3D_Iterate(CT_List,US_Fine,...
    DynRng,Inc,Init_Ang,Init_Pos);

%RngInc=[3,3,3;1,1,1];
DynRng=[max(AngPos(:,1:3));min(AngPos(:,1:3))];
for k=1:3
    if abs(DynRng(1,k)-DynRng(2,k))<3
        DynRng(1,k)=DynRng(1,k)+2;
        DynRng(2,k)=DynRng(2,k)-2;
    end
end

Inc=[1,1,1];

[Table.AngF,Chart.AngF]=Rotation_3D_Iterate(CT_List,US_Fine,...
    DynRng,Inc,Init_Ang,Table.PosF(1,1:3));

Fine_AngPos=[Table.AngF(:,1:3),Table.PosF(:,1:3),Table.AngF(:,4)];

%% Step 3: Initialize Super Fine Volume and Variables
Init_Ang=Fine_AngPos(1,1:3); %Initial angle
Init_Pos=Fine_AngPos(1,4:6)*(Scale(3)/Scale(4)); %Initial position

CT_SFine=Vol_Scale(CT,Scale(4));
US_SFine=Vol_Scale(US,Scale(4));
CT_List=Vol2List(CT_SFine);
%% Step 3: Iterate Super Fine Volume Rotations
%RngInc=[2,2,2;1,1,1];

DynRng=[max(Fine_AngPos(:,4:6));min(Fine_AngPos(:,4:6))]*2;
for k=1:3

```

```

    if (DynRng(1, k) - DynRng(2, k)) < 2
        DynRng(1, k) = DynRng(1, k) + 1;
        DynRng(2, k) = DynRng(2, k) - 1;
    end
end
Inc = [1, 1, 1];
[Table.PosSF, Chart.PosSF] = Translation_3D_Iterate(CT_List, US_SFine, ...
    DynRng, Inc, Init_Ang, Init_Pos);

%RngInc = [1, 1, 1; 1, 1, 1];
DynRng = [max(AngPos(:, 1:3)); min(AngPos(:, 1:3))];
for k = 1:3
    if (DynRng(1, k) - DynRng(2, k)) < 2
        DynRng(1, k) = DynRng(1, k) + 1;
        DynRng(2, k) = DynRng(2, k) - 1;
    end
end
Inc = [1, 1, 1];
[Table.AngSF, Chart.AngSF] = Rotation_3D_Iterate(CT_List, US_SFine, ...
    DynRng, Inc, Init_Ang, Table.PosSF(1, 1:3));

SFine_AngPos = [Table.AngSF(:, 1:3), Table.PosSF(:, 1:3), Table.AngSF(:, 4)];

CT_List = Vol2List(CT);
%% Step 3: Iterate Full Volume Rotations
%RngInc = [2, 2, 2; 1, 1, 1];
Init_Ang = Fine_AngPos(1, 1:3); %Initial angle
Init_Pos = Fine_AngPos(1, 4:6) * (Scale(4)); %Initial position

DynRng = [max(SFine_AngPos(:, 4:6)); min(SFine_AngPos(:, 4:6))] * 2;
for k = 1:3
    if (DynRng(1, k) - DynRng(2, k)) < 2
        DynRng(1, k) = DynRng(1, k) + 1;
        DynRng(2, k) = DynRng(2, k) - 1;
    end
end
Inc = [1, 1, 1];
[Table.PosFin, Chart.PosFin] = Translation_3D_Iterate(CT_List, US, ...
    DynRng, Inc, Init_Ang, Init_Pos);

%RngInc = [1, 1, 1; 1, 1, 1];
DynRng = [max(AngPos(:, 1:3)); min(AngPos(:, 1:3))];
for k = 1:3
    if (DynRng(1, k) - DynRng(2, k)) < 2
        DynRng(1, k) = DynRng(1, k) + 1;
        DynRng(2, k) = DynRng(2, k) - 1;
    end
end
Inc = [1, 1, 1];
[Table.AngFin, Chart.AngFin] = Rotation_3D_Iterate(CT_List, US, ...
    DynRng, Inc, Init_Ang, Table.PosFin(1, 1:3));

Fin_AngPos = [Table.AngFin(:, 1:3), Table.PosFin(:, 1:3), Table.AngFin(:, 4)];
end

```

```

function
[Error_Table,Error_Chart]=Translate_3D_Iterate(CT_List,US,DynRng,Inc,Init_Ang
,Init_Pos)

PosX_N=1+(DynRng(1,1)-DynRng(2,1));
PosY_N=1+(DynRng(1,2)-DynRng(2,2));
PosZ_N=1+(DynRng(1,3)-DynRng(2,3));

Error_Chart_Columns=PosX_N;
Error_Chart_Rows=PosY_N*PosZ_N;
Error_Chart=zeros(1+Error_Chart_Rows,2+Error_Chart_Columns);

%Translate in 3 DOF
for XP=1:PosX_N
    for YP=1:PosY_N
        for ZP=1:PosZ_N
            Position1=(DynRng(2,1)+Inc(1)-1)+(XP*(Inc(1))-1)-Inc(1);
            Position23(1)=(DynRng(2,2)+Inc(2)-1)+(YP*(Inc(2))-1)-Inc(2);
            Position23(2)=(DynRng(2,3)+Inc(3)-1)+(ZP*(Inc(3))-1)-Inc(3);
            E_Col=2+1+(XP-1);
            E_Row=1+1+((YP-1)*PosZ_N)+(ZP-1);

            %CT_New_List=Vol_AngPos(CT_List,Init_Ang,[Position1,Position23]);
            %CT_New_Vol=List2Vol_Presized(CT_New_List,size(US));

            %Error_Chart(E_Row,E_Col)=Error_Sampler(CT_New_Vol,US,2);
            Error_Chart(1,E_Col)=Position1;
            Error_Chart(E_Row,1:2)=Position23';
        end
    end
end

parfor k=1:(size(Error_Chart,2)-2)
    Err_Col=Error_Chart(:,k+2);
    for j=1:(size(Error_Chart,1)-1)
        Position1=Error_Chart(1,k+2);
        Position23=Error_Chart(j+1,1:2);
        CT_New_List=Vol_AngPos(CT_List,Init_Ang,[Position1,Position23]);
        CT_New_Vol=List2Vol_Presized(CT_New_List,size(US));
        Err_Col(j+1)=Error_Sampler(CT_New_Vol,US,2);
    end
    Err_Chart(:,k+2)=Err_Col;
end
Error_Chart(2:end,3:end)=Err_Chart(2:end,3:end);
%Select the top 5 translations
Top=5;
Error_Only=Error_Chart(2:end,3:end);
[Error_Val,Error_Row]=mink(Error_Only,Top);
Error_Locus=zeros(Top*size(Error_Only,2),3);
for j=1:size(Error_Only,2)
    for k=1:Top
        Error_Locus(k+Top*(j-1),1)=Error_Val(k,j);
        Error_Locus(k+Top*(j-1),2)=j;
        Error_Locus(k+Top*(j-1),3)=Error_Row(k,j);
    end
end
end

```

```

Sort_Err_Min=sortrows(Error_Locus);
Error_Table=zeros(Top,4);
for k=1:Top
    Error_Table(k,1)=Error_Chart(1,Sort_Err_Min(k,2)+2);
    Error_Table(k,2:3)=Error_Chart(Sort_Err_Min(k,3)+1,1:2)';
    Error_Table(k,4)=Sort_Err_Min(k,1);
end
%Error_Table(Top+2,:)=std(Error_Table);
Error_Table(Top+1,:)=[Init_Pos,Error_Only(ceil(size(Error_Only,1)/2),ceil(size(Error_Only,2)/2))];
end

```



```

function
[Error_Table,Error_Chart]=Rotation_3D_Iterate (CT_List,US,DynRng,Inc,Init_Ang,
Init_Pos)

AngX_N=1+(DynRng (1,1)-DynRng (2,1));
AngY_N=1+(DynRng (1,2)-DynRng (2,2));
AngZ_N=1+(DynRng (1,3)-DynRng (2,3));

Error_Chart_Columns=AngX_N;
Error_Chart_Rows=AngY_N*AngZ_N;
Error_Chart=zeros (1+Error_Chart_Rows,2+Error_Chart_Columns);

%Translate in 3 DOF
for XR=1:AngX_N
    for YR=1:AngY_N
        for ZR=1:AngZ_N
            Angle1=(DynRng (2,1)+Inc (1)-1)+(XR*(Inc (1))-1)-Inc (1);
            Angle23 (1)=(DynRng (2,2)+Inc (2)-1)+(YR*(Inc (2))-1)-Inc (2);
            Angle23 (2)=(DynRng (2,3)+Inc (3)-1)+(ZR*(Inc (3))-1)-Inc (3);
            E_Col=2+1+(XR-1);
            E_Row=1+1+( (YR-1)*AngZ_N)+(ZR-1);

            %CT_New_List=Vol_AngPos (CT_List,[Angle1,Angle23],Init_Pos);
            %CT_New_Vol=List2Vol_Presized (CT_New_List,size (US));

            %Error_Chart (E_Row,E_Col)=Error_Sampler (CT_New_Vol,US,2);
            Error_Chart (1,E_Col)=Angle1;
            Error_Chart (E_Row,1:2)=Angle23';
        end
    end
end

parfor k=1:(size (Error_Chart,2)-2)
    Err_Col=Error_Chart (:,k+2);
    for j=1:(size (Error_Chart,1)-1)
        Angle1=Error_Chart (1,k+2);
        Angle23=Error_Chart (j+1,1:2);
        CT_New_List=Vol_AngPos (CT_List,[Angle1,Angle23],Init_Pos);
        CT_New_Vol=List2Vol_Presized (CT_New_List,size (US));
        Err_Col (j+1)=Error_Sampler (CT_New_Vol,US,2);
    end
    Err_Chart (:,k+2)=Err_Col;
end
Error_Chart (2:end,3:end)=Err_Chart (2:end,3:end);
%}
%Select the top 5 translations
Top=5;
Error_Only=Error_Chart (2:end,3:end);
[Error_Val,Error_Row]=mink (Error_Only,Top);
Error_Locus=zeros (Top*size (Error_Only,2),3);
for j=1:size (Error_Only,2)
    for k=1:Top
        Error_Locus (k+Top*(j-1),1)=Error_Val (k,j);
        Error_Locus (k+Top*(j-1),2)=j;
        Error_Locus (k+Top*(j-1),3)=Error_Row (k,j);
    end
end

```

```

end
Sort_Err_Min=sortrows(Error_Locus);
Error_Table=zeros(Top,4);
for k=1:Top
    Error_Table(k,1)=Error_Chart(1,Sort_Err_Min(k,2)+2);
    Error_Table(k,2:3)=Error_Chart(Sort_Err_Min(k,3)+1,1:2)';
    Error_Table(k,4)=Sort_Err_Min(k,1);
end
%Error_Table(Top+2,:)=std(Error_Table);
Error_Table(Top+1,:)=[Init_Ang,Error_Only(ceil(size(Error_Only,1)/2),ceil(size(Error_Only,2)/2))];
end

```

```

function [CT,US,Transform_C,Min_Error,QC]=C_ICP_Registration(CT,US,QC)

CT_PointCloud=pointCloud(CT.SurfList);
US_PointCloud=pointCloud(US.List);
Inlier_List = [0.6, 0.7, 0.8];
Grid_List = [5, 7];

Min_Error = 10000;

for i = 1:size(Inlier_List, 2)
    for j = 1:size(Grid_List, 2)

        inlier = Inlier_List(i);
        grid = Grid_List(j);

        CT_PointCloud_D = pcdownsampling(CT_PointCloud, 'gridAverage', grid);
        US_PointCloud_D = pcdownsampling(US_PointCloud, 'gridAverage', grid);

        % Performs the ICP registration:
        [tform, ~, ~] = pcregistericp(CT_PointCloud_D, US_PointCloud_D,...
            'Metric','pointToPlane',...
            'InlierRatio', inlier,...
            'MaxIterations', 100);

        CT_PointCloud_T = pctransform(CT_PointCloud, tform);

        [CT_Vol_Temp, US_Vol_Temp,~,~,~,~] =
Vol_Rewindow(round(CT_PointCloud_T.Location),US.List);

        Error = Error_Sampler(CT_Vol_Temp, US_Vol_Temp, 1);

        if Error < Min_Error
            Min_Error = Error;
            CT.Vol_H = CT_Vol_Temp;
            CT.IR_List = round(CT_PointCloud_T.Location);
            Transform_C = tform.T;
        end
    end
end

%% Save Output Data to File for QC
[CT.Vol_H,US.Vol_H,~,~,Temp_Center]=Vol_Rewindow(CT.IR_List,US.List);
QC=QC_Check(CT.Vol_H, US.Vol_H,Temp_Center,QC);
end

```

```

function [Error]=Error_Sampler(CT_Vol,US_Vol,Sample)
Err=zeros(size(US_Vol,3),1);
for k=1:Sample:size(US_Vol,3)
    %Err(k)=immse(CT_Vol(:,:,k),US_Vol(:,:,k)); %Use if unsure about
    %datatypes. Need to make sure they're the same!
    x = double(CT_Vol(:, :, k));
    y = double(US_Vol(:, :, k));
    Err(k) = (norm(x(:) - y(:), 2).^2) / numel(x);
    %CT_Vol=uint8(CT_Vol);
    %Err(k)=ssim(x,y);
    %Err(k)=mi(x,y);
    %Err(k)=corrcoef(x,y);
end
Error=sum(Err);

function[List]=Vol2List(Volume)
Frames=size(Volume,3);
list_size=0;
for j=1:Frames
    [X,~]=find(Volume(:,:,j));
    list_size=list_size+size(X,1);
end
List=zeros(list_size,3);
list_start=1;

for j=1:Frames
    [X,Y]=find(Volume(:,:,j));
    list_end=list_start+size(X,1)-1;
    List(list_start:list_end,1)=Y-1;%Swap Y and X from Vol to List
    List(list_start:list_end,2)=X-1;
    List(list_start:list_end,3)=j-1;
    list_start=list_end+1;
end

end

function [Volume]=List2Vol(List)
%% Repopulate Volume Stack
>List=sortrows(List,3);
%Initialize blank volume based on range (max/min) of values.

Delta=max(List)-min(List);
List=List-min(List)+1;
Volume=zeros(Delta(2),Delta(1),Delta(3),'logical');

%Check each row for coordinates and repopulate volume
List_Size=size(List,1);
k=1; Frm=1;
for k=1>List_Size
    Volume(List(k,2)+1,List(k,1)+1,List(k,3)+1)=1;
end
end

```

```

function [New_List,Center] = Vol_AngPos(List,Ang,Pos)
%% Transform PNG Stack
V_size=size(List,1);
Center=round(sum(List)/size(List,1),0);
List=List-Center;
%Add 4th column for translation and rotation compatibility
List(:,4)=1;
T_Mat=Transform_Matrix_ZXYT(Ang,Pos);
New_List=zeros(V_size,4);
New_List=List*T_Mat;
New_List=round(New_List,0);
New_List=New_List(:,1:3)+Center;
end

function [New_List] = Vol_AngPos_Origin(List,Ang,Pos)
%% Transform PNG Stack
V_size=size(List,1);

%Add 4th column for translation and rotation compatibility
List(:,4)=1;
T_Mat=Transform_Matrix_ZXYT(Ang,Pos);
New_List=zeros(V_size,4);
New_List=List*T_Mat;
New_List(:,4)=[];
New_List=round(New_List,0);
%New_List=unique(New_List,'rows');

end

function[Full_Rot]= Transform_Matrix_ZXYT(Ang,Pos)
Translation=...
[1, 0, 0, 0;...
0, 1, 0, 0;...
0, 0, 1, 0;...
Pos(1), Pos(2), Pos(3), 1];

%Rotation Matrix XYZ
Xrot=...
[1, 0, 0, 0;...
0, cosd(Ang(1)), sind(Ang(1)), 0;...
0, -sind(Ang(1)), cosd(Ang(1)), 0;...
0, 0, 0, 1];

Yrot=...
[cosd(Ang(2)), 0, -sind(Ang(2)), 0;...
0, 1, 0, 0;...
sind(Ang(2)), 0, cosd(Ang(2)), 0;...
0, 0, 0, 1];

Zrot=...
[cosd(Ang(3)), sind(Ang(3)), 0, 0;...
-sind(Ang(3)), cosd(Ang(3)), 0, 0;...
0, 0, 1, 0;...
0, 0, 0, 1];

Full_Rot=Zrot*Xrot*Yrot*Translation;

```

```

function [Heat]=Vol2Heat (Volume)
Heat=uint16 (zeros (size (Volume,2) ,size (Volume,3) ));
for n=1:size (Volume,3)
    for j=1:size (Volume,2)
        %Find non-zero values
        if sum (any (Volume (:,j,n)))>0 %Check if column has any non-zero values
            %Find location of all non-zero values
            Location=find (Volume (:,j,n));
            Heat (j,n)=Location (1);
        else
            Heat (j,n)=0;
        end
    end
end

function
[Vol1,Vol2,List1,List2,List_Center,MM_Compare]=Vol_Rewindow (List1,List2)

[MM1,~,~]=Vol_Sizing (List1);
[MM2,~,~]=Vol_Sizing (List2);
for k=1:3
    MM_Compare (1,k)=MM1 (k,1);
    MM_Compare (2,k)=MM2 (k,1);
    MM_Compare (1,k+3)=MM1 (k,2);
    MM_Compare (2,k+3)=MM2 (k,2);
end

List_Center=[max (MM_Compare (:,4) )-min (MM_Compare (:,1) ) , ...
    max (MM_Compare (:,5) )-min (MM_Compare (:,2) ) , ...
    max (MM_Compare (:,6) )-min (MM_Compare (:,3) ) ];

List_Center (2,:) =min (MM_Compare (:,1:3) );

List1=List1-List_Center (2,:);
List2=List2-List_Center (2,:);

List_Size=[List_Center (1,2) ,List_Center (1,1) ,List_Center (1,3) ];
Vol1=List2Vol_Presized (List1,List_Size);
Vol2=List2Vol_Presized (List2,List_Size);
end

```

## Appendix 7: Navigation Code

```
function [CT2,US2,Transform]=ICP_Registration(CT_Spine)
%%%%%%%%%%%%%%%%%%%%%%%%%%%%%%%%%%%%%%%%%%%%%%%%%%%%%%%%%%%%%%%%%%%%%%%%
% ICP_Registration
% Last Modified by Andrew Chan - Utter Matlab Noob, October 2019
%
% Purpose: Used to perform a complete registration using the ICP Algorithm
%
% Inputs to be updated:
% 1: The Inlier_List and Grid_List vectors can be altered if one wants to
%     narrow or widen the breadth of registration settings that are performed
%
% Inputs: CT_A, the logical volume of the vertebrae to be registered
% Outputs: tform: The transformation matrix of ICP registration
%
%%%%%%%%%%%%%%%%%%%%%%%%%%%%%%%%%%%%%%%%%%%%%%%%%%%%%%%%%%%%%%%%%%%%%%%%

clear tform Transform_B Vol3D_B Vol3D_R Vol3D_T Vol3D_F

[filename, pathname]=uigetfile('..\5 Current Data\*.mat','Select .mat file');

fprintf('\nPart A: Image Processing\n');

tic
[US_A,Center,Y_Ang_Init]=A_Image_Processing(filename, pathname);
elapsedTime(1)=toc

fprintf('\nPart B: Preregistration\n');

%File Select:
levelname=filename(1:2);
switch levelname
    case 'T3'
        CT=CT_Spine.CT_T3;
    case 'T4'
        CT=CT_Spine.CT_T4;
    case 'T5'
        CT=CT_Spine.CT_T5;
    case 'T6'
        CT=CT_Spine.CT_T6;
    case 'T7'
        CT=CT_Spine.CT_T7;
    case 'T8'
        CT=CT_Spine.CT_T8;
    case 'T9'
        CT=CT_Spine.CT_T9;
    case 'T1'
        level_name_3char=filename(1:3);
        switch level_name_3char
            case 'T10'
                CT=CT_Spine.CT_T10;
            case 'T11'
                CT=CT_Spine.CT_T11;
            case 'T12'
```

```

        CT=CT_Spine.CT_T12;
    case 'T13'
        CT=CT_Spine.CT_T13;
    case 'T14'
        CT=CT_Spine.CT_T14;
    otherwise
        CT=CT_Spine.CT_T1;
    end
case 'L1'
    CT=CT_Spine.CT_L1;
case 'L2'
    CT=CT_Spine.CT_L2;
case 'L3'
    CT=CT_Spine.CT_L3;
case 'L4'
    CT=CT_Spine.CT_L4;
case 'L5'
    CT=CT_Spine.CT_L5;
end

tic
[CT2, US2, Rot_Center, Transform_B, QC] = B_Preregistration(CT, US_A, Center,
Y_Ang_Init);
elapsedTime(2)=toc

fprintf('\nPart C: ICP Registration\n');

tic
[CT2, US2, Transform_C, Min_Error, QC]=C_ICP_Registration(CT2, US2, QC);
elapsedTime(3)=toc

%% Output Registration Data
Name = strcat(filename(1:end-4), '-Reg');
Full_Name=strcat(pathname, Name, '.mat');
%save(Full_Name, 'CT2', 'US2'); Only for archival purposes

fprintf('\nICP RMSE: %f. \n', Min_Error);
fprintf('\nPart B Transform for Unity:\n')

Transform_B(:,1)=-Transform_B(:,1);
Transform_B(:,3)=-Transform_B(:,3);
Transform_B(3,:)=-Transform_B(3,:);

disp(Transform_B);

% Obtain the quaternion representation of the transformation matrix
[x, y, z, w] = Extraction(Transform_C);
y = -y;

fprintf('Part C Rotation Quaternion:\n')
fprintf('(X,Y,Z,W) = (%f, %f, %f, %f)\n', x, y, z, w);

fprintf('\nPart C Translation:\n')
Translation = Transform_C(4, 1:3)*0.2;
Translation(2) = -Translation(2);

```



```
fprintf('X,Y,Z) = (%f, %f, %f)\n', Translation(1), Translation(2), ...
    Translation(3));

Transform = zeros(5, 4);
Transform(1:3, 1:3) = Transform_B;
Transform(4, :) = [x y z w];
Transform(5, 1:3) = Translation;

Transform_Write_to_OBJ(Transform,filename(1:end-4));
elapsedTime(4)=toc

end
```

```

function [S]=Transform_Write_to_OBJ(Transform,filename)

%formatSpec='What %1.1f, %1.1f, %1.1f';
%A=fprintf(formatSpec,Transform(1,:))
file_level=filename(1:2);
file_id=filename(3:end);
if file_level(2)=='1'
    file_level=filename(1:3);
    file_id=filename(4:end);
end
file_id=filename(3:end);
S = ['usemtl clear', newline, S];
S = ['mtllib bone_clear.mtl', newline, S];
S = ['###Material Header', newline, S];

OBJName=strcat('..\5 Current Data\OBJ Files\',file_level, '.obj');
S = fileread(OBJName);

C_Trans=mat2str(Transform(5,1:3),4);
C_Trans=strcat('#',C_Trans);
S = [C_Trans, newline, S];

C_Rot=mat2str(Transform(4,:),4);
C_Rot=strcat('#',C_Rot);
S = [C_Rot, newline, S];

B_Trans=mat2str(Transform(3,1:3),4);
B_Trans=strcat('#',B_Trans);
S = [B_Trans, newline, S];

B_US_Rot=mat2str(Transform(2,1:3),4);
B_US_Rot=strcat('#',B_US_Rot);
S = [B_US_Rot, newline, S];

B_CT_Rot=mat2str(Transform(1,1:3),4);
B_CT_Rot=strcat('#',B_CT_Rot);
S = [B_CT_Rot, newline, S];

S = ['###Rotation Header', newline, S];

%FID='T5_New.obj';
FID = fopen(strcat('..\5 Current Data\',file_level,file_id, '.obj'), 'w');
if FID == -1, error('Cannot open file %s', OBJName); end
fwrite(FID, S, 'char');
fclose('all');

```

```

using Dummiesman;
using System.IO;
using UnityEngine;
using System.Collections;
using System.Collections.Generic;
using SimpleFileBrowser;

public class Vertebrae_Import : MonoBehaviour
{
    string objPath = string.Empty;
    string error = string.Empty;
    GameObject loadedObject;

    void Start()
    {
        // Set filters (optional)
        FileBrowser.SetFilters(true, new FileBrowser.Filter("OBJ Files",
".obj"), new FileBrowser.Filter("Text Files", ".txt", ".pdf"));
        FileBrowser.SetDefaultFilter(".obj");
        FileBrowser.SetExcludedExtensions(".lnk", ".tmp", ".zip", ".rar",
".exe");
        FileBrowser.AddQuickLink("Users", "C:\\Users", null);
        StartCoroutine(ShowLoadDialogCoroutine());
    }

    IEnumerator ShowLoadDialogCoroutine()
    {
        // Show a load file dialog and wait for a response from user
        // Load file/folder: file, Initial path: default (Documents), Title:
"Load File", submit button text: "Load"
        yield return FileBrowser.WaitForLoadDialog(false, @"C:\Users\Andrew
Chan\Documents\V1 3DUS NAVIGATION", "Load File", "Load");

        // and the path to the selected file (FileBrowser.Result) (null, if
FileBrowser.Success is false)
        Debug.Log(FileBrowser.Success + " " + FileBrowser.Result);
        string objPath = FileBrowser.Result;
        string mtlPath = @"C:\Users\Andrew Chan\Documents\V2 3DUS
NAVIGATION\5 Current Data\bone_clear.mtl";
        if (!File.Exists(objPath))
        {
            error = "File doesn't exist.";
        }
        else
        {
            if (loadedObject != null)
                Destroy(loadedObject);
            loadedObject = new OBJLoader().Load(objPath,mtlPath);
            error = string.Empty;
        }
    }
}

```

```

/*
 * Copyright (c) 2019 Dummiesman
 *
 * Permission is hereby granted, free of charge, to any person obtaining a
copy
 * of this software and associated documentation files (the "Software"), to
deal
 * in the Software without restriction, including without limitation the
rights
 * to use, copy, modify, merge, publish, distribute, sublicense, and/or sell
 * copies of the Software, and to permit persons to whom the Software is
 * furnished to do so, subject to the following conditions:
 *
 * The above copyright notice and this permission notice shall be included in
 * all copies or substantial portions of the Software.
*/

```

```

using System.Collections.Generic;
using System.IO;
using UnityEngine;
using System;
using Dummiesman;
#if UNITY_EDITOR
using UnityEditor;
#endif

namespace Dummiesman
{
    public enum SplitMode {
        None,
        Object,
        Material
    }

    public class OBJLoader
    {
        //options
        /// <summary>
        /// Determines how objects will be created
        /// </summary>
        public SplitMode SplitMode = SplitMode.Object;

        //global lists, accessed by objobjectbuilder
        internal float[] Rot_array_f = new float[16];
        internal List<Vector3> Vertices = new List<Vector3>();
        internal List<Vector3> Normals = new List<Vector3>();
        internal List<Vector2> UVs = new List<Vector2>();

        //materials, accessed by objobjectbuilder
        internal Dictionary<string, Material> Materials;

        //file info for files loaded from file path, used for GameObject
naming and MTL finding
        private FileInfo _objInfo;

#if UNITY_EDITOR
        [MenuItem("GameObject/Import From OBJ")]

```

```

        static void ObjLoadMenu()
        {
            string pth = EditorUtility.OpenFilePanel("Import OBJ", "",
"obj");
            if (!string.IsNullOrEmpty(pth))
            {
                System.Diagnostics.Stopwatch s = new
System.Diagnostics.Stopwatch();
                s.Start();

                var loader = new OBJLoader
                {
                    SplitMode = SplitMode.Object,
                };
                loader.Load(pth);

                Debug.Log($"OBJ import time: {s.ElapsedMilliseconds}ms");
                s.Stop();
            }
        }
    #endif

    /// <summary>
    /// Helper function to load mtlLib statements
    /// </summary>
    /// <param name="mtlLibPath"></param>
    private void LoadMaterialLibrary(string mtlLibPath)
    {
        if (_objInfo != null)
        {
            if (File.Exists(Path.Combine(_objInfo.Directory.FullName,
mtlLibPath)))
            {
                Materials = new
MTLLoader().Load(Path.Combine(_objInfo.Directory.FullName, mtlLibPath));
                return;
            }

            if (File.Exists(mtlLibPath))
            {
                Materials = new MTLLoader().Load(mtlLibPath);
                return;
            }
        }

        /// <summary>
        /// Load an OBJ file from a stream. No materials will be loaded, and
        will instead be supplemented by a blank white material.
        /// </summary>
        /// <param name="input">Input OBJ stream</param>
        /// <returns>Returns a GameObject represeting the OBJ file, with each
        imported object as a child.</returns>
        public GameObject Load(Stream input)
        {
            var reader = new StreamReader(input);

```

```

//var reader = new StringReader(inputReader.ReadToEnd());

Dictionary<string, OBJObjectBuilder> builderDict = new
Dictionary<string, OBJObjectBuilder>();
OBJObjectBuilder currentBuilder = null;
string currentMaterial = "default";

//lists for face data
//prevents excess GC
List<int> vertexIndices = new List<int>();
List<int> normalIndices = new List<int>();
List<int> uvIndices = new List<int>();

//helper func
Action<string> setCurrentObjectFunc = (string objectName) =>
{
    if (!builderDict.TryGetValue(objectName, out currentBuilder))
    {
        currentBuilder = new OBJObjectBuilder(objectName, this);
        builderDict[objectName] = currentBuilder;
    }
};

//create default object
setCurrentObjectFunc.Invoke("default");

string[] Rot_set_strings = new string[16];
string txt;
int counter = 0;
float angle;
Vector3 axis;

// Read each line from the file
while ((txt = reader.ReadLine()) != null) && (counter <= 5))
{
    txt = txt.Substring(2, txt.Length - 3);
    Debug.Log(txt);
    string[] set_strings = txt.Split(' ');

    switch (counter)
    {
        case 1:
            Rot_set_strings[0] = set_strings[0];
            Rot_set_strings[1] = set_strings[1];
            Rot_set_strings[2] = set_strings[2];
            break;
        case 2:
            Rot_set_strings[3] = set_strings[0];
            Rot_set_strings[4] = set_strings[1];
            Rot_set_strings[5] = set_strings[2];
            break;
        case 3:
            Rot_set_strings[6] = set_strings[0];
            Rot_set_strings[7] = set_strings[1];
            Rot_set_strings[8] = set_strings[2];
            break;
        case 4:

```

```

        Rot_set_strings[9] = set_strings[0];
        Rot_set_strings[10] = set_strings[1];
        Rot_set_strings[11] = set_strings[2];
        Rot_set_strings[12] = set_strings[3];
        break;
    case 5:
        Rot_set_strings[13] = set_strings[0];
        Rot_set_strings[14] = set_strings[1];
        Rot_set_strings[15] = set_strings[2];
        break;
    }
    counter = counter + 1;
}

for (int i = 0; i < 16; i++)
{
    Rot_array_f[i] = float.Parse(Rot_set_strings[i]);
}

//var buffer = new DoubleBuffer(reader, 256 * 1024);
var buffer = new CharWordReader(reader, 4 * 1024);

//do the reading
while (true)
{
    buffer.SkipWhitespaces();

    if (buffer.endReached == true) {
        break;
    }

    buffer.ReadUntilWhiteSpace();

    //comment or blank
    if (buffer.Is("#"))
    {
        buffer.SkipUntilNewLine();
        continue;
    }

    if (Materials == null && buffer.Is("mtllib")) {
        buffer.SkipWhitespaces();
        buffer.ReadUntilNewLine();
        string mtlLibPath = buffer.GetString();
        LoadMaterialLibrary(mtlLibPath);
        continue;
    }

    if (buffer.Is("v")) {
        Vertices.Add(buffer.ReadVector());
        continue;
    }

    //normal
    if (buffer.Is("vn")) {
        Normals.Add(buffer.ReadVector());
    }
}

```

```

        continue;
    }

    //uv
    if (buffer.Is("vt")) {
        UVs.Add(buffer.ReadVector());
        continue;
    }

    //new material
    if (buffer.Is("usemtl")) {
        buffer.SkipWhitespaces();
        buffer.ReadUntilNewLine();
        string materialName = buffer.GetString();
        currentMaterial = materialName;

        if (SplitMode == SplitMode.Material)
        {
            setCurrentObjectFunc.Invoke(materialName);
        }
        continue;
    }

    //new object
    if ((buffer.Is("o") || buffer.Is("g")) && SplitMode ==
SplitMode.Object) {
        buffer.ReadUntilNewLine();
        string objectName = buffer.GetString(1);
        setCurrentObjectFunc.Invoke(objectName);
        continue;
    }

    //face data (the fun part)
    if (buffer.Is("f"))
    {
        //loop through indices
        while (true)
        {
            bool newLinePassed;
            buffer.SkipWhitespaces(out newLinePassed);
            if (newLinePassed == true) {
                break;
            }

            int vertexIndex = int.MinValue;
            int normalIndex = int.MinValue;
            int uvIndex = int.MinValue;

            vertexIndex = buffer.ReadInt();
            if (buffer.currentChar == '/') {
                buffer.MoveNext();
                if (buffer.currentChar != '/') {
                    uvIndex = buffer.ReadInt();
                }
            }
            if (buffer.currentChar == '/') {
                buffer.MoveNext();
                normalIndex = buffer.ReadInt();
            }
        }
    }

```



```

        }
    }

    // "postprocess" indices
    if (vertexIndex > int.MinValue)
    {
        if (vertexIndex < 0)
            vertexIndex = Vertices.Count - vertexIndex;
        vertexIndex--;
    }
    if (normalIndex > int.MinValue)
    {
        if (normalIndex < 0)
            normalIndex = Normals.Count - normalIndex;
        normalIndex--;
    }
    if (uvIndex > int.MinValue)
    {
        if (uvIndex < 0)
            uvIndex = UVs.Count - uvIndex;
        uvIndex--;
    }

    // set array values
    vertexIndices.Add(vertexIndex);
    normalIndices.Add(normalIndex);
    uvIndices.Add(uvIndex);
}

// push to builder
currentBuilder.PushFace(currentMaterial, vertexIndices,
normalIndices, uvIndices);

// clear lists
vertexIndices.Clear();
normalIndices.Clear();
uvIndices.Clear();

continue;
}

buffer.SkipUntilNewLine();
}

// finally, put it all together
GameObject obj = new GameObject(_objInfo != null ?
Path.GetFileNameWithoutExtension(_objInfo.Name) : "WavefrontObject");

obj.transform.localScale = new Vector3(-1f, 1f, 1f);

obj.transform.Rotate(Rot_array_f[0], Rot_array_f[1],
Rot_array_f[2], Space.World);
obj.transform.Rotate(Rot_array_f[3], Rot_array_f[4],
Rot_array_f[5], Space.World);
obj.transform.Translate(Rot_array_f[6], Rot_array_f[7],
Rot_array_f[8], Space.World);
// Quaternion Rot_Fin = new Quaternion();

```

```

        //Rot_Fin.Set(Rot_array_f[9], Rot_array_f[10], Rot_array_f[11],
Rot_array_f[12]);
        //Quaternion Rot_Fin = Quaternion.Euler(Rot_array_f[9],
Rot_array_f[10], Rot_array_f[11]);
        Quaternion Rot_Fin = new Quaternion(Rot_array_f[9],
Rot_array_f[10], Rot_array_f[11], Rot_array_f[12]);
        Rot_Fin.ToAngleAxis(out angle, out axis);
        obj.transform.RotateAround(Vector3.zero, axis, angle);
        //obj.transform.Translate(Rot_array_f[12], Rot_array_f[13],
Rot_array_f[14], Space.World);
        obj.transform.Translate(Rot_array_f[13], Rot_array_f[14],
Rot_array_f[15], Space.World);

        foreach (var builder in builderDict)
        {
            //empty object
            if (builder.Value.PushedFaceCount == 0)
                continue;

            var builtObj = builder.Value.Build();
            builtObj.transform.SetParent(obj.transform, false);
        }

        return obj;
    }

    /// <summary>
    /// Load an OBJ and MTL file from a stream.
    /// </summary>
    /// <param name="input">Input OBJ stream</param>
    /// /// <param name="mtlInput">Input MTL stream</param>
    /// <returns>Returns a GameObject represeting the OBJ file, with each
imported object as a child.</returns>
    public GameObject Load(Stream input, Stream mtlInput)
    {
        var mtlLoader = new MTLLoader();
        Materials = mtlLoader.Load(mtlInput);

        return Load(input);
    }

    /// <summary>
    /// Load an OBJ and MTL file from a file path.
    /// </summary>
    /// <param name="path">Input OBJ path</param>
    /// /// <param name="mtlPath">Input MTL path</param>
    /// <returns>Returns a GameObject represeting the OBJ file, with each
imported object as a child.</returns>
    public GameObject Load(string path, string mtlPath)
    {
        Debug.Log("what's not again going on");
        _objInfo = new FileInfo(path);
        if (!string.IsNullOrEmpty(mtlPath) && File.Exists(mtlPath))
        {
            var mtlLoader = new MTLLoader();
            Materials = mtlLoader.Load(mtlPath);
        }
    }

```

```

        using (var fs = new FileStream(path, FileMode.Open))
        {
            return Load(fs);
        }
    }
    else
    {
        using (var fs = new FileStream(path, FileMode.Open))
        {
            return Load(fs);
        }
    }
}

/// <summary>
/// Load an OBJ file from a file path. This function will also
attempt to load the MTL defined in the OBJ file.
/// </summary>
/// <param name="path">Input OBJ path</param>
/// <returns>Returns a GameObject representing the OBJ file, with each
imported object as a child.</returns>
public GameObject Load(string path)
{
    return Load(path, null);
}
}
}

```